JOURNAL OF APPLIED PHYSICS

Vol. 31, No. 2 February, 1960

Thermally Etched Copper Crystal. See Page 225.

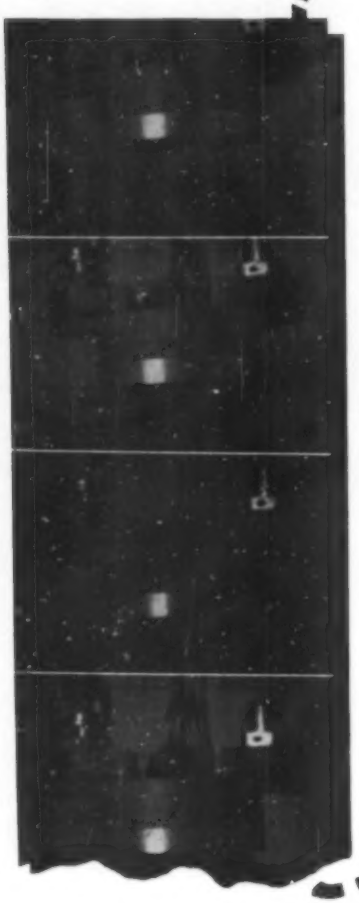

WHAT IS IT YOU NEED TO KNOW...

about the four winds?

Meteorology is one of the strong points in the activity of the Research & Development Division. The special instrument shown above was created by this group to meet vertical-gustiness-measurement needs of Dugway Proving Ground of the U. S. Army Chemical Corps. Now in continuous service, this first-of-its-kind instrument was produced, from concept to finished hardware, in a neat though admittedly hectic ninety days.

about energy and motion?

One of our product divisions packages up explosive energy into ingenious devices which turn, twist, chop, push, or pull things aboard missiles in flight. So naturally, the R&D people get involved in similar projects. Above is a series of Dynafax pictures of an explosive-actuated electrical disconnect in operation. This is known as playing both ends against the middle, since the facilities and knowledge of our own photo-instrumentation product department are brought into the situation as well.

Availability of such facilities as a Model 189 Framing Camera and related items has recently led R&D scientists into an investigation of electrets. This is one, at right. A charged plastic plate, 4 by 4 in., is punctured at the bottom center and the charge forms the pathway shown. One of the more interesting points is that it all happens in something less than 0.58 microseconds.

about your career?

Openings exist in the Beckman & Whitley R&D Division staff. If your background falls into any of these areas, we invite your inquiry. Besides great technical interest, there are such inducements as climate and general living conditions to consider. Contact Tom Holland, director.

These are just a few of the things going on in the Beckman & Whitley Research & Development Division. The combination of backgrounds, talents, and technical facilities is available to government and industry for the solution of the unusual range of problems which lie in these general areas. For specific details, contact Tom Holland, director.

Beckman & Whitley

SAN CARLOS 8 • CALIFORNIA • U.S.A.

JOURNAL OF APPLIED PHYSICS

Vol. 31, No. 2 FEBRUARY, 1960

In This Issue

Development of Facets, Spirals, and Etch Pits on Copper Crystals by Heating to High Temperatures in High Vacua . . . . . F. W. Young, Jr., and A. T. Gwathmey 225

Factors Affecting the Ductility and Strength of NaCl Single Crystals Tested in Flexure . C. A. Stearns, A. E. Pack, and R. A. Lad 231

Torsion Induced Recrystallization of Molybdenum and Tungsten Filaments . . . . . F. E. Gifford and E. A. Coomes 235

Determination of Magnetization Distribution in Thin Films Using Electron Microscopy . Harrison W. Fuller and Murray E. Hale 238

Effect of Electron Irradiation and Subsequent Thermal Treatment on Young's Modulus of Copper . A. Sosin and L. L. Bienvenue 249

Effect of Specimen Delocalization in Electron Diffraction Studies of Gas Molecules . . . . . L. S. Bartell 252

Experimental Investigation of a High-Energy Density, High-Pressure Arc Plasma . . . . . Edward A. Martin 255

Diffusion Coefficients, Solubilities, and Permeabilities for He, Ne, H_2, and N_2 in Vycor Glass . . C. C. Leiby, Jr., and C. L. Chen 268

Submillimeter Wave Maser . . . . . Saul M. Bergmann 275

Propagation of Large Amplitude Waves in Annealed Aluminum . . . . . James F. Bell 277

Growth, Structure, and Properties of Graphite Whiskers . . . . . Roger Bacon 283

Ion Drift in an *n-p* Junction . . . . . E. M. Pell 291

Diffusion of Boron into Silicon . . . . . A. D. Kurtz and R. Yee 303

Rolling Friction of Polymeric Materials. I. Elastomers . . . . . Donald G. Flom 306

Photoelectronic Analysis of High Resistivity Crystals: (a) GaAs, (b) Sb_2S_3 . . . . . Richard H. Bube 315

Thermal Initiation of Explosives . . . . . John Zinn and Charles L. Mader 323

Single Crystal Tungstates for Resonance and Emission Studies . . . . . L. G. Van Uitert and R. R. Soden 328

Effect of the Polarity of the III–V Intermetallic Compounds on Etching . . . . . J. W. Faust, Jr., and A. Sagar 331

Effect of Oxide Layers on the Diffusion of Phosphorus into Silicon . . . . . R. B. Allen, H. Bernstein, and A. D. Kurtz 334

Theory of Fast-Wave Parametric Amplification . . . . . Curtis C. Johnson 338

Observations on MnBi Films during Heat Treatment . . . . . Ludwig Mayer 346

Detailed Study of Switching Current in Barium Titanate . . . . . M. E. Drougard 352

Decay of Wax Electrets . . . . . M. M. Perlman 356

Theory of Non-Newtonian Flow. III. A Method for Analyzing Non-Newtonian Flow Curves . . . . . Wan Kyue Kim, Nishio Hirai, Taikyue Ree, and Henry Eyring 358

Mobility of Edge Dislocations in Silicon-Iron Crystals . . . . . Dale F. Stein and J. R. Low, Jr. 362

Single-Velocity Equivalents for Multivelocity Electron Streams . . . . . Glenn A. Gray 370

On the Concept of Fictitious Surface Charges of an Electron Beam . . . . . E. L. Chu 381

Method for the Detection of Flaws in Yttrium Iron Garnet Crystals . . . . . E. Buehler and M. Tanenbaum 388

Thermal Attenuation of Nonlinear Stress Waves . . . . . Sven Treitel 391

Operating Characteristics of a Molecular-Beam Maser . . . . . H. G. Venkates and M. W. P. Strandberg 396

Ion Energies in a Cold Cathode Discharge in a Magnetic Field . . . . . John Backus and Norman E. Huston 400

Structure in Vitreous Silicate Fibers as Shown by Small-Angle Scattering of X-Rays . . . . . W. O. Statton and L. C. Hoffman 404

Precision Lattice Parameter Measurements of Cold-Worked Metals . . . . . Robert Asimow 410

Microwave Study of Afterglow Discharge in Water Vapor . . . . . Susumu Takeda and Arwin A. Dougal 412

Absorption and Reflection Spectrum of a Plasma . . . . . W. D. Hershberger 417

Monoenergetic Neutron Irradiation of Germanium . . . . . O. L. Curtis, Jr., and J. W. Cleland 423

Microwave Determination of Plasma Density Profiles . . . . . Charles B. Wharton and Donald M. Slager 428

Letters to the Editor:

Improvement of Semiconductor Surfaces by Low Melting Glasses, Possibly Functioning as Ion Getters . . . . . S. S. Flaschen, A. David Pearson, and I. L. Kalnins 431

High-Power Effects in Ferrimagnetic Resonance . . . . . P. E. Seiden and H. J. Shaw 432

Flow of Magnesium Oxide Single Crystals . . . . . D. S. Thompson and J. P. Roberts 433

Thermal Stress Analysis and Grueneisen's Relation . . . . . A. M. Freudenthal 434

Elastic Moduli of Face-Centered Cubic Cobalt . . . . . R. Dean Dragsdorf 434

Effect of Gas Pressure and Cone Angle on the Velocities of Electrically Excited Shock Waves . . . Philip J. Hart 436

Observation of Néel Walls in Thin Films . . . . . Harvey Rubinstein, Harrison W. Fuller, and Murray E. Hale 437

Three-Dimensional Wedge Impact on a Compressible Fluid . . . . . S. F. Borg 438

On the Reflection of Electromagnetic Waves from a Medium Excited by Acoustic Waves . . . . . Hans J. Schmitt and Dipak L. Sengupta 439

Bulk Densities of Separated Copper Isotopes . . . . . D. D. Snyder 440

Reciprocity Law Failure in ZnO and Se . . . . . Joze Kostelec 441

"Spontaneous Magnetic Anisotropy" in Polycrystalline Thin Films . . . . . W. Andrä, Z. Málek, W. Schüppel, and O. Stemme 442

Pulsed Field Millimeter Wave Maser . . . . . L. R. Momo, R. A. Myers, and S. Foner 443

Noise Temperature Measurement on a Traveling-Wave Maser Preamplifier . R. W. DeGrasse and H. E. D. Scovil 443

Penetration Depth Investigation of Gas Cleanup with Radioactive Tracers . C. Y. Bartholomew and A. R. LaPadula 445

Erratum: Diffraction by a Slit . . . . . Robert Plonsey and Hwei-Piao Hsu 445

Books Reviewed 445

Index to Advertisers xxxiv

JOURNAL OF APPLIED PHYSICS

A journal of general physics and its applications to other sciences and to industry

Published by the

American Institute of Physics

GOVERNING BOARD

Ralph A. Sawyer, *Chairman*

Walter S. Baird
J. G. Baker
Jesse W. Beams
R. H. Bolt
Harvey Brooks
J. W. Buchta
J. H. Dillon
Vernet E. Eaton
Herbert A. Erf
S. A. Goudsmit
W. W. Havens, Jr.
Winston E. Kock
R. Bruce Lindsay
Walter C. Michels
C. J. Overbeck
G. E. Pake
Joseph B. Platt
John Strong
George E. Uhlenbeck
V. F. Weisskopf

ADMINISTRATION

Elmer Hutchisson
Director

Henry A. Barton
Associate Director

Wallace Waterfall
Secretary and Treasurer

Ruth F. Bryans
Publication Manager

W. C. Kelly
Director of Education Projects

Eugene H. Kone
Director of Public Relations

Alice Mastropietro
Circulation Manager

Kathryn Setze
Assistant Treasurer

Edward Tober
Manager, Production and Distribution

Theodore Vorburger
Advertising Manager

Emily Wolf
Office Manager

Editor

James A. Krumhansl

Editorial Board

J. H. Crawford
Arthur Kantrowitz
A. F. Kip
J. E. Goldman
J. L. Tuck
C. A. Wert
Herman A. Haus
C. Lester Hogan
R. S. Rivlin

THE JOURNAL OF APPLIED PHYSICS is devoted to general physics and its applications to other sciences, to engineering, and to industry. Previous to 1937, this journal was called PHYSICS.

The JOURNAL OF APPLIED PHYSICS welcomes articles of two distinct kinds: (1) Descriptions of new results in experimental or theoretical physics which are of general interest to physicists. The author should explain his contribution in such a way that a physicist or engineer in another field of specialization can appreciate its objectives and essential features. (2) Critical reviews of particular areas of physics or surveys of extensive investigations at a single laboratory. Authors contemplating writing such should correspond with the Editor before they begin writing.

The JOURNAL OF APPLIED PHYSICS welcomes letters to the editor which describe in a few words the content of laboratory reports and theses and which tell readers how they may obtain copies of such reports.

Manuscripts should be submitted to the Editor, James A. Krumhansl, Rockefeller Hall, Cornell University, Ithaca, New York. Authors should read the "Information for Contributors," facing page 1 of the January issue, before writing articles or letters. The *Style Manual* of the American Institute of Physics is also helpful to writers preparing manuscripts for journals published by the American Institute of Physics. It can be obtained for $1.00 from the American Institute of Physics, 335 East 45 Street, New York 17, New York.

Corrected proofs and all correspondence concerning papers in the process of publication should be addressed to the Publication Manager, American Institute of Physics, 335 East 45 Street, New York 17, New York.

Subscriptions, renewals, and orders for back numbers should be addressed to the American Institute of Physics, 335 East 45 Street, New York 17, New York.

Subscription Price	U.S. and Canada	Elsewhere
To members of member organizations of the American Institute of Physics and Affiliated Societies ..	$12.00	$13.00
To all others	14.00	16.00

Back Number Prices

Yearly back number rate when complete year is available: $17.00.
Single copies: $1.75 each (exception: March, 1958—$3.00 each).

Changes of address should be sent to the American Institute of Physics.

Advertising rates supplied on request. Orders, advertising copy, and cuts should be sent to the American Institute of Physics.

Second-class postage paid at Lancaster, Pa.

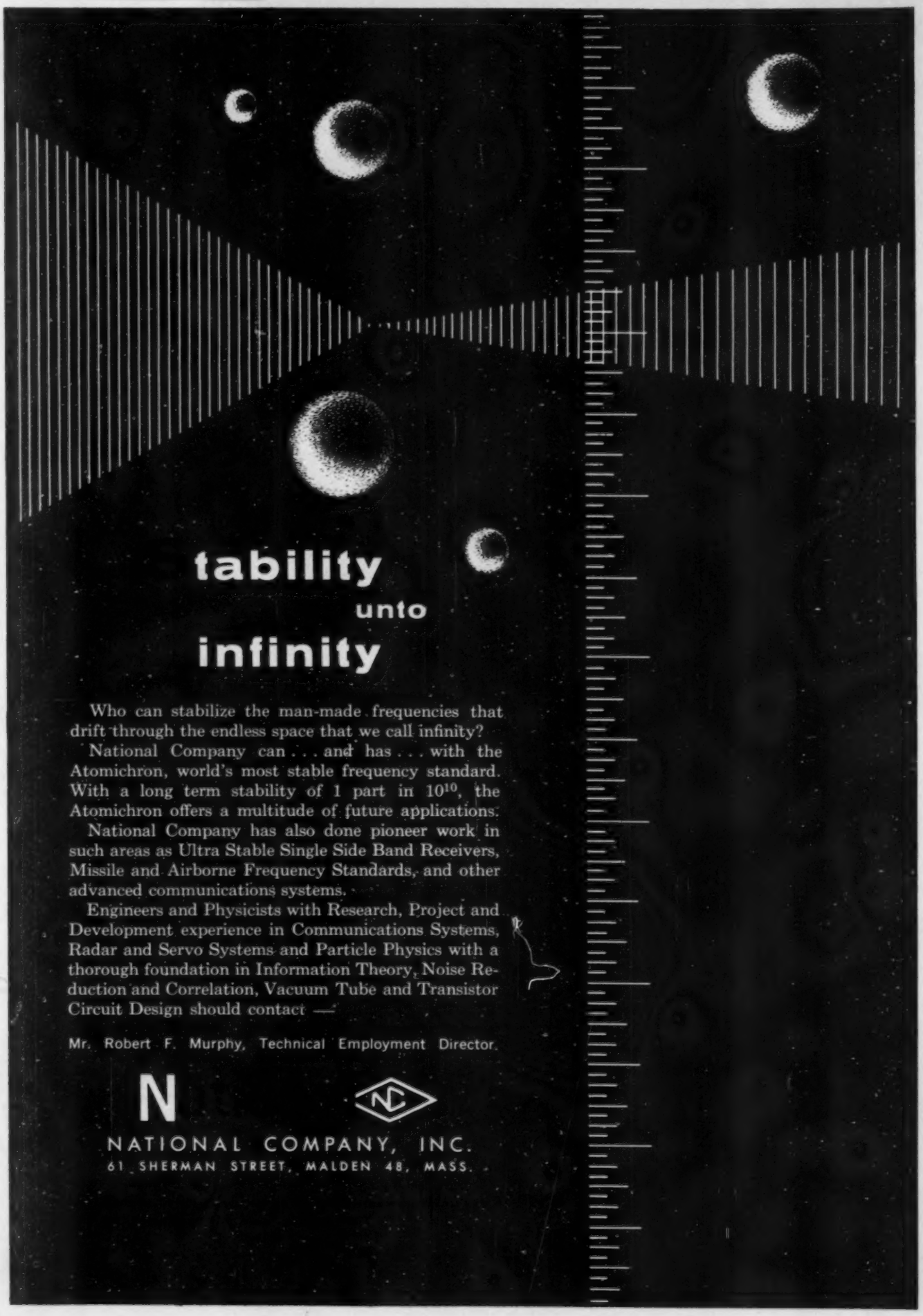

tability unto infinity

Who can stabilize the man-made frequencies that drift through the endless space that we call infinity?

National Company can . . . and has . . . with the Atomichron, world's most stable frequency standard. With a long term stability of 1 part in 10^{10}, the Atomichron offers a multitude of future applications.

National Company has also done pioneer work in such areas as Ultra Stable Single Side Band Receivers, Missile and Airborne Frequency Standards, and other advanced communications systems.

Engineers and Physicists with Research, Project and Development experience in Communications Systems, Radar and Servo Systems and Particle Physics with a thorough foundation in Information Theory, Noise Reduction and Correlation, Vacuum Tube and Transistor Circuit Design should contact —

Mr. Robert F. Murphy, Technical Employment Director.

N

NATIONAL COMPANY, INC.

61 SHERMAN STREET, MALDEN 48, MASS.

We promise that you will hear from us within one week!

important openings for senior E.E.'s and Physicists
to assume responsibility for development of

new infrared search systems

Progress of the Hughes Infrared and Guidance Department reflects Hughes overall growth. In the past ten years, employment has risen from under 2,000 to over 34,000 in the several semi-autonomous divisions of Systems Development, Research, Commercial Products, Ground Systems, Communications and Manufacturing. The infrared activity includes these typical projects:

These activities have created a number of new openings for graduate engineers and physicists with analytical and inventive abilities.
You are invited to investigate these openings if you have several years of applicable experience in infrared optics or electronics, and can assume responsibility for systems analysis and preliminary design.
The importance of infrared development at Hughes is shown in substantial development contracts and in the fact that Hughes is investing its own funds in further exploration.

1. **Air-To-Air Missiles**
2. **AICBM**
3. **Air-To-Air Detection Search Sets**
4. **Satellite Detection & Identification**
5. **Infrared Range Measurement**
6. **Detection Cryogenics**
7. **Detector Application Physics**
8. **Optical Systems Design**

We invite your earliest inquiry.
Wire collect, or airmail resume directly to:

Mr. William Craven, *Manager, Infrared*
Hughes Systems Development Laboratories
Culver City, California

HUGHES

© 1959 HUGHES AIRCRAFT COMPANY

Write for reprints of these important technical papers, written by Hughes staff members...
Infrared Search-Systems Range Performance: R. H. Genoud /Missiles Seekers and Homers: W. A. Craven, et al.
Servomechanisms Design Considerations for Infrared Tracking Systems: J. E. Jacobs /Simulation of Infrared Systems: H. P. Meissinger

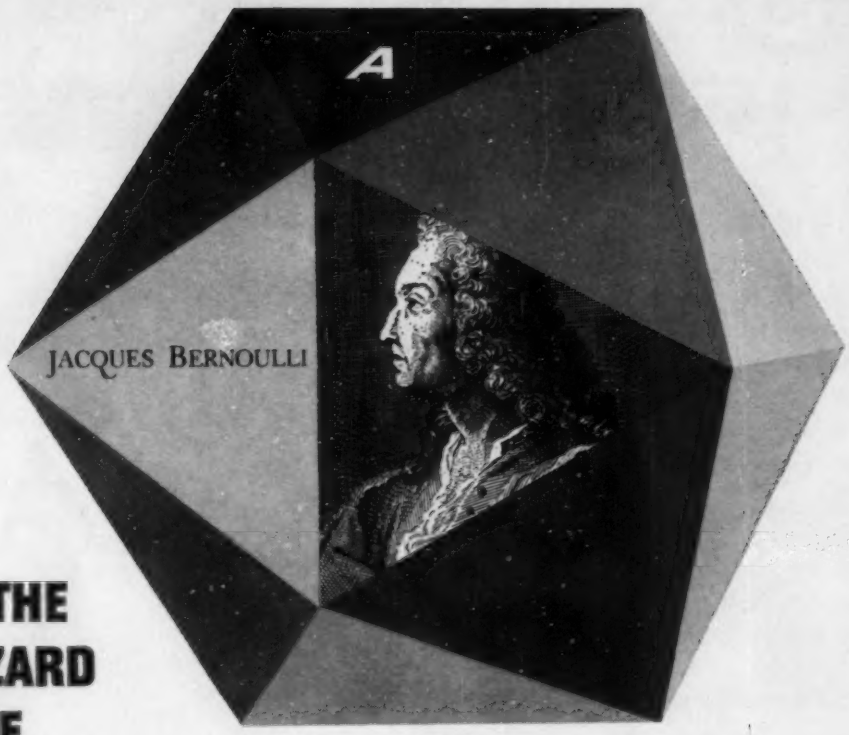

THE WIZARD OF ODDS

He solved a telephone traffic problem two centuries ago

Jacques Bernoulli, the great Swiss mathematician, pondered a question early in the 18th century. Can you mathematically predict what will happen when events of chance take place, as in throwing dice?

His answer was the classical Bernoulli binomial distribution—a basic formula in the mathematics of probability (published in 1713). The laws of probability say, for instance, that if you roll 150 icosahedrons (the 20-faced solid shown above), 15 or more of them will come to rest with side "A" on top only about once in a hundred times.

Identical laws of probability govern the calls coming into your local Bell Telephone exchange. Suppose you are one of a group of 150 telephone subscribers, each of whom makes a three-minute call during the busiest hour of the day. Since three minutes is one-twentieth of an hour, the probability that you or any other subscriber will be busy is 1 in 20, the same as the probability that side "A" of an icosahedron will be on top. The odds against 15 or more of you talking at once are again about 100 to 1. Thus it would be extravagant for the Bell System to supply your group with 150 trunk circuits when 15 are sufficient for good service.

Telephone engineers discovered at the turn of the century that telephone users obey Bernoulli's formula. At Bell Telephone Laboratories, mathematicians have developed the mathematics of probability into a tool of great economic value. All over the Bell System, the mathematical approach helps provide the finest telephone service using the least possible equipment. The achievements of these mathematicians again illustrate how Bell Labs works to improve your telephone service.

BELL TELEPHONE LABORATORIES

World center of communications research and development

TRANSISTOR MEN

Your future advancement lies in Delco Radio's Semiconductor Program in the fields of germanium and silicon transistors, silicon rectifiers, and solar cells.

In expanding its semiconductor line, Delco Radio offers unusual opportunities in research engineering and production. We are vitally interested in hiring men with experience in the following areas:

- **SEMICONDUCTOR DEVICE DEVELOPMENT**

  We need men with experience in the techniques of semiconductor device development including alloying and diffusion.

  We need a man with experience in the chemistry of semiconductor devices.

  We need a man with experience in semiconductor materials to lead a program on metallurgical research of new semiconductor materials.

  We need a man with experience in semiconductor device encapsulation.

- **PROCESS ENGINEERING**

  We need several men for production set-up and trouble shooting.

- **EQUIPMENT DEVELOPMENT**

  We need men to develop automatic and semi-automatic fabrication equipment.

PROGRESS=OPPORTUNITIES

Delco Radio has long been the World Leader in the production of auto radios and is becoming a leader in the semiconductor field. The semiconductor applications which we see are staggering. We're anxious to get more experienced personnel, and responsible positions are open to those who qualify.

GM
DELCO RADIO

If you're interested in becoming a member of our GM team, send your resume today to the attention of Mr. Carl Longshore, Supervisor Salaried Employment.

DELCO RADIO DIVISION OF GENERAL MOTORS
KOKOMO, INDIANA

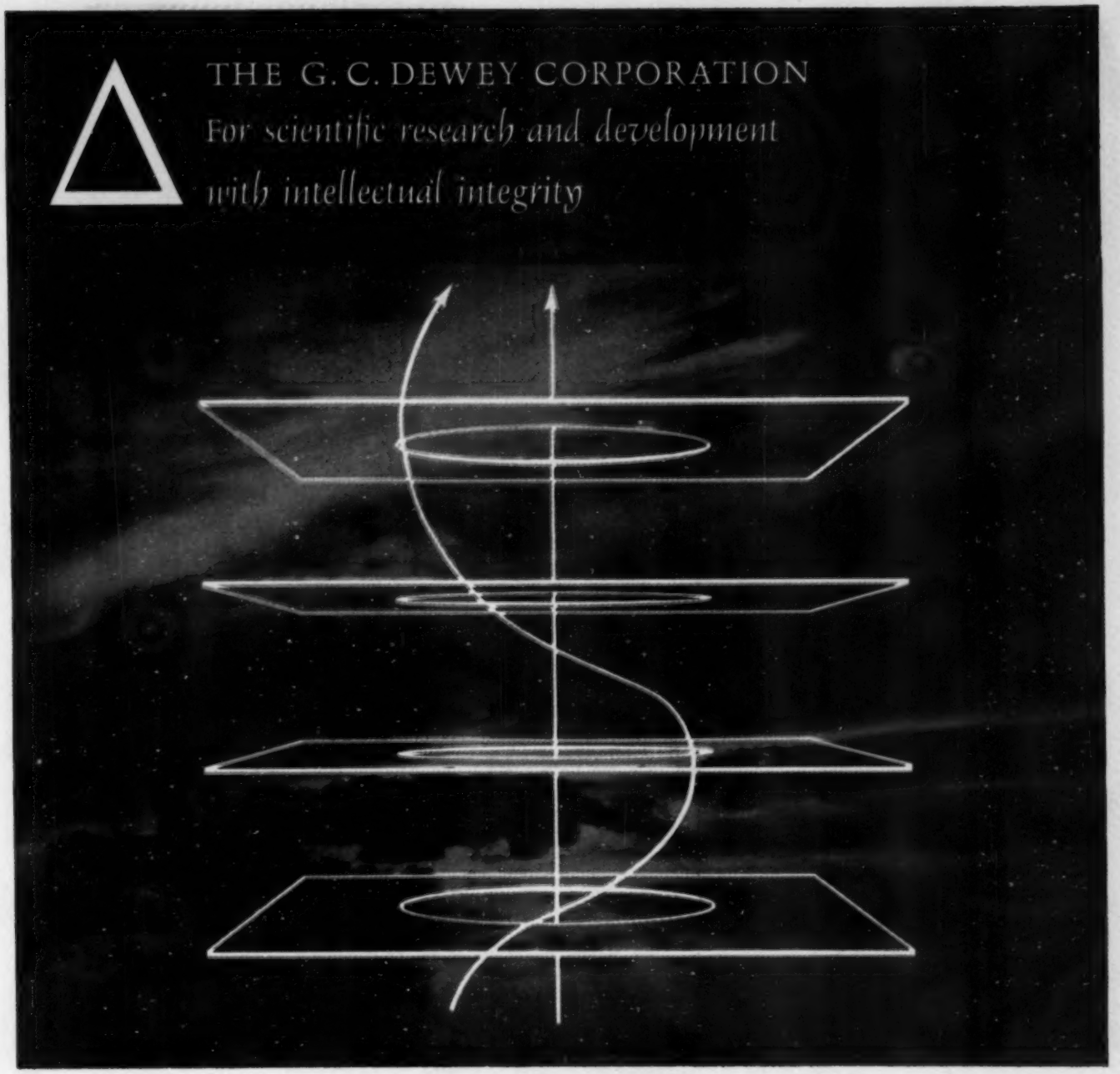

SCIENTIFICALLY ORIENTED to achieve significant results for government and civilian agencies–in the broad areas of defense physics...weapons system concepts and evaluation...electronic technology–this organization applies creative scientific thinking...to advanced problems of nuclear and plasma physics...to unique computer programming techniques...to original electronic design criteria...to systems analyses that meet measure of effectiveness standards.

THE G. C. DEWEY CORPORATION, 202 East 44th Street, N. Y. C. 17

Physicists, mathematicians and engineers with advanced degrees, write for information on professional career opportunities.

ENGINEERS • SCIENTISTS

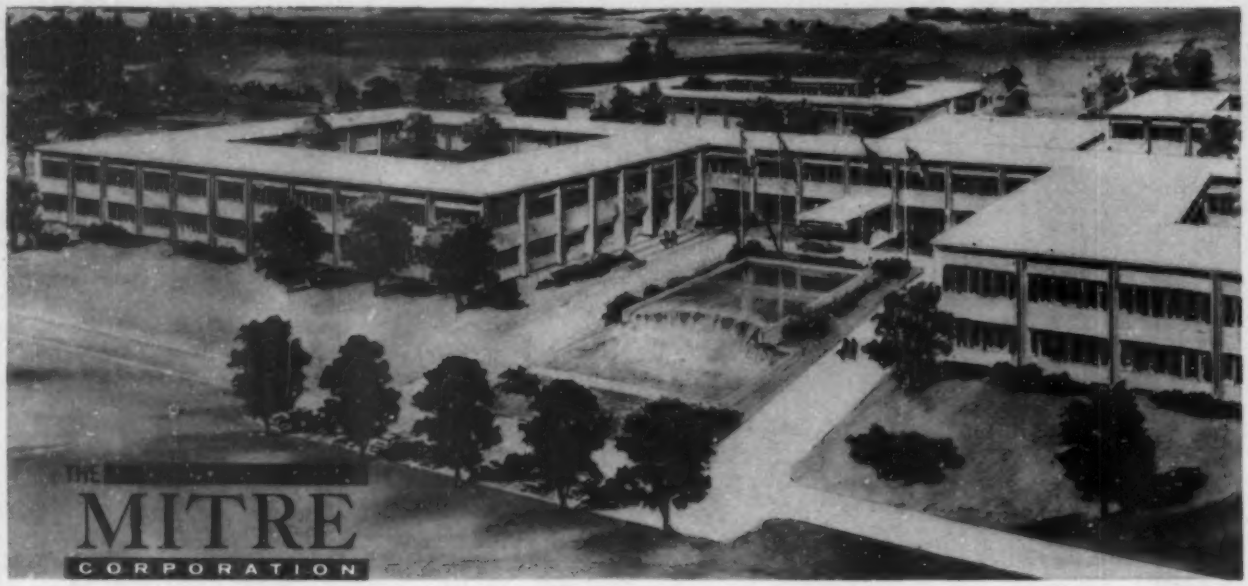

Announces

NEW HEADQUARTERS UNDER CONSTRUCTION IN SUBURBAN BOSTON

MITRE'S new headquarters will serve a Technical Staff that has established, and is daily adding to, its reputation in large-scale systems design and development. Located in Bedford, Massachusetts it affords engineers and scientists an opportunity to pursue long-term, challenging work programs with an expanding organization in an environment of professional and cultural excitement.

If you possess a baccalaureate or advanced degree in engineering, mathematics or the physical sciences, you are invited to inquire about career opportunities in these areas:

- **SYSTEM DESIGN**
- **COMPONENT DEVELOPMENT**
- **RADAR SYSTEMS**
- **OPERATIONS ANALYSIS**
- **WEAPONS SYSTEM INTEGRATION**
- **COMMUNICATION SYSTEMS**
- **ELECTRONIC WARFARE**
- **INTEGRATED SYSTEM EVALUATION**
- **COMPUTER PROGRAMMING**
- **PROGRAM LOGISTICS**

To arrange an immediate confidential interview, direct your inquiries to:
Dana N. Burdette, Personnel Director, Dept. 1-MD

THE MITRE CORPORATION

244 Wood Street – Lexington 73, Massachusetts

KEITHLEY MODEL 150 MICRO VOLT-AMMETER

MEASURES DOWN TO 0.03 μv AND 2 x 10⁻¹² AMPERE

The Keithley 150 sets new standards in sensitivity, stability and noise figure for dc microvoltmeters. It also serves as an amplifier, null detector, micro-microammeter, and (with an external voltage supply) meg-megohmmeter. Functions and measurement spans include:

DC Voltmeter, 1 microvolt to 1 volt full scale
Ammeter, 10^{-10} to 10^{-3} ampere full scale
DC Amplifier, gains of 10 to 10,000,000
Null Detector, with 0.5 to 2 second period.

OTHER FEATURES of the 150 include zero suppression of up to 100 times full scale; optional floating or grounded input; high input resistance; zero stability as a voltmeter within ±0.1 microvolt per day, and within $\pm 2 \times 10^{-11}$ ampere per day as an ammeter; short term noise within 0.03 microvolt peak to peak (0.006 microvolt RMS). The 150 is rugged, relatively insensitive to vibration, 60-cycle fields, or thermal EMF's. It is available in either rack or cabinet packaging.

USES of the 150 encompass nearly every branch of research and engineering. Examples include measuring the outputs from strain gages, thermopiles, thermocouples, bolometers, phototubes, ionization chambers, scintillation counters, and barrier layer cells. Other applications are found in cell studies, electrochemical potentials, corrosion work, molecular-weight analysis, Hall effect studies.

DETAILED DATA about the 150 Micro Voltammeter are now available in Keithley Engineering Notes, Vol. 7 No 1. A request will bring your copy promptly.

BRIEF SPECIFICATIONS

dc voltage: 13 ranges in 1X and 3X steps from ±1 microvolt to ±1 volt full scale.

current: 17 ranges in 1X and 3X steps from $\pm 10^{-10}$ to $\pm 10^{-3}$ ampere full scale.

zero stability: within 0.1 microvolt per day, or 2×10^{-11} ampere per day.

noise: less than 0.006 microvolt RMS as a voltmeter; less than 2×10^{-12} ampere as an ammeter.

accuracy: voltage, ±2% of full scale on all ranges; current, ±3% on all ranges.

zero suppression: up to 100 times full scale.

response speed: 0.5 to 2 seconds.

gain: 10,000,000 maximum.

output: ±10 v and 5 ma for full scale deflections

price: $675.00

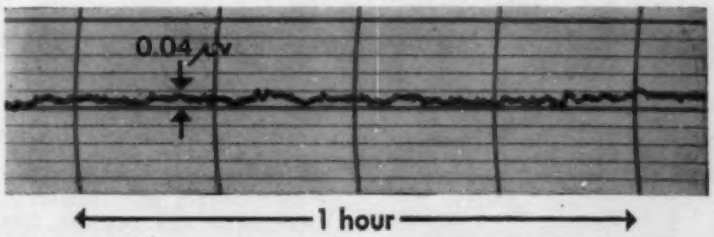

Long-term drift of the Model 150 is shown in the above recording. A 1000-ohm resistance was connected across the input. Note the very low peak to peak noise, even at this slow paper speed.

KEITHLEY INSTRUMENTS, INC.
12415 EUCLID AVENUE CLEVELAND 6, OHIO

PHYSICISTS

Opportunities in advanced reactor development at The Knolls Atomic Power Laboratory. The new groups being formed around key members of KAPL's professional staff afford physicists who join us now, unusual opportunities to work in close liaison with acknowledged leaders in reactor technology. Experimental facilities for nuclear investigations at KAPL rank with the finest in the nation and include seven reactor critical assemblies, one of which permits study of core configurations at power reactor temperatures and pressures. You are invited to inquire about the following openings: **Experimental Physicists** to plan, conduct and interpret results of reactor physics experiments. Develop new critical experiments, techniques and analytical methods of solving experimental reactor physics problems. Assist in the formulation and direction of critical experimentation. Should have MS or PhD in Physics. **Analytical Physicists** to interpret physics data and its application to design. Develop theory, analyze phenomena and predict nuclear performance and characteristics of reactors. Should have MS or PhD in Nuclear Engineering or Physics. **Nuclear Analysts** to evaluate reactor nuclear designs, using analytical and machine computational techniques. Predict nuclear performance of reactors. Develop and improve analytical techniques for the solution of nuclear design problems. Qualifications should include MS in Engineering or Physics with experience in nuclear analysis of reactors. **Also Openings in these areas:** Advanced Mathematics / Computer Programming / Controls Development / Coolant Chemistry & Engineering / Electrical Design / Facilities & Construction / Shielding Design / Heat Transfer, Fluid Flow / Instrumentation Development / Mass Spectrometry / Materials Application / Mechanical Design / Physical Metallurgy / Powerplant Equipment / Pressure vessel Design / Radiochemistry / Radiological Engineering / Reactor Plant Operation / Solid State Physics / Stress Analysis / Systems Analysis / Welding & Fabrication / X-Ray Diffraction.

ADVANCED DEGREE PROGRAM KAPL is now considering recent graduates in ME, Met, Met E, ChE, Physics, EE, Nuclear and Marine E for its advanced degree program in nuclear engineering in conjunction with Rensselaer Polytechnic Institute. Applicants should have strong interest in nuclear field and must have graduated in upper 10% of their class. Selection of candidates will be completed by April 1; classes begin September, 1960. Write for further details.

Please forward your resume in confidence, including salary requirement, to Mr. A. J. Scipione, Dept. 37-MB. U.S. Citizenship Required

Knolls Atomic Power Laboratory

OPERATED FOR A.E.C. BY

GENERAL ELECTRIC

SCHENECTADY, N.Y.

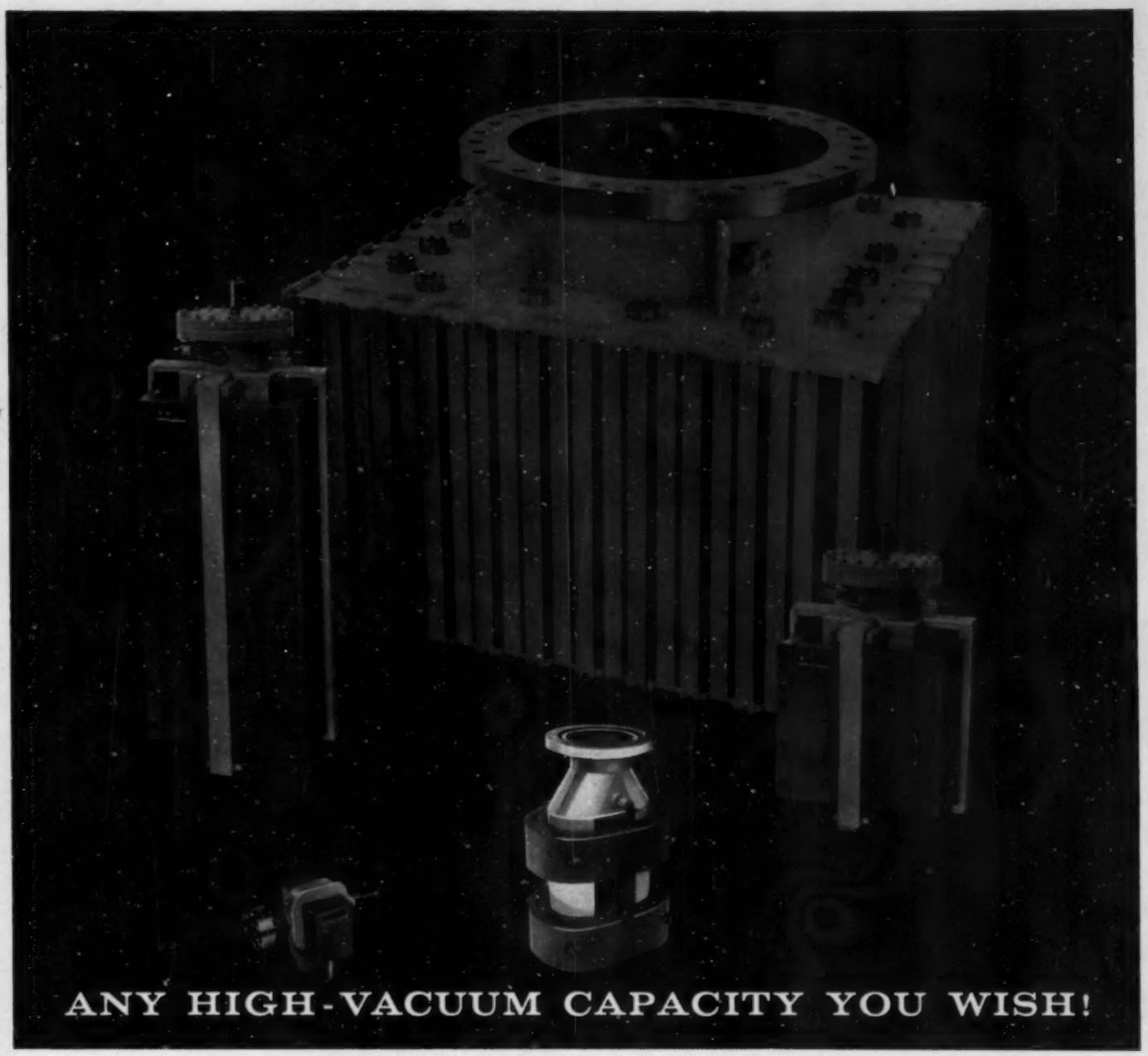

ANY HIGH-VACUUM CAPACITY YOU WISH!

The 40 liter/second Vaclon® High Vacuum Pump, emphasized above, is just one of a great variety of Varian Vaclon Pump sizes available from stock. These include ½, 1, 5, 40, 100, 140, 280, 1000, 3000, 5000 and 10,000 liter/second capacities. Other sizes available on custom order.

All these pumps give extremely clean vacuums to below 10^{-10} mm Hg, have no moving parts or fluids, and operate without attention or service.

The Vaclon High Vacuum Pump is a fully electronic device and is a Varian "First." Unique both in principle and advantages, it has been accepted as an efficient, reliable laboratory and production tool throughout the world.

A comprehensive brochure and technical data sheets are available by writing Vacuum Products Division.

COMPLETE VARIAN VACION HIGH-VACUUM SYSTEM

VARIAN associates

PALO ALTO 36, CALIFORNIA

Representatives throughout the world

KLYSTRONS, WAVE TUBES, GAS SWITCHING TUBES, MAGNETRONS, HIGH VACUUM EQUIPMENT, LINEAR ACCELERATORS, MICROWAVE SYSTEM COMPONENTS, NMR & EPR SPECTROMETERS, MAGNETS, MAGNETOMETERS, STALOS, POWER AMPLIFIERS, GRAPHIC RECORDERS, RESEARCH AND DEVELOPMENT SERVICES

Lockheed Missiles and Space Division Offers

PHYSICISTS

Unusual Opportunities in Research and Development

Important career positions are available at Lockheed Missiles and Space Division at its new facilities on the beautiful San Francisco Peninsula — one of the choicest living areas in the nation. Headquarters for the Division are at Sunnyvale, California, with Research and Development facilities located in the Stanford Industrial Park in nearby Palo Alto. Equipment and facilities are completely modern and include one of the largest computer centers in the world. Interesting opportunities exist for physicists to contribute to the solution of new problems in the fields listed at the right. Please write: Research and Development Staff, Dept. B-32, 962 West El Camino Real, Sunnyvale, California. U.S. citizenship or existing Department of Defense clearance required.

SPACE PHYSICS

Advanced degree preferred, for work in basic research on the physics of the earth's upper atmosphere and beyond. Typical projects include: measurement of atmospheric composition and density at satellite altitudes; laboratory experiments on upper atmospheric atomic and molecular reactions; hydromagnetic interactions with the earth's magnetic fields; simulation and study of meteor impacts; and particle radiation.

INFRARED AND OPTICS

Advanced degree in E.E. or physics preferred, with experience in infrared systems research and development, or electrical engineers with background in electronics information theory; servomechanisms; specialized circuitry, as in low-level voltage circuits, or physicists with background in optics or semiconductors. For work in infrared physics research; advanced systems development, or physical measurements in infrared. Research is also being conducted in optical devices and systems, including scanners, encoders, detectors, and read-out devices.

SOLID STATE DEVICES

Advanced degree required, Ph.D. preferred, in E.E. or physics and evidence of creative, original work through published articles, patents or superior Ph.D. theses for research work in one or more of the following: thermoelectric; photovoltaic; lumistor; ferrite; logic component; sensor; thermistor; or cryogenic devices. Also, materials analysis and evaluation; processing techniques; design and development of novel electronic devices and components; circuit analysis; circuit topology; or microminiaturization.

Lockheed / MISSILES AND SPACE DIVISION

Systems Manager for the Navy POLARIS FBM; the Air Force AGENA Satellite in the DISCOVERER Program and the MIDAS and SAMOS Satellites; Air Force X-7; and Army KINGFISHER

SUNNYVALE, PALO ALTO, VAN NUYS, SANTA CRUZ, SANTA MARIA, CALIF. · CAPE CANAVERAL, FLA. · ALAMOGORDO, N.M. · HAWAII

TIFFEN OPTICAL FACILITIES FOR SCIENCE AND INDUSTRY

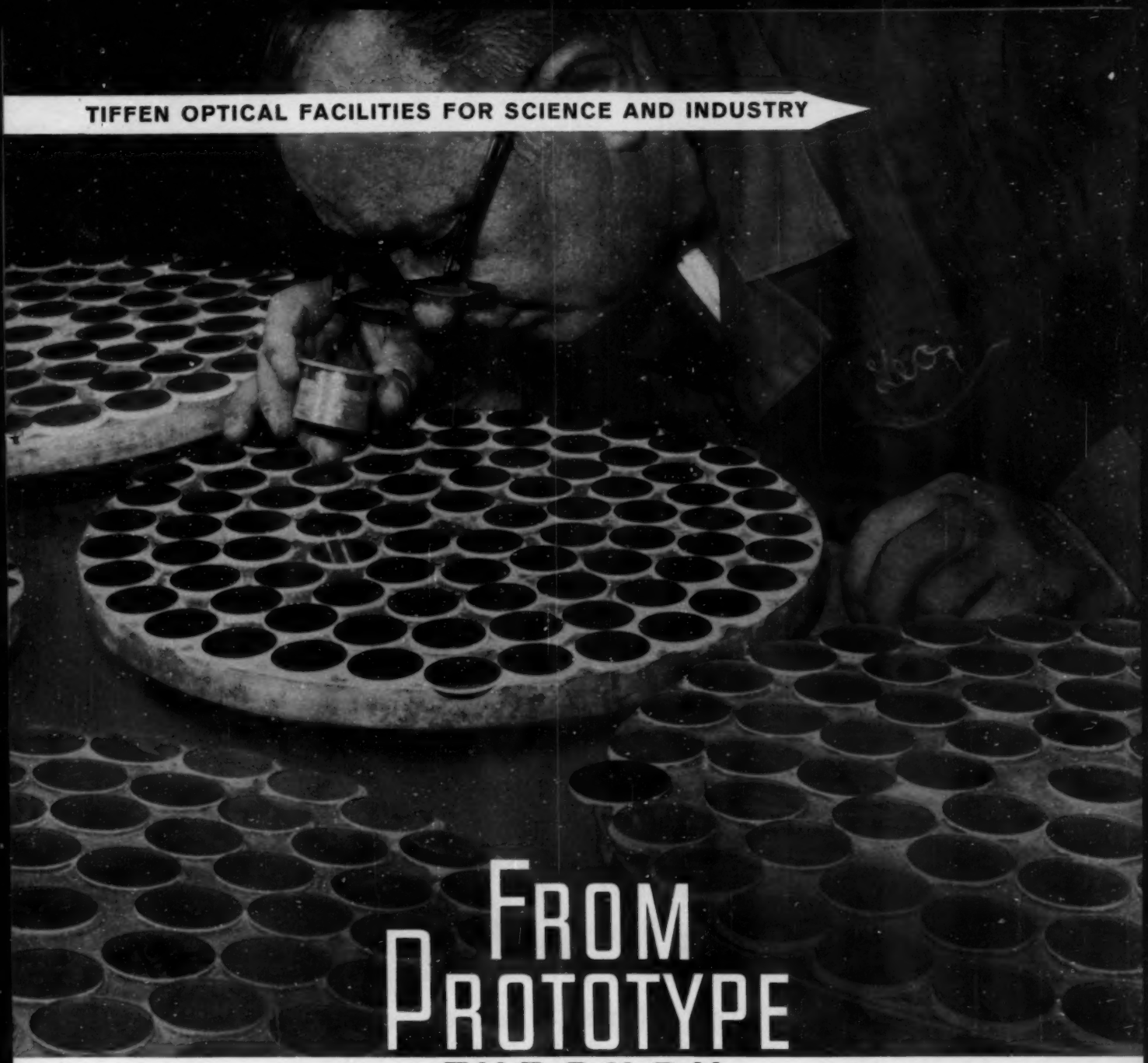

FROM PROTOTYPE THROUGH PRODUCTION

A unique integration of prototype and production facilities . . . that is TIFFEN! For over a decade, government agencies, leading industrial firms and photographic studios have turned to TIFFEN for precision photographic optical accessories.

Now, TIFFEN offers their specialized experience and greatly expanded facilities to all industry employing optics in their product. TIFFEN's major facilities are described below, and are constantly being augmented to conquer specialized problems.

BLANCHARDS ... flat grinding to .00005". Diamond grinding wheels for shaping to .0001" tolerances. Sizes to 18" dia. ***EDGING*** . . . glass and ceramics, to tolerances less than .001", up to 20" dia. Precision bevels and odd shapes ground. ***DRILLING*** . . . dia. from .010" to 12", concentric to within .0005", on glass, ceramics, silicon, germanium, etc. ***GRINDING & POLISHING***. . . from subminiature optics 1mm dia. to mirrors 24" dia., to within 1/10 wavelength in flatness, less than 2 seconds of arc in parallel. Roof prisms to 2 seconds of accuracy. ***COATING*** . . . high vacuum deposition of all types of material. Hot and cold magnesium fluoride coating, partial coatings for beam splitters and metallic neutral density filters. Aluminizing, with silicon monoxide overcoat, for high reflection mirrors. A battery of 22" bell-jars, temperature and humidity controlled dept. ***COLOR LABORATORY*** . . . includes Densichron, Beckman Du Spectrophotometer, Weston Foot Lambert Meter, environmental test equipment, etc. ***FILTERS*** . . . laminated glass equal in environmental tests to solid glass, with superior color control. All colors and curves, .040 to 12" dia., thickness .025" to 1", resolution to 100 lines per mm. ***MACHINING*** . . . multi-spindle automatics to 4", secondary machines to 10" capacity. Thread cutting, Whitworth, English and metric, with single point tools. High precision lens barrels and metallic optical parts. ***TOOL ROOM*** . . . modern 23" swing lathes, grinders, millers. All tools and jigs manufactured internally.

Special problems? Write, call or visit: **TIFFEN OPTICAL CO., 84 Jane St., Roslyn Hgts., L. I., N. Y.** West Coast Rep.: CRAIG CORP., 3410 So. La Cienega Blvd., Los Angeles 16, Cal.

TIFFEN DELIVERS THE GOODS!

Varian V-4012A Laboratory Magnet

From the standard Varian V-4012A 12-inch Laboratory Magnet, performance is unmatched in providing the user with a ***maximized product*** of the three important magnetic-field parameters: (1) field strength, (2) permissible sample volume in the air gap, and (3) field uniformity over the sample volume.

Because when one magnet parameter goes up another goes down, the true measure of the magnet's quality and usefulness is the ***field-volume-uniformity*** combination and the wide range over which each may be varied. The typical field plot at the right demonstrates that even at a field as high as 20,000 gauss, the Varian V-4012A can accommodate a useful-sized sample within its volume of high-homogeneity field. This 20,000 gauss performance is an achievement that has utilized highly advanced design and shimming techniques. It reflects Varian Associates' unique understanding acquired from years of continuous and productive research in magnet technology.

But the full extent of the inherent quality of the V-4012A is revealed by its convertibility to another highly useful but specialized type of magnet. Any new Varian V-4012A can now be converted in the

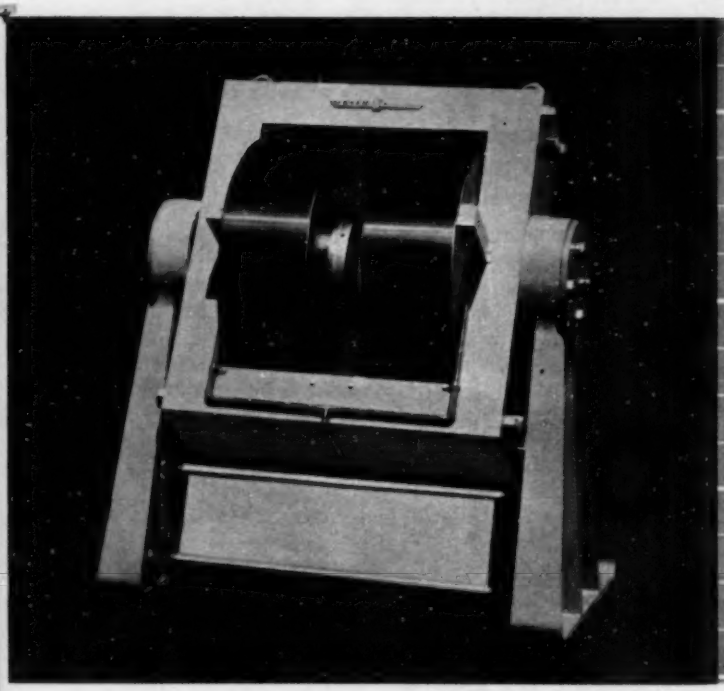

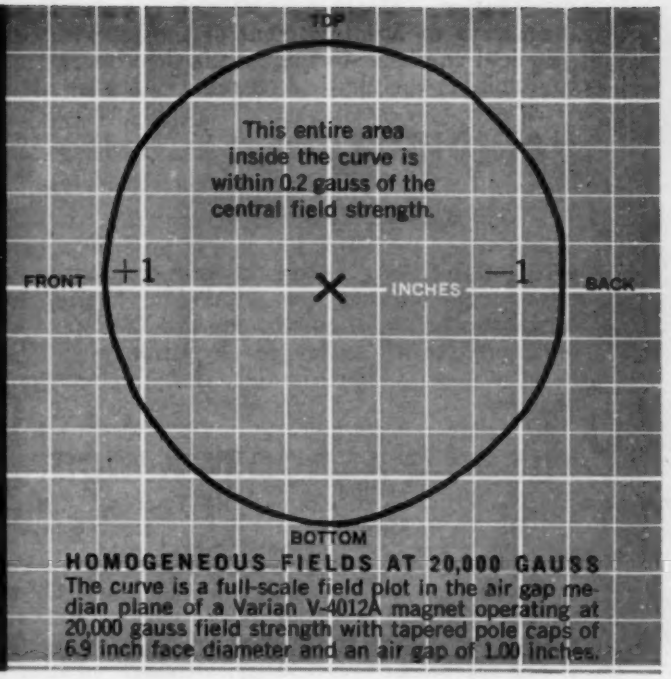

HOMOGENEOUS FIELDS AT 20,000 GAUSS
The curve is a full-scale field plot in the air gap median plane of a Varian V-4012A magnet operating at 20,000 gauss field strength with tapered pole caps of 6.9 inch face diameter and an air gap of 1.00 inches.

field to what we designate as a V-4013 – the ultra-precise magnet that Varian developed to make possible the 60-megacycle High Resolution NMR Spectrometer. The magnet-dependent resolution of this spectrometer is as high as one part in 200,000,000 for a spinning cylindrical proton sample of 4 mm diameter in a 14,100 gauss field.

Choosing a Varian Magnet for your laboratory is an act of foresight. Not only will its performance serve for today's uses, but tomorrow's can be accommodated as well.

Varian Associates manufactures a line of 4, 6, and 12-inch laboratory magnet systems including rotating models and adjustable yoke types. For literature describing all types, write the Instrument Division.

The Varian Magnet Standard:
Unmatched performance through unique understanding.

VARIAN associates
PALO ALTO 36, CALIFORNIA

NMR & EPR SPECTROMETERS, MAGNETS, MAGNETOMETERS, GRAPHIC RECORDERS, FLUXMETERS, MICROWAVE TUBES, MICROWAVE SYSTEM COMPONENTS, HIGH VACUUM EQUIPMENT, LINEAR ACCELERATORS, RESEARCH AND DEVELOPMENT SERVICES

MECHANICAL RADIATION

By R. B. LINDSAY, Brown University. *McGraw-Hill International Series in Pure and Applied Physics.* Ready in February.

The book provides an introduction to wave motion at the senior-graduate level, using mechanical radiation as the principal vehicle, but laying stress on these aspects common to all kinds of wave propagation. Mechanical relation is presented in the broad sense in integrated form by bringing together a unified treatment of the most significant radiation aspects of acoustics. Though the principal emphasis throughout is theoretical, the author has not allowed the mathematical analysis to dominate the physical meaning of the results.

RADIOISOTOPE TECHNIQUES

By RALPH T. OVERMAN, Oak Ridge Institute of Nuclear Studies; and HERBERT M. CLARK, Rennselaer Polytechnic Institute. Now Available, $10.00.

A laboratory textbook designed to give the principles and typical procedures of working with radioactive materials. Discussions and techniques are included relative to the detection of radiation, errors in radioactivity measurements, the preparation of radioactive sources, the laboratory characterizations of radiation, the standardization of radioactive sources and the calibration of radiation detectors, the rates of radioactive processes, radiochemical separation methods, and applications of radioisotopes. Approximately 1,000 references to literature dealing with these techniques are included.

MISSILE AERODYNAMICS

By JACK N. NIELSEN, VIDYA, Inc. *McGraw-Hill Series in Missile and Space Technology.* Ready in March.

This volume presents a rational and connected account of principles of missile aerodynamics. It treats the subjects of bodies, wings, and tails and the interactions between them which are particularly important for missiles. Various methods are presented for determining the airflow about missiles, including the vortices which are frequently very prominent in the flow. The book is directed at the supersonic speed range, although most of the results are also applicable to subsonic speeds.

BOUNDARY LAYER THEORY, *Second Edition*

By HERMANN SCHLICHTING, University of Braunschweig, Germany. Translated by Dr. J. KESTIN, Brown University. *McGraw-Hill Mechanical Engineering Series.* Ready in April.

A general up-dating of a reference book written principally for practicing and research engineers doing advanced work in Fluid Mechanics, and for students of aerodynamics and such allied subjects as require a thorough knowledge of the dynamics of viscous flow. The book gives a connected and logical exposition of that branch of Fluid Mechanics which deals with flows in boundary layers.

Send for copies on approval

McGraw-Hill
BOOK COMPANY, INC.
330 West 42nd Street New York 36, N.Y.

Breakthrough in Radiation Detection!

The new Hughes Solid State Detector (housed in the transistor can on the tip of this complete alpha survey meter) is the smallest...fastest...simplest...and most accurate charged particle detector ever devised.

SMALL: 1mm square—1cm square
FAST: Response time less than one nanosecond
SIMPLE: Operates on 6-12 volts
ACCURATE: Better than 1% particle energy resolution.

Hughes is already providing equipment using these detectors in conjunction with fast electronic circuits, memory devices and read out equipment.

Hughes Nuclear Electronics Laboratory specializes in radiation——its measurement, production and application——with off-the-shelf products, custom products, research studies, and design and construction of facilities. We welcome your inquiry.

Please write, wire or call:
Mr. Ben W. Davis, Hughes Nuclear Electronics Laboratory, P.O. Box 90515-A, International Airport Station, Los Angeles 45, California

Creating a new world with ELECTRONICS

HUGHES

© 1960 HUGHES AIRCRAFT COMPANY

Hughes offers you complete, proven capabilities in radiation... detectors, handling equipment, sources, analysis of effects

MOBOT Mark I is first of a family of mobile, remote controlled handling machines using TV vision and electronic controls. Wall or crane mounted Mobots and rough terrain Mobots are among those currently under development.

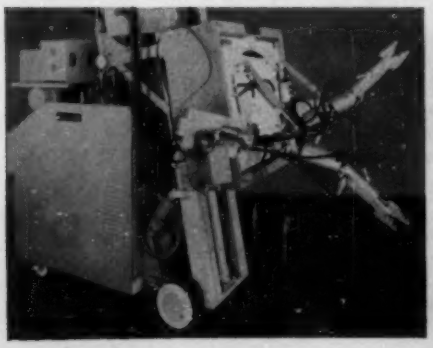

Hughes Research Linac has 3 times the current of comparable machines...over ½ amp. available at 1 to 10 μs pulse width. They are available in many configurations for research in the effects and other applications of high gamma radiation.

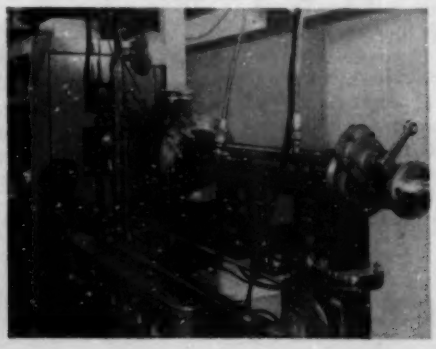

Shown is the effect of pulsed (low dose, high rate) radiation on a vacuum tube amplifier. For the past three years Hughes has been studying transient and permanent radiation effects on materials, components and systems.

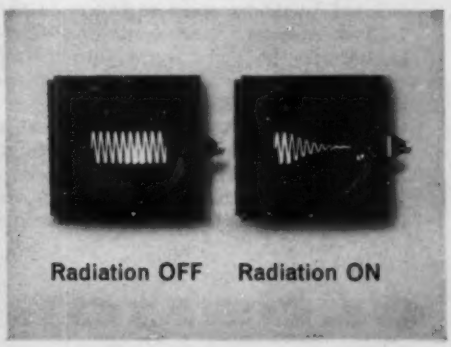

Radiation OFF Radiation ON

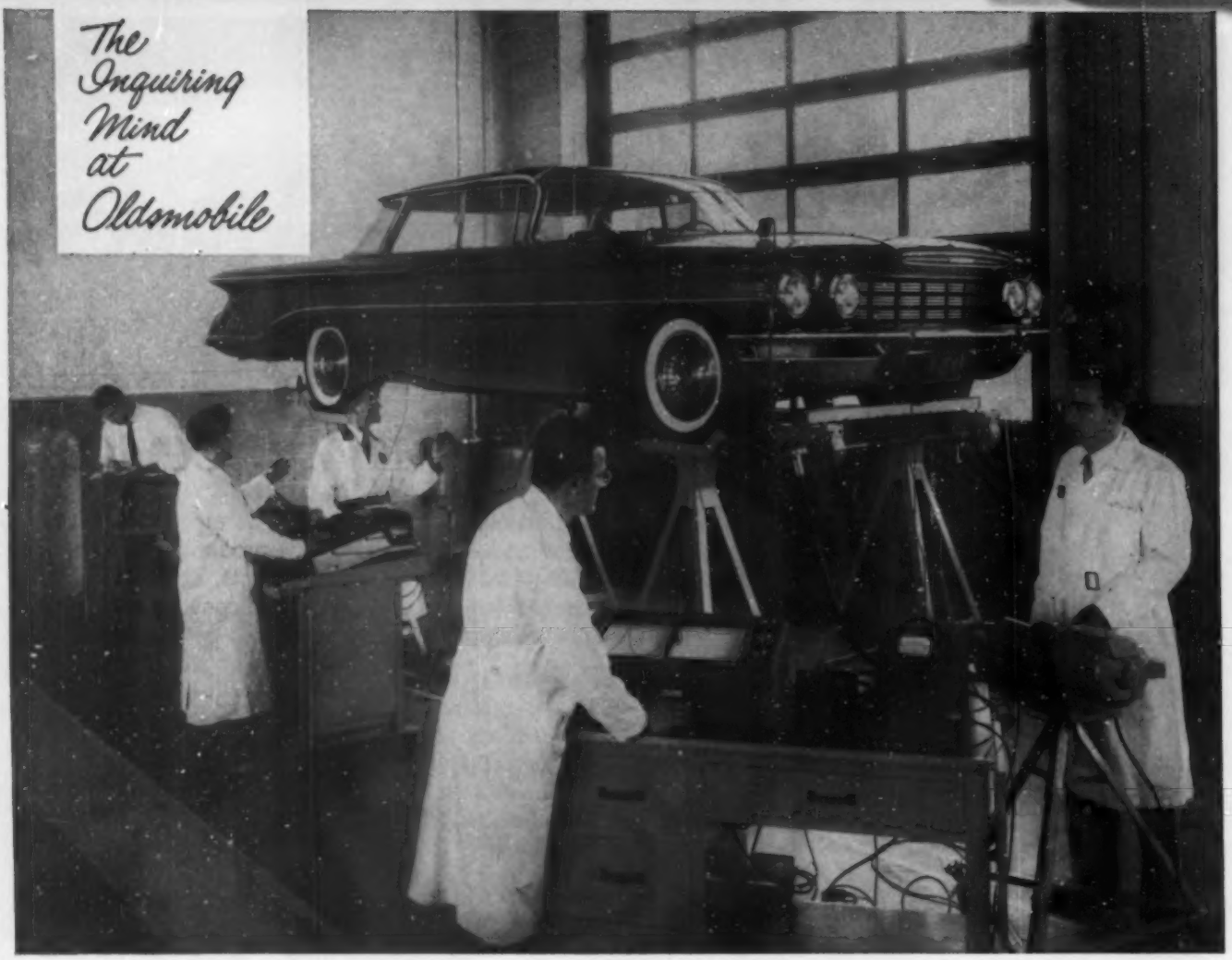

no. 10 OF A SERIES

IT'S THE QUIETEST RIDE YOU'VE EVER TRIED!

New Vibra-Tuned Body Mountings—electronically located at the nodal points of the frame by Oldsmobile engineers—produce an exceptionally quiet and satisfying ride.

Quietness in a fine automobile is a mark of superior quality. To make the 1960 Oldsmobile the quietest, most comfortable car on the road, Oldsmobile engineers have developed many advanced testing techniques to insulate against all types of road noise.

One of the unique ways in which noise and vibration are isolated by Oldsmobile engineers is through Vibra-Tuned body mountings. These mountings—direct attaching points between the body and frame—are critical to comfort and to the life of the car. If they are not properly placed, severe road vibrations can literally shake the car apart in a few thousand miles. But, by using the most advanced electronic measuring techniques, a softer and quieter ride is achieved by placing the body mounts at the nodal points of the frame. In this way, inherent road vibrations and shocks are practically isolated from the passenger compartment.

In the "tuning" of the chassis and body, the car is subjected to severe shaking, at a frequency of 7½ to 15 cycles per second, by a mechanical oscillator to produce torsional and bending moments. By using numerous electronic pick-ups, movement of the frame and body at a given point can be determined quickly and translated into an accurate magnitude vs. frequency curve through an X-Y plotter. By a complete and thorough examination of the entire car in such a manner, it can be determined where the "dead" or nodal points are on the frame, and the body mounts can then be scientifically placed. Then, after being located, the hysteresis characteristics of the body mounts are determined to give the most satisfying ride.

These methods, and many more up-to-the-minute techniques, have enabled Oldsmobile engineers to build consistently fine quality automobiles year after year. Visit your local authorized Quality Dealer and drive a 1960 Oldsmobile. See why it's the most satisfying car you've ever known . . . *the finest the medium-price class has to offer!*

OLDSMOBILE DIVISION • GENERAL MOTORS CORPORATION

OLDSMOBILE **Where Proven Quality Is Standard!**

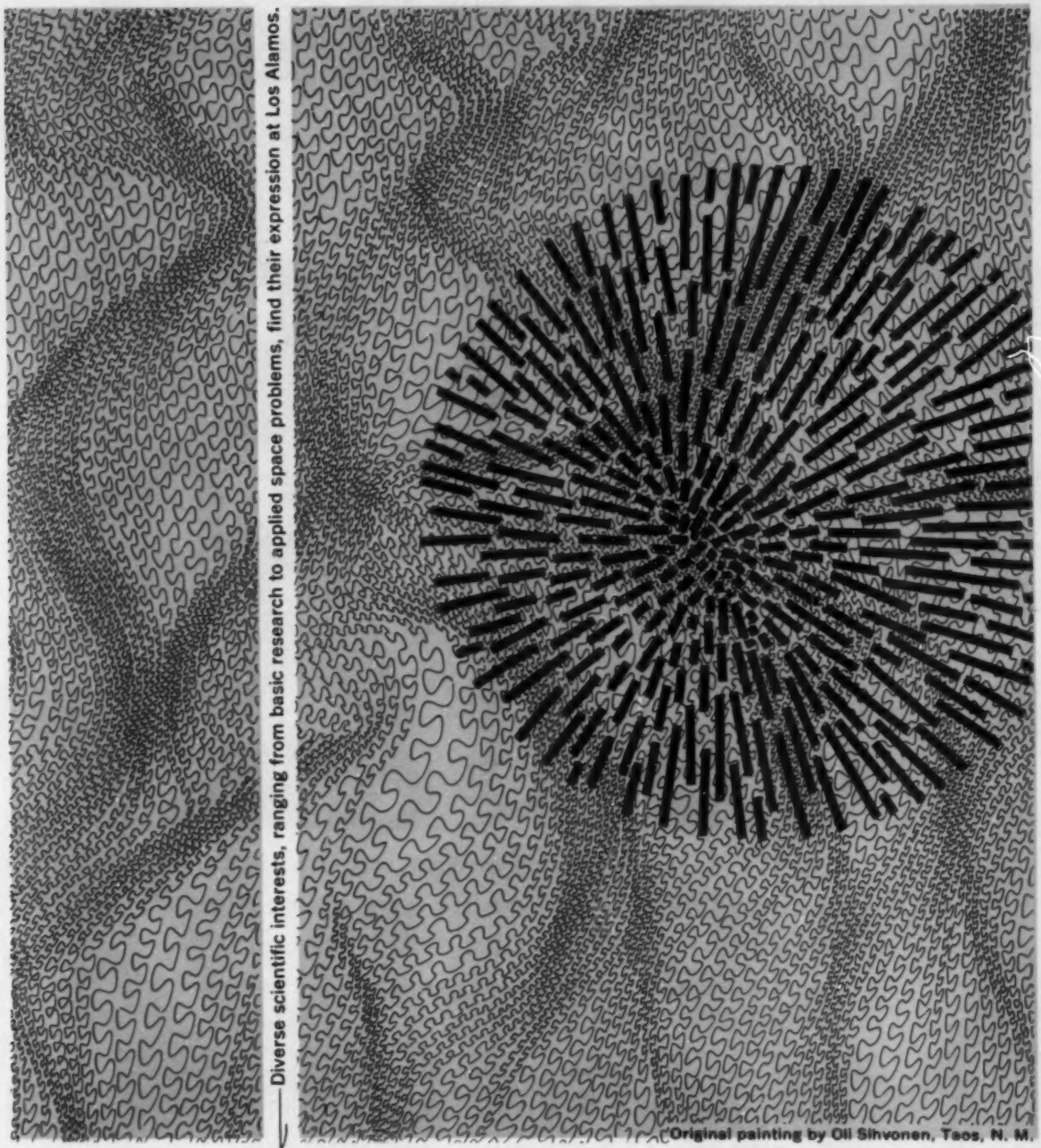
Diverse scientific interests, ranging from basic research to applied space problems, find their expression at Los Alamos.
Original painting by Oli Sihvonen, Taos, N. M.

For employment information write: Personnel Director, Department 60-18

los alamos
scientific laboratory
OF THE UNIVERSITY OF CALIFORNIA
LOS ALAMOS, NEW MEXICO

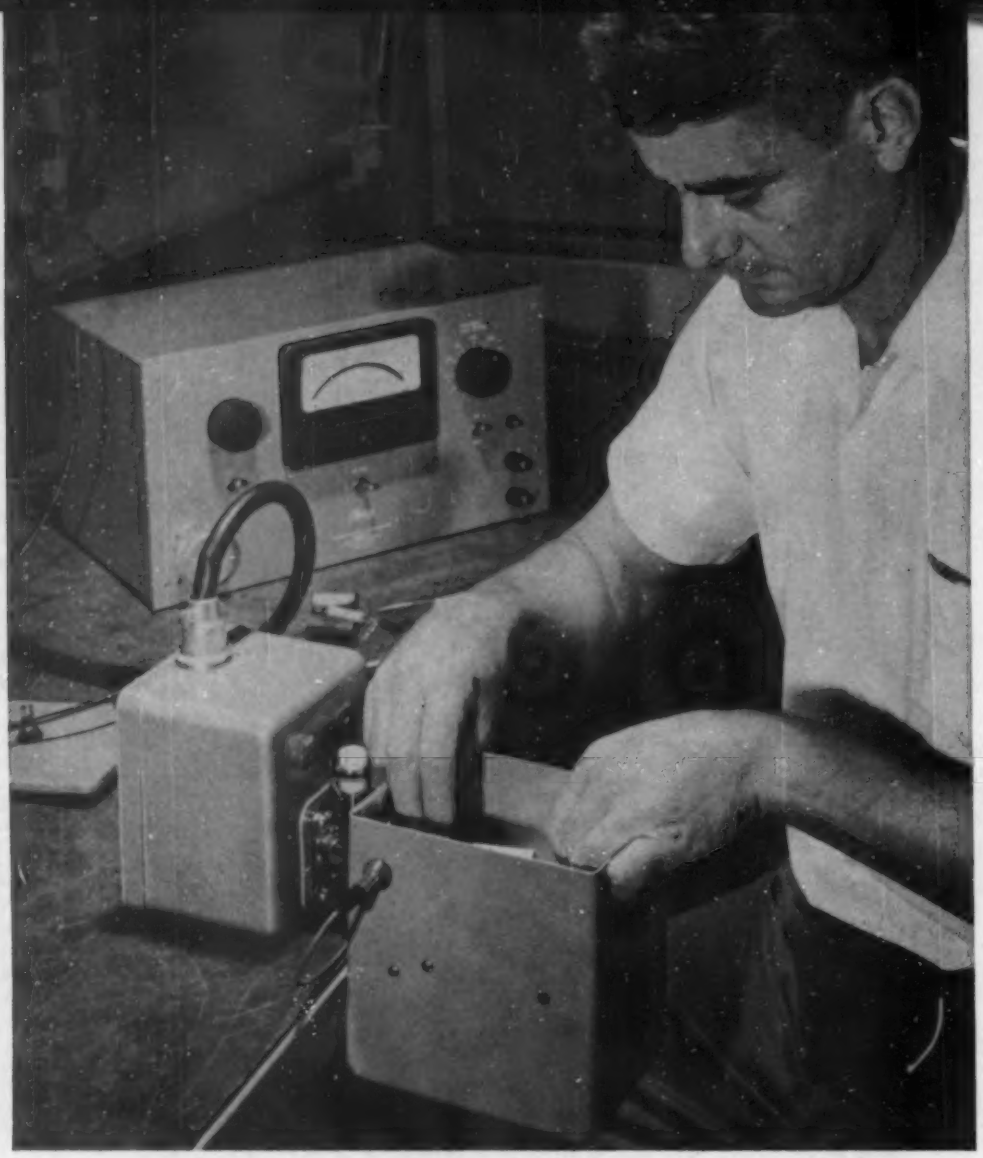

Cary Electrometers measure insulation resistance of 10^{15} ohms at potentials of one volt or less with ±1% accuracy

Provide fast accurate leakage measurements; eliminate instrument loading of the test circuit

In addition to measuring large resistance values Cary Electrometers are used for measuring charging phenomena, hysteresis and photo effects of semi-conductors and insulating materials. Applications include air ionization studies, measurement of ion currents in mass spectrometry, radioactivity measurements of solids, liquids and gases and Hall effect studies.

Cary Electrometers detect currents as small as 10^{-17} amperes; charges to 6×10^{-16} coulombs; and voltages as low as 20 microvolts.

High stability (less than 5×10^{-17} amperes steady drift), high accuracy (±0.25% using a precision potentiometer), and operation independent of changes in vacuum tube and component characteristics are just a few of the features contributing to the superior performance of Cary Electrometers.

Choose from several models: MODEL 31 for measuring currents from grounded sources and voltages from ungrounded sources; MODEL 31V for voltage measurements from grounded sources; MODEL 31-31V for measuring voltage or current from grounded sources.

Cary INSTRUMENTS

Additional information
on Cary Electrometers and Accessories is yours for the asking.
Write for data file R14-20

Electrometers • UV–Visible–Near IR and Raman Spectrophotometers

APPLIED PHYSICS CORPORATION • 2724 So. Peck Rd., Monrovia, Calif.

MATHEMATICIANS

DUALITY THEORY IN REACTOR DESIGN CALCULATION

Because reactor design parameters require efficient neutron transport calculations, mathematicians at the Bettis Atomic Power Laboratory considered extracting information from the adjoint Monte Carlo problem in which neutron trajectories are essentially reversed in time. Thus by using the duality theory to satisfy neutron flux and importance function, sampling models were modified in a systematic manner thereby optimizing computing efficiency.

If you are a mathematician with an advanced degree and are interested in pursuing a career in reactor and nuclear system mathematics and are a U. S. citizen, write to: Mr. M. J. Downey, Dept. B-34, Bettis Atomic Power Laboratory, Westinghouse Electric Corporation, P. O. Box 1526, Pittsburgh 30, Pennsylvania.

$$\varphi(\underline{r},\underline{E}) = \iint K(\underline{r},\underline{E};\underline{r}',\underline{E}')\,\varphi(\underline{r}',\underline{E}')\,d\underline{r}'d\underline{E}' + S(\underline{r},\underline{E})$$

$$\iint \Sigma(\underline{r},\underline{E})\,\varphi(\underline{r},\underline{E})\,d\underline{r}d\underline{E} = \iint S(\underline{r},\underline{E})\,\eta(\underline{r},\underline{E})\,d\underline{r}d\underline{E}$$

$$\eta(\underline{r},\underline{E}) = \iint K(\underline{r}',\underline{E}';\underline{r},\underline{E})\,\eta(\underline{r}',\underline{E}')\,d\underline{r}'d\underline{E}' + \Sigma(\underline{r},\underline{E})$$

BETTIS ATOMIC POWER LABORATORY

Westinghouse

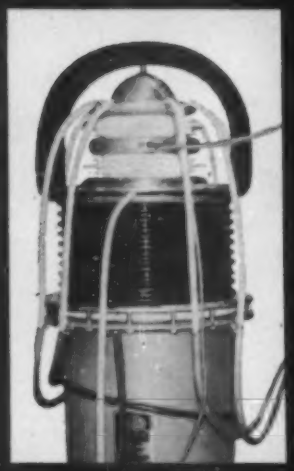

600,000 amperes help harness H-power

At the historic Geneva Atoms-For-Peace Conference, Los Alamos scientists unveiled Scylla—a fusion device used to heat a plasma of ionized heavy hydrogen particles millions of degrees by blasting it with a 600,000-ampere thunderbolt.

Surrounding the heart of this thermonuclear machine is a bank of Tobe low-inductance, energy-storage capacitors...each rated at 100,000 volts, each capable of a 20,000 megawatt peak surge.

Why Tobe capacitors? Because only Tobe, with over 30 years of capacitor experience, could meet the rigid design specifications set for the project. Tobe capacitors can meet yours, too. We invite inquiries for a single energy storage capacitor or a complete energy storage system including capacitors, racks, interconnecting lines, protective devices and charging power supply.

For further technical information or engineering aid, write to Cornell-Dubilier Electric Corp., Marketing Office, Norwood, Mass.

CDE **CORNELL-DUBILIER ELECTRIC CORPORATION**
Affiliated with **Federal Pacific Electric Company**

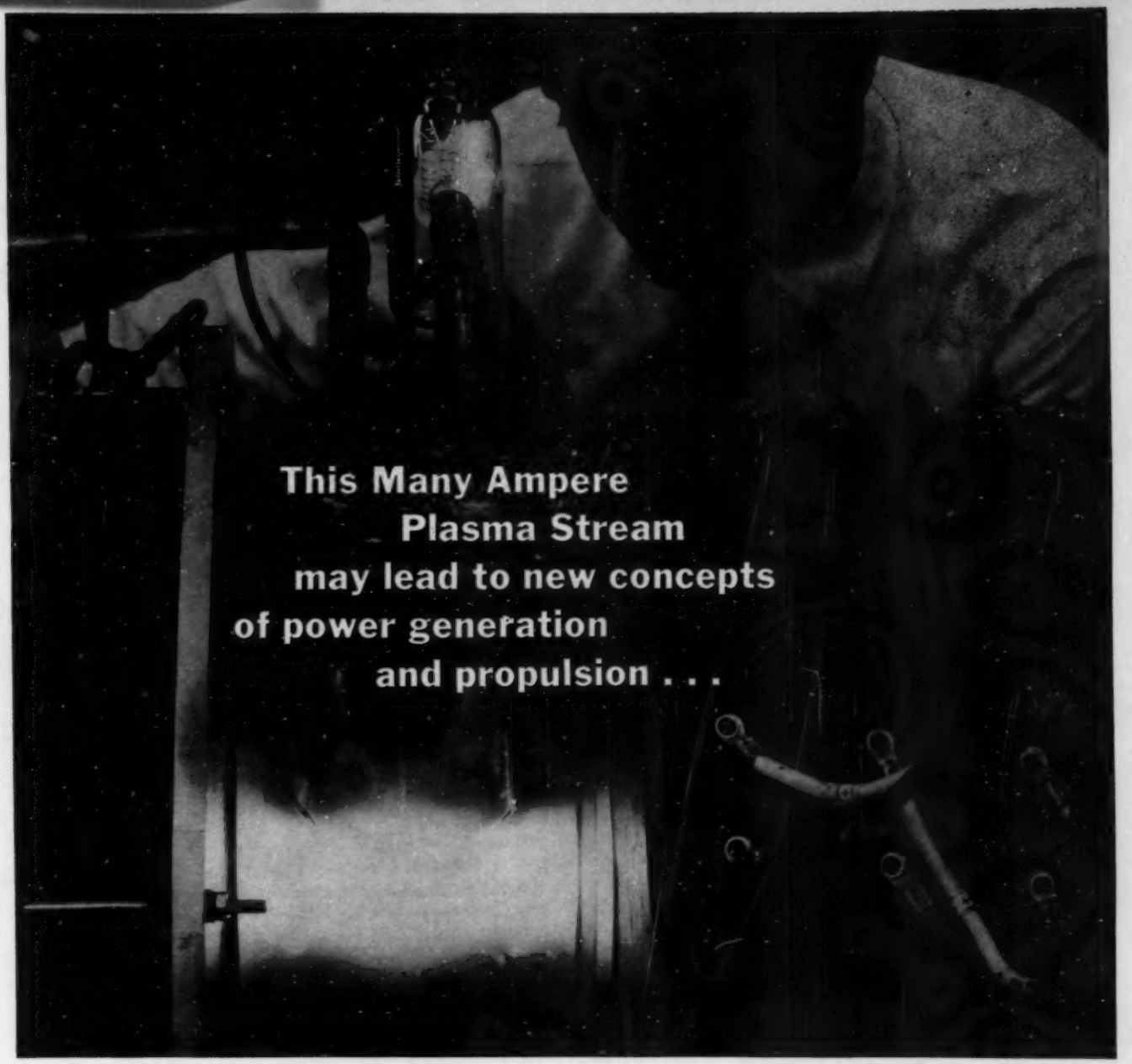

A many-ampere source of ions, this device is believed to be the most powerful in operation in any laboratory Already it is providing new insight into thermonuclear fusion. It may lead to new concepts in propulsion including a method of producing thrust for missions beyond the earth's atmosphere.

Accomplishments like this are the result, we believe, of a unique research environment. Among other things, we encourage independence of scientific thought and action. And, we make determined efforts to free scientists from tedious routine — help direct their full mental powers towards scientific achievement.

Complex calculations, for instance, are handled by the nation's largest industrial computational facility. Unusual assistance — at operational and theoretical levels — is available from outstanding leaders in other disciplines.

We believe that this combination of facilities and services is unequaled. If you are interested in corporate-sponsored studies into the fundamental nature of matter in an environment where success comes easier, write today.

Please write to Mr. W. N. Walsh, or phone Hartford, Conn., JAckson 8-4811, Ext. 7145

Research Opportunities
in many areas . . .

Solid State Physics
Plasma Physics
Gaseous Electronics
Chemical Kinetics
Particle Physics
Nuclear Engineering
Surface Chemistry
Cryogenics
Energy Conversion

RESEARCH LABORATORIES
UNITED AIRCRAFT CORPORATION
400 Main Street, East Hartford 8, Conn.

Symbol of UAC RESEARCH . . . creative research

American Institute of Physics

A Federation of

Professional Societies in Physics

The American Institute of Physics is the coordinating and unifying organization in the field of physics. All of the societies listed below are Members, Associates or Affiliates of the Institute. Eight journals are published by the Institute for the Member Societies. These, together with fourteen journals owned by the Institute, constitute a coordinated publishing program of high standards, efficiency, and economy.

The Institute also carries on other activities designed to advance physics and to serve the public interest through physics. It maintains a free Placement Service for the use of employers and of physicists seeking jobs. It works with the Societies in seeking cooperation with other fields of science, with departments of the Federal government, with educational institutions, and with industrial organizations.

Corporate Associates: A special class of membership is available to corporations who pay minimum annual dues of $350, for which they may receive certain journals, programs of meetings of societies, and other privileges.

Student Sections: College physics students may form local organizations which may become Student Sections of the Institute.

Information: Address Wallace Waterfall, Secretary, 335 East 45 Street, New York 17, N. Y. for information about the Institute and its activities. For information about any Member Society, address its Secretary.

MEMBER SOCIETIES:

AMERICAN PHYSICAL SOCIETY

The Society has as its object the advancement and diffusion of the knowledge of physics. All branches of fundamental and applied physics are generally included in its scope. Both experimental and theoretical researches are reported in its journals and meetings.

Dues: Members, $15; Fellows, $25.

Address: Karl K. Darrow, Secretary, Columbia University, New York 27, New York.

OPTICAL SOCIETY OF AMERICA

The Society devotes itself to the advancement of optics, pure and applied, in all its branches. Its scope includes research in fundamental optics as well as problems concerned with design and production of optical instruments.

Dues: Associate Members, $13.00; Regular Members and Fellows, $17.00; Student Members, $2.00; Corporation Members, $125.00 minimum; Patrons, $1000.

Address: Mary E. Warga, Executive Secretary, ACS Building, 1155 16th Street, N.W., Washington 6, D. C.

ACOUSTICAL SOCIETY OF AMERICA

The Society's purpose is to increase and diffuse the knowledge of acoustics and promote its practical applications. The scope includes fundamental researches on the intensity, transmission, and absorption of sound; also on noise, reverberation in rooms, the processes of speech and hearing, the performance and reproduction of music, etc.

Dues: Associate Members, $10; Members and Fellows, $15; Sustaining Members, not less than $100.00.

Address: Wallace Waterfall, Secretary, 335 East 45 Street, New York 17, New York.

AMERICAN ASSOCIATION OF PHYSICS TEACHERS

Whereas the other Societies are mainly concerned with research, this Association has provided a much needed forum for the discussion of the problems of teaching. In cooperation with the other groups, the Association promotes the advancement of physics and emphasizes its place in the general culture.

Dues: Members, $7.50; Junior Members, $4.00; Sustaining Members, $200.00.

Address: Frank Verbrugge, Secretary, Univ. of Minnesota, Minneapolis 14, Minn.

SOCIETY OF RHEOLOGY

This small but active society is composed of physicists, chemists, and engineers interested in "rheology," which is defined as the science of deformation and flow of matter.

Dues: Members, $6.00; Sustaining Members, $25.00.

Address: W. R. Willets, Secretary-Treasurer, Titanium Pigment Corp., 99 Hudson Street, New York 13, N. Y.

ASSOCIATE MEMBER SOCIETIES:

American Crystallographic Association

Address: Leroy E. Alexander, Secretary, Mellon Institute, 4400 Fifth Avenue, Pittsburgh 13, Pa.

American Astronomical Society

Address: J. Allen Hynek, Secretary, Smithsonian Astrophysical Observatory, 60 Garden Street, Cambridge 38, Mass.

AFFILIATED SOCIETIES:

American Society for Metals • Cleveland Physics Society • Electron Microscope Society of America • Foundation for Instrumentation Education and Research, Inc. • Philosophical Society of Washington • Physical Society of Pittsburgh • Physics Club of Chicago • Physics Club of Lehigh Valley • Physics Club of Philadelphia • Sigma Pi Sigma

Inquiries regarding membership in the Affiliated Societies may be sent to the American Institute of Physics, 335 East 45 Street, New York 17, New York. Such inquiries will be forwarded to the respective secretaries.

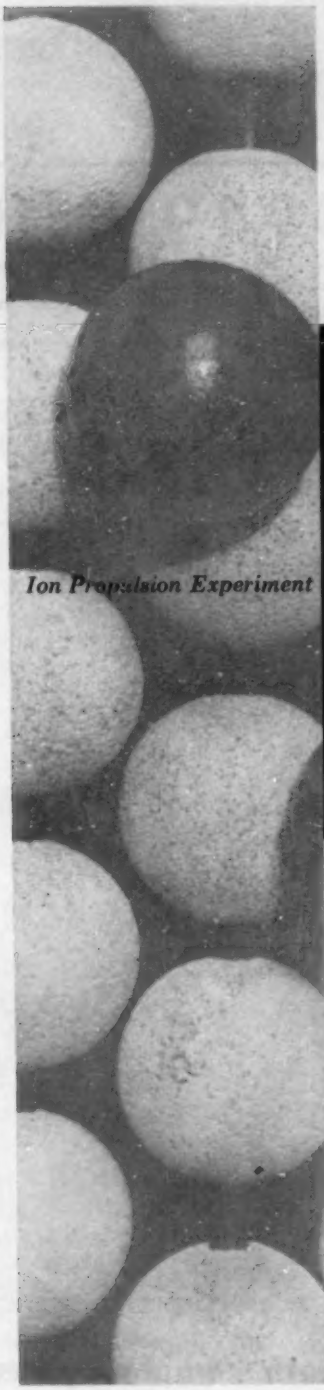

Ion Propulsion Experiment

An announcement of importance to PHYSICISTS

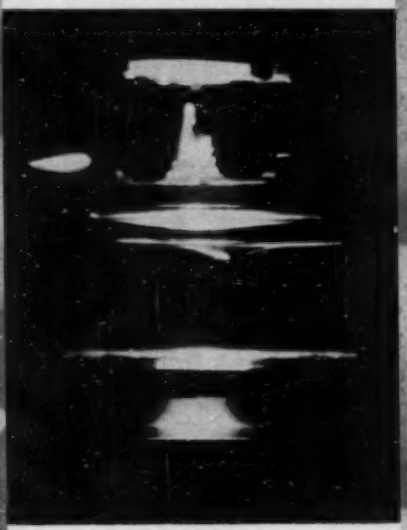

Only occasionally do *truly* outstanding professional opportunities with a vital, growing organization become available. New and expanding programs in the Fluid Physics Division of EOS* have created positions of this exceptional caliber for both theoretical and applied physicists.

These rewarding appointments on the technical staff will be concerned with pioneering efforts in the fields of . . .

Magnetohydrodynamics
Electrically Exploding Wires
Electromagnetics
Nuclear and Molecular Physics
Ion and Plasma Propulsion

Creative scientists — men with ideas and curiosity — who hold an advanced degree and have pertinent research experience, are invited to write in confidence to the Senior Technical Staff Placement Director for additional information.

*Founded in 1956, Electro-Optical Systems is conducting advanced research and development programs in solid state devices, energy research and advanced power systems, fluid physics, advanced electronics and space defense systems.

E
O
S

ELECTRO-OPTICAL SYSTEMS, INC.
MUrray 1-0408

150 NORTH VINEDO AVE.
PASADENA, CALIFORNIA

Up-to-date! — NEW 1959 Edition
WELCH CHART OF THE ATOMS

All specific information including a tabulation of principal isotopes now arranged for greater clarity • Nobelium 102 (most recent discovery) included

Improved readability • Large size—42 X 58 inches • Lithographed in 6 colors
Lists latest atomic weights compiled by International Union for Pure & Applied Chemistry

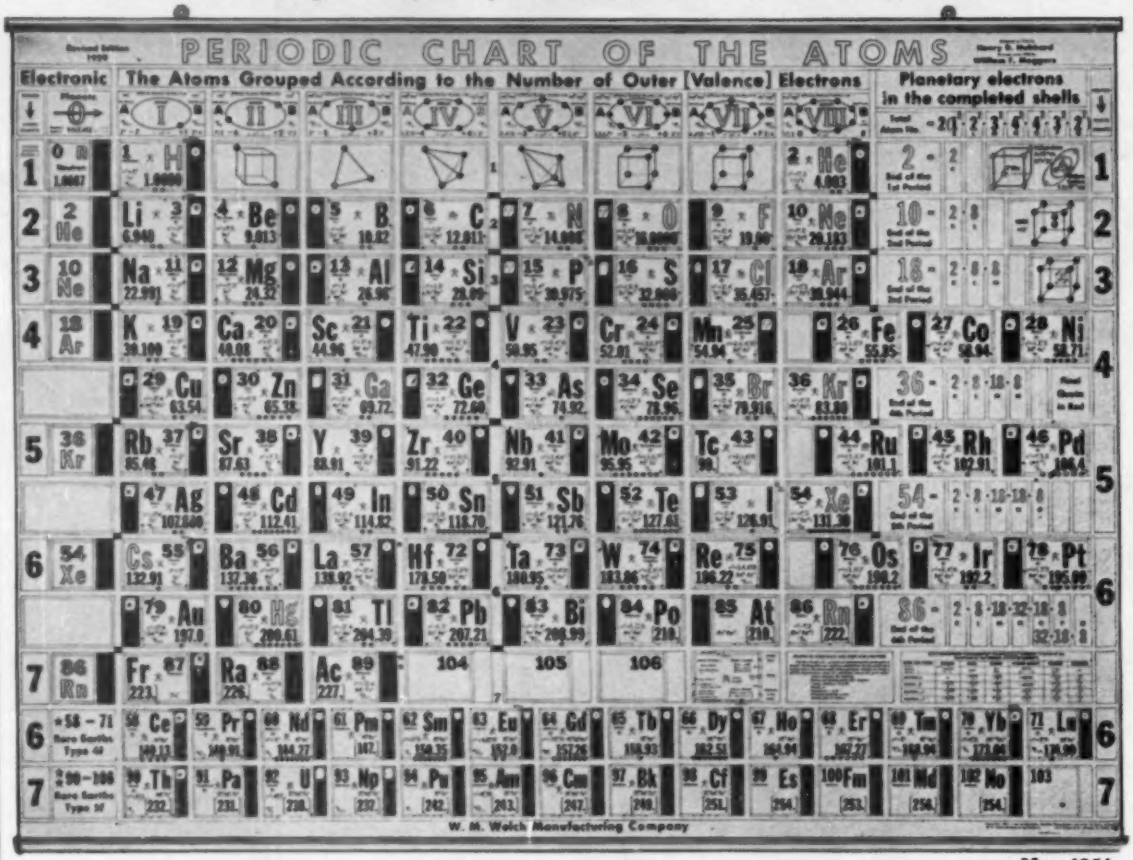
PERIODIC CHART OF THE ATOMS
Electronic
The Atoms Grouped According to the Number of Outer [Valence] Electrons
Planetary electrons in the completed shells
W. M. Welch Manufacturing Company

No. 4854.

Chart and 48-page Key Booklet both completely revised
by Dr. William F. Meggers, National Bureau of Standards

No. 4854. CHART OF THE ATOMS—1959 Edition. Lithographed in six colors on heavy chart paper, coated with a plastic film especially treated to prevent glare, with formed-metal chart molding at top and bottom with eyelets for hanging and a 48-page key booklet.....Each $7.50

Write for Complete Circular

W. M. WELCH SCIENTIFIC COMPANY
DIVISION OF W. M. WELCH MANUFACTURING COMPANY
ESTABLISHED 1880
1515 Sedgwick Street, Dept. C-1 Chicago 10, Illinois U. S. A.
Manufacturers of Scientific Instruments and Laboratory Apparatus

Journal
of
Applied Physics

Volume 31, Number 2 February, 1960

Development of Facets, Spirals, and Etch Pits on Copper Crystals by Heating to High Temperatures in High Vacua*

F. W. Young, Jr.,† and A. T. Gwathmey
Cobb Chemical Laboratory, University of Virginia, Charlottesville, Virginia

(Received March 3, 1959)

Single crystal spheres of OFHC and 99.999% copper were heated to temperatures of 950 to 1075° in high vacua. In the case of the OFHC copper, facets parallel to the (111), (110), and (100) planes were formed over relatively large areas centered at the respective poles, and with some of these crystals spiral facets were formed around the (111) pole. When an OFHC crystal was heated in a copper cup, an appreciable number of pits were formed. In the case of the 99.999% copper, facets parallel to the (111) and (100) planes were formed in small areas around the respective poles, and at certain temperatures etch pits were formed. An attempt was made to interpret the difference in the size of the facets formed on the two types of crystals in terms of the influence of impurities on the rates of evaporation. It was proposed that the etch pits formed at dislocations in the crystal, although there was not a one-to-one correspondence between pits and dislocations.

INTRODUCTION

When metal crystals are heated to high temperatures in high vacua or in the presence of various gases, facets are generally developed. In the case of heterogeneous catalytic reactions on the surface of a single crystal of copper, studies carried out in this laboratory[1] have shown that the surface rearranges to expose certain facets which depend on the nature and concentration of the reacting gases and on the conditions of the experiment. In an effort to understand the principles which control the stability of crystal faces under various conditions, it is of interest to determine the facets which form when a crystal is maintained at a high temperature in a high vacuum. The question of the stability of faces is also of major importance in attempting to prepare for detailed study plane surfaces of single crystals.

Past studies on thermal etching have been reviewed by Shuttleworth[2] who studied the thermal etching of polycrystalline silver in oxygen. Menzel[3] has investigated the behavior of copper crystals at high temperatures under a variety of conditions, and Suzuki[4] has observed the behavior of polycrystalline copper near its melting point in a low vacuum. Young[5] has reported preliminary results on copper crystals. Moore[6] has studied in more detail the etching of single crystal and polycrystalline silver in oxygen. It is also possible to develop etch pits by thermal etching, as reported by the above authors and by Hendrickson and Machlin[7] on silver.

The studies described in this paper are concerned with the development of facets, etch pits, and spirals on single crystals of copper which were heated to high temperatures in high vacua.

EXPERIMENTAL

Single crystals of copper in the form of spheres, $\frac{1}{4}$ to $\frac{5}{8}$ in. in diam, were used in these experiments. Some of the spheres were machined from large single crystal rods, while other crystals were grown with a hemispherical end so that no cutting or mechanical polishing was

* The cover picture shows a single crystal sphere of copper, thermally etched at 1025°C in high vacuum and then lightly oxidized at 200°C. Photograph made with a single light directed at the (111) pole by K. R. Lawless at the University of Virginia.

† Present address: Solid State Division, Oak Ridge National Laboratory, Oak Ridge, Tennessee.

[1] A. T. Gwathmey and A. F. Benton, J. Chem. Phys. **8**, 569 (1940).
A. T. Gwathmey and R. E. Cunningham, J. chim. phys. **51**, 497 (1954).

[2] R. Shuttleworth, Metallurgia **38**, 125 (1948).

[3] E. Menzel, Z. Physik **132**, 508 (1952).

[4] H. Suzuki, J. Phys. Soc. Japan **10**, 981 (1955).

[5] F. W. Young, Jr., J. Appl. Phys. **27**, 554 (1956); Bull. Am. Phys. Soc. Ser. II, **1**, 139 (1956).

[6] A. J. Moore, Acta Met. **6**, 293 (1958).

[7] A. A. Hendrickson and E. S. Machlin, Acta Met. **3**, 64 (1955).

Copyright © 1960 by the American Institute of Physics.

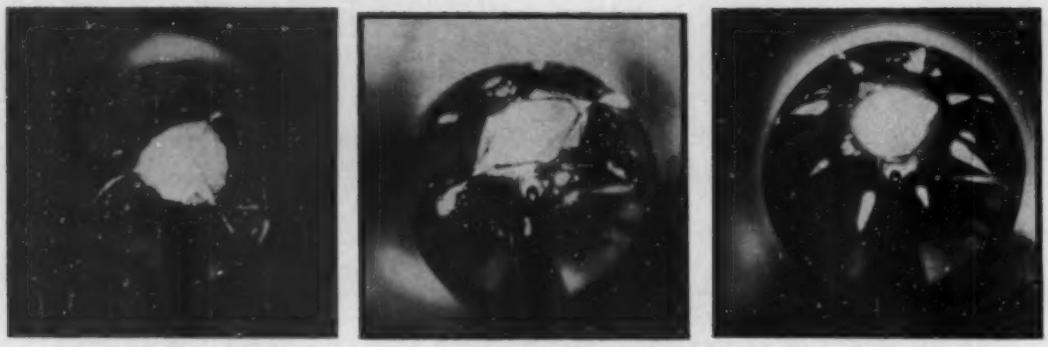

(a) (b) (c)

FIG. 1. Reflections from the poles of OFHC copper crystal after heating to 1000°C in high vacuum. (a) (111), (b) (110), (c) (100).

necessary. All of the crystals were grown in a graphite crucible by the Bridgman technique. No effect of the rate of growth ($\frac{3}{4}$ to $2\frac{1}{4}$ in./hr) or of the vacuum during growth (1×10^{-5} to 2.5×10^{-3} mm Hg) was seen on the subsequent etching behavior. Crystals grown from OFHC and from 99.999% copper were investigated.‡

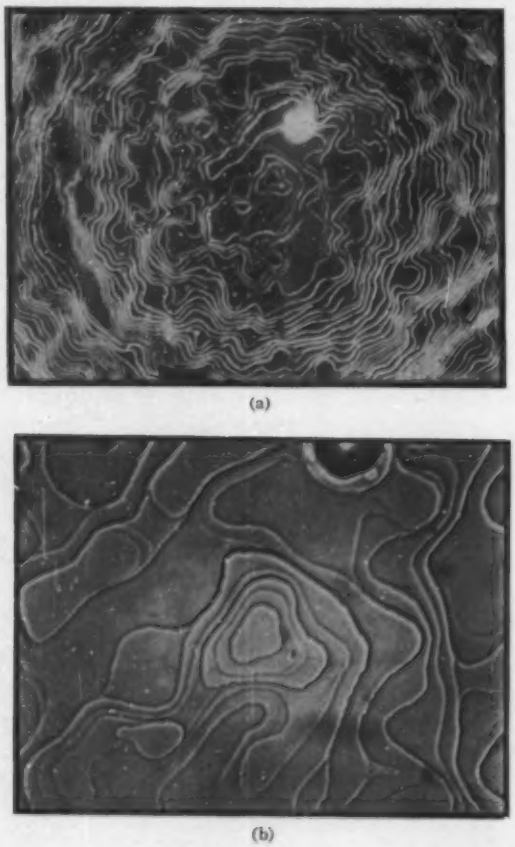

(a) (b)

FIG. 2. (111) pole of OFHC copper crystal after heating to 1000°C in high vacuum. (a) 300× dark field, (b) 600×.

In all cases the crystals were polished electrolytically in a H_3PO_4-H_2O bath (60 wt.% H_3PO_4), washed carefully in distilled water and dried in a jet of oxygen as described previously.[5] After this treatment the surface of the crystal was of such smoothness that it was not possible to focus on it with a metallurgical microscope at 1000 ×.

The crystal was suspended on a Vycor hook in a 200-ml Pyrex bulb which was attached to an all-glass high vacuum system, and the tube through which the crystal was introduced was sealed off. After annealing the crystal in pure hydrogen at 500°C for one hour, the system was evacuated and baked out at 450°C for about ten hours. The pressure was approximately 2×10^{-9} mm Hg after cooling the system to room temperature. The crystal was then heated to the desired temperature with an induction coil which was placed around the outside of the Pyrex bulb. Temperatures were measured with an optical pyrometer, and corrections were made for nonblackbody conditions. Absolute values of the temperature were accurate to ±20°C. However, the reproducibility in obtaining a given temperature was somewhat better, probably ±5°C.

Since the crystal was isolated from the bulb by the Vycor hook, the glass walls remained cool. As the temperature was raised the pressure in the system increased because of evolution of gas from the crystal, but after a short time a pressure of 1×10^{-8} to 5×10^{-9} could be maintained with the temperature of the crystal near the melting point. At temperatures above approximately 925°C the vapor pressure of copper became appreciable in the system, and copper was deposited on the glass walls. After heating, the crystal was cooled in the vacuum to room temperature, removed from the apparatus, and examined in a beam of light and with the optical microscope.

A few experiments were carried out with the crystal suspended in a thin walled OFHC or 99.999% copper cup, which in turn was suspended on the Vycor hook as

‡ The 99.999% copper was obtained from American Smelting and Refining Company. A spectrographic analysis was furnished which indicated no impurities were detected in their analysis. A representative analysis of the OFHC copper showed some fifteen impurities, the largest in amount being 0.002% sulfur, and indicated the copper to be 99.98% pure.

[5] Young, Cathcart, and Gwathmey, Acta Met. 4, 145 (1956).

described above. The cup had previously been electropolished and heated in a high vacuum. Both the cup and the crystal were heated with the induction coil, and any difference in temperature between them was not detectable with the optical pyrometer (accuracy of measurement ±5°C).

RESULTS

Different types of surface structure were obtained with the two types of crystals.

Crystals Grown from OFHC Copper

A crystal which had been machined from a single crystal rod and polished as described was heated in high vacuum to 1000°C for about 10 min. When it was examined in a beam of light, reflections were seen from the (111) and (110) poles and from the area around the (100) pole, as shown in Fig. 1. There were no reflections immediately at the (100) pole. The various reflections indicated that facets parallel to the (111), (110), and (100) planes were formed during the heating. Photomicrographs taken at the (111) pole are shown in Fig. 2. It can be seen that an initially smooth surface has been converted to a stepped or terraced surface, the flat portions of the steps being (111) planes. The orientation of the plane of the risers of the steps varied more or less continuously around the (111) pole, and the step height was $\sim 1\ \mu$. A photomicrograph taken at the (110) pole is shown in Fig. 3. The general appearance was similar to that seen at the (111) pole, with the exceptions that in certain directions from the (110) pole the risers were (111) planes and the step height was lower. Microscopic examination of the (100) pole showed a few small pits and a slight waviness, but there was no step formation as seen about the other two poles. Near the (100) pole, in all directions from it, facets were observed, such as are shown in Fig. 4, and a few pits were also seen among the facets. The faceted region at the (111) pole was larger than those at the other two poles. The facet structure in regions which were not near the three major

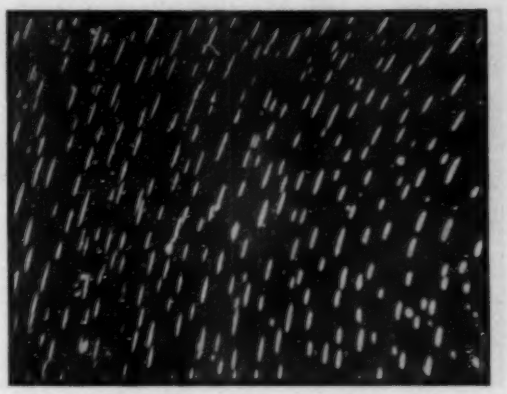

FIG. 4. Near (100) pole of OFHC copper crystal after heating to 1000°C in high vacuum. 300× dark field.

poles was a rather complicated combination of the facets around the (111), (110), and (100) poles. The formation of the facets did not appear to be particularly dependent on the time of heating. For short times (approximately 2 min) the facets were the same as those described above, but not as well formed. For times greater than 10 min, they were the same as those described. The same results were obtained on crystals heated in the range 950°–1050°C.

A second crystal was heated to 1075°C in high vacuum. On subsequent examination the results were essentially the same as before, except that the edges of the steps had become less wavy. This was particularly observable at the (111) pole where the steps had become more nearly circular, as seen in Fig. 5. For many crystals so heated, spirals were formed at the (111) poles, as shown in Fig. 6, and reported previously by Young.[5] The crystal shown in Fig. 6 was oxidized slightly after the thermal etching in order to improve the contrast for photographing. The formation of spirals at the (111) poles was reproducible with a given crystal.

The results described above were reproduced on some twenty crystals. A crystal was suspended in a copper cup made of OFHC copper, as described above, and heated to 1075°C for about 5 min. In this experiment

FIG. 3. (110) pole of OFHC copper crystal after heating to 1000°C in high vacuum. 1200×.

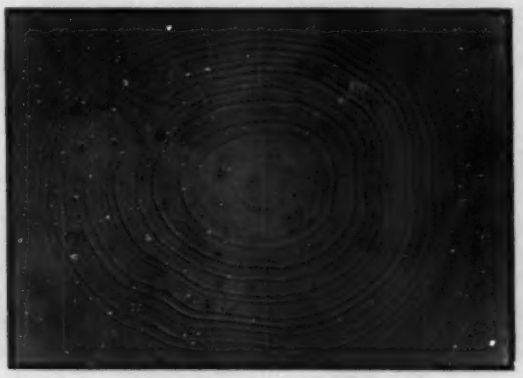

FIG. 5. (111) pole of OFHC copper crystal after heating to 1075°C in high vacuum. 000×.

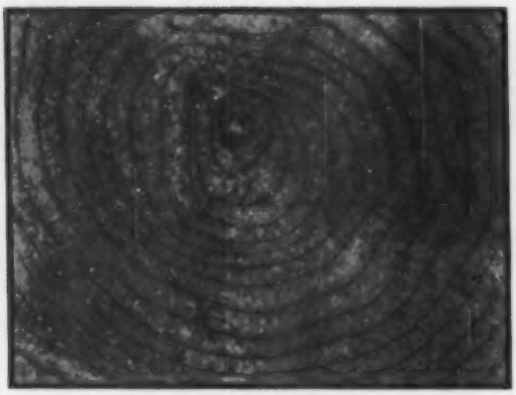

FIG. 6. Single spiral around (111) pole of an OFHC copper crystal after heating to 1075°C in high vacuum. 600×.

the crystal was more nearly in equilibrium with its vapor. Subsequent examination showed facets similar to those described above, with the exception that the step height was lower. Pits were also seen over the surface of the crystal, as shown in Fig. 7. The number of pits varied with orientation: at the (111) pole $-3\times10^6/cm^2$; near the (111) pole $-2\times10^7/cm^2$; at the (110) $-2\times10^6/cm^2$; and at the (100) $-1\times10^7/cm^2$. The number of pits which were developed was a function of the temperature of etching.

Crystals Grown from 99.999% Copper

A crystal which had been grown as a hemisphere and had not been mechanically polished was electropolished and then was heated to 1075°C in high vacuum for about 10 min. Very faint reflections from the (111) and (100) poles could be seen in a beam of light. Microscopic examination showed small steps around the (111) and (100) poles, as shown in Figs. 8 and 9. The steps extended a relatively small distance away from the poles, and no steps or facets were seen elsewhere on the crystal. The well-defined steps were $\sim0.1\ \mu$ in height immediately around the (111) pole, while the steps around the (100) pole were smaller and poorly defined. There were plateaus both near the poles and distributed among the steps, and in general a tiny pit could be detected in each plateau. Also there were pits with steps down into the pit, which in at least some cases could be resolved as a spiral step.

A crystal was heated to 1020°C in high vacuum for about 10 min. Subsequent examination revealed steps around the (111) and (100) poles as above, but the steps were smaller and less distinct. There were no pits similar to those described above, but a large number of small pits were observed about the (111) and (100) poles (see Fig. 10). The density of the pits was less immediately at the poles, and relatively few pits were seen elsewhere on the crystal. The maximum number of pits observed was approximately $1\times10^7/cm^2$.

A crystal was heated to 970° in high vacuum for about 10 min. Microscopic examination showed steps and pits around the (111) pole similar to those described after heating to 1020°C. Elsewhere on the crystal no steps were seen and the number of pits was relatively small.

The foregoing results were obtained from repeated experiments with some fifteen crystals. One crystal was machined and mechanically polished prior to electropolishing and thermal etching, with no apparent change in the facets formed.

A few experiments were carried out in which a crystal was suspended inside a copper cup and heated in high vacuum. If the cup was made of 99.999% copper, facets similar to those described above were seen on the crystal. If the cup was made of OFHC copper, it was found that the facet formation was very similar to that described under "Crystals Grown from OFHC Copper." Apparently some of the OFHC copper with its impuri-

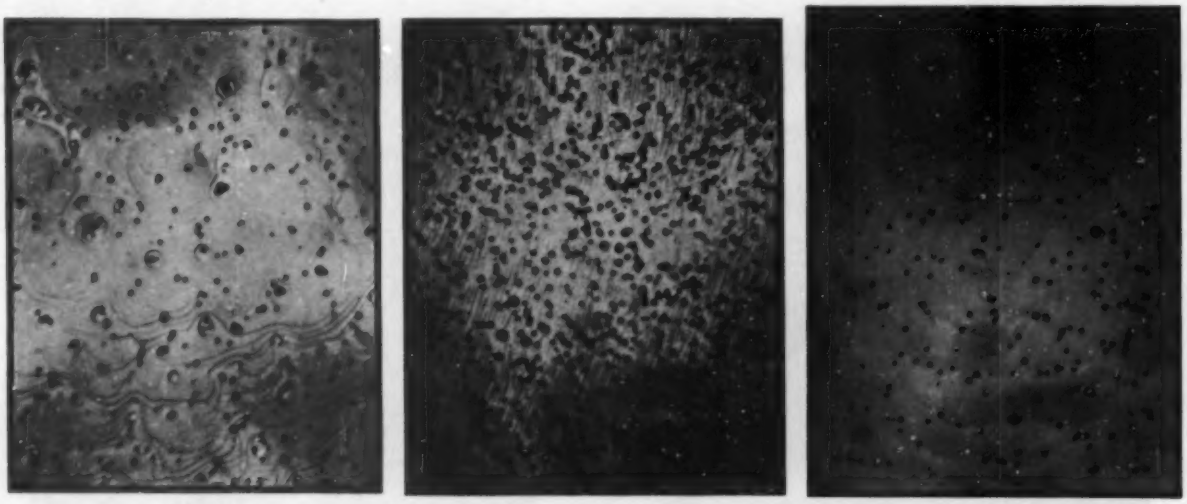

(a) (b) (c)

FIG. 7. Pits on OFHC copper crystal heated in a copper cup to 1075°C in high vacuum. 600×. (a) (111), (b) near (111), (c) (110).

ties evaporated and condensed onto the crystal of 99.999% purity causing it to behave similarly to an OFHC crystal. The crystal was then electropolished and heated in high vacuum without the cup, and results typical of the 99.999% copper crystals were obtained.

DISCUSSION

For purposes of discussion, the more important results may be summarized as follows. The evaporation of copper from spherical OFHC crystals resulted in the formation of (111), (110), and (100) facets over relatively large areas centered around the respective poles. In some cases spirals were formed around the (111) pole. When an OFHC crystal was heated in a copper cup, an appreciable number of pits was formed. In the case of crystals of 99.999% copper, (111) and (100) facets were formed over relatively small areas centered at the respective poles. Thus, the area on the sphere over which the facets formed was much smaller with the purer copper. When a crystal of 99.999% copper was heated in a cup made of OFHC copper, results similar to those given by an OFHC crystal were obtained.

The striking difference in the thermal etch patterns formed on the two types of crystals emphasizes the importance of the purity of the copper. It should be noted that the purities given (99.98% for OFHC and 99.999% for the purer material) represent values for the copper before the crystals were grown. No information is available on the final purity of the crystals as used. Also, the perfection of these crystals, in terms of dislocations and point imperfections, is not known.

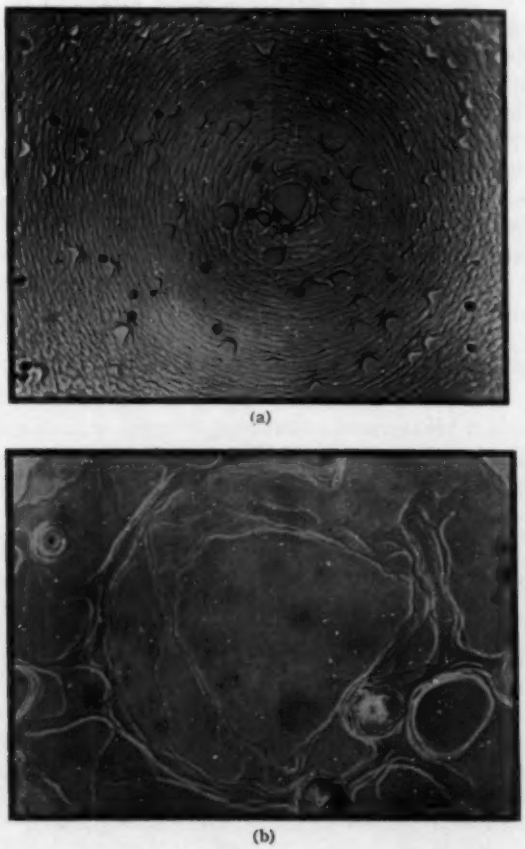

(a)

(b)

FIG. 8. (111) pole of 99.999% copper crystal after heating to 1075°C in high vacuum. (a) 150×, (b) 900×.

FIG. 9. (100) pole of 99.999% copper crystal after heating to 1075°C in high vacuum. 150×.

It is not clear whether surface energies play a role in the formation of the facets in these experiments. Obviously, the crystal was not in equilibrium with its vapor. Although an attempt was made to approach equilibrium by enclosing the crystal in a copper cup, the difference in temperature between the crystal and the cup was too great to attain equilibrium.§ Numerical values for the relative surface energies of the low index faces have been determined from these data by using a method similar to that of Moore,[6] but, since nonequilibrium conditions existed, such a determination neglects the possibility of a reasonable kinetic mechanism which could account for the arrangements of steps that were observed. A mechanism whereby large steps could be formed on evaporation of crystals is proposed by

FIG. 10. Pits on 99.999% crystal near (111) after heating to 1020°C in high vacuum. 600×.

§ A difference in temperature between the cup and the crystal of one degree (accuracy of measurement ±5°) would mean that the system was far from equilibrium.

Cabrera[9] and by Frank[9] in a kinematic theory of crystal growth and dissolution. Therefore, a determination of relative surface energies from these experiments is not necessarily correct at this time. Further experiments and more careful examination of the facets with the electron microscope are required to clarify the relation between facet formation and surface energy.

The influence of impurities on the rates of evaporation probably played an important role in determining the size of the facets which were formed. Starting from a smooth spherical surface with steps of atomic dimensions, a faceted surface with steps approximately 1 μ in height was produced on OFHC copper crystals by evaporation. An important question is why the atomic-size steps changed into large steps. Consider two surfaces, A and B, which have the same average orientation. Surface A is composed of facets separated by larger steps, while surface B is composed of the same facets separated by monoatomic steps. Then surface A would have the lower surface energy, because of the smaller number of edge positions in A as compared to B. Thus, if there were some mechanism to cause atomic-size steps to form large steps during the evaporation process, it is probable that the larger steps would be stabilized because of the lower surface energy. The presence of impurities in the copper could account for the formation of the large steps in the following way. Evaporation probably occurs from the edges of steps. The steps are moved across the surface as evaporation occurs, and, if the impurities in the crystal have less tendency to evaporate than the copper, impurity atoms would accumulate at the steps. The accumulation of impurity would cause a step to slow down in its motion across the surface, and other steps to catch up with it. Thus, large steps would be formed, and they would be stabilized because of the lower surface energy, as described above. Such a mechanism could account for the large difference in step height noted between OFHC and 99.999% copper crystals.

It seems reasonable to assume that the pits formed during evaporation were related to dislocations.[4,7] For OFHC copper, few pits were formed when the crystal was heated without the cup. This suggests that under these conditions the lateral rate of advance of the steps is equal to or greater than the evaporation rate from the dislocations. It follows that dislocations are not important sources of steps for these conditions of evaporation. The difference in energy required to evaporate two atoms, one at a dislocation and one not at a dislocation, is a small quantity compared to the total evaporation energy.[10] For the nonequilibrium conditions, this small difference in energy would not be enough to promote evaporation at dislocations over evaporation elsewhere, and thus the dislocations would not play an important role in the evaporation of OFHC copper.

Under the more nearly equilibrium conditions of heating in the cup, the small energy difference between atoms at dislocations and atoms elsewhere becomes significant, and pits are formed at dislocations. For these conditions dislocations can be an important source of steps on OFHC copper, as is evident at the (111) pole, Fig. 7(a), where the number of steps is small and where a series of small steps around some pits can be seen. At orientations such that a large number of steps is present, the dislocations do not appear to be so important as sources of steps [see Fig. 7(b)].

For the 99.999% copper, pits were formed on some planes under nonequilibrium conditions of evaporation. The number of pits was a function of the temperature of etching. No satisfactory explanation can be given at present for the differences in the conditions necessary for the formation of pits on the two kinds of copper.

The conditions for formation of the pits, presumably at dislocations, are rather critical. The fact that the number of pits formed was a function of the temperature of etching for both OFHC and 99.999% crystals indicates that there was not a one-to-one correspondence between pits and dislocations. The observed difference in number of pits on different crystal planes probably does not imply that there were different numbers of dislocations ending on the several planes. Other techniques of observing dislocations,[11] such as the observation of etch pits formed in solutions, indicate that the number of dislocations does not vary so markedly with orientation.

ACKNOWLEDGMENT

It is a pleasure to acknowledge many valuable discussions with Professor N. Cabrera of this Laboratory. This work was supported in part by the Office of Naval Research.

[9] N. Cabrera and D. A. Vermilyea, *Growth and Perfection of Crystals*, edited by Doremus, Roberts, and Turnbull (John Wiley & Sons, Inc., New York, 1958), p. 393; F. C. Frank, *ibid.*, p. 411.

[10] N. Cabrera, *Semiconductor Surface Physics*, edited by R. H. Kingston (University of Pennsylvania Press, Philadelphia, 1957), p. 327.

[11] F. W. Young, Jr., J. Appl. Phys. **29**, 760 (1958).

JOURNAL OF APPLIED PHYSICS VOLUME 31, NUMBER 2 FEBRUARY, 1960

Factors Affecting the Ductility and Strength of NaCl Single Crystals Tested in Flexure

C. A. Stearns, A. E. Pack, and R. A. Lad
Lewis Research Center, National Aeronautics and Space Administration, Cleveland, Ohio
(Received July 6, 1959)

An experimental investigation has revealed that the initial deformation of NaCl single crystals is anelastic rather than Hookean. This anelastic deformation is manifested by a low slope foot in the load-deflection curve. The magnitude of the foot is dictated by the pretreatment given the specimen. Treatments which increase or decrease the fresh dislocation density respectively increase or decrease the length of the initial anelastic foot.

The order of increasing ductility and strength with specimen pretreatment was found to be (1) heated at 135°C, (2) as cleaved, (3) coated with silver, (4) heated at 135°C and then water polished, (5) water polished and then coated with silver, (6) water polished, (7) water polished and then heated at 135°C, (8) annealed at 700°C, and (9) annealed at 700°C and then water polished.

The experimental results have been discussed in terms of the role played in deformation and fracture by surface cracks, grown-in dislocations, and fresh dislocations.

INTRODUCTION

RECENT experiments with single-crystal NaCl and MgO have shown that these materials possess a fair degree of inherent ductility at room temperature.[1–3] These experiments also indicate that the ductility and strength are extremely dependent on both the mode of specimen preparation and the treatment of the specimen after preparation. Many of the findings can be interpreted to indicate that the nature of the surface is the prime factor governing the behavior of the specimen. For example, the ductility of old cleaved crystals of NaCl can be substantially increased by treatments such as surface dissolution with water, coating with a thin (25 A) layer of silver, or deposition of a thin film of stearic acid. However, other means for changing ductility and strength, for example, annealing and quenching, which have a predominant effect in the bulk rather than in the surface, suggest that possibly more than just the nature of the surface is involved.

The purpose of this paper is to describe the results obtained in two sets of carefully controlled experiments on NaCl single crystals. In these experiments the effects on ductility were studied in relation to water treatment, annealing conditions, surface coating, quenching, and x-irradiation. The results were examined in terms of present concepts of the role played in deformation and fracture by surface cracks, grown-in dislocations, and dislocations introduced during the cleavage process.

The work reported in this paper was performed in a manner designed to minimize the difficulties usually encountered in an investigation of this type. The specimens used in each set of experiments were taken from a single melt and had identical histories. The flexure specimens varied only slightly in dimensions so that direct comparison of the load-deflection curves could be made.

[1] Gorum, Parker, and Pask, J. Am. Ceram. Soc. **41**, 161 (1958).
[2] Lad, Stearns, and Del Duca, Acta Met. **6**, 610 (1958).
[3] E. Aerts and W. Dekeyser, Acta Met. **4**, 557 (1956).

EXPERIMENTAL

Specimens

The material used in this study was Harshaw single-crystal NaCl. The specimens in group I were from a single melt and were supplied in the form of crystals cleaved to the approximate dimensions of 3×7×40 mm. The specimens in group II were cleaved in our laboratory from larger pieces all from another single melt. All specimens were cleaved at least thirty days prior to treatment or testing.

Water Polishing

Two water polishing procedures were employed. Specimens to be completely water polished were immersed successively for 15 sec in four 25 ml volumes of distilled water at room temperature. They were then rinsed with dry methanol and air dried. The second procedure was used when only part of the specimen was to be water polished. In this case, the specimen face was passed successively over water saturated cotton and methanol saturated cotton and finally air dried.

Annealing

Specimens to be annealed were placed directly into a quartz tube closed at one end. All anneals were done in air and at a temperature of 700±10°C followed by a 24 hr furnace cool.

X-Irradiation

Specimens to be irradiated were wrapped in aluminum foil and mounted on the end of the shaft of a 4-rpm clock motor. The specimens were rotated with their long dimension normal to the x-ray beam. The x-ray tube was a Machlett AEG-50 having a tungsten target and a beryllium window. The tube was operated at 50 kv and 30 ma.

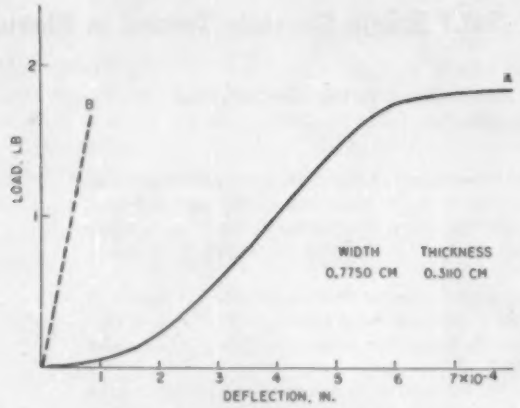

FIG. 1. Initial portion of load-deflection curve for NaCl single-crystal specimen. A is the experimental curve and B is the calculated Hooke's law line.

Flexure Tests

Specimens were tested in flexure in an Instron Tensile Testing Machine equipped with a compression type load cell and bending jig. The four-point loading method subjects an extended area of the specimen to a constant bending stress; this condition was deemed necessary to obtain representative data for specimens having a distribution of nucleation sites for destructive crack formation. The reactance and loading points, rigidly attached to the load cell and movable crosshead, respectively, were 0.1035 in blades of Monel ground to a 0.0625-in. radius at the specimen contact end. The distance between centers of the loading points was 1.1770 in. and the moment arm was 0.2690 in. The bending jig was aligned in the testing machine to within 0.0001 in.

The Instron is generally considered to be a hard machine. However, in these experiments, the load cell deflection was great enough to be an important factor and correction was always made for this factor. The load cell deflection coefficient for the load cell used was experimentally determined to be 1.00×10^{-4} in. per lb of load.

All the bend tests were run in air at room temperature and at a constant bending rate of 0.002 in. per min. The data were obtained in the form of strip chart traces.

Load-strain data were obtained in some experiments by use of wire resistance strain gauges bonded with Duco cement to the tension and/or compression faces of the specimens. The bond was cured for 50 hr at room temperature. Strains were measured with an SR-4 strain indicator.

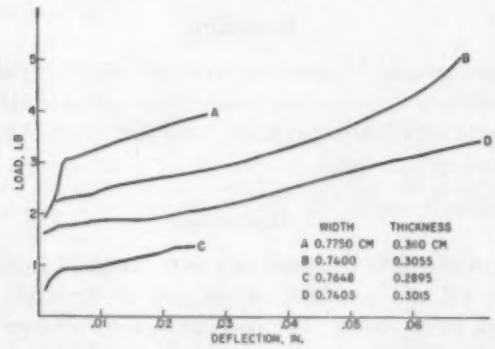

FIG. 2. Load-deflection curves for NaCl single-crystal specimens. A is the curve for an as-cleaved specimen, B is for a specimen water polished on the tension side, C is for a specimen water polished on the compression side, and D is for a specimen water polished on both the tension and compression sides.

RESULTS

General Characteristics of Load-Deflection Curves

Figure 1 shows the initial portion of the load-deflection curve for an as-cleaved specimen. The most striking feature exhibited by the specimens tested was the existence of an initial anelastic region having an extremely low slope. The Hooke's law line calculated from the elastic constant is included in the figure for comparison.

TABLE I. Effects of treatments on length of foot of load-deflection curve for NaCl specimens from group I.

Number of specimens	Treatment	Foot length $\times10^4$, in.
7	As cleaved	2.5±0.3
5	Annealed 24 hr at 700°C	2.4±0.3
7	Completely water polished	0.6±0.1
4	X-irradiated 72 hr	11.8±2.1
5	Quenched from 700°C in CCl_4	4.6±0.5

Flexure tests were run on polycrystalline nickel and copper specimens of small dimensions in order to insure that the load-deflection curves were characteristic of the NaCl and not an artifact of the test procedure. The nickel and copper specimens yielded straight lines and the resultant Young's moduli agreed excellently with literature values. These results also showed that the reproducibility of the test was within ±5%.

Load-strain data obtained with strain gauges mounted on the tension and compression faces of the specimen also indicated the lack of a Hooke's law region. In addition, it was found in these experiments that the load-compressive strain and the load-tensile strain curves differed in shape. Simultaneously recorded load-deflection curves were identical to those for crystals without strain gauges. Thus, the presence of strain gauges did not affect the deformation behavior.

Cyclic stressing showed the initial deformation to be anelastic. When a specimen was loaded within this range and immediately unloaded, recovery occurred over a period of several hours. The photoelastic strain patterns observed through a polariscope also showed the same slow recovery. The experiment could be re-

peated any number of times provided that enough time was allowed for the recovery to take place.

Effect of Specimen Pretreatment

The length of the initial "foot" of the load-deflection curve was found to depend in a marked way on the type of pretreatment of the specimen. The foot length was taken to be the intercept of an analytically determined tangent drawn through the point of inflection. Foot lengths for a variety of treatments are listed in Table I. A fourfold variation occurs between cleaved and water polished specimens, and x-irradiation produces even greater changes.

The effect of pretreatment on the deflection at failure D_F and the load at failure L_F are indicated in Table II. The values listed are averages and the indicated limits are computed probable errors. The deflection at fracture was affected by pretreatment in a more pronounced way than was the load at fracture. Thirty-six fold changes in D_F occurred, while L_F varied by less than a factor of six.

TABLE II. Deformation and load at failure for NaCl specimens of group II subjected to pretreatment.

Number of specimens	Treatment	$D_F \times 10^4$, in.	L_F, lb
11	As cleaved	47±5	2.1±0.2
5	Annealed 24 hr at 700°C	710±40	7.1±2.0
5	Annealed 24 hr at 700°C and water polished	1450±160	14.5±3.9
5	Heated 1 hr at 135°C	38±5	2.2±0.3
5	Heated 1 hr at 135°C and water polished	165±44	3.3±0.3
10	Water polished	343±53	3.2±0.2
6	Water polished and heated 1 hr at 135°C	367±98	4.8±0.5
5	Water polished and coated with silver	176±11	2.4±0.5
5	Coated with silver	112±23	2.7±0.6

Pronounced variations in behavior were noted when only portions of a specimen were water polished. In Fig. 2 are shown the results of such experiments. When both the tension and compression faces were water polished the resultant curve was identical to that for a completely polished crystal. This result was taken to indicate that the nature of the side surfaces plays little or no role in the plastic bending behavior.

Annealing of the cleaved specimens increased their ductility with little alteration of the fracture load (Fig. 3), while quenching increased the fracture load but did not alter the ductility. X-irradiation (Fig. 4) for periods as long as 72 hr always decreased ductility. The 72 hr irradiation produced the least ductile specimens tested. The fracture stress was changed very little.

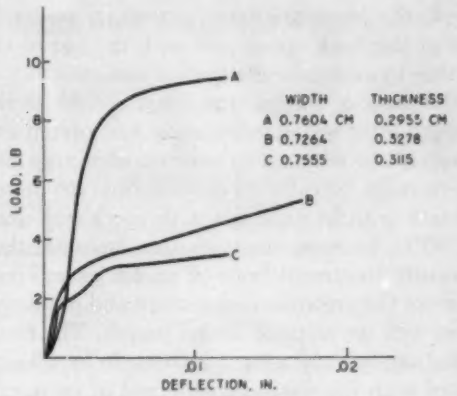

FIG. 3. Load-deflection curves for NaCl single-crystal specimens. A is the curve for a specimen quenched from 700° to 25°C in CCl_4, B is for a specimen annealed 40 hr at 700°C, and C is for an as-cleaved specimen.

DISCUSSION

Recent work[4,5] on the nature of the dislocation loops introduced into a crystal by cleavage indicates that they may be primarily responsible for the initial anelastic region (or "foot") of the load deflection curve. The dislocation loops introduced during cleavage are more numerous in the surface layers than in the interior. They have been found to move readily on the application of low stress, probably because they are not encumbered by a Cottrell atmosphere. The flexure test emphasizes these characteristics because the applied stress is a maximum in the surface region.

It is proposed that the application of low stress causes the loops introduced by cleavage to expand until they interact with the stress fields of dislocations which remain static under the low applied stress. The expansion of any particular loop will cease when the opposing stress balances the applied stress; for these low stresses this will be long before they interact strongly enough to cause permanent locking. When the applied stress is

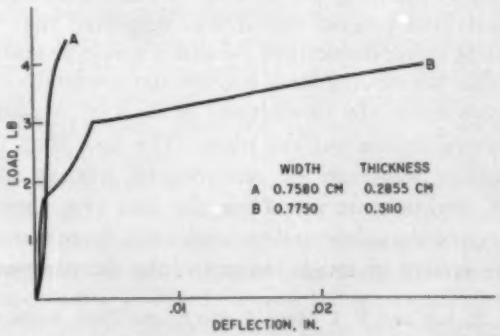

FIG. 4. Load-deflection curves for NaCl single-crystal specimens. A is the curve for a specimen x-irradiated for 72 hr and B is for an as-cleaved specimen.

[4] Stokes, Johnston, and Li, Third Technical Report under Office of Navy Research Project NOnr-2456(.00) NR-039-04.

[5] J. J. Gilman and W. G. Johnston, *Dislocations and Mechanical Properties of Crystals* (John Wiley & Sons, Inc., New York, 1957).

removed, the loops are free to contract under the influence of the back stress and with the aid of thermal activation to overcome dissipative forces.

On the basis of this picture, the fourfold decrease in foot length after water polishing is interpreted as being the result of the removal by solution of a large majority of the cleavage introduced dislocations. An increase in foot length is to be expected with specimens quenched from 700°C to room temperature, because the high temperature treatment boils off vacancies and impurity atoms from the grown-in dislocations and produces more loops as well as loops of longer length. The results on x-irradiation, namely a large increase in foot length, are in accord with the softening observed in creep of NaCl after short irradiation.[6] In that case it was proposed that the first effect of irradiation by x-rays was to disperse vacancy clusters which were in the vicinity of dislocations. The lack of any change in foot length for the annealed specimens is believed to be due to the fact that our specimens were heated rapidly. Kear and Pratt[7] have shown that (because of the stress gradients resulting from the low thermal conductivity) slip lines are produced in ionic crystals by up-quenching. Apparently the increase in dislocation concentration produced by the up-quench masked the anticipated decrease in foot length.

In addition to causing marked changes in the length of the initial portion of the load-deformation curve, the various methods of pretreating the specimens also affected the deformation and load at fracture. Since most of these treatments primarily affected the surface regions of the crystals, their possible role in the nucleation and growth of cracks might be worthy of consideration.

Earlier work by Metz and Lad,[8] on nucleation sites for the crystallization of evaporated silver films, indicated that linear sites having an average length of 10^{-4} cm and occurring in concentrations of $10^5/cm^2$ can be made to form on water polished annealed crystals by heating in the range 50° to 200°C. These sites form by an activated process and it was suggested that they might be either dislocation—vacancy arrays or cracks—and that the driving force was the stress introduced by the conversion (by dissolution) of an interior plane to a nonequilibrium surface plane. The fact that these nucleation sites can be removed by heating above 200°C makes more attractive the idea that they are arrays of dislocations and vacancies which are attracted to the surface by image forces and the thermodynamic requirement that their concentration be greater in the surface layers than in the interior.

A cleaved surface would also be expected to contain crack nucleation sites of the above-mentioned type because cleavage creates a nonequilibrium surface. In addition, the surface will contain many other sites such as steps and possibly cracks together with stress concentrations which can aid in the development of large cracks. Electron diffraction studies of x-irradiated NaCl surfaces have illustrated the role of surface stresses in the disorientation of NaCl surfaces by x-ray irradiation.[9] Cleaved crystals were disrupted much more readily than were annealed or water polished ones.

The findings of this investigation lend credence to the picture that the ductility is limited by the stress required to form and propagate the fatal crack, and that treatments which eliminate crack nuclei or make their formation more difficult tend to result in higher ductility and fracture stress. The order of increasing ductility as well as stress at fracture is just that which would be predicted by a consideration of the types of crack nucleation sites which might be present and also the ease with which they would be expected to form and propagate.

The increase in ductility and fracture stress obtained by coating with a thin layer of silver might be interpreted as due to the relief of surface flaws. However, it is apparent that possible surface reactions with atmospheric gases must be investigated in more detail before further speculation can be made regarding either crack formation or the role of evaporated films.

CONCLUSIONS

The load-deflection curves for NaCl single crystals tested in flexure show an inital anelastic region rather than the conventional linear Hooke's law region. The magnitude of this anelastic region or "foot" is dictated by the type of treatment given the specimen. This can be understood in terms of the dislocation loops introduced into the specimen during the cleavage process and the effects of various treatments on the number and/or properties of these dislocation loops.

The flexure tests showed that the order of increasing ductility with treatment is (1) heated at 135°C, (2) as cleaved, (3) coated with silver, (4) heated at 135°C and water polished, (5) water polished and coated with silver, (6) water polished, (7) water polished and heated at 135°C, (8) annealed at 700°C, and (9) annealed at 700°C and water polished. The variation of deformation and load at fracture with these treatments indicates that the nucleation and growth of cracks are the primary factors governing ductility and strength.

[6] R. A. Lad and F. I. Metz, J. Mech. and Phys. Solids **4**, 28 (1955).
[7] B. H. Kear and P. L. Pratt, Acta Met. **6**, 457 (1958).
[8] F. I. Metz and R. A. Lad, J. Phys. Chem. **60**, 277 (1956).
[9] H. R. Leider, Phys. Rev. **101**, 56 (1956).

Torsion Induced Recrystallization of Molybdenum and Tungsten Filaments*

F. E. GIFFORD† AND E. A. COOMES
University of Notre Dame, Notre Dame, Indiana
(Received July 23, 1959)

When an optimum amount of permanent twist is introduced in 3- to 10-mil filaments of molybdenum or tungsten, single crystals up to 15 cm in length grow by either the moving gradient or Robinson techniques. About 5 turns per inch for W at 2500°K or for Mo at 1650°K was favorable. Although there is evidence of perfection in the volume of the crystals, the twist leaves a threadlike surface imperfection which remains even after severe heat treatment at evaporation temperatures.

INTRODUCTION

ALTHOUGH large single crystals of refractory metals have been grown by floating zone melting[1] in self-supporting rods of large diameter, recrystallization by grain growth in fine filaments of tungsten and molybdenum, of interest to workers in electron emission and surface physics, lacks a well understood and satisfactorily reproducible technique. In the case of tungsten, good single crystals occupying the entire cross section and as long as 10 cm have been grown[2,3] in 3- to 5-mil 218 nonsag wire from a lot drawn before World War II. When the die marks were removed by careful grinding,[4] either of two techniques produced usable crystals. Nichols[2] utilized the moving gradient method; the filament mounted in vacuum is subjected to a temperature discontinuity moved along the wire at a fixed rate. In the simple implementation[2] of this method, the temperature step is provided at the surface of a mercury column which is lowered at the desired rate, while the section of filament above is maintained at a constant temperature optimum for growth. In the Robinson method the filament, mounted in vacuum, is held at some constant temperature for a number of hours, and grain growth proceeds by a simple thermally activated process[3] for which heating is continued until grain boundaries no longer advance. Recrystallization was complete after 18 hr for the special prewar 218 wire at 2000°K. Although grain growth terminates in a definite time at a definite temperature, the length and perfection of any single crystal produced varies from filament to filament.

The foregoing methods, however, did not produce[5] long single crystals in filaments of postwar 218 wire. Recently these two methods were instrumented in this laboratory and crystals were grown by both techniques when applied to the special prewar tungsten filament, but five other sources of 3- to 5-mil 218 wire drawn in prewar and postwar eras never recrystallized to lengths of more than a few wire diameters. No improvement or modification resulted on variations in grinding, electrolytic polishing, or insertion of permanent stretch in graduated amounts from zero to yield point. Identical negative results followed in the case of molybdenum, for which no favorable lot of crystal-growing wire has been found.

Gifford's experiment[6] demonstrated that recrystallization over centimeters of length could be produced in 3- to 10-mil molybdenum or tungsten filaments taken from any lot of wire at hand and without mechanical grinding, if a prescribed amount of permanent twist were uniformly inserted and favorable temperature chosen. Experimental details are given below.

EXPERIMENTAL

A chosen length of raw filament wire was mounted taut between two aligned heads fixed at constant distance apart, and one head then rotated until desired amount of twist existed. Uniformity and pitch were examined under a 100-power optical microscope. Length was standardized at 10 in. and twists up to 20 turns per inch (TPI) were used (Mo filaments broke at about 30 TPI). With the twist inserted, recrystallization proceeded equally well by both moving gradient and Robinson methods, and crystals were identified by their thermionic emission *vs* orientation in a cylindrical electron projection tube.[2] A lowering rate of 0.5 in./hr was always used in the moving gradient method, since this was not a critical parameter. The sequence of pictures in Fig. 1 is a typical record of the effect of twist on recrystallization by the gradient method. The 5-mil molybdenum filaments represented here were taken from the same spool of wire; the growing temperature was 2000°K. In Fig. 1(A), the case of no twist, and 1(H), first twisted 10 TPI right followed by 10 TPI left, there is no evidence of recrystallization, although the die marks appear prominently in the projection pattern. In Fig. 1(B) and (C) with ½ and 1 TPI respectively die marks still show on the surface, but crystal growth extending across the wire diameter is evident, a crystal 5 cm long having grown in the 1 TPI wire. For 2, 5, 10, and 20 TPI, Fig. 1(D) to (G), the die marks have receded to a single threadlike imper-

* This work supported in part by Office of Naval Research and U. S. Atomic Energy Commission.
† Now at Bendix Corporation, Detroit, Michigan.
[1] David, Calverly, and Lever, J. Appl. Phys. **27**, 195 (1956).
[2] M. H. Nichols, Phys. Rev. **57**, 297 (1940).
[3] C. S. Robinson, J. Appl. Phys. **13**, 647 (1942).
[4] Johnson, White, and Nelson, Rev. Sci. Instr. **9**, 253 (1939).
[5] G. E. Moore (private communication).
[6] F. Gifford and E. Coomes, Bull. Am. Phys. Soc. Ser. II, **1**, 333 (1956).

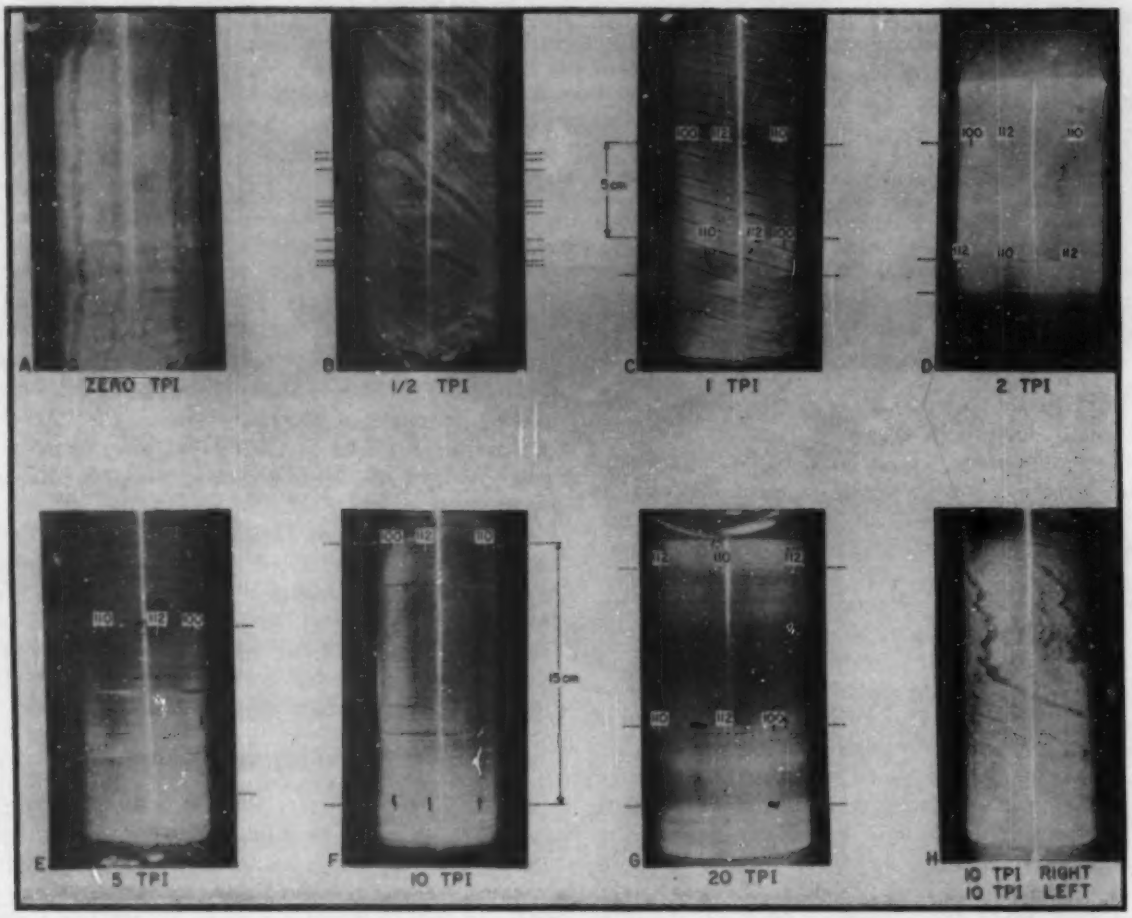

FIG. 1. Electron projection patterns showing the effect of twist on crystal growth in 5-mil molybdenum filaments. The permanent twist in turns per inch (TPI) inserted before heating is indicated at each picture. Gradient method at 2000°K was used (see text). Horizontal dotted lines show limits of grain growth; crystal directions were identified from thermionic emission *vs* orientation plot. Die marks are prominent in (A), (B), (C), and (H); in (D), (E), (F), and (G) a threadlike imperfection with pitch of twist remains. At (F) entire filament has converted to a single crystal.

fection on the surface, and crystals up to 15 cm in length have grown. In case (F) the *entire* length of mounted wire has become a single crystal. Identification of crystal directions indicated in the figures was made by comparison with the Nichols pattern.[2]

Figures 2 and 3 give results of the Robinson technique with the same lot of 5-mil Mo wire. For Fig. 2(A) to (E), five lengths were twisted to 10 TPI and each heated 15 hr in vacuum in the range 1300°–1900°K. Recrystallization occurred between 1550°–1750°K, with

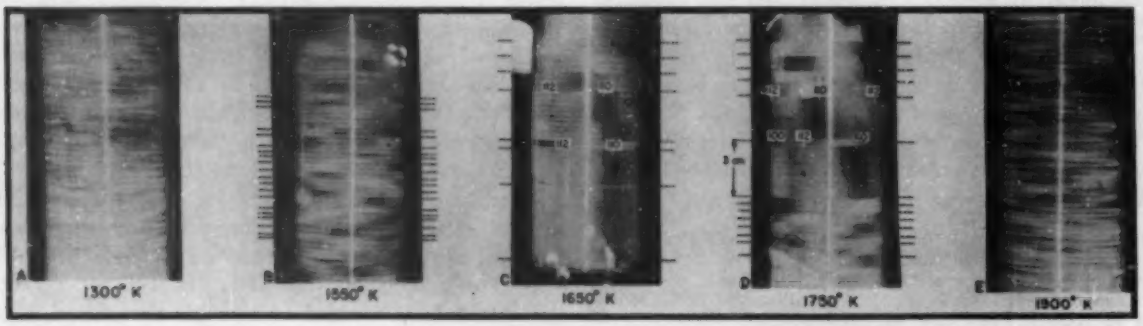

FIG. 2. Electron projection patterns showing the effect of temperature on crystal growth by the Robinson method for previously twisted 5-mil molybdenum filaments. All filaments were twisted 10 TPI and heated for 15 hr at temperatures indicated. Longest perfect crystal grew at 1650°K, shown at (C).

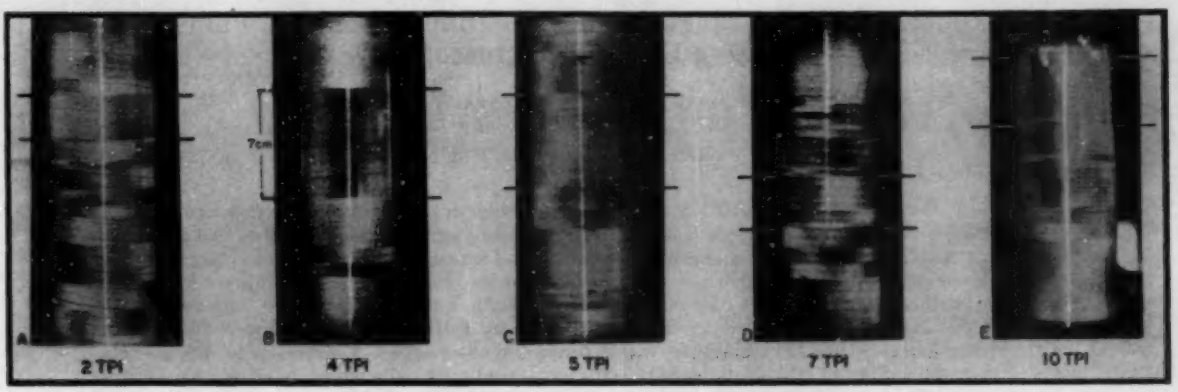

FIG. 3. Crystal growth as a function of twist in 5-mil molybdenum from the same lot used in Fig. 2. Robinson method at 1650°K was employed. Longest perfect crystal was obtained for 4 TPI, shown at (B).

longest crystal at 1650°K, Fig. 2(C). Crystal growth at 1650°K with the twist varied from 2 to 10 TPI is shown in Fig. 3(A) to (E); each of these filaments has single crystals, with the longest in the 4 TPI wire, Fig. 3(B).

Shilts[7] utilized an experimental program with the Robinson method embracing the two procedures represented by Figs. 2 and 3 to obtain the optimum twist-temperature conditions for W and Mo wire. While there was variation from source to source because of difference in impurity content and history of manufacture, such a condition could always be found. In our experiments the best parameters were found to be: ~5 TPI, ~2500°K for tungsten, giving 10-cm crystals; and ~5 TPI, ~1650°K for molybdenum, giving 7-cm crystals. Figure 4 shows two large crystals grown in tungsten[8] by this program.

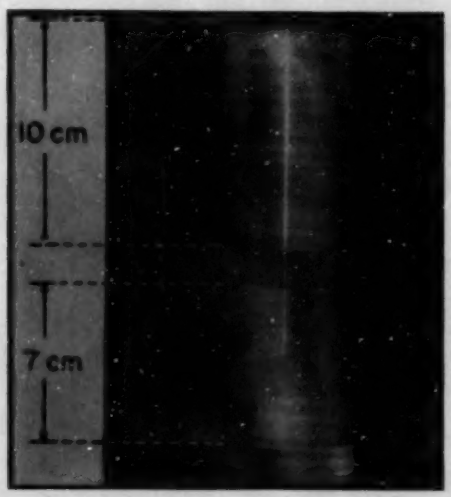

FIG. 4. Crystal growth in 5-mil tungsten postwar 218 wire. Twist of 4 TPI was inserted, and recrystallization carried out by Robinson method at 2550°K.

[7] J. Shilts and E. Coomes, Bull. Am. Phys. Soc. Ser. II, 1, 333 (1956).

[8] J. Menard, Master's Thesis, University of Notre Dame (1957).

DISCUSSION

A method to completely remove the surface imperfection which appears as a bright threadlike emission pattern with the same pitch as the twist [cf. Fig. 1(F) and (G)] has not been found. Even after prolonged heating at temperatures where rapid evaporation occurs the imperfection may be optically observed. Laue x-ray patterns taken at intervals along the (110) plane on specimens such as that shown in Fig. 1(F) before severe heating reveal a single crystal with some strain. When emitter tips etched from a crystal are examined by field ion microscopy,[9] freedom from imperfections at least near the axis of the wire is confirmed. There is some evidence that the threadlike imperfection on a 5 TPI Mo crystal is too localized to affect the single-crystal work function pattern: photoelectric Schottky plots[10] taken after prolonged heating reveal no fine scale patch structure, and the work function obtained from these data agrees with the Fowler determination.[11]

The physics of the crystal growth as influenced by the torsional strain needs further study. If the effect of twisting were simply to break up fibers, recrystallization then proceeding according to the small grain hypothesis,[3] the result given in Fig. 1(H) is difficult to explain. Since the wire does not melt, presumably the crystal grows as a result of competition between the absorption of crystallites activated by thermal energy input and the suppression of nuclei around which new crystallites form. Since the latter process is dependent upon concentration of lattice imperfections, the large strain introduced by twisting might exert a strong control.

[9] E. W. Müller (private communication).

[10] D. W. Juenker, J. Appl. Phys. 28, 1398 (1957).

[11] Results of Juenker and Jaklevic (to be published) for the use of which the authors express their appreciation.

Determination of Magnetization Distribution in Thin Films Using Electron Microscopy*

HARRISON W. FULLER AND MURRAY E. HALE
Computer Products Division, Laboratory for Electronics, Inc., Boston, Massachusetts
(Received September 22, 1959)

Some new developments are reported in the technique of observing magnetization in thin ferromagnetic films by transmission electron microscopy, and the results of some observations are described that contribute to an understanding of the magnetic character of thin films. Two modes of operation of a microscope are explained, one using projector magnification alone, and one using both objective and projector lenses. The intensity distribution images of the magnetization distribution in a thin film is derived from the Lorentz force acting on an electron passing through the film. The intensity distributions for some simple domain walls are computed and compared in various ways with experimental observations. A magnetization ripple model is proposed and justified to explain an intensity texture observed principally when projector magnification alone is used. The texture is shown to be an orthogonal map of the magnetization of the film, and to be of use in interpreting wall structures. High magnification and resolution wall micrographs are obtained using objective magnification, and a direct measurement of the wall thickness and shape can be made in this way. 180° walls in a Fe-Ni alloy film of about 200 A thickness are found to have a width of $2\delta = 1500$ A, using the wall model $\cot^{-1}\theta = -\sinh x/\delta$. The effect of finite resolution on the measurements is discussed. It is shown that the magnetization distribution of a wall can be obtained from the measured intensity distribution by inverting the parametric equation solution for the intensity distribution.

INTRODUCTION

SEVERAL means have been used for observing domains and domain walls in thin ferromagnetic films. Fowler and Fryer[1] used the Kerr magneto-optic effect to view domains in Permalloy films, while others have employed the Faraday magneto-optic effect.[2,3] Williams and Sherwood[4] and Huber, Smith, and Goodenough[5] have used powder patterns to great advantage in detailed studies of domain walls in thin films. Mayer[6] has shown that a representation of domain walls in films can be obtained by techniques of electron mirror microscopy, wherein the trajectory of a reflected electron is influenced by the external fields of domain walls.

An electron-optical method of viewing domain walls in thin films was more recently demonstrated[7] that employs a standard transmission electron microscope. In this method the electrons pass through the film, and the direct interaction of the electron with the specimen magnetization is responsible for the imaging. The present paper presents further developments of the method, and demonstrates how this means of observation is capable of giving quantitative descriptions of the magnetization distributions in thin films that could at best be deduced only indirectly by other means.

Figure 1 shows an electron micrograph of domain walls in a thin film using one mode of operation of a standard instrument. Note the alternation of dark and light wall images due to the divergence or overlap of the beam of electrons after passing through the deflecting magnetization of the specimen.[7] In this mode of operation of the microscope a very large amount of divergence or overlap can occur. The mode of operation

FIG. 1. Electron micrograph of domain walls in a Permalloy film using projector magnification only. Grid spacing is 200/in.

* This work was supported in part by Bell Helicopter Corporation through Contract Nonr-1670(00), and by Office of Naval Research Information Systems Branch under Contract Nonr-2676(00).

[1] C. A. Fowler, Jr., and E. M. Fryer, Phys. Rev. **100**, 746 (1955).
[2] Williams, Sherwood, Foster, and Kelly, J. Appl. Phys. **28**, 1181 (1957).
[3] M. E. Hale, Fifth Symposium of the American Vacuum Society, Paper No. 41, (1958).
[4] H. J. Williams and R. C. Sherwood, J. Appl. Phys. **28**, 553 (1957).
[5] Huber, Smith, and Goodenough, J. Appl. Phys. **29**, 294 (1958).
[6] L. Mayer, J. Appl. Phys. **28**, 975 (1957).
[7] Hale, Fuller, and Rubinstein, J. Appl. Phys. **30**, 789 (1959).

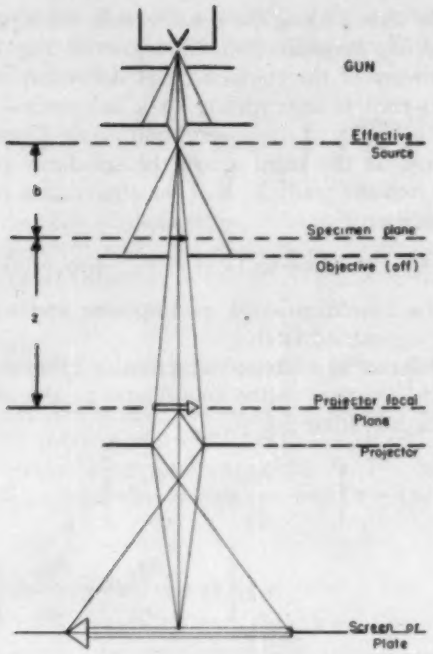

FIG. 2. Operation of electron microscope to obtain magnetization images using projector magnification only.

is shown schematically in Fig. 2, where it is seen that the principle features are: extreme overfocusing of the condenser to give a small, distant, effective illuminating source; inoperative objective, except for small fields to cause film switching; and finally, full projector magnification of the unfocused shadow-image appearing at the projector focal plane a distance z below the specimen.

A second mode of instrument operation using the objective lens will be described in a later section, following a treatment of what can be learned by use of the first mode. The primary advantage of the first mode is the great sensitivity of such an observation to relatively small and slow variations in the magnetization of a specimen.

ELECTRON TRAJECTORIES

The effect on the trajectory of an electron passing through a magnetized film will now be considered in order quantitatively to account for the domain wall images that have been observed. The expression for the force on an electron traveling through a magnetized medium still appears to be a matter of controversy, and an exact expression may be dependent on the velocity of the electron.[8] The present calculations are based on the force expression

$$\mathbf{F}=-\frac{e}{c}(\mathbf{v}\times\mathbf{B})=-\frac{4\pi e}{c}(\mathbf{v}\times\mathbf{M}), \qquad (1)$$

where e is the electronic charge (esu), c the velocity of light, $\mathbf{v}$ the velocity of the electron, $\mathbf{B}$ the flux density (gauss), and $\mathbf{M}$ the magnetization of the medium. It is clear from experimental observations that $(\mathbf{v}\times\mathbf{H})$ is not the correct expression to use for this case. The subsequent development neglects demagnetizing and externally applied fields, and it will be shown in special cases of interest that the existence of even large demagnetizing fields does not influence the principle results, though this is not universally true. Magnification by lenses in the electron-optical system, furthermore, are not included in the development, since the inclusion of appropriate factors is straightforward except for one case that will be noted.

Figure 3 shows a top and side view of the geometry of a film and electron trajectories, assuming no objective or projector magnification. The film of thickness τ in the x, y plane is shown containing a Neel wall[9] of width $2a$ along the y axis, with center at $x=0$. The electrons are assumed to arrive at the specimen parallel to the z axis, and enter the film perpendicular to the plane of the film; a correction for electron-source divergence is added later.

Using a left-handed coordinate system, and assuming a deflecting force is exerted on the electrons only by the film magnetization and only during their transit through the film, Eq. (1) gives

$$\mathbf{F}=-4\pi\frac{ev_0}{c}(\mathbf{z}_1\times\mathbf{M})=4\pi\frac{ev_0}{c}(M_x\mathbf{y}_1-M_y\mathbf{x}_1), \qquad (2)$$

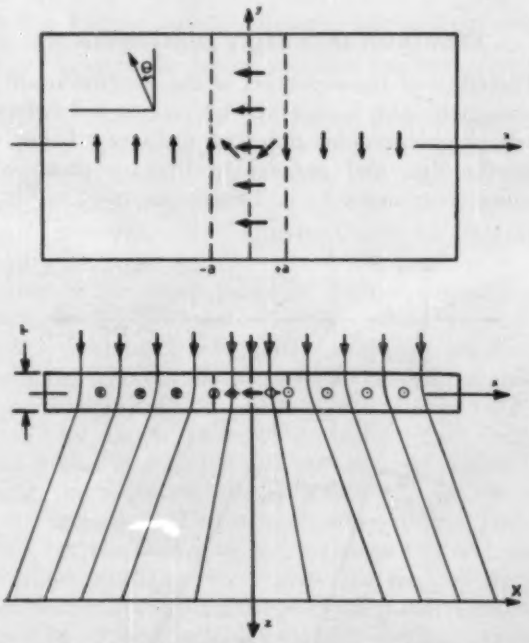

FIG. 3. Electron trajectories as a result of passing through thin film containing divergent Neel wall.

[8] W. K. H. Panofsky and M. Phillips, *Classical Electricity and Magnetism* (Addison-Wesley Publishing Co., Inc., Reading, Massachusetts, 1955), p. 128.

[9] L. Neel, Compt. rend. **241**, 533 (1955).

where $v_0=(2Ve/m)^{\frac{1}{2}}$ is the speed of the electron, V the microscope accelerating potential (esu), and m the electronic mass. The total angular deflection of the electron is assumed to be small so that M_z is not effective.

From the equation of motion for the electron,

$$F=m(\ddot{x}\mathbf{x}_1+\ddot{y}\mathbf{y}_1), \tag{3}$$

combined with Eq. (2), the deflection velocities are obtained:

$$\begin{aligned}\dot{x}&=-4\pi e v_0 M_y t/mc,\\ \dot{y}&=4\pi e v_0 M_x t/mc.\end{aligned} \tag{4}$$

These expressions hold for the time interval during which the electron is traversing the thickness of the specimen. Thus assuming that $\dot{z}=v_0$, and that t starts at zero and extends to $t=\tau/v_0$, the angular deflections are obtained:

$$\begin{aligned}\phi_x&=\frac{dx}{dz}=-\Phi M_y/M_s,\\ \phi_y&=\frac{dy}{dz}=\Phi M_x/M_s,\\ \Phi&\equiv\frac{4\pi\tau}{c}\left(\frac{e}{2Vm}\right)^{\frac{1}{2}}M_s,\end{aligned} \tag{5}$$

where M_s is the saturation magnetization of the specimen. The approximation is made that Φ is very small, so that the x or y deflection, when an electron emerges from the film, is much less than τ.

ELECTRON INTENSITY DISTRIBUTION

The effect of the deflection of the electron beam by the magnetic film is observed by placing a fluorescent screen or photographic film at a distance z below the magnetic film, and parallel to the x,y plane with specified coordinates X, Y. This is illustrated in Fig. 3,

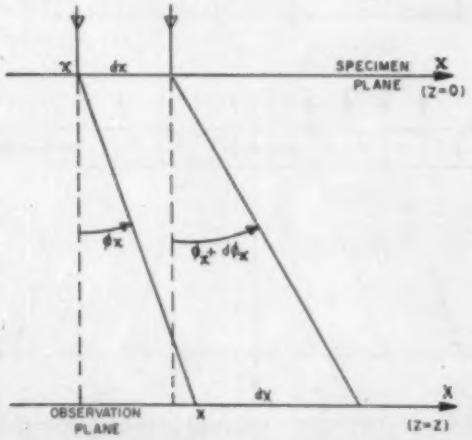

FIG. 4. Trajectory geometry for calculation of intensity distribution at observation plane.

where the view is along the $+y$ direction. With projector and objective magnification still neglected, Fig. 4 shows the geometry of the component of deflection in the x direction that is appropriate to a calculation of the electron intensity at the observation plane. From Fig. 4 it is seen that the point x,y in the specimen plane is mapped into the point X, Y of the observation plane in accordance with

$$\mathbf{x}_1X+\mathbf{y}_1Y=\mathbf{x}_1[x+z\phi_x(x,y)]+\mathbf{y}_1[y+z\phi_y(x,y)], \tag{6}$$

where the aforementioned assumptions and approximations are carried forth.

For differential changes in x and y, the resulting differential changes in the coordinates at the observation plane are, from Eq. (6),

$$\begin{aligned}\mathbf{x}_1dX+\mathbf{y}_1dY=\mathbf{x}_1&\left[dx+z\frac{\partial\phi_x}{\partial x}dx+z\frac{\partial\phi_x}{\partial y}dy\right]\\ &+\mathbf{y}_1\left[dy+z\frac{\partial\phi_y}{\partial y}dy+z\frac{\partial\phi_y}{\partial x}dx\right],\end{aligned} \tag{7}$$

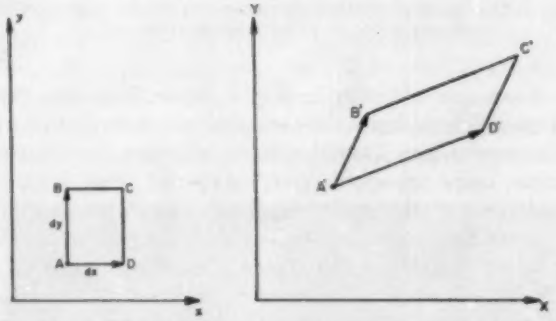

FIG. 5. Mapping of element of area in x, y plane to element of area in X, Y plane by electron deflections.

saving only first-order terms. The mapping of an element of area $dxdy$ into the X, Y plane is shown in Fig. 5, as indicated by Eq. (7). Note that a rectangular area is mapped into a parallelogram; the corresponding specimen and observation plane elements of area are given by:

$$\begin{aligned}|(\mathbf{x}_1dx)\times(\mathbf{y}_1dy)|\rightarrow\Bigg|&\left[\mathbf{x}_1\left(dx+z\frac{\partial\phi_x}{\partial x}dx\right)+\mathbf{y}_1z\frac{\partial\phi_y}{\partial x}dx\right]\\ &\times\left[\mathbf{y}_1\left(dy+z\frac{\partial\phi_y}{\partial y}dy\right)+\mathbf{x}_1z\frac{\partial\phi_y}{\partial x}dx\right]\Bigg|,\end{aligned} \tag{8}$$

or

$$\begin{aligned}|dxdy|\rightarrow\Bigg|&\left(dx+z\frac{\partial\phi_x}{\partial x}dx\right)\left(dy+z\frac{\partial\phi_y}{\partial y}dy\right)\\ &-z^2\frac{\partial\phi_y}{\partial x}\frac{\partial\phi_x}{\partial y}dxdy\Bigg|.\end{aligned} \tag{9}$$

If I_0 is taken as the uniform intensity of electrons over

the x,y plane at $z=0$, a point in the x,y plane contributes to the intensity at a point in the X, Y plane in accordance with

$$I(X,Y)=I_0\left|\left(1+z\frac{\partial\phi_x}{\partial x}\right)\left(1+z\frac{\partial\phi_y}{\partial y}\right)-z^2\frac{\partial\phi_y}{\partial x}\frac{\partial\phi_x}{\partial y}\right|^{-1}, \quad (10)$$

using the ratio of elementary areas indicated in Eq. (9). Equations (6) and (10) constitute a solution for the intensity distribution in the X, Y plane as parametric equations in x and y.

INTENSITY DISTRIBUTION FOR SIMPLE WALLS

Assume the magnetization of the simple Neel wall in Fig. 3 to rotate uniformly from the $\pm y$ direction to the $\mp y$ direction within the wall width $2a$. The magnetization distribution would then be

$$\begin{aligned}&\mathbf{M}=\pm\mathbf{y}_1M_s, \quad -\infty<x\lesseqgtr-a,\\ &\mathbf{M}=\mp\mathbf{x}_1M_s\sin\theta\pm\mathbf{y}_1M_s\cos\theta, \quad -a\lesseqgtr x\lesseqgtr+a, \qquad (11)\\ &\mathbf{M}=\mp\mathbf{y}_1M_s, \quad +a\lesseqgtr x<\infty, \quad \theta=\pi(x+a)/2a,\end{aligned}$$

where the divergent case shown in Fig. 3 is described by the upper signs, and the convergent case by the lower signs.

Using Eq. (11) in Eqs. (5), (6), and (10), the reduced form of the parametric equations is

$$\begin{aligned}&I(U,V)/I_0=1, \quad U=u\mp R, \quad V=v, \quad u\lesseqgtr-1;\\ &I(U,V)/I_0=\left(1\pm\frac{\pi R}{2}\cos\frac{\pi}{2}u\right)^{-1}, \quad U=u\pm R\sin\frac{\pi}{2}u, \qquad (12)\\ &\qquad\qquad V=v\mp R\cos\frac{\pi}{2}v, \quad -1\lesseqgtr u\lesseqgtr 1;\\ &I(U,V)/I_0=1, \quad U=u\pm R, \quad V=v, \quad u\gtreqless 1;\end{aligned}$$

where

$$u\equiv x/a, \quad v\equiv y/a, \quad U\equiv X/a, \quad V\equiv Y/a,$$
$$R\equiv\frac{z\Phi}{a}=\frac{4\pi M_s\tau z}{ac}\left(\frac{e}{2Vm}\right)^{\frac{1}{2}}. \qquad (13)$$

Calculations of the intensity distribution in Eq. (12) are plotted in Fig. 6(a) for the divergent case and in Fig. 6(b) for the convergent case for various values of the parameter R. Electron deflections in the y direction are not considered since they do not influence the intensity distribution. Note that the maximum distance an electron is deflected is $z\Phi$, so the parameter R of Eq. (13) can be thought of as the amount of overlap or divergence relative to the wall width.

From Fig. 6(a) it is seen that the region of low intensity broadens with increasing R, approaching a rectangular distribution of width $2(R+1)$. The intensity at the center becomes $I(0)/I_0\rightarrow 2/\pi R$ as $R\rightarrow\infty$. In

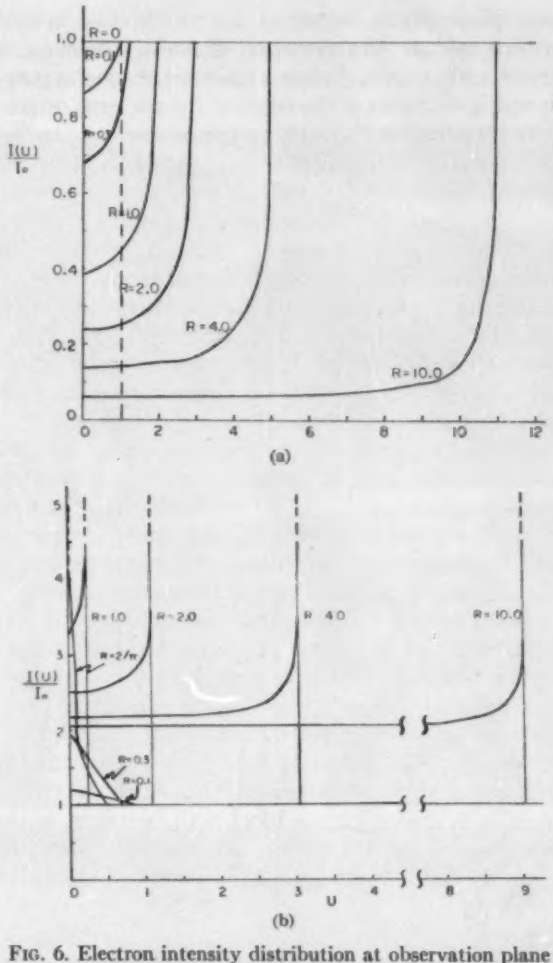

FIG. 6. Electron intensity distribution at observation plane for wall of uniformly rotating magnetization through wall width $2a$. Upper: divergent case. Lower: convergent case. $R=z\Phi/a$.

Fig. 6(b) the intensity distribution narrows and peaks at $U=0$, until $R=2/\pi$; then with increasing R two symmetrical infinite peaks move out from the center, located in the region of $U=\pm(R-1)$. The distribution again approaches rectangularity, and the central intensity becomes $I(0)/I_0\rightarrow 2+2/\pi R$ as $R\rightarrow\infty$. The nature of the sharp peaks in the convergent case is discussed in a later section.

A typical value for overlap or divergence distance predicted theoretically is $2z\Phi\doteq 10^{-3}$ cm, taking material and instrumental values of $4\pi M_s=10^4$ gauss, $\tau=250$ A, $V=75$ kv, and $z=15$ cm. The observed dark and light line widths of Fig. 1 would appear to be 4×10^{-4} cm, using the fact that the specimen grid is 200 mesh (200 grids/in.). The magnification of the projector need not be taken into account since this lens simply refocuses on the screen or plate the electron distribution that exists at the projector focal plane. A correction must be applied to this measured width, however, in view of angular divergence of the illuminating source in the microscope. In Fig. 2 it is seen that the shadow image of the grid will be magnified at the projector

focal plane by a factor of $z(z+b)^{-1}$. The intensity pattern due to the presence of walls, however, will depend only on the distance z, since the overlapping or diverging electrons at the edges of the patterns originate from very nearly the same point in the specimen for narrow walls. The observation shown in Fig. 1 was made with a Philips EM75B instrument, in which $z \doteq b$, so that the corrected experimental pattern width is 8×10^{-4} cm. The agreement between predicted and experimental widths is adequate considering the experimental uncertainty in the values of M_s and τ.

In the above-mentioned experimental case, $R\sim10^2$ for a wall width $2a\sim10^3$ A. The use of large-R approximations is warranted, therefore, for this mode of microscope operation. The observed uniformity of the intensity across either a converging or diverging wall pattern in Fig. 1 is in agreement with the calculated intensities for $R\gg1$. Note that for $R\sim10^2$, $I(0)/I_0\sim10^{-2}$ for diverging walls so that normal random scattering mechanisms probably contribute the major part of the actual intensity at the center of the dark patterns.

From Eq. (13) it is seen that the overlap distance is proportional to V^{-1}. This proportionality was experimentally confirmed by photographing the same walls using different values of accelerating potential V.

A uniform-rotation model for a Bloch wall similar to the Neel-wall description of Eq. (11) gives an intensity distribution identical to that for the Neel wall. The y deflection is absent for the Bloch wall, however, so that $V\equiv v$ replaces the V expression in Eq. (12). Note that for these simple wall models only $M_y(x)$ enters the intensity expressions. Since demagnetizing fields have only x and z components, these fields will only translate electrons in the y direction, and not influence the intensity distribution calculations.

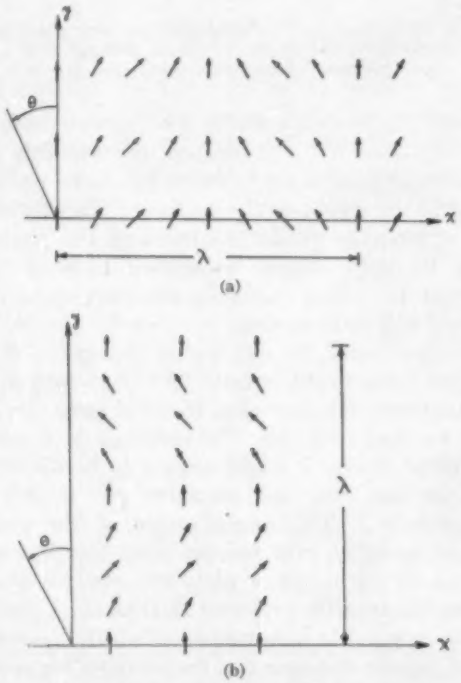

FIG. 7. Magnetization ripple model. Upper: lateral ripple. Lower: longitudinal ripple.

INTENSITY DISTRIBUTION FOR MAGNETIZATION RIPPLE

The large-R electron micrograph in Fig. 1 exhibits a quite complex magnetization distribution in places, and an intensity texture is clearly visible in the regions between major intensity variations. The following discussion proposes a model for the source and nature of this texture, and shows how the texture can be used easily to determine complicated magnetization distributions in thin films that could only indirectly be deduced by other techniques.

Two ways in which the quasi-periodic intensity variations in Fig. 1 could be manifested are shown in Fig. 7. In these diagrams it is assumed that a small-amplitude (sinusoidally) periodic variation in the magnetization direction occurs either along a direction perpendicular to or parallel to the direction of net magnetization, and the distribution is termed lateral or longitudinal "magnetization ripple." The wavelength, λ, of the variation and the maximum angular excursion, θ_0, are assumed equal in each case. Contributions to the total energy of the specimen from exchange and anisotropy, as a result, are identical for the two models, leaving only the magnetostatic self-energy as a criterion for which configuration is energetically more favorable.

The distribution for sinusoidal magnetization ripple is

$$\mathbf{M}=-\mathbf{x}_1M_s\sin\theta+\mathbf{y}_1M_s\cos\theta, \tag{14}$$

where $\theta=-\theta_0\sin(2\pi x/\lambda)$ for the lateral case, and $\theta=-\theta_0\sin(2\pi y/\lambda)$ for the longitudinal case. Lateral magnetization ripple gives a magnetostatic self-energy of

$$E\doteq kM_s^2\theta_0^2/\lambda^2, \tag{15}$$

where k is a proportionality constant, and $\theta_0\ll1$, while longitudinal magnetization ripple gives

$$E\doteq kM_s^2\theta_0^4/2\lambda^2, \tag{16}$$

indicating that for the same values of λ and small θ_0 the longitudinal configuration is much more likely.

From Eqs. (5), (6), (10), and (14) the intensity distribution for the lateral case is

$$I(X,Y)/I_0\doteq\left|1+\frac{\pi z\Phi\theta_0^2}{\lambda}\sin\frac{4\pi x}{\lambda}\right|^{-1},$$

$$X\doteq x-z\Phi+\frac{z\Phi\theta_0^2}{4}\cos\frac{4\pi x}{\lambda},\quad \theta_0\ll1, \tag{17}$$

$$Y\doteq y+z\Phi\theta_0\sin\frac{2\pi x}{\lambda},$$

while for the longitudinal case there results

$$I(X,Y)/I_0 \doteq \left|1+\frac{2\pi z\Phi\theta_0}{\lambda}\cos\frac{2\pi y}{\lambda}\right|^{-1},$$

$$X \doteq x - z\Phi + \frac{z\Phi\theta_0^2}{4}\cos\frac{4\pi y}{\lambda}, \qquad (18)$$

$$Y \doteq y + z\Phi\theta_0\sin\frac{2\pi y}{\lambda}, \quad \theta_0 \ll 1.$$

It is seen from Eqs. (17) and (18) that the intensity variations for the longitudinal case are greater than those for the lateral case by a factor of $2/\theta_0$. From Eq. (18) it is seen that overlap begins at $2\pi z\Phi\theta_0/\lambda = 1$, but in most experimental cases, $2\pi z\Phi\theta_0/\lambda \ll 1$, for which Eq. (18) becomes

$$I(Y)/I_0 \doteq 1 - \frac{2\pi z\Phi\theta_0}{\lambda}\cos\frac{2\pi Y}{\lambda}. \qquad (19)$$

Note that the more favorable longitudinal magnetization ripple leads to bands of uniform intensity running perpendicular to the principal magnetization direction, and this is substantially what is observed experimentally (Fig. 1) assuming that the magnetization of a domain is ordinarily closely parallel to the wall direction. The intensity streaks resulting from longitudinal magnetization ripple appear, therefore, to represent an accurate orthogonal map of the magnetization distribution in the plane of a thin film, and the detailed distribution is easily read from a micrograph. The dark branching walls in the middle right-hand window of Fig. 1, for example, are seen to be 90° walls. The magnetization distribution for a terminating domain can similarly be deduced from the ripple pattern in the middle-left window of Fig. 1.

If the ripple lines make angles of α_1 and α_2 with a wall on either side of a (straight) wall segment, the overlap or divergence distance (for large R) should be

$$D = z\Phi(\sin\alpha_1 + \sin\alpha_2). \qquad (20)$$

Measurements on the walls of Fig. 1 substantiate Eq. (20).

Intensity ripples similar to those of Fig. 1 were measured on a photographic plate with a microdensitometer to determine the order of magnitude of θ_0. The intensity variations, after a correction of the data for film blackening, were $\pm 10\%$ about a mean value, corresponding to a small value of $2\pi z\Phi\theta_0/\lambda$ in Eq. (19). The value of $z\Phi$ was determined from the overlap for 180° walls, and a value of $\lambda \sim 2\times 10^{-4}$ cm was determined by averaging the ripple wavelengths on the plate. The result was an experimental value of $\theta_0 \sim 10^{-2}$, emphasizing the sensitivity of large-R electron microscope observations.

The observation of magnetization ripples lends confirming evidence to the magnetization buckling model for thin-film switching previously proposed.[10]

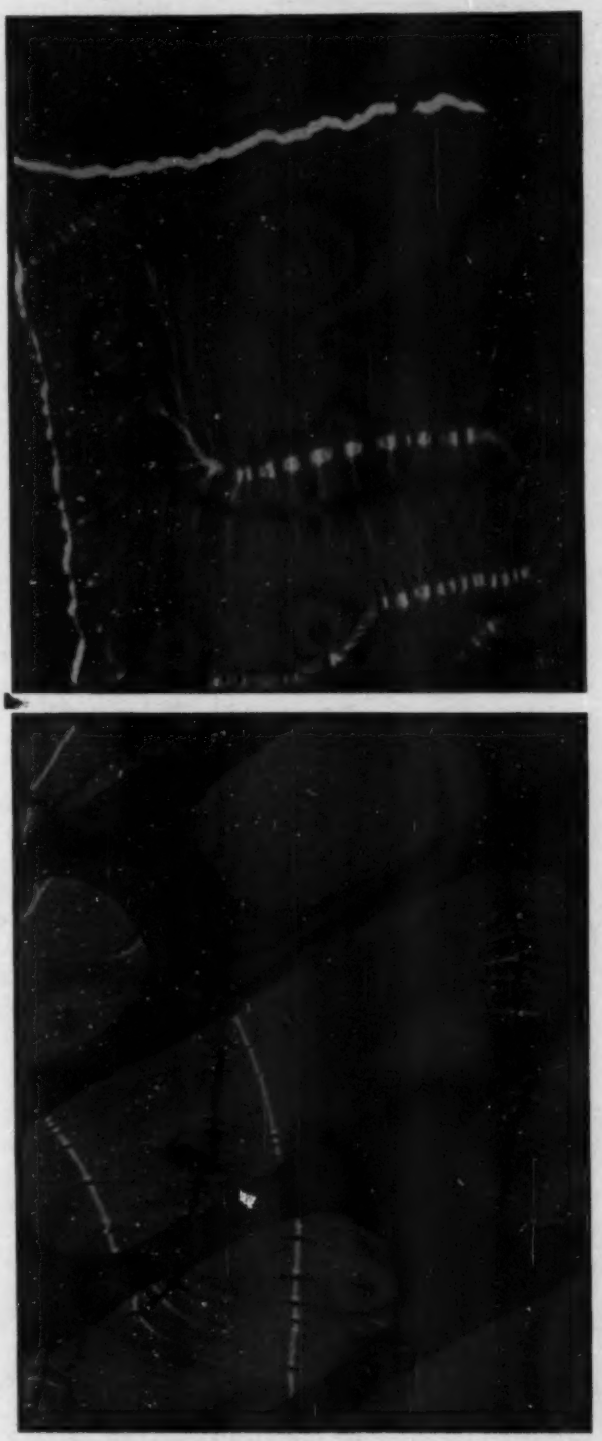

FIG. 8. Cross-tie walls in Permalloy films viewed by large-R electron microscope operation.

[10] H. W. Fuller and H. Rubinstein, J. Appl. Phys. **30**, 84S (1959).

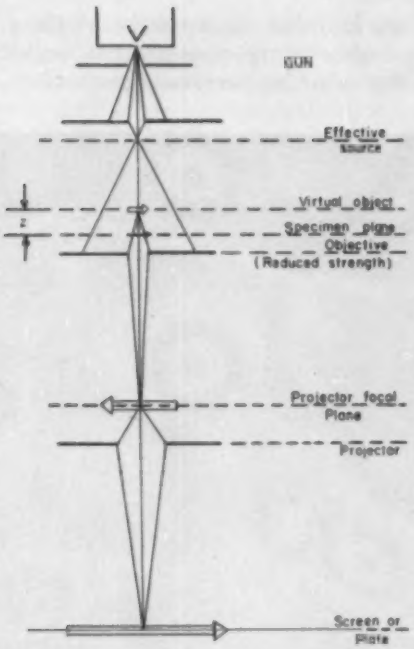

FIG. 9. Operation of electron microscope for high resolution and magnification magnetization images using objective and projector lenses.

Figure 8 shows two large-R micrographs of cross-tie walls; the intensity distribution is in accord with the model for cross-tie walls proposed by Huber *et al.*[5]

HIGH RESOLUTION BY USE OF OBJECTIVE LENS

The large-R micrographs discussed previously were obtained with projector magnification alone (Fig. 2), while the objective lens was used at very low currents only as a useful external field source to cause wall motion and domain formation in the specimen. A second mode of operation of a standard instrument is shown in Fig. 9 where the objective assumes a function closer to that of normal microscope operation. The objective is operated at reduced strength to focus a virtual object plane, a distance z above the specimen, on the projector focal plane, as shown in Fig. 9.

Operation of the objective at a reduced current is experimentally necessary in this mode since full objective field results in the elimination of domain walls in the thin-film specimens. Although the reduced objective field is maintained accurately normal to the film specimen by careful adjustment, the observations so far have been limited to films of relatively high coercive force.

Since the focal length of a magnetic lens is a function of H^2/V, where H indicates the field strength at some reference point in the lens and V is the accelerating potential,[11] the objective operated at reduced strength can be refocused on the specimen by a suitable reduction of V. Such in-focus observations were made, although the use of small values of V results in a serious loss of intensity at the screen. Note that at focus the electron deflections caused by the specimen magnetization do not result in domain wall images at the screen or photographic plate. This is because the magnetic angular deflections are well within the angular aperture of the objective lens, and as for any scattering mechanism in this event, the deflected electrons are returned to the correct point in the image plane. Defocusing by a distance z is necessary, therefore, to the production of a magnetization image (cf. Fig. 6 for $R \rightarrow 0$), although the use of the objective in this way allows a selection of the value of z that can be arbitrarily close to zero, and permits using the high-resolution capabilities of the instrument.

The formulation of the magnetization imaging process was based on the electron intensity distribution a distance z *below* the specimen plane (cf. Figs. 2 and 3). The present mode of operation, from Fig. 9, establishes the effective observation plane *above* the specimen. Since electron trajectories occurring below the specimen must be projected up through the specimen to establish the virtual object, converging trajectories become diverging, and vice versa, at the virtual object. This inversion fits the analytical formulation completely if the value z for the virtual object is taken as a negative quantity. Negative values of R [Eq. (16)] similarly assume significance in this case.

For the mode of operation using the objective, the magnifications of the objective and projector lenses are again easily taken into account in the intensity distribution expressions, with the simplification that in this case the value of z is ordinarily quite small compared with b in Fig. 2 so that a correction for magnification due to source divergence need not be made.

HIGH-RESOLUTION OBSERVATIONS AND WALL MEASUREMENT

Figure 10 shows a familiar domain wall pattern viewed at high magnification and resolution by the use of objective lens magnification. Note that the fine structure of the magnetic film, although out of focus, can be seen. Small imperfections are visible at the tips of pointed domains, and are probably responsible for holding the wall in place in the high objective field.

Note in Fig. 10 that the light (converging) wall is significantly narrower than the dark (diverging) wall, in agreement with the results shown in Fig. 6. The wall shown in Fig. 10 was measured to compare the experimental and predicted intensity distributions at low values of R.

The analytical wall model used in the comparison was a more realistic one that results from calculating the spin distribution for minimum total energy contributed to by exchange and either anisotropy or magnetostatic

[11] C. E. Hall, *Introduction to Electron Microscopy* (McGraw-Hill Book Co., Inc., New York, 1953), p. 91.

energy.[12] The magnetization distribution for this wall is based on the angular dependence (cf. Fig. 3)

$$\theta = -\cot^{-1}[\sinh(x/\delta)], \tag{21}$$

giving the magnetization distribution

$$\mathbf{M} = \pm \mathbf{x}_1 M_s \operatorname{sech}(x/\delta) \mp \mathbf{y}_1 M_s \tanh(x/\delta) \tag{22}$$

for a wall along the y axis.

Substitution of Eq. (22) in the parametric equations for the intensity distribution, Eqs. (7) and (11), gives

$$\begin{aligned} I(U)/I_0 &= |1 \pm R \operatorname{sech}^2 u|^{-1}, \\ U &= u \pm R \tanh u, \\ V &= v \mp R \operatorname{sech} v, \end{aligned} \tag{23}$$

where, as before, $u = x/\delta$, $v = y/\delta$, $U = X/\delta$, $V = Y/\delta$, and $R = z\Phi/\delta$. The upper and lower signs again refer to divergent and convergent cases respectively, and the intensity distributions computed for these two cases are shown in Fig. 11. The principal features of the distributions are similar to those of Fig. 5 for the uniform rotation model.

To compare the experimental intensity distribution for the walls shown in Fig. 10 with the result in Eq. (23), the photographic plate was examined with a microdensitometer, and transmission curves were obtained for scans across the light and dark walls. The transmission data were then converted to intensity with a calibration curve for the emulsion. A single value of $R = 0.3$ was selected for the theoretical curves that caused the experimental intensity distributions to best match the theoretical result in peak excursions, and a value of δ was selected [Eq. (24)] by fitting the experimental scale to the theoretical curves. The theoretical distributions are shown in Fig. 12 together with the scaled experimental points. The two-parameter fitting of a single curve in this fashion would not be particularly significant perhaps, but the simultaneous fitting of the two curves in Fig. 12 seems to strongly substantiate the present development.

A value of $\delta = 750$ A was used in Fig. 12, so that the experimentally measured domain wall width is $2\delta = 1500$ A (for about 100° rotation). The measured width is of the right order according to theoretical calculations for Neel-wall widths in 200 A films of 50-50 Fe-Ni.[13] The experimental data for the divergent wall show an intensity overshoot on either side of the pattern, and also a clear asymmetry. Both effects can

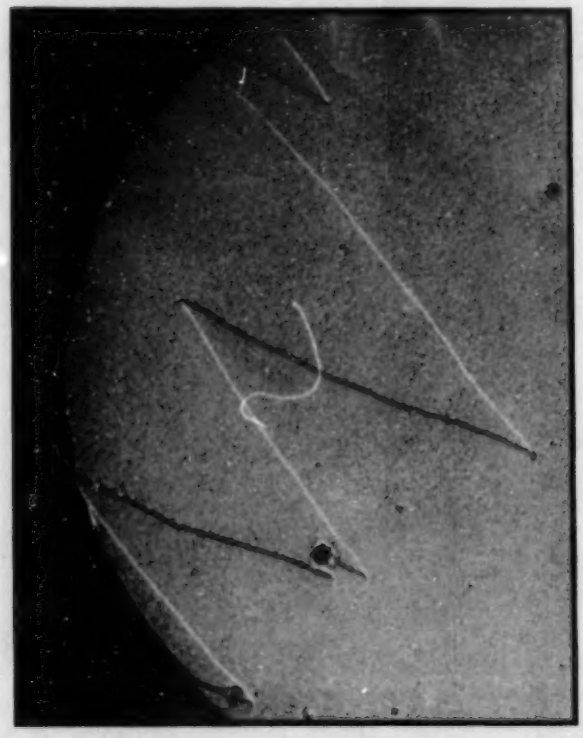

FIG. 10. High-resolution image of domain walls in 50-50 Fe-Ni film using objective magnification. Picture is about five microns wide.

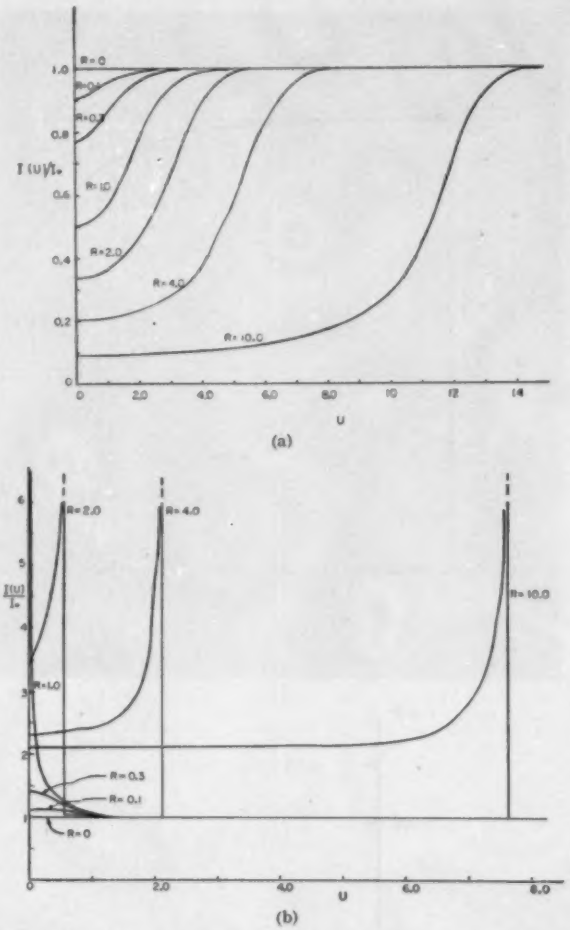

FIG. 11. Electron intensity distribution at observation plane for wall of shape $\cot^{-1}\theta = -\sinh(x/\delta)$. Upper: divergent case. Lower: convergent case. $R = z\Phi/\delta$.

[12] C. Kittel, Revs. Modern Phys. 21, 541 (1949).

[13] R. J. Spain (unpublished work).

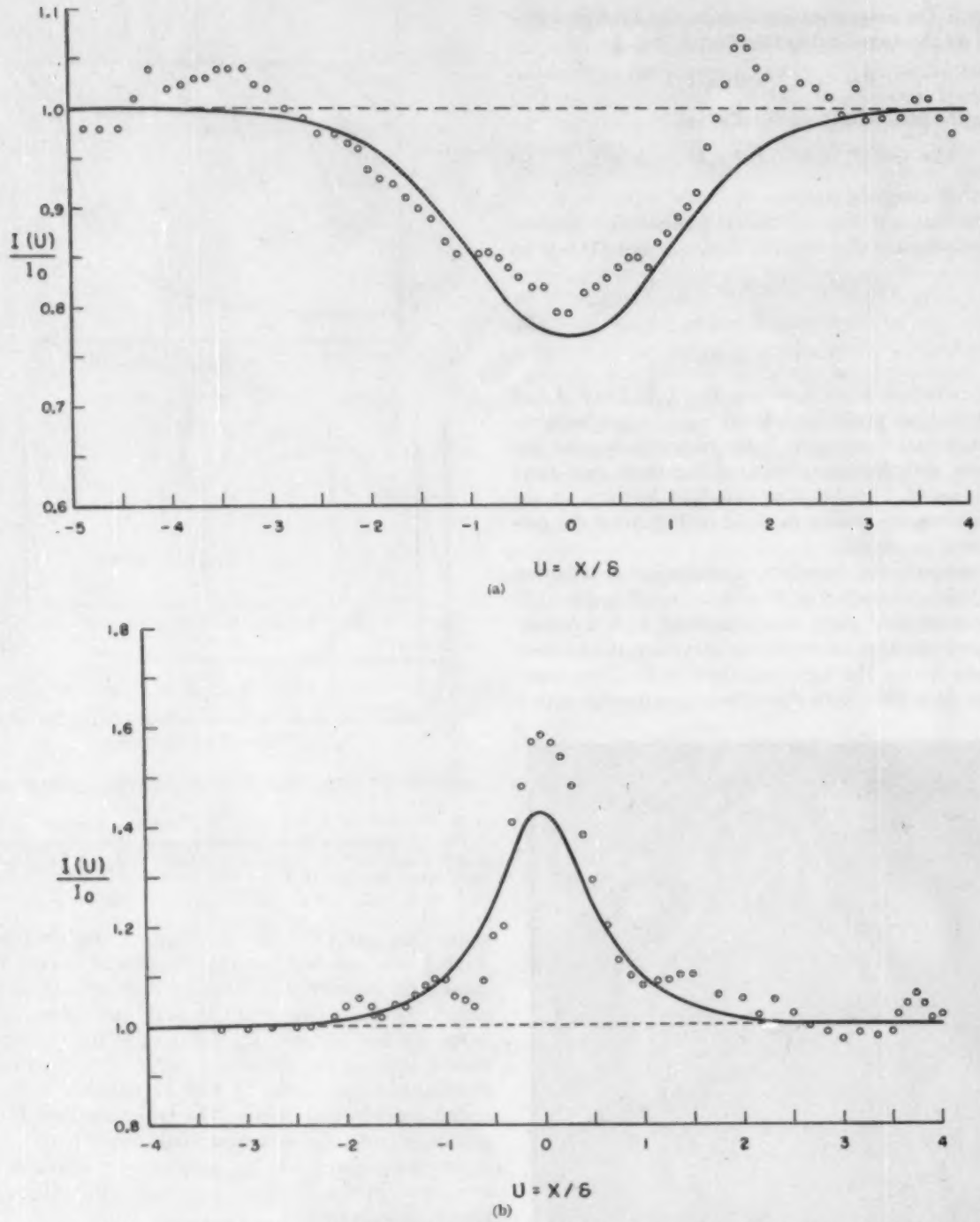

FIG. 12. Comparison of measured and theoretical intensity distributions for walls in 50-50 Fe-Ni film (Fig. 10). Upper: divergent case. Lower: convergent case. $R=0.3$, $\delta=750$ A.

be accounted for by concluding that the wall is not exactly parallel to the magnetization of the domains that it separates.

Other domain walls are shown in Fig. 13 viewed at high magnification and resolution by use of objective lens magnification. These walls are much wider, in general, than those of Fig. 10, but they apparently have complicated magnetization structures on a small scale. It appears that the wall in the middle photograph is a broad Neel wall with a crossover in the direction of wall rotation, probably a Bloch region, at the center of the picture. Neel-wall segments of this kind have been

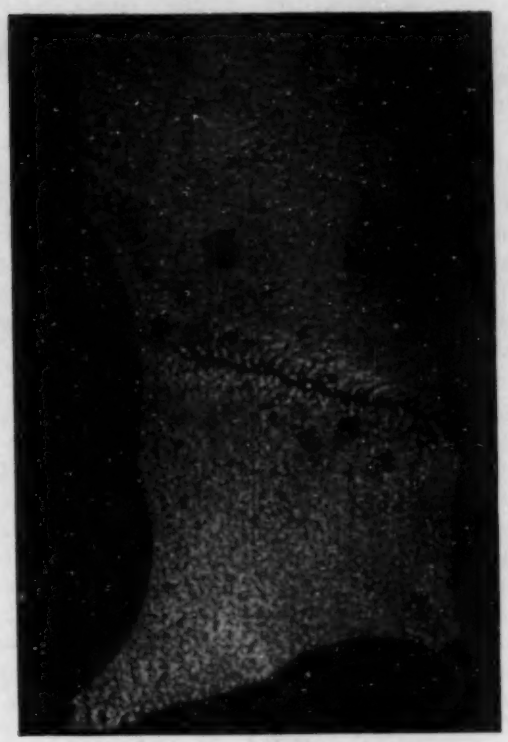

(a)

(c)

(b)

FIG. 13. High-resolution images of magnetization distribution in thin films of Permalloy using objective magnification. Pictures are about ten microns wide.

observed with powder patterns.[10] The irregular edges of the pictures in Fig. 13 are caused by the shadow of the objective aperture through which the films are viewed.

EFFECT OF FINITE RESOLUTION

For the mode of operation using the objective lens the resolution of the instrument should be as high for the magnetic images as it would be for focused images of

objects in the virtual object plane of the reduced-strength objective, even though the specimen plane is badly out of focus during magnetic observations. For the EM75B this resolution is in the order of 50–100 A. In comparing theoretical and measured intensity distributions for narrow walls, therefore, a correction of the theoretical curves should be made to account for the effects of finite resolution. This can be done by computing a new intensity distribution,

$$I'(X)=\frac{1}{2\Delta X}\int_{X-\Delta X}^{X+\Delta X} I(X')dX', \tag{24}$$

where $2\Delta X$ is the (rectangularly shaped) resolution referred to the observation plane.

The effect of finite resolution is important in considering the significance of the infinite intensity peaks that occur at sufficiently large values of R for a convergent wall (cf. Fig. 6). If U_0 in the observation plane is taken as the point of infinite intensity, corresponding to u_0 in the specimen plane, then from Eq. (23),

$$I_0/I(U_0)=|1-R\,\mathrm{sech}^2u_0|=0, \quad R>1, \tag{25}$$

and from Eqs. (25) and (23),

$$\begin{aligned} u_0&=\pm\cosh^{-1}R^{\frac{1}{2}},\\ U_0&=\pm\cosh^{-1}R^{\frac{1}{2}}\mp R^{\frac{1}{2}}(R-1)^{\frac{1}{2}}. \end{aligned} \tag{26}$$

The form of $I(U)$ in the neighborhood of U_0 is found by defining $U\equiv U_0+\eta$, $u=u_0+\epsilon$, $\epsilon,\eta\ll 1$, from which it develops that

$$\frac{I(\eta)}{I_0}\doteq\tfrac{1}{2}|\eta|^{-\frac{1}{2}}\left(\frac{R}{R-1}\right)^{\frac{1}{4}}. \tag{27}$$

In any practical intensity observation the resolution of the measurement is finite, so that the practically measured peak intensity with a spatial resolution of ΔU is

$$\begin{aligned} \frac{2}{\Delta U}\int_{U_0}^{U_0+\Delta U}\frac{I(U)}{I_0}dU&=\frac{1}{\Delta U}\int_0^{\Delta U}|\eta|^{-\frac{1}{2}}\left(\frac{R}{R-1}\right)^{\frac{1}{4}}d\eta\\ &=2\left(\frac{R}{R-1}\right)^{\frac{1}{4}}(\Delta U)^{-\frac{1}{2}}, \quad R>1. \end{aligned} \tag{28}$$

The measured intensity at the U_0 peaks, therefore, is finite for a finite resolution. The special case of $R=1$ gives a similar result.

MAGNETIZATION DISTRIBUTION FROM INTENSITY DISTRIBUTION

The expressions for the electron intensity distribution given by Eqs. (6) and (10) can be inverted in certain cases. Assuming a variation of magnetization in only one (x) direction, and assuming no overlap ($dx/dX\geqslant 0$), the intensity distribution is given by the parametric equations

$$\begin{aligned} \frac{I(X)}{I_0}&=\frac{dx}{dX}=\left[1-\frac{z\Phi}{M_s}\frac{dM_y}{dx}\right]^{-1},\\ X&=x-\frac{z\Phi M_y}{M_s}. \end{aligned} \tag{29}$$

From Eq. (30),

$$\begin{aligned} \frac{dM_y}{dx}&=\frac{M_s}{z\Phi}\left[\frac{I(X)}{I_0}-1\right]\frac{dX}{dx},\\ M_y(x)&=\frac{M_s}{z\Phi}\int\left[\frac{I(X)}{I_0}-1\right]dX, \end{aligned} \tag{30}$$

giving $M_y(x)$ from data available in the observation plane. Also from Eq. (29),

$$x(X)=\int\frac{I(X)}{I_0}dX, \tag{31}$$

so that Eqs. (30) and (31) constitute a parametric integral equation solution for the magnetization distribution in a thin film for no overlap.

ACKNOWLEDGMENTS

The authors wish to acknowledge the assistance of members of the Applied Physics Group of the Computer Products Division at Laboratory for Electronics, Inc. The authors wish to thank H. Rubinstein and R. J. Spain for helpful discussions.

Effect of Electron Irradiation and Subsequent Thermal Treatment on Young's Modulus of Copper*

A. Sosin and L. L. Bienvenue
Atomics International, A Division of North American Aviation, Canoga Park, California
(Received June 3, 1959)

Measurements of Young's modulus of copper following high energy electron irradiation and subsequent heat treatment are reported. The modulus is observed to increase following short exposures at −190°C in three separate temperature regions, centered at approximately −45°C, −5°C, and +80°C. These modulus increases are discussed in terms of the various point defects created by the bombarding electrons.

INTRODUCTION

SEVERAL investigations[1–5] have been made of the effects of high energy radiation on the elastic moduli and internal friction of high purity copper. The majority of work reported has been concerned with the manner in which these properties change when irradiated at a fixed temperature. All such investigations show that the elastic moduli are increased as a result of irradiation, except perhaps for extremely long exposures.

Figure 1 presents the results previously reported[1] for a sample irradiated near liquid nitrogen temperature (hereafter called LN irradiation). All modulus measurements were made at −196°C. This irradiation was carried out using 1-Mev electrons. It was shown that this modulus behavior—the fast rise and subsequent saturation—could be understood if the defects created in a region of about a three atom radius around dislocation lines were effective in pinning the dislocation. The interpretation of the data followed a theory due to Mott.[6] In this theory, the "modulus defect" ΔE is due to the bowing out of dislocation segments under the action of the applied stress. The modulus defect is given by the expression

$$\Delta E/E = -(1/6)Nl^2, \qquad (1)$$

where l is the average length of the dislocation and N is its density (lines/cm²). The effect of the irradiation is to shorten the average length of dislocation segments, thus eliminating or reducing the modulus defect. However, work by Thompson, Blewitt, and Holmes[3] shows that some defect which is mobile near 45°K also contributes to dislocation pinning in the case of neutron irradiation. It is necessary, therefore, to re-examine the model for our LN irradiation effects. This is discussed further in the rest of this paper.

We also reported[1] that warming to room temperature after a short 1-Mev electron irradiation near liquid nitrogen temperature also caused an increase in Young's modulus and that irradiation near 0°C (hereafter called RT irradiation) was similar to LN irradiation but that the rate of modulus increase was faster in RT irradiation. The present paper is a more detailed investigation of these temperature effects.

EXPERIMENTAL

The method of measurement was essentially the same as previously reported. That is, annealed (one hour at 450°C) polycrystalline 99.999% pure copper foils were mounted in the form of cantilever beams and vibrated in resonance. The resonant frequency varied from 400 to 600 cps, depending on sample dimensions. The fractional change in modulus induced by the various treatments is approximately twice the fractional change in resonant frequency. The precision of the frequency measurements was about ±0.03 cps. Typical specimen dimensions were 0.2 in. by 0.4 in. by 6 mils, with the small dimension parallel to the electron beam. The samples were cooled or heated by conduction, having been carefully soldered at one end to a massive copper block. The maximum strain amplitude was estimated to be about 10^{-5}.

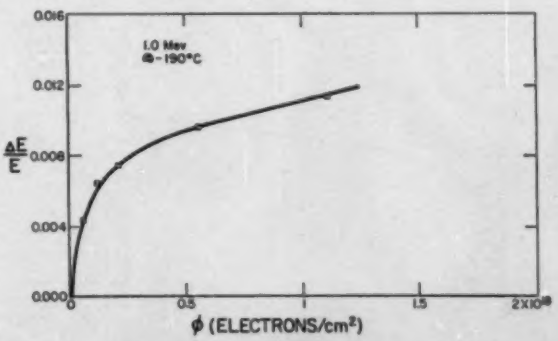

FIG. 1. Fractional change in Young's modulus as a function of electrons exposure. All measurements were made at −196°C.

* This work was performed under contract to the U. S. Atomic Energy Commission.

[1] H. Dieckamp and A. Sosin, J. Appl. Phys. **27**, 1416 (1956).
[2] D. O. Thompson and D. K. Holmes, J. Appl. Phys. **27**, 191 (1956); **27**, 713 (1956).
[3] Thompson, Blewitt, and Holmes, J. Appl. Phys. **28**, 742 (1957).
[4] R. S. Barnes and N. H. Hancock, Phil. Mag. **29**, 527 (1958).
[5] D. O. Thompson and V. K. Paré, Bull. Am. Phys. Soc. Ser. II, **4**, 136 (1959).
[6] N. F. Mott, Phil. Mag. **43**, 1151 (1952); also J. Friedel, Phil. Mag. **44**, 444 (1953).

RESULTS

In all the figures presented, squares denote measurements at −196°C; open circles, measurements at 0°C; and filled circles, measurements at the temperature shown on the abscissa.

Figure 2 presents the results for a RT irradiated sample. All modulus measurements were made at 0°C. This irradiation and all subsequent irradiations discussed were carried out using 0.75-Mev electrons. It is important to note that the electron flux necessary to produce an equivalent amount of modulus increase is drastically reduced in the higher temperature irradiation. A precise comparison of damage rate is precluded since samples treated under nominally identical conditions failed to show reproducibility in absolute electron flux for a given damage rate to better than a factor of two or three.

To determine in what manner the temperature effects enter, several coarse pulse-annealing experiments were performed. A typical result is shown in Fig. 3. The sample was first given what was then believed to have been relatively short LN irradiation of 7.5×10^{15} e/cm^2. The subsequent tempering treatment produced no changes up to −100°C, then essentially eliminated the modulus defect between −100°C and −50°C. These results were unexpected since measurements of electrical resistivity fail to indicate a defect which is mobile in this temperature region. It will be seen, however, that this modulus behavior is connected with the *relatively long* LN irradiation given these samples.

To resolve further the recovery behavior, a shorter LN irradiation was performed. In this case, the measurement procedure was changed. Prior to irradiation, the temperature dependence of the modulus was measured over the range from −196°C up to +30°C. Following irradiation, two more warm-ups were made. In this way, the temperature dependence could be subtracted, yielding that portion of the modulus behavior due to imperfections. The results are presented in Fig. 4. It is clear that two recovery stages are present, centered at about −45°C and −5°C. Since an additional irradiation following these thermal treatments produced a further modulus increase, it can be concluded that each defect migration in each of these recovery stages had proceeded to a state of completion determined by the concentration of defects introduced by the first irradiation.

Figures 5 and 6 show that still another recovery stage may be observed at higher temperature, namely at about 80°C. In the first case, a sample was given a slight LN irradiation, then warmed to 0°C; in the second case, the sample was RT irradiated. Pulsing was carried out in each case for the temperature range 0°C to 100°C. Each sample shows this recovery stage. However, there is some difference in the modulus behavior approaching this stage.

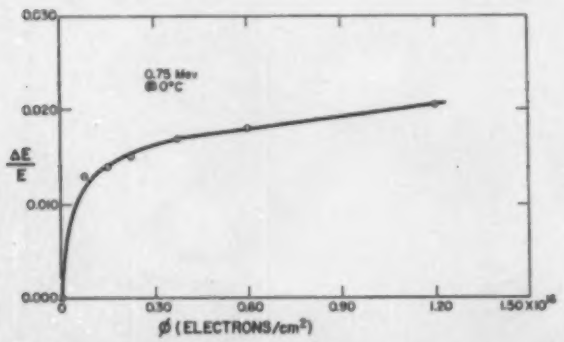

FIG. 2. Fractional change in Young's modulus as a function of electron exposure. All measurements were made at 0°C.

DISCUSSION

The results presented above clearly show three stages of recovery between −190°C and +100°C. These data in themselves do not lead to a unique atomistic interpretation. However, we will show that these data may be interpreted in a manner consistent with a model deduced from other measurements (e.g., electrical resistivity). The cited references[7,8] should be consulted for a more complete discussion of the model as it is used to explain the various stages of defect migration referred to herein.

+80°C: Migration of Stage IV Defects to Dislocations

These defects are believed to be single vacancies, as discussed elsewhere.[7,8] The temperature observed in the present experiment is somewhat lower than usually associated with stage IV in copper. Since the modulus change is nonlinear in its dependence on number of pinning agents (vacancies, in this case), the earlier arriving vacancies contribute disproportionally more than later vacancies. These vacancies have, however, migrated only a relatively short distance to reach dislocation.

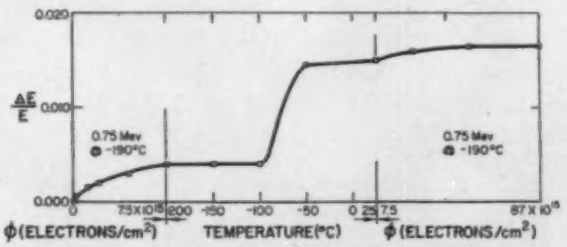

FIG. 3. Effect of thermal treatment below 0°C on Young's modulus after a mild exposure. All measurements were made at −196°C.

[7] A. Seeger, *Metallurgy and Fuels, Vol. III, Progress in Nuclear Energy Series*, edited by H. M. Finniston and J. P. Howe (Pergamon Press, London) (to be published).

[8] Meechan, Sosin, and Brinkman (to be published).

−5°C: Migration of Stage III Defect to Dislocations

In accord with an interpretation developed elsewhere,[8] these defects are believed to be symmetric interstitials. (A symmetric interstitial is an atom located in the center of a face-centered cubic unit cell.) Again the "center" temperature is lower than previously found in electron-irradiated copper where electrical resistivity has been measured. The explanation of this lowering is the same as offered previously in connection with stage IV recovery.

−45°C: Migration of Converted Interstitial Atoms

There is little or no indication of this stage through electrical resistivity measurements. Thus a bulk migration is probably not involved. It is believed that electron-irradiation will produce an appreciable concentration of crowdions. (A crowdion is a linear configuration of N atoms occupying (N-1) lattice site in a closed-packed direction, where $N \simeq 7$.) Some of these will be dynamically driven into the stacking fault regions of extended dislocations and converted to symmetric interstitials. They will, however, probably overshoot somewhat, coming to rest a few atom distances away from the stacking fault ribbon. When the temperature is increased to a point somewhat below the region in which interstitials removed from dislocations can execute sufficient number of jumps to reach a sink or trap, these interstitials will easily make the few jumps required to move into the stacking fault. Basically, therefore, the modulus increases at −45°C and −5°C are of similar origin. We may identify the recovery at −45°C as nonrandom motion of symmetric interstitials to dislocations and the recovery at −5°C as random motion of symmetric interstitials to dislocations.

It is interesting to attempt to explain the observation by Thompson, Blewitt, and Holmes[3] of a modulus rise near 45°K (−228°C). More specifically, the modulus was observed to be affected by imperfections throughout the temperature range between 39°K and 53°K. In the present interpretation, crowdions migrate in this temperature region. The crowdions which encounter dislocations during random migration will cause dislocation pinning in the same manner as caused by other point defects. Furthermore, there would appear to be no nonrandom motion of defects to dislocation in this temperature region. This is in accord with our interpretation since only crowdions stopped near dislocations should execute such a nonrandom migration. These crowdions are, however, converted to symmetric interstitials which migrate at a high temperature.

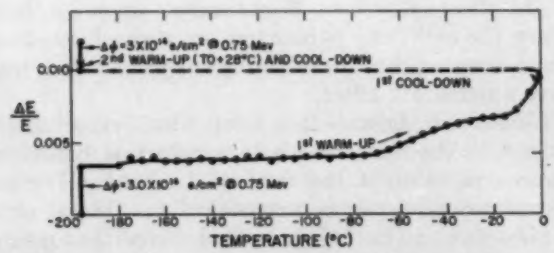

FIG. 4. Effect of thermal treatment below 0°C on Young's modulus after a low exposure. All measurements were made at the temperature shown on the abscissa. The temperature dependence of the modulus has been subtracted.

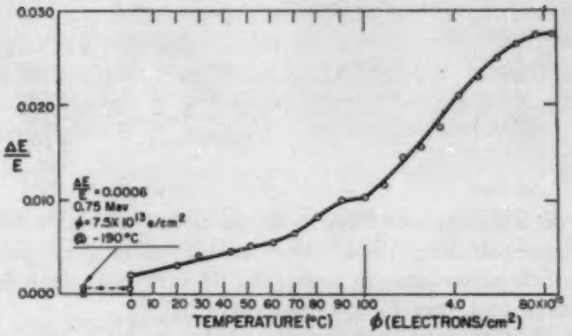

FIG. 5. Effect of thermal treatment above 0°C on Young's modulus after a slight LN exposure. Circles indicate measurements at 0°C; squares indicate measurements at −196°C. The arrows indicate the changes observed on warming from −196°C to 0°C.

Finally, we may estimate the density of dislocations, N, and average length, l, from Eq. (1). It is observed that prior to irradiation $\Delta E/E \simeq 0.02$ for all samples investigated. We will assume that N remains constant during radiation and that l is decreased from its initial value, l_0. Consider the possible values for these parameters listed in Table I.

Here $c_0 = N/l_0$ is the number of pinning points per cm³ located at dislocations. These may be either impurity atoms or dislocation nodes. Referring to Fig. 4, we see that a flux of 3×10^{14} e/cm² in a LN irradiation introduces a change in $\Delta E/E$ of about 0.004, implying a 10% change in l due to a 10% increase in the number of pinning points. From resistivity data, we estimate the number of point defects which have been created by the radiation and which were sufficiently mobile to

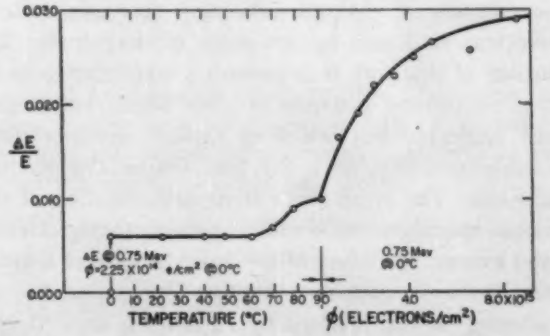

FIG. 6. Effect of thermal treatment above 0°C on Young's modulus after a short RT exposure. All measurements were made at 0°C.

TABLE I. Dislocation parameters.

	N (cm^{-2})	l (cm)	c_0 (cm^{-3})
(a)	10^6	1.5×10^{-4}	7×10^{9}
(b)	10^7	5.0×10^{-5}	2×10^{11}
(c)	10^8	1.5×10^{-6}	7×10^{12}

reach dislocations lines to be about 3×10^{12} cm^{-3}. This figure excludes those close interstitial-vacancy pairs which recombine on annealing at very low temperatures[9] and, therefore, do not affect $\Delta E/E$.

It is obvious that the parameters N and l_0 in (c) of Table I are not very likely. It seems unlikely that appreciably more than 0.1% of the mobile defects will reach dislocations rather than other sinks. This is indicated by the fact that the concentration of defects giving rise to a change in modulus around −45°C must be very small, yet the change in $\Delta E/E$ is comparable with the change induced during the LN irradiation. The observed second-order kinetics found in stage III in resistivity measurements following electron irradiation[10] also indicate that the number of mobile defects reaching dislocations rather than other sinks is small. Thus it appears that the concentration of contributing dislocations is between 10^6 cm^{-2} and 10^7 cm^{-2} with an average length of about 10^{-4} cm. An appreciably smaller concentration of contributing dislocations is not excluded by these data but is unlikely since l_0 then becomes unreasonably large.

[9] Corbett, Smith, and Walker (to be published).
[10] C. J. Meechan and J. A. Brinkman, Phys. Rev. **103**, 1193 (1956).

TABLE II. Proposed for defect migration.

Temperature region	Defect	Type of motion
−228°C	Crowdion	Random
−45°C	Symmetric interstitial	Nonrandom
−5°C	Symmetric interstitial	Random
+80°C	Vacancy	Random

CONCLUSION

The observed increases in Young's modulus due to irradiation and warming can be interpreted using a dislocation-pinning model. In this model, the defects responsible for pinning are given in Table II.

ACKNOWLEDGMENTS

The authors wish to thank J. A. Brinkman and C. E. Dixon for critical readings of the manuscript.

JOURNAL OF APPLIED PHYSICS VOLUME 31, NUMBER 2 FEBRUARY, 1960

Effect of Specimen Delocalization in Electron Diffraction Studies of Gas Molecules*

L. S. BARTELL
Institute for Atomic Research and Department of Chemistry, Iowa State College, Ames, Iowa
(Received November 25, 1958)

The effect upon a normal electron diffraction pattern of an extraneous uniform distribution of the gaseous specimen is considered quantitatively. It is shown that the delocalization of gas may lead to errors in internuclear distances of several thousandths of an Angstrom unit or more in conventional experiments. Equations are presented for the correction of experimental data.

OVER the last decade improvements in experimental and interpretive procedures have increased the accuracy of electron diffraction determinations of molecular structure by an order of magnitude. The purpose of this note is to present a quantitative treatment concerning a source of error which has largely been neglected but which is capable of interfering, possibly seriously, with the precision of the modern technique. The error arises from delocalization of the gaseous specimen and is always present to a greater or lesser extent. The effect of the finite breadth of a localized gas sample upon the atomic and molecular electron scattering curves, denoted by I_A and I_M respectively, has been treated in some detail by Bauer *et al.*[1] and by Karle and Karle.[2] The effect upon I_A of a uniform delocalization of gas throughout the diffraction chamber has also received attention.[1] No quantitative treatment of the effect of uniform delocalization upon I_M, from which the molecular parameters are derived, has been given, however, but the following analysis shows it may have a significant effect.

Almost all failures to meet ideal experimental diffraction conditions result in a reduction below the theoretical value of the ratio of I_M to I_A. The experimental efficiency is represented by the value $R = \{(I_M/I_A)_{\text{expt}}/(I_M/I_A)_{\text{ideal}}\}$ called the index of resolution. In the following development we will assume, in

* Work was performed in the Ames Laboratory of the U. S. Atomic Energy Commission. Contribution No. 686.

[1] Harvey, Keidel, and Bauer, J. Appl. Phys. **21**, 860 (1950).
[2] I. L. Karle and J. Karle, J. Chem. Phys. **18**, 963 (1950).

accordance with experience with our particular apparatus, that the major factor responsible for values of R lower than unity is uniformly delocalized gas.

The intensity, I_T, received on a flat photographic plate from gas located at a distance L' from the plate is of the form[3]

$$I_T(\mathfrak{R},L')=\frac{K\Phi\{Z-F(s)\}^2}{(\mathfrak{R}^2+L'^2)s^4}\left\{1+c\int^{\infty}P(r)\frac{\sin sr}{sr}dr\right\}$$
$$=I_A+I_M \qquad (1)$$

where $\mathfrak{R}$ is the plate radius, $\Phi(\mathfrak{R})$ the rotating sector function, and $P(r)$ is the probability distribution in internuclear distance, r. The natural angular diffraction variable is $s=2k\sin(\frac{1}{2}[\arctan\mathfrak{R}/L'])$, where $k=2\pi/\lambda_e$. The intensity for an arbitrary density distribution, $\rho(L')$, of gas along the path of the electron beam is

$$I_T(\mathfrak{R})\simeq\int_0^L\rho(L')I_T(\mathfrak{R},L')dL', \qquad (2)$$

where L is the distance from the plate to the aperture at the gas nozzle, provided the beam trap is not close to the nozzle. Equation (2) can be integrated if the reasonable approximations are introduced that $\{Z-F(s)\}\simeq Zs^2/(s^2+s_1^2)$, where s_1 is a constant characteristic of the atomic radius, and that

$$P(r)=(2\pi l^2)^{-\frac{1}{2}}\exp(-[r-r_0]^2/2l^2) \qquad (3)$$

where l is the rms amplitude of vibration and r_0 is the effective internuclear distance. The results calculated for the scattering by equal numbers of localized and uniformly delocalized molecules are as follows:

$$I_A(\text{deloc})\simeq\tfrac{1}{2}I_A(\text{loc})\left\{1+\frac{\mathfrak{R}^2}{L^2}+\frac{4}{5}\left(\frac{s_1L}{k\mathfrak{R}}\right)^2-\frac{4}{35}\left(\frac{s_1L}{k\mathfrak{R}}\right)^4+\cdots\right\} \qquad (4)$$

$$I_M(\text{loc})\simeq cI_A(\text{loc})\{\exp(-l^2s^2/2)\}\{(\sin sr_0)/sr_0\} \qquad (5)$$

and

$$I_M(\text{deloc})\simeq cI_A(\text{loc})\{\exp(-l^2s^2/2)\}\times\left[\frac{\{n(\sin sr_0)/sr_0\}+\cos sr_0}{n^2+(sr_0)^2}\right] \qquad (6)$$

where n is determined by the average value of the exponent in the expression $I_A(\mathfrak{R})=K'\mathfrak{R}^{(1-n)}$ over the range of interest. The precise value of n does not greatly affect the correction sought and hereafter the value $(20)^{\frac{1}{2}}$ will be adopted. The range of validity of Eqs. (4)–(6) is from $s\sim 2s_1$ to $s\sim 70A^{-1}$ for 40-kv electrons. It is seen that $I_A(\text{loc})$ is very nearly three times $I_A(\text{deloc})$, as assumed in the following, except at very small and very large angles, for equal numbers of molecules involved. If the index of resolution, R, is less than unity because of a background of delocalization, the implied ratio of delocalized to localized molecules is $3(1-R)/R$.

The cosine term in Eq. (6) shifts the phase of the molecular scattering features, resulting in an apparent shift in r_0. The appropriate superposition of Eq. (6) and Eq. (5) gives, very nearly,

$$I_M(\text{tot})\simeq cRI_A(\text{tot})\{\exp(-l^2s^2/2)\}\times\{\sin[s(r_0+\Delta r)]\}/sr_0 \qquad (7)$$

over the entire range of interest of s, where

$$\Delta r\simeq 3r_0(1-R)/\{[20+(sr_0)^2]R\}. \qquad (8)$$

If the conventional correlation method is used to deduce r_0, the quantity Δr must be subtracted from the apparent r_0 at each point of correlation in order to arrive at the true value of r_0.

As a rule, internuclear distances are determined most easily from the radial distribution function, $f(r)$, so it is of particular interest to determine the correction, Δr_{RD}, for this method of analysis. From the defining relation

$$f(r)=\int_0^{s_m}sR(I_M/I_A)_{\text{theor}}\exp(-bs^2)\sin sr\,ds+\int_{s_m}^{\infty}s(I_M/I_A)_{\text{expt}}\exp(-bs^2)\sin sr\,ds \qquad (9)$$

it can be shown that

$$f(r)\simeq(cR/2r_0\lambda)(\pi/2)^{\frac{1}{2}}\exp(-[r-r_0]^2/2\lambda^2), \qquad (10)$$

where $\lambda^2=2b+l^2$. If the shift in $f(r)$ in the vicinity of r_0 caused by a shift in r_0 of magnitude Δr is computed from Eq. (9) and compared with the shift, $(\partial f/\partial r_0)\Delta r_{RD}$, computed from Eq. (10), it is found that

$$\Delta r_{RD}=\int^{\infty}\Delta r\,s^2\exp(-\lambda^2s^2/2)ds\Big/\int_0^{\infty}s^2\exp(-\lambda^2s^2/2)ds, \qquad (11)$$

provided Δr is small compared with r_0. The correction, Δr_{RD}, is again to be subtracted from the apparent r_{RD} to obtain the true r_0. An approximate analytic expression for Δr_{RD} can be developed, giving

$$\Delta r_{RD}=\{3(1-R)\lambda^2/[(1-\eta)Rr_0]\}g(y,z) \qquad (12)$$

with

$$g(y,z)\simeq\exp(10z^2)\left\{\exp(10z^2)-\left(\frac{2}{\pi}\right)^{\frac{1}{2}}yz\left[1+\frac{10}{y^2}-\frac{z^2y^2}{6}\right]\right\},$$

[3] P. Debye, J. Chem. Phys. 9, 55 (1941).

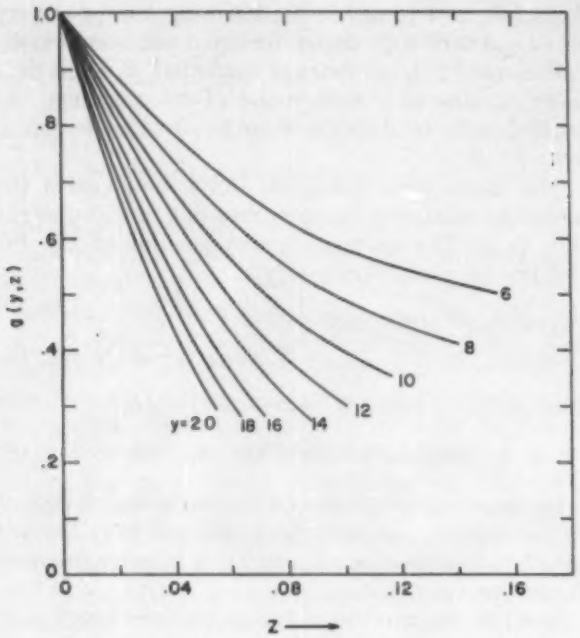

FIG. 1. The function $g(y,z)$ for representative values of y and z.

where $y^2=[20+(s_m r_0)^2]$, $z=\lambda/r_0$, and $\eta=0$ if the $f(r)$ input theoretical r_0 is without error. If, alternatively, the $f(r)$ input theoretical r_0 is consistent with the apparent output r_0, $\eta\simeq(2/\pi)^{\frac{1}{2}}\lambda^3 s_m^3(1-0.3\lambda^2 s_m^2)/3$. The function $g(y,z)$ is plotted for a representative range of variables in Fig. 1.

The error in approximation (12) would be only a few percent if the experimental intensity background could be drawn objectively and precisely. In practice, the background is drawn by successive approximations to internal experimental consistency, and accordingly, the background drawn in the most arbitrary region at small s, where Δr is the largest, is almost certainly prejudiced in a direction to reduce the $\Delta r(s)$. This makes an exact correction impossible, but an approximate compensation, suggested by the requirement that the background be smooth, is to use in Eq. (12) a value of s_m larger than the true s_m by an amount of 3 or 4 units. This does not greatly alter the result, as is shown below.

Unless R is very small, the error introduced into l by uniform gas spread is negligible. This is in contrast to the effect of finite sample size where the error in r_0 may be negligible and the error in l appreciable.

It can be seen that Δr is largest when l is large and r_0 is small. It can be expected, therefore, that bonded hydrogen distances will be affected to an appreciably greater extent than other common distances. Experimental results for ethylene[4] illustrate the magnitude of corrections to be expected. The index of resolution was found to be only 0.76. From the principal structural parameters $r(\mathrm{C-H})\simeq 1.084$ A, $l(\mathrm{C-H})\simeq 0.080$ A, $r(\mathrm{C=C})\simeq 1.333$ A, and $l(\mathrm{C=C})\simeq 0.044$ A, with $b=0.0021$, it is readily calculated that $\Delta r_{RD}=0.0057$ A for C−H and 0.0031 A for C=C if $s_m=3$ A^{-1}. If s_m is increased to 7 A^{-1}, the corrections decrease somewhat to 0.0042 A and 0.0024 A, respectively.

It can be seen that the correction, while small, is significant for accurate work. There has been an unfortunate tendency of workers in the field to omit the reporting or even the determination of R. Values of R lower than 0.3 can easily occur in conventional experiments, according to Bauer *et al.*,[1] although values greater than 0.9 were obtained routinely in the earlier patterns taken with the University of Michigan apparatus.[5] While the best guarantee of accuracy is to obtain experimental indices of resolution approaching unity, it is helpful to have a means of compensating for the imperfections that remain.

[4] L. S. Bartell and R. A. Bonham, J. Chem. Phys. **31**, 400 (1959).
[5] L. O. Brockway and L. S. Bartell, Rev. Sci. Instr. **25**, 569 (1954).

JOURNAL OF APPLIED PHYSICS VOLUME 31, NUMBER 2 FEBRUARY, 1960

Experimental Investigation of a High-Energy Density, High-Pressure Arc Plasma

EDWARD A. MARTIN
The University of Michigan, Ann Arbor, Michigan
(Received September 21, 1959)

The underwater spark is utilized to study the fundamental parameters of a plasma at 30 000°K and 10 000 atmos pressure. The 25-kv spark is obtained by underwater discharge of capacitors having a stored energy of 1800 joules, the inertia of the water providing the confinement necessary to develop high pressures. Phenomena relating to the initiating wire (exploded wire) are discussed. Kerr cell photographs show that spherical structures are formed around both electrodes under certain conditions. A possible explanation is postulated. A detailed energy balance and particle balance are carried out. The results show that the plasma has great capability to store energy in dissociation, excitation, and ionization without a corresponding increase in temperature. The plasma is 30% ionized and the total particle density is about 2×10^{27} per cubic meter. At this density the plasma radiates a blackbody spectrum. Pressures are obtained by calculation based on the rate of spark channel expansion and the shock properties of water. The plasma is found to have an internal pressure of the same order of magnitude as the external pressure because of interparticle Coulomb forces. Plasma conductivity calculated from equations of Gvosdover and Spitzer and Harm agree very well with the experimental value. The study is basically experimental, with the emphasis in interpretation being placed on reliability of the conclusions rather than on refined accuracy.

INTRODUCTION

THERE are two serious experimental obstacles which hinder the study of physical conditions within a high-pressure, high-temperature gas. Confinement of the gas to maintain its pressure requires thermal and mechanical properties of the chamber material which are beyond those presently available; and energy must be continually supplied to the gas at a high rate to replenish that lost by radiation. For these reasons, studies of steady state gases have been primarily concerned with temperatures not exceeding 10 000 °K and with pressures below 1000 atmos. If the studies are carried out on a transient basis, however, one can extend appreciably the pressure and temperature ranges to higher values. The underwater spark, produced by the rapid discharge of a capacitor across underwater electrodes, is an experimentally convenient means of producing and studying a highly ionized, high-pressure, high-temperature gas (plasma).

When a spark takes place under water, the heated spark plasma tends to expand. The mechanical inertia of the surrounding water resists this expansion, resulting in the development of high pressures. The objective, therefore, is to supply the maximum possible power to spark channel while the volume is still small. This calls for a maximum rate of current rise together with high spark resistance. The high pressures tend to increase spark resistance by reducing the degree of ionization and by reducing the mobility of the charged plasma particles.

The underwater spark has been used for many years as a spectroscopic light source. With a stored energy of several joules per discharge the radiant output has a continuum in the ultraviolet which is useful for absorption studies. The underwater spark may also find application as a photographic light source of high brilliance,[1] a subaqueous sound source,[2] or a pressure source. The emphasis in the present investigation, however, is to treat the underwater spark as a research tool for the study of high-energy plasmas. By its use information has been obtained concerning the physical conditions existing within a plasma at temperatures up to 30 000 °K and at pressures of the order of 10 000 atmos.

To establish the orders of magnitude involved, the final results will be briefly summarized. The underwater spark is produced by a 25-kv discharge from a 5.8 μf capacitor. At the moment of peak current, which is 85 000 amp, the spark plasma radiates a continuous spectrum corresponding to a black body at 29 900°K. The external pressure produced by the channel is 8300 atmos. The electrical power input is 390 megawatts. The total particle density within the plasma is about 2×10^{27} per cubic meter; and the plasma is 30% ionized. The plasma exhibits such a large capability to store energy in the form of dissociation, excitation, ionization, and kinetic energy of random motion of the constituent particles that most of the electrical energy input to the spark is initially stored within the channel. This energy is then relatively slowly dissipated (slow on the time scale of the spark processes) as mechanical work to generate a shock wave and as thermal radiation from the surface. The particle density in the channel is great enough so that the radiation emitted is more characteristic of a solid than a gas, and the importance of Coulomb interparticle forces makes the use of the ideal gas law invalid as an equation of state.

The actual measurement procedure consisted of determining the power input to the spark as a function of time by means of a discharge-circuit energy balance.

[1] H. C. Early and E. A. Martin, *Communication and Electronics* (American Institute of Electrical Engineers, New York, 1956), Vol. 22, p. 788.
[2] H. H. Rust and H. Drubba, Z. angew. Phys. 5, 251 (1953).

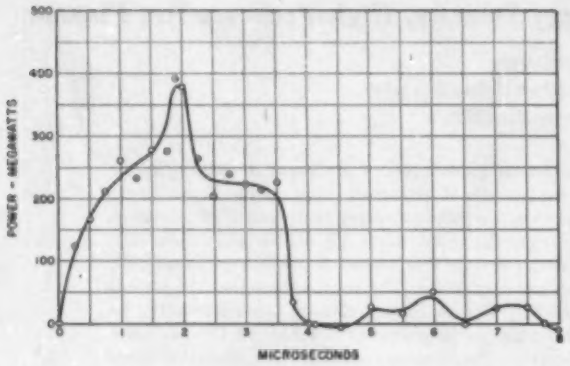

FIG. 1. Power delivered to the 25-kv underwater spark channel by the discharge circuit.

Subμsec Kerr cell camera photographs of the spark channel provided the channel size as a function of time. The channel pressure was determined from the rate of channel expansion and the shock characteristics of water. The channel temperature was determined by means of absolute measurements of the visible radiation. By use of these four fundamental spark parameters, a detailed energy balance for the plasma was carried out as a function of time. This energy balance involved the degrees of dissociation, excitation, and ionization within the channel. The conclusions which were reached are self-consistent as well as consistent with the work of others.

THE DISCHARGE CIRCUIT

The attainment of high pressure and high temperatures within the spark channel requires that the initial rate of current rise be maximized. To this end, the circuit was constructed to have as short leads as possible, and the leads consisted of closely spaced wide copper strips insulated to withstand the capacitor voltage used. The existence of high voltage and high current in the circuit required careful attention to electrical shielding and grounding; otherwise, large spurious signals induced in the triggering and measuring circuits invalidated the experimental data.

The electrical properties of the discharge circuit were as follows: The capacitors consisted of five 1-μf, 25-kv units connected in parallel and mounted inverted at the top of a metal cabinet. The electrical circuit was closed by means of a manually operated air gap, initiating the discharge through the underwater electrodes. On the microsecond time scale of the underwater spark, the 0.01 μsec breakdown time of the air gap could be treated as instantaneous closure of the circuit. The small energy dissipated in this air gap was taken into account in the circuit energy balance. A 15-gal covered water tank was positioned directly below the capacitors. A 3-in. diam window was located in the side of the tank so that photographs could be taken and light measurements made. Since the spark took place only $4\frac{3}{4}$ in. from the window, the shock wave accompanying the spark rendered the use of glass impractical. The material which was finally found to be successful was $\frac{5}{16}$ in. Plexiglas clamped between sheet rubber gaskets.

Current measurements were made by use of a folded ribbon shunt and recording oscilloscope (Tektronix 513-D and Polaroid camera). The shunt resistance and inductance were 0.00693 ohm and 2×10^{-11} henry. Maximum rate of change of current in the discharge circuit, 6×10^{10} amp/sec, would thus induce about one volt compared to the peak resistive voltage of 590 v.

The discharge circuit parameters were experimentally determined by use of conventional measurement equipment or by short-circuiting part of the discharge circuit and noting the current resulting from reduced voltage discharges. The methods used allowed for skin and proximity effects in the discharge circuit and for the effects of induced currents in the shielding cabinet. All values of circuit parameters were checked by approximate calculations based on physical dimensions. The effective series resistance and inductance of the energy storage capacitors were obtained by measurement. The results of the circuit measurements may be briefly summarized. The effective capacitance of the energy storage capacitors was 5.8 μf, the effective series inductance of the entire circuit was 0.26 μh, and the effective series resistance (including the contributions from the manual air gap and the current shunt) was 0.0422 ohm.

CIRCUIT ENERGY BALANCE

The circuit energy balance as a function of time was carried out by use of the measured spark current and the circuit parameters, the spark being treated as a passive circuit element. The current was integrated to obtain capacitor voltage. The derivative of current furnished the inductive voltage. By subtracting resistive and inductive powers from the capacitor power, the power to the spark was obtained (Fig. 1). These measurements and calculations were checked for accuracy by continuously accounting for all of the energy originally stored in the capacitor. This revealed that the errors in the circuit energy balance were of the order of one percent. A summary of these calculations is presented in Table I. The useful product of the energy balance is column 8 which gives the cumulative energy which has been supplied to the spark at any instant of time. It should be noted that half of the energy originally stored in the capacitors was transferred to the spark channel at 8 μsec. This high efficiency of energy transfer is jointly a result of high spark resistance caused by high plasma pressure and by low circuit inductance and resistance.

KERR CELL CAMERA

The Kerr cell camera photographs of the underwater spark yielded the rate of growth of the spark channel as well as much qualitative information. The Kerr cell utilized nitrobenzene as the active liquid. HN22 high

TABLE I. Circuit energy balance.

1 Time μsec	2 Current amp	3 Calculated capacitor voltage kv	4 Calculated instantaneous capacitor output power megawatts	5 Calculated instantaneous inductance input power megawatts	6 Calculated instantaneous resistive power megawatts	7 Instantaneous power to spark megawatts	8 Cumulative energy into spark joules	9 Error of circuit energy balance joules
0	0	25.00	0	0	0	0	0	0
¼	13 700	24.71	338	206	7.9	124	19	+4
½	31 000	23.76	736	527	40.5	168	54	+16
¾	46 600	22.08	1030	725	92.0	213	102	+18
1	58 700	19.84	1164	757	145	262	158	−13
1¼	70 100	17.05	1196	756	207	233	220	−9
1½	78 300	13.96	1094	558	258	278	286	−6
1¾	83 400	10.37	864	293	294	277	359	−10
1.9	85 000	8.19	696	0	305	391	413	+7
2	84 500	6.70	566	−113	301	378	451	+1
2¼	81 500	3.10	252	−292	280	264	528	−17
2½	76 900	−0.28	−21.6	−475	250	203	588	−13
2¾	69 000	−3.40	−234	−674	201	239	644	−17.5
3	57 300	−6.20	−356	−720	139	225	699	−33
3¼	44 700	−8.40	−376	−675	84.4	214	755	−24
3½	29 800	−10.00	−298	−464	37.5	128	809	−13.5
3¾	15 450	−11.00	−170	−214	10.1	34	835	−5.5
4	3 090	−11.40	−35.2	−39.8	4.0	½	838	−6
4½	−19 050	−10.60	+202	194	15.4	−7	837	−9
5	−34 600	−8.40	291	214	50.5	26	839	−3.5
5½	−42 900	−5.00	214	118	77.9	18	851	−6.5
6	−43 600	−1.30	56.6	−73.6	80.1	50	868	−9
6½	−38 400	+2.30	−88.4	−151	62.1	½	878	−7
7	−27 000	5.10	−138	−194	30.8	25	886	−12.5
7½	−10 420	6.75	−70.5	−102	4.6	27	899	−16
8	+7 820	6.81	+53.2	+62.5	2.6	−12	902	−16
							Magnitude of average error	11.7 joules

extinction Polaroids were used. All optical surfaces were adjustable so that not only extinction but also parallelism could be attained; this was found necessary in order to eliminate ghost images produced by multiple reflection. The cell was left open to the atmosphere so that changes in atmospheric pressure or temperature could not strain the windows. Contamination of the nitrobenzene through the small venting hole did not impair the operation of the cell. Evidently the pulse duration of ¼ μsec was not long enough to allow field-distorting space charges to accumulate within the liquid. The light-to-dark ratio was sufficiently high so that no photographic exposure could be detected when the spark was caused to take place with no voltage pulse applied to the Kerr cell electrodes. A 6-in. camera lens was used, the spark being in such a position as to result in an image on the film about 1.8 times actual size. The photographic speed of the entire optical system was about f/40.

The Kerr cell required a 7-kv pulse. This was obtained by use of a voltage-fed pulse network switched by means of a 5C22 hydrogen thyratron triggered by a 2D21 thyratron. The continuously adjustable delay trigger output of the oscilloscope was generally used, which gave delay times as short as one μsec after initiation of spark current flow. For shorter delays the 5C22 was triggered directly by the discharge circuit through an RC delay circuit.

SPHERICAL STRUCTURES

Initial work with the underwater spark was carried out at 4 to 10 kv using a storage capacitor of 11 μf. The sudden application of voltages of this magnitude to underwater electrodes which are approximately 1.5 cm apart does not result in immediate breakdown. There is a time lag of random duration during which a current of about one amp flows. At the lower capacitor voltages the breakdown lag may be several millisec. When the voltage is increased, the duration may be only 10 or 100 μsec. Photographs taken when breakdown finally does occur reveal spherical structures on the electrodes (Fig. 2). These structures have interesting properties. The sphere on the positive electrode is always larger. Surface textures vary from cloudy to glossy smooth. The spheres have not been observed for water temperatures above 15°C, but they grow quite readily at 10°C. Occasionally breakdown failed to occur at the lower voltages because the capacitor charge was depleted by the prebreakdown current. Even in this case the spheres were formed, a fact which was established by photographing them with an auxiliary flash light source. Under this condition, there was no detectable mechanical disturbance in the water, indicating that the spheres did not represent an appreciable change in water density. It is noteworthy that these spheres were consistent in their uniformly spherical structure, because the original electric field between the parallel rod electrodes was far

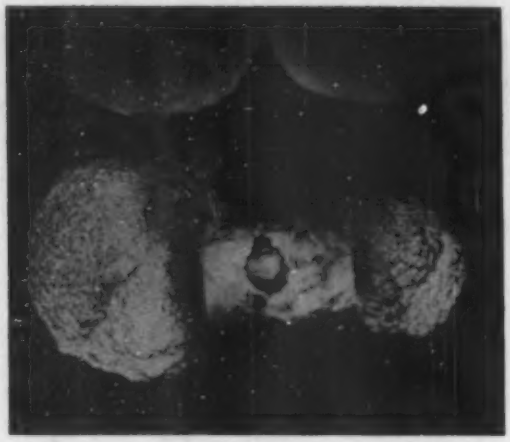

FIG. 2. Kerr cell photograph of a 6-kv underwater spark 10 μsec after breakdown. Left electrode positive.

from spherically symmetric. If a dielectric barrier was inserted between the electrodes to delay breakdown, the spheres grew very large, and while doing so they refused to contact a solid surface. The breakdown path always appeared to terminate at the centers of the spheres. In lieu of a better hypothesis, these spheres may possibly be regions of spontaneous electric polarization somewhat analogous to the magnetic domains in a ferromagnetic material. The surfaces of the spheres would then become visible because of an abrupt change in the dielectric constant of the water.

STREAMER BREAKDOWN

When the capacitors were charged to voltages of the order of 20 kv or more, breakdown took place so rapidly that the spheres did not form. The breakdown sequence resembled that which occurs in gases. One or both electrodes originated streamers. When a conducting path was established, the unsuccessful streamers became dormant, and their presence was revealed in the photographs by the light from the main discharge channel. The breakdown process required times of the order of several microseconds for voltages of the order of 20 kv.

INITIATING WIRE

The random duration of the prebreakdown period and the irregular, unpredictable path of the spark made correlation of data taken on different sparks very difficult. Also, the spheres, when present, tended to mask the channel geometry. These difficulties were all circumvented by initiating the spark with a fine wire between the electrodes. The resulting uniform, straight, circular cylinder, free of spheres, enabled the association of a definite and measurable geometry with the spark channel. In addition, the sparks became quite reproducible from one to the next. A large number of Kerr cell photographs and current oscillograms were taken to check reproducibility. Excellent consistency of the data justified the use of instantaneous measurements on successive sparks at increasingly later delay times as a means of obtaining the spark behavior as a function of time.

It was established that the metal of the initiating wire played no significant part in the plasma phenomena of the spark channel. Even though the atoms of the initiating wire were more highly ionized than the other particle components of the plasma, they neither contributed an appreciable number of particles nor stored an appreciable amount of energy. When larger size initiating wires were used at low voltages, a dip in the current shown by the current oscillogram revealed the moment at which the wire vaporized. For 3-mil copper wire at 6 kv, the vaporization time was about one μsec. However, for the spark measurements described in this paper, one-mil tungsten wire was used. In this case, the vaporization took place essentially instantaneously on the microsecond time scale of the spark.

It has been predicted on the basis of similarity that a spark channel in a gas under very high pressure should consist of a very fine filament. Such a channel, because of lateral instability, should continually be whipping about within the luminous column, successively exciting and ionizing small volume elements of the plasma and then moving on and leaving those elements to radiate the stored energy until the next lateral trip. It is not necessary to postulate that particles would have to attain a lateral velocity corresponding to the velocity of the filamentary channel, since the channel is merely a path of high ionization. This path could move at very high lateral velocities, too high to be revealed by a $\frac{1}{4}$-μsec photographic exposure. Various attempts were made to cause the postulated fine channel to reveal itself. The spark was initiated adjacent to a transparent material (plastic, mica, or glass) and then photographed through the resulting "window" before the material was destroyed, in order to see into the luminous column. Also, initiating wires were bent into hairpin shapes, or two underwater sparks were initiated parallel to each other, in an effort to make the mutual magnetic fields drive the fine channel out of the luminous column. Among the large number of Kerr cell pictures which were made, not one showed any evidence of the predicted fine filamentary channel.

STRIATIONS

Photographs of underwater sparks initiated by a relatively large diameter wire showed transverse striations during the early stages of spark development. They were occasionally very clear and sharply delineated. The spacing was a function of the initiating wire diameter but was relatively unaffected by changes in wire material. These striations were originated by unduloids, the succession of droplets which is formed when a wire is rapidly melted by an electric current. The unduloids are formed by the self-magnetic field of the wire acting on the current carried by the wire, the so-called pinch

effect. This effect, if acting alone, would constrict the wire at random intervals. The high degree of regularity of the unduloids, and hence of the observed striations, may be explained by considering the instability of a liquid cylinder caused by surface tension. The surface tension tends to cause the liquid cylinder to break up into uniformly spaced droplets, the spacing being dependent on the diameter of the wire. The spacing may be predicted on the basis of the work of Lord Rayleigh.[3] Surface tension provides the initial small regularly spaced constrictions in the wire cross section which are then amplified by the relatively much greater magnetic pinch forces. Therefore, at some stage of the vaporizing process, the initiating wire must consist of a succession of metallic droplets separated by short arcs in the metal vapor. The spacings of the striations observed on the Kerr cell photographs of the underwater spark were compared with the predicted values based on Rayleigh's work. The spacings were found to be one-half and one-fourth (but not one-third) the predicted values. This indicates that secondary and tertiary unduloids are formed.[4] In the case of a one-mil tungsten wire vaporized at 25 kv, the striations are not in evidence. Either they are unresolved in the photographs or are incompletely formed because of the short duration of the liquid phase.

CHANNEL GROWTH

The size of the channel of the underwater spark, a consistently uniform circular cylinder, may be scaled from the Kerr cell photographs. When this is done for successively later times in the spark cycle, a growth curve is obtained. For the 25-kv, 5.8-μf spark studied in this work, the diameter of the channel in millimeters was

$$D = 1.8t^{0.52}, \tag{1}$$

where t is the time in μsec after current initiation. The length of the spark was 1.5 cm, determined by electrode separation. In other similar spark sequences at different values of voltage and storage capacitance, the exponent of t was always found to be close to one-half.

SPARK CHANNEL PRESSURE

The rapid transfer of a large amount of energy into the small volume of the spark channel raises its temperature and tends to make it expand. The enveloping medium opposes this expansion, the amount of opposition being dependent on the medium density and relatively independent of hydrostatic pressure. For this reason, sparks in liquids develop high transient pressures which result in production of shock waves. The shock wave is made evident by the loud metallic report which is heard when the pressure pulse reaches the walls of the water tank.

Consideration was given to the problem of measuring the pressures in the vicinity of the underwater spark. An electromechanical device is not feasible. A response time of less than one μsec, a pressure range up to 50 000 atmos or so, very small size, extreme ruggedness, and insensitivity to rapidly varying electric and magnetic fields are characteristics which are not presently available in any transducer. Since the underwater spark will punch slugs from sheet metal, a rough index of the pressure range was established by calculating the static pressures necessary to shear a corresponding amount of metal. A second approximate measurement of the pressures in the water adjacent to the spark channel was made by measuring the amount of compression of the water. Compression modifies the index of refraction of the water, and hence an optical measurement of the change of index is sufficient to establish the pressure. This measurement indicated pressures in the range 2500 to 5000 atmos, but the accuracy was not suitable for present purposes. Further attempts to measure pressure based on determining the amount of adiabatic compression of small bubbles of hydrogen located close to the spark were not successful.

Pressures adjacent to the surface of the underwater spark may, however, be obtained by calculation based on rate of channel expansion. These pressures depend only on the hydrodynamic properties of water and on the rate of expansion of the cylindrical spark channel, provided that negligible water is inducted into the spark channel through the channel wall. As a result of the channel particle balance calculations soon to be described, it was established that the amount of water consumed at the channel wall was sufficiently small so that the pressure calculations were not rendered inaccurate. For example, at the time of current maximum the measured rate of channel expansion was 348 m/sec. Induction of water through the channel wall accounted for a wall velocity of only 10 m/sec.

Explicit calculation of the pressures produced at an arbitrary point in the water surrounding the expanding cylinder, whether formulated in the Euler or the Lagrange form, is difficult because of the high degree of nonlinearity. If, however, one is satisfied with a partial solution, calculations suitable for present requirements may be obtained. The procedure involves using the Rankine-Hugonoit shock wave relations in differential rather than in incremental form, yielding the pressure and pressure gradient at the surface of the expanding cylinder. One does not obtain information concerning the pressure distribution throughout the entire compressed region surrounding the cylinder. The solution obtained may be treated as the two inner boundary conditions for the more complete pressure calculation. The details of the pressure calculation will not be presented here; only the resulting equations will be given. The shock characteristics of water are taken to be given by

$$P = A(\rho/\rho_0)^7 - B, \tag{2}$$

[3] Lord Rayleigh, Proc. London Math. Soc. **10**, 4 (1878).
[4] W. Kleen, Ann. Physik **403**, 579 (1931).

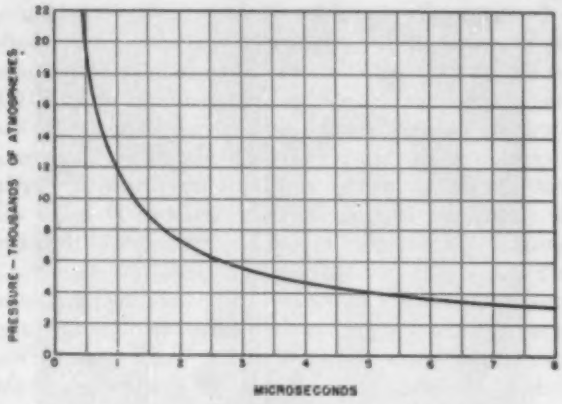

FIG. 3. Calculated pressure developed at the surface of a 25-kv underwater spark channel.

where P is pressure in atmos, ρ is the density at pressure P, ρ_0 is the normal density, and A and B are constants, equal to about 3000 atmos but differing by 1 atmos. Further, the separable-energy character of water is utilized so that only the relations concerning conservation of mass and momentum need be used. One may omit the small refinement of the solution resulting from consideration of the conservation of energy. The equations which result, giving the pressure and pressure gradient on the expanding cylinder surface, are

$$(P+B)^{3/7}=\left(\frac{3\rho_0^{1/2}}{7^{1/2}A^{1/14}}\right)U+B^{3/7}, \tag{3}$$

$$\frac{dP}{dr}=\frac{-(\rho_0)^{1/2}(dP/dt)}{7^{1/2}A^{1/14}(P+B)^{3/7}}-\frac{7(P+B)}{3r}+\frac{7(P+B)^{4/7}B^{3/7}}{3r}, \tag{4}$$

where U is the velocity of the cylinder wall (m/sec), r is the cylinder radius (meters), t is the time (sec), P is the pressure at the cylinder surface (newtons/meter^2), and ρ_0, A, and B are from Eq. (2) (MKS units). The value of dP/dt in Eq. (4) is obtained by differentiation of Eq. (3).

A plot of the pressure on the surface of the 25-kv underwater spark as a function of time is given in Fig. 3. The pressure curve has an infinite value at zero time because the exponent of the expansion relation, Eq. (1), is less than unity. The accuracy of measurement of spark diameters at times less than $\frac{1}{2}$ μsec was critically dependent on timing of the Kerr cell camera, and also the photographs have a finite exposure interval of $\frac{1}{4}$ μsec. Therefore, the expansion curve should not be considered valid during this early interval. The pressure curve should be considered as starting at zero initially and rapidly rising to a pressure of the order of 20 000 atmos in about $\frac{1}{2}$ μsec. The pressures given in Fig. 3 agree well with those obtained by measuring the change in optical index of the water, and are of the same order as the static pressures necessary to punch slugs from sheet metal.

MEASUREMENT OF TEMPERATURE

The underwater spark at high power levels emits a bluish-white flash of light. This light furnishes a means of measuring the temperature of the spark as a function of time. In general, the light emitted by a gas discharge will consist of spectral lines, recombination continua, and electron acceleration radiation (bremsstrahlung). For practical purposes, the light from a low pressure gas discharge below $\frac{1}{10}$ atmos is a pure line spectrum characteristic of the gas. As gas pressures are increased through the range from about $\frac{1}{10}$ atmos to several hundred atmos, the spectral lines broaden as a result of Doppler effect, collisional damping, Stark effect, and Zeeman splitting in the randomly varying local magnetic fields. Also, the recombination continuum becomes appreciable because of an increasing amount of volume recombination. As an example, hydrogen at approximately 30 atmos emits a continuous spectrum. The distribution of spectral intensity within the continuum, however, follows no simple mathematical law. Temperatures in many types of discharge may be determined by measuring the amount of spectral line broadening, the relative intensity of spectral lines, or the distribution of intensity in spectral bands. Such temperatures are not necessarily the temperatures corresponding to the average random thermal energy of any particular type of particle in the discharge. In general, unless there is thermal equilibrium among the various particle types, temperatures obtained by such measurements cannot be interpreted as temperature in the usual sense. Measurements carried out by two different methods will generally yield widely differing results.

As the gas pressure of an electrical discharge is progressively increased above approximately 200 atmos, the irregularities in the continuous spectrum which are caused by spectral lines or groups of spectral lines become submerged in the continuum. This continuum is produced partly by electron-ion recombination. However, at very high particle densities approaching the order of magnitude encountered in solid materials, the major contribution to the continuum is from electron acceleration radiation. The constituent plasma particles lose their individual spectral character. The plasma radiates a spectrum more characteristic of a solid than a gas. If certain conditions are fulfilled, the plasma should be expected to radiate a continuum having the spectral distribution of a black body. The measurements made during this investigation indicate that a high power underwater spark does radiate a blackbody spectrum.

There are two requirements which must be met in order for the continuum to have a blackbody distribution. First, all particle types within the plasma must be

in thermal equilibrium. This condition is approached when the freedom with which energy may be exchanged between different particle types is large enough so that the electrical input power to the plasma, which is primarily delivered to the electrons only, is transmitted to the other classes of particle types with only a small temperature difference being necessary. The freedom of energy transfer between the electrons and other particle types is measured by an accommodation time constant, which is determined by the rate of energy transfer through the mechanisms of elastic collisions, inelastic (dissociating, exciting, and ionizing) collisions, and radiant transfer. The over-all time constant (when all three mechanisms are operative) will of course always be shorter than the time constant for any one mechanism of transfer alone. A calculation on the basis of only one mechanism will give an upper limit to the true time constant. An accommodation time constant for the 25-kv spark being treated here, calculated on the basis of only elastic collisions between the electrons and ions of the plasma, gives a value of the order of 10^{-10} sec. The factors which enter into this calculation are the spark plasma temperature and particle densities. Thus, on the microsecond time scale of the underwater spark, the constituent particle types of the plasma may be considered to be in thermal equilibrium.

The second requirement for blackbody radiation is that the particle density must be great enough to render the plasma opaque to radiation which is in the spectral region of interest. From the viewpoint of photons, the mean free path of a photon must be small compared to the dimensions of the plasma. If this condition is satisfied, then a quantum which originates within the volume of the plasma is absorbed and re-emitted many times before escaping from the surface. When all particles with which the photon interacts have the same temperature, the situation is analogous to the absorption and re-emission of radiation within a blackbody enclosure at a uniform internal surface temperature. The plasma of the underwater spark is highly opaque. All Kerr cell photographs have failed to define any detail within the plasma volume. Also, for various reasons, the spark has been allowed to engulf a solid object during the course of its expansion. In the resulting Kerr cell photographs, the image of the object is sharply terminated at the channel surface. This evidence of opacity in the visible spectrum is the basis for concluding that the plasma has a very great absorption coefficient for radiation in the wavelength range in which the temperature measurements were made.

The spectrum of the light from the underwater spark was obtained by means of a quartz spectrograph. The spectral range covered was 3400 to 6900 A, and the exposures were time integrated over the entire spark history. Line structure could not be detected in the continuum. No attempt was made to determine spectral intensity as a function of wavelength because of the time-integrated nature of the exposures.

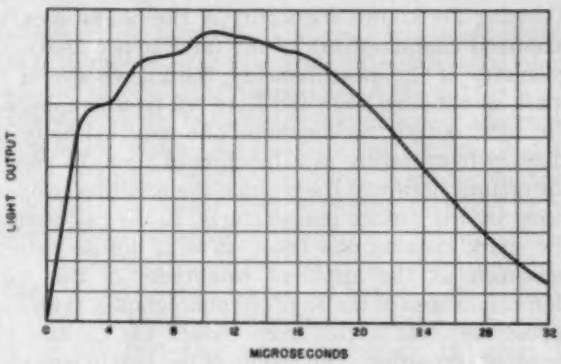

FIG. 4. Oscillogram of light output at 4190 A from the 25-kv underwater spark.

A conventional method of measuring the temperature of a body emitting a blackbody spectrum is to measure the relative spectral intensity at two wavelengths. However, when the temperatures are in the range of 30 000 °K or above, the method is of low accuracy if the measurements are made in the visible region of the spectrum. The visible region falls at wavelengths well beyond the maximum of the blackbody curve plotted on a wavelength scale, so that the ratio of the two measured intensities is a very insensitive function of the temperature. Therefore the temperature of the underwater spark was measured by determining the absolute intensity at a single wavelength. As a check, two completely independent measurements were made, one at the red end of the spectrum, and one at the blue end. Interference filters were used to isolate a known narrow spectral band, and vacuum phototubes were used. The phototube circuit for each measurement was enclosed in a shielding aluminum container together with the battery. The load resistor was made smaller than is typical in order to reduce the circuit time constant. Thorough checks were carried out to insure that the circuit frequency response and linearity were suitable, and that stray pickup and gas amplification were not present in sufficient amount to affect the measurements. The phototubes were calibrated against a tungsten ribbon standard lamp, which in turn had been calibrated by the use of optical pyrometers.

An oscillogram of the light output at 4190 A is shown in Fig. 4. An immediately evident significant fact is that the light output persists for about 30 μsec, whereas almost all of the electrical energy input is delivered to the spark in 4 μsec. This is evidence that the major amount of energy to the spark is stored within the plasma, this energy then being relatively slowly dissipated as the spark channel expands and cools. The light output oscillograms are shaped by the combined effects of channel expansion and decreasing temperature. As a result, oscillograms taken at the red end of the spectrum show the light output reaching a maximum slightly later than the light output at the blue end, but the total duration is approximately the same in both cases.

Utilizing the known sensitivity of the phototubes, the passband characteristics of the interference filters, the geometry of the measurements, the known size of the spark as obtained from the Kerr cell photographs, and the light output oscillograms, one may calculate the channel temperature as a function of time. In view of the opaque nature of the plasma, the resulting temperatures are the surface temperatures. In the calculations, the spark channel was taken to be a diffuse radiator inasmuch as the apparent brightness of the spark channel, as seen in the Kerr cell photographs, is uniform across the cross section even though the channel is a figure of revolution. The results of the two independent temperature measurements are presented in Fig. 5. Agreement is very good, tending to confirm the conclusion that the spark radiates as a black body.

In other temperature measurements which were made during the course of this study, the temperature measured at the red end of the spectrum has consistently been slightly lower than that obtained from the blue measurement. There are two possible causes for this discrepancy. If the spark channel surface has an emissivity less than unity, even though it may be independent of wavelength, then the true channel temperature would be greater than either of the measured values, and the blue measurement would give the higher value. The second possible cause is that the plasma absorption coefficient for red radiation may be somewhat greater than that for blue radiation.[5] If this is the case, the blue radiation will come from deeper layers within the spark channel where the temperature is somewhat higher.

The internal temperatures in the spark plasma are undoubtedly higher than the surface temperatures obtained from the preceding measurements. However, several considerations lead to the conclusion that these temperatures are not higher by a great factor. The first consideration is based on the apparent absence of a fine filamentary current-carrying channel within the luminous column of the spark. In addition, small calculated pinch pressures as compared to the total plasma pressure lead to the conclusion that the current density is substantially uniform across the spark cross section. Since most of the electrical energy supplied to the spark is stored in the plasma, any small volume unit will receive and store about the same amount of energy as any other volume unit, and thus will attain about the same temperature. There is no reason to require that there be an appreciable thermal gradient within the plasma in order to carry energy to the channel walls. The thermal conductivity of the plasma, to be calculated later, is low enough so that it would require a central temperature of about 3 million degrees in order to transmit to the channel walls the amount of power necessary to convert liquid water to channel plasma. Ion recombination on the channel wall will be shown to be more than adequate to supply this amount of power. The major power loss from the spark is that used in generating the shock wave. If all elemental volumes of the spark plasma expand uniformly, then this major energy loss is supplied without the necessity of a large thermal gradient to transport energy from the central regions of the channel to the spark environment. Further evidence that the spark does not have a central hot core is the inability of the ratio of channel cross-sectional area to lateral area to affect such spark parameters as light output, intrinsic brightness, peak current, and current damping. Photographs, light measurements, and current oscillograms were made with the underwater spark flattened between closely spaced surfaces. In spite of the consequent increase in the ratio of surface area to volume, the major parameters were not significantly altered. This behavior could not be expected if the central temperature were as much as an order of magnitude greater than the surface temperature. Finally, for the purposes of the energy balance to be described next, the central temperature is not of critical concern, since its value does not affect appreciably the energy balance. The density of energy storage in the spark plasma was found to be almost directly proportional to pressure and almost independent of temperature up to temperatures as high as 200 000°K.

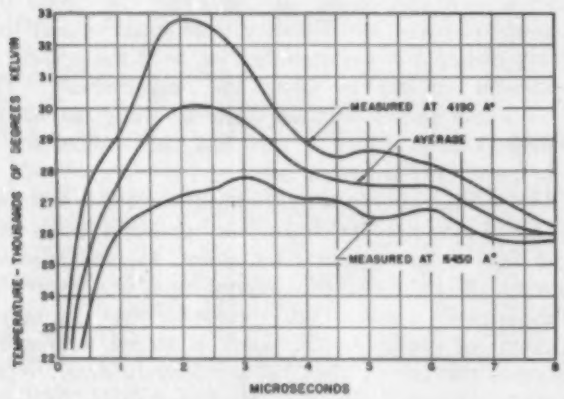

FIG. 5. Temperature of the underwater spark as determined by two independent measurements at two wavelengths. Note depressed zero.

[5] A star at 29 000°K should have a greater absorption coefficient for red light than for blue light. See L. H. Aller, *Astrophysics, the Atmospheres of the Sun and Stars* (Ronald Press Company, New York, 1953), p. 186.

THE SPARK ENERGY BALANCE

The preceding work has made available the spark channel size, the electrical input energy, the pressure, and the temperature as functions of time. These four parameters are the basis for a spark channel energy balance. The procedure will be concisely summarized. One begins with the total electrical energy which has been supplied to the spark by the discharge circuit previous to a selected instant of time. From this, one subtracts the total energy which has been lost from the channel by radiation, mechanical work, and thermal

conduction. Energy utilized at the channel wall to vaporize, dissociate, excite, and ionize incoming water should not be subtracted, since this energy is retained within the channel. The result obtained by this procedure is the energy actually resident within the channel at the selected instant of time.

The second part of the energy balance consists of employing the pressure, the temperature, the Saha and Boltzmann equations, and a plasma equation of state to obtain the plasma energy stored in the form of particle kinetic energy, dissociation, excitation, and ionization. The procedure may be termed a particle balance. The resulting plasma energy density multiplied by the spark channel volume yields the total energy stored in the spark channel. This result should agree with the channel energy obtained by the first method. The two procedures just described were used to calculate the stored energy as a function of time for the first eight μsec after initiation of current through the spark. These first eight μsec constitute the most interesting period of the spark history.

As suggested above, energy may be removed from the spark channel by radiation, by mechanical work to generate the shock wave, and by thermal conduction to the surrounding water. The radiant power output may be calculated using the Stephan Boltzmann law and the spark channel dimensions. The mechanical power output may be computed as the product of channel external pressure, wall velocity, and wall area. The power loss caused by thermal conduction is difficult to compute since the problem involves transient heat flow in which the dimensions of the hot body are changing and the hot surface is continually absorbing the adjacent water. Approximate calculations lead to a value of about 2 megawatts, which is small compared to the other two losses. Also, the heat transferred to the hottest water adjacent to the channel is reintroduced into the channel when this water is subsequently inducted. The thermal conduction loss will therefore be neglected. Calculated power losses at various moments due to radiation and mechanical work are given in Table II. Integrals of these losses furnish the total energies lost. These losses may be subtracted from the discharge circuit input energy to obtain the energy stored in the spark channel. The results are given in column 10 of Table II, and are plotted as Curve A in Fig. 6.

PARTICLE BALANCE

The second part of the energy balance requires that the number density of the various particle types in the spark plasma be determined. In general, one could write a complete set of particle balance equations involving as variables the number densities of all types of particles which could conceivably be found to exist in the plasma. This would involve all possible atom types in a wide range of conditions of association, excitation, and ionization. These particle balance equations,

TABLE II. Spark energy balance.

1 Time μsec	2 Channel diameter meters ($\times 10^{-6}$)	3 Channel volume cubic meters ($\times 10^{-6}$)	4 Channel wall velocity meters/sec	5 Calculated external pressure atmos	6 Shock wave power megawatts	7 Shock wave energy joules	8 Radiant power megawatts	9 Radiant energy joules	10 Channel energy (Curve A, Fig. 6) joules
0	0	0	∞	∞	∞	...	0	0	0
¼	0.813	7.8	913	32 300	112.6	27.5	0.346	0.075	−8.6
½	1.25	18.4	657	19 400	75.0	44.5	1.41	0.300	+9.6
¾	1.55	28.3	541	14 200	56.1	65.6	2.10	0.714	35.7
1	1.80	38.1	471	11 600	46.2	78.4	2.84	1.32	78.5
1¼	2.02	48.0	423	9960	40.1	89.2	3.56	2.12	128.7
1½	2.22	57.0	388	8800	35.6	98.7	4.30	3.11	184
1¾	2.41	68.3	361	7900	32.4	107	5.10	4.30	247
1.9	2.51	74.3	348	7600	31.2	112	5.42	5.10	296
2	2.58	78.3	338	7300	30.0	115	5.58	5.64	330
2¼	2.75	89.0	320	6810	28.2	122	6.06	7.10	399
2½	2.91	99.6	305	6320	26.4	129	6.29	8.65	450
2¾	3.05	109.5	291	6040	25.2	135	6.48	10.3	498
3	3.20	121	280	5640	23.8	142	6.59	11.9	545
3¼	3.34	132	268	5350	22.5	147	6.42	13.5	594
3½	3.46	141	259	5150	21.8	153	6.28	15.1	641
3¾	3.60	153	251	4850	20.6	158	6.15	16.7	660
4	3.72	163	243	4700	20.0	163	6.06	18.2	656
4½	3.96	184	230	4410	18.9	173	6.24	21.2	643
5	4.17	204	219	4070	17.5	182	6.40	24.4	633
5½	4.39	227	208	3870	16.7	190	6.70	27.6	633
6	4.60	249	200	3720	16.1	198	7.00	31.2	638
6½	4.79	270	193	3530	15.4	206	6.83	34.6	637
7	4.98	292	186	3380	14.8	214	6.55	38.0	634
7½	5.17	315	180	3280	14.4	221	6.42	41.2	637
8	5.34	336	174	3080	13.5	228	6.52	44.5	629

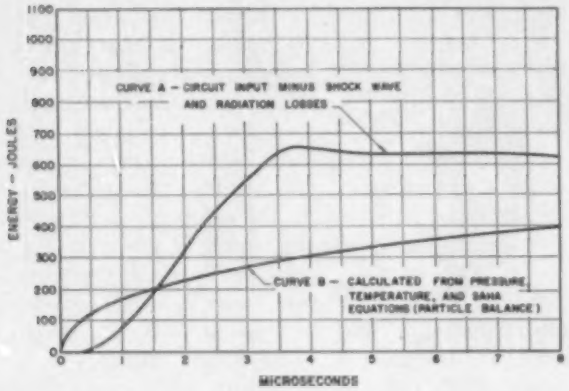
CURVE A – CIRCUIT INPUT MINUS SHOCK WAVE AND RADIATION LOSSES
CURVE B – CALCULATED FROM PRESSURE, TEMPERATURE, AND SAHA EQUATIONS (PARTICLE BALANCE)
ENERGY – JOULES
MICROSECONDS

FIG. 6. Energy stored in the 25-kv underwater spark channel. Summary of results of the entire energy balance.

involving Saha ionization equations and dissociation equations, will be a nonlinear set, and hence, explicit solutions will be inconveniently complicated as far as algebraic manipulation is concerned. In the present study, this complication in obtaining the particle balance solution was avoided by assuming initially that certain particle types were present in negligible amounts in the plasma, and hence, the appropriate terms in the equations could be neglected. The resulting particle balance solutions then supplied information which could be used to confirm that the original assumptions were in fact correct.

The types of particles which could conceivably be found in the underwater spark plasma are water molecules, oxygen molecules, hydrogen molecules, ozone molecules, oxygen atoms in all degrees of excitation and ionization, hydrogen atoms in all degrees of excitation (and singly ionized), tungsten atoms in all levels of excitation and ionization, copper atoms (from the electrodes) in all levels of excitation and ionization, hydroxyl (OH) groups, and negative hydrogen ions formed by electron attachment. This list could be made more extensive by adding such molecules as copper oxide and by considering that all molecule types may themselves be excited or ionized.

Copper will be eliminated from consideration, since there is not sufficient time for copper to migrate from the electrode regions into the spark. The kinetic theory calculated mobility for copper (an upper limit to the true value) is 2.4×10^{-6} m²/sec v, and the typical electrical gradient is 3.3×10^{5} v/meter. This gives a migration distance of only 2×10^{-5} m in 24 μsec. This is small compared to the spark length of 1.5×10^{-2} m. Tungsten may also be eliminated from consideration. It will be shown later that the tungsten atoms are multiply ionized, but since there are so few of them present compared to the total particle density, they store a negligible amount of energy and contribute a negligible number of free electrons to the plasma. Subsequent analysis will also show that there is a negligible amount of second ionization of the oxygen atoms, so that only neutral and singly ionized oxygen need be considered. Ozone, hydroxyl groups, and negative hydrogen ions will be considered to exist in negligible numbers, since they are either unstable at high temperatures or have small dissociation energies.

The degrees of dissociation of water, oxygen, and hydrogen molecules were investigated using the dissociation relation of Gibson and Heitler.[6] This relation strictly applies only to diatomic molecules, but was also applied to the triatomic water molecule by choosing the moment of inertia and characteristic frequency to obtain the minimum degree of dissociation. It was found that undissociated water constitutes at most less than 1% of the total number of particles present in the plasma. As applied to oxygen molecules, the dissociation relation showed that there are less than 3% as many oxygen molecules as there are oxygen atoms present. The fraction of hydrogen molecules was similarly found to be much less than 3% of the number of hydrogen atoms present. The conclusion was therefore reached that undissociated molecules constitute at most only several percent of the total number of plasma particles and may therefore be neglected.

The remaining numerically important particle types were determined by solving the following simultaneous particle-balance equations:

$$N_{\mathrm{HI}}+N_{\mathrm{HII}}+N_{\mathrm{OI}}+N_{\mathrm{OII}}+N_e=N, \tag{5}$$

$$N_{\mathrm{HI}}+N_{\mathrm{HII}}=2N_{\mathrm{OI}}+2N_{\mathrm{OII}}, \tag{6}$$

$$N_{\mathrm{HII}}+N_{\mathrm{OII}}=N_e, \tag{7}$$

$$N_{\mathrm{HII}}N_e=N_{\mathrm{HI}}S_{\mathrm{H}}, \tag{8}$$

$$N_{\mathrm{OII}}N_e=N_{\mathrm{OI}}S_{\mathrm{O}}, \tag{9}$$

where N is the total particle density, N_e is the electron density, N_{HI} is the hydrogen atom density, N_{HII} is the hydrogen ion density, S_{H} is the Saha factor for hydrogen, and O subscripts designate similar terms for oxygen. These equations were supplemented by a large number of Boltzmann excitation relations. Since each Boltzmann relation introduced one unknown term as well as supplying one equation, the excitation relations were subsequently introduced after the above particle balance equations were solved. The Saha factor is given by

$$S=\frac{2B'(T)}{B(T)}\left(\frac{2\pi m_e k}{\mathrm{h}^2}\right)^{\frac{3}{2}}T^{\frac{3}{2}}\exp\left(\frac{-11\,600V}{T}\right), \tag{10}$$

where $B(T)$ is the atom partition function, $B'(T)$ is the ion partition function, m_e is the electron mass, and V is the ionization potential in volts. Other terms have the usual meanings.

The particle balance equations were completely solved for three selected instants of time during the spark cycle: one-half μsec, 1.9 μsec (current maximum), and 4 μsec (first current zero). The value of N was ob-

[6] G. E. Gibson and W. Heitler, Z. Physik **49**, 465 (1928).

tained by employing the ideal gas law as the equation of state of the plasma. Subsequently, it will be concluded that the plasma has an internal pressure caused by interparticle Coulomb fields, and hence the N obtained is only an approximation. The pressure term in the ideal gas law included not only the calculated external pressure (7600 atmos at 1.9 μsec) but also the average pinch pressure (735 atmos at 1.9 μsec). The partition functions, which are nonconvergent infinite series, were evaluated by a simplified form of the method of excluded volumes of Urey and Fermi.[7] This concept of excluded volumes also leads to appropriately reduced ionization potentials. The solutions to the particle balance equations at current maximum, including the excitation as obtained from the Boltzmann relations, are presented in Table III. To each particle type in this table there may be ascribed a certain amount of energy. This in general consists of water vaporization energy, dissociation energy, excitation energy, ionization energy (based on reduced ionization potentials), and kinetic energy of thermal motion. The ionization energies have been associated with the product ions, leaving only the kinetic energy of random motion to be ascribed to the resultant electrons. This obviated subdividing the electrons into groups according to their origin, and therefore simplified the calculations. The appropriate energies per particle at current maximum are given in column 3 of Table III. The resulting energy densities per particle type are given in column 4. Summation of column 4 gives the energy density in the plasma at current maximum, 3.08×10^{9} joules/meter^3. A similar procedure carried out at $\frac{1}{2}$ and at 4 μsec yielded stored energies of 7.0×10^{9} and 1.8×10^{9} joules/meter^3 respectively. Calculations showed that a negligible amount of energy was stored by induced polarization of the hydrogen atoms and the oxygen atoms and ions.

TABLE III. Particle balance at 1.9 μsec (current maximum, 85 000 amp).

Particle type	Particle density (per cubic meter) ($\times10^{24}$)	Energy per particle (ev)	Energy density (joules per cubic meter) ($\times10^{9}$)
Neutral hydrogen			
ground state	6.75	7.2	7.78
first excited state	0.52	17.4	1.45
Ionized hydrogen	3.01	17.7	8.55
Neutral oxygen			
ground state	2.48	7.2	2.86
first excited state	0.645	9.2	0.950
second excited state	0.055	11.4	0.101
third excited state	0.061	16.5	0.162
Ionized oxygen			
ground state	0.977	17.7	2.77
first excited state	0.675	21.0	2.27
second excited state	0.210	22.7	0.764
third excited state	0.0092	32.6	0.048
fourth excited state	0.0042	40.8	0.027
Electrons	4.48	3.9	3.05
Total	2.02×10^{27}		3.08×10^{9}

[7] R. H. Fowler, *Statistical Mechanics* (Cambridge University Press, Cambridge, 1936), second edition.

TABLE IV. Stored energy density in water (excitation energy neglected).

Pressure atmos	Temperature (°K)	Energy density (joules per cubic meter)
4 150	31 500	1.45×10^{9}
8 300	31 500	2.80×10^{9}
20 000	31 500	6.38×10^{9}
8 300	40 000	2.73×10^{9}
8 300	60 000	2.62×10^{9}
8 300	200 000	2.78×10^{9}

Highly ionized tungsten from the initiating wire contributes an additional 0.72×10^{9} joules per cubic meter at 200 000°K.

The known volume of the tungsten initiating wire, together with simultaneous Saha equations, allowed the number densities of tungsten atoms in various stages of ionization to be determined. Appropriately reduced ionization potentials were used. The results showed that at current maximum in the underwater spark, most of the tungsten was singly and doubly ionized, the populations of these two levels being about equal. The consequent density of stored energy was found to be $\frac{1}{2}$% of the energy density stored by dissociation, excitation, and ionization of water. The tungsten also contributed a negligible number of particles to the channel in comparison with those furnished by the water. Similarly, the amount of second ionization of oxygen may be determined. The results showed that there was about 0.05% as many doubly ionized oxygen ions as singly ionized ions, so that the resultant energy storage was negligible.

An interesting result of the calculations of energy density may be obtained by taking the ratio of energy density to channel pressure (including average pinch pressure) and plotting the result as a function of time. The ratio is found to be constant to an accuracy of about 12%. This proportionality of energy density to pressure was investigated further by applying the particle balance equations to the products of dissociation of water over a more extended pressure and temperature range than is encountered in the underwater spark. The results, which neglect energy of excitation, are summarized in Table IV. Over the range of pressures and temperatures calculated, the energy density is approximately proportional to pressure and almost independent of temperature. By making use of this constant ratio between energy density and pressure, and employing the volume of the spark as obtained from the Kerr cell photographs, one may plot a curve of total energy stored in the underwater spark as a function of time. The result is shown as Curve B in Fig. 6. This curve constitutes the second part of the energy balance. Agreement between Curves A and B would indicate complete accounting for all of the energy in the spark channel at any instant of time.

DISCREPANCIES IN THE ENERGY BALANCE

The differences between Curves A and B may be qualitatively and semiquantitatively resolved. The fact that Curve A goes slightly negative reveals that the calculated external pressures were somewhat too large, which indicates that the actual rate of channel growth was less than that used in the calculations. The method of determining the rate of channel growth introduces some uncertainty, but a major factor is the effect of optical magnification as a result of the pressure gradient adjacent to the spark channel surface. The shock wave calculations lead to a pressure gradient of 5.8×10^7 atmos/m at $\frac{1}{2}$ μsec and 2.15×10^7 atmos/m at 1 μsec. These pressure gradients were converted to refractive index (n) gradients by assuming $n-1$ to be proportional to mass density. Appreciable curvature of a light ray results, and the consequent effect on the apparent channel size was approximately determined graphically by ray tracing. The amount of magnification at $\frac{1}{2}$ and 1 μsec was of the order of 15%. The consequent change in the channel growth curve tends to raise Curve A, since the calculated mechanical work output and radiated energy are both reduced. It also tends to lower Curve B, since the lower pressure leads to a lower energy density which, in conjunction with the smaller spark volume, gives a lower channel energy. After the first μsec or so the preceding effects become unimportant, since the larger channel diameter and the lower pressure gradient yield less channel magnification.

The differences between Curves A and B at times substantially later than 1.6 μsec are probably caused by inaccuracy of Curve B due to the use of the ideal gas law as the equation of state of the plasma. The particle density within the plasma is of the order of $\frac{1}{10}$ of that found in solids or liquids, and the degree of ionization is approximately 30%. Under such conditions the plasma cannot be expected to behave as an ideal gas. The deviation from ideal behavior may be obtained by calculating the internal pressure which is produced by the interparticle Coulomb fields.

The general pressure relations for any gas are included in the equation,

$$P_{\text{external}}+P_{\text{pinch}}+P_{\text{attraction}}=P_{\text{kinetic}}+P_{\text{repulsion}}, \quad (11)$$

where P_{external} is the calculated pressure which generates the shock wave, P_{pinch} is the average pinch pressure, $P_{\text{attraction}}$ and $P_{\text{repulsion}}$ are the components of pressure ascribable to attractive and repulsive forces between particles, and P_{kinetic} is the component of pressure (NkT) resulting from kinetic motion of the particles. The separation of the attraction and repulsion pressures is somewhat artificial; the two are usually combined and calculated from the interparticle force law in the form of the second virial coefficient. The resulting pressure may be placed on the left side of Eq. 11 as $P_{\text{attraction}}-P_{\text{repulsion}}$. It is then referred to as the internal pressure. Knowledge of the external, pinch, and internal pressures thus enables one to compute the kinetic pressure and, therefore, the true particle density.

There are two basic reasons why the conventional integral expressions for the internal pressure cannot be applied to the present case involving a highly ionized gas. The first of these is concerned with the long-range nature of the Coulomb force law. The integrals involved are derived on the assumption of binary collisions only. Closely related to this is the fact that the integrals are nonconvergent for interparticle force laws which decrease less rapidly than the inverse fourth power of the particle separation. For an inverse-square law of force, the motion of a particle is appreciably affected by particles well beyond the nearest neighbors. This suggests that the concepts of mean free path and binary collisions have no place in the analysis of highly ionized gases. The second basic reason why the usual integral forms for the internal pressure cannot be used is that they are based on the assumption of identical force laws between all particle types. For a highly ionized gas there are repulsion forces between some pairs of particles, attraction forces between other pairs, and negligibly small forces (due to polarization and short-range interactions) between other pairs. As a result, another approach must be used to evaluate the internal pressure in a highly ionized plasma. The approach used here is based on the concept of the Debye shielding distance. If the particle densities already calculated are used, the Debye length is found to be about 4 A for the plasma of the underwater spark. This length gives the order of magnitude of the distance beyond which only collective particle motions exert an appreciable effect on the motion of a given particle. However, for the same conditions, the average particle separation is found to be about 10 A. These results suggest that the entire plasma surrounding a given particle may be treated as a polarizable continuum; i.e., individual interactions of a given particle with its nearest neighbors may be neglected.

Consider a sphere surrounding any particular plasma ion (Fig. 7). Choose the radius of the sphere so that its volume is the average volume per particle of the plasma. Polarization of the plasma by the ion may be represented by a surface charge density uniformly distributed over the surface of the sphere. If one computes the forces between the central ion and the enclosing spherical charge shell (allowing for mutual repulsion between the

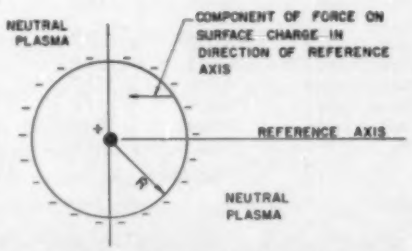

FIG. 7. Calculation of internal pressure within the plasma.

charges on the shell), one finds there is a net force holding any two hemispheres of the outer shell together. This net force divided by the cross-sectional area of the sphere is a measure of the internal pressure caused by the interparticle Coulomb forces. The result is

$$P_{\text{internal}} = \frac{q^2}{32\pi^2\epsilon_0 R^4} \tag{12}$$

where q is the charge on the ion, R is the radius of the enclosing sphere (meters), and ϵ_0 is the dielectric constant of free space (MKS rationalized units). This equation may be solved simultaneously with Eq. (11) for the particle density N in terms of external and pinch pressures and temperature. When applied to the conditions in the underwater spark at current maximum, this procedure yields a total particle density of 2.5×10^{27} particles/meter^3, and an internal pressure of 2170 atmos. This result has significance in that it indicates that the internal pressures are of the same order of magnitude as the external pressures, and hence should not be neglected. The new value of N thus obtained may be used as the basis of a revised particle balance. It would be found that a greater amount of energy would be stored in the spark channel than is indicated by Curve B of Fig. 6. This would serve to bring the two energy balance curves into better agreement. The discrepancy between Curves A and B at times later than 1.6 μsec may conceivably be treated as an experimental measure of the magnitude of the internal pressure within the plasma.

ADDITIONAL CONCLUSIONS BASED ON THE PARTICLE BALANCE

The particle densities obtained from the energy balance calculations may be utilized to obtain additional information about the underwater spark plasma. If the amount of water in the channel (based on the particle balance) is plotted *vs* time, one may obtain the rate of induction of water through the spark channel wall. At current maximum, this is found to be 10^{25} molecules/sec, requiring an inducting power of 55 megawatts. It should be noted that this power does not leave the channel. It is improbable that this amount of power is transferred to the channel wall from the core by thermal conduction. The thermal conductivity of the plasma, soon to be computed, is sufficiently low so that a central temperature on the spark axis of several million degrees would be required. Temperatures of this order are not to be expected in view of the insensitivity of the major spark parameters to changes in surface to volume ratio as mentioned earlier. If the surface recombination rate is computed, however, and one assumes that all ions impinging on the channel wall do recombine, then an energy of 348 megawatts is available. Therefore, only one-eighth of the ions striking the wall need recombine in order to furnish the necessary induction energy. The rate of induction of water molecules also allows one to determine the rate of radial expansion of the channel wall caused by water induction. The result at current maximum is 10 m/sec, which is not large enough to invalidate the hydrodynamic pressure calculation described earlier.

The electrical conductivity of the plasma should not be computed on the basis of the usual kinetic theory concept of a mean free path because of the importance of the Coulomb interparticle fields. Gvosdover has developed an expression for the effective collision cross section for electrons moving through positive ions.[8] If the Gvosdover cross section is used in computing the electrical conductivity of the underwater spark plasma at current maximum, the result is 5.4×10^4 mhos/m. Spitzer and Harm have developed a theory for the electrical conductivity of a completely ionized plasma.[9] Their theory applied to the underwater spark plasma at current maximum yields an electrical conductivity of 10×10^4 mhos/m. Both of these computed conductivities are in good agreement with the value experimentally obseved in this study. The experimental conductivity at current maximum is 5.6×10^4 mhos/m.

The theory of Spitzer and Harm yields a thermal conductivity for the underwater spark plasma at current maximum of 86 w/m °K. This theory is based on the kinetic motion of the plasma particles only, and neglects contributions to the thermal conductivity caused by radiation exchange and gradients of dissociation, excitation, and ionization. Preliminary order-of-magnitude calculations indicate that these latter mechanisms do not contribute significantly to the thermal conductivity of the underwater spark plasma.

The channel wall of the underwater spark is a complex region. The temperature gradient is very large so that thermodynamic equilibrium cannot be expected to exist among the particles. The differing coefficients of diffusion of electrons and ions in the plasma establish a large electrical gradient across the wall. The magnetic field in this region is about 13.5 webers/m^2 (135 000 gauss) at current maximum. Also, the degrees of dissociation, excitation, and ionization change rapidly across this region. Finally, the channel wall is probably not a gas-to-liquid interface because the pressures are very much higher than the critical pressure of water. The channel wall may therefore be considered to be a transition region of small but finite thickness where all physical characteristics vary continuously from cool liquid water to highly ionized plasma.

ACKNOWLEDGMENTS

The author is indebted to W. G. Dow and H. C. Early for their many helpful discussions. The work was supported in part by the U. S. Army Office of Ordnance Research.

[8] H. Maecker, Ergeb. exakt. Naturw. **25**, 310 (1951).
[9] L. Spitzer and R. Harm, Phys. Rev. **89**, 977 (1953).

Diffusion Coefficients, Solubilities, and Permeabilities for He, Ne, H_2, and N_2 in Vycor Glass*

C. C. Leiby, Jr., and C. L. Chen
Department of Electrical Engineering, University of Illinois, Urbana, Illinois
(Received May 11, 1959)

The permeability of a Vycor filter (680 cm² area and 0.25 mm thick) is given for helium at six temperatures ranging from 299°K to 723°K, for neon and hydrogen at 673°K and 723°K, and for nitrogen at 673°K. The observed values and their temperature dependences are in good agreement with corresponding values for fused quartz reported elsewhere. Values of the diffusion coefficient of these gases in Vycor also were obtained experimentally, enabling calculation of their solubilities. Helium appears to deviate from activated diffusion in Vycor somewhere between 100° and 26°C. Its permeation velocity and diffusion coefficient at 26°C are larger than expected for activated diffusion, while its solubility at 26°C is one-half its value at 100°C. These changes suggest that some structure sensitive diffusion process begins to dominate the activated or solution process at these lower temperatures. Helium flow rates through the filter as high as 2100 mm Hg (0°C)×cc/hr at a filter temperature of 450°C and a pressure difference of 35 cm Hg (0°C) were observed. On the basis of observed permeation rates for the above gases, it is estimated that the filtered helium has an impurity content of less than 1/50th of its unfiltered value.

I. INTRODUCTION

RECENT experiments in this laboratory have indicated the need for helium gas of a higher purity than is commercially available. To obtain this higher purity it was decided to effect an impurity separation by means of a suitable permeable membrane. The work of Norton[1] indicated that Corning Vycor glass might prove adequate for this purpose, providing the membrane were thin enough and of sufficient area to filter practical amounts of gas. Since Norton's values for helium permeation in Vycor cover a range of temperatures from −78°C to 25°C, it was necessary to determine whether an extrapolation of his data to higher temperatures (where the permeation velocity should be greatly enhanced) was valid. Also it was considered necessary to find the permeation velocities for other gases which might be present in commercially available "spectroscopically pure" helium in order to determine the possible reduction in impurity content that could be effected by the filter. Further, since the sensitivity of the method employed in measuring these permeation rates was quite good, it was also decided to include measurements of the diffusion coefficients for the above gases in Vycor. Knowledge of the permeation velocities and diffusion coefficients of these gases enables their solubilities to be calculated. These measurements were deemed worthwhile inasmuch as the only published values for the interaction of gases with Vycor glass known to us are the three permeation velocities for helium (at −78°, 0°, and 25°C) reported by Norton.[1]

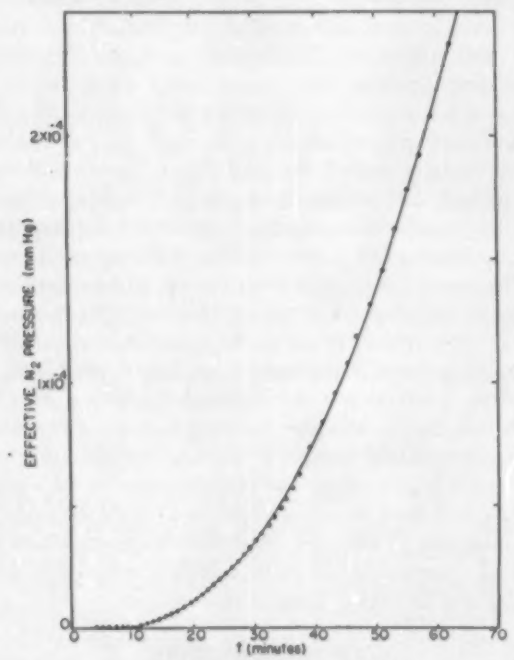

FIG. 1. Helium permeation in Vycor at room temperature immediately after admission of helium to the filter, demonstrating the time transient which was characteristic of all of the gases reported in this paper. (The units of "Eff. N_2 Pressure" are explained in Sec. V.)

II. PRINCIPLE OF THE EXPERIMENT

The determination of the permeation velocity K of a gas through a membrane is easily obtained in terms of the membrane area A and thickness d, the pressure difference Δp across the membrane, and the rate of pressure increase dp/dt inside a known volume V on the low-pressure side of the membrane, via the relation:

$$dp/dt = K(A/Vd)\Delta p. \quad (1)$$

The units in which K is expressed depend upon the chosen units of area, thickness, volume, pressure, and time. Hence they may differ from observer to observer. The units chosen in this report are those employed by

* This research was sponsored by the Air Force Cambridge Research Center.

[1] F. J. Norton, J. Am. Ceram. Soc. 36, 90 (March, 1953).

Barrer[2] and Norton,[1] namely: K[cc of gas at NTP/sec/cm² area/mm thickness/cm Hg press. diff. (0°C)]. In order to obtain the diffusion coefficients of gases in Vycor, the method described by Rogers, Buritz, and Alpert[3] was used. In this method the initial time variation of gas current density through the membrane immediately after admission of the gas to the filter may be used to determine the diffusion coefficient.

The solutions to the time dependent diffusion equation

$$-D\nabla^2 n = \partial n/\partial t \tag{2}$$

in plane geometry are[3]

$$\frac{dp}{dt} = \frac{ADS}{Vd}\Delta p\left[1+\sum_{m=1}^{\infty} 2\cos\pi m \exp(-m^2\pi^2 Dt/d^2)\right] \tag{3}$$

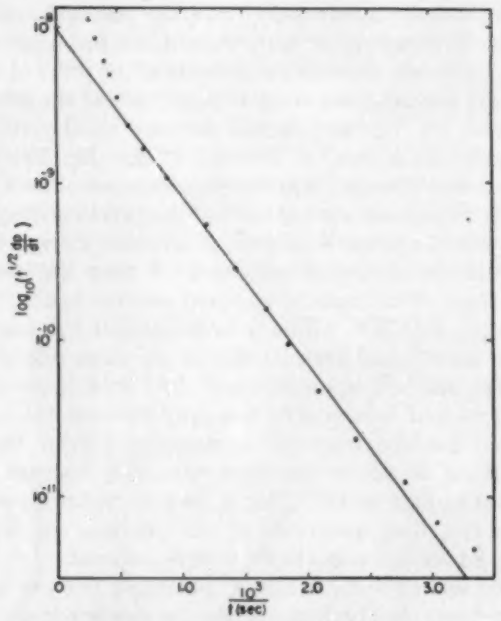

FIG. 2. Data presentation for "early approximation" (helium at room temperature in Vycor glass).

or its transform

$$\frac{dp}{dt} = \frac{2AS}{V}\left(\frac{D}{\pi t}\right)^{\frac{1}{2}}\Delta p \sum_{m=0}^{\infty}\exp\left[-\left(\frac{d^2(2m+1)^2}{4Dt}\right)\right] \tag{4}$$

where S is the solubility and D is the diffusion coefficient of the gas in the membrane. Because of the large diameters of the cylindrical membranes used in our experiment, the application of these plane geometry solutions to our data involves an error of less than 0.01%.

For large values of t, Eq. (3) reduces to:

$$dp/dt = (DS)(A/Vd)\Delta p \tag{5}$$

[2] R. M. Barrer, *Diffusion in and Through Solids* (Cambridge University Press, London, 1951).

[3] Rogers, Buritz, and Alpert, J. Appl. Phys. **25**, 868 (1954).

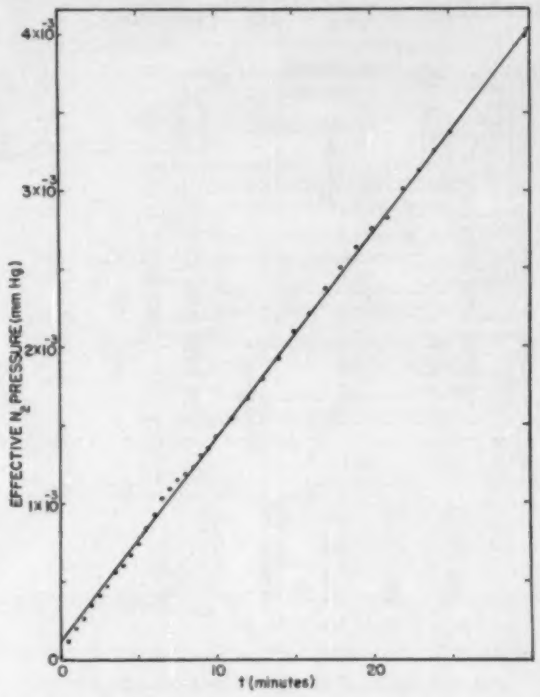

FIG. 3. Helium permeation in Vycor at room temperature several days after admission of helium to the filter, demonstrating the steady-state permeation rate. (The units of "Eff. N_2 pressure" are explained in Sec. V.)

which by identification with Eq. (1) yields:

$$K = DS. \tag{6}$$

Equation (4) converges rapidly for small values of t and may be written:

$$\ln[t^{\frac{1}{2}}(dp/dt)] = \ln[(2AS/V)\Delta p(D/\pi)^{\frac{1}{2}}] - d^2/4Dt \tag{7}$$

for "early" times.

Hence observation of $p(t)$ from the time of admission of gas to the filter will enable determination of the diffusion coefficient [from the slope of $\ln(t^{\frac{1}{2}}dp/dt)$ *vs* $1/t$] for early times, while the permeation velocity may be determined [by Eq. (1)] at late times when dp/dt is a constant. From these, by a suitable choice of units for K and S, Eq. (6) may be used to determine the solubility of a gas in the membrane. Figures 1, 2, and 3 are representative of the data plots used for these determinations.

III. EXPERIMENTAL ARRANGEMENT

The system used for these experiments is shown schematically in Fig. 4. The portion of the diagram enclosed by the dashed line is baked out at 400°C prior to each run. The vacuum apparatus (gauges, valves, etc.) in this portion of the system is of the ultra-high vacuum type described by Alpert.[4] The cross-hatched outline of the oven contains four cylindrical Vycor

[4] D. Alpert, J. Appl. Phys. **24**, 860–876 (1953).

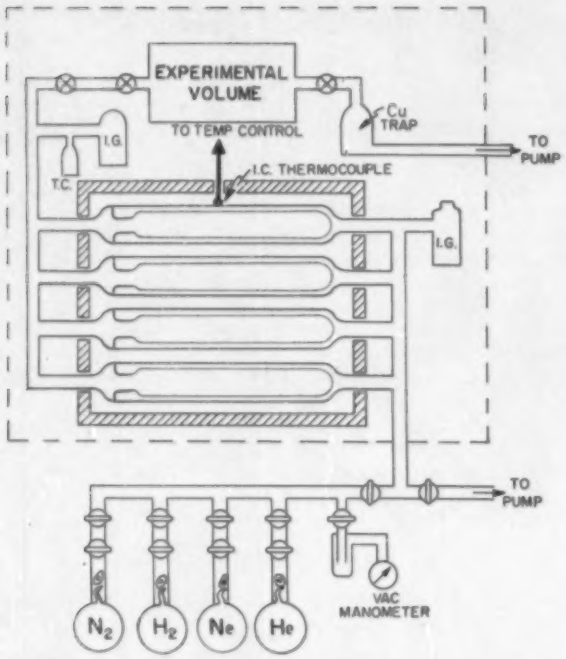

FIG. 4. Diagram of the experimental vacuum system.

membranes having an average thickness of 0.25 mm (estimated error, ±20%) and a total area of 680 cm² (±2%). The remainder of the glass inside this oven (graded seals and Pyrex tubing) has a wall thickness of 1.8 mm or more. The oven itself was Transite lined with Apollo metal and sealed with asbestos tape to prevent air circulation from the outside. Temperature variations within the oven in the vicinity of the filter elements were measured and found to be less than ±10°C at an oven temperature of 400°C. The Brown temperature control held the temperature to within ±5°C throughout the experiments. It was necessary, however, to apply an "idling current" to the oven heating elements during "off" periods of the temperature control at the higher oven temperatures, in order that the temperature drop should not exceed more than a few degrees during such periods.

The "experimental" volume shown in Fig. 4 consisted of a cataphoresis pump[5] (for separation from the discharge region of any noble gas impurities which might remain after filtration), and a volume in which electrical discharges are established for the investigation of plasma phenomena. The electrodes of the cataphoresis pump and discharge region, as well as their supports, were made of high-purity titanium metal, so that any chemically active impurities could be continuously gettered during plasma experiments.

The region lying outside the dashed line contained two independent sets of pumps and the gas manifold. The greased stop cocks on the "dirty" side of the filter were assumed to contribute no significant amount of impurity to the gas which was to be filtered because of the high pressure of that gas and the belief that such impurities (air, moisture, and hydrocarbons) would be of too large a molecular diameter to permeate the filter at any measureable rate.

The residual pressure on the dirty side before gas fill was determined by an RCA 1949 ion gauge. The gas fill pressure was measured by means of a vacuum manometer, and its accuracy (checked by volume division calculations) was found to be ±0.3 cm Hg.

The residual pressure on the "clean" side of the system before gas was admitted to the filter was measured by a Westinghouse WL 5966 (Alpert type) ionization gauge.

IV. EXPERIMENTAL PROCEDURE

The high vacuum portion of the system was thoroughly baked out at 400°C and the portions external to the bakeout region were flamed. At the conclusion of this process, an ultimate pressure of the order of 10^{-10} mm Hg was achieved on the "clean" side of the system, whereas the best obtainable pressure on the "dirty" side was of the order of 10^{-7} to 10^{-8} mm Hg. This procedure was followed prior to the admission of each gas.

The filter oven was then raised to operating temperature and baked out until residual pressure rises on both sides of the system, when closed off from the pumps, stabilized. This usually required several hours. (For example, at 400°C, ultimate oven bakeout was reached when the residual pressure rise on the clean side of the system reached approximately 10^{-7} mm Hg/hr, i.e., the expected helium diffusion rate[5] through the outer Pyrex envelope from the atmosphere.) Prior to the admission of gas to the filter, this filter bakeout was carried as high as 475°C for as long as twenty hours to guarantee that quantities of the previous gas which went into solution in the filter were removed.

The seal on the gas bottle containing the gas to be filtered was then broken, and the gas slowly admitted to the filter. This procedure occupied (roughly) two minutes. The Alpert valve to the pumps was then closed and "snap" pressure readings taken at specific time intervals. Because of the strong (ion) pumping action of the WL 5966 ion gauge, it was necessary to make these readings in as short a time as possible. After some practice, this reading interval was shortened to approximately two seconds. Shorter reading periods proved impossible because of the inertia of the microammeter.

Repeated pressure readings were made until the pressure reached approximately 2×10^{-3} mm Hg. At this pressure, the gauge became nonlinear and it was necessary to pump out the "clean" side of the system and commence anew. This process was repeated until two or three successive runs gave the same rate of increase of pressure with time. To identify each gas (except nitrogen), a high-frequency discharge was established in the filtered gas and its characteristic color observed.

[5] R. Riesz and G. H. Dieke, J. Appl. Phys. **25**, 196–201 (1954).

V. CORRECTIONS TO THE EXPERIMENTAL DATA

Inasmuch as different parts of the experimental apparatus were at different temperatures, it was necessary to measure volumes and temperatures in order to calculate effective 0°C pressures. These pressure calculations were corroborated by direct measurement of the pressure of a definite quantity of helium in the clean side of the system with the filter oven at room temperature and at 400°C. The room temperature pressure employed for this measurement was approximately 10^{-3} mm Hg. (Approximately the same pressure of helium was introduced on the "dirty" side of the filter to avoid permeation effects during these pressure-temperature measurements.) This pressure was chosen in order to guarantee that the same molecular flow conditions prevailed as prevailed in the experimental runs.

The ion gauge sensitivity to helium was measured by means of a precalibrated RCA 1946 thermocouple gauge. The helium permeation rate through the filter was allowed to reach a steady state as measured by the ion gauge. This rate was then extrapolated in time, and compared with later pressure values measured independently by the thermocouple gauge. The sensitivity thus determined was in good agreement with the value given by Dushman and Young.[6] Hence it was decided to use their relative sensitivities for expressing all of our ion-gauge pressure data in terms of "effective N_2 pressures."

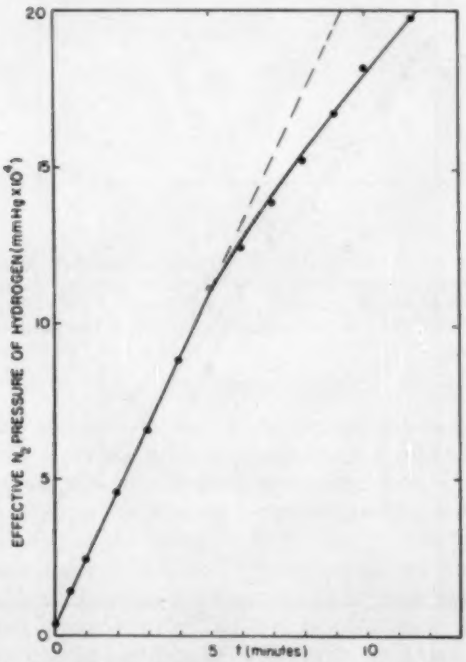

FIG. 5. Hydrogen pressure in the "clean" side of the system at 400°C as a function of time. These values were observed 7 hours and 20 minutes after the admission of hydrogen to the filter and represent the "steady-state" permeation rate. The effect of hydrogen gettering by the room temperature titanium electrodes is evident.

[6] S. Dushman and A. H. Young, Phys. Rev. Letters **68**, 278 (1945).

TABLE I. Observed steady-state values of dp/dt and permeation velocities in Vycor glass.

Gas	T(°C)	Δp(cm Hg)0°C	V(cc)	dp/dt(atmos/sec)0°C	K ($\times 10^9$)
He	26	46.2	1830	2.48×10^{-9}	0.036
	100	29.4	1830	6.59	0.151
		38.4		8.94	0.157
	200	38.4	1830	4.09×10^{-8}	0.873
	300	21.2	1830	7.08	2.26
	400	20.2	1590	1.60×10^{-7}	4.65
				1.67	4.86
	450	19.1	1590	2.24	6.88
	455	35.0	1830	4.20	8.07
Ne	400	17.4	1830	1.22×10^{-9}	0.048
				1.27	0.050
				1.23	0.048
	450	17.1	1830	2.24	0.090
				2.24	0.090
H_2	400	17.4	1830	3.36×10^{-9}	0.132
				3.50	0.138
				3.53	0.139
	450	17.1	1830	8.06	0.324
				7.40	0.298
				8.43	0.339
N_2	400	17.4	1830	1.6×10^{-11}	0.00063

While not of the nature of a correction, the error introduced by active gettering by the titanium electrodes had to be taken into account in the hydrogen and nitrogen runs. Since the gettering rate is proportional to the system pressure, the observed permeation rates were expected to be relatively unaffected by this process at extremely low pressures, but increasingly affected as the system pressure increased. Hence, once constant permeation rates at low pressures had been observed for these chemically active gases, steady-state permeation was assumed to hold and deviations from constant dp/dt at higher system pressures were taken to be a measure of the titanium gettering rate. Figure 5 is a representative plot for H_2 which clearly demonstrates this gettering effect.

VI. EXPERIMENTAL RESULTS

Immediately after admission of each gas to the filter, dp/dt (the rate of increase of gas pressure in the "clean" side of the system) exhibited a transient behavior similar to that shown in Fig. 1 for helium at room temperature. These data were then replotted in the manner of Fig. 2, permitting direct determination of the diffusion coefficient according to Eq. (7).

After a period of time (ranging from 4½ to 24 hours) steady-state permeation rates were observed. In general these values were much larger than those observed in the transient period. Figure 3 (a plot of pressure *vs* time for room temperature helium in the steady-state permeation period) demonstrates this increase. These steady-state values of dp/dt were used [see Eq. (1)] in calculating the permeation velocities listed in Table I.

The activation energies for activated diffusion of

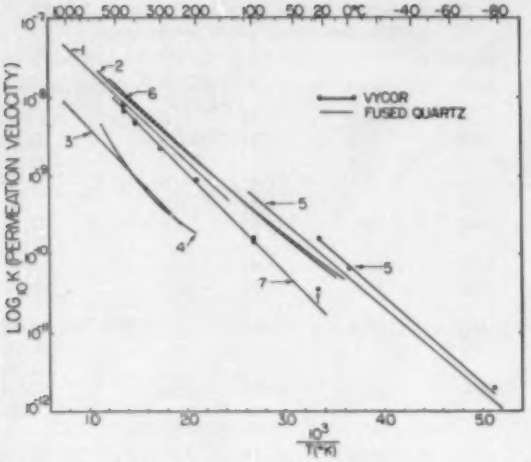

FIG. 6. Permeation velocity K of helium in Vycor and fused quartz glasses *vs* the reciprocal of the absolute temperature. K is in units of cm³ (NTP)/sec/cm² area/mm thickness/cm Hg press. diff. (0°C). Vycor: •—•; fused quartz: —. 1, T'Sai and Hogness[14]; 2, Braaten and Clark[15]; 3, Barrer[16]; 4, Williams and Ferguson [G. A. Williams and J. B. Ferguson, J. Am. Chem. Soc. 44, 2160 (1922)]; 5, Norton[1]; 6, Jones[13]; 7, Present experiment.

helium in Vycor and fused quartz, as determined from the slopes of the curves shown in Fig. 5, are listed in Table II.

Figures 6, 7, 8, and 9 are plots of the permeation velocities in Vycor of helium, neon, hydrogen, and nitrogen, respectively. The corresponding values for these gases in fused quartz also are plotted for purposes of comparison.

The solubilities of the gases observed were obtained by substitution of the permeation velocities (in units of

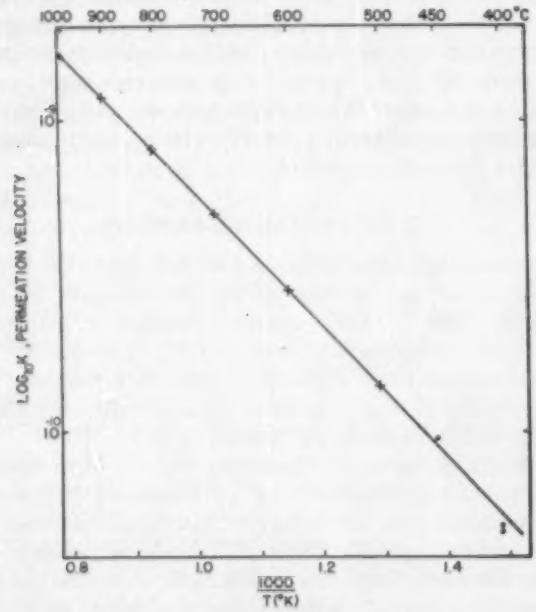

FIG. 7. Permeation velocity K of neon in Vycor and fused quartz glasses *vs* reciprocal of the absolute temperature. K is in units of cm³ (NTP)/sec/cm² area/mm thickness/cm Hg press. diff. (0°C). +, T'Sai and Hogness[14] (fused SiO_2); •, our values (Vycor).

TABLE II. Activation energies for helium in Vycor and fused quartz.

Glass	Activation energy (calories/deg C)	Observer
Fused quartz	5600	T'Sai and Hogness[14]
	5390	Braaten and Clark[15]
	5700	Barrer[2]
Vycor	4900	Norton[1]
	5900	Present report

cc (NTP)/sec/cm²/cm thickness/atmos. press. diff. (0°C)) and diffusion coefficients into Eq. (6). Both the solubilities and diffusion coefficients are given in Table III.

Observed helium filtering rates of our Vycor membrane at various temperatures are given in Table IV. In terms of time required to fill the experimental portion of our system with filtered gas, at 455°C the 1830-cc system can be filled with purified helium to a room temperature pressure of 30 mm Hg in approximately 26 hours.

The gettering effect of the room temperature titanium electrodes (approximately 120 cm² total surface area) was evident for hydrogen at higher system pressures. (See Fig. 5.) Calculations of the "sticking ratio" for H_2

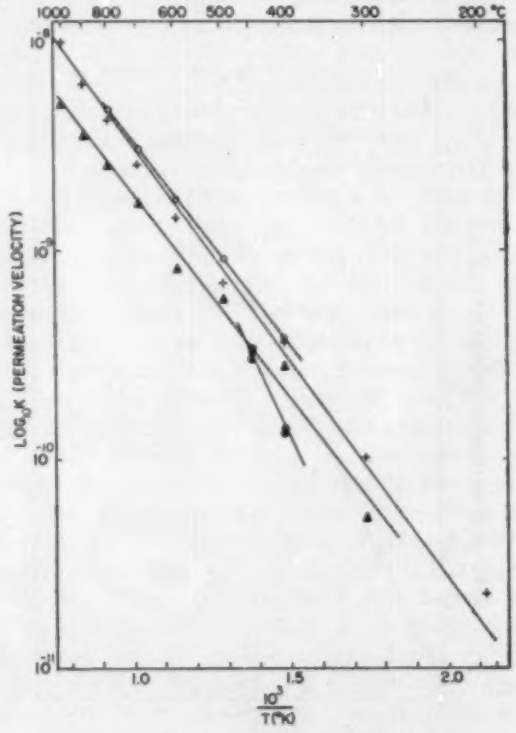

FIG. 8. Permeation velocity K of hydrogen in Vycor and fused quartz glass *vs* reciprocal of the absolute temperature. The disparity in our results may be attributed to a changing gettering rate of the titanium electrodes in the system. K is in units of cm³ (NTP)/sec/cm² area/mm thickness/cm Hg press. diff. (0°C). Fused SiO_2: +—+, Barrer[16]; ○—○, Williams and Ferguson (Fig. 6, reference 4); Johnson and Burt (see Fig. 9); Vycor: •—•, our values.

on our electrodes yielded values fifty times less than those observed by Stout and Gibbons.[7] This is reasonable inasmuch as our titanium was not cleaned by preheating of 1100°C as was that of Stout and Gibbons. More interesting was the observed time dependent gettering of nitrogen. The effect of room temperature gettering in nitrogen was unexpected, and indeed not noticeable until approximately forty hours had elapsed. From this time on, until the conclusion of the run at the end of some 56 hours, the system pressure dropped continuously in spite of a continuous influx of permeating nitrogen gas.

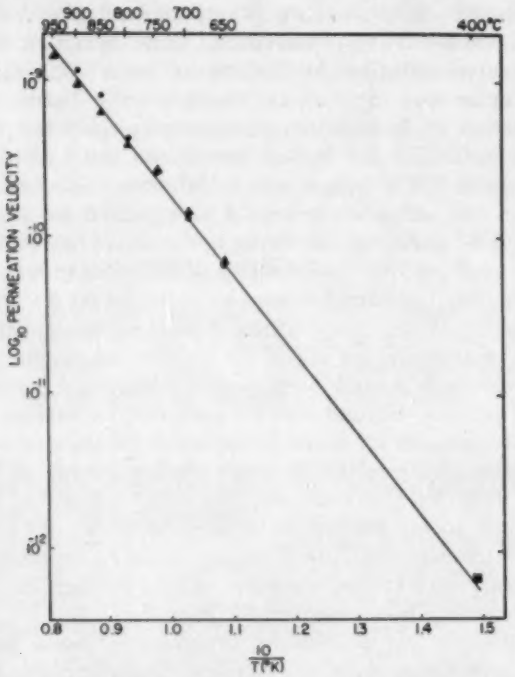

FIG. 9. Permeation velocity of nitrogen in Vycor and fused quartz. K in units of cc(NTP)/sec/cm²/mm thickness/cm Hg press. diff. (0°C). Fused SiO_2: ▲, Barrer[16]; ●, Johnson and Burt [J. Johnson and R. Burt, J. Opt. Soc. Am. 6, 734 (1922)]; Vycor: ■, our value.

VII. DISCUSSION

The observed values of the permeation velocity for helium in Vycor glass demonstrate a temperature dependence which is in good agreement with a replot of data reported by Norton[1] for much lower temperatures. However, when compared to an extrapolation of Norton's curve to higher temperatures, our values are considerably lower. Since our standard error is estimated to be approximately 20%, it is concluded that this difference is significant. Differences in glass samples could be responsible; however it should be pointed out that both Alpert's values[3] (which were obtained by the same techniques as were employed in this investigation) and those of McAfee[8] (who used a technique similar to that used by Norton) for helium permeation in Pyrex glass were also consistently lower than Norton's corresponding values.

TABLE III. Diffusion coefficients and solubilities in Vycor glass.

Gas	T(°C)	D(cm²/sec)	S(cc/cc/atmos)
He	26	6.3×10^{-8}	0.0043
		5.9×10^{-8}	0.0046
	100	1.26×10^{-7}	0.0094
Ne	400	6.0×10^{-8}	0.006
H_2	400	1.50×10^{-7}	0.007
N_2	400	10^{-8}—10^{-7}	10^{-5}—10^{-4}

Helium, neon, and nitrogen permeation velocities in Vycor glass seem to be in good agreement with previously published values for these gases in fused quartz (see Figs. 6, 7, and 9). However, since only one value was obtained for nitrogen, and that only with great difficulty, there is a possibility that its agreement is fortuitous. The permeation velocities of hydrogen in Vycor also lie in the range of hydrogen permeation velocity data for fused quartz, but they have a much steeper slope. This may have been caused by room temperature gettering of the hydrogen by the titanium electrodes in the system.

The activation energy for the diffusion of helium through Vycor reported here is slightly higher than the values reported by other observers for helium diffusion in fused quartz. This is reasonable inasmuch as approximately 3% impurity remains in the SiO_2 structure of Vycor. Norton[1] reports a much lower activation energy for helium in Vycor, but his value was based upon three data points and may be subject to some ambiguity.

The apparent similarity of permeation processes in Vycor and fused quartz is interesting. The solubilities, permeabilities, and activation energies for gases in these glasses seem to be essentially the same. Actually, this should be expected as the two glasses have approximately the same density, composition, and working characteristics, but it is interesting in view of their completely different modes of manufacture.

Vycor is formed from a melt of SiO_2 and B_2O_3. When cool, the formed object is immersed in an acid which removes all but a few percent of the B_2O_3. The remain-

TABLE IV. Observed helium filtering rates of a Vycor membrane. (680 cm² area, 0.25 mm thickness.)

Filter temp. (°C)	Δp(cm Hg)0°C	Q(mm Hg×cc/hr)0°C
26	46.2	12.3
100	29.4	33.0
	38.4	49.0
200	31.4	256
300	21.2	465
400	20.2	696
	20.2	730
450	19.1	1410
455	35.0	2100

[7] V. L. Stout and M. D. Gibbons, J. Appl. Phys. **26**, 1488–1492 (1955).

[8] K. B. McAfee, Jr., J. Chem. Phys. **28**, 218–229 (1958).

ing structure (which is extremely porous) is then heated to a sintering temperature at which it shrinks to approximately two-thirds of its previous size. In this finished state, Vycor exhibits no apparent porosity. However, the very nature of this manufacturing process lends credence to the belief that finished Vycor may possess innumerable submicroscopic voids of molecular dimensions, and that these voids may be responsible for the large permeation velocities reported here.

Although fused quartz is manufactured in a different manner, because of its above-mentioned similarities to Vycor, one might hazard the guess that it too possesses such submicroscopic voids. Bridgeman[9] has investigated the behavior of fused quartz and Vycor under extremely high pressures. Their pressure thresholds for permanent compaction and their density increases at twice threshold pressure were observed to be almost the same. X-ray diffraction of compacted specimens (some having a density comparable to that of crystalline quartz) revealed no change in the length of the Si—O bond, hence the structural changes must have occurred on a larger scale, i.e., by the collapse of voids of molecular size and larger. Rayleigh's[10] value for the permeation velocity of helium through crystalline quartz, which is less than 10^{-4} times the permeation velocity for helium in fused quartz, also tends to support this view.

Barrer[2] has postulated a structure sensitive diffusion process for gases at low temperatures in fused quartz. He found a permeation velocity for helium in fused quartz which, in the light of his data for higher temperatures, was too high to be attributed to an activated (or solubility) process. This same effect is evident in the data of Braaten and Clark,[11] and is quite pronounced in the data of Burton, Braaten, and Wilhelm.[12]

Jones[13] obtained a convex curve when he attempted to plot his data for the permeation velocity of helium in fused quartz as $K=Ae^{-Q/RT}$ and noted that Ferguson and Williams and others[14,15] had found this same curvature. Upon plotting his data as $K=BT^{\frac{1}{2}}e^{-Q/RT}$ he obtained a straight line.†

This possible $T^{\frac{1}{2}}$ dependence of the permeation velocity of helium in silica glasses may indicate the existence of a molecular streaming process taking place through extremely small voids and/or channels of near molecular dimensions. The apparent cross-sectional area (as defined by the wall potentials) of such a void or channel, as seen by an incident gas molecule, would depend upon the energy of that molecule.‡ Also, if one assumes that there is a distribution of void or channel sizes, the *number* of voids or channels (per unit area of glass surface) which are large enough to permit molecular streaming to take place will also depend upon the average energy of the gas molecules. Hence the streaming rate depends strongly upon the average separation of the wall potentials and upon their profile; i.e., the permeation process would exhibit an "activation energy" dependence as well as a $T^{\frac{1}{2}}$ dependence. This mechanism is suggested in order to explain our results, since they cannot be explained in terms of purely activated lattice diffusion, or purely grain-boundary diffusion, or a purely molecular streaming process. We have observed the same deviation from activated diffusion for helium at room temperature in Vycor (see Fig. 6) as was found by Barrer (see reference 2). In addition, we observed a room temperature solubility for helium which was one-half of its observed 100°C value, and a diffusion coefficient 3.3 times the value which would be expected for purely activated diffusion. According to the above mechanism, one would expect the solubility of the glass to increase as more of its volume becomes accessible to gas molecules with increasing temperature. Also, one would expect that a temperature would be reached where most of the channels or voids were participating in the permeation process. Beyond this temperature, no further increase in solubility would be expected. On the contrary, because of the relatively small binding energy of Si^{++} and O^{--} for gas molecules (McAfee[8] calculates this binding energy for helium to be of the order of kT for room temperature), the solubility would be expected to decrease with further increases in temperature. Such a decrease has been observed by Jones.[13]

Although our plausibility argument is based upon the permeation data, the physical characteristics, and the mode of manufacture of two specific glasses, namely, Vycor and fused quartz, it should be noted that McAfee,[8] in his interesting work with helium permeation in Pyrex under tensile stress, was also led to postulate the existence of submicroscopic diffusion channels in Pyrex. Thus it is possible that "channels" or "voids" play an important role in the diffusion of gases in a wide variety of glasses.

VIII. ACKNOWLEDGMENTS

The authors would like to acknowledge the assistance and encouragement given them by Dr. A. A. Dougal and the discussions with Mr. P. Knorr who also fabricated the glass system.

[9] P. W. Bridgeman, J. Appl. Phys. **24**, 405 (1953).
[10] Lord Rayleigh, Proc. Roy. Soc. (London) **156A**, 350 (1936).
[11] E. O. Braaten and G. Clark, J. Am. Chem. Soc. **57**, 2714 (1935).
[12] Burton, Braaten, and Wilhelm, Can. J. Research **21**, 497 (1933).
[13] W. M. Jones, J. Am. Chem. Soc. **75**, 3093 (1953).
[14] L. S. T'Sai, and T. R. Hogness, J. Phys. Chem. **36**, 2595 (1932).
[15] R. M. Barrer, J. Chem. Soc. **1934**, 378 and reference 2.

† Owing to the magnitudes of the experimental values of K, T, and Q, it should be noted that the power of T used in this latter expression could vary over a small range of values and still give a reasonable fit within the accuracy of the data.

‡ T'Sai and Hogness[14] postulated a channel diffusion mechanism, in which channel size increased with increasing temperature, in order to explain their observations, but were unable to explain how these channels could expand over fortyfold as their data required. Alty [T. Alty, Phil. Mag. **15**, 1035 (1933)] later proposed the overlapping wall potential concept to explain such a channel widening effect, but he did not agree with the idea of a channel diffusion process.

Submillimeter Wave Maser

SAUL M. BERGMANN
Laboratory for Electronics, Boston, Massachusetts
(Received July 30, 1959)

It is shown that coherent emission between the levels $3^2P_{\frac{1}{2}}-3^2P_{\frac{1}{2}}$ for Na atoms enclosed in a resonant cavity should occur at a rate greater than in free space where transition probabilities are very low. It is therefore proposed to operate a maser at the submillimeter wavelengths corresponding to these transitions ($\nu=5.18\times10^{11}\text{sec}^{-1}$) using a dielectric tube resonator as the cavity. An input and output coupling scheme is discussed.

INTRODUCTION

MASER operation at infrared and optical frequencies has been considered by Schawlow and Townes.[1] These workers have suggested favorable transition probabilities for maser action at the near infrared. It is tempting to investigate the possibilities of maser operation at the far infrared frequencies. In this respect maser operation for doublet states in the submillimeter wave range might prove to be feasible.

DIELECTRIC TUBE RESONATOR

A hollow dielectric rod will only support certain modes which it will propagate with little loss. The phase velocity V_p of the wave will have a lower bound as well as an upper bound given by the relation

$$\epsilon^{-\frac{1}{2}}\leqslant V_p\leqslant c,$$

where ϵ is the dielectric constant of the tube and c is the velocity of light in vacuum.

If both ends of the tube are short circuited by metallic plates the cavity thus formed will exhibit properties which are important for submillimeter wavelength applications. The Q of the cavity will be high, of the order of 10^4. The mode discrimination is very effective. The dimensions of the cavity can be made large compared to a wavelength. A detailed study of the properties of the dielectric tube resonator has been made by Becker.[2]

$(3^2P_{\frac{1}{2}}-3^2P_{\frac{1}{2}})$ TRANSITIONS IN Na

The electric dipole transition for the $(3^2P_{\frac{1}{2}}-3^2P_{\frac{1}{2}})$ states in sodium is "forbidden." However the magnetic dipole transition probability is allowed but very small. In order to get an idea of this order of magnitude of the lifetime τ_m of this transition the ratio of the magnetic dipole to the electric dipole transition probability is approximately given by

$$\frac{\text{magnetic dipole}}{\text{electric dipole}}\sim\alpha^2\lambda_e{}^3/\lambda_m{}^3,$$

where α is the fine structure constant 1/137, λ_e is the wavelength corresponding to the $3^2P_{\frac{1}{2}}-3^2S_{\frac{1}{2}}$ transition, and λ_m is the wavelength corresponding to the $3^2P_{\frac{1}{2}}-3^2P_{\frac{1}{2}}$ transition.

If a lifetime of 10^{-8} sec for $3^2P_{\frac{1}{2}}-3^2S_{\frac{1}{2}}$ is assumed, a simple calculation shows that the lifetime τ_m is of the order of 10^2. One should remember however that this would correspond to a radiation into free space, and not into a single mode, such as would be the case if the atom were enclosed in a resonant single mode cavity. In the latter case, the coupling between the atom and the field is increased. This was recognized by Purcell[3] who found for the expression of the spontaneous transition probability for the case of resonance between atom and cavity

$$16\pi^2Q\mu^2/hV,$$

where μ is the dipole moment, V the volume of the cavity, and Q the quality factor of the cavity.

The transition probability is then increased by a few orders of magnitude.

Since spontaneous emission probability and induced emission probability are related, any enhancement of the former will result in an increase of the latter. The great enhancement of several orders of magnitude of the spontaneous emission probability owing to the presence of the resonant cavity as compared to free space emission has been demonstrated by Jaynes.[4]

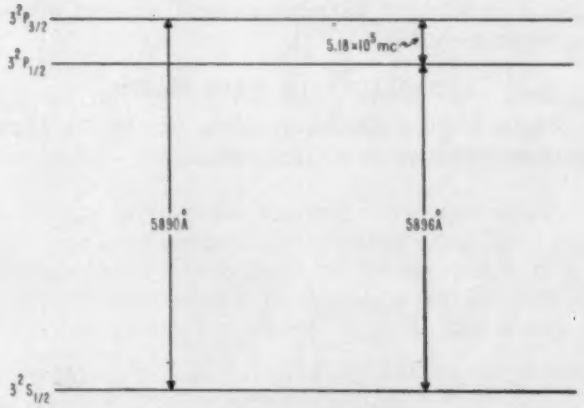

FIG. 1. Na energy levels.

[1] A. L. Schawlow and C. H. Townes, Phys. Rev. 112, 1940 (1958).
[2] R. C. Becker, Technical Report No. 2, U. S. Atomic Energy Commission Contract No. AT(11-1)-392.
[3] E. M. Purcell, Phys. Rev. 69, 681 (1946).
[4] E. T. Jaynes, M. L. Report No. 502, May, 1958, Stanford University.

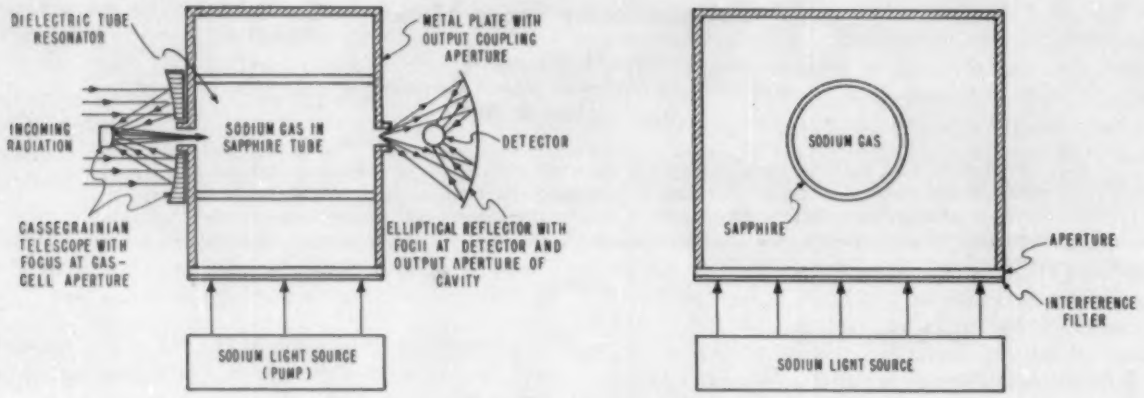

FIG. 2. Submillimeter wave maser amplifier.

It is therefore proposed to enclose Na atoms in a dielectric tube resonator. Optical pumping is carried out between $3^2S_{\frac{1}{2}}$ and $3^2P_{\frac{1}{2}}$ levels so that there would be a population inversion between the $3^2P_{\frac{1}{2}}$ and $3^2P_{\frac{3}{2}}$ levels.

The magnetic dipole moment between the $3^2P_{\frac{1}{2}}$ and $3^2P_{\frac{3}{2}}$ states is of the order of one Bohr magneton.

It can be shown that the excess number of excited states N per cm^3 needed for the onset of oscillations is given by

$$N \geqslant \pi\Delta\nu/2h\gamma^2Q,$$

where

$$\gamma = 1.76\times10^7 \text{ sec}^{-1} \text{ oersted}^{-1},$$

$$h = 6.62\times10^{-27} \text{ erg sec}.$$

The pump power required is given by

$$P = Nh\nu_{13}W_{13}$$

where ν_{13} is the frequency corresponding to transitions between the $3^2P_{\frac{1}{2}}$ and $3^2S_{\frac{1}{2}}$ levels, and W_{13} is the transition probability between these same levels.

If we assume, as Schawlow and Townes[1] did, that the line narrowing due to maser action is of the order of 10^6, we have $\Delta\nu = 10^2$ sec^{-1}. Suppose further that $Q = 10^4$ and $W_{13} = 10^8$ sec^{-1}, the pump power P required will be approximately 250 mw.

SUBMILLIMETER WAVE MASER

Figure 1 gives the energy levels for the Na atom between which maser action is sought.

Figure 2 describes the general setup of the proposed maser. Coupling into and out of the cavity is achieved by mirrors shaped so as to provide foci at the points of coupling. The detector, which is sensitive at these frequencies, has been described by H. Happ *et al.*[5] An interference filter is introduced so as to eliminate the $3^2P_{\frac{1}{2}}-3^2S_{\frac{1}{2}}$ line of the source since its presence would seriously prevent population inversion between the desired levels.

CONCLUSION

It would appear that resonant coupling between atomic systems and radiation, when the former are enclosed in a high Q resonant cavity, would favor coherent emission between levels for which ordinarily emission is very small. A maser is proposed which could act either as an amplifier or as an oscillator at submillimeter waves.

ACKNOWLEDGMENTS

Thanks are extended to Dr. I. R. Senitzky for many illuminating discussions and for access to his unpublished work. Thanks are extended to Professor P. D. Coleman, Professor L. Bradley, Dr. A. L. Schawlow, and Dr. A. Yariv for stimulating discussions.

[5] Happ, Eckhardt, Genzel, Sperling, and Weber, Z. Naturforsch. **12a**, 522 (1957).

JOURNAL OF APPLIED PHYSICS VOLUME 31, NUMBER 2 FEBRUARY, 1960

Propagation of Large Amplitude Waves in Annealed Aluminum

JAMES F. BELL
The Johns Hopkins University, Baltimore, Maryland
(Received July 20, 1959)

An experimental study of large amplitude compression waves in annealed aluminum for the case of constant velocity impact has given a close agreement with the strain rate independent theory of one-dimensional plastic wave propagation. Radial effects in the first diameter are observed and calculations of Poisson's ratio indicate the presence of relatively large dilatation. Propagation velocities, maximum strain, and energy considerations are in agreement with predictions from the slopes of the static stress-strain curve. These data were obtained using the author's diffraction grating technique for measuring strain and surface angle.

INTRODUCTION

IN a recent paper[1] an experimental study of plastic wave propagation in annealed aluminum was presented. These data, which were obtained by means of observing the dynamic behavior of spectral lines from diffraction gratings ruled upon specimens undergoing constant velocity compression impact, were in agreement with some of the predictions of the strain rate independent theory of plastic wave propagation in solids. Thus the theoretical requirement that each level of strain be propagated with a constant velocity was shown to be valid for this case of constant velocity impact. These results, however, gave a dynamic stress-strain curve considerably below the static curve, and also showed final maximum strains below those which are predicted from the slopes of the static curve.

The discovery of a systematic error[2] in the electronics of the signal from one of the two spectral orders measured has necessitated the repetition of the earlier tests. This error, which affected the rise time of one signal, did not influence the constancy of the relative time for propagation at each level of strain, but did affect the magnitude. The strain data of the repeated and extended experiments again have given constant velocity of propagation of each level of strain and, in addition, are in very good agreement with the propagation velocities determined from the slopes of the static stress-strain curve. The maximum strain levels for varied impact velocities, at positions of two or more diameters from the impact face, are also those predicted from the static stress-strain curve.

The nonapplicability of the static stress-strain curve in the earlier data was thought to be associated with the large specimen diameter of 1 in. However, the present results indicate that radial effects, at least in soft aluminum, are confined to the first diameter and a half from the impact face. To further investigate the diametral effects and the assumption of one-dimensionality, data were obtained on thin walled aluminum tubes in constant velocity impact. Calculations also were made of Poisson's ratio for both thin walled tubes and solid specimens. All these results, as well as the obtaining of a close energy balance before and after impact, have shown agreement with the one-dimensional strain rate independent theory of finite amplitude plastic wave propagation.

THE EXPERIMENTAL RESULTS

The strain rate independent theory of plastic wave propagation was independently proposed in varied form by several investigators.[3–6] In LaGrangian formulation, the equation of motion is given as

$$\rho(\partial^2 u/\partial t^2)=\partial\sigma/\partial x, \tag{1}$$

where u is the particle displacement, and σ the stress. If σ is assumed to be a function of strain only, then the above becomes

$$\rho(\partial^2 u/\partial t^2)=(\partial\sigma/\partial\epsilon)(\partial\epsilon/\partial x), \tag{2}$$

where $\epsilon=\partial u/\partial x$. If $\epsilon=f(x/t)$, then it may be shown[7] that solutions of the above are obtained for the case of constant velocity impact where

$$c_p=\left(\frac{\partial\sigma/\partial\epsilon}{\rho}\right)^{\frac{1}{2}} \tag{3}$$

represents the velocity of propagation as a function of strain, and

$$v=\int_0^{\epsilon} c_p d\epsilon \tag{4}$$

is obtained as the relation between strain level and particle velocity v. The maximum strain for constant velocity impact is reached when v rises to the impact velocity v_0.

A constant velocity impact requires that one end of the specimen be subjected to a velocity step, after which this velocity is maintained for the duration of time in which measurement is to be made. Experimentally this may be obtained in several ways. In these tests, an

[1] James F. Bell, J. Appl. Phys. **30**, 196 (1959).
[2] James F. Bell, J. Appl. Phys. (to be published).
[3] Th. von Karman, NDRC Report A 29, OSRD 365 (1942).
[4] G. I. Taylor, British Official Report RC 329 (1942).
[5] M. P. White and L. Griffis, NDRC Report A72, OSRD 742 (1942).
[6] K. A. Rakhmatulin, Appl. Math. and Mech. **9**, 91–100 (1945).
[7] H. Kolsky, *Stress Waves in Solids* (Oxford University Press, London, 1953).

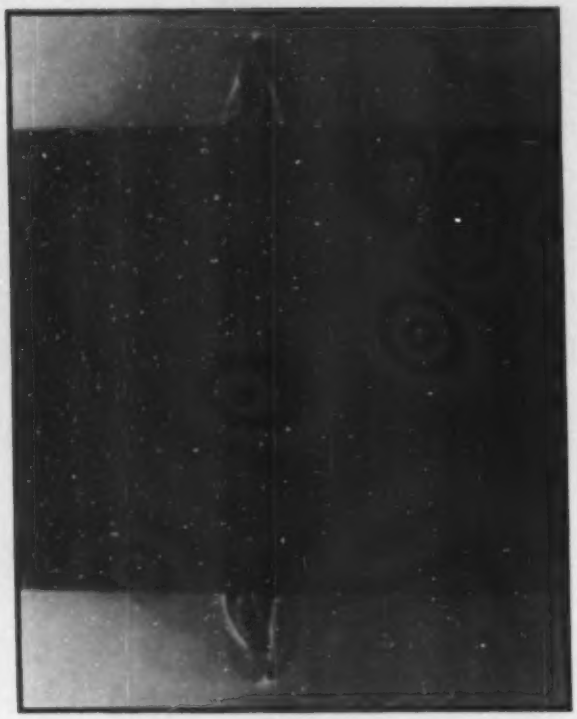

FIG. 1. A spark photograph of the colliding specimens within 1 μsec after impact. The symmetry of the escaping air pattern is related to the dynamic alignment.

initially stationary annealed aluminum specimen of 0.990 in. diam and 10 in. long was struck axially by an identical moving specimen. The constant impact velocity v_0 at the interface was one-half the hitter velocity.

The experimental procedure used was to conduct a number of tests with measurements made at several stations along the specimens and for different impact velocities. One specimen was shot from a smooth bore air gun of matching internal diameter, and the other was supported by four ball bearings located at the far end of the specimen and arranged to permit free axial displacement. Prior to the test, these specimens were aligned optically with 5 in. of the hitter inside the gun. The gun was sufficiently ported at the muzzle so that constant velocity impact was obtained. Dynamic checks of alignment of the square ended specimens were made from spark photographs taken within 1 μsec of impact (Fig. 1). In the photograph the symmetry of the air escaping from between the two specimen faces has been found to be quite sensitive to the degree of alignment. During a test, the two bars are essentially in free flight in the axial direction. The hitter velocity was determined by measuring the time to travel a known distance by means of an electronic counter. A second counter was used to determine the final velocity of the initially stationary specimen. This latter measurement was made at the end of the specimen away from impact.

An agreement with theory would require that the velocities of propagation of each level of strain, as measured by the time of arrival at various positions, should

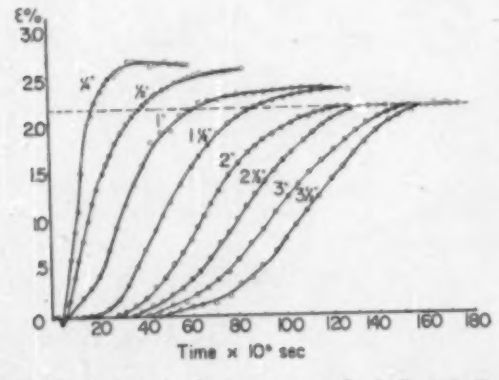

FIG. 2. Typical strain-time curves at the indicated distances from the impact face, for an impact of approximately 66.5 ft/sec. The dotted line at 2.2% is the maximum value computed from the static stress-strain curve for this impact velocity.

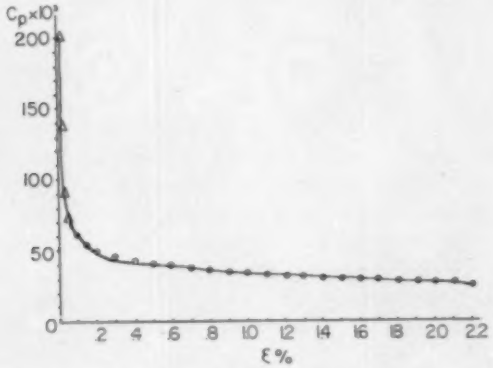

FIG. 3. A comparison of wave propagation velocities averaged from 50 dynamic tests with those determined from the slopes of the static stress-strain curve (solid line). The vertical scale is in inches per second.

be constant. If they are constant, these propagation velocities, c_p, can then be used in Eq. (4) to obtain the velocity-strain curve and a comparison may be made with the results computed from the slopes of the static stress-strain curve. In addition, if accurate data in the low strain region are obtained, the stress-strain curves themselves may be compared, since from (3)

$$\sigma = \int_0^{\epsilon} \rho c_p^2 d\epsilon. \tag{5}$$

In Fig. 2 a series of tests at positions from $\frac{1}{4}$ in. to $3\frac{1}{2}$ in. are shown. All tests in Fig. 2 are for an impact velocity v_0 of approximately 66.5 ft/sec. From three to five tests have been conducted at each station. A detailed examination of the strain data from 50 specimens has shown that propagation velocities are constant and in very close agreement with the values given from the slopes of the static stress-strain curve.

Figure 3 is a comparison of the velocities of propaga-

tion calculated from the slopes of the static stress-strain curve with those obtained from averaging all data at positions from ½ in. to 3½ in. The agreement is excellent.

In Fig. 4 the solid curve is that obtained from integrating Eq. (4) from the slopes of the static stress-strain curve, and the circles represent final maximum strain obtained at two or more diameters from impact for several impact velocities. Again there is agreement between the dynamic and static values. Included in these data are a few maxima obtained earlier with angular incident light[8] and a calibration method which did not involve the systematic error referred to previously.

Increasing the impact velocity has the effect of increasing the strain-time slopes at higher strain levels (Fig. 5), although below 80 ft/sec propagation velocities c_p are independent of impact velocity. A slight trend toward higher propagation velocities has been observed at 80 ft/sec, which is the object of study in a test series in progress, using a higher velocity air gun.

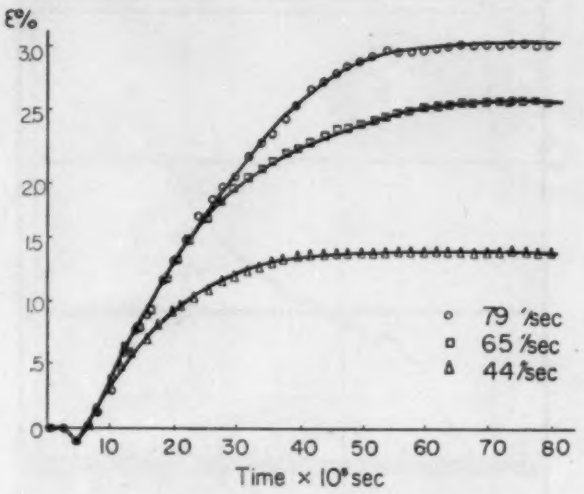

FIG. 5. Strain-time curves for different impact velocities. All measurements were made at one-half diameter from impact.

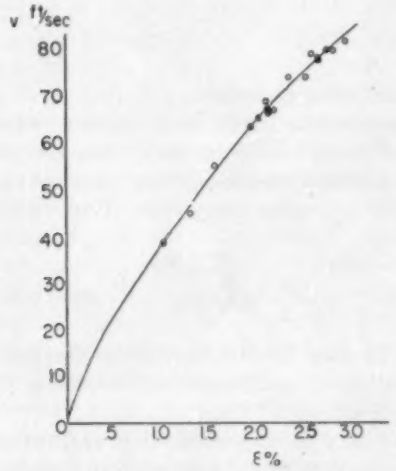

FIG. 4. Impact velocity *vs* maximum dynamic strain at two or more diameters from impact.

In order to integrate Eq. (5) so as to obtain a dynamic stress-strain curve, it is necessary to obtain accurate strain-time data below 500 μin./in. To achieve the accuracy required, it is necessary to use gratings of approximately 45 000 lines/in. Although current studies will include measurement with this increased sensitivity, all of the data given here were obtained from 0.005 in. long, 30 720 lines/in. gratings. However, tests were made using A-8 wire resistance strain gauges for strains up to 500 μin./in. The strain propagation velocities from these tests are shown as triangles in Fig. 3.

The aluminum used in these studies was commercial 1100F, which was annealed for two hours at 1100°F and furnace cooled. Selected specimens were examined microscopically to be certain that the grain size was sufficiently small so that at least twenty or more grains were contained in the area of the diffraction grating used for measurement.

In order to obtain reliable static stress-strain data, a total of eight tests were made: two at constant strain rate, four on a standard hydraulic machine at a variable strain rate, and two tests were conducted in an independent laboratory. A load cell was calibrated by dead weight test, and then used to obtain an absolute load level. Although the constant strain rate curves were slightly higher, with somewhat higher slopes, the calculation of c_p from the slopes of all these tests gave only very small variations. All specimens were 0.990 in. in diam, 3 in. long, and selected from the annealed rods used in the dynamic tests. The solid line of Fig. 6 is an average of the variable strain rate tests.

One aspect of the calculation of a dynamic stress-strain curve may be seen in the A-8 wire resistance strain gauge test shown in Fig. 7. The effect of what appears to be a Pochhammer-Chree dispersion at the elastic limit in the strain below 200 μin/in. will lower the dynamic curve by approximately 400 psi stress.

The curve of Fig. 6 was obtained by assigning the bar velocity, $c_0=(E/\rho)^{\frac{1}{2}}$, where E is Young's modulus

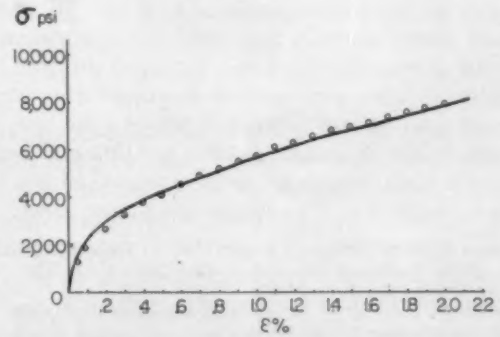

FIG. 6. Dynamic *vs* static (solid line) stress-strain curves.

[8] James F. Bell, J. Appl. Phys. **27**, 1109 (1956).

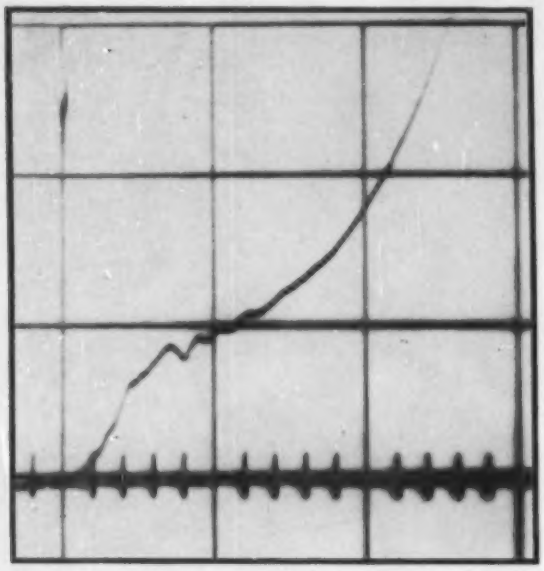

FIG. 7. An oscillogram of the initial elastic front for a 3% plastic wave showing dispersion at the elastic limit. The vertical scale is 0.02% strain per major division. The horizontal scale is 20 μsec per major division.

for aluminum for initial elastic strains. This assumption that the small initial front travels with the bar velocity would seem reasonable for the purpose of a comparison with the static curve whose modulus is E in this elastic region.

The use of Eq. (5) to obtain a dynamic stress-strain curve places such great emphasis upon the low strain region where propagation velocities are large that small variations in four A-8 wire resistance strain gauge tests are sufficient (since the c_p's are squared) to give a shift of several hundred psi in the dynamic stress-strain curve.

The diffraction grating technique for measuring strain has been discussed in several papers.[9-11] The results in all the present series of tests were obtained from 30 720 lines/in. gratings which had a gauge length of 0.005 in. and measurements were made of the behavior of the two first-order 5461 λ green lines of the mercury arc with normal incident light. As has been shown in the above references, the sum of the two angular changes is proportional to the surface angle, and the difference is proportional to strain. The normal uniform monochromatic light field was larger than the expected grating displacement. V-shaped slits and photomultiplier tubes were used, as described elsewhere,[8,10] and each grating was calibrated prior to the test. The reproducibility of data at a given position and impact velocity is such that strain level variations of less than 5% are obtainable. The largest maximum strain was 3%. This value is that for the largest velocity obtainable with the present air gun for a 1 in. diam, 10 in. long aluminum specimen, i.e., a hitter velocity of 160 ft/sec giving an impact velocity of 80 ft/sec, and for a grating location of $\frac{1}{2}$ in.

In a recent paper[1] a method was given for determining Poisson's ratio from these data provided there was sufficient axiality in the impact and also assuming that the radial strain was uniform across a diameter. This latter assumption is a consequence of the introduction of one-dimensionality. Poisson's ratio was shown to be given by

$$\nu=-\frac{1}{\epsilon}\int_0^{\epsilon}\frac{\alpha}{r(\partial\epsilon/\partial x)}d\epsilon, \tag{6}$$

where α is the surface angle, and r the radius of the specimen.

In this integral $\partial\epsilon/\partial x$ may be replaced by $(1/c_p)\times(\partial\epsilon/\partial_t)$ since by definition

$$c_p=-\frac{\partial\epsilon/\partial_t}{\partial\epsilon/\partial x} \tag{7}$$

for constant velocity impact.

This substitution for $\partial\epsilon/\partial x$ in (6) permits the calculation of Poisson's ratio for each test, independent of slopes, at adjacent positions, using values of c_p obtained earlier from averaging many tests. Thus we have

$$\nu=-\frac{1}{\epsilon}\int_0^{\epsilon}\frac{\alpha c_p}{r\partial\epsilon/\partial_t}d\epsilon \tag{8}$$

where $\partial\epsilon/\partial_t$ may be measured from the slopes of the strain-time curve, and α for corresponding time from the same test.

In Fig. 8 may be seen strain-time and corresponding surface angle time data from tests at $\frac{1}{2}$ diam, 2 diam, and $3\frac{1}{2}$ diam from the impact face for an impact velocity of approximately 66.5 ft/sec in each case. Figure 9 gives the corresponding values of Poisson's ratio as

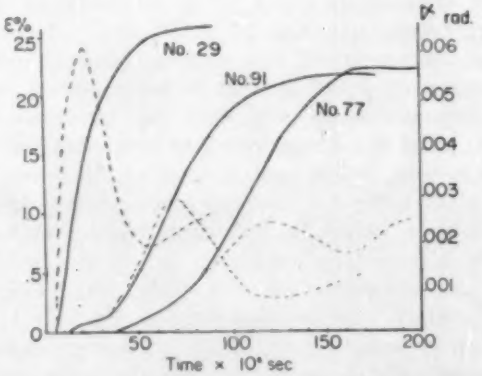

FIG. 8. Strain time and corresponding surface angle time (dotted curves) at $\frac{1}{2}$ diam (No. 29), 2 diam (No. 91), and $3\frac{1}{2}$ diam (No. 77) from the impact face.

[9] James F. Bell, Technical Report No. 4, Department of the Army, BRL, Contract No. DA 36-034-ORD-1363, The Johns Hopkins University (June 1956).

[10] James F. Bell, 3d U. S. National Congress of Applied Mechanics, Proceedings (June, 1958).

[11] James F. Bell, Proc. Soc. Exptl. Stress Anal. (to be published).

determined from these data, using Eq. (8). This delay in the increase in Poisson's ratio suggests the influence of radial acceleration in increasing the amount of dilatation in the immediate vicinity of impact, and may account for the higher maximum strains in the first $1\frac{1}{2}$ diam, shown in Fig. 2.

It is regarded as further evidence for the assumption of one-dimensionality, even for these large diameter specimens, that Poisson's ratio increases from $\frac{1}{3}$ to $\frac{1}{2}$. Because of difficulties in determining $\partial\epsilon/\partial_t$ at very low strain levels, it has been necessary arbitrarily to assume Poisson's ratio to be $\frac{1}{3}$ at 0.1% strain in order to perform the integration of Eq. (8). An examination of the errors present in this calculation has shown that for experimental errors in changing diffraction angles resulting in a 5% error in strain, Poisson's ratio also may be obtained within 5%. Variations of surface angle computed from the same changing diffraction angles are such that larger differences in Poisson's ratio are observed at a given position. These differences are attributed to small variations in axiality of impact. It is thought that simultaneous measurement on opposite sides of the same specimen will provide an average surface angle from which more reproducible results may be obtained. Equipment to permit such simultaneous measurement is at present in construction. The static stress-strain tests have shown that Poisson's ratio begins to increase at 100 μin./in.

In nearly all cases the calculated values of Poisson's ratio are between $\frac{1}{3}$ and $\frac{1}{2}$, except for measurements at $\frac{1}{2}$ in. or less from the impact face, where values below $\frac{1}{3}$ are calculated. For example, a value of 0.2 has been obtained at $\frac{5}{32}$ inch from the impact face. In any event, the trend shown in Fig. 9 is present in all tests; namely, that Poisson's ratio increases more rapidly with increasing distance from impact, and in nearly all cases it has reached a value of $\frac{1}{2}$ before maximum strain is reached. These Poisson's ratio data have been used to determine the amount of dilatation in the propagating plastic wave. Whereas relatively large dilatation is present in the first diameter, a very small amount is found at larger distances from impact.

In order to investigate further the assumption of one-dimensionality present in these studies, three tests were conducted in thin walled tubes having the same outside diameter as the solid specimens. The wall thickness was $\frac{1}{8}$ in. and the outside diameter, 0.990 in. The hitter specimen and initially stationary specimen were both tubes, and the material was annealed aluminum bored from the same material as the solid specimens. Although strain-time slopes slightly steeper than for solid specimens were encountered, the strain propagation velocities, strain maxima, and Poisson's ratio detail were the same as for the solid specimens.

Of particular interest in these tests is the surface angle behavior. For the case of a straight-fronted extensional wave in a plate one would expect the surface angle to be symmetrical with respect to the middle

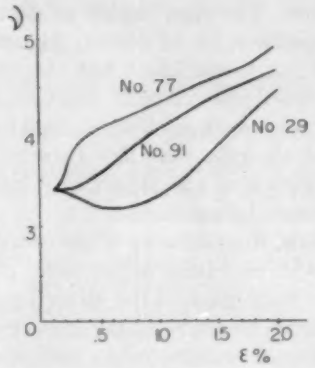

FIG. 9. Poisson's ratio *vs* strain for the three tests shown in Fig. 8.

surface. The angle of the inner surface of a hollow tube, however, must move in the same direction as the outer surface and in the ratio of the radii, if uniform axial stress is present. A comparison of surface angle in the two cases would vary inversely as the wall thickness, or the tube angle in this case would be eight times that for the equivalent plate, and of the same magnitude as that of the solid specimen. In all three cases the maximum surface angles were the same as for the solid specimens measured at similar distances from the impact face.

Since the strain behavior would seem to be essentially one-dimensional, and since Poisson's ratio was $\frac{1}{2}$ at maximum strain for most cases, maximum strain may be computed from the change in specimen diameter associated with impact. This maximum strain determined from the change in specimen diameter produced by the impact may then be compared with the maximum strain given by the diffraction gratings.

If $u_r = \nu r\epsilon$ is the radial displacement, then

$$\epsilon_{\max} = \frac{(u_r)_{\max}}{r\nu} = 4(u_r)_{\max} \tag{9}$$

for $r = \frac{1}{2}$ in. Checks of specimen diameters before and after impact agree with maxima obtained from gratings, after a small allowance is included for unloading. Specimens initially circular, whose impact velocities were 66.5 ft/sec or higher, exhibited a slight but definite oval cross section after impact. This effect, although small, was found over the entire strained portion of the specimen.

If the distribution of strain at the time when the elastic front has reached the far end of the specimen is used to determine the work done, and the kinetic energy is determined from the distribution of particle velocity as given from Eq. (4), their sum may be compared with the initial kinetic energy of the hitter before impact. The energy per unit volume of deformation was obtained from the area under the stress-strain curve of Fig. 6. A difference of less than 2% is obtained in this

energy balance. The distribution of kinetic energy in the hitter specimen is, of course, higher than in the initially stationary specimen, but the strain distributions are assumed symmetrical. Since 50 dynamic tests and 8 static tests were involved in making this energy balance, it is thought that this correlation offers the strongest evidence of the strain rate independent behavior of annealed aluminum.

A check of the final velocity of the initially stationary specimen has given values of the order of five to eight ft/sec higher than one-half the hitter velocity, or what has been referred to above as the impact velocity. This suggests reflected strain levels sufficient to unload elastically the plastically strained regions of the specimens. An attempt to calculate a final energy balance including the reflected unloading wave did not meet with success. An experimental study of such interaction, including internal reflection, would seem to be desirable.

One phenomenon present in these data, and shown in Figs. 2 and 5, is what appears to be small tension precursors at $\frac{1}{4}$ and $\frac{1}{2}$ diam from impact. This effect has disappeared by 1 diam and is only barely visible at $\frac{3}{4}$ diam. It is also associated primarily with higher impact velocities. This effect has recently been identified as the refraction of one of the diffraction images during the passage of the leading edge of the air pulse escaping from between the two colliding specimen faces (Fig. 1). The introduction of deflection shields has eliminated the tension spike but has not otherwise affected the results.

DISCUSSION OF RESULTS, AND CONCLUSIONS

It would appear that these experimental results in annealed aluminum are in agreement in every respect with the predictions of the one-dimensional strain rate independent theory of plastic wave propagation. The strain propagation velocities are given by the slopes of the static stress-strain curve. Although strain propagation velocities are constant from $\frac{1}{2}$ diam to at least $3\frac{1}{2}$ diam, larger strain maxima are obtained in the first $1\frac{1}{2}$ diam. The maximum strain at 2 or more diam is that predicted by the slopes of the static stress-strain curve. The higher maxima in the region of impact is attributed to the large radial acceleration associated with the more rapidly increasing strain. The low values of Poisson's ratio and corresponding large dilatation which have been observed below 1 diam are consistent with this assumption. It should be emphasized that experiments in progress in other materials have not given indication that this type of wave propagation is to be universally expected.

The results given in this paper differ in generality with those reported earlier by Johnson, Wood, and Clark.[12] Their experiments consisted of compression impact of annealed aluminum rods with a hardened elastic rod of another material on which measurements could be made with wire resistance gauges. Since the stresses determined by that method were those at the impact interface where the present results have indicated higher strains are to be expected, it is possible that the apparent lack of agreement is attributable to the effect of radial acceleration and increased dilatation near impact. The contact of a hard and soft material would have the effect of increasing the radial resistance even more. An additional difference between those experiments and these presented here is that the impact ends of the former were formed with an initial radius, whereas the latter involved square ended specimens. Studies with 0.001 in. long gratings located 0.010 in. from the impact face are in progress at the present time, as well as variation of specimen diameter, in order to examine in more detail the behavior in this region near impact.

The reported results are limited to 3% strain, or impact velocities of 80 ft/sec, and all measurements were confined to the first $3\frac{1}{2}$ diam. Similar studies for strains up to 10% are in progress, using a higher velocity air gun than that used in these tests. Measurements also are being made at larger distances than $3\frac{1}{2}$ in. from the impact face. Some additional difficulties are encountered in increasing this distance since a considerably larger uniform light field is required. Studies of constant velocity impact in aluminum at temperatures up to within a few degrees of the melting point also are in progress since the grating technique has been found to be applicable under these conditions.

ACKNOWLEDGMENTS

This investigation has been sponsored by the U. S. Army, Office of Ordnance Research. The invaluable assistance of Mr. John Suckling, Research Assistant, is appreciated.

The author wishes to thank Mrs. Patricia Jones who performed most of the calculations, Mr. Jacob Wenig for the spark photography, and Mr. Stanley Klein for his contribution to the electronics.

[12] Johnson, Wood, and Clark, J. Appl. Mech. **20**, 206 (1953).

JOURNAL OF APPLIED PHYSICS VOLUME 31, NUMBER 2 FEBRUARY, 1960

Growth, Structure, and Properties of Graphite Whiskers

ROGER BACON
Research Laboratories, National Carbon Company, Division of Union Carbide Corporation, Cleveland 1, Ohio
(Received August 5, 1959)

Graphite whiskers have been grown in a dc arc under a pressure of 92 atmospheres of argon and at 3900°K. They are embedded in a solid matrix of graphite which builds up by diffusion of carbon vapor from the positive to the negative electrode. Diameters range from a fraction of a micron to over five microns, with recoverable lengths up to 3 cm. They consist of one or more concentric tubes, each tube being in the form of a scroll, or rolled-up sheet of graphite layers, extending continuously along the length of the whisker, with the c axis exactly perpendicular to the whisker axis. They exhibit a high degree of flexibility, tensile strengths up to 2000 kg-mm^{-2}, Young's modulus in excess of 7×10^{12} dyne-cm^{-2}, and values of room-temperature resistivity of around 65 μohm-cm, which approximates the single crystal value.

INTRODUCTION

FILAMENTS of graphite have been observed by many workers.[1–8] They have been found, often by accident, as deposits on various substrates inside furnaces containing hydrocarbon gases or carbon monoxide. Substrate temperatures have varied from 350° to 2500°C. A wide range of sizes has been found, roughly from 0.01 micron to 200 microns in diameter and up to 5 cm in length. They have been observed in the form of helices[4,6,8] and, in one remarkable case, as loops and as an interconnected network of branches.[8]

Several authors observed or postulated that the growth occurred from catalyst particles. In some cases, such particles were found on the growing end of the filament[4,5,6,8]; in other cases, they appeared to have been left behind, serving only to initiate growth of the filament, which then continued to grow unaided.[2,3,7] Filaments have been found growing on graphite, silica, a ceramic thermocouple tube, fire brick, iron oxide and on particles of iron, cobalt, nickel, and lampblack. The growth in the presence of iron, cobalt, nickel, or their oxides or carbides, generally occurs at relatively low temperatures (350–600°C), whereas temperatures in excess of about 1000°C seem to be required for growth on the remaining materials where the "catalyst" conceivably could be a particle of soot in every case.

Hillert and Lange[8] observed thick filaments, up to 200 microns diameter and often over 50 mm long in the hottest (1000°C) zone of a silica tube furnace. Filaments as thin as 0.01 micron were found at a zone of lower temperature. The thin filaments were hollow tubules similar to those observed by other workers.[5,6] Although polycrystalline, there was a high degree of preferred orientation, the c axis being roughly perpendicular to the filament axis, with a deviation of about 10°. The thicker filaments were similarly oriented and the authors presented evidence which shows that they probably result from a thickening process which takes place after the formation of the primary thin filaments. Measurements by this author of the strengths of these filaments, kindly supplied to him by Dr. Hillert, yielded a maximum tensile strength of 155 kg mm^{-2} obtained with a filament of 12 microns diameter. Smaller filaments, which doubtless would have yielded higher values, were too brittle to handle with the testing apparatus available.

Meyer[7] has observed filaments grown at temperatures above 2000°C micrographs of which look very similar to those of Hillert and Lange and show a similar preferred orientation.

The filaments to be described in the present communication have been reported previously.[9–11] They differ radically from those of the above-mentioned investigators in several respects. They are formed at graphite arc temperatures and are found embedded in a solid matrix of graphite from which they must be extracted. They are very flexible but exceedingly strong. Although they are not single crystals in a strict sense, they consist of cylindrical layers, or actually scroll-like formations, of graphite sheets extending *continuously* along the length of the filament, the c axis being oriented exactly perpendicular to the filament axis. Hence, they behave essentially like single crystals with respect to properties measured along the filament axis.

Although the highly anisotropic crystal structure of graphite limits comparison between graphite whiskers and whiskers of other materials,[12] the former show a

[1] R. Iley and H. L. Riley, J. Chem. Soc. **1948**, 1362.
[2] P. A. Tesner and A. I. Echeistova, Doklady Akad. Nauk S.S.S.R. **87**, 1029 (1952).
[3] L. V. Radushkevich and V. M. Lukýanovich, Zhur. Fiz. Khim. **26**, 88 (1952).
[4] Davis, Slawson, and Rigby, Nature **171**, 756 (1953).
[5] Hofer, Sterling, and MacCartney, J. Phys. Chem. **59**, 1153 (1955).
[6] Davis, Slawson, and Rigby, Trans. Brit. Ceram. Soc. **56**, 67 (1957).
[7] L. Meyer, Z. Krist. **109**, 61 (1957).
[8] M. Hillert and N. Lange, Z. Krist. **111**, 24 (1958).
[9] Roger Bacon and J. C. Bowman, Bull. Am. Phys. Soc. Ser. II, **2**, 131 (1957).
[10] Roger Bacon, Bull. Am. Phys. Soc. Ser. II, **3**, 108 (1958).
[11] Roger Bacon, *Growth and Perfection of Crystals*, edited by Doremus, Roberts, and Turnbull (John Wiley & Sons, Inc., New York, 1958), p. 197.
[12] Recent articles on whiskers may be found in *Growth and Perfection of Crystals*, edited by Doremus, Roberts, and Turnbull (John Wiley & Sons, Inc., New York, 1958), including review articles by F. R. N. Nabarro and P. J. Jackson, p. 11, and by S. S. Brenner, p. 157. See also: S. S. Brenner, Science **128**, 569 (1958).

similarly high degree of crystal perfection and very high tensile strength, as observed in a variety of other whiskers, both metallic and nonmetallic.

METHOD OF GROWTH

The graphite whiskers are grown in a dc graphite arc under a high pressure of inert gas. A positive upper graphite electrode one-half inch in diameter is used to strike an arc against a carbon block, the whole being contained inside a pressure vessel which is provided with the means for feeding the rod downward as it is consumed. Graphite vaporizes from the tip of the rod and immediately condenses to a solid on the block (with roughly 20% loss to other parts of the chamber) building up a solid cylindrical deposit having a slightly larger diameter than the rod itself. This deposit (which we term a "boule") grows like a stalagmite at the rate of about one-half inch per minute until it reaches a length of five or six inches.

The whiskers are embedded in this solid graphite boule and are extracted simply by breaking the boule open. A given whisker pulls out of one-half of the broken boule, remaining firmly anchored in the other half. Lengths of up to 3 cm are found protruding from the exposed surfaces. Diameters generally fall in the range of one to five microns, although ribbons with thicknesses of a fraction of a micron also are found. Many hundreds of whiskers typically are found on each surface.

The density of whiskers is greatest in the central portion of the boule cross section. This is because they tend to grow axially upward along the boule, but also slightly inward, that is, in a direction perpendicular to the concave growing surface of the boule. X-ray back reflection photographs have been taken from interior surfaces of boules which were split longitudinally. No preferred orientation was found; hence, the whiskers, which are highly oriented, represent a small fraction of the total mass of the material, and the matrix in which they grow is composed of a dense polycrystalline graphite with random orientation of the grains.

The range of pressures under which whiskers will grow is only a few atmospheres, with the optimum pressure believed to be about 92 atmospheres. This is just under the triple point pressure, which has been reported by Basset[13] to be 100 atmospheres, a value we have confirmed using both resistance heating and arc heating. The sublimation temperature of graphite at this pressure has been determined by Jones[14] to be about 3900°K.

The dc arc is operated at 75–80 volts and 70–75 amperes for best whisker growth. A ballast resistance of about 0.15 ohm is in series with the arc and the line voltage is 90 volts.

The method of boule growth is an application at lower pressures of a method developed in these Laboratories by Jones for the arc melting of graphite. His process was first carried out at pressures above the triple point so that solidification of the boule occurred from the liquid phase rather than from the vapor. The boule material under these conditions consists of comparatively large needles oriented perpendicular to the concave growing surface and showing a large degree of preferred orientation, the c axis being roughly perpendicular to the needle axis.

PROPERTIES

a. External Appearance and Shape

Under a low power microscope, a crop of whiskers looks like a bundle of Christmas tinsel, the sides showing the high reflectivity characteristic of the basal planes of the graphite crystal. Under higher power, it becomes evident that, although some whiskers are ribbon-shaped, most are thick whiskers with either cylindrical surfaces or somewhat irregularly flattened surfaces. The sides of cylindrical whiskers can be deliberately flattened by mechanical pressure and it was believed until recently that all whiskers grow in a cylindrical form, either circular or elliptical, becoming deformed in the process of extraction from the boule. However, recent work by Bryant[15] indicates that a prismatic form is common in the as-grown whiskers. These whiskers were freed from the surrounding matrix by heating in air and etching away the boule material.

b. Flexibility and Strength

Manipulation of the whiskers indicates that they are very flexible and strong. They may be kinked back and forth dozens of times without breaking. Once kinked, a whisker may be straightened and will recover to a considerable extent its resistance to further kinking.

Under tension, the whiskers exhibit exceedingly high strengths, the highest observed value being 2000 kg mm^{-2}. This corresponds to a maximum elastic strain of about 2%. In most cases, failure occurs at the grip and it is usually observed that the whisker actually pulls out of the grip leaving a thin outer sheath behind. Graphite has a very low shear strength along the layer planes and shearing stresses are high in the region near the grips. The highest observed strengths are found with thin ribbon-shaped whiskers where a large gripping surface-to-volume ratio minimizes this difficulty.

c. Young's Modulus

The Young's modulus along the whisker axis is currently being investigated. This modulus is the reciprocal of the single crystal elastic compliance constant, s_{11}. No previous determinations have been made, for

[13] J. Basset, J. phys. radium **10**, 217 (1939).
[14] M. T. Jones and William Weltner, Jr., Fourth Biennial Conference on Carbon, University of Buffalo (1959).
[15] Paul Bryant (private communication).

the evident reason that no suitable samples have been available heretofore. A value of 7×10^{12} dynes cm^{-2} can be reported as a lower limit, but it is believed that the true value may be as high as 10×10^{12} dynes cm^{-2}. (The experimental difficulty again is the problem of gripping the whisker for the application of tension. Near the grips, only the outer layers are in tension so that the effective cross-sectional area is less than the measured area.) An unpublished calculation by Eatherly of these Laboratories, based on data from benzene spectra, predicts a value for $1/s_{11}$ of 10×10^{12} dynes cm^{-2} with an estimated accuracy of $\pm20\%$.

d. Resistivity

The room temperature resistivities were measured on several graphite whiskers from the same boule specimen. The cross-sectional areas were determined with only fair accuracy by measuring the diameter under a 600-power microscope. In the case of elliptical cross sections, the major and minor axes were measured to aid in calculating the cross section. Seven out of eight whiskers yielded values between 60 and 76 μohm-cm. This range in values could easily be accounted for by the error in cross-sectional area measurement. Annealed and purified single crystal flakes show room temperature resistivities as low as 40 μohm-cm,[16] whereas that of bulk polycrystalline graphite is usually above 800 or 1000 μohm-cm along the extrusion axis. Since graphite is intermediate between a semiconductor and a metal in its electrical characteristics, its resistivity is very sensitive to impurity content and crystal perfection. Furthermore, it is highly anisotropic; the resistivity along the c axis (i.e., normal to the basal plane) is some two to three orders of magnitude higher than that in the basal plane.

A more sensitive test of the crystal perfection is the temperature dependence of the resistivity at low temperatures. Figure 1 shows this behavior for several types of graphite samples, including two whiskers. A total of sixteen whiskers was measured at three or four points, from room temperature down to liquid helium temperature. Whisker A in Fig. 1 exhibited behavior nearest to that of pure annealed single crystal flakes.[16] Two other whiskers showed similar behavior. Whisker B is typical of the behavior of most of the remaining whiskers: a slight rise in resistance down to liquid-nitrogen temperature followed by a rapid drop to the temperature of liquid helium. Carefully handled samples of carbon filaments, coated by pyrolytic decomposition of hydrocarbon gases and having a high degree of preferred orientation, exhibit a temperature behavior similar to that of the whiskers.[17] The corresponding behavior of bulk polycrystalline graphite is, by contrast, a monotonic increase in resistivity as one lowers the temperature down to liquid helium.

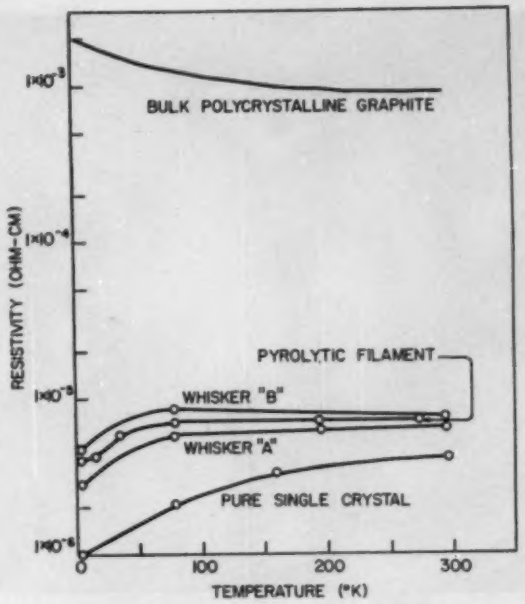

FIG. 1. Resistivity *vs* temperature for several graphites.

STRUCTURE OF GRAPHITE WHISKERS

a. X-Ray Diffraction

Several whiskers mounted with their axes perpendicular to the x-ray beam (copper $K\alpha$ radiation) gave (00.2) reflections with the diffracted beam perpendicular to the whisker axis. This was expected since it was already evident that the basal planes must be parallel with the whisker axis. A result unexpected at that time, however, was that the reflection was observed at all orientations of the whisker as it was rotated about its axis. This meant either that the whisker was a bundle of randomly oriented fibers or that the graphite basal planes were bent into tubes or scrolls. Because the diffraction spots were sharp, it seemed unlikely that a random arrangement of individual fibers could be responsible, for the fibers would be expected to have dimensions along the c axis of the order of 100 A or less where diffraction broadening would become appreciable. In these patterns, other reflections are observed which showed broadening characteristic of graphite with stacking faults.

One whisker having a flat, ribbon-like shape was mounted for x-ray diffraction in the same manner as above, but this time the (00.2) reflection was observed at only one orientation. The (00.4) reflection was then observed after rotating the whisker about its axis through the predicted angle of 14°, the difference in Bragg angles for the two reflections using copper $K\alpha$ radiation. This showed that in the case of ribbon whiskers, at least, the graphite layer planes were oriented parallel with the surface.

[16] D. E. Soule, Phys. Rev. **112**, 698 (1958).
[17] Bowman, Krumhansl, and Meers, Industrial Carbon and Graphite Conference, London, 1957 (Society of Chemical Industry), p. 52.

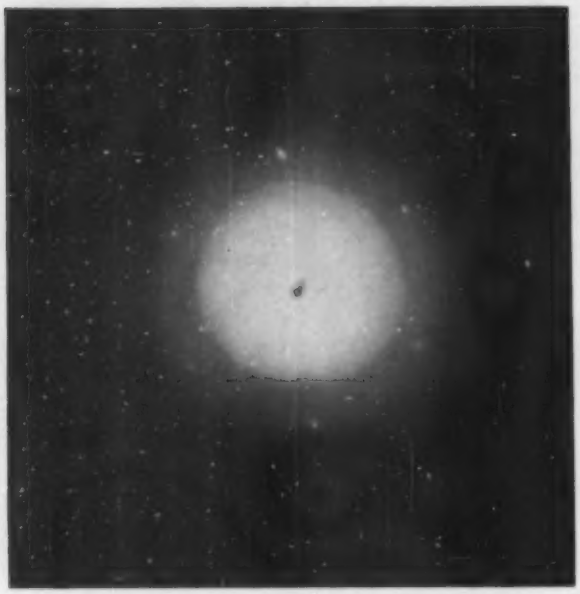

FIG. 2. Single crystal electron diffraction pattern from whisker fragment.

b. Electron Diffraction

Figure 2 shows a single-crystal electron diffraction pattern obtained with an RCA model EMU-3B electron microscope from a very thin flake of graphite which had peeled off from the main body of a whisker. The flake was nearly perpendicular to the incident electron beam and hence only the hexagonal array of spots of type (*hk*.0) appear.

Most of the electron diffraction patterns were obtained from the main whisker itself and hence resulted in a more complicated array of spots. In many cases, the (00.2) and sometimes the (00.4) spots appeared (for example, see Fig. 4) owing to the bending of the layer planes into a cylindrical form, which thereby allowed the direction of the whisker axis on the diffraction pattern to be determined (since the *c* axis is perpendicular to it). Finally, in the majority of cases, several hexagonal arrays appeared in the pattern, misoriented one with another by rotations about the *c* axis.

Figure 3 shows a pattern which is clearly equivalent to a single crystal rotation pattern, although the whisker was held stationary during the exposure. The axis of the whisker is approximately vertical with the page. The apparent rotation results from the fact that the whisker consists of graphite sheets bent around some axis (in this case, a [210] axis) to form a tube.

FIG. 3. Single crystal electron diffraction pattern from cylindrical whisker.

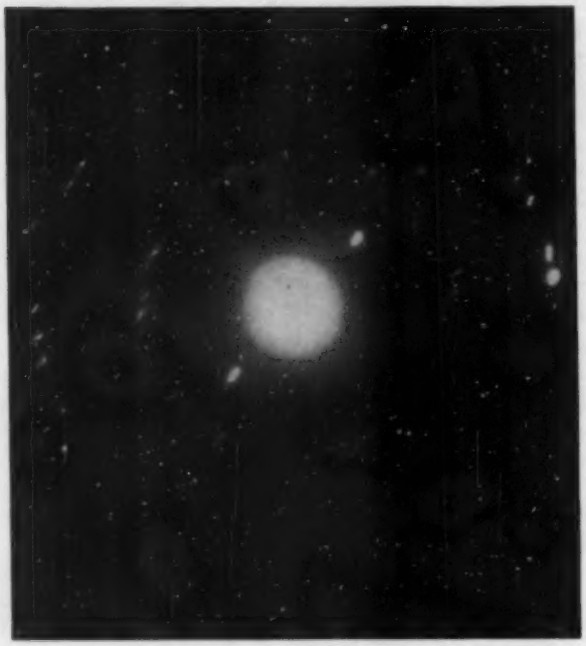

FIG. 4. Electron diffraction pattern from triple-tube whisker of Fig. 5.

Figure 4 shows the electron diffraction pattern of a whisker, the electron micrograph of which appears in Fig. 5. The pattern shows the (00.2) and (00.4) spots and hence the whisker axis is along the direction perpendicular to the line joining these spots. Figure 5 suggests that the whisker, the end of which has been tapered in step-wise fashion in a mechanical tensile test, consists of three more or less well-defined concentric tubes. (The tubes have become partially flattened or otherwise distorted.) The diffraction pattern shows that each "spot" is triple, arising from three layers misoriented successively by about six degrees. Now, in a single crystal pattern, the innermost ring in the hexagonal array of (*hk*.0) spots consists of the six

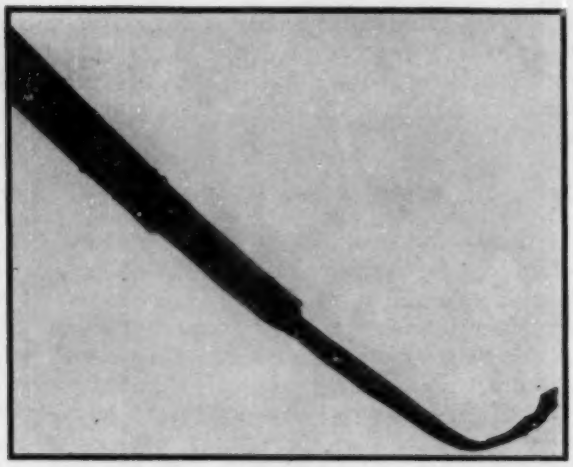

FIG. 5. Electron micrograph of whisker end showing three concentric tubes. (7700×.)

{10.0} reflections, but in this pattern we find twelve such reflections for each of the three crystal layers consisting of two interleaved sets of six. In each case, the second set of six reflections is obtained from the first set by a 180° rotation about the whisker axis. We thus have direct evidence from this diffraction pattern that any given single crystal layer is bent around into a cylinder or scroll; it diffracts the incident electron beam twice—once at the "front side" of the whisker and again at the "back side."

c. Electron Microscopy

Clear evidence of the fact that the graphite whiskers are composed of cylindrical layers is presented in the electron micrographs of Figs. 5 to 9. Figure 5 is an example of the commonly observed fact that a decrease in diameter is accompanied by circumferential steps on the whisker and an increase in the transparency to the electron beam. Similar effects may be seen in Fig. 9. In Fig. 6, which shows a tip that has been field evaporated in a field emission microscope, the steps silhouetted on opposite sides of the whisker are remarkably similar. Exposed edges at the points of termination of cylindrical layers are "frayed" by the high field, but the smooth sides attest to the fact that the cylindrical

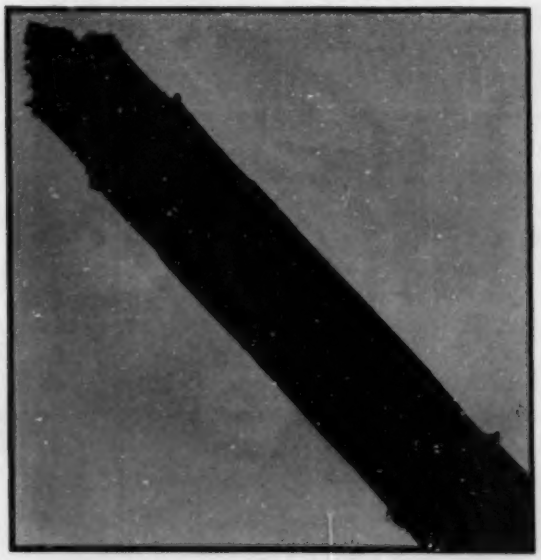

FIG. 6. Whisker whose tip has been evaporated in a field emission microscope. (2500×.)

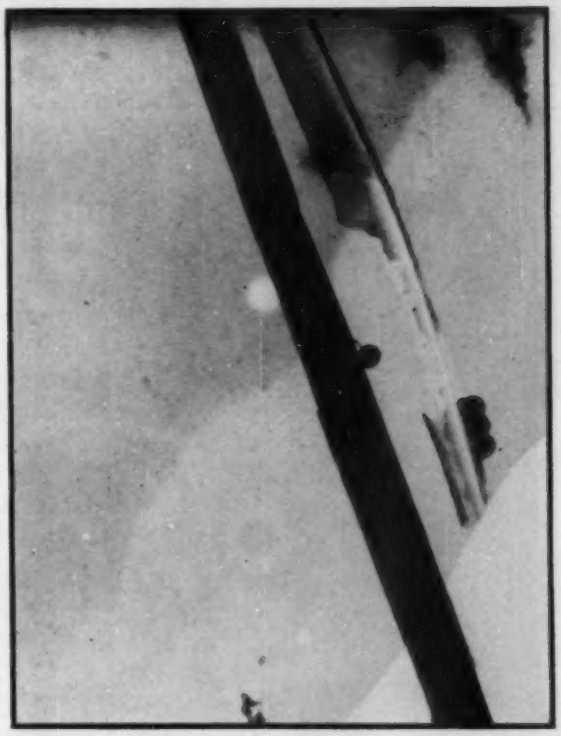

FIG. 7. Whisker with a peeled-off cylindrical sheath. (12 300×.)

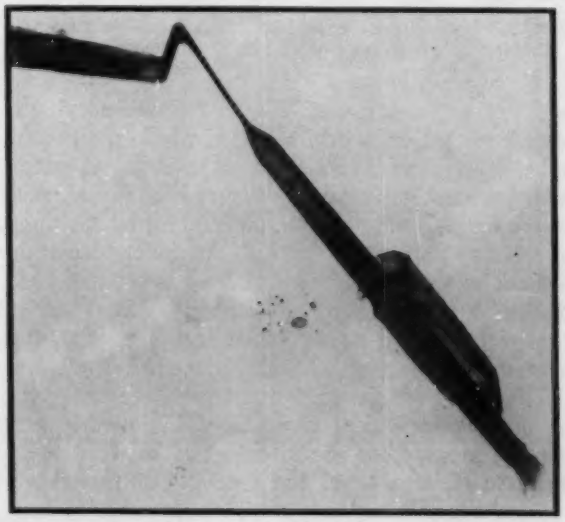

FIG. 8. Hollow tube collapsed into a ribbon. (6300×.)

FIG. 9. Thin ribbon-shaped whisker exhibiting Moiré pattern. Picture includes both edges of the 2 μ wide whisker. (24 000×.)

surfaces are undamaged. Figure 7 shows a cylindrical sheath peeled off from its parent whisker. (The small spheres seen are Dow latex balls used to calibrate the instrument magnification.) Figure 8 shows a whisker whose outer layers were "exploded" off by the passage of a heavy current through it. The inner core appears to be a hollow tube, part of which has collapsed into a ribbon. Figure 9, showing a ribbon with small step changes in width accompanied by changes in transparency, exhibits, in addition, a moiré pattern[18] consisting of equally spaced interference bands oriented along three equivalent crystallographic directions. The pattern arises from the interference between the undeviated electron beam and a doubly diffracted beam, the second diffraction occurring at a crystal layer misoriented with the layer producing the first diffraction by a rotation of about 0.3° about the c axis. The bands are perpendicular to the {10.0} planes which give rise to them.

[18] For a similar pattern obtained from boron nitride see: J. F. Goodman, Nature **180**, 425 (1957).

d. Evidence for a Scroll Structure

The observations of the structure of graphite whiskers which have been presented thus far have demonstrated that they consist of cylindrical or prismatic layers of graphite extending over large distances along the axes of the whiskers. The observations have neither suggested nor precluded the possibility that the structure is actually a scroll such as the model sketched in Fig. 10 where a graphite sheet (presumably consisting of several monolayers) overlaps itself and continues to wind around the whisker axis many times rather than joining opposite edges after a single turn to form a perfect cylinder. The scroll structure is somewhat more attractive from the standpoint of growth mechanism as it provides a means for the simultaneous thickening and elongation of the whisker. The fact that this actually is the structure was made evident by observations in which a section of a whisker was exploded by the sudden passage of a large current through it. The result, a good example of which is shown in Fig. 11, was that very large sheets were peeled off with lateral dimensions many times the circumference of the whisker itself. These observations are consistent only with the scroll structure model.

DISCUSSION

a. Relationship between Structure and Physical Properties

One obvious result of the cylindrical structure of graphite whiskers is that they have sides which are essentially perfect. Except for the edge of the final turn of the scroll, the only boundary on the outside surface consists of a tightly bonded hexagonal layer of the graphite crystal with no exposed edges at which tearing under stress can initiate. As a result, severe deformation

FIG. 10. Model of graphite whisker scroll structure.

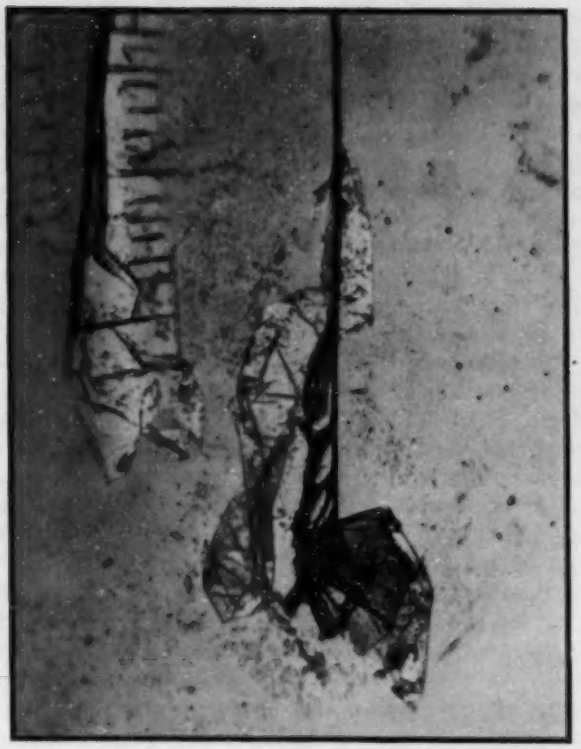

FIG. 11. Optical micrograph of electrically exploded whisker. (260×.)

like that shown on the side of the ribbon of Fig. 12 does not result in tearing, but only in a crinkling of the edge. The exceedingly high strengths observed in these whiskers is thus accounted for so long as one is able to apply tension uniformly to the whisker, i.e., without a large shear component of stress parallel to the whisker axis. Likewise, the remarkable ability of the whiskers to withstand repeated kinking without appreciable loss of strength can be understood.

The measurement of macroscopic properties along the axis of the whisker should result in nearly single crystal values, as has been observed in the case of resistivity and elastic modulus, because the whisker is a structure of continuous graphite layers and is essentially a single crystal insofar as properties measured along its axis are concerned. Most properties measured in the basal plane are independent of direction within the plane so that disorientations between the several component layers of the whisker will not alter the results.

The imperfections which could cause deviations from perfect single crystal properties are: (1) stacking faults, which are presumably unimportant unless they occur with great frequency since interplanar bonding in graphite is very weak; (2) bending of layers, which is probably serious only when the curvature is large, such as results from inclusions between planes or damage from handling; (3) impurities, which can cause local mechanical stresses as well as affect electrical properties; (4) abrupt discontinuance of a layer at some point along the length of the whisker; such boundaries never have been definitely observed within the whisker, but only on the outside layer where in some cases, at least, they are the result of deliberate or unavoidable damage such as occurs during extraction from the boule; (5) twinning, which may account for the prismatic forms of some whiskers. No quantitative evaluation of the effects of these imperfections can be made at the present time.

b. Nucleation and Growth Kinetics

Since direct observation of the growth of graphite whiskers has been impossible, and since they are not grown in an isolated state but must be extracted from a solid matrix, one can only speculate as to the mechanisms of nucleation and subsequent growth, taking into account their cylindrical structure and comparisons with graphite fibers formed by decomposition of hydrocarbons or carbon monoxide.

It is commonly observed when carbon is deposited from a vapor that graphite layers tend to orient themselves parallel with the substrate surface. This has been observed in the case of evaporated films,[19] and in the case of pyrolytic coatings, including the thickening of the graphite fibers cited in the introduction. Hillert and Lange[8] showed that in the primary hollow filament itself, the *c* axis was preferentially perpendicular to the filament axis, fundamentally as the result of graphite layers forming parallel with the surface of a catalyst particle. Other workers have likewise observed or postulated nucleation from a catalyst particle.[5,6] Similarly, tubes of cuprene, grown by polymerization of acetylene in the presence of copper, have been observed with a

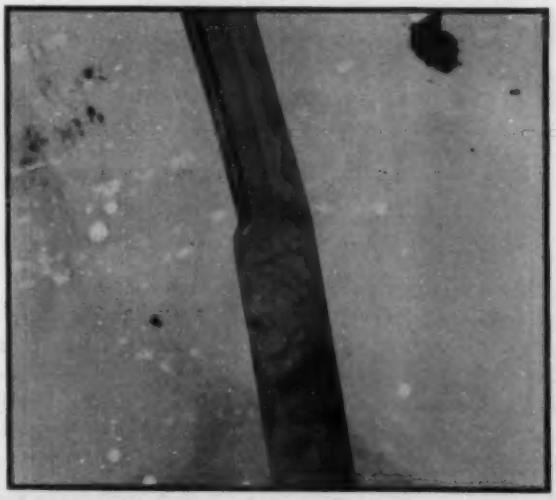

FIG. 12. Electron micrograph of ribbon-like whisker showing severe damage at edge without tearing. (3500×.)

[19] D. E. Palin, Nature **178**, 809 (1956).

variety of cross sections attributed to the size and shape of the catalyst particle.[20]

The tendency for graphite crystals to nucleate with layers parallel to the surface substrate is presumably the result of the lowering of the surface energy of the embroyonic graphite layer crystal. During subsequent growth, the crystal layers will tend to follow substrate surface contours in competition with the resistance of the layers to bending.

A possible mechanism of whisker growth, then, is described as follows. A very thin graphite sheet or ribbon coils itself up (possibly wrapping around a fortuitously situated graphite particle) in order to reduce its surface energy. If the resulting cylinder or scroll is properly oriented, with its axis parallel to the general growth direction, then it can grow rapidly in the direction of increasing length, while thickening simply by tangential growth in spiral fashion. Every so often, the tangential growth may stop and be superseded by a new growth layer which nucleates on the whisker surface, the new layer possibly being misoriented with respect to the old by a rotation about the c axis. All of the layers then propagate themselves as the whisker grows in length.

Since the growing tip of the whisker is a stable structure growing in the fast growth direction (i.e., perpendicular to the c axis), it is reasonable to suppose that the tip grows slightly ahead of the general solid surface. In fact, it is observed that whiskers will grow right through layer-like discontinuities transverse to the boule which are formed under certain conditions as the result of large fluctuations in the arc current. The boule itself is very weak at these discontinuities, and yet the growth of some whiskers, at least, is quite unaffected by their occurrence.

[20] John H. L. Watson and K. Kaufmann, J. Appl. Phys. **17**, 996 (1946).

The formation of the boule occurs under very nearly equilibrium conditions. On the assumption that the vaporization coefficient of the dominant gas species is near unity, a calculation using kinetic theory shows that the carbon vapor pressure at the evaporating surface of the anode is lower than the equilibrium vapor pressure of 90 atmospheres by only 0.01 to 0.1 atmosphere. The arc gap between electrodes seems to be no greater than one-tenth millimeter, so that anode and cathode surface temperatures are not greatly different. The transfer of carbon vapor across the gap may be shown to be a diffusion-limited process.

These near-equilibrium conditions at very high temperatures undoubtedly are responsible for the high degree of crystal perfection found in these whiskers as compared to the graphite filaments studied by other workers. It is of interest to note, furthermore, that at these temperatures, the larger molecular species begin to dominate in the vapor. C_3 may be the dominant species, but according to calculations by W. Weltner[21] at these Laboratories, and by Pitzer and Clementi,[22] there is a good probability that C_5 and higher molecular species exist in appreciable quantities, particularly under conditions approaching equilibrium. The dominance of these higher species may be of some significance in the nucleation of whiskers.

ACKNOWLEDGMENTS

The author wishes to thank R. Sprague for his patient performance of many experimental observations and tests, Karl Meyer for the electron micrographs and diffraction patterns, and numerous other members of the laboratory staff for their help and interest in this work.

[21] W. Weltner, Jr. (unpublished).

[22] Kenneth S. Pitzer and Enrico Clementi, J. Am. Chem. Soc. **81**, 4477 (1959).

JOURNAL OF APPLIED PHYSICS VOLUME 31, NUMBER 2 FEBRUARY, 1960

Ion Drift in an n-p Junction*

E. M. PELL
General Electric Research Laboratory, Schenectady, New York
(Received August 19, 1959)

If a reverse bias is applied to an n-p junction at a sufficiently elevated temperature to give either the donor or the acceptor ions appreciable mobility, the ions will drift in the electric field of the junction to produce an intrinsic semiconductor region between the n and p regions. Such ion drift offers a simple and straightforward method for investigating diffusion constants, as well as chemical interactions within the host lattice which affect this diffusion. Preliminary results indicate its feasibility for measuring the diffusion constant of Li in Si to as low as 10^{-18} cm²/sec and also for measuring the effect of Li-oxygen and Li-acceptor interactions in decreasing the diffusion rate. Intrinsic regions resulting from ion drift have been used to produce diodes with breakdown in excess of 4000 volts from low resistivity silicon. In addition, they can be used to extend the frequency range of devices by virtue of the decrease in junction capacitance associated with such an incorporated intrinsic region. Ion drift has also been used for the fabrication of analog transistors, an early unit having an input impedance of 6 megohms, a power gain of 17 db and a voltage gain of 4.

INTRODUCTION

USING the techniques to be described, it is possible to produce an intrinsic region between two heavily and oppositely doped semiconducting regions. This is of significance as a means for studying the drift-diffusion process and also as a new technique in device technology.

Since the ion drift process occurs on a microscale, measured distances being of the order of the width of the n-p junction, it is admirably suited to the measurement of small diffusion rates. The process is simple and straightforward and involves but few assumptions and parameters; one can hence have a high degree of confidence in the results. Because of the method's high sensitivity, (2.5×10^{-17} cm²/sec has been reliably measured with diffusion times of the order of hours; 10^{-18} cm²/sec appears quite reasonable) it can be used to measure diffusion rates at relatively low temperatures, where chemical interactions are expected to affect the diffusion rate,[1-3] and it leads directly to the value of the binding energy in such interactions. Because it sensitively measures the diffusion rate at very low concentrations (10^{13} atoms per cc or lower for Li in Si) it can measure the effect of chemical constituents which are present in comparably low concentrations.

In device technology, the advantages of p-i-n diode structures and related transistor structures as a means of increasing the breakdown voltage and high-frequency limit have long been known.[4,5] The ion drift technique offers another method for achieving such structures. It eliminates the need for using material of intrinsic resistivity and hence may prove useful with semiconductors of low purity. Also, it offers a new degree of freedom in controlling device geometry, particularly on the microscale; and it may therefore prove applicable in certain special areas of device technology. Its usefulness in achieving complex geometries is illustrated by its adaptability to making an analog transistor structure—so called because it is exactly analogous to the structure of the vacuum tube, inclusive of control grid, with a drift region composed of intrinsic semiconductor replacing the vacuum of its counterpart. The concept of such a structure probably antedates the transistor. Possible forms have been described in detail,[6] and a close variant has been produced,[7] but only with the ion drift technique has it now become possible to achieve the exact counterpart of the vacuum tube.

The method for achieving an intrinsic region by use of ion drift relies on the drift of donor and/or acceptor ions in the field of a reverse-biased n-p junction. It will be demonstrated that the ions drift in such a way as to almost perfectly compensate each other. The temperature at which this occurs must, of course, be sufficiently high to make either the donor ions or the acceptor ions mobile, but not so high that the semiconductor becomes intrinsic and the n-p junction disappears.

PRINCIPLES OF THE ION DRIFT PROCESS

We shall consider the drift of Li^+ ions, which are donors, in p-type Si, the latter being produced, for example, by doping with boron during the crystal growth. The acceptor is initially present uniformly throughout the Si to a level of N_A acceptors per cc. Lithium is then diffused into the silicon from a surface source of N_0 donors per cc, where $N_0 \gg N_A$, until an n-p junction is produced internally at the position $x=c$, as

* The research reported in this paper has been partly sponsored by the Electronics Research Directorate of the Air Force Cambridge Research Center, Air Research and Development Command, under contract AF 19(604)-5551. It has been presented, in part, at the May, 1959 meeting of the Electrochemical Society.

[1] Reiss, Fuller, and Morin, Bell System Tech. J. **35**, 535 (1956).
[2] J. P. Maita, J. Phys. Chem. Solids **4**, 68 (1958).
[3] E. M. Pell, *Proceedings of the Brussels Conference on Solid State Physics, 1958* (to be published).
[4] A. Uhlir, Jr., Proc. Inst. Radio Engrs. **46**, 1099 (1958), and references therein.
[5] J. M. Early, Bell System Tech. J. **33**, 517 (1954).
[6] W. Shockley, Proc. Inst. Radio Engrs. **40**, 1289 (1952).
[7] Statz, Pucel, and Lanza, Proc. Inst. Radio Engrs. **45**, 1475 (1957).

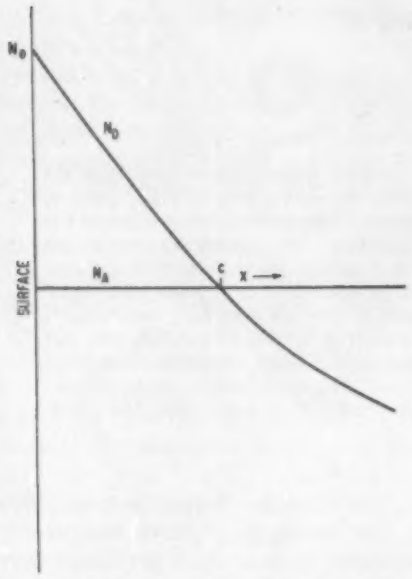

FIG. 1. Impurity distribution after preliminary lithium diffusion.

in Fig. 1. For diffusion temperatures sufficiently high that drift in the built-in field of the junction is negligible, the initial donor concentration as a function of the distance, x, from the surface is described by[8]

$$N_D = N_0 \operatorname{erfc}[x/2(D_0 t_0)^{\frac{1}{2}}] \quad (1)$$

where D_0 is the diffusion constant at the temperature of this initial diffusion and t_0 is the duration of the diffusion period. We shall consider only the region of large x in the neighborhood of $x=c$, with $c \gg (D_0 t_0)^{\frac{1}{2}}$. In this region Eq. (1) can be approximated by the first term of a series expansion, giving

$$N_D \simeq (2N_0(D_0 t_0)^{\frac{1}{2}}/x\sqrt{\pi}) \exp(-x^2/4D_0 t_0). \quad (2)$$

At $x=c$, this equation becomes equal to N_A, permitting an evaluation of $N_0(D_0 t_0)^{\frac{1}{2}}$. Substituting this in Eq. (2),

$$N_D \simeq (N_A c/x) \exp[-(x^2-c^2)/4D_0 t_0]. \quad (3)$$

We note, for future use, that for values of x in the neighborhood of c, Eq. (1) can be expanded by Taylor's formula to give

$$N_D \simeq N_A[1-(x-c)/L+(x-c)^2/2L+\cdots] \quad (4)$$

where $L \equiv 2D_0 t_0/c$. The slope at $x=c$ is $(-N_A/L)$.

If a reverse bias is now applied to this n-p junction, an electrostatic field (E) will be present in the space charge region extending a short distance in both directions from $x=c$. This field will exert a force tending to move the positively charged Li^+ ions from the Li-rich side of the junction to the Li-deficient side. Such Li-ion motion will occur in a reasonable time, provided the temperature is sufficiently high to give the Li^+ ions appreciable mobility (μ). The number of Li^+ ions per cm^2 moved across the junction in time t will be $E\mu N_A t$, the N_A arising from the fact that the field exists only in the region where $N_D \simeq N_A$. This relation depends on the assumption that the field is large enough so that $E\mu N_D \gg D\nabla N_D$, i.e., so that the drift exceeds any diffusion which can occur. In this case the Li^+ concentration at $x<c$ will decrease and the Li^+ concentration at $x>c$ will increase. The Li^+ concentration cannot, however, fall below N_A at $x<c$ because the excess acceptors in such a region would change the space charge so as to increase the field on the excess Li^+ side and decrease it on the opposite side, thus increasing the Li^+ flow into the deficit region until it disappeared. For similar reasons, the Li^+ concentration cannot rise above N_A at $x>c$. The value of N_D will, therefore, tend toward N_A at $x<c$ and rise toward N_A at $x>c$, thereby producing an intrinsic region and extending the region in which the driving field, E, is present. This is illustrated in Fig. 2, which shows the impurity concentrations after such a drift period. In this figure, the gradient of N_D at the steep region near $x=a$ will be given roughly by $D\nabla N_D = E\mu N_D$ since it is this concentration gradient in the zero-field region that supplies ions by diffusion to the drift region. Because of the large E the concentration gradient of N_D in this diffusion region will hence generally be steep relative to the initial gradient. The steep region near $x=b$ can be even steeper than the one near $x=a$ because of ion pairing.[1] We shall approximate both steep regions by vertical lines. The amount of Li drifted in time t is then represented by the shaded area, or

$$\int_0^t E\mu N_A dt = \left(\int_a^c N_D dx\right) - (c-a)N_A = (b-c)N_A - \int_c^b N_D dx. \quad (5)$$

Using Eq. (1) for N_D and integrating by parts there is obtained

$$\int E\mu N_A dt = cN_0 \operatorname{erfc}[c/2(D_0 t_0)^{\frac{1}{2}}] - aN_0 \operatorname{erfc}[a/2(D_0 t_0)^{\frac{1}{2}}] + [2N_0(D_0 t_0)^{\frac{1}{2}}]/\sqrt{\pi}[\exp(-a^2/4D_0 t_0) - \exp(-c^2/4D_0 t_0)] - (c-a)N_A \quad (6)$$

with a similar expression involving b and c. To find the behavior near $t=0$, for $W \ll L$, the erfc and the exponential can be expanded about c, giving

$$\int E\mu dt \simeq (c-a)^2/2L + (c-a)^3/6L^2 \simeq (b-c)^2/2L - (b-c)^3/6L^2 \quad (7)$$

[8] Carslaw and Jaeger, *Conduction of Heat in Solids*, (Oxford University Press, London, 1959), second edition, p. 60. There may be some error caused by built-in fields if the concentration near the surface is high enough to make a part of this region extrinsic during the diffusion;[17] this effect will be neglected here.

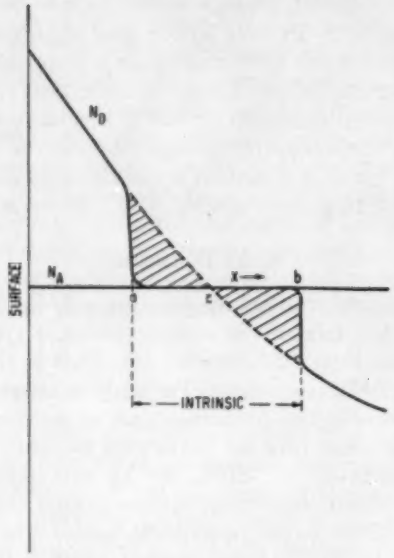

FIG. 2. Impurity distribution after ion drift.

from which, with further manipulation, there is obtained for $W=(b-a)\ll L$:

$$\int E\mu dt \simeq (W^2/8L), \tag{8}$$

with an error less than $W^2/27L^2$, as obtained by calculating the next term. Thus, for drift in a constant field, the square of the junction width will be proportional to the drift time; or for a constant applied voltage (approximately equal to the field times the junction width), the cube of the junction width will be proportional to the drift time.

For t very long or for $W\gg L$, on the other hand, it is not convenient to expand the erfc and exponential in Eq. (6) about c because too many terms would be required for a good approximation. It is in this case more appropriate to use the asymptotic series for the erfc of large agument, giving

$$\int E\mu dt \simeq L\{(c^2/a^2)\exp[(c^2-a^2)/4D_0t_0]-1\}+a-c$$
$$\simeq b-c-L\{1-(c^2/b^2)\exp[(c^2-b^2)/4D_0t_0]\}. \tag{9}$$

This yields, for $(b-c)\gg(c-a)\gg L$, and hence for $W\simeq(b-c)$,

$$\int E\mu dt \simeq W. \tag{10}$$

The junction width will now be proportional to the drift time for constant field, or the square of the junction width will be proportional to the drift time for constant voltage. For t very long, the source becomes very "stiff" because the intrinsic region has moved back to a steep region of N_D at $x<c$, and growth occurs primarily at $x>c$, where each increment in x must be filled with donors to the constant concentration N_A.

These preliminary remarks have been intended to describe the physics of the drift process in easily understood terms, and mathematical complications arising from the initial space charge width have been neglected. In order to confirm the model experimentally, it is necessary to include these complexities, and also to include accurately the effect of varying E for constant applied voltage. This has been done in the Appendix, to which reference will be made in discussing the experimental results.

EXPERIMENTAL TECHNIQUES

1. Normal Technique

The ion drift process is straightforward and involves the measurement of but few parameters. In the simplest case, namely the measurement of ion mobility after appreciable initial drift, one needs to measure only the junction area and the variation of capacitance with time with constant applied voltage. Normal precautions are necessary in making contact to the sample to ensure that the junction capacitance, and not some capacitance associated with the contact, is measured. This generally requires the use of some form of alloyed or diffused contact to the p-type region. We have successfully used alloyed Al, alloyed Au, and diffused B. Since the Li-diffused n-type region has very low resistivity at the surface, a simple pressure contact to this region generally suffices. In Si of less than 10 ohm-cm resistivity, measurements can be made in room air with little danger that inversion layers will affect the capacitance measurement. It is advantageous to use a high-sensitivity bridge with provision for measuring direct capacitance exclusive of stray capacitance via ground; it is also advantageous for the measuring instrument to afford dc continuity so that bias voltage can easily be supplied in series with bridge and sample. Because of the loss associated with the reverse leakage current, the use of a high-frequency bridge (e.g., 100 kc) is recommended; and because of the voltage dependence of the junction capacitance, the ac measuring voltage of the bridge should be small.[9]

2. Inversion Layers

In higher resistivity Si, inversion layers become troublesome because they add to the junction capacitance and often vary in an unpredictable fashion. Their presence has been confirmed and their behavior studied in high resistivity samples by observing the change in contact potential with weak illumination, using a chopped-light technique. Since the Li^+ gradient is quite steep and hence inhibits inversion a very short distance from the junction on the Li^+ side, this trouble generally

[9] In the present experiments, a Boonton 74-C capacitance bridge was used.

is most serious on the p-type side. In 100 ohm-cm Si, inversion can be controlled satisfactorily by the use of a dip in dilute (about 0.1%) sodium dichromate solution after etching the junction, with subsequent measurements made in dry oxygen.[10] In 1000 ohm-cm Si, such treatment has not sufficed, and to prevent surface inversion effects it has been necessary to make the surface strongly p-type by a two hour diffusion of B at 1150°C (after a one-minute treatment in BCl_3 at 1150°C)[11] followed by a subsequent removal of the amorphous boron by an etching process.[12] Subsequent to this surface treatment, one face is ground off and the Li alloying and diffusion performed on this face in the manner to be described. The thin shell (of the order of 1 μ thick) of high-conductivity B-doped Si cannot in any case contribute appreciably to the capacitance, but its effect is additionally minimized in that it, too, becomes intrinsic in the drift process. This boron-diffused layer has a further usefulness in affording a low resistance contact to the sample. This contact is made by electroplating the p-type skin with gold prior to the Li diffusion. Electroless Ni plating has also been used, but it leads to heat-treatment effects from diffusion of Ni into the Si during the Li diffusion, these effects showing up as resistivity changes and hence junction capacity changes during the first few hours at room temperature after the Li diffusion.

3. Heat Treatment Effects

In 1000 ohm-cm Si, even though produced by the floating zone process, impurities can be introduced during the predrift treatments which lead to changes in sample resistivity. Although such heat treatment effects have been noticed, they are not serious in practice, being present only in very high resistivity Si and only for the first few hours at room temperature. They do not affect the results at long t, and for higher temperature ion drift their effects can be eliminated by allowing the sample to stand for a few hours at room temperature, without applied drift voltage, previous to the drift. The high-temperature boron diffusion does not seem to be responsible for such heat treatment. The Li diffusion step seems rather to be the cause in that it permits the simultaneous diffusion of an impurity (probably copper) into the sample, which causes resistivity changes having time constants of the order of hours at room temperature—similar in some respects to the effect of Ni, but generally going in the opposite direction. We believe the troublesome impurity to be copper because it has an appropriate diffusion rate, and its deliberate introduction produced a similar, but enhanced, effect. When it is necessary to observe the initial drift, it has been found that this effect can be greatly minimized, though never entirely removed in 1000 ohm-cm Si, by very lightly gold plating the entire sample, producing little more than a haze, subsequent to grinding the sample face for Li diffusion. The sample is then heated overnight at 320°C, enabling the Au to act as a chemical getter in removing the Cu. In the Li diffusion, the Li is added on top of this gold film so that the Au will be present during the Li diffusion.

4. Li Diffusion

Li is normally added by painting a Li-in-oil suspension[13] on one face of the sample, which is typically of dimensions 1 cm×0.3 cm×0.3 cm. This is then dried at about 200°C in helium. For drift measurements at long t, where initial phenomena are of no concern, the Li diffusion can then be performed by simply raising the temperature to 450°C for 1½ minutes, without worrying about what may happen during the ensuing quench. Where initial phenomena are of concern, it is necessary to ensure a fast quench so that these phenomena will not occur during the quench itself. It is also desirable to know the diffusion time and temperature accurately to give an additional means, other than initial capacitance, for calculating the initial Li^+ distribution. We have used a graphite double-strip heater, forming an approximate blackbody enclosure, with the sample resting flat upon the lower strip and within a few millimeters of the upper strip. To ensure accurate measurement of the diffusion time, an initially-peaked current wave form has been used to heat the graphite

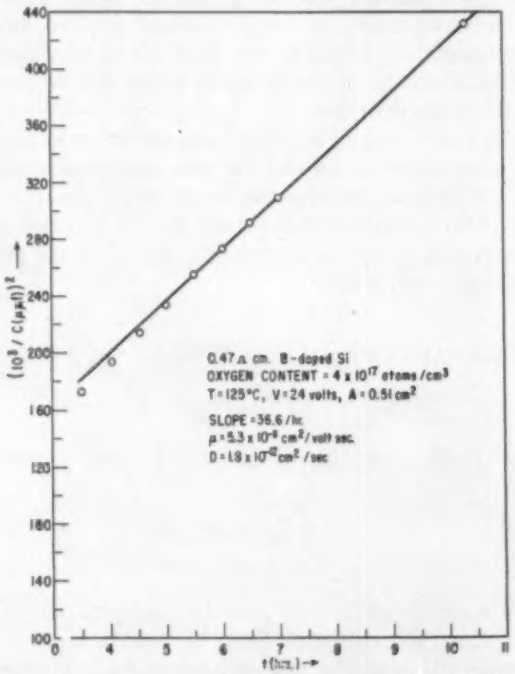

FIG. 3. $(1/C)^2$ vs time at long t.

[10] H. Nelson and A. R. Moore, RCA Rev. **17**, 5 (1956).
[11] *Transistor Technology III* (D. Van Nostrand Company, Inc., Princeton, New Jersey, 1958).
[12] M. Waldner (private communication).
[13] 30% Li, 70% mineral oil, 1.7% oleic acid; available from the Lithium Corporation of America.

strips to 450°C in about one second. Temperature has been monitored by a calibrated lead sulfide cell and chopper and manually maintained at 450°C during the diffusion period. A fast quench has been obtained by blowing the sample with a high-velocity nitrogen jet into a room-temperature ethylene-glycol bath about 6 in. distant, taking care to ensure a straight line, nonturbulent path. After the quench, the sample is etched quickly in dilute white etch and mounted in the measuring jig, generally under a flowing dry oxygen ambient. If the reverse current is too high, the unit is re-etched until the loss component falls within the tolerance of the bridge.

VERIFICATION OF THE ION DRIFT MODEL

Since the model as developed in the first section and in the Appendix relies on various approximations to predict the behavior over a range of physical parameters, one would like to verify each of these approximations experimentally. In this section, those conclusions of the model which can be subjected to experimental test will be enumerated and compared with experiment.

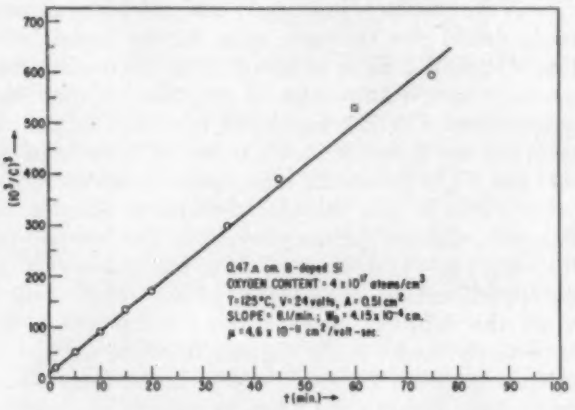
0.47 Ω cm. B-doped Si
OXYGEN CONTENT = 4 x 10^17 atoms/cm^3
T = 125°C, V = 24 volts, A = 0.51 cm^2
SLOPE = 6.1/min.; W0 = 4.15 x 10^-4 cm.
μ = 4.6 x 10^-11 cm^2/volt-sec.
(10^3/C)^2 →
t (min.) →

FIG. 4. $(1/C)^2$ *vs* time at short t.

1. For constant applied voltage, the square of the junction width should vary linearly with time at long t. Such behavior has been observed for every sample tested. An example is exhibited in Fig. 3. The square of the reciprocal capacitance, and hence the square of the width, is seen to approach a straight line asymptotically at long t.

2. For constant applied voltage, the cube of the junction width should vary linearly with time at short t, when $W_0 \ll L$. Such behavior is illustrated in Fig. 4, for the same sample of Fig. 3 discussed in the preceding paragraph. Another example is illustrated in Fig. 9.

3. The slope at $t=0$ should be uniquely related to the slope at long t, in accordance with Eq. (A37) of the Appendix. This can be verified by comparing the mobility calculated from Fig. 3, using Eq. (A8) of the Appendix, with the mobility calculated from Fig. 4,

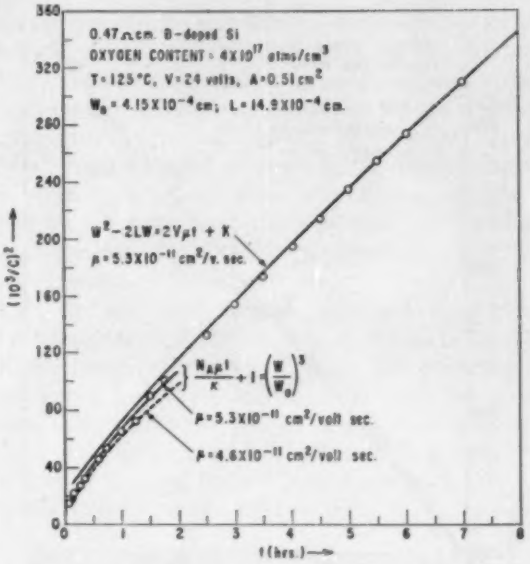
0.47 Ω cm. B-doped Si
OXYGEN CONTENT = 4 X 10^17 atms/cm^3
T = 125 °C, V = 24 volts, A = 0.51 cm^2
W0 = 4.15 X 10^-4 cm; L = 14.9 X 10^-4 cm.
W^2 − 2LW = 2Vμt + X
μ = 5.3 X 10^-11 cm^2/v. sec.
(10^3/C)^2 →
μ = 5.3 X 10^-11 cm^2/volt sec.
μ = 4.6 X 10^-11 cm^2/volt sec.
t (hrs.) →

FIG. 5. $(1/C)^2$ *vs* time, calculated and experimental.

using Eq. (A21) of the Appendix. The two mobilities are 5.3×10^{-11} cm^2/volt sec and 4.6×10^{-11} cm^2/volt sec, respectively. This constitutes good agreement. The discrepancy could arise either from an error in the determination of the area, or from an error in the value of N_A as determined from the resistivity. The latter seems more likely in view of the spread in the values of N *vs* ρ reported in the literature. We used a value of 4.3×10^{16}/cm^3 for N_A in this 0.47 ohm-cm Si, using the data of Prince.[14] A value of 3.73×10^{16}/cm^3 for N_A would have resulted in perfect agreement in the μ obtained from Fig. 3 with that obtained from Fig. 4. Other values of N_A obtained from the literature[15] range from 3.5×10^{16}/cm^3 [16] to 8×10^{16}/cm^3 [15] for this resistivity.

The results can be displayed in a different form by using the calculated μ to plot two theoretical curves for short t and long t, using Eqs. (A10) and (A22) of the Appendix, and comparing these with the experimental data. This has been done in Fig. 5. Again the agreement is excellent.

4. Also in accordance with Eq. (A37) of the Appendix, the initial slope should become more nearly equal to the final slope, on a plot of W^2 *vs* time, as the resistivity of the starting material increases. This is illustrated by Fig. 6, which shows that in high resistivity silicon (1800 ohm-cm) the initial slope becomes indistinguishable from the final slope. It is possible, of course, that a different initial slope exists for too short a time to be seen, i.e., that the time constant for the

[14] M. B. Prince, Phys. Rev. **93**, 1204 (1954).
[15] G. Backenstoss, Phys. Rev. **108**, 1416 (1957), and references cited therein.
[16] F. J. Morin and J. P. Maita, Phys. Rev. **96**, 28 (1954), with N_A calculated from the conductivity mobility given by their Figs. 11 and 14.

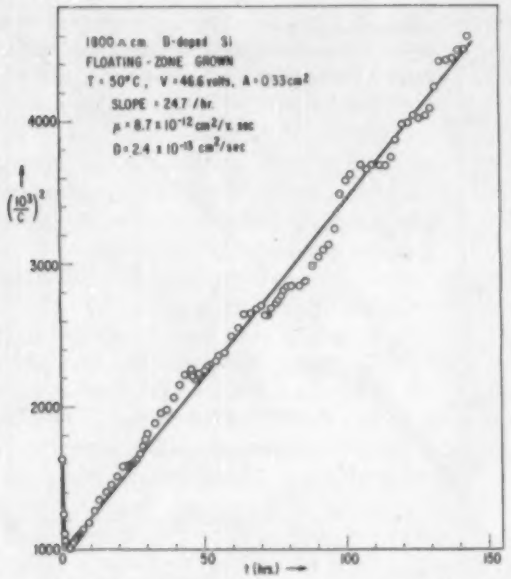

FIG. 6. $(1/C)^2$ *vs* time in 1800 ohm-cm Si.

disappearance of an initial region of different slope decreases as the resistivity increases. The present treatment does not answer such a question. The conservative interpretation of Fig. 6 is that it does not disagree with Eq. (A37) of the Appendix. The initial drop in Fig. 6 is felt to be caused by a heat treatment effect, as discussed in the section on experimental techniques. The fluctuations in the data are typical of high resistivity samples, and their cause has not been determined. The fact that the measured capacitances are here very small, as low as 15 $\mu\mu$f, will introduce some statistical fluctuation. In addition, the presence of fluctuations in resistivity could lead to such data fluctuations.

5. If ion drift produces the impurity distribution indicated in Fig. 2, then the space charge will be largely localized near *a* and *b*, and the capacitance should hence become essentially independent of voltage after ion drift. A typical *C-V* characteristic after ion drift is reproduced in Fig. 7. The significant feature is that the capacitance becomes independent of voltage only above the voltage which was applied during the ion drift and exhibits a roughly $V^{-\frac{1}{2}}$ dependence below this voltage. This has been checked for other drift voltages. The $V^{-\frac{1}{2}}$ region indicates that there is some uncompensated charge present in the region which we have called intrinsic. It is therefore important to know whether the quantity of uncompensated charge is significant—in particular, whether the field can be treated as constant throughout the drifted region, as we have done, or whether this region should be treated as a gradient junction with the field dropping to zero at the edges. The precision of the *CV* characteristic is insufficient to answer this question. But an argument can be made which indicates that the constant field approximation is the best one to use, as follows: The ion current at the position of E_{max} is given by $E_{max}\mu N_A$. If the field drops to a small value at the edge of the junction, i.e., if the junction is gradient-type, this quantity is equal to $(dN/dx)W^2\mu N_A/8\kappa$, where E_{max} has been determined by solving Poisson's equation for a gradient-type junction. W is the junction width and κ the dielectric constant. If the field drops to a small value at the edge of the junction, this same current would at that point need to be carried by diffusion. But the diffusion current is just $D(dN/dx)$, where dN/dx at the junction edge is comparable to dN/dx at the position of E_{max} in a gradient junction. The ratio of this value for the diffusion current to the preceding value for the field current is thus $8\kappa kT/W^2qN_A=(1.2\times10^6)/W^2N_A$, where k is Boltzmann's constant and q is the electronic charge. In our samples of smallest $W(\sim10^{-3}$ cm) and smallest $N_A(\sim10^{13}$ cm$^{-3})$ this ratio is only about 10%, indicating that diffusion is incapable of supporting the ion current near the junction edge and that the electric field must hence be appreciable near the junction edge—in fact, nearly as large as at the position of E_{max}.

6. If the quench is sufficiently fast, the initial capacitance should give the same value for the initial junction width, W_0, as is obtained from calculating this quantity from a knowledge of the diffusion time and temperature. The junction width is related to the capacitance by $W_0=1.06\ A/C_0$, where A is the area in cm^2 and C_0 is the initial capacitance in micro-microfarads. W_0 is also related, through a solution of Poisson's equation, to the gradient at the junction by $W_0=(12\kappa VL/qN_A)^{\frac{1}{3}}$ where $L=N_A/(dN/dx)$ and V is the applied voltage. L is given by $2D_0t_0/c$, where D_0 and t_0 are the diffusion constant and the diffusion time, respectively, and c is the distance from the surface to the junction [see Eq. (4)], which can be found from the complementary error function solution to the diffusion equation [see Eq. (1)]. In a typical junction so tested (the same junction described by Figs. 3–5), W_0 determined from the initial capacitance, making a slight correction for ion drift occurring at room temperature prior to the measurement, was 4.94×10^{-4} cm. Calculated from D_0 and t_0, the corresponding value was 4.15×10^{-4} cm. The former value is subject to two errors: (a) if the quench is faulty, some drift may occur

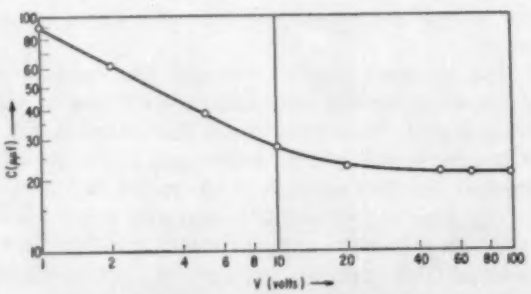

FIG. 7. Capacitance-voltage characteristic after ion drift at 24 volts.

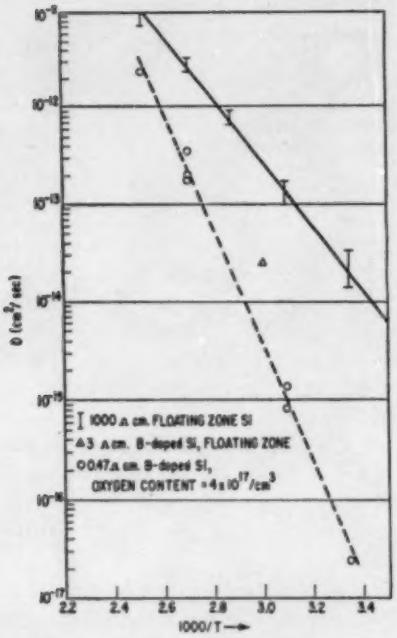

FIG. 8. Diffusion rate of Li in Si; preliminary results.

in the built-in field during the quench, causing the measured $1/C$, and hence W_0, to be too large; and (b) if the alloying is at all spotty, the value used for the area will be too large, leading also to a W_0 which is too large. The latter value for W_0 is hence felt to be the more accurate; though it, too, is subject to a small error because of the effect of the built-in field in the extrinsic region during the diffusion, arising from the disparity in diffusion rates of electrons and ions.[17] Note that W_0 cannot generally be found by extrapolating drift data to zero time, especially in high temperature runs, because the zero of time is not accurately known, some ion drift inevitably occurring while the sample is brought to temperature. With a slower quench, W_0 from the initial capacitance was generally significantly too large, suggesting that some ion drift took place during the quench itself, probably from the built-in field of the junction. For example, one ohm-cm p-type Si becomes intrinsic around 350°C; at this temperature the diffusion constant of Li is of the order of 10^{-8} cm²/sec and μ of the order of 10^{-7} cm²/volt sec, leading to drift rates of the order of 10^{-4} cm/sec for a junction 10^{-4} cm wide with 0.1 volt for the "built-in" junction voltage.

7. If there are no systematic errors present in the analysis of the model, and if precautions are taken to use Si of sufficient purity and resistivity that the Li remains unassociated with impurities or acceptors, then the ion drift rate should yield reasonable values for the diffusion rate of Li in Si. A series of measurements using 1000 ohm-cm vacuum-grown floating-zone Si gave a diffusion constant of $6\times10^{-4}\exp(-0.61q/kT)$ cm²/sec, using the data from these measurements alone (see Fig. 8, which will be described further in a subsequent section). This is to be compared to a value of $23\times10^{-4}\times\exp(-0.66q/kT)$ cm²/sec obtained from high-temperature measurements[18] and $23\times10^{-4}\exp(-0.72q/kT)$ cm²/sec obtained from low-temperature measurements.[19] The present data and those of reference 18 can be joined by a straight line which falls within the experimental error of both the present measurements and those of reference 18.

8. If the ion drift rate does indeed measure the diffusion constant of the Li, then it should be possible, at these temperatures, to decrease the drift rate by using lower resistivity silicon such that ion paring effects are significant,[1] or by using silicon of high oxygen content such that Li-O complex formation is significant.[3] Both of these effects have been observed, and will be noted in the next section.

MEASUREMENT OF DIFFUSION RATES WITH ION DRIFT

The ion drift technique is inherently very sensitive for measuring drift and hence diffusion rates both because of the very high near-breakdown field which can be used and because the measuring rod is so short, being the width of an n-p junction. (The measuring rod has a slight further virtue in that it becomes longer as the experiment proceeds, permitting the convenient measurement of a wide range of diffusion rates in a single experiment.) With Li in Si, we commonly measure diffusion rates over four decades in a single experiment by varying the temperature. This is illustrated in Fig. 8 which gives preliminary results from such a measurement in crucible grown Si which contained about 10^{18} oxygen atoms/cc from 9 μ infrared absorption measurements.[20] The diffusion rate at 25°C was derived from the data illustrated in Fig. 9, which is a measure of the

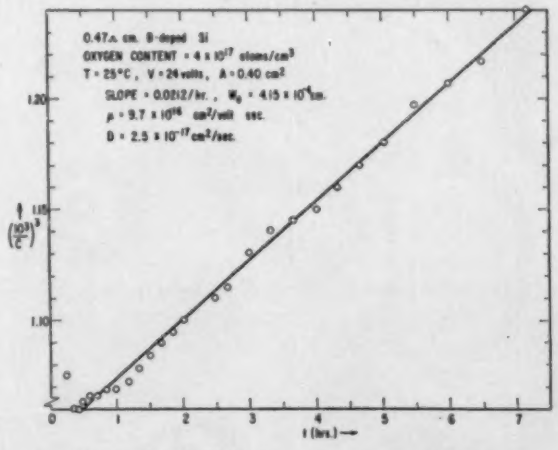

FIG. 9. Initial intrinsic region growth at 25°C.

[17] F. M. Smits, Proc. Inst. Radio Engrs. **46**, 1049 (1958).

[18] C. S. Fuller and J. C. Severiens, Phys. Rev. **96**, 21 (1954).

[19] J. P. Maita, J. Phys. Chem. Solids **4**, 68 (1958).

[20] W. Kaiser and P. H. Keck, J. Appl. Phys. **28**, 882 (1957).

initial junction growth when the measuring rod was shortest and the measurement most sensitive. From the appearance of these data it is estimated that a diffusion constant as small as 10^{-13} cm²/sec could be measured with good accuracy. Figure 8 also includes data from floating-zone Si of 1000 ohm-cm resistivity, which are indicative of the diffusion rate of free Li^+ in Si.

The results described in the preceding paragraphs are intended only to be illustrative of the use of ion drift in diffusion measurements. They are neither final nor complete, and estimation of errors and reconciliation with other experiments have not been completed. Final results and conclusions will be the subject of future reports. The general features—in particular, the effect of the oxygen in decreasing the diffusion rate, are real and are in general agreement with previous findings.[8] Similar effects, as suggested by the single point for 3 ohm-cm Si, should be observed in floating-zone Si of higher acceptor concentration, such that ion-pair relaxation times are within the period of the experiment, and will be used to measure ion pairing phenomena.[1] By appropriate choice of resistivity and temperature it should also be possible to measure the relaxation times for such pairing and complexing phenomena; present data show such effects but they have not yet been made quantitative.

The large effect of oxygen upon the diffusion rate, especially at low temperatures, combined with the sensitivity of the ion drift technique, should make it useful for measuring oxygen content at low concentrations. Since the model for Li-O interaction is simple and is felt to be well understood,[8] confidence in the results should be correspondingly high. We estimate that an oxygen concentration as small as 10^{15} atmos/cc should be accurately measurable by drifting at a temperature of 0°C.

Because the ion drift rate is measured at low concentrations of the diffusant (about 10^{13}/cc in 1000 ohm-cm Si) it can reveal chemical interactions between the diffusant and constituents which may themselves be present only in very low concentration, for example because of limited solubility.

INTRINSIC REGION FORMATION FOR DEVICES

In a diode structure, the incorporation of an intrinsic region by ion drift leads to a lower capacitance and a lower electric field for a given applied voltage. For example, a diode having a breakdown voltage in excess of 4 kv has been produced using Si with a resistivity of 20 ohm-cm. There would seem to be no inherent limit to the PIV that can be achieved, though the forward characteristic would of course suffer if the junction width exceeded the diffusion length. Also, at high PIV, surface breakdown becomes a problem (the 4 kv unit was immersed in silicone oil to prevent air breakdown). In a similar manner, the decreased capacitance resulting from ion drift might be advantageously used in improving high frequency response, for example, by the use of ion drift in achieving PNIP or NPIN transistor structures.

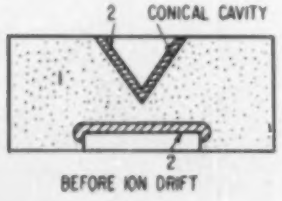

FIG. 10. Formation of analog transistor; configuration after initial diffusion. Region 1: p-type Si; reg. 2: n-type Si from Li diffusion.

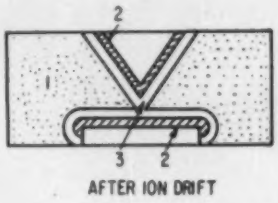

FIG. 11. Formation of analogtransistor; configuration after ion drift. Region 1: p-type Si; reg. 2: n-type Si; reg. 3: intrinsic Si from ion drift.

A more fascinating function of ion drift is its use to produce complex microgeometries. For example, its use permits the fabrication of true analog transistor structures, in which a space-charge limited current flows through an intrinsic semiconducting medium under the control of a grid, exactly as in a vacuum tube. Thyratron analogs are also possible by combining electron and hole currents in the same structure. One method for achieving an analog transistor structure is illustrated in Fig. 10 and Fig. 11. The former illustrates the geometry subsequent to the diffusion of the mobile impurity; the latter illustrates the geometry after sufficient ion drift to produce an aperture in the intervening low-resistivity semiconductor. By applying appropriate biases, as in Fig. 12, one of the initially diffused regions becomes the source (analogous to the cathode), the other initially diffused region becomes the drain (analogous to the anode), and the intervening low-resistivity region with its aperture becomes the grid. Several such devices have been constructed; one exhibited an input resistance of 6 megohms, a power gain of 17 db and a voltage gain of 4. In addition to the advantage of high input impedance, such a device has the further advantage that its properties are essentially independent of temperature, below the temperature at which diffusion destroys the geometry. For good frequency response, a different geometry with a smaller input capacitance would be required. In principle, the presence of the field in the drift region would improve the frequency response through its decrease of the transit time, but the high input capacitance prevents this advantage from being realized here.

One would expect to observe space-charge limited emission in such analog transistor structures.[21,22] In a p-i-p structure, made by Li-ion drift and with a grid

[21] N. F. Mott and R. W. Gurney, *Electronic Processes in Ionic Crystals*, (Oxford University Press, 1940), p. 172.
[22] A. Rose, Phys. Rev. 97, 1538 (1955).

aperture which happened to be too large to exhibit control, it appeared that space-charge limited emission was observed. The current varied as V^2 and the current had a magnitude of 1 ma with 1 volt applied. This is consistent with space-charge limited emission for an area of 0.01 cm^2 and a separation of 0.004 cm, these values being reasonable though not independently measured for this unit. In another unit with smaller grid aperture, such that the unit exhibited power gain, the current depended linearly on voltage at lower voltages and increased slightly more slowly with voltage at higher voltages; this observation is not understood but has not been pursued further.

No extensive study of the effect of the Li diffusion and ion drift upon carrier lifetime has been made nor have any special efforts been made to keep the lifetime high. Carrier lifetimes at least as high as 160 μsec, and also as short as 3 μsec, (in drifted units without B skin) have been observed by the diode recovery method.[23] In another unit which was subjected to an initial B diffusion step at 1150°C as described in a previous section, the lifetime was about 3 μsec, with forward and reverse characteristics in reasonable agreement with this lifetime. Since Li is a shallow donor, it would not by itself be expected to decrease the lifetime,[23] but whatever is responsible for the heat treatment to which reference has previously been made could also affect the lifetime, as could high-temperature heat cycles.[23] With Li, it is possible to avoid high-temperature heat cycles, and it may hence prove more feasible to retain high lifetimes with this diffusant. Reasonable lifetime would be of importance in obtaining a good forward characteristic in a high-voltage p-i-n junction; it would be of less importance in an analog transistor because here the field makes transit times small.

The useful life of ion drift devices depends upon many factors. High-temperature storage life without applied potential is limited by the time it takes for diffusion to smear out the intrinsic region. High-temperature life with applied field depends on the time it takes the Li^+ available in the source to all drift through the unit. In an analog structure, the grid aperture must not change appreciably, imposing a more stringent limitation on allowable drift during the useful life, though geometries are possible which minimize this problem by use of a nonuniform initial distribution of what would in the present examples be the immobile acceptor ions. In Li-Si diodes using oxygen to slow the Li diffusion (see previous section), reasonable operating lifetimes with voltage applied at temperatures up to 125°C and reasonable storage lifetimes without applied voltage at temperatures up to 75°C should be attainable. Higher operating temperatures would require the use of a slower diffusant or a different host lattice, subject of course to the limitation that drift must occur at a temperature such than an n-p junction exists. The number of possible choices for such other materials is enlarged by the fact that they need not be of high purity.

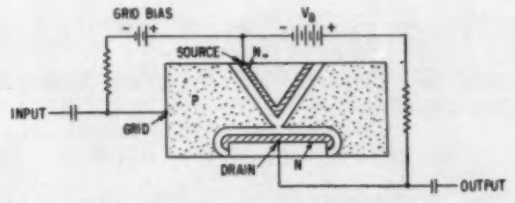

FIG. 12. Circuit for analog transistor.

[23] G. Bemski, Proc. Inst. Radio Engrs. 46, 990 (1958), and references cited therein.

CONCLUDING REMARKS

The primary intent of this paper has been to describe and analyze a new technique for producing an intrinsic region in semiconductors. Data have been presented to illustrate the features of the kinetics and to experimentally confirm the results of the analysis. The significance of the method as a research tool and also its possible usefulness in the device area have been briefly described and illustrated.

ACKNOWLEDGMENTS

The author is deeply appreciative of many ideas originating in discussions with other members of the Semiconductors Studies Section of the General Electric Research Laboratory, particularly R. N. Hall, F. S. Ham, E. O. Kane, and A. G. Tweet. For the experimental results, he is largely indebted to the capable efforts of D. J. Locke.

APPENDIX

This appendix will present an analysis of the increase in junction width with ion drift for constant applied voltage, V, for a mobile donor ion of concentration $N(x)$ diffused into a crystal having a uniform concentration, N_A, of immobile acceptor ions.

Approximation for Long t and $W \gg L$

The starting point will be Eq. (10) of the text:

$$\int E\mu dt \simeq L\{(c^2/a^2)\exp[(c^2-a^2)/4D_0t_0]-1\}+a-c$$
$$\simeq b-c-L\{1-(c^2/b^2)\exp[(c^2-b^2)/4D_0t_0]\}. \quad \text{(A1)}$$

Although E can in general be obtained from V only through a detailed knowledge of intrinsic region width and space charge region distribution, some simplification results at long t because the space charge width becomes negligible relative to the intrinsic width. This occurs both because the intrinsic region becomes constantly wider and because the space charge region becomes constantly narrower, the latter resulting from the fact that the required space charge is equal to

voltage times capacitance and hence decreases as the capacitance decreases. The early stages of growth can be avoided by dealing with the differential form of Eq. (A1), which gives μ in terms of the growth rate at long t. For somewhat shorter t, the differential form can be integrated and the integration constant evaluated from the data at long t. The resulting relation between junction width and time can be compared with experiment to check the range of validity of the simplifying assumptions.

From the first and third equalities of Eq. (A1), for $(b^2-c^2)\gg 4D_0t_0$ (which is essentially for $W\gg L$),

$$\int E\mu dt\simeq b-c-L. \tag{A2}$$

Approximating E by V/W,

$$\int (V/W)\mu dt\simeq b-c-L. \tag{A3}$$

The term equal to c can be eliminated by using the second and third equalities of Eq. (A1), subject to the previous approximations:

$$W/L\simeq (c^2/a^2)\exp[(c^2-a^2)/4D_0t_0]. \tag{A4}$$

Since $L=2D_0t_0/c$ [from Eq. (4)], this yields

$$(c-a)=L\ln(W/L) \tag{A5}$$

so that, from Eq. (A3), and also noting that $W=b-a$,

$$\int (V/W)\mu dt=W-L-L\ln(W/L). \tag{A6}$$

Differentiating, there is obtained

$$dW/dt=V\mu/W(1-L/W) \tag{A7}$$

giving

$$d(W^2)/dt=2V\mu/(1-L/W), \tag{A8}$$

or

$$d(W^2)/dt\simeq 2V\mu \quad \text{for} \quad W\gg L. \tag{A9}$$

L is related to the space charge width, W_0, of the initial gradient-type junction by $L=(W_0^2N_A/12\kappa V)$, obtained in the usual fashion by integrating the field across the initial junction.

Equation (A7) can be integrated, giving

$$W^2-2LW=2V\mu t+K \tag{A10}$$

where K, the integration constant, must be determined experimentally because the integral is wrong at short t, when $E\neq(V/W)$.

In Eqs. (A7) and (A8), the L in the denominator results from the fact that the intrinsic region grows at a finite rate toward the side of high Li^+ concentration, as well as in the direction of low Li^+ concentration where most of the growth takes place.

The above expressions will be correct only when diffusion can be neglected relative to drift in the field. In cases of strong ion pairing or small fields this condition might not be fulfilled, and dW/dt could be appreciably reduced or even zero. This would arise because the boundary of the intrinsic region on the high Li^+ side would move continuously toward the other boundary because of Li^+ diffusion.

Approximation for Short t and $W\ll L$

From Eq. (8) of the text,

$$\int E\mu dt\simeq W^2/8L. \tag{A11}$$

But $L=N_A/(dN_D/dx)|_{x=c}$ [see Eq. (4)], and the gradient at $x=c$ can be written in terms of the space charge width prior to ion drift, W_0, by integration of Poisson's equation, as $(dN_D/dx)|_{x=c}=12\kappa V/W_0^3$, where κ is the dielectric constant and V is the voltage across the junction, giving

$$\int E\mu dt\simeq 3W^2\kappa V/2N_AW_0^3. \tag{A12}$$

From now on we wish to distinguish between the intrinsic region width, W_I, the space-charge region width, W_{sc}, and the total junction width, $W=W_I+W_{sc}$, so that Eq. (A12) becomes

$$E_I\mu dt\simeq 3W_I^2\kappa V/2N_AW_0^3. \tag{A13}$$

We must next evaluate E_I/V as $f(W_I,W_{sc})$ and then rewrite $f(W_I,W_{sc})$ as $F(W,W_0)$. To evaluate E_I/V we approximate the space charge by a linear gradient with half of the space charge width and intrinsic region width on either side, as in Fig. 13. There is obtained

$$E(l)=\int \rho dl/\kappa=(l\nabla N/2\kappa)(W_I+W_{sc}-l), \tag{A14}$$

and

$$E_{max}=(W_{sc}\nabla N/4\kappa)(W_I+W_{sc}/2). \tag{A15}$$

This E_{max} is the E which exists throughout the intrinsic region and is hence the E_I to be used in our expression for E_I/V. V is found through a further integration of Edl:

$$V=(W_{sc}\nabla N/4)(W_{sc}W_I+W_I^2+W_{sc}^2/3). \tag{A16}$$

Dividing Eq. (A16) by Eq. (A15) and noting that $W_{sc}=W-W_I$,

$$3V/2E_I=W+W_I-WW_I/(W+W_I); \tag{A17}$$

W_I can be eliminated by noting that at $t=0$, $V=\nabla NW_0^3/12\kappa$ (from the usual expression for a gradient-type junction, as obtained from integrating Poisson's equation). Using this value for V in Eq. (A16)

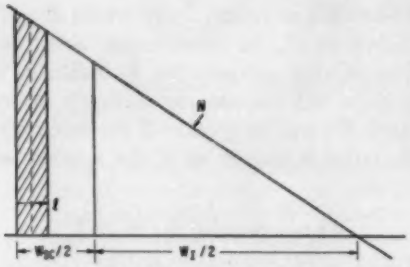

FIG. 13. Approximate impurity distribution at short t.

and eliminating W_{sc} as before there is obtained

$$W_I=(W^3-W_0^3)^{\frac{1}{3}}. \tag{A18}$$

Using Eqs. (A17) and (A18) with Eq. (A13), there is obtained for $x\equiv W/W_0$,

$$dx/dt=(N_A\mu/\kappa)(x^3-1)^{\frac{1}{3}}/\{2x^2[x+(x^3-1)^{\frac{1}{3}} -(x^3-1)^{\frac{1}{3}}x/[x+(x^3-1)^{\frac{1}{3}}]]\} \tag{A19}$$

which, for large x, becomes

$$dx/dt\simeq N_A\mu/3x^2\kappa, \tag{A20}$$

or

$$d(x^3)/dt\simeq N_A\mu/\kappa. \tag{A21}$$

According to Eq. (A19), as x approaches unity, dx/dt approaches zero. But the above approximations are not valid in this region, for they neglect the initial transport of ions by the field throughout the space charge region. It will be shown subsequently that the exact solution for $d(x^3)/dt$ at $t=0$ is just the same as that given by Eq. (A21). Since our experiments do not suggest any S-shaped character to the true behavior, it seems reasonable that Eq. (A21) is obeyed throughout the initial range, in which case it can be integrated to give

$$x^3=N_A\mu t/\kappa+1, \tag{A22}$$

the one being necessary to make x equal to one at the origin.

A plot of W^2 *versus* time will hence have an initial region where the curvature is negative; in this region the junction width is less than a few L, where L is defined in connection with Eq. (4). At this stage the junction is increasing in width toward both the Li-rich and Li-deficient sides, with an ever-increasing amount of Li^+ transport being required for a given incremental increase in junction width. Finally, when the junction width greatly exceeds L, the curvature becomes zero, in accordance with Eqs. (A8) and (A9). In this region growth is primarily toward the Li-deficient side, with each increment of junction width requiring essentially the same amount of Li^+ transport.

Exact Solution at $t=0$, for $W\ll L$

We shall consider the simplified case where the initial Li^+ concentration near the junction can be approximated by a linear gradient. Near $t=0$, the Li^+ concentration as a function of time will be approximated by the first two terms of a power series. The field and voltage will then be determined as a function of time near $t=0$, and from them it will be possible to find dW/dt at $t=0$.

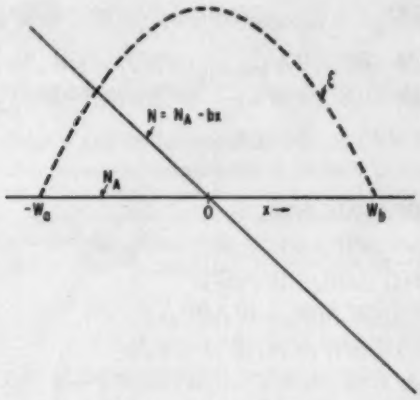

FIG. 14. Initial field and impurity concentrations.

In accordance with Fig. 14,

$$N(x,t)|_{t=0}=N_A-bx. \tag{A23}$$

Near $t=0$, the first two terms of a power series for N gives

$$N(x,t)=N(x,0)+t(dN/dt)(x,0). \tag{A24}$$

But at any x,

$$\frac{dN}{dt}=-E\mu\frac{dN}{dx}+D\frac{d^2N}{dx^2}-N\mu\frac{dE}{dx}. \tag{A25}$$

Noting also that in this particular case $d^2N/dx^2=0$, Eq. (A24) becomes

$$N(x,t)=N_A-bx+t\mu[bE-(dE/dx)(N_A-bx)]. \tag{A26}$$

For E, we can use the initial field, which for this gradient-type junction is $(1/\kappa)(bW_0^2/8-bx^2/2)$, where b here is the gradient, giving

$$N(x,t)=N_A-bx+(t\mu/\kappa) \times[b^2W_0^2/8+bxN_A-3bx/2]. \tag{A27}$$

Knowing $N(x,t)$, it is possible to find E and V. To find E, one integrates the charge density:

$$E=\int\rho dx=\int(N-N_A)dx. \tag{A28}$$

Making use of the boundary condition that $E=0$ at $x=W_b$, this gives

$$\kappa E=-bx^2/2+bW_b^2/2+(t\mu/\kappa)[(b^2W_0^2/8)(x-W_b) +N_Ab(x^2/2-W_b^2/2)-b^2(x^3/2-W_b^3/2)] \tag{A29}$$

with an identical expression, changed only by the substitution of $(-W_a)$ for W_b, corresponding to the boundary condition $E=0$ at $x=(-W_a)$.

To find V, E is integrated from $(-W_a)$ to W_b, giving

$$V=bW_a^3/3+bW_b^3/3+(t\mu/\kappa)[(b^2W_0^2/16)(W_a^2-W_b^2) -(N_Ab/3)(W_a^3+W_b^3)-(3b^2/8)(W_a^4-W_b^4)]. \quad (A30)$$

To find dW/dt, the differential of Eq. (A30) is next taken, noting that V is constant:

$$0=bW_a^2dW_a+bW_b^2dW_b +(t\mu/\kappa)[(b^2W_0^2/8)(W_adW_a-W_bdW_b) -N_Ab(W_a^2dW_a+W_b^2dW_b) -(3b^2/2)(W_a^2dW_a-W_b^2dW_b)] +(\mu dt/\kappa)[(b^2W_0^2/16)(W_a^2-W_b^2) -(N_Ab/3)(W_a^3+W_b^3)-(3b^2/8)(W_a^4-W_b^4)]. \quad (A31)$$

Initially, $W_a=W_b=W_0/2$, $dW_a=dW_b=dW/2$, and $t=0$, giving

$$0=bW_0^2dW/4-\mu N_AbW_0^3dt/12\kappa. \quad (A32)$$

This leads to

$$(dW/dt)|_{t=0}=N_A\mu W_0/3\kappa, \quad (A33)$$

and since $d(W^2)/dt=3W^2dW$, and for $x\equiv W/W_0$,

$$[d(x^3)/dt]|_{t=0}=N_A\mu/\kappa, \quad (A34)$$

which is the same as Eq. (A21), as noted earlier.

It is also possible to find the ratio of the initial slope, $d(W^2)/dt|_{t=0}$, to the final slope given by Eq. (A9):

$$(d(W^2)/dt)|_{t=0}=2WdW/dt|_{t=0}=2N_A\mu W_0^2/3\kappa; \quad (A35)$$

$$(d(W^2)/dt)|_{t=\infty}=2V\mu=2\mu bW_0^3/12\kappa. \quad (A36)$$

Noting that $b=N_A/L$, this gives

$$\text{initial slope/final slope}=4L/W_0. \quad (A37)$$

This will be valid, of course, only where W_0 is initially small relative to L, in accordance with the initial assumptions of this section, but it indicates that the change in slope will become decreasingly noticeable as W_0 increases. W_0 will be greater if the resistivity of the starting material is greater or if the applied voltage is greater.

Approximation for $W_0 \gg L$

In high-resistivity material, it is possible for W_0 to exceed L for voltages normally applied. In this case, the appropriate starting point becomes Eq. (10) of the text, which for $W_0 \gg L$ becomes

$$\int E\mu dt \simeq W \quad (A38)$$

giving

$$d(W^2)/dt \simeq 2V\mu \text{ at long } t. \quad (A39)$$

As before, for short t when W_0 is comparable with W, E cannot be approximated by V/W. A solution in this range would require a procedure similar to that used in obtaining Eq. (A22), except that a linear gradient approximation such as the one of Fig. 13 is not appropriate when $W_0 \gg L$. Because of this added complication it has not yet proved feasible in the present case to find the slope analytically at short t. In view of experimental results such as those of Fig. 6, and in view of the trend suggested by Eq. (A37), it is tentatively assumed that the initial slope is the same as the final slope of Eq. (A39).

JOURNAL OF APPLIED PHYSICS VOLUME 31, NUMBER 2 FEBRUARY, 1960

Diffusion of Boron into Silicon*

A. D. KURTZ† AND R. YEE
Semiconductor Division, Minneapolis-Honeywell Regulator Company, Boston, Massachusetts
(Received June 24, 1959)

The diffusion of boron into silicon has been investigated over a temperature range of 1050°C to 1350°C using an open-tube vapor-solid diffusion technique at atmospheric pressure. A *p-n* junction method of measuring the diffused layer was used to determine the diffusion constant. Lower diffusivities and a somewhat lower activation energy, ($\Delta H = 81$ kcal) were obtained than those reported previously.

The difference is attributed to variation of diffusivity with surface concentration and is discussed on the basis of field-aided diffusion theory.

INTRODUCTION

FULLER and Ditzenberger[1] have studied the diffusion of boron in silicon over the temperature range from 950°C to 1275°C using the closed tube diffusion method. Under the conditions of their investigation boron surface concentrations of order 10^{21} to 10^{22} atoms/cm^3 were obtained. The high density of diffused impurity indicates that field aided diffusion probably occurred. The present investigation studies boron diffusion in silicon over approximately the same temperature range using open tube diffussion methods, but under conditions where field aided diffusion is not appreciable.

For the case of a constant concentration diffusing source, solution of the differential diffusion equation yields the result

$$C = C_s \operatorname{erfc}\left(\frac{x}{2(Dt)^{\frac{1}{2}}}\right) \tag{1}$$

where C_s is the surface concentration, C the concentration at a distance x from the surface, erfc is the complementary error function, t the duration of the diffusion process, and D the diffusion constant, which is determined by the diffusing species and the medium through which it diffuses. The temperature dependence of the diffusion constant is given by $D = D_0 \varepsilon^{-\Delta H/RT}$, where ΔH is the activation energy and T the temperature of diffusion, so that measurements of D as a function of temperature enable one to evaluate ΔH and D_0. To solve Eq. (1) for the diffusion constant, D, the *p-n* junction depth was measured optically from metallographic cross sections and by careful lapping and thermal probing. The surface concentration, C_s was obtained from measurement of the sheet resistivity of the diffused layer and making appropriate corrections based on the functional relationship of $1/\rho_s x_0$ to C_s given by Backenstoss.[2]

* This research was supported in part by the Air Force Contract, AF-19(604)-4099.

† Now at Kulite Semiconductor Products, Ridgefield, New Jersey.

[1] C. S. Fuller and J. A. Ditzenberger, J. Appl. Phys. **27**, 544 (1956).

[2] G. Backenstoss, Bell System Tech. J. **37**, 699 (1958).

EXPERIMENTAL PROCEDURE

The apparatus for vapor-solid diffusion at atmospheric pressure consists essentially of a zirconium silicate or a fused silica tube extending through two controlled temperature zones, the first zone being used to control the volatility of the impurity diffusant and the second zone to heat the silicon samples. A flowing gas carries the impurity vapors past the silicon samples with an increasing temperature gradient being maintained between the two zones to prevent the redeposition of the vapor before reaching the silicon. B_2O_3 was used as the diffusant in these investigations, and the boron vapor was carried past the silicon samples using prepurified nitrogen as the carrier gas at a flow rate of 400 ml per min in furnace tubes of one inch inside diameter. The silicon was held vertically in a slotted fused silica sample holder, and an alundum container was used for B_2O_3. Pt-Pt 13% Rh thermocouples and automatic controllers regulated the temperature to ±3°C. Wafers 0.5 in×0.5 in×0.015 in. were cut parallel to the (111) crystallographic direction from single crystal, *n*-type silicon (Sb doped), lapped plane with Carborundum A-1000 Finishing Compound, and etched to a mirror polish in a mixture of concentrated HF and HNO_3. The final sample thickness was approximately 12 mils. The silicon retained a bright surface without pitting when prepurified nitrogen was used as the carrier gas. The bulk resistivity of the silicon samples showed little change after being heated at the temperatures of diffusion, but in calculations involving the resistivity of the bulk silicon those values are used which were measured after diffusion.

When Eq. (1) is solved for D, the following result is obtained:

$$D = \frac{1}{4t}\left\{\frac{x}{\arg \operatorname{erf}[1-(C/C_s)]}\right\}^2. \tag{2}$$

Letting C_0 be the impurity concentration of the base material, then a junction is obtained at the plane of intersection where $C = C_0$. The value of the diffusion constant, D, may be calculated from Eq. (2) using this value for C, and measured values of the junction depth, $x = x_0$, and the surface concentration, C_s.

In order to measure the *p-n* junction depth accurately,

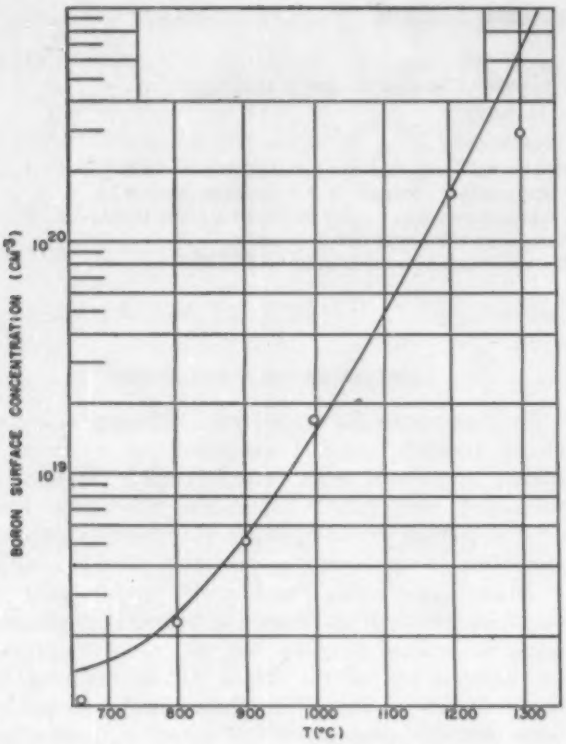

FIG. 1. Boron surface concentration *versus* B_2O_3 source temperature.

each diffused sample was cut in half and the junction depth measured by two separate methods, optically, and by careful lapping and thermal probing while measuring the change in conductivity through the diffused layer at each lapping. For the optical method the samples were mounted in a transparent potting compound and lapped and polished to expose a cross section. Great care must be taken during this operation to preserve the outer edges of the sample since distances are measured from this reference. Several staining techniques were used to define the *p-n* junction, the most successful being a quick swab of the cross section with an etch made from 20 cc of HF and a drop of HNO_3. Staining is completed in about two seconds. Photomicrographs of the stained cross section enable junction depths to be measured to at least ± 0.05 mil. The alternative method of determining the junction depth involves successive lappings with thermal probing to check conductivity type and four-point probe resistivity measurements after each lapping. Lapping increments of 0.05 mil were made. Junction depth determinations using the thermal probe and conductivity reversal data, and metallographic sections agreed to ± 0.05 mil.

As mentioned earlier, the surface concentration was obtained from a four-point probe sheet resistivity measurement of the diffused layer and determining C_s from curves of $1/\rho_s x_0$ *versus* C_s given by Backenstoss.[2] The dependence of the boron surface concentration with the B_2O_3 source temperature has been plotted in Fig. 1.

RESULTS AND DISCUSSION

A temperature range of 1050°C to 1350°C was investigated with results as summarized in Table I. The surface concentrations of the diffused layer were of the order of 5×10^{18} per cm³. A plot was made of the logarithm of the diffusion constant against the reciprocal of the absolute temperature, Fig. 2. From the slope of this plot an activation energy, ΔH, of 81 kcal is obtained. This value of activation energy is in good agreement with the 85 kcal reported by Fuller and Ditzenberger[1] and 81 kcal reported by Dunlap.[3] The value of D_0, however, is approximately one-half that reported by Fuller and Ditzenberger.[1] Points in the plot of Fig. 2 represent mean values of the computed D values listed in Table I, while the bar lines denote the limits of deviation from the mean.

The lower values of the surface concentrations of the diffused layer in this investigation can account for the lower diffusivities as compared with Fuller and Ditzenberger's work.[1] The effect on the diffusion constant of a highly doped layer in the surface region has been discussed by Bardeen, Brattain, and Shockley[4] and Reiss, Fuller, and Morin.[5] Physically a field arises from the large difference in diffusion constants of the ionized boron atoms and the holes associated with

TABLE I. Diffusion data.

Run No.	Temp. (°C)	Time (hr)	Junction depth (microns)	Surface concent. (cm^{-3})	Diffusion const. (cm^2/sec^{-1})	Mean value for diff. const. (cm^2/sec^{-1})
1	1058	14.75	3.56	2.0×10^{18}	8.5×10^{-14}	7.9×10^{-14}
			3.30	4.0×10^{18}	6.5×10^{-14}	
			3.56	7.0×10^{18}	6.8×10^{-14}	
2	1100	71.0	12.7	4.5×10^{18}	1.8×10^{-13}	2.0×10^{-14}
			11.4	5.0×10^{18}	1.5×10^{-13}	
			14.2	4.0×10^{18}	2.3×10^{-13}	
			13.5	4.1×10^{18}	2.2×10^{-13}	
3	1124	48.0	14.5	6.1×10^{18}	3.3×10^{-13}	3.1×10^{-13}
			14.2	2.5×10^{18}	3.6×10^{-13}	
			11.9	4.1×10^{18}	2.3×10^{-13}	
4	1193	13.5	11.4	2.0×10^{17}	1.2×10^{-12}	1.0×10^{-12}
			9.41	1.6×10^{17}	9.1×10^{-13}	
			9.92	3.0×10^{17}	9.1×10^{-13}	
			10.7	1.9×10^{17}	1.1×10^{-13}	
5	1238	16.4	20.3	1.6×10^{18}	2.3×10^{-12}	2.5×10^{-12}
			23.6	3.0×10^{18}	2.8×10^{-12}	
			20.6	1.6×10^{18}	2.3×10^{-12}	
6	1300	15.0	38.2	5.9×10^{18}	7.2×10^{-12}	7.8×10^{-12}
			41.2	6.4×10^{18}	8.3×10^{-12}	
7	1300	16.25	38.1	3.2×10^{18}	7.3×10^{-12}	7.6×10^{-12}
			38.1	3.5×10^{18}	7.3×10^{-12}	
			38.1	4.7×10^{18}	6.3×10^{-12}	
			43.2	4.3×10^{18}	8.4×10^{-12}	
8	1342	5.0		5.5×10^{18}	1.1×10^{-11}	1.5×10^{-11}
				5.5×10^{18}	1.2×10^{-11}	
				3.5×10^{18}	1.9×10^{-11}	
				3.2×10^{18}	2.0×10^{-11}	

[3] Dunlap, Bohm, and Mahon, Phys. Rev. **96**, 822(A) (1954).
[4] Bardeen, Brattain, and Shockley, J. Chem. Phys. **14**, 4 (1946).
[5] Reiss, Fuller, and Morin, Bell System Tech. J. **35**, 535 (1956).

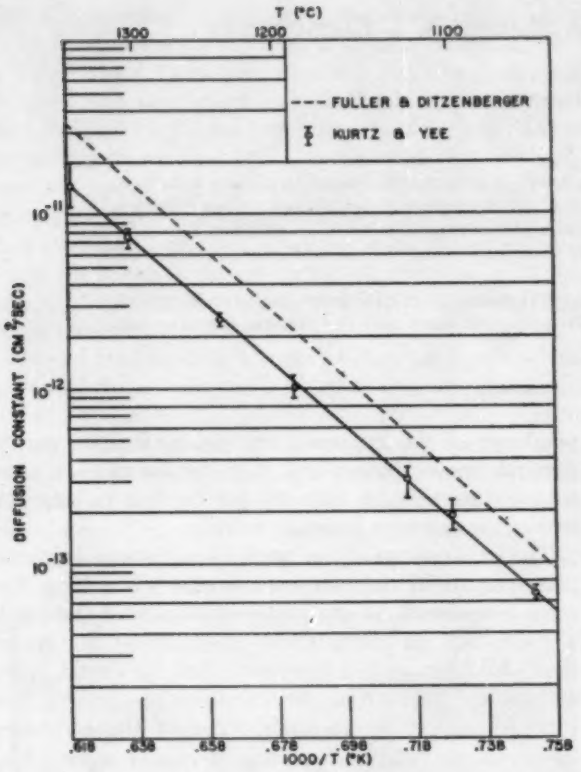

FIG. 2. Diffusion constant of boron in silicon.

them. The holes would ordinarily tend to diffuse away faster than the ions, thus creating a space charge. To prevent this a field is set up to keep the two distributions identical. The magnitude of the field may be determined by considering the two resulting currents, that of holes and ions.

$$J_p=-qD_p(\partial p/\partial x)+q\mu_p pE,$$
$$J_B=-qD_B(\partial C_B/\partial x)-q\mu_B C_B E.$$

The currents must be equal, and, if there is to be no net space charge,

$$p=C_B+n$$

and

$$np=n_i^2.$$

Then, equating the currents and solving for the field, E:

$$E=\frac{kT}{q}\frac{(1/C_B)(\partial C_B/\partial x)(D_p[1+(n_i/p)^2]^{-1}-D_B)}{[D_p+D_B+D_p(n_i^2/C_B p)]}.$$

For conditions of temperature and boron concentration such that $n_i \ll C_B$, and since $D_B \ll D_p$, the field equation reduces to

$$E=(kT/qC_B)(\partial C_B/\partial x).$$

When this value is substituted in the equation for the current density of diffusing boron ions, and using $\mu_B=G_q$ and $D_B=GkT$, where G is the microscopic mobility; that is, the velocity attained by an atom under unit applied force, there results a doubling of the effective diffusion constant. The doubling of the diffusivity would arise only under extrinsic conditions, that is $n_i \ll C_B$. Impurity concentrations in this work were approximately 5×10^{18} cm^{-3}, while the intrinsic carrier concentrations[6] for the diffusion temperatures used are in excess of 10^{19} cm^{-3}. Thus, field aided diffusion should not be observed in this investigation. Fuller and Ditzenberger,[1] however, report surface concentrations of order 10^{21} to 10^{22} cm^{-3} indicating that the density of impurity carriers exceeds the density of intrinsic carriers and one might expect doubling of the diffusion constant. A plot of Fuller and Ditzenberger's[1] data has been included in Fig. 2. The dissimilar results of the two investigations are adequately explained by field aided diffusion theory. The slight convergence of the two curves at the lower temperatures may indicate that some field aided diffusion occurred in this investigation, since at the lower diffusion temperatures, the data indicates C_s is not excessively larger than n_i.

ACKNOWLEDGMENTS

The authors wish to thank H. Halpin for his technical assistance in performing the experiments, and J. Kennedy and H. Halpin for evaluation of the data.

[6] F. J. Morin and J. P. Maita, Phys. Rev. **96**, 28 (1954).

JOURNAL OF APPLIED PHYSICS VOLUME 31, NUMBER 2 FEBRUARY, 1960

Rolling Friction of Polymeric Materials. I. Elastomers

DONALD G. FLOM
General Electric Research Laboratory, Schenectady, New York
(Received July 6, 1959)

Coefficients of friction for the rolling of steel balls on butyl, silicone and Neoprene elastomers have been measured in the temperature range of 25 to 100°C. For equivalent amounts of deformation rolling friction is directly proportional to dynamic mechanical losses measured by a rebound method. In addition, the coefficients of friction vary directly with (load)$^{\frac{1}{3}}$ and inversely with (ball radius)$^{\frac{1}{3}}$. These results are in agreement with recent theoretical predictions.

The high mechanical losses and rolling friction for the butyl elastomer at 25°C drop sharply on increasing the temperature to 100°C. For the silicone and the Neoprene the losses and the friction decrease only slightly with increase in temperature.

INTRODUCTION

RECENT studies have shown that the major contribution to the rolling frictional properties of materials may be found in the dynamic mechanical losses of these materials. As a quantitative test of the theory proposed by Bueche and Flom,[1,2] rolling friction and dynamic loss studies have been carried out on three elastomers of widely different mechanical properties—unfilled butyl,* Neoprene GN, and silicone SE 450.

In the rolling friction measurements, the effects of load, speed, temperature, and ball radius were studied. In the dynamic loss measurements a rebound method was used, the frequencies of stress being obtained from measured times of impact.

For each of the three elastomers the coefficient of friction was found to depend on load and on ball size in the manner predicted from theory. In the speed and temperature effects, the moderate but significant deviations from theory indicated the necessity, in a real material, of using a distribution of retardation times for the calculation of the friction coefficient rather than a single retardation time.[2] Furthermore the direct dependence of the measured friction coefficients on the dynamic losses showed that it is simpler in most cases to use this relation directly for further calculations without recourse to assumed models.

The implications of this work lie in the new emphasis placed on speed and temperature effects in rolling. The same considerations apply to well-lubricated sliding. It is probable that unexplained speed effects for rubber tires sliding on wet surfaces described by Tabor, Giles, and Sabey[3] arise from the variation of dynamic loss with frequency. In addition, some of the roughness effects in the lubricated sliding of rubber reported by Denny[4] can very likely be explained on the basis of such losses.

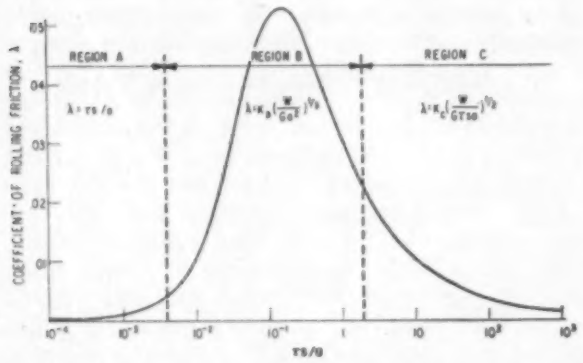

FIG. 1. Rolling friction of a sphere on a base material with single retradation time. $W=100$ grams, $G=10^6$ grams/cm², and $a=0.1$ cm.

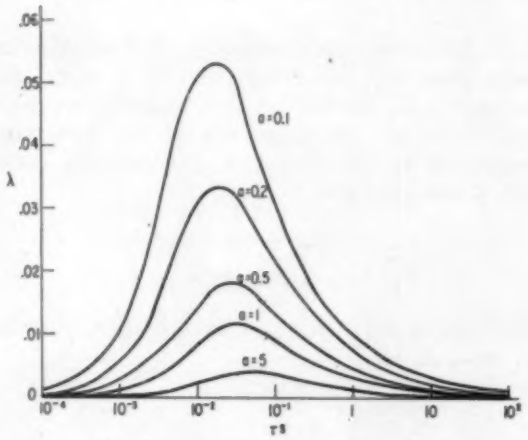

FIG. 2. Effect of sphere radius on rolling friction. $W=100$ grams and $G=10^6$ grams/cm².

BRIEF REVIEW OF PAST WORK

In 1952 Tabor correlated the low-speed friction of spheres rolling on rubber with the hysteresis losses in rubber as determined directly by normal loading.[5] He

[1] A. M. Bueche and D. G. Flom, Wear **2**, 168 (1959).
[2] D. G. Flom and A. M. Bueche, J. Appl. Phys. **30**, 1725 (1959).
* The butyl elastomer was prepared from a recipe similar to that given by de Mey and van Amerongen.[21]
[3] Tabor, Giles, and Sabey, Engineering **186**, 838 (1958).
[4] D. F. Denny, Proc. Phys. Soc. (London) **B66**, 721 (1953).
[5] D. Tabor, Phil. Mag. **43**, 1055 (1952).

and his co-workers subsequently extended these ideas to lubricated sliding on rubber and to other materials.[3,6–10]

Bueche and Flom demonstrated experimentally and theoretically how speed and temperature effects could be introduced by considering the dynamic mechanical properties of materials.[1,2] They showed that with increasing speed the coefficient of friction should go through a maximum the position of which would depend in a known manner on the temperature. Essentially the same result was obtained for rolling cylinders by May, Morris, and Atack[11] using somewhat different theoretical models.

In the treatment of a sphere rolling on a softer base material the assumption was made that the properties of the base material could be represented by a parallel spring-dashpot model. This would have a retardation time τ equal to η/G where η is viscosity and G is shear modulus. The friction coefficient λ was then found to depend on τ, the speed of rolling s, and ball radius a in the manner depicted in Fig. 1. It was also shown that

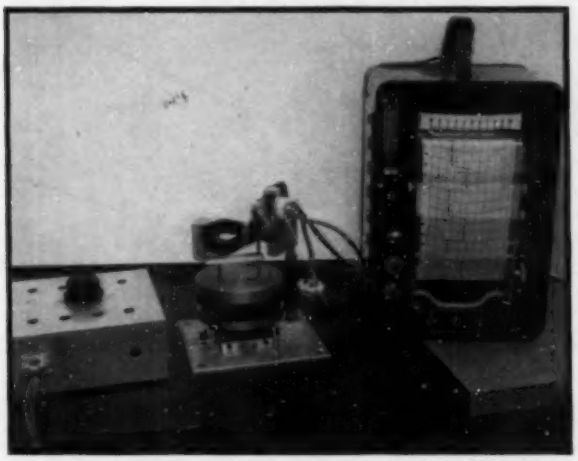

FIG. 3. Over-all view of rolling friction apparatus.

λ may be expressed in terms of ϕ (the ratio of the radius of contact, l, to the radius of the sphere, a) by means of the equation

$$\lambda = K_\phi \phi. \tag{1}$$

K_ϕ in this expression is not constant but increases with increasing $\tau s/a$. Since ϕ decreases with increasing $\tau s/a$, the value of λ in Eq. (1) thus goes through a maximum as required. Equation (1) is a general expression for λ which reduces, in the appropriate regions of $\tau s/a$, to the following expressions giving the functional dependence of λ on the load W and on G, τ, s, and a.

[6] D. Tabor, Brit. J. Appl. Phys. **6**, 79 (1955).
[7] D. Tabor, Proc. Roy. Soc. (London) **A229**, 198 (1955).
[8] D. Tabor, Lubrication Eng. **12**, 379 (1956).
[9] J. A. Greenwood and D. Tabor, Proc. Phys. Soc. (London) **71**, 989 (1958).
[10] D. Atack and D. Tabor, Proc. Roy. Soc. (London) **A246**, 539 (1958).
[11] May, Morris, and Atack (private communication).

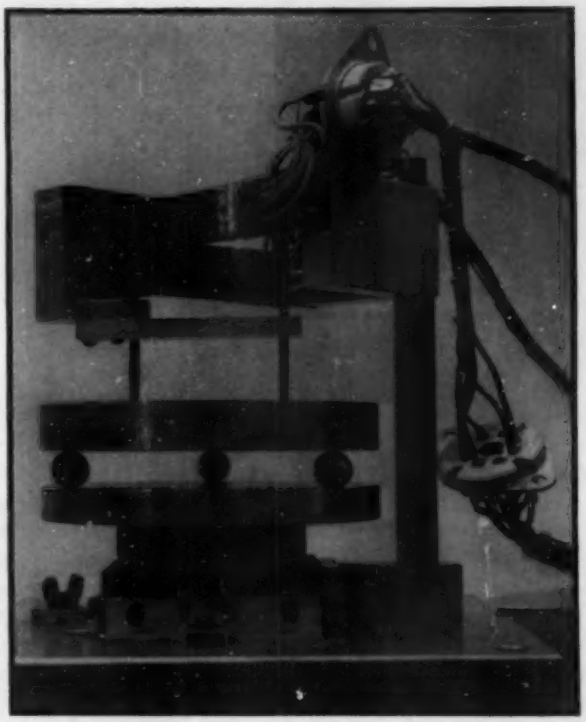

FIG. 4. Closeup of rolling friction apparatus.

Region A (*small* $\tau s/a$)

$$\lambda = \tau s/a. \tag{2}$$

Region B (*intermediate* $\tau s/a$)

$$\lambda = K_B (W/Ga^2)^{\frac{1}{2}}. \tag{3}$$

Region C (*large* $\tau s/a$)

$$\lambda = K_C (W/G\tau sa)^{\frac{1}{2}}. \tag{4}$$

These expressions are also given in Fig. 1. K_B and K_C are variable coefficients which are related directly to the dynamic losses in the material.

The effect of ball radius on λ can be seen more clearly by reference to Fig. 2. From this plot it is obvious that measurements of λ as a function of s and a quickly serve to identify the region of $\tau s/a$ in Fig. 1 which is applicable to the case in hand.

ROLLING FRICTION

Apparatus and Procedure

Photographs of the rolling friction apparatus are shown in Figs. 3 and 4. A schematic diagram of the main element is shown in Fig. 5. The apparatus consists essentially of two horizontal disks separated by three balls, the composite being similar in geometry to that of a thrust bearing. The lower disk is driven in rotation by a variable speed motor and gear reducer under the bench top. The upper disk (which in the present study carried the elastomer sample) is con-

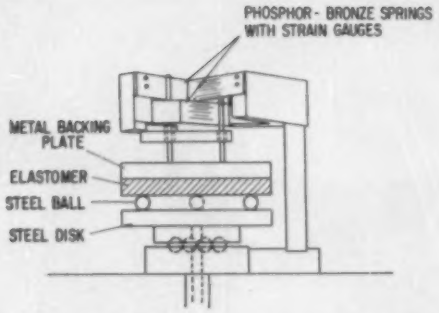

FIG. 5. Schematic diagram of rolling friction apparatus.

strained from rotating by two projecting pins which are loosely coupled to a pair of phosphor-bronze springs. Strain gauges attached to the springs are used for measuring the force in rotation. The normal load is the dead weight of the upper disk plus any additional weights which might be placed on it. The balls are kept in position during assembly by a shallow circumferential groove in the lower disk. The groove radius is large enough (1.10 inch) to insure essentially sphere-on-plane contact between the balls and the disk. Thus, additional friction due to sliding is not introduced unless the speed is allowed to become unusually high and centrifugal forces become appreciable.

Two sets of disks were used in the elastomer study having radii of $1\frac{3}{8}$ and $2\frac{1}{4}$ inches, respectively. Since the balls were positioned by the groove in the lower disk, they rolled in tracks of either 1 or 2 inch radius (also referred to as pitch radius) depending upon the set of disks being used. For the measurements at elevated temperatures, a furnace consisting of a glass tube wound with electric heating tape was used to enclose the disk combination. The temperature was measured with a copper-copnic boot type thermocouple (0.18 inch o.d.) inserted directly into the elastomer.

In making the friction measurements it was found that rotation in one direction only gave poor results because the constraining spring system seldom returned to exactly the same zero point on stopping the disks. However, one-half the sum of the spring deflections resulting from disk rotation in both directions was very reproducible even when the friction was very low, e.g., steel balls and steel disks (F less than $\frac{1}{2}$ gram). This was therefore used as the friction force. An additional feature of the measurement was that the rolling friction proved relatively insensitive to atmospheric and surface conditions, thus indicating that bulk properties were the most important factors involved.

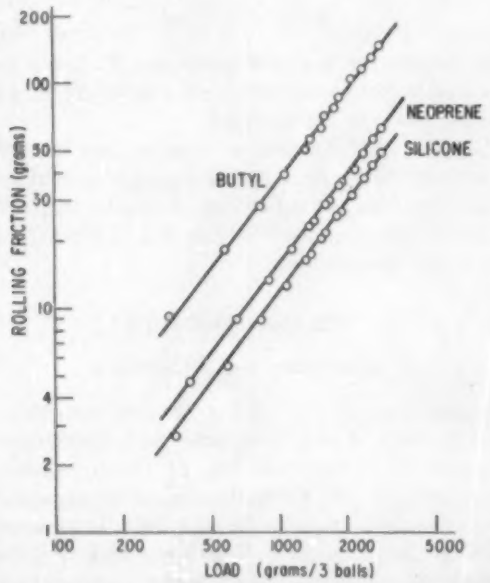

FIG. 6. Effect of load on friction for steel balls rolling on elastomers. $a=0.635$ cm and $s=15$ cm/sec. Slopes of straight lines $=1.3$.

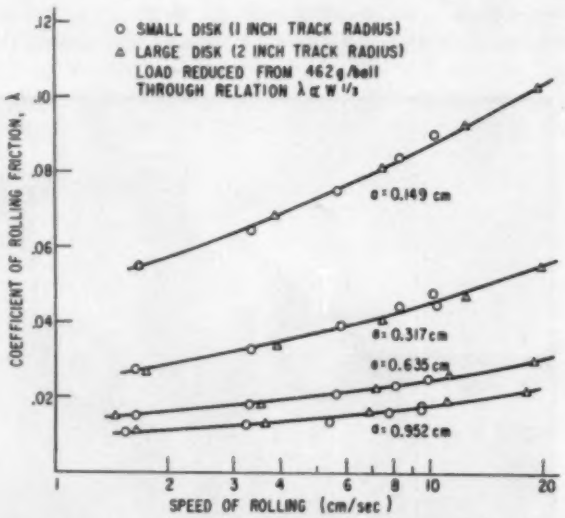

FIG. 7. Effect of speed on friction for steel balls rolling on butyl elastomer. $W=173$ grams/ball.

The rolling friction of steel balls between two steel disks was some 100 times less than that for a similar combination employing an elastomer disk (with metal backing). As a result the contribution of the steel could be neglected in the measurements of elastomer friction. For both steel and elastomers, or combinations thereof, the addition of lubricants such as cetane, oleic acid, glycerine, MoS_2, and graphite did not lower the friction. On the other hand, the use of small balls (e.g., $\frac{1}{8}$ inch) and a highly viscous liquid such as glycerine resulted in increased friction.

Finally, the rolling friction was found to be independent of the size of disks used (i.e., $1\frac{3}{8}$ or $2\frac{1}{4}$ inch radius). In this work, then, the contribution resulting from spin as discussed by Johnson[12,13] were negligible. This would not necessarily hold for speeds and ball radii outside the range of the present study.

[12] K. L. Johnson, J. Appl. Mech. **25**, 332 (1958).
[13] K. L. Johnson, J. Appl. Mech. **25**, 339 (1958).

Load, Speed, and Ball Size

The effect of load over a range of 300 to 3000 grams (on 3 balls) at a constant rolling speed of 15 cm/sec, is shown in Fig. 6. In the case of each elastomer the straight line through the experimental points has a slope of 1.3. This is the theoretical slope which would be expected for λ falling in the region of intermediate $\tau s/a$ (Region B in Fig. 1). Additional measurements of λ *vs* load for the silicone elastomer at a series of different ball radii also gave curves with slopes of 1.3.

The effects of speed and ball radii for steel balls rolling on butyl are shown in Fig. 7. Comparison of these curves with the ones in Fig. 2 indicate the extent of broadening of the elastomer curves as opposed to those for an ideal material with a single retardation time. Similar behavior was exhibited by the silicone elastomer (Fig. 8). The fact that the λ curves for silicone

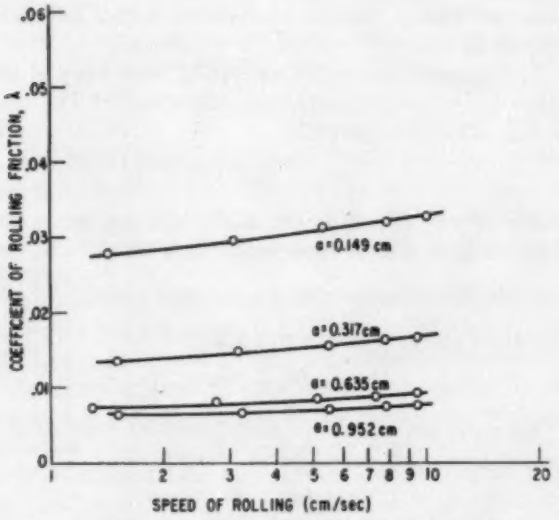

FIG. 8. Effect of speed on friction for steel balls rolling on silicone elastomer. $W = 176$ grams/ball.

were flatter and lower in magnitude than those for butyl was to be anticipated from the results of the dynamic loss measurements described later.

The direct dependence of λ on $W^{\frac{1}{3}}$ and on $a^{-\frac{1}{3}}$ for the butyl elastomer is shown in Fig. 9 where the data have been reduced to the same load and radius. Only in the case of the larger balls was there any tendency for deviation from theoretical behavior.

Effect of Temperature

In the foregoing description of the effects of load, speed, and ball radius, only functional relationships were established. To provide a quantitative test of the theory, the rolling friction was measured as a function of temperature for each elastomer and these results were then compared with the theoretical friction, also as a function of temperature. The experimental results are given by the solid curves in Fig. 10. The theoretical

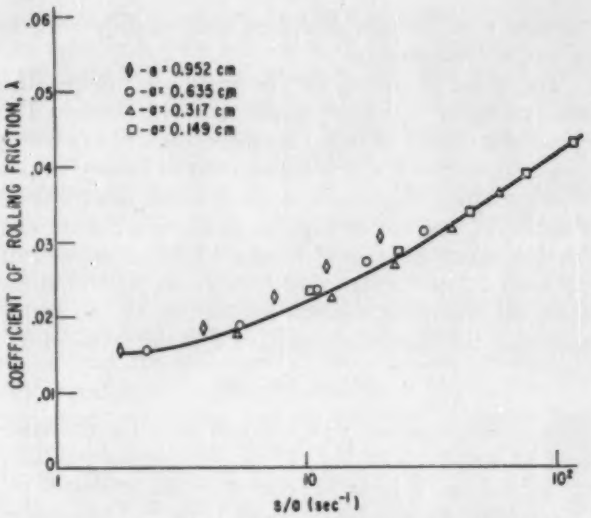

FIG. 9. Rolling friction of steel balls on butyl. Data reduced to radius of 0.952 cm through relation $\lambda \propto a^{-\frac{1}{3}}$. $W = 462$ grams/ball.

results are given by the dotted curves and were obtained in a manner to be described presently. As may be noted, the coefficient of rolling friction was relatively high for the butyl elastomer at 25°C but on increasing the temperature to 100°C, the friction dropped sharply. For the silicone and Neoprene, on the other hand, the

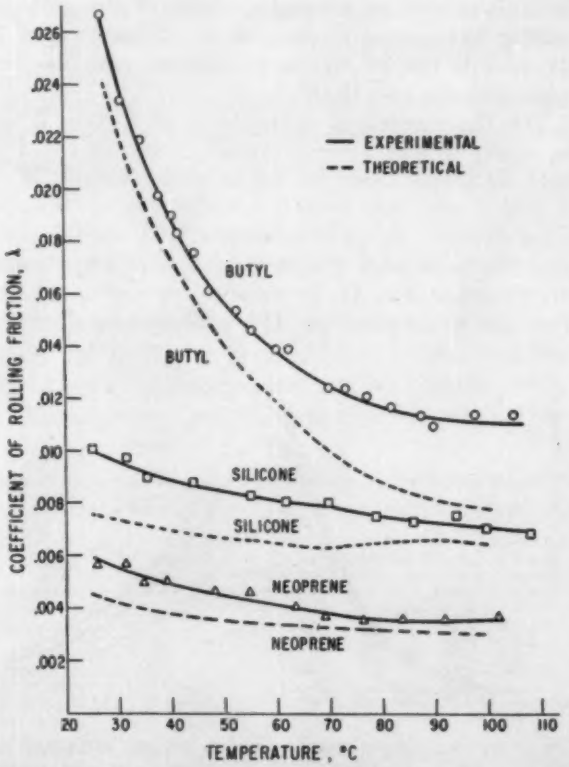

FIG. 10. Rolling friction of steel balls on elastomers. Butyl, $W = 173$g/ball; silicone, $W = 176$g/ball; and Neoprene, $W = 177$g/ball.

coefficient of friction decreased only slightly with increase in temperature.

The speed of rolling for the friction *vs* temperature measurements was held constant at 15 cm/sec. This speed was chosen so that a frequency of stress in rolling could be obtained which approached as closely as possible the stress frequencies of the dynamic loss measurements, yet was not so high as to introduce additional friction effects because of localized heating or centrifugal forces. The rolling stress frequencies were obtained from the following relation between ϕ, W, G, and a, assuming the elastomers to have Poisson ratios of 0.5:

$$W=5.33Ga^2\phi^3. \tag{5}$$

This is the equation which would hold for the lower part of Region B in Fig. 1,[2] i.e., the region indicated by Figs. 7 and 8 to be of interest in the present work.

To obtain a value for G, Shore Type "A" Durometer measurements were made. The calibration curves of Scott[14] were used for conversion of Durometer readings to modulus values. This procedure might be open to some question since G would be expected to vary with rolling speed and with temperature. These effects would tend to counteract one another, however, and the net change would be small compared to the much greater change in dynamic loss. The following values of G (in g/cm^2) were obtained: butyl, 3.7×10^3; silicone, 5.6×10^3; Neoprene, 1.55×10^4. Taking a rolling distance of $4l$ as comprising a complete cycle of stress, the resulting frequencies, ν, given by Eq. (5) were then 18, 24, and 35 cps for the butyl, silicone, and Neoprene experiments, respectively.

For the theoretical calculations of friction it was necessary to plot a curve similar to that in Fig. 1 for each elastomer, using the appropriate constants W, G, a, and s, and then from a knowledge of τ (obtained from dynamic loss measurements) pick off the corresponding value of λ. The curves of λ *vs* $\tau s/a$ so obtained are shown in Fig. 11. It remained to evaluate τ as a function of temperature. This will now be discussed.

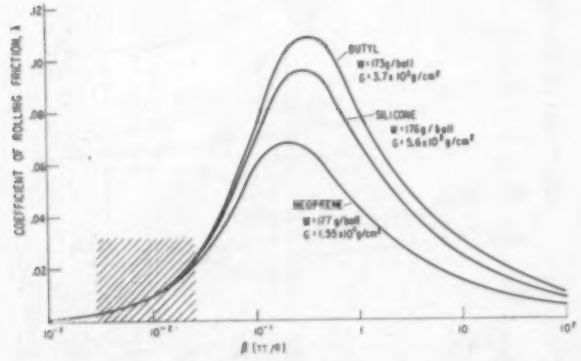

FIG. 11. Theoretical friction for steel balls ($a=0.635$ cm) rolling on elastomers. Shaded area indicates region of applicability in present study.

[14] J. R. Scott, Rubber Chem. and Technol. **28**, 1071 (1955).

DYNAMIC LOSSES

Viscoelastic Relationships

In determining the elastic loss in a material it is convenient to represent the dynamic shear modulus as a complex quantity, G^*. The stress-strain relationship is then

$$\sigma=G^*\epsilon \tag{6}$$

where $G^*=G'+iG''$. G' is the real component of the modulus and is that stress which is in phase with the strain divided by the strain. G'' is the imaginary component of the modulus and is that stress which is 90° out of phase with the strain divided by the strain. G' is also referred to as the storage modulus and G'' is referred to as the loss modulus. The ratio G''/G' is the tangent of the phase angle δ by which the stress leads the strain and is called the loss tangent. It is this quantity which serves as the starting point for calculations of rolling friction coefficients based on elastic hysteresis losses.

The rebound method of measuring losses may be considered as a special case of free vibration[15,16] The stress in Eq. (6) is then given by

$$\sigma=-(M/c)D^2\epsilon \tag{7}$$

where $D^2=\partial^2/\partial t^2$, M is the mass, and c is a constant depending on sample dimensions such that

$$\text{force/displacement}=c(\text{stress/strain}). \tag{8}$$

Equation (6) may be rewritten as

$$-(M/c)D^2\epsilon=G'\epsilon+iG''\epsilon. \tag{9}$$

[This equation is of the same form as that used in torsion pendulum experiments, namely

$$-(I/c)D^2\theta=G'\theta+iG''\theta$$

where I is the moment of inertia and θ is the angle of twist.[17]]

Equation (9) may be solved by considering the stress and strain to be sinusoidal. This is not completely correct since the strain is actually a damped sinusoid but the resulting error is small. We express the strain then as

$$\epsilon=\epsilon_0 e^{(i\omega-\lambda)t}. \tag{10}$$

Here ω is circular frequency ($\omega=2\pi\nu$) and $e^{-\lambda t}$ is a term which expresses the decay of strain with time.

Combining (10) and (9) we get

$$-(M/c)(-\omega^2-2i\omega\lambda+\lambda^2)=G'+iG''$$

or

$$(M/c)(\omega^2-\lambda^2)+(2Mi\omega\lambda/c)=G'+iG''. \tag{11}$$

From this equation we readily see that

$$G'=(M/c)(\omega^2-\lambda^2)$$

[15] R. S. Marvin, Ind. Eng. Chem. **44**, 696 (1952).
[16] S. D. Gehman, Rubber Chem. and Technol. **30**, 1202 (1957).
[17] L. E. Nielsen, Rev. Sci. Instr. **22**, 690 (1951).

and

$$G''=(2\omega M\lambda/c) \tag{12}$$

and finally

$$\tan\delta=G''/G'=[2\omega\lambda/(\omega^2-\lambda^2)]. \tag{13}$$

If the period of oscillation is given by $T=(2\pi/\omega)$ and the logarithmic decrement is given by $\Delta=\ln\{[\epsilon(t_0)]/[\epsilon(t_0+T)]\}$ then

$$\Delta=(2\pi\lambda/\omega)=\lambda T. \tag{14}$$

Substitution of (14) into (13) then gives

$$\tan\delta=G''/G'=[4\pi\Delta/(4\pi^2-\Delta^2)]. \tag{15}$$

In the case of impact the logarithmic decrement is obtained directly from the relation

$$\Delta=2.303\log(h_1/h_2) \tag{16}$$

where h_1 is the height of the ball before release and h_2 is the height of rebound.

In most dynamic studies $\tan\delta$ is sufficiently small so that Eq. (15) can be written as

$$\tan\delta\simeq(\Delta/\pi). \tag{17}$$

In the present case it was found that if this approximation were used for butyl elastomer at 25°C the resulting error would be slightly greater than 20%. For calculations in this work, then, Eq. (15) was used without change.

To determine τ, its relation to dynamic loss and frequency is needed. Unfortunately, this relation is not easy to obtain experimentally and a detailed knowledge of the distribution of retardation times is ordinarily required. On the other hand, it has been fairly well established that the maximum in $\tan\delta$ occurs when $\omega\tau=1$. Furthermore, when $\omega\tau\ll1$, $\tan\delta$ is directly proportional to $\omega\tau$ and when $\omega\tau\gg1$, $\tan\delta$ is directly proportional to $1/\omega\tau$. For the present work the approximate relation was used

$$\tan\delta=2(\tan\delta)_{\max}[\omega\tau/(1+\omega^2\tau^2)] \tag{18}$$

which satisfied the necessary boundary conditions. It should be pointed out that for butyl elastomer Eq. (18) cannot be correct on the high-frequency side of the loss maximum. Studies on polyisobutylene (essentially the unvulcanized form of butyl elastomer)[18] have shown a secondary inflection in the loss curve at high frequencies which could not be obtained from a relation of the form of Eq. (18). In the present work however, the loss data were obtained on the low-frequency side of the maximum so Eq. (18) could be used with confidence.

Rebound Measurements

For the loss measurements a steel ball ($\frac{1}{2}$ inch in diameter) was dropped from a height of 30 cm to a horizontal elastomer surface and the height of rebound read visually from a vertical scale. The elastomer was in the form of a disk $2\frac{3}{4}$ inches in diameter and $\frac{1}{2}$ inch thick. This was backed up by a steel disk of the same diameter and of slightly greater thickness. Losses at the interface between the elastomer and the steel were minimized by bonding the two with pressure sensitive tape in addition to a screw extending through the centers of the disks.

The method of release was magnetic, i.e., the ball was suspended at the end of a soft iron rod extending through an electrically energized coil; when the circuit was opened, the ball would drop. While this procedure was entirely satisfactory, it was later found that an even more convenient method consisted of suspending the ball by suction from the end of a rigidly clamped rubber hose connected to the house vacuum line. Interruption of the vacuum then caused the ball to drop. The precision with which the ball could be made to hit a prescribed area of the elastomer surface was determined by dusting the surface lightly with talc and then measuring the diameter of the impression left by the ball during impact. It was found that 5 or 6 impacts could be made without significantly increasing the diameter of the ball impression. Neither did the dusting procedure affect the height of rebound. On the other hand, successive impacts resulted in an increase in rebound and a reproducible value was reached only after 3 or 4 impacts. This effect has been reported previously and is apparently a well-known phenomenon in rubber technology.[19,‡]

By enclosing the elastomer with a Nichrome-wound glass furnace, the dynamic loss could be measured over a range of temperatures extending to more than 100°C. The temperature was measured with a boot-type copper-copnic thermocouple inserted directly into the elastomer at a point about 1 inch from the impact area.

The dynamic loss data at 25°C for the three elastomers are given in Table I. These results, together with those at higher temperatures, are plotted in Fig. 12. The agreement with data in the literature for ma-

Table I. Dynamic mechanical properties of elastomers at 25°C.

Elastomer	Dynamic loss ($\tan\delta$)	Time of impact (millisec) Photo-tube method	Strain gauge method	Electrical contact method	Stress frequency (cps)	Maximum load in impact (g)
Neoprene	0.27	1.5	≃2	1.2	417	≃800
Silicone	0.20	2.7	≃3	2.0	250	≃700
Butyl	1.05	3.5	≃4	1.7	294	≃500

[18] Ferry, Grandine, and Fitzgerald, J. Appl. Phys. **24**, 911 (1953).

‡ *Note added in proof.*—As Dr. Tabor has kindly pointed out, this phenomenon is equivalent to a "closing up" of the hysteresis loop with successive stress cycles.

[19] J. H. Dillon and S. D. Gehman, Rubber Chem. and Technol. **20**, 827 (1947).

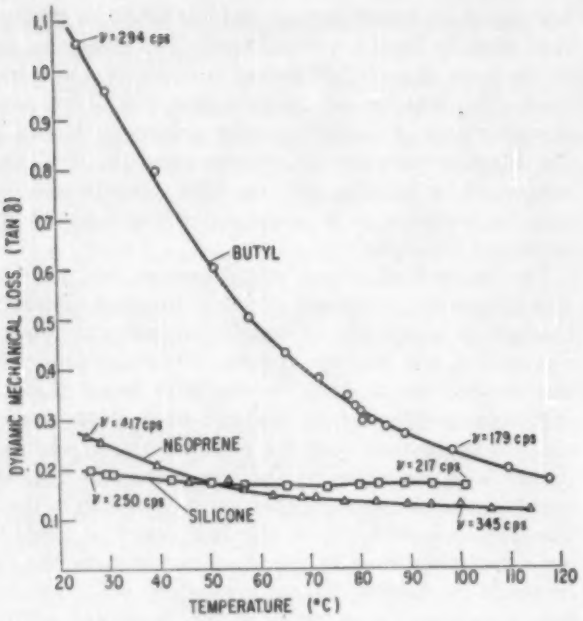

FIG. 12. Dynamic mechanical losses of elastomers in rebound.

terials of presumably the same composition is good.[20–25] The stress frequencies associated with the losses, reported alongside the curves, were obtained from measurements of impact times, now to be described.

Times of Impact

The times of impact were measured by three different methods. These served as independent checks on one another. In the first, a light beam passing through a tiny slit positioned in the plane of the elastomer surface and falling on a phototube was interrupted by the ball during the period of the deformation. A time interval meter was used to measure the duration of light interruption.

In the second method a pin, attached to a coupled pair of phosphor-bronze springs, was inserted into the elastomer from the side such that the tip was a few mm below the point of impact. Deformation of the elastomer during impact resulted in a deflection of the spring system and this deflection was measured by means of strain gauges. This method gave only a rough measure of the time of impact because the signal was superimposed on that resulting from the natural frequency of the spring system. However, the method was valuable in another sense in that an estimate of the maximum force developed during impact could be obtained.

The third method for measuring time of impact, and the one which proved most useful, was to place two tiny platinum wires (2-mil diam) on the elastomer surface such that their ends were separated by a small gap—of the order of 0.4 mm—in the center of the impact region. When included in an electrical circuit, these wires would give rise to a short-circuit by contact with the steel ball during impact. The resulting signal was displayed on an oscilloscope and photographed. Since the wires were extremely small (less than 1% of the maximum area of contact) they exerted negligible effect on either the height of rebound or the diameter of the ball impression formed. The impact times obtained in this way were the most reproducible of the three times measured.

The results of all three techniques are given in Table I. The reason for the consistent difference in impact times measured by the different methods may be seen in Fig. 13. The duration in each case is depicted as that required for the impact to progress from stage 1 to stage 3. In the phototube method [Fig. 13(A)] the time measured was greater than that of actual physical contact but less than the period of compressive strain. In the strain gauge method [Fig. 13(B)] the time measured was that of compressive strain. In the electrical contact method [Fig. 13(C)] the time was that of actual physical contact or stress. The difference between the times as measured by the different methods was greatest for the materials of lowest moduli and/or greatest elastic loss. Because of this relationship, it appears that in principle at least impact time measurements such as these could be used to determine dynamic properties independently of rebound height measurements. The conditions of contact in rolling corresponded

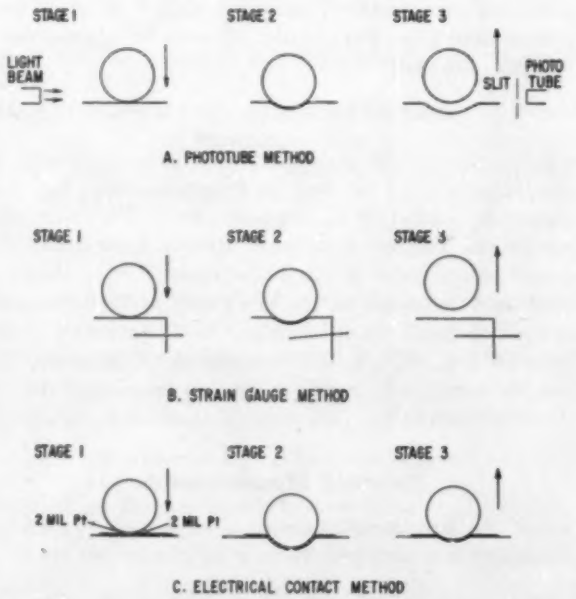

FIG. 13. Stages of deformation during impact time measurements.

[20] K. Schmieder and K. Wolf, Kolloid Z. **134**, 149 (1953).
[21] S. de Mey and G. J. van Amerongen, Rubber Chem. and Technol. **29**, 1215 (1956).
[22] Ivey, Mrowca, and Guth, J. Appl. Phys. **20**, 486 (1949).
[23] Ferry, Fitzgerald, Johnson, and Grandine, J. Appl. Phys. **22**, 717 (1951).
[24] A. W. Nolle, J. Polymer Sc. **5**, 1 (1950).
[25] G. W. Painter, Trans. Am. Soc. Mech. Engrs. **76**, 1131 (1954).

most closely to those obtained in the electrical contact method for measuring impact times. Hence, the data obtained from the latter were used for calculations of the frequencies listed in Table I. Here the impact was considered as half a cycle of stress where one cycle defined in the usual dynamic sense includes both compression and tension.

In addition to measurements at room temperature, the impact times were also measured at 100°C, using the electrical contact method. The resulting frequencies are given alongside the curves in Fig. 12.

Dynamic Losses at Reduced Frequencies

The frequencies of stress in rebound were higher than could be obtained conveniently in the rolling experiments as carried out. Hence the two experiments could not be compared directly. Fortunately, it is a characteristic of dynamic mechanical properties in viscoelastic materials that temperature and frequency are interchangeable, i.e., an increase in frequency is tantamount to a decrease in temperature, and vice versa. The reason for this is that temperature exerts its effect predominantly through τ and since τ appears only in the product $\omega\tau$ [see e.g. (18)], any change in response produced by a change in τ can be offset by a change in ω. The details of reducing data to a single temperature or frequency have been thoroughly explained by Ferry and co-workers.[26] It is assumed that when the temperature is changed from a reference temperature T_0 to another temperature T, every retardation time (or relaxation time depending on the experiment) is multiplied by an empirical factor a_T. The reduced frequency, ω_R, is then given by

$$\omega_R = \omega a_T. \tag{19}$$

Once the a_T factors have been obtained experimentally for a given material, log a_T can be plotted against $10^3/T$ and the resulting curve can be used to reduce the dynamic data to that for any frequency desired.

In this study, a_T factors for the elastomers were not available. However, comparison with the data of other workers could be made. In the case of butyl, for example, Ferry *et al.* have shown that the a_T values for polyisobutylene can be used since the two materials are essentially of the same composition.[23] (At extremely low frequencies this would not be expected to hold because of the cross-linking in the elastomer.) Making use of this fact, the loss data for butyl at the frequencies in rebound were reduced to obtain the losses at 18 cps, the frequency of stress in the rolling experiments.

In similar fashion, the silicone and Neoprene loss data were reduced to 24 cps and 35 cps, respectively. In the case of the silicone an estimate of a_T was obtained from the data of Painter[25] and in the case of Neoprene from the data of Nolle.[21] The reduced loss data for all three elastomers are shown in Fig. 14. As may be seen, the reduction procedure resulted in a general decrease in loss which was most pronounced at the lower temperatures.

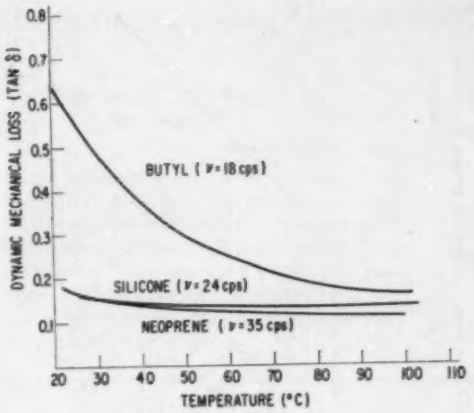

FIG. 14. Reduced loss data for elastomers.

By means of the loss curves in Fig. 14 and with the aid of Eq. (18), τ could be evaluated. Since none of the rebound loss measurements covered a sufficient range to include $(\tan\delta)_{max}$, an estimate of this value was necessitated. In the case of butyl elastomer, Ivey, Mrowca, and Guth reported $(\tan\delta)_{max} \approx 1.0$[22] while deMey and van Amerongen gave $(\tan\delta)_{max} \approx 1.5$.[21] A value of 1.3 was therefore used in the present work. This also served as a good estimate of $(\tan\delta)_{max}$ for Neoprene. In the case of silicone the work of others[25,27] indicated a lower $(\tan\delta)_{max}$ so a value of 1.0 was chosen.

When multiplied by the constant s/a, the τ values obtained showed that the region of applicability in the present study was that indicated by shading in Fig. 11. The theoretical values of λ obtained therefrom were plotted to give the dotted curves in Fig. 10.

In view of the many assumptions required in the calculations, the agreement of the curves in Fig. 10 can be considered quite satisfactory. It should be noted that the deviations in each case are in the direction which one would expect for a theory based on a single retardation time instead of a distribution of retardation times. The use of a distribution would tend to produce higher λ values at the outer ends of the curves in Fig. 11. At the same time, a distribution would tend to lower the maximum λ so that on the basis of our present treatment we would expect to obtain theoretical λ's higher than the experimental ones if we were operating in the central region of the curve.

ROLLING FRICTION AND DYNAMIC LOSS

That the coefficient of rolling friction is directly proportional to the dynamic loss for each elastomer is illustrated in Figs. 15, 16, and 17. Here λ has been plotted as a function of $(W/Ga^2)^{\frac{1}{2}} \tan\delta$ rather than $\tan\delta$ alone so that comparison of the three elastomers can be made at equivalent deformations. While the

[26] Ferry, Fitzgerald, Grandine, and Williams, Ind. Eng. Chem. 44, 703 (1952).

[27] I. L. Hopkins, Trans. Am. Soc. Mech. Engrs. 73, 195 (1951).

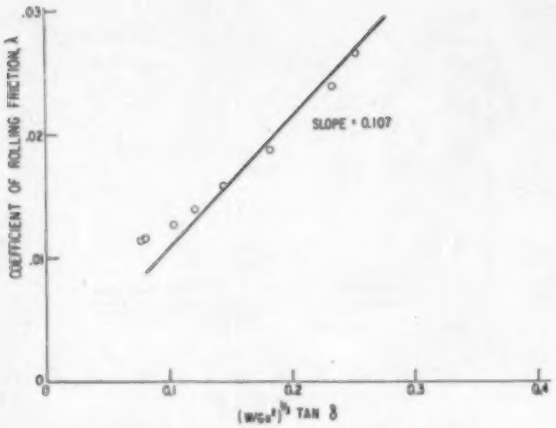

FIG. 15. Relation between rolling friction and dynamic losses for butyl elastomer.

straight lines in these plots do not all pass through zero, the departures from this are small. In the case of the butyl experiments there were unavoidable heat effects on the strain gauges which lowered the precision of the friction measurements at the higher temperatures. Hence the experimental points corresponding to the lower temperatures are somewhat favored in Fig. 15.

It is obvious that having determined the slopes of

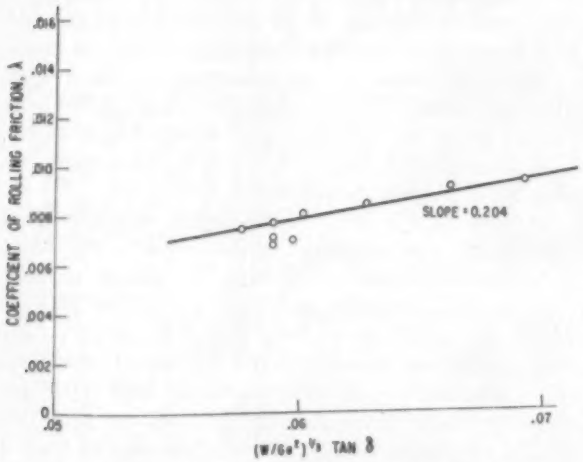

FIG. 16. Relation between rolling friction and dynamic losses for silicone elastomer.

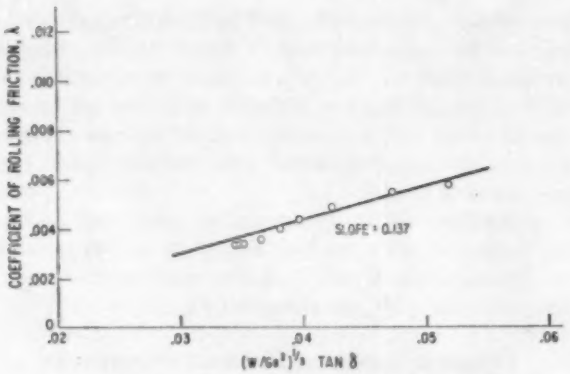

FIG. 17. Relation between rolling friction and dynamic losses for Neoprene elastomer.

the straight lines in Figs. 15, 16, and 17, λ for these elastomers could be calculated for any temperature and for any rolling speed providing tanδ were known over a broad frequency and/or temperature range. For many materials this information is either readily available or more convenient to obtain than direct friction measurements. Conversely, rolling friction studies could be used to measure dynamic losses in materials. This has, in effect, been done in the work of Bulgin and Hubbard on rubbers[28] and in the work of Drutowski on metals.[29]

The treatment used for rolling friction would also apply to well-lubricated sliding as indicated in the work of Tabor and co-workers[3,9,10] and Bueche and Flom.[1] It is probable that some of the roughness effects described by Denny for the lubricated sliding of rubber[4] could be explained on the basis of dynamic mechanical losses. In addition, the variation of dynamic losses with frequency could give rise to previously unexplained speed effects for rubber tires on wet surfaces described by Tabor, Giles, and Sabey.[3]

ACKNOWLEDGMENT

The author gratefully acknowledges helpful discussions with Dr. A. M. Bueche during the course of this work.

[28] D. Bulgin and G. D. Hubbard, Trans. Inst. Rubber Ind. **34**, 201 (1958).

[29] R. C. Drutowski, Annual Meeting American Society of Mechanical Engineers, New York, November 30–December 5, 1958.

JOURNAL OF APPLIED PHYSICS VOLUME 31, NUMBER 2 FEBRUARY, 1960

Photoelectronic Analysis of High Resistivity Crystals: (a) GaAs,* (b) Sb_2S_3

RICHARD H. BUBE
RCA Laboratories, Radio Corporation of America, Princeton, New Jersey
(Received August 10, 1959)

A series of photoelectronic measurements has been used to obtain information about the following basic properties of high resistivity crystals: (1) majority carrier lifetime, (2) band gap, (3) activation energy for dark conductivity, and (4) activation energies and densities of trapping centers for carriers. Such measurements have been made on representative high resistivity *n*-type crystals of GaAs and Sb_2S_3. The results are reported here together because both crystals show evidence for trapping of photoexcited carriers by compensated donor centers of the same type as those which uncompensated give rise to the normal dark conductivity. Additional data on Sb_2S_3, together with other results on similar crystals, suggest that these same uncompensated donor centers may play an important role in the recombination process.

INTRODUCTION

TECHNIQUES of photoelectronic analysis[1,2] used commonly to investigate photoconductivity in such insulators as cadmium sulfide can be profitably applied to other high-resistivity semiconductors and insulators. This paper describes such measurements on high-resistivity GaAs crystals, perhaps more commonly investigated in the lower resistivity semiconductor range,[3] and on high-resistivity Sb_2S_3 crystals, perhaps more commonly investigated in the still higher resistivity evaporated layer form.[4] The results provide data on the band gap, the majority carrier lifetime, the activation energy for dark conductivity, and the density and depth of trapping centers. Both GaAs and Sb_2S_3 show trapping of photoexcited carriers by compensated donor centers.

EXPERIMENTAL

Crystals of GaAs were grown from the melt and were supplied by R. V. Jensen and P. G. Herkart. High-resistivity crystals were found intermittently as the result of a program to purify GaAs. In some cases impurities were deliberately added, but in most of the crystals, indirect variations in impurity and imperfection content resulted from the choice of different raw materials and possible contamination during preparation.

Crystals of Sb_2S_3 were grown by I. J. Hegyi from the vapor over a melt in a sealed tube. Three representative runs are described; in one the melt contained excess Sb, in the second the melt contained excess S, and in the third the melt contained stoichiometric proportions of Sb and S.

The following measurements were made on each crystal, provided with ohmic contacts, and measured in an atmosphere of dry helium.

(*1*) *Photocurrent vs light intensity.*—Excitation was either by an incandescent lamp directly or through a Bausch & Lomb grating monochromator. Variations in light intensity were obtained with neutral wire-mesh filters which were capable of accurately covering a light intensity range of seven orders of magnitude. These measurements were used to obtain (a) the power dependence of photocurrent on light intensity as a guide to the proper correction of monochromator curves of spectral response; (b) values of photoconductivity gain,[5] i.e., the number of charges passing through the crystal for each photon absorbed; and (c) values of majority carrier lifetime, which can be calculated, for photoconductivity primarily associated with only one type of carrier, from the following equation:

$$\tau_{maj} = (L^2 G/\mu V) \qquad (1)$$

L is the inter-electrode spacing, G is the gain, μ is the carrier mobility, and V is the applied voltage.

(*2*) *Spectral response of photoconductivity.*—Excitation was by a Bausch & Lomb grating monochromator. Data were corrected so that the resultant curves represent photocurrent per photon as a function of wavelength. These measurements were used to obtain (a) the band gap from the photoconductivity maximum as a function of wavelength; and (b) an indication of the purity and perfection of the crystals by the sharpness of the photoconductivity cutoff at wavelengths longer than the absorption edge.

(*3*) *Dark conductivity vs temperature.*—The dark conductivity was measured for dark currents in excess of 10^{-11} amp using a Leeds and Northrup micromicroammeter with a Leeds and Northrup X-Y recorder. In most cases this gave values of dark conductivity covering five or more orders of magnitude. The slope of the conductivity-temperature curve was used to obtain the activation energy of the conductivity generation process.

(*4*) *Thermally stimulated current vs temperature.*—The sample was cooled to liquid nitrogen temperature and then exposed to exciting radiation. After a period of excitation, the radiation was removed and the crystal

* Work on GaAs crystals was supported under Air Force Contract AF 33(616)-5029.

[1] R. H. Bube, *Photoconductivity of Solids* (John Wiley & Sons, Inc., New York, to be published).

[2] R. H. Bube, in *Solid State Physics*, edited by F. Seitz and D. Turnbull (Academic Press, Inc., to be published).

[3] H. P. R. Frederikse and R. F. Blunt, Proc. Inst. Radio Engrs. **43**, 1828 (1955); Barrie, Cunnell, Edmond, and Ross, Physica **20**, 1087 (1954).

[4] Forgue, Goodrich, and Cope, RCA Rev. **12**, 335 (1951).

[5] A. Rose, Proc. Inst. Radio Engrs. **43**, 1850 (1955).

was heated at a linear rate of 0.5°/sec in the dark. The measured current, in excess of the normal dark current, is contributed by carriers being freed from trapping centers. The maxima of such a curve of thermally stimulated current *vs* temperature can be correlated with the trap depths involved, and the trap densities can be obtained from the area under the curve. On the basis of the reasonable assumption that the thermally stimulated current is contributed by majority carriers, i.e., those carriers for which the majority carrier lifetime has been determined, and that these majority carriers are electrons in the *n*-type samples measured, the trap depth may be calculated:

$$E_{trap}=E_{fn}=kT\ln(N_c/n) \tag{2}$$

where E_{fn} is the distance of the steady-state electron Fermi level below the bottom of the conduction band, T is the temperature of the thermally stimulated current maximum, N_c is the effective density of states in the conduction band, and n is the density of free carriers at the thermally stimulated current maximum (calculated from the conductivity†). The density of traps of a given depth can be determined from the area A under that portion of the curve:

$$N_t=\frac{A}{e\mathcal{V}G} \tag{3}$$

where N_t is the trap density, e is the electronic charge, $\mathcal{V}$ is the volume of the crystal, and G is the gain calculated for steady-state excitation of a photocurrent with magnitude equal to that of the average thermally stimulated current.

In the event of the existence of a hole trap, its depth could be calculated from the *p*-type conductivity attending its emptying from an equation similar to Eq. (2):

$$E_{trap}=E_{fp}=kT\ln(N_v/p) \tag{4}$$

where N_v is the effective density of states in the valence band. The calculation of the trap density according to Eq. (3), however, might be in considerable error if the majority carrier (electron) lifetime were used to calculate the gain G, rather than the hole lifetime. All of the trap depths and densities given in Table I have been calculated assuming that they were electron traps; later discussion indicates that one of these may be a hole trap, and therefore the densities listed for it may be in error.

The effects measured are almost certainly indications of bulk properties of the material rather than surface properties. The following evidence can be presented to support this statement: (1) typical dimensions of a GaAs crystal are $10\times2\times2$ mm³; the surface-to-volume ratio is therefore some 10^2 times smaller than for high-resistivity platelets of CdS for which volume properties have been measured by these techniques; (2) Hall effect and PEM measurements made on these crystals by Meyerhofer, Glicksman, and Amith indicate volume properties consistent with those measured in this investigation; (3) photoconductivity characteristics and trap densities obtained from a large GaAs crystal were essentially identical with these same quantities determined from small sections cut from this large crystal.

† For calculations, a mobility value of 1000 cm/volt sec was used, substantiated by Hall effect data.

GaAs RESULTS

A tabular summary of the experimental results is given in Table I for the nine crystals of *n*-type GaAs described in this paper.

Photocurrent *vs* Light Intensity

The dependence of photocurrent on light intensity is summarized in the final column of Table I. Values of n varied between 0.5 and 1.0, an average value being about 0.7.

Calculated values of majority carrier lifetime are given in the next-to-last column of Table I. Lifetimes varied over a wide range, from 2×10^{-9} sec to 2×10^{-2} sec in extreme cases. The longest lifetimes seemed to occur in the more conducting samples. A long majority carrier lifetime implies the capture of photoexcited minority carriers at sites in the crystal where recombination with free majority carriers is unlikely. The difference between majority carrier lifetimes at room temperature and liquid nitrogen temperature is a direct measure of the variation of photosensitivity with temperature. In some cases there was an increase in sensitivity on cooling, in others a decrease, but in most samples the over-all difference was less than or equal to an order of magnitude. The exception to this was sample GAJ-10, which at low light intensities at liquid nitrogen temperature had a majority carrier lifetime 10^4 times larger than at room temperature.

Spectral Response of Photoconductivity

Most photoconductors show a maximum of photosensitivity at a wavelength close to that corresponding to the absorption edge or band gap. This maximum arises because of surface absorption with lower lifetime for shorter wavelengths, and decreased absorption for longer wavelengths. Almost without exception, the band gap obtained from photoconductivity data is a lower limit to the actual band gap. The data given in the third column from the right in Table I show that the room temperature gap is 1.39 ev in all but one of the samples, and that the liquid nitrogen temperature gap is 1.47 or 1.48 ev, giving a temperature coefficient of band gap of about -4.0×10^{-4} ev/deg. It has been customary to consider the band gap of GaAs to be 1.35 ev[3]; the current data suggest that a somewhat higher value by 3% to 5% may be more accurate. This

TABLE I. Summary of photoelectronic data on *n*-type GaAs crystals.

Sample No.	*RT* conduct. mho/cm	Conduct. slope, ev	Therm. stim. current		*PC* band gap, ev		Maj. τ, μsec		$\Delta i a L^n / n$	
			E, ev	N_t, cm^{-3}	*RT*	90°K	*RT*	90°K	*RT*	90°K
GAJ 7	5×10^{-9}	0.675	0.32 0.56	10^{17} 2×10^{17}	1.39	1.47	0.04	0.002	0.70	0.66
GAJ 333	4×10^{-9}	0.61	$\leq$0.20 0.46 0.54	$\geq2\times10^{18}$ 3×10^{15} 2×10^{17}	1.39	···	0.02	0.1	0.83	0.73
GAG 410	10^{-8}	0.47	$\leq$0.22 0.56	$\geq3\times10^{16}$ 4×10^{16}	···	1.48	7	26	0.59	0.95
GAG 450	10^{-6}	0.43 0.058 (low *T*)	···	···	···	···	0.1	0.003	0.69	0.92
GAJ 11-4	8×10^{-9}	0.64 0.27 (low *T*)	$\leq$0.27 0.54	$\geq6\times10^{15}$ 10^{16}	1.39	1.48	0.07	0.2	0.95	0.65
GAJ 10	8×10^{-5}	0.57 0.23 (low *T*)	$\leq$0.20 0.31 0.35 0.41	$\geq3\times10^{14}$ 10^{15} 2×10^{15} 6×10^{17}	···	1.47	2	139 25 000 (low *L*)	0.62	0.72 0.57 (low *L*)
GAF 26	3×10^{-6}	0.53	$\leq$0.19 0.44 0.53	$\geq10^{17}$ 10^{16} 2×10^{15}	1.39	1.48	1	0.1	0.72 0.61 (low *L*)	0.64
GAJ 15-2	1.6×10^{-9}	0.715	$\leq$0.22 0.63	$\geq2\times10^{17}$ 10^{15}	1.42	···	0.6	0.06	0.76	0.79 0.56 (low *L*)
GAG 514	4×10^{-9}	0.71 0.48 (low *T*)	$\leq$0.21 0.57	$\geq3\times10^{16}$ 3×10^{16}	1.39	···	0.07	0.2	0.80	0.66

is particularly true since the crystal with the highest room temperature resistivity, GAJ-15-2, indicates a photoconductivity band gap of 1.42 ev at room temperature. Spectral response curves for four of the crystals are shown in Figs. 1, 2, 3, and 5.

If there were no levels in the forbidden gap, the photoconductivity would drop many orders of magnitude once the exciting wavelength exceeded that of the absorption edge. The failure of the spectrum to behave in this way is an indication of levels in the forbidden gap from which carriers can be excited to the free state. In the case of *n*-type photoconductivity, the pronounced long-wavelength response of all the spectral response curves indicates considerable density of levels from which electrons can be excited to the conduction band; compensated acceptor levels or un-ionized donor levels would behave in this way. Since the response extends well below 0.9 ev, the lowest energy photons used in these measurements, the indication is that the highest lying of these levels lie well up toward or above the center of the forbidden gap.

The spectral response curves shown in Fig. 1 for sample GAJ-7 are reasonably typical of most of the samples. Strikingly different is the curve of Fig. 2 for sample GAJ-15-2, the highest resistivity sample examined; here surface-absorbed light is as effective as volume-absorbed light so that the sharp maximum is absent, and there is an appreciably abrupt drop in photosensitivity as soon as the wavelength exceeds that of the absorption edge.

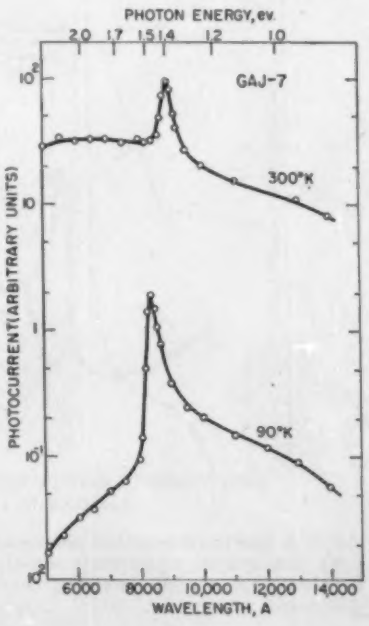

FIG. 1. Spectral response of photoconductivity in GaAs crystal GAJ-7, at room temperature and at 90°K.

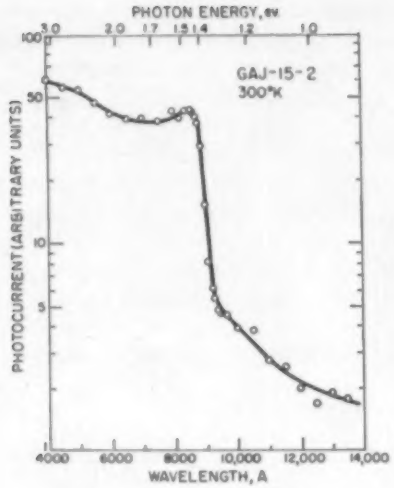

FIG. 2. Spectral response of photoconductivity in GaAs crystal GAJ-15-2 at room temperature.

The spectrum of sample GAJ-11-4 at 90°K, shown in Fig. 3, shows a sharp minimum of sensitivity due to the existence of strong infrared quenching in this sample. The infrared quenching spectrum was analyzed and is shown in Fig. 4. Quenching extends almost from the band gap to a low-energy cutoff of about 1.15 ev. If we again assume that *n*-type photoconductivity is involved, this quenching observation indicates a "sensitizing" level lying about 0.3 ev below the conduction band, with large cross section for photoexcited holes and a subsequent small cross section for photoexcited electrons. The same crystal shows a dark conductivity activation energy of 0.27 ev at low temperatures which may correspond to the same level. Such infrared quenching was found in only one other GaAs crystal, not included in this report. The quenching phenomenon is restricted to low temperatures, because at room temperature, for example, these levels are acting only as trapping centers.

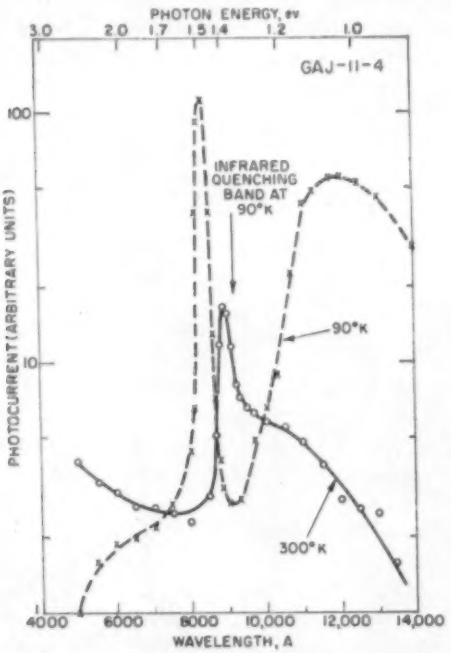

FIG. 3. Spectral response of photoconductivity in GaAs crystal GAJ-11-4, at room temperature and at 90°K. Note the evidence for the sharp infrared quenching band in the low-temperature spectrum.

Sample GAJ-10, for which the low-temperature spectral response is given in Fig. 5, is that sample for which very high photosensitivity was observed at low temperatures. The temperature dependence of the photocurrent is shown in Fig. 6. Upon cooling below room temperature, the photosensitivity increases almost exponentially with $1/T$ to a maximum at about 65°K, to a value over two orders of magnitude greater than its room temperature value. The photosensitivity at 65°K, in fact, is 30 mho cm²/watt, an order of magnitude or more greater than that found in normal photosensitive CdS crystals. The slope of the nearly exponential portion of the curve corresponds to an activation energy of 0.08 ev.

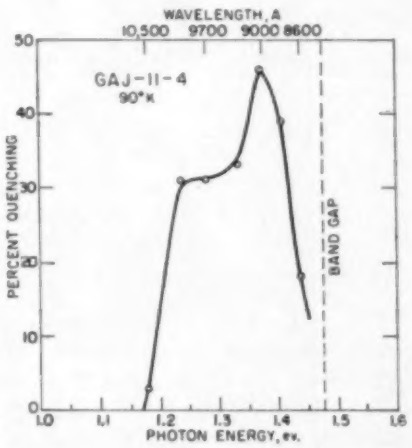

FIG. 4. Infrared quenching spectrum for GaAs crystal GAJ-11-4 at 90°K. The structure of the spectrum is probably not basically significant.

Dark Conductivity *vs* Temperature

For five of the crystals only one slope was found over the entire conductivity range measured, whereas for the other four crystals a smaller slope was found at low temperatures. Since the crystals involved were partially compensated *n*-type, with N_D donors partially compensated by N_A acceptors, in the range where $n \ll N_A$,[1]

$$E_f = E + kT \ln\left[\frac{N_A}{N_D - N_A}\right] \qquad (5)$$

where E_f is the distance between the bottom of the conduction band and the Fermi level, and E is the activation energy of the uncompensated donor centers. Since the slope of a plot of ln conductivity *vs* $1/T$ is given by:

$$\text{slope} = \frac{T}{k}(dE_f/dT) - \frac{E_f}{k} \qquad (6)$$

the slope is equal to $-E/k$.

The dark conductivity activation energies at higher temperatures suggest three levels: one at about 0.5 ev below the conduction band (0.47, 0.43, 0.53 ev), a second at about 0.6 ev below the conduction band (0.61, 0.64, 0.57 ev), and a third at about 0.7 ev below the conduction band (0.675, 0.715, 0.71 ev). (The calculation of these energy values assumes that the temperature dependence of the density of conduction band states cancels out the temperature dependence of the mobility. Some experimental evidence indicates that the mobility may be fairly invariant with temperature; under this condition, the same data give activation energies about 0.04 ev lower in any specific case.) In general, the lower activation energies are found in the more conducting samples. In an intrinsic sample, the activation energy would be ½ the band gap, or assuming a band gap of 1.4 ev, about 0.7 ev. In such an intrinsic material, the room temperature dark conductivity should be about 10^{-9} mho/cm. Sample GAJ-15-2 comes closest to fulfilling these criteria, although it is almost certainly not an intrinsic sample. See Fig. 7.

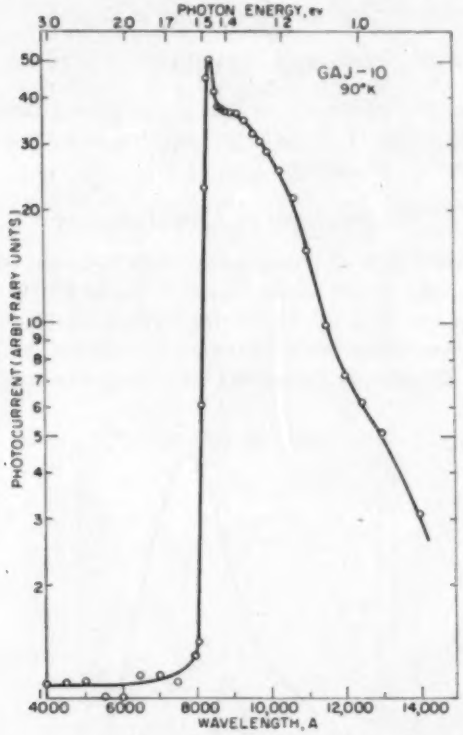

FIG. 5. Spectral response of photoconductivity in GaAs crystal GAJ-10 at 90°K.

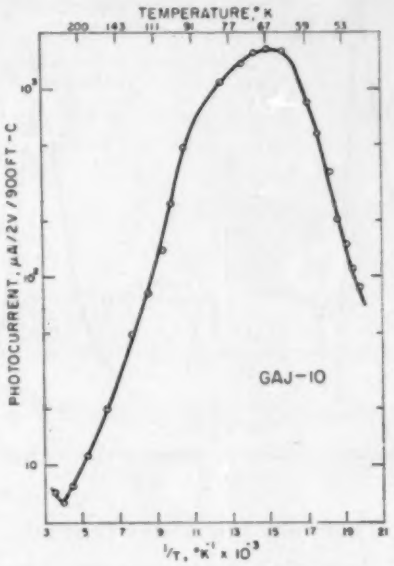

FIG. 6. Temperature dependence of photocurrent for GaAs crystal GAJ-10. Maximum sensitivity reached at 65°K is an order of magnitude greater than that of sensitive CdS crystals.

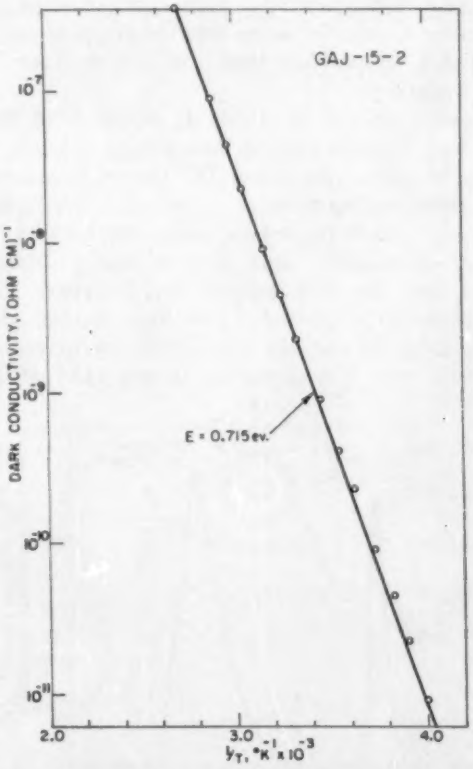

FIG. 7. Temperature dependence of dark conductivity in GaAs crystal GAJ-15-2, showing activation energy of ½ the band gap. Data points are only illustrative since the data were taken from a continuous recording.

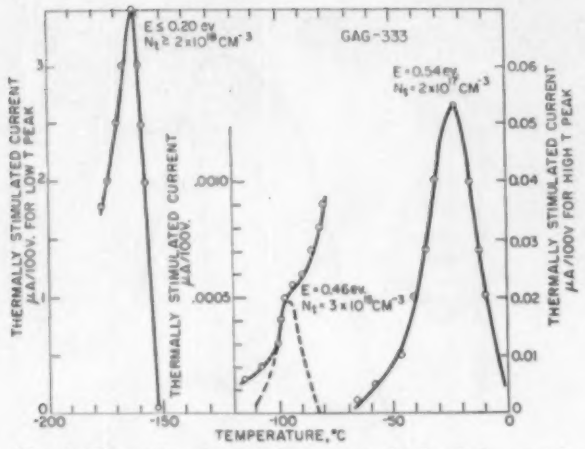
GAG-333
E ≤ 0.20 ev
E = 0.54 ev
E = 0.46 ev
THERMALLY STIMULATED CURRENT μA/100V. FOR LOW T PEAK
THERMALLY STIMULATED CURRENT μA/100V.
THERMALLY STIMULATED CURRENT μA/100V FOR HIGH T PEAK
TEMPERATURE, °C

FIG. 8. Thermally stimulated current peaks for GaAs crystal, GAG-333. Note the change in scale for the different peaks.

Thermally Stimulated Current

Table I shows that there are at least two principal trapping centers in each crystal. One of these is shallow with an activation energy ≤ 0.2 ev; it appears in every crystal except GAJ 7. This trapping center might be a compensated donor center, but since it appears with very high density in low resistivity samples, such as GAJ 333 and GAJ 15-2, it might equally well be a hole trap rather than an electron trap. The experimental fact that the thermally stimulated current drops essentially to zero between this low-temperature peak and higher temperature peaks, is also in favor of the latter hypothesis.

In every crystal of Table I, except GAJ 10 and GAJ 15-2, a deep trap is found lying 0.55 ± 0.02 ev below the conduction band. The thermally stimulated peak corresponding to this trap occurs in that temperature range where the *n*-type dark conductivity is becoming appreciable, and the thermally stimulated current and the dark current are frequently of the same order of magnitude. The high conductivity of sample GAJ 10 excludes the possibility of observing this peak even if present. In crystal GAJ 15-2, the crystal with the highest resistivity and dark conductivity activation energy, the deep trap observed has a significantly higher activation energy, about 0.63 ev. In other crystals of this same type isolated examples have been found where traps of depth 0.63 ev and 0.70 ev are measured in the same sample. It is proposed that these trapping centers are compensated donor centers, the same donor centers as give rise to the measured dark conductivity. The 0.55 ev peak commonly found may well be made up of unresolved 0.5 and 0.6 ev components.

As shown in Table I, trap densities vary from 10^{15} to 10^{18} cm^{-3}. The smallest density of deep traps is found in the highest resistivity sample, GAJ 15-2. Typical thermally stimulated current curves for samples GAG 333 and GAJ 15-2 are shown in Figs. 8 and 9. Note that a different current scale is used for each peak.

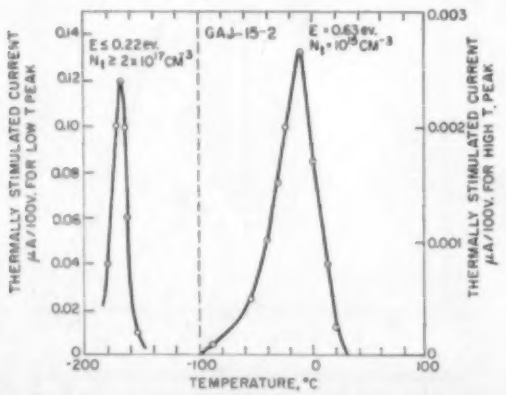
GAJ-15-2
E ≤ 0.22 ev
E = 0.63 ev
THERMALLY STIMULATED CURRENT μA/100V. FOR LOW T PEAK
THERMALLY STIMULATED CURRENT μA/100V. FOR HIGH T PEAK
TEMPERATURE, °C

FIG. 9. Thermally stimulated current peaks for GaAs crystal GAJ-15-2. Note the change in scale for the two peaks.

Sb_2S_3 RESULTS

A tabular summary of the experimental results is given in Table II, for the three crystals of *n*-type Sb_2S_3 described in this paper.

Photocurrent *vs* Light Intensity

The variation of photocurrent with light intensity is summarized in the last column of Table II. At room temperature n is 0.5 in all the crystals, and at liquid nitrogen temperature n is between 0.6 and 1.0. Majority carrier lifetimes lie between 1 and 10 microseconds.

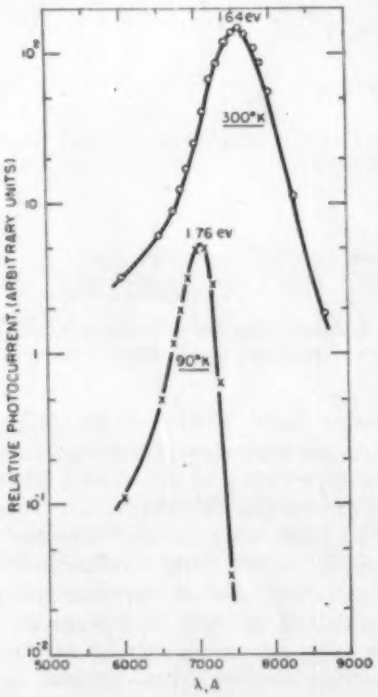

FIG. 10. Spectral response of photoconductivity in Sb_2S_3 crystal grown over a melt with stoichiometric proportions, at room temperature and at 90°K.

TABLE II. Summary of results on *n*-type Sb_2S_3 crystals.

Sample	Dark cond. at *RT*, mho/cm	Dark cond. slope, ev	Sens. at *RT*, mho/cm²/watt	*PC* band gap, ev 300°K	*PC* band gap, ev 90°K	Therm. stim. current *E*, ev	Therm. stim. current N_t, cm⁻³	Photocurrent *vs* *T* i(90°K)/i(min)	Photocurrent *vs* *T* *T*, °K for i(min)	Photocurrent *vs* *T* i(300°K)/i(min)	$\Delta i_n L^n$ 300°K	$\Delta i_n L^n$ 90°K
Excess Sb	3×10^{-8}	0.52	7×10^{-4}	1.65	1.77	0.34	4×10^{15}	3	173	5	0.51	0.62
						0.61	4×10^{16}					
Stoichiomet.	6×10^{-8}	0.60	5×10^{-4}	1.63	1.76	0.58	2×10^{17}	6	143	12	0.49	0.76
Excess S	8×10^{-9}	0.61	2×10^{-5}	1.63	1.76	0.57	6×10^{16}	3	158	14	0.53	0.94

Spectral Response of Photoconductivity

Photoconductivity-determined band gaps for Sb_2S_3 are about 1.64 ev at room temperature and 1.76 ev at liquid nitrogen temperature, corresponding to a temperature coefficient of band gap of -5.7×10^{-4} ev/deg. Typical spectral response curves, for the "stoichiometric" Sb_2S_3 crystals, are given in Fig. 10. The "stoichiometric" crystals were the only ones to show an infrared quenching effect. At liquid nitrogen temperature, quenching of photoconductivity was caused by light with energy as high as 1.65 ev, with low-energy cutoff at 0.95 ev; the spectrum is shown in Fig. 11. The effect in Sb_2S_3 is therefore similar to that in GaAs in that the "sensitizing" centers involved have levels lying above the middle of the gap.

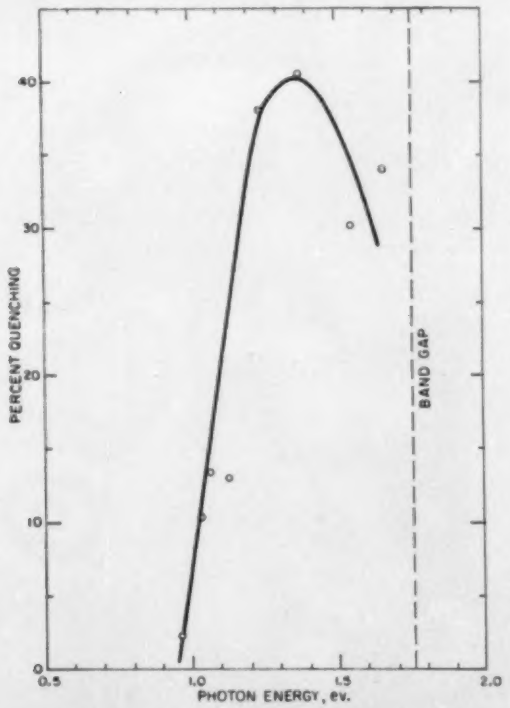

FIG. 11. Infrared quenching spectrum for Sb_2S_3 crystal grown over a melt with stoichiometric proportions. Measured at 90°K.

Dark Conductivity *vs* Temperature

All three of the crystals showed comparable dark conductivity, except for the slightly lower value obtained for those crystals grown from a melt with excess S. The activation energy for dark conductivity was also essentially the same in all three crystals, lying between 0.5 and 0.6 ev.

Thermally Stimulated Current

Except for the 0.34-ev level in the "excess Sb" sample, all thermally stimulated current peaks had to be obtained by subtraction of a relatively large dark current from the total current. Figure 12 shows the

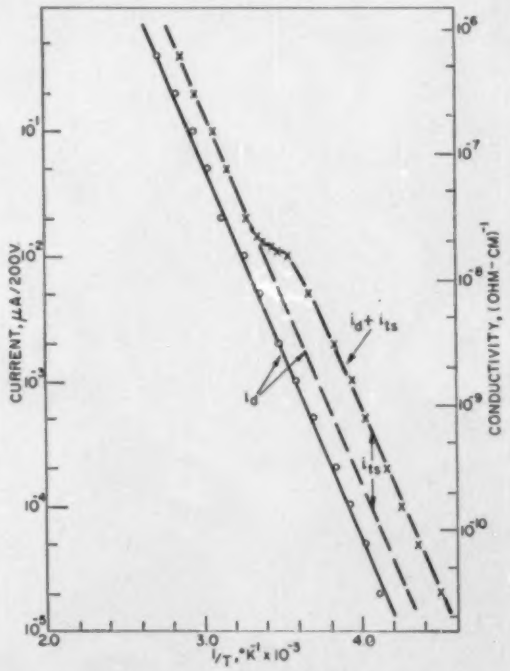

FIG. 12. Dark conductivity, and total conductivity after low-temperature photoexcitation, as a function of temperature for Sb_2S_3 crystal grown over a melt with excess S. Mismatch of the two curves at high temperature can be neglected as due to a slight nonreproducibility.

data for the "excess S" crystal. The absolute difference between the high temperature conductivities is the result of a slight nonreproducibility in the measurement and can be neglected. A comparison of the activation energies for dark conductivity with the recurring trap energy obtained from thermally stimulated current data, together with the shape of the curves of Fig. 12, indicates that the thermally stimulated current arises from trapping of carriers by compensated donors with level about 0.6 ev below the bottom of the conduction band. This is analogous with the results obtained with GaAs.

Photosensitivity *vs* Temperature

The photocurrent in all three samples shows a minimum at about 160°K, increasing by between 3 and 6 when the temperature is decreased to 90°K, and increasing by between 5 and 14 when the temperature is increased to 300°K. Only in the "excess S" sample did the photocurrent level off with increasing temperatures, up to about 350°K.

A photocurrent that increases in magnitude over the same temperature range that the dark conductivity is increasing and of appreciable magnitude, suggests that the un-ionized centers giving rise to the conductivity are playing an important role as recombination centers. Such behavior has been reported in certain CdSe crystals,[6] In_2S_3 crystals,[7] HgI_2 crystals,[8] and has been found also in Ga_2Se_3[9] crystals. Thus a single set of centers can have three well defined functions: (a) uncompensated, increase the dark conductivity as they become thermally ionized; (b) uncompensated and unionized, determine recombination kinetics; and (c) compensated, trap photoexcited majority carriers, giving rise to thermally stimulated current and decreased speed of response.

[6] R. H. Bube and L. A. Barton, J. Chem. Phys. **29**, 128 (1958).
[7] R. H. Bube and W. H. McCarroll, J. Phys. Chem. Solids **10**, 333 (1959).
[8] R. H. Bube, Phys. Rev. **106**, 703 (1957).
[9] R. H. Bube and E. L. Lind (unpublished data).

SUMMARY

Photoelectronic analysis of high-resistivity *n*-type GaAs and Sb_2S_3 give the following major results.

The band gap of GaAs may well be 3% to 5% higher than the 1.35-ev value commonly reported in the past, i.e., 1.39–1.42 ev at room temperature. The band gap of Sb_2S_3 at room temperature is 1.64 ev. Temperature coefficients of band gap are -4.0×10^{-4} ev/deg for GaAs, and -5.7×10^{-4} ev/deg for Sb_2S_3.

Evidence is obtained for the existence of the following levels in GaAs: donor levels lying 0.5, 0.6, and 0.7 ev below the bottom of the conduction band, and an acceptor level lying 0.2 ev above the top of the valence band. Compensated donor levels act as electron traps; compensated acceptor levels act as hole traps. Uncompensated donor levels give rise to the observed *n*-type conductivity. In Sb_2S_3, similar evidence is obtained indicating that the dark conductivity arises from uncompensated donors lying 0.6 ev below the bottom of the conduction band, and that trapping is associated with the compensated portion of these donors.

The observation of an increasing photosensitivity in that temperature range where the dark conductivity is also of appreciable magnitude and increasing rapidly, suggests that un-ionized uncompensated donors in Sb_2S_3 and similar materials play an important role in recombination of photoexcited carriers.

A few isolated cases of low-temperature infrared quenching of photoconductivity were found in both GaAs and Sb_2S_3 crystals, the effect being similar in both crystals in that the levels involved lay above the middle of the band gap.

ACKNOWLEDGMENTS

The author is indebted to L. R. Weisberg, R. V. Jensen, P. G. Herkart, I. J. Hegyi, and J. Blanc for supplying the various crystals used in this investigation; to M. L. Schultz for assistance in obtaining the low-temperature data on GaAs crystal GAJ 10; and to L. R. Weisberg for helpful discussions.

JOURNAL OF APPLIED PHYSICS VOLUME 31, NUMBER 2 FEBRUARY, 1960

Thermal Initiation of Explosives

JOHN ZINN AND CHARLES L. MADER*
University of California, Los Alamos Scientific Laboratory, Los Alamos, New Mexico
(Received July 29, 1959)

Numerical solutions have been obtained for the nonlinear heat conduction equations arising in the theory of thermal explosions. Explosion times are calculated for externally heated spheres, cylinders, and slabs of several explosive materials, and the results are shown to agree with experiment.

INTRODUCTION

IF an explosive is heated or cooled, and if it decomposes according to a single first-order rate process, its internal temperature should be described by the equation,[1]

$$-\lambda\nabla^2T+\rho C(\partial T/\partial t)=\rho QZe^{-E/RT}. \quad (1)$$

Here T is temperature in °K, λ is thermal conductivity (cal deg^{-1} cm^{-1} sec^{-1}), ρ is density (g cm^{-3}), C is heat capacity (cal g^{-1} deg^{-1}), Q is heat of decomposition (cal g^{-1}), Z is collision number (sec^{-1}), E is activation energy (cal M^{-1}), R is the gas constant (1.987 cal M^{-1} deg^{-1}).

It will be assumed that the above constants are independent of temperature.

The Laplacian operator ∇^2, in the special cases of spheres, infinitely long cylinders, or infinite slabs, reduces to

$$(\partial^2/\partial x^2)+(m\partial/x\partial x),$$

if we require that the heating be uniform over the surface, ($m=0$ for slabs, 1 for cylinders, and 2 for spheres).

Where the reaction-heating term $(\rho QZ)\exp(-E/RT)$ is zero, Eq. (1) reduces to the well-known heat equation. In the one-dimensional case (infinite slab) this is

$$\partial^2T/\partial x^2=\rho C\partial T/\lambda\partial t. \quad (2)$$

Under the boundary conditions $T=f_0(x)$, when $t=0$ and $T=T_1$ at $x=0$ and $x=2a$, Eq. (2) has the solution:

$$T(x,t)=T_1+\frac{1}{a}\sum_{n=1}^{\infty}\exp\left(-\frac{n^2\pi^2\lambda t}{4\rho Ca^2}\right)\times\sin\frac{n\pi x}{2a}\int_0^{2a}[f_0(x)-T_1]\sin\frac{n\pi x}{2a}dx. \quad (3)$$

If at any time the temperature $f_0(x)$ is known at a sufficient number of points, the integrals can be evaluated numerically; thus the temperature distribution at later times can be calculated.

When the self-heating term is nonzero, we have for the infinite slab,

$$-\lambda(\partial^2T/\partial x^2)+\rho C(\partial T/\partial t)=\rho QZe^{-E/RT},$$

which has not been solved analytically. However, numerical solutions can be obtained in the following manner.

Suppose the time scale to be divided into equal intervals each τ sec long. We imagine that the heat of reaction is not liberated continuously, but instead is added to the system batchwise at the end of each interval. For purposes of calculating the amount of reaction heat liberated at any point in an interval τ it is convenient to assume that the temperature remains constant during τ, an approximation which improves as the intervals are made shorter. Thus, if in the absence of reaction during τ we calculate that the temperature at some point should be T, we can estimate that the reaction that has occurred in the interval should actually raise the temperature at the point to $T+(QZ\tau/C)\exp(-E/RT)$.

Suppose the slab is initially at a uniform low temperature T_0. At time zero the two faces at $x=0$ and $x=2a$ are suddenly raised to a higher temperature T_1. Treating the problem for the first small interval τ_1 as though the slab were inert, we obtain an approximation to the temperature distribution $T(x,\tau_1)$ after τ_1 sec, as given by Eq. (3), where $f_0(x)$ is set equal to T_0 and $t=\tau_1$. Due to the chemical reaction which will have occurred, this first estimate of the temperature should be revised to $T(x,\tau_1)+(QZ\tau_1/C)\exp[-E/RT(x,\tau_1)]$. During the next interval τ_2 the slab is again treated as inert, and a first approximation to the temperature is again given by Eq. (3), where this time we must set $f_0(x)$ equal to $T(x,\tau_1)+(QZ\tau_1/C)\exp[-E/RT(x,\tau_1)]$, and t equal to τ_2. Again the temperature rise due to reaction is added on. This process is repeated either until a steady state is attained, or until the temperature at some point in the slab reaches some very high value which may be said to define an explosion.

An exactly analogous technique has been applied to cylinders, where the inert heat equation takes the form,

$$\partial^2T/\partial r^2+(\partial T/r\partial r)=\rho C\partial T/\lambda\partial t.$$

Under the boundary conditions $T=f_0(r)$ when $t=0$ and

* Work performed under the auspices of the U. S. Atomic Energy Commission.
[1] D. A. Frank-Kamenetskii, Acta Physiochim. U.R.S.S. **10**, 365 (1939).

$T=T_1$ for $r=a$, this has the solution

$$T(r,t)=T_1+\frac{2}{a^2}\sum_{n=1}^{\infty}\frac{\exp[-(g_n^2\lambda t/\rho Ca^2)]}{J_1^2(g_n)}$$

$$\times J_0\left(\frac{g_n r}{a}\right)\int_0^a r(f_0(r)-T_1)J_0\left(\frac{g_n r}{a}\right)dr, \quad (4)$$

where the g_n are the roots of the zero-order Bessel function J_0.

The procedure has also been applied to spheres. Here the inert heat equation is

$$\partial^2T/\partial r^2+2\partial T/r\partial r=\rho C\partial T/\lambda\partial t,$$

and under the boundary conditions $T=f_0(r)$ when $t=0$ and $T=T_1$ for $r=a$ this has the solution:

$$T(r,t)=T_1+\frac{2}{ar}\sum_{n=1}^{\infty}\exp\left(-\frac{n^2\pi^2\lambda t}{\rho Ca^2}\right)$$

$$\times\sin\frac{n\pi r}{a}\int_0^a r(f_0(r)-T_1)\sin\frac{n\pi r}{a}dr. \quad (5)$$

The calculations were carried out on an IBM-704 digital computer.

RESULTS—GENERAL

The gross results of the calculations are not at all unexpected and might be summarized as follows.

If a given explosive in a charge of a given size and shape has its surface maintained at a temperature higher than a certain critical value, which we designate by T_m, it will eventually explode. If the surface temperature is kept below T_m a thermal explosion will not occur. This critical temperature decreases as the dimensions of the charge are increased.

If the charge is initially at room temperature, and its surface temperature is then raised to T_1, where T_1 is above T_m, the explosion will occur after a certain induction time which depends on the explosive, the geometry of the charge, and T_1. If T_1 is only slightly higher than the critical temperature T_m the induction time is relatively long, and the explosion develops at the center of the charge. With increasingly higher values of T_1 the induction time becomes progressively shorter and the explosion commences progressively closer to the surface. (See Figs. 1 and 2.) For a given value of T_1 the induction times for small charges are much shorter than for large ones.

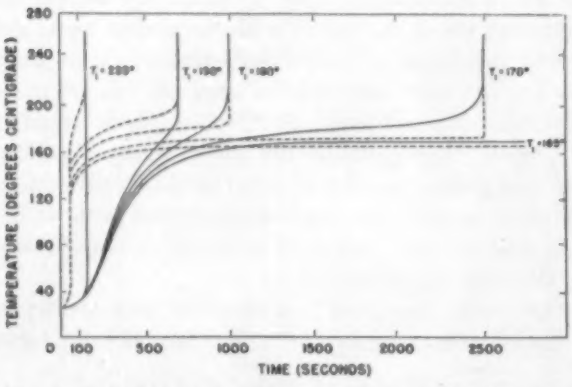

FIG. 1. Temperature *vs* time at two locations within a 1 in. diam sphere of RDX initially at 25°C for various values of T_1. Solid curve: $r/a=0$ (center of sphere); Dashed curve: $r/a=0.9$.

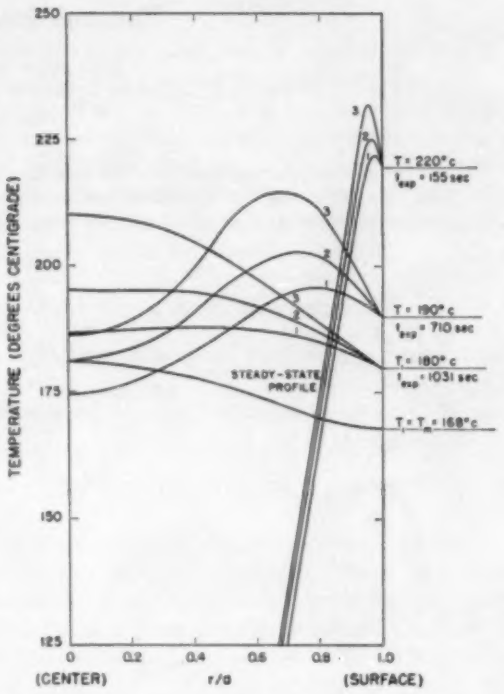

FIG. 2. Temperature profiles for times near the end of the induction period, as calculated for 1 in. spheres of RDX initially at 25°C. Curve 1: $t=0.90t_{exp}$; Curve 2: $t=0.95t_{exp}$; Curve 3: $t=0.98t_{exp}$. Also shown is the steady-state profile at the critical temperature, T_m.

Figure 1 shows the calculated variation of temperature with time at two locations within a 1-in sphere of RDX for various values of T_1. For relatively low surface temperatures the hottest region prior to explosion is at the center. Points near the surface remain relatively cool until the end of the induction period, suffering a discontinuous jump at the time of explosion. Somewhat the reverse situation applies when T_1 is high. The same facts are evident from Fig. 2, where the temperature *vs* position profiles are shown for various times near the end of the induction period.

For charges of a given size, shape, and composition it is convenient to plot logarithms of the calculated explosion times *vs* the reciprocal of the surface temperature T_1, where the charges all start out at a uniform low temperature T_0. For slabs, cylinders, and spheres these plots are linear over quite a large region, but bend upward sharply near the critical temperature T_m. At T_m

they become vertical, indicating an infinitely long induction period.

Frank-Kamenetskii[1] and Chambré[2] have solved Eq. (1) under the steady state condition $\partial T/\partial t=0$, obtaining the following expression for critical temperature in terms of the related physical parameters:

$$T_m=\frac{E}{2.303R\log(\rho a^2QZE/\lambda RT_m^2\delta)}, \tag{6}$$

where $\delta=0.88$ for slabs, 2.00 for cylinders, and 3.32 for spheres. This equation can be quickly solved by iteration and gives values for T_m which are in agreement with those obtained from the present calculated $\log t_{exp}$ *vs* $1/T_1$ curves.

It will be noted from the method of calculation and from the form of Eqs. (3)–(5) that for a given shape only three parameters are used to describe the charge, namely $\rho a^2QZ/\lambda$, E, and $\lambda/\rho Ca^2$, instead of seven independent ones. Thus one can make the following generalizations: (1) Changing Q by a multiplicative factor is entirely equivalent to changing Z; (2) In the same way, ρ, a^2, and $1/\lambda$ are equivalent; (3) E and C are independent of the others.

The t_{exp} *vs* $1/T_1$ relationship is of the form

$$t_{exp}=\frac{\rho Ca^2}{\lambda}F(E/T_m-E/T_1), \tag{7}$$

where F is a function depending only on the type of geometry (spheres, cylinders, or slabs) and the initial temperature T_0. Values of F as a function of the argument, $E/T_m-E/T_1$ are plotted in Fig. 3 for spheres, cylinders, and slabs, all initially at 25°C. Since T_m is given by Eq. (6), the relationship (7) together with Fig. 3 makes possible the calculation of explosion times for spheres, cylinders, or slabs of any arbitrary explosive (when ρ, C, a, λ, Z, Q, and E are known).

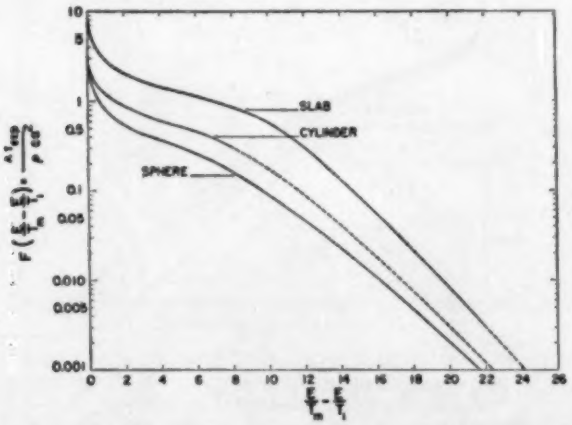

FIG. 3. Graphs of $\lambda t_{exp}/\rho Ca^2$ *vs* $E/T_m-E/T_1$ for spheres, cylinders, and slabs, all initially at 25°C.

[2] P. L. Chambré, J. Chem. Phys. **20**, 1795 (1952).

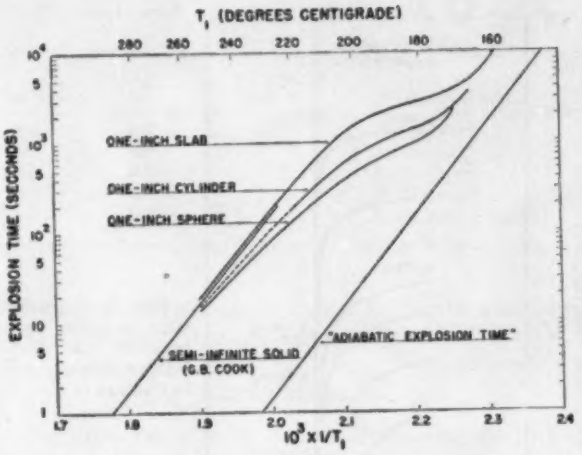

FIG. 4. Explosion times *vs* $1/T_1$ for RDX in various geometries. Initial temperature = 25°C.

Figure 4 shows the calculated explosion times *vs* temperature for three particular cases, namely 1 in. RDX spheres, cylinders, and slabs. The results can be explained qualitatively as follows. The critical temperatures T_m below which no explosions are obtained are related to the rate at which heat can escape to the surface, which in turn is related to the surface-to-volume ratio. The surface-to-volume ratios of spheres, cylinders, and slabs are respectively $3/a$, $2/a$, and $1/a$, if a represents radius or half-thickness. Thus for a given value of a the slab should have the lowest critical temperature. At relatively low temperatures explosion times are related to surface-to-volume ratios in the opposite manner. The sphere, having the smallest volume to be heated per unit surface, will explode the fastest.

Although at relatively low temperatures geometry has an important influence on induction times, its effect becomes less pronounced as temperature is increased. This is associated with the fact that for high external temperatures explosions begin near the surface of the explosive while the interior is still cool. Above 270°C the log t_{exp} *vs* $1/T_1$ plots for 1 in. RDX spheres, cylinders, and slabs are coincident (Fig. 4). Moreover they are coincident with the plots obtained by G. B. Cook[3] for a semi-infinite solid heated at its single surface. Cook's line, adjusted to correspond to our own choice of physical parameters, is included in Fig. 4.

Also plotted in Fig. 4 are "adiabatic" explosion times, defined by the relation

$$t_{exp}=\int^{T_{exp}}\frac{C}{QZ}\exp(E/RT)dt\cong\frac{CRT_1^2}{QZE}\exp(E/RT_1).$$

Physically this represents the time it would take for an infinite mass of explosive to ignite if it were initially at the uniform temperature T_1. The adiabatic explosion

[3] G. B. Cook, Proc. Roy. Soc. (London) **246**, 154 (1958).

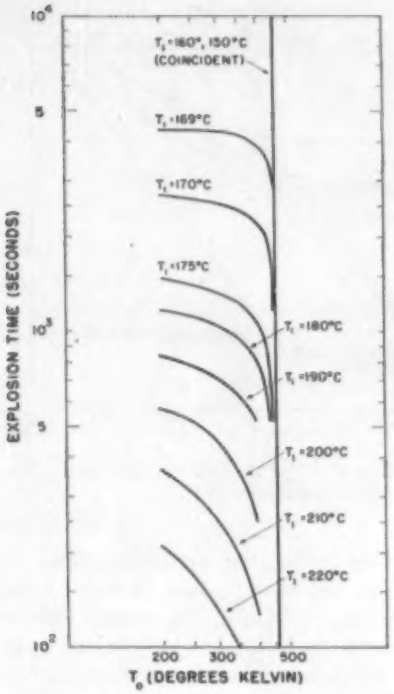

FIG. 5. Explosion time *vs* initial temperature for 1-in. RDX spheres at various values of T_1.

time is necessarily shorter than explosion times obtained on raising only the surface of the explosive to T_1.

The effect of initial temperature on explosion times has been investigated only for the case of spheres. Plots of explosion times for 1 in. RDX spheres *vs* their initial temperature T_0 are shown in Fig. 5, for various values of the surface temperature T_1. The following qualitative observations can be made: (1) If the explosive is initially cold, and its surface is raised to a temperature only slightly above T_m, the precise value of the initial temperature is relatively unimportant. The body of the explosive heats relatively quickly to T_1, regardless of the initial temperature. Then commences the slow process of self-heating, which takes up the major part of the induction period. For higher values of T_1 this is no longer the case. The self-heating process takes proportionately less time, and it is strongly influenced by conduction of heat to the cold interior; (2) If the initial temperature is less than T_1, and T_1 is lower than the critical temperature T_m no thermal explosions can occur. However, if T_0 exceeds T_1 (a rather hypothetical situation), explosions may occur even when the surface temperature is lower than T_m. For every value of T_1 below T_m there is a "critical" value of T_0 which, if exceeded, will lead to an explosion. This is related to the matter of "hot spots"[4] and will not be discussed further here.

Corresponding to the reduced explosion time plots of Fig. 3, in Fig. 6 the quantity $\lambda t_{exp}/\rho Ca^2$ is plotted *vs* $E/T_m - E/T_1$ for spheres with various initial temperatures. Figure 6, together with Eqs. (6) and (7), makes possible the calculation of explosion time for any sphere with any value of T_0.

The present calculational technique is limited in practice to temperatures not too far in excess of T_m. Within this region the reaction rate term is relatively small; hence the size of the time intervals τ can be made large enough to allow the Fourier series in (3), (4), and (5) to converge at a reasonable rate. By varying τ it is found that accuracy suffers at temperatures where $(QZ\tau/C)\exp(-E/RT)$ exceeds 1°C.

For economy of computing time it has been necessary to write a series of machine programs for each of the geometries considered. To cover a region of temperatures near to or lower than T_m a program is used which carries the Fourier series summations over sixteen terms and performs integrations by means of Simpson's rule. When more terms are considered Simpson's rule becomes inefficient, and it has been necessary to use a method which is similar in principle to that of Filon[5] although not requiring that the region of integration be divided into equally spaced intervals.[6] The most extensive machine programs extend the Fourier summations over 500 terms, allowing τ to be as small as $5\rho Ca^2/\lambda \times 10^{-6}$.

SPECIFIC CALCULATIONS

Reliable thermochemical data for explosives are quite scarce. Much of the available literature is abstracted in Picatinny Arsenal Report 1740 (1958), and the parameters used in these calculations are mostly from this source. For other parameters where no data exist, one is forced to guess, and the guesses which appear here are probably reliable to within a factor of three.

Literature values for E and Z are generally in poor agreement. The uncertainties are of such magnitude as

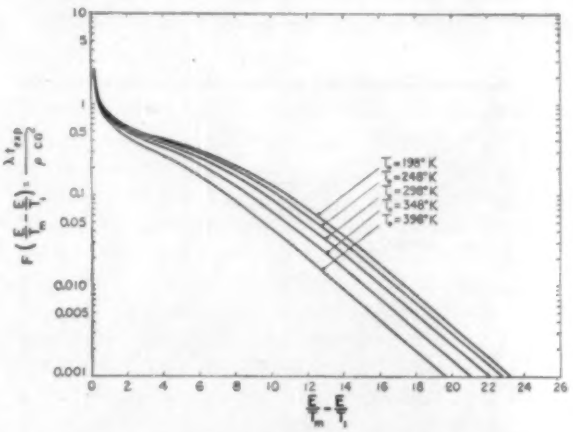

FIG. 6. Graphs of $\lambda t_{exp}/\rho Ca^2$ *vs* $E/T_m - E/T_1$ for spheres with various initial temperatures.

[4] E. K. Rideal and A. J. B. Robertson, Proc. Roy. Soc. (London) **A195**, 135 (1948).

[5] L. N. G. Filon, Proc. Roy. Soc. (Edinburgh) **49**, 38 (1928–1929).

[6] John Zinn, Commun. Assoc. Computing Machinery (to be published).

Table I. Parameters used in the calculations.

Explosive	ρ (g/cc)	C cal/g/°C	λ cal/°C/cm/sec	Q cal/g	Z sec^{-1}	E kcal/M	Source of E and Z
RDX	1.8	0.5	0.0007	500	$10^{18.5}$	47.5	Robertson[8]
75/25 cyclotol	1.7	0.5	0.0007	375	$10^{18.5}$	47.5	Robertson[8]
50/50 pentolite	1.65	0.5	0.0005	250	$10^{20.1}$	52.3	Robertson[9]
TNT	1.6	0.5	0.0005	500	$10^{11.4}$	34.4	Robertson[10]
TNT	1.6	0.5	0.0005	500	$10^{17.2}$	43.4	Cook and Abegg[11]

to overshadow any uncertainties arising from the other parameters. Experiments at this Laboratory[7] tend to confirm the kinetic constants determined by Robertson[8,9] for RDX and PETN, and these were used in the calculations. For TNT, on the other hand, values of E and Z were determined both by Robertson[10] and by Cook and Abegg,[11] and their disagreement causes a difference of 90° in T_m as calculated by Eq. (6).

Data on heats of decomposition are nonexistent. The value of 500 cal/g is assumed here for all explosives considered.

For mixed explosives like pentolite and cyclotol, the induction times are determined almost entirely by the more reactive component. The TNT acts mainly as a diluent, since it does not decompose appreciably below temperatures where self-heating by the other component is extremely fast. Thus for 50/50 pentolite we assume that the activation energy has the value appropriate for PETN (52.3 kcal per M), and the QZ has one-half the PETN value.

Log t_{exp} *vs* $1/T_1$ curves have been calculated for 1-in. cylinders of each of the explosives tested in Table I, using the parameters indicated. The curves are shown in Fig. 7 along with experimental points.

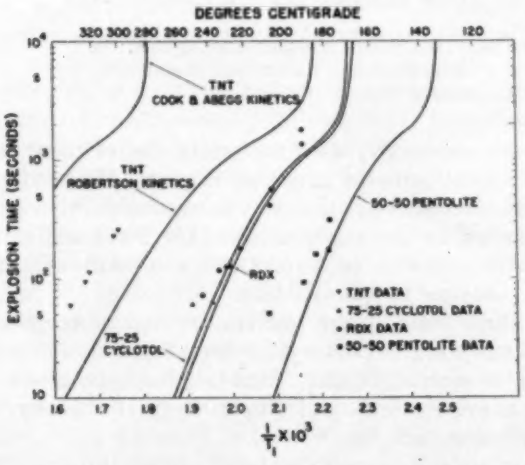

FIG. 7. Comparison of experimental and calculated induction times for various explosives.

EXPERIMENTAL

The experiment to be described was not specifically designed to fit the present model. Historically the shots preceded the calculations by a few years. Nevertheless, the resemblance is strong and a comparison of the data with the theory is of interest.

The main difference between the idealized model and "reality" lies in the fact that most explosives melt before much decomposition occurs. In all cases the kinetic parameters used in the calculations were determined above the melting point. However, no attempt has been made to allow for the changes in heat transfer properties that must take place when the explosive melts. The experimental arrangement is shown in Fig. 8. Before firing the thin-walled cylindrical capsule containing the pressed or cast explosive is suspended above the Dural heating block as shown. When the heating block has

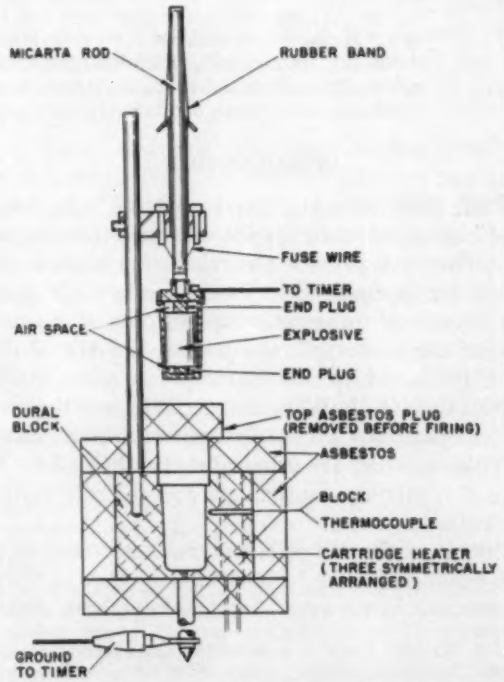

FIG. 8. The experimental arrangement.

[7] Rogers, Yasuda, and Zinn, Anal. Chem. (submitted for publication).
[8] A. J. B. Robertson, Trans. Faraday Soc. 45, 85 (1949).
[9] A. J. B. Robertson, J. Soc. Chem. Ind. (London) 61, 221 (1948).
[10] A. J. B. Robertson, Trans. Faraday Soc. 44, 977 (1948).
[11] M. A. Cook and M. T. Abegg, Ind. Eng. Chem., 48, 1090–1095 (1956).

Additional line broadening effects can be related to the nuclear magnetic moments of neighboring ions and random ordering, particularly of ions with different valence states. Calcium tungstate is exceptional in that its constituent ions have very low nuclear magnetic moments throughout. The isotopes which have nuclear magnetic moments occur to the extent of 0.13% in calcium, 14% in tungsten, and 0.04% in oxygen. Further, the moments possessed by these isotopes are quite small in comparison to the values possessed by atoms such as aluminum, sodium, and fluorine.

Measurements made by C. F. Hempstead[9] of these Laboratories on samples of $Na_{0.5}Y_{0.5}WO_4$ and $CaWO_4$, both containing Gd and having the scheelite structure, show large differences in line width although these crystals were prepared under the same conditions. The line width observed in $CaWO_4$ was less than 6 Mc (as low as $1\frac{1}{2}$ Mc was measured for very dilute manganese in $CaWO_4$). The line width for Gd observed in $Na_{0.5}Y_{0.5}WO_4$, in comparison, was approximately 600 Mc. This marked increase may be attributed to the effects of random ordering of Na^+ and Y^{3+} in the 8-fold sites in the scheelite structure and in some degree to the larger nuclear magnetic moments of Na^+ and Y^{3+}. When the ordering of these is completely random, the odds are roughly 10 to 1 that the electric fields resulting from variable arrangements of Na^+ and Y^{3+} in the nearest 8-fold sites about those containing Gd^{3+} will be different. By comparison, when Na^+ and Gd^{3+} are randomly distributed in $Ca_{0.99}Gd_{0.005}Na_{0.005}WO_4$, the odds are less than 1 to 100 that anything but Ca^{2+} will be located in the nearest 8-fold sites to Gd^{3+}. Thus, it is possible that the effects of random ordering are decreased by a factor of as much as 1000 in the $CaWO_4$.

Calcium tungstate can be considered nearly ideal as a host lattice for the study of many paramagnetic ions. The chemical stability of this compound and the tungstates of Mg, Zn, and Cd as compared to water soluble salts is also of considerable advantage. The $SrWO_4$ and $BaWO_4$ compositions offer one possible advantage over $CaWO_4$ for applications involving optical transitions in that the former do not show a broad band luminescence under 2537 A excitation as do $CaWO_4$ and the other tungstates discussed.

[9] C. F. Hempstead and K. D. Bowers (to be submitted to Phys. Rev).

ACKNOWLEDGMENTS

We wish to thank K. D. Bowers for his very helpful discussions on the properties of paramagnetic materials, and M. Peter and C. F. Hempstead for permission to cite their line width measurements.

Effect of the Polarity of the III-V Intermetallic Compounds on Etching

J. W. Faust, Jr., and A. Sagar
Westinghouse Research Laboratories, Pittsburgh 35, Pennsylvania

(Received August 10, 1959)

For the III-V intermetallic compounds, the ⟨111⟩ directions are polar axes. The shape of etch pits bounded by crystallographic planes and the presence or absence of pits at dislocations are influenced by the effect of the polar axes on the etch rates. Studies of these effects are reported for several etches on InSb, InAs, GaSb, and GaAs. Correlation of these studies with published x-ray investigations shows that these etches reveal dislocations and truncated pyramidal pits only on {111} surfaces that are at the group III end of the polar axis. A difference in the shape of the pits on opposite {100} surfaces was found and is explained by means of the polar axes.

THE III-V intermetallic compounds have a zinc-blende structure, which belongs to the space group $F\bar{4}3m$ in the Hermann-Mauguin notation, or Td^2 in the older Schoenflies notation. The crystal model for this structure is shown in Figure 1 where the atoms marked *A* represent elements of group III of the periodic system and the atoms marked *B* represent group V elements. In assigning planes and directions to this model, we have used the convention of Dewalt,[1] i.e., the {111} plane containing atoms of group III is the $(\bar{1}\bar{1}\bar{1})$ plane. Examination of this structure shows that the {111} planes are composed entirely of either *A* atoms or *B* atoms. Along any specific [111] direction these planes form a series of pairs, each pair containing a plane of *A* atoms followed by a plane of *B* atoms. In the opposite direction, $[\bar{1}\bar{1}\bar{1}]$, the order is reversed, i.e., the plane of *B* atoms is followed by a plane of *A* atoms. For such a structure the [111] direction is known as the polar axis.

The polar axis has been shown to cause a difference in the behavior of several processes on opposite {111} planes (for example (111) and $(\bar{1}\bar{1}\bar{1})$). The piezoelectric effect[2] as well as differences in the action of etches at dislocations,[3–5] the rates of anodic oxidation,[1] and the thickness of the oxide layer formed by anodic and chemical oxidation[6] have been reported for InSb. The difference in shape of characteristic etch pits[7] has been reported for various surfaces of GaAs.

Recently special x-ray techniques have been used to identify the {111} surfaces upon which dislocations have been revealed by etching. The results are reported in.[8,9] Our etching studies on the III-V intermetallic compounds have yielded some interesting observations that are pertinent to these two recent papers and a difference, which has apparently gone unnoticed, in the etch figures on {001} surfaces.

{111} SURFACES

One part of the etching investigation consisted of studying the action of a number of different etches on the same face of a slice. Slices of InSb, InAs, GaSb, and GaAs were cut with two large faces parallel to {111} planes. A mark was placed on one of the large faces of each slice to distinguish it from the other face. The two large faces of the slices were lapped with 3200-mesh alundum before etching. The etches contained an oxidizing agent, complexing agent, and modifiers except for an etch for InAs, which simply consisted of conc HCl. The composition of the etches are given in Table I. All of the etches were acidic except the one containing NaOH, which was basic.

The appearance of the surfaces produced by the etches can be divided into four types: (1) relatively smooth, with dislocations revealed as conical pits or as pyramidal pits; (2) relatively smooth, with no pits;

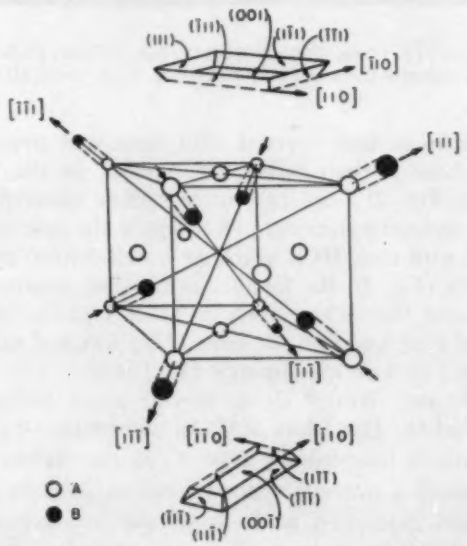

FIG. 1. Structure of the III-V intermetallic compounds and sketch of pits on opposite {001} planes. Open circles denote group III atoms, black circles group V.

[1] J. F. Dewalt, J. Electrochem. Soc. **104**, 244 (1957).
[2] J. H. Wasilik and R. B. Flippen, Phys. Rev. Letters **1**, 332 (1958).
[3] R. E. Maringer, J. Appl. Phys. **29**, 1261 (1958).
[4] J. D. Venables and R. M. Broudy, J. Appl. Phys. **29**, 1025 (1958).
[5] J. W. Faust, Jr., paper presented at Electrochem. Society Meeting, Cincinnati, May, 1955 (unpublished).
[6] Lavine, Rosenberg, and Gatos, J. Appl. Phys. **29**, 1131 (1958).
[7] H. A. Schell, Z. Metallkunde **48**, 158 (1957).
[8] J. G. White and W. C. Roth, J. Appl. Phys. **30**, 946 (1959).
[9] E. P. Warekois and P. H. Metzger, J. Appl. Phys. **30**, 960 (1959).

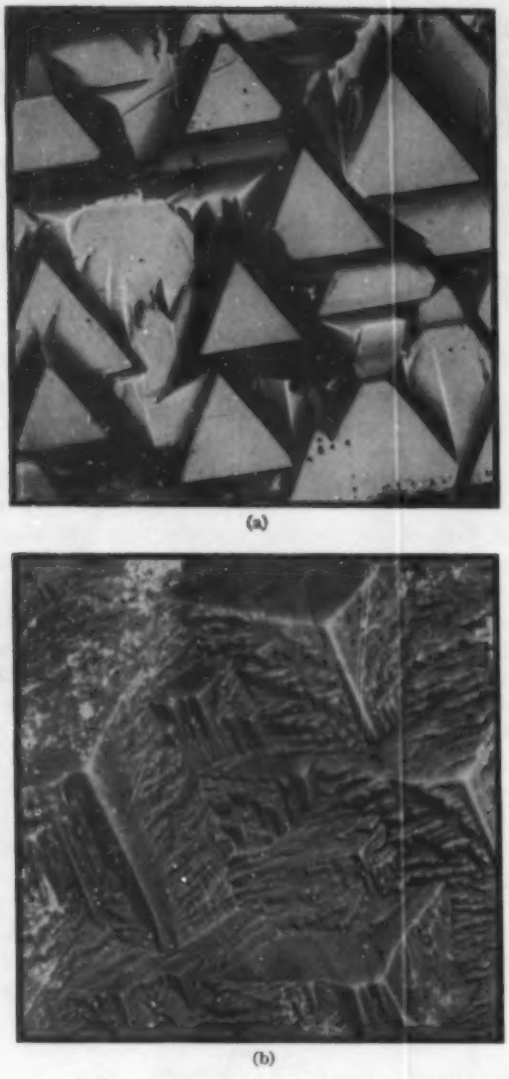

FIG. 2. (a) $(\bar{1}\bar{1}\bar{1})$ face. (200×) (b) (111) face. (500×) Etch figures on opposite faces of {111} InAs slice. Etch: conc. HCl.

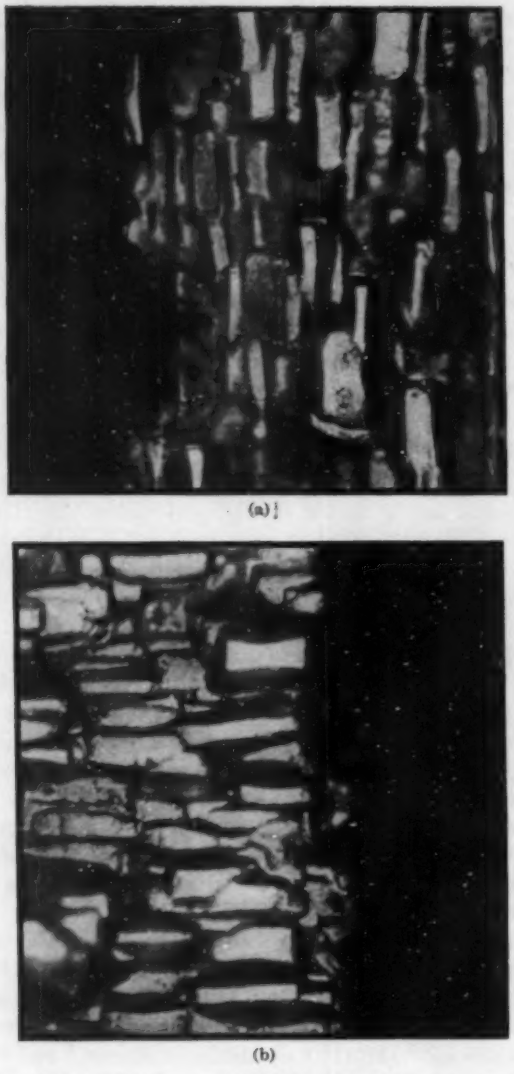

FIG. 3. (a) (001) face. (b) $(00\bar{1})$ face. Etch figures on opposite faces of {001} GaSb slice (500×). Etch: 1 part H_2O_2; 1 part HCl; 2 parts H_2O. Edge is parallel to a [110] direction.

(3) entire surface covered with truncated pyramidal pits whose bottom facets are parallel to the {111} planes (Fig. 2); and (4) entire surface covered with poorly defined pyramidal pits except in the case of InAs etched with conc HCl, which gave well-defined pyramidal pits (Fig. 2). We found that for each intermetallic compound the etches given in Table I produced surfaces of type 1 or 3 on the same {111} face and surfaces of type 2 or 4 on the opposite {111} face.

Roth and White[8] using special x-ray techniques identified the {111} face of GaAs that produced pits at dislocations (our surface type 1) as the surface that contained Ga atoms (i.e., the Ga end of the polar axis). Warekois and Metzger,[9] using similar techniques, showed that for InAs, pits were produced at dislocations on the {111} surface that contained In atoms. Thus, from these two papers and from our results, it seems evident that the {111} faces that yield surfaces of types 1 and 3 are the faces containing the group III atoms, or using the notation of Dewalt,[1] the $(\bar{1}\bar{1}\bar{1})$ planes.

By studying the shape of the truncated and untruncated pyramidal pits and their growth on repeated etching, we can say that the $(\bar{1}\bar{1}\bar{1})$ planes have a slower etch rate than the (111) planes. We have determined the etch rates, from weight loss measurements on these two planes of GaSb, and we find no discrepancy with the conclusions arrived at from the pit studies.

{100} SURFACES

Another symmetry property of this structure is that the cube axes are not simple fourfold axes but are fourfold inversion axes. Such a symmetry axis should

result in a difference in the etch pits on opposite faces cut parallel to {001} planes. We have been able to demonstrate this effect on GaSb and InSb. The photomicrographs given in Fig. 3 are the (001) and (00$\bar{1}$) surfaces of GaSb etched in 1 part conc HCl, 1 part conc H_2O_2 and 2 parts water. The edge shown in these photomicrographs lies along a [110] direction. One can see that the pits are rectangular rather than square and that the pits on the (00$\bar{1}$) are rotated 90° to those on the (001). Optical goniometric measurements show the flat bottoms to be {001} planes and the side facets to be {111} planes. Figure 1 shows clearly that this effect is a direct result of the polar ⟨111⟩ axes. Looking at the top plane, the (001), we see that the [111] and [$\bar{1}\bar{1}$1] directions have the same polarity but opposite to the [1$\bar{1}$1] and [$\bar{1}$11] directions. Since planes of opposite polarity have different etch rates, the pits will be rectangular as we have found. The [111] and [$\bar{1}\bar{1}$1] directions are the normals to the fast etching planes, and thus these planes should bound the pits along the long axis on the (001) planes, as shown in the pit drawing at the top of the figure. Looking at the bottom plane, the (00$\bar{1}$), we see that the polarity of all these directions is reversed, resulting in a 90° rotation of the pits with respect to the pits on the (001) face. The pit drawing for the (00$\bar{1}$) face is shown at the bottom of the figure.

The polar nature of the [111] axes does not affect the shapes of the pits found by etching with molten metals.[10]

TABLE I.

Intermetallic compound	Etch	
InSb	H_2O_2:HF:H_2O	1:1:4
	HNO_3:HF:H_2O	1:1:4
	HNO_3:HF	1:1
InAs	conc HCl	
	H_2O_2:HF:H_2O	1:1:4
	HNO_3:H_2O_2:tartaric acid[a]	1:1:6
	HNO_3:HF:acetic acid:Br_2	75:15:15:.06
GaSb	H_2O_2:HCl:H_2O	1:1:2
	HNO_3:tartaric acid[a]	1:3
	HNO_3:HF:H_2O	1:1:1
GaAs	H_2O_2:HF:H_2O	1:1:4
	HNO_3:tartaric acid[a]	3:1
	HNO_3:HCl:H_2O	1:1:2
	H_2O_2:NaOH[a]	3:1

[a] 40% aqueous solution.

ACKNOWLEDGMENTS

The authors wish to acknowledge the assistance of J. Patchel and Miss S. Warner.

[10] A. Sagar, thesis, University of Pittsburgh, 1959 (unpublished). A paper on etching by molten metals (to be published).

Effect of Oxide Layers on the Diffusion of Phosphorus into Silicon*

R. B. Allen, H. Bernstein, and A. D. Kurtz†
Semiconductor Division, Minneapolis-Honeywell, Boston, Massachusetts
(Received August 17, 1959)

The diffusion of phosphorus from the vapor phase into single crystal silicon has been studied. The experimental data are analyzed in terms of a two-layer diffusion model, leading to the determination of a diffusion constant for phosphorus in the oxide. The resulting diffusion constant at 1150°C is found to be 2.1×10^{-15} cm/sec[2] with an activation energy of 1.4 ev.

I. INTRODUCTION

FROSCH and Derick[1] have found that a thermally grown silicon oxide film can be used to impede the diffusion of certain of the Group III and Group V impurities into bulk silicon. The technique of "oxide masking" has been employed in the fabrication of double-diffused silicon transistor structures, notably the NPN "mesa" transistor, in which the geometry of the emitter region is controlled by diffusing phosphorus into a silicon crystal through a hole in the oxide. This investigation is intended to study the diffusion of phosphorus from the vapor phase in the temperature range 1125°C to 1250°C through oxide films 0.1 μ to 0.4 μ thick grown in wet nitrogen gas at 1250°C. Preliminary results of a similar investigation have been reported by Sah, Sello, and Tremere.[2] The degree to which a film can mask under specific conditions of oxidizing time and temperature, diffusion time and temperature, and diffusant vapor pressure can be determined by measuring the concentration of phosphorus just beneath the oxide layer relative to the concentration which results when no film is present. A simple diffusion model has been analyzed involving a composite solid in which the diffusion constant of phosphorus in the oxide layer is found to be about three orders of magnitude smaller than the diffusion constant reported by Fuller and Ditzenberger[3] for phosphorus in bulk silicon. The concentration of phosphorus which has penetrated the oxide film is found to decrease rapidly with increasing oxide thickness and decreasing diffusion time and temperature, in qualitative agreement with the predictions of the theoretical model.

II. DIFFUSION MODEL

A one-dimensional diffusion model is considered, consisting of a slab of medium 1 (oxide) of finite thickness x_0 on a semi-infinite block of medium 2 (bulk silicon). The boundary between the two media is taken to be at $x=0$. The concentration of the diffusant species (phosphorus) as a function of distance and time is denoted by $C_1(x,t)$ in region 1 and $C_2(x,t)$ in region 2 with respective diffusion constants D_1 and D_2. Under the conditions of open-tube diffusion from the vapor phase the concentration of phosphorus at the oxide surface, $x=-x_0$, is assumed to be held constant at a value C_0 for the duration of the diffusion. Consequently the solution of the diffusion equation:

$$\begin{aligned} D_1\frac{\partial^2 C_1(x,t)}{\partial^2 x}&=\frac{\partial C_1(x,t)}{\partial t}, \quad \text{region 1 } -x_0<x<0,\\ D_2\frac{\partial^2 C_2(x,t)}{\partial^2 x}&=\frac{\partial C_2(x,t)}{\partial t}, \quad \text{region 2 } 0<x<\infty, \end{aligned} \tag{1}$$

with the initial and boundary conditions:

$$C_1=C_2=0, \qquad x>-x_0 \text{ and } t\leq 0, \tag{2}$$

$$C_1(-x_0,t)=C_0, \qquad t>0, \tag{3}$$

$$C_1(0,t)=C_2(0,t)\equiv C_s(t), \qquad t>0, \tag{4}$$

$$D_1\frac{\partial C_1}{\partial x}=D_2\frac{\partial C_2}{\partial x}, \qquad \text{at } x=0 \text{ and } t>0, \tag{5}$$

$$C_2(x,t)\to 0, \qquad \text{as } x\to\infty, \tag{6}$$

is found from standard treatments[4] to be

$$C_1(x,t)=C_0\sum_{n=0}^{\infty}\left(\frac{1-k}{1+k}\right)^n\left\{\operatorname{erfc}\left[\frac{(2n+1)x_0+x}{L_1}\right]-\left(\frac{1-k}{1+k}\right)\operatorname{erfc}\left[\frac{(2n+1)x_0-x}{L_1}\right]\right\}$$

in the region

$$(-x_0<x<0); \tag{7}$$

$$C_2(x,t)=\frac{2kC_0}{1+k}\sum_{n=0}^{\infty}\left(\frac{1-k}{1+k}\right)^n\operatorname{erfc}\left[\frac{(2n+1)x_0}{L_1}+\frac{x}{L_2}\right] \tag{8}$$

in the region

$$(0<x<\infty)$$

* This research was supported in part by the Air Force Contract AF-19(604)-4099.
† Now at Kulite Semi-Conductor Products, Inc., Ridgefield, N. J.
[1] C. J. Frosch and L. Derick, J. Electrochem. Soc. **104**, 547 (1957).
[2] Sah, Sello, and Tremere, Bull. Am. Phys. Soc. Ser. II, 4, 157 (1959).
[3] C. S. Fuller and J. A. Ditzenberger, J. Appl. Phys. **27**, 544 (1956).
[4] H. S. Carslaw and J. C. Jaeger, *Conduction of Heat in Solids* (Clarendon Press, Oxford, England, 1959), second edition, p. 318.

where $k \equiv (D_1/D_2)^{\frac{1}{2}}$ and

$$L_1 \equiv (4D_1t)^{\frac{1}{2}} = \text{diffusion length in oxide}$$
$$L_2 \equiv (4D_2t)^{\frac{1}{2}} = \text{diffusion length in bulk.}$$

Figure 1 illustrates schematically the distribution in the composite layer. Conditions (5) and (6) assume that there is no discontinuity in diffusant concentration or diffusant current across the boundary at $x=0$; that is, no segregation of the diffusant in the oxide. Equations (7) and (8) can be greatly simplified if the condition $x_0/L_1 \geq 1$ is obeyed, since the complementary error function decreases very rapidly with increasing argument. Consequently only the zero order term need be retained in the summations. The inner surface concentration C_s in this approximation is given simply by

$$C_s \simeq 2k/1+kC_0 \operatorname{erfc}(x_0/L_1). \quad (9)$$

If the bulk contains a uniform initial concentration C_B of opposite conductivity type than the diffusant, a PN junction will result at a depth x_j when $C_s > C_B$. x_j is determined by setting $C_2(x,t)=C_B$ in Eq. (7) with the result:

$$C_B \simeq 2k/1+kC_0 \operatorname{erfc}[(x_0/L_1)+(x_j/L_2)]. \quad (10)$$

The effectiveness of an oxide film as a mask against the penetration of the diffusant into the bulk is determined essentially by the ratio C_S/C_B; that is, if $C_S/C_B<1$, we say that the oxide has masked, since the initial concentration is only partially compensated and no junction forms. If $C_S/C_B>1$, then only partial masking is achieved. In the limit as the oxide thickness approaches zero, the diffusant concentration in the bulk is given exactly by the equation

$$C_2(x,t)=C_0 \operatorname{erfc}(x/L_2), \quad (11)$$

and $C_s=C_0$.

The diffusion constant D_1 associated with the oxide can be determined in the following way. A "mask-failure" condition[2] is established by proper choice of diffusion time and temperature and oxide thickness such that the bulk is just compensated at the interface ($x=0$). For this situation, Eq. (9) can be written:

$$C_B \simeq \frac{2k}{1+k} C_0 \operatorname{erfc}\left[\frac{x_0^M}{(4D_1t^M)^{\frac{1}{2}}}\right] \quad \text{for} \quad \frac{x_0^M}{4D_1t^M} \geq 1, \quad (12)$$

where the superscript M refers to the "mask failure" condition. Consequently by fixing the bulk concentration C_B, surface concentration C_0, and the parameter k for a fixed diffusion temperature, the diffusion constant D_1 can be calculated from

$$D_1 = \frac{(x_0^M)^2}{4t^M} \frac{1}{\operatorname{arg}^2\left[\operatorname{erfc}\left(\frac{2k}{1+k}\frac{C_B}{C_0}\right)\right]}. \quad (13)$$

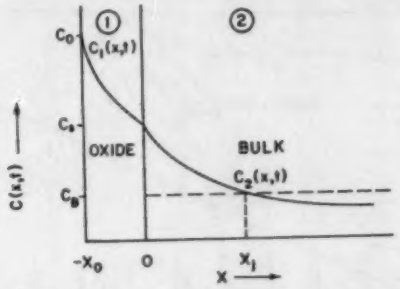

FIG. 1. Diffusant concentration distribution for the composite model.

Although the value of k depends upon D_1 itself, D_1 as calculated from Eq. (13) is relatively insensitive to the value of k chosen; for example, an uncertainty of an order of magnitude in k is reflected as an uncertainty of a factor of less than two in D_1. A rough estimate of k can be made by varying the oxide thickness for the condition of partial masking and measuring the change in junction depth, other factors being constant. According to Eq. (10), we have

$$x_0+kx_j = \text{constant}. \quad (14)$$

However, a linear relationship between junction depth and oxide thickness can hold only for the larger values of x_0, that is, the condition of almost masking. For smaller values of x_0, Eq. (7) for the distribution in the distribution in the bulk can no longer be approximated by a single term and Eq. (14) breaks down.

III. EXPERIMENTAL PROCEDURE

Slices $\frac{1}{2}$ in. sq were cut parallel to the (111) crystallographic direction from approximately 15Ω cm p-type single crystal silicon (boron-doped). The slices were lapped with No. 600 grit, and their resistivity measured by a four point probe method.[5] The samples were finally lapped with No. 1800 grit and etched to a mirror finish in CP4 etch. The final sample thickness was approximately 13 mils.

The silicon samples were oxidized for varying times in an open tube of fused silica-alumina (triangle H-5 Mullite) of $1\frac{1}{4}$ in. i.d. with a flow rate of 1.5 l/min of nitrogen bubbled through water held at 30°C. The samples were held at 1250°C as monitored by a Pt-Pt 13% Rh thermocouple. One side of each sample was then etched in concentrated HF to remove the oxide.

The phosphorous diffusion was carried out in a $1\frac{1}{4}$ in. i.d. quartz tube extending through two independently controlled temperature zones. A flow of 0.5 l/min of dry nitrogen was maintained through the tube. In the first, or source, zone, P_2O_5 held in a fused silica holder was maintained at a temperature of 225°C. In the second, or diffusion, zone, the silicon samples were held vertically in a fused silica holder at constant tempera-

[5] F. M. Smits, Bell System Tech. J. 37, 711 (1958).

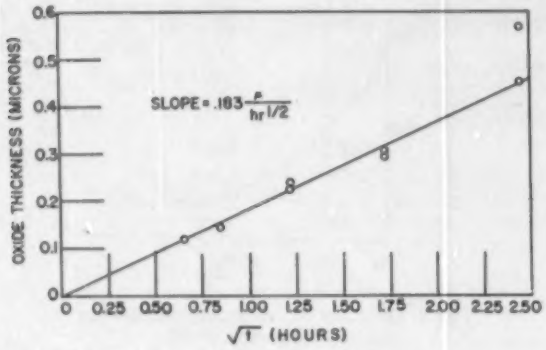

FIG. 2. Oxide thickness *vs* oxidation time. The films were grown in wet N_2 at 1250°C with a gas flow rate of 1.5 l/min.

tures in the range from 1125°C to 1250°C. Pt-Pt 13% Rh thermocouples and automatic controllers regulated the temperatures to ±3°C.

The thickness of the oxide layer for several oxidizing times was determined by differential weighing in the following manner. The samples were first degreased in trichlorethylene, dried in air, and then weighed on a microbalance. After etching in HF for a time sufficiently long to remove all the oxide, the samples were dried and reweighed. Unoxidized samples were carried through the same procedure as a control. The density of the oxide layer was assumed to be that of SiO_2, namely 2.2 g/cc. A plot of the oxide thickness versus the oxidizing time[6] is given in Fig. 2. The growth was found to be parabolic in agreement with Atalla, Tannenbaum, and Scheibner.[7]

The junction depths were determined by successive parallel lappings using a pressure sensitive micrometer to measure the thickness of material removed. Junction position was determined by observing a change in conductivity type with a thermal probe and a peak in

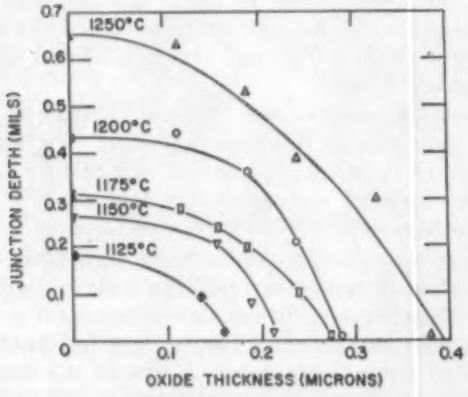

FIG. 3. PN junction depth *versus* oxide thickness for phosphorus diffused into 15 ohm-cm p-type silicon. P_2O_5 source held at 225°C. Dry N_2 carrier gas at a flow rate of 0.5 l/min for a diffusion time of 3 hr.

[6] K. C. Nomura and R. J. Hager (private communication).
[7] Atalla, Tannenbaum, and Scheibner, Bell System Tech. J. **38**, 749 (1959).

successive four point probe reading. The junction depth was checked by metallographic sectioning with a low angle jig and staining with a HF and HNO_3 acid etch.[3] Surface concentrations were calculated from the sheet resistivities and junction depths of the diffused layers by the method of Backenstoss.[8]

IV. EXPERIMENTAL RESULTS AND DISCUSSION

A plot of the junction depth versus oxide thickness is given in Fig. 3 for three hour diffusions under the conditions stated in the previous section. A growth of oxide on the etched side of the silicon samples was found to occur during the course of the P_2O_5 diffusion. The thickness of this layer was judged by interference colors to be of the order of 0.1 μ; therefore, a correction to the oxide thickness as determined from the oxidizing time in wet N_2 was made in Fig. 3. Using Eq. (14) and the experimental points where the junction depth is small we obtain values of k which are given in Table I.

From the values of k shown in Table I and the diffusion time and oxide thickness for zero junction depth D_1 is calculated by Eq. (13). The concentration of phosphorous C_0 at the surface of the oxide is assumed to be equal to the surface concentration measured on the etched side of the sample. The diffusion constant for phosphorus in silicon oxide as a function of temperature is shown in Fig. 4. For comparison the diffusion constant for phosphorus in silicon reported by Fuller and Ditzenberger[3] is also shown. The temperature dependence of the phosphorous diffusion constant in silicon oxide is given by

$$D_1 = D_0 \exp(-E_a/Kt), \tag{15}$$

where D_0 is 3.9×10^{-12} cm²/sec and E_a is 1.4 ev (32 Kcal/M). This is in reasonable agreement with the value of 1.5 ev given by Sah, Sello, and Tremere.[2] This value of activation energy is smaller than that for the diffusion of Group III and V impurities in silicon.

Experimental data on the surface concentration immediately under the oxide are given in Fig. 5 for a constant diffusion time, carrier gas flow, and source temperature. There is qualitative agreement with Eq. (9) in that the surface concentration increases with increasing diffusion temperature and decreases with increasing oxide thickness. The quantitative agreement with Eq. (9) is not good even if the higher order terms

TABLE I. Experimental values of k by Eq. (14).

Temperature	k
1250°C	1.43×10^{-2}
1200°C	9.75×10^{-3}
1175°C	2.04×10^{-2}
1150°C	1.57×10^{-2}
1125°C	9.74×10^{-3}

[8] G. Backenstoss, Bell System Tech. J. **37**, 699 (1958).

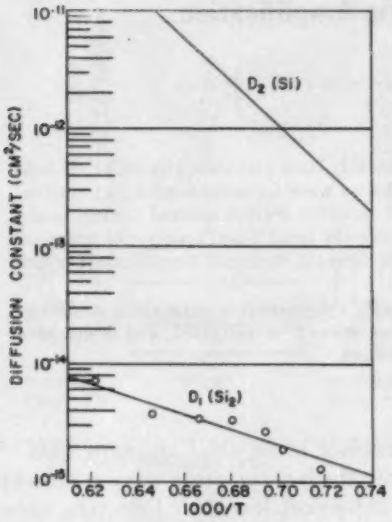

FIG. 4. Diffusion constants for phosphorus in bulk silicon (after Fuller and Ditzenberger[3]) and in silicon oxide as a function of temperature.

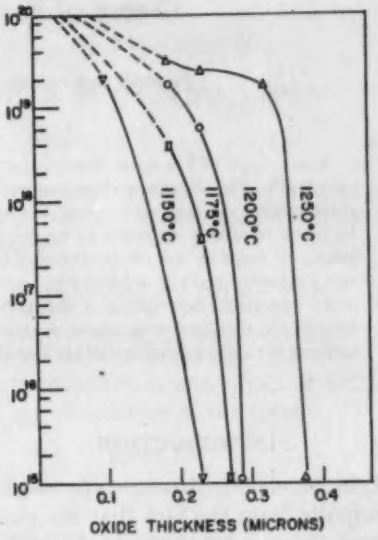

FIG. 5. Experimental values of surface concentration *versus* oxide thickness for several temperatures for the conditions of Fig. 3. The dotted portions of the curves are extrapolations suggested by the theory.

of Eq. (8) are retained in Eq. (9). The experimental curves show a slower decrease of surface concentration with oxide thickness than predicted by Eq. (9).

The theoretical values of the surface concentration are extremely sensitive to the experimentally determined values of the oxide thickness and the diffusion constant for the oxide. In the range of larger oxide thickness where approximations of Eq. (9) are more valid, there are experimental difficulties in measuring the surface concentration because the junction depth is small and the relative error is large. The accumulation of oxide on the etched side of the silicon sample during diffusion complicates the determination of the concentration. C_0 on the oxide layer. On the other hand the functional dependence of Eq. (13) is such that the experimental values for the diffusion of phosphorus in silicon oxide are fairly accurate.

ACKNOWLEDGMENTS

The authors wish to acknowledge the assistance of R. Reed in the diffusion experiments, and J. Kennedy for providing metallographic sections for junction depth evaluation. We are greatly indebted to K. C. Nomura and R. J. Hager of the Minneapolis Research Center, Hopkins, Minnesota, for measuring the thickness of oxide layers.

JOURNAL OF APPLIED PHYSICS VOLUME 31, NUMBER 2 FEBRUARY, 1960

Theory of Fast-Wave Parametric Amplification

CURTIS C. JOHNSON
Research Laboratories, Hughes Aircraft Company, Culver City, California
(Received May 1, 1959)

A new type of low-noise beam-type parametric amplifier has recently been introduced by Adler, Hrbek, and Wade. This device is characterized by its use of the fast-cyclotron wave for amplification purposes instead of the conventionally used slow space-charge wave. The fast-cyclotron wave is selected because it can be made relatively noiseless by appropriate coupling processes. Since the input beam noise is the principal source of noise in beam-type tubes, a very great reduction in noise figure is obtained. Amplification of the fast-cyclotron wave is achieved by use of the parametric principle.

An analytical description of the device is presented which includes a discussion of parametric amplification of the fast-cyclotron wave. A method of coupling to cyclotron waves is investigated, and design procedures for establishing optimum low-noise characteristics are outlined.

INTRODUCTION

NOISE in conventional beam-type amplifiers stems principally from the fact that the electron beam must originate from a hot cathode. Extensive work to reduce this beam noise has resulted in noise figures of approximately 3.5 db at 3 kMc.[1] In the conventional beam-type amplifier the slow space-charge wave is employed to obtain gain. Since the slow wave exhibits negative ac power flow, all the beam noise cannot be removed.

It is well known that the fast wave carries positive ac energy where it would be possible to remove or couple out any beam noise. The next logical step in the development of a truly low-noise beam-type amplifier would be to use the fast wave. Conceivably, the noise could be entirely removed from the fast wave, prior to its amplification. Unfortunately, this type of device is not possible with conventional amplification processes, where the fast wave can only be reduced in amplitude.

Work along these lines has recently been stimulated by the application of a new principle. This principle, recently discussed in the literature by Landon[2] and Suhl,[3] states that energy can be extracted from a system consisting of a driven energy-storage element coupled to a resonant circuit. Amplifiers based on this principle are called variable-parameter or parametric amplifiers. Although most of the work has been devoted to devices without beams, where clearly low-noise characteristics can be obtained since there is no hot cathode, this principle also has an important application to beam-type devices. It provides for the first time a method for establishing a growing fast wave.

An investigation of this parametric amplification process for space-charge waves has been carried out by Louisell and Quate.[4] It is also possible to utilize the fast and slow *cyclotron* waves present on a beam drifting in the presence of an axial magnetic field.[5,6] To date, results with the fast-cyclotron wave are most promising; Adler *et al.*[5] report less than 1-db tube noise figure at 500 Mc.

This paper presents a first-order theory describing the parametric amplification of cyclotron waves. Following a description of the proposed device, the nature of cyclotron waves existing on an electron beam is investigated. The cyclotron-wave description of the stream is then employed in determining the growing-wave behavior in the pump region and the excitation of the waves in the couplers. Finally, input conditions are applied, and an expression for gain is derived.

PRINCIPLE OF OPERATION

The device to be described consists essentially of an input coupler to remove beam noise and apply the signal to the fast-cyclotron wave, a pump cavity to amplify this wave, and an output coupler. The slow-cyclotron wave does not enter the picture, as the couplers couple effectively only to the fast wave. A simplified diagram of the device is shown in Fig. 1.

The beam, with noise modulation on both the fast and slow cyclotron waves, enters the input coupler. The coupler is designed to remove all the noise power from the fast wave during its transit time. Since this design also coincides with the point of best match into the coupler, the signal can be optimally applied to the beam at the same time. For the particular case of $\omega=\omega_c$, a coupler suitable for this use has been described by Cuccia.[7] Basically, a transverse rf field is set up across the beam, which interacts with the stream under conditions where the apparent rf frequency seen by the stream equals the cyclotron frequency. This will occur under two conditions; when the coupler-wave velocity is greater or smaller than the beam velocity. In each case, the apparent frequency or "slip" frequency must be ω_c. For fast-wave coupling, the coupler wave must

[1] M. Currie and D. Forster, Proc. Inst. Radio Engrs. **46**, 570–579 (1958).
[2] J. D. Laudon, RCA Rev. **10**, 387–396 (1949).
[3] H. Suhl, Phys. Rev. **106**, 384–385 (1957).
[4] W. H. Louisell and C. F. Quate, Proc. Inst. Radio Engrs. **46**, 707–716 (1958).
[5] Adler, Hrbek, and Wade, Proc. Inst. Radio Engrs. **46**, 1756–1757 (1958).
[6] R. Adler, Proc. Inst. Radio Engrs. **46**, 1300–1301 (1958).
[7] C. C. Cuccia, RCA Rev. **10**, 270–303 (1949).

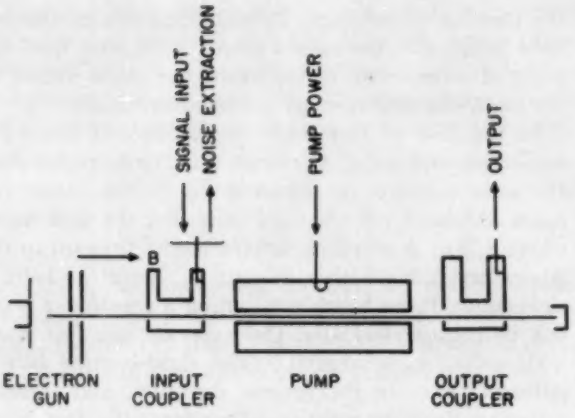

FIG. 1. Schematic diagram of parametric fast-cyclotron wave, low-noise tube.

travel faster than the beam when $\omega > \omega_c$. The coupling process effectively interchanges the beam fast-wave noise power and signal power, as demonstrated by Cuccia. After the stream leaves the input coupler, no more noise-reduction processes occur. The output coupler delivers the noiseless amplified fast-wave beam energy to the load and puts the load noise power on the stream, which is of no consequence since the amplifying process is now complete.

A growing fast wave is obtained in the pump region by driving the orbiting electrons to ever-increasing radii with electric fields. The electric-field pattern, oscillating at $\omega_p \approx 2\omega_c$, consists of two counterrotating components, one of which is in synchronism with the electrons. Energy is transferred from the pump fields to the electrons as they rotate synchronously. For an exponentially growing wave, the pump fields must vary linearly with radius. This gives a value of gain which is independent of input level for small signals. Appropriate pump field patterns can be obtained from quadrupole structures and from many common wave-guide cavities, such as the TE_{11} square guide or the TE_{20} rectangular guide.

The beam motion and energy-exchange processes in the couplers and the pumper will be considered in detail in the following sections.

CYCLOTRON WAVES

An electron beam drifting in the presence of an axial magnetic field supports not only two space-charge waves, but also two cyclotron waves. Space-charge waves arise because of the space-charge restoring forces. In a similar way cyclotron waves are supported by magnetic restoring forces. Space-charge waves are excited by longitudinal disturbances, whereas cyclotron waves require transverse excitation. Except for this, the two sets of waves are remarkably similar.

To obtain the cyclotron-wave equations, an analysis is made of beam behavior in the presence of an axial magnetic field. If space-charge forces are neglected, the force equation is

$$d\bar{v}/dt = -\eta(\bar{v} \times \bar{B}), \tag{1}$$

which is rewritten for the purposes here as

$$\partial\bar{v}/\partial t + (\bar{v} \cdot \bar{\nabla})\bar{v} = -\eta(\bar{v} \times \bar{B}). \tag{2}$$

For a one-dimensional model, where there are no x and y variations and $dz/dt = u_0$, (2) reduces to two components equations

$$(\partial v_x/\partial t) + u_0(\partial v_x/\partial z) = -\eta v_y B \tag{3}$$

$$(\partial v_y/\partial t) + u_0(\partial v_y/\partial z) = +\eta v_x B. \tag{4}$$

The unknown quantities v_x and v_y can be best obtained by applying a trial solution of the form

$$v_x = v_0 e^{j\omega t - \Gamma z} \tag{5}$$

$$v_y = A v_x. \tag{6}$$

Combining (5) and (6) with (3) and (4), one obtains

$$A = \pm j \tag{7}$$

$$j\omega - u_0\Gamma = \mp j\omega_c. \tag{8}$$

Now the complete expression for v_x and v_y can be written as

$$v_x = v_0 \exp j\{\omega t - \beta_e[1 \pm (\omega_c/\omega)]z\} \tag{9}$$

$$v_y = \pm j v_x. \tag{10}$$

From (9) and (10) it is seen that there are two wave solutions, a slow-wave (upper sign) and a fast-wave (lower sign) solution. The phase velocity of the fast and slow waves are, respectively,

$$v_f = \frac{u_0}{1 - (\omega_c/\omega)} \tag{11}$$

$$v_s = \frac{u_0}{1 + (\omega_c/\omega)}. \tag{12}$$

The separation in velocities arises from the presence of the magnetic field; hence the waves have been termed cyclotron waves. These velocities are plotted *versus* ω/ω_c in Fig. 2. The slow wave is always positive, but less than u_0. The fast wave has a negative phase velocity when $\omega/\omega_c < 1$ and a positive velocity always greater than u_0 when $\omega/\omega_c > 0$. There is a singularity at $\omega/\omega_c = 1$, where the fast-wave velocity goes to infinity. This is the region where the coupler described by Cuccia operates.

Notice from (10) that the two waves are rotating in opposite directions. The velocities expressed in (9) and (10) describe *beam* motion, not particle motion. It is apparent that the beam shapes are different in the two cases, since the waves are counter-rotating. The frequency and sense of rotation of the beam intersecting a plane of constant z can be found from the above velocity relations. From (9) and (10), with z equal to

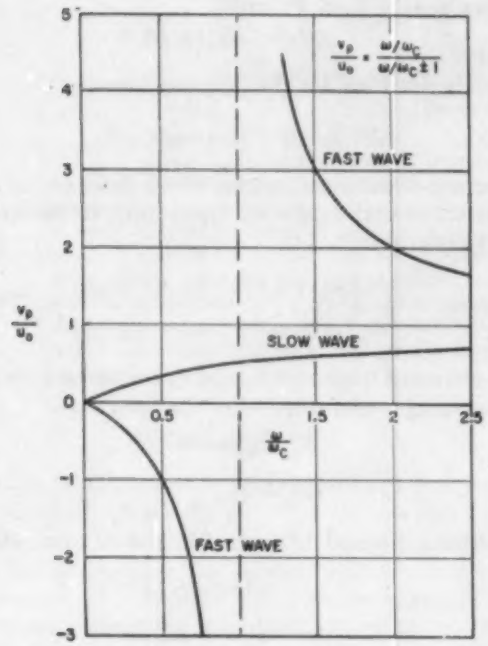

FIG. 2. Cyclotron-wave velocities. The fast- and slow-cyclotron wave velocities are plotted *versus* ω/ω_c.

a constant,

$$v_x = v_1 \cos\omega t \tag{13}$$

$$v_y = \mp v_1 \sin\omega t. \tag{14}$$

It is seen from these relations that the fast wave (lower sign) intercepts the plane in a clockwise sense at frequency ω, and the slow wave (upper sign) in a counterclockwise sense at frequency ω. Of course, the beam must intercept the plane at frequency ω in order to excite the signal frequency in a coupler. The wavelength of the cyclotron waves can be found from (9) also. If t is held constant, it is seen that

$$v_x = v_1 \cos\beta_c z\left[1 \pm (\omega_c/\omega)\right]z, \tag{15}$$

from which one obtains

$$\lambda = \frac{2\pi u_0}{\omega_c}\left[\frac{\omega_c/\omega}{1 \pm (\omega_c/\omega)}\right]. \tag{16}$$

It is now easy to see how the beam is shaped under fast- or slow-wave excitation. When $\omega > \omega_c$, the wave velocity is positive and greater than u_0 for fast-wave excitation. In the reference frame of the wave, the electrons are moving in the negative z direction, as in Fig. 3. The individual electrons must rotate as shown in the presence of the magnetic field as they move through the circuit field pattern. The beam is shaped into a left-handed helix. This helix in the laboratory frame moves forward with velocity v_p, since it is stationary in the reference frame of the wave. The individual electrons in the beam are moving with axial velocity u_0 and are rotating in such a way as to maintain this moving helical shape. By imagining this left-handed helix striking a constant-z plane, it is seen that the point of intersection of the beam and plane rotates in the clockwise direction, as shown theoretically.

In the case of slow-wave excitation *and* fast-wave excitation with $\omega < \omega_c$, the beam velocity is greater than the wave velocity. As shown in Fig. 4, this causes the beam to form a right-handed helix. For the slow wave, where $v_p > 0$, this helical pattern moves forward in the laboratory frame with a velocity v_p. Since the helix is right-handed, the beam rotation on a constant-z plane will be counterclockwise. However, for the fast wave with $\omega < \omega_c$, v_p is negative. The right-handed helical pattern moves in the reverse direction, and thereby causes a *clockwise* rotation. Therefore, the fast wave always causes a clockwise rotation and the slow wave always causes a counterclockwise rotation as predicted from (13) and (14).

By knowing how the beam behaves under fast- or slow-cyclotron wave excitation, it is possible to draw some conclusions about the rf power flow associated with each wave. A wave is called a positive ac energy carrier if its energy increases when energy is supplied to it, and a negative ac energy carrier if its energy decreases when energy is applied. It is well known that the fast space-charge wave carries positive ac power, since the stream energy increases when this wave is excited. This increase in energy is accomplished by electrons bunching in the accelerating phase. The slow space-charge wave carries negative ac power, since the stream energy is decreased when a slow wave is excited. Here the bunches form in the decelerating phase. The energy carried by the two waves is equal in magnitude and opposite in sign.

It can be readily shown that the fast- and slow-cyclotron waves behave in a similar way. The energy exchange between an electron and a wave is proportional to the force times the particle velocity.

$$\mathcal{E} \propto \bar{F} \cdot \bar{v}. \tag{17}$$

In the case of a traveling wave moving in synchronism with the beam pattern, it is seen that energy is exchanged by both the longitudinal and transverse fields. The transverse fields can give energy only to the stream, since they drive the electron around its orbit. The longitudinal fields give energy to the stream when $u_0 < v_p$ (see Fig. 3) since the beam is deflected into ac-

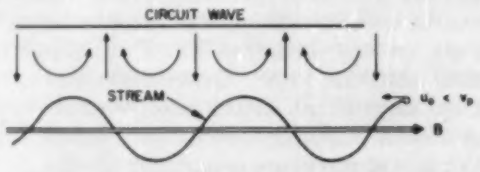

FIG. 3. Beam shape under fast-wave excitation where $\omega/\omega_c > 1$. The beam acquires the left-handed helical shape as shown. In the laboratory reference frame, this beam shape moves forward with velocity v_p.

celerating fields. When $u_0 > v_p$, the beam is deflected into decelerating fields (see Fig. 4) and energy is taken from the stream. For typical transverse-field slow-wave structures, one can write the following expressions for peak energy transfer due to the transverse and longitudinal fields.

$$|\hat{\mathcal{E}}_t| = r_0 \omega_c E_0 \tag{18}$$

$$|\hat{\mathcal{E}}_l| = u_0 E_0 \sinh \gamma r_0. \tag{19}$$

γ is the wave propagation constant and r_0 is the cyclotron radius. Since the energy exchange is periodic with time, the ratio of the average energy transfers is equal to the ratio of the peak energy transfers.

$$\left|\frac{\mathcal{E}_l}{\mathcal{E}_t}\right| = \frac{\gamma u_0}{\omega_c}\left(\frac{\sinh \gamma r_0}{\gamma r_0}\right). \tag{20}$$

For small γr_0, this reduces to

$$\left|\frac{\mathcal{E}_l}{\mathcal{E}_t}\right| = \frac{\omega}{\omega_c}\frac{u_0}{v_p}. \tag{21}$$

The total energy transfer is the sum of the two energy contributions.

$$\mathcal{E} = \mathcal{E}_t[1 + (\mathcal{E}_l/\mathcal{E}_t)]. \tag{22}$$

For the slow wave, where $\mathcal{E}_l/\mathcal{E}_t$ is negative, the total energy is found by combining (12) and (21) with (22).

$$\frac{\mathcal{E}_{\text{slow}}}{\mathcal{E}_t} = -\frac{\omega}{\omega_c}. \tag{23}$$

For the fast wave, the expression for $\mathcal{E}_l/\mathcal{E}_t$ is found by combining (11) with (21).

$$\frac{\mathcal{E}_{l\ \text{fast}}}{\mathcal{E}_t} = \frac{\omega}{\omega_c} - 1. \tag{24}$$

When $\omega < \omega_c$, the wave velocity is negative, and $\mathcal{E}_l/\mathcal{E}_t$ should be negative (Fig. 4). For the special case $\omega = \omega_c$, $\mathcal{E}_l = 0$. This is the case of the Cuccia coupler, where $\mathcal{E}_l = 0$ since there are no longitudinal fields. When $\omega > \omega_c$, the wave velocity is positive, and $\mathcal{E}_l/\mathcal{E}_t$ should be positive (Fig. 3). Note that (24) satisfies these requirements based on the physical considerations. Combining (24) with (22), one obtains

$$(\mathcal{E}_{\text{fast}}/\mathcal{E}_t) = +(\omega/\omega_c). \tag{25}$$

Since the value of $\mathcal{E}_t$ is positive and the same in magnitude for each case, it is clear that the fast wave accepts energy and the slow wave delivers energy in equal amounts. Equal excitation of both waves therefore requires no net power. The analogy with the space-charge waves is now complete, because both sets of waves have the same power-flow characteristics.

It is important to determine the nature of ac power flow on cyclotron waves, since this limits the use of each

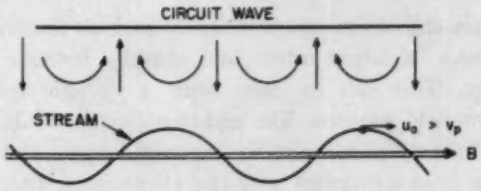

FIG. 4. Beam shape under slow-wave excitation or fast-wave excitation where $\omega/\omega_c < 1$. The beam acquires this right-handed helical shape. This beam shape moves forward for the slow wave and backward for the fast wave at the appropriate velocities.

wave. For instance, conventional amplification processes involving energy transfer by decelerating bunches of electrons can be carried out only with the slow wave. Only a negative ac energy carrier can be amplified by removing energy. Removing energy from the slow space-charge wave is accomplished in the conventional traveling-wave tube, and removing energy from the slow cyclotron wave is a process involved in the magnetron-type device. In parametric devices, noise power is removed from the beam wave before amplification takes place. This removal can be accomplished only when the wave is a positive energy carrier. Since the fast space-charge wave satisfies this requirement, it is possible to utilize this wave to obtain a low-noise device. It has been shown that the fast cyclotron wave also carries positive energy, and a successful low-noise tube built by Adler[5] demonstrates this fact. After the noise power has been removed from the fast wave by taking energy from the wave, the signal can be amplified by supplying energy to the wave. The process by which this is done is described in a later section.

To complete the discussion of cyclotron waves, it should be pointed out that the waves present in crossed-field tubes are almost identical to the waves described here. The principal difference is that the stream rotates in a plane parallel to the axis rather than in a plane perpendicular to the axis. This must be the case because B is now perpendicular to the axis and the electrons must rotate around the B vector. By running through a similar analytical procedure, one gets a set of equations analogous to (9) and (10).

$$\begin{aligned} v_x &= v_0 \exp j\{\omega t - \beta_e[1 \pm (\omega_c/\omega)]z\} \\ v_z &= u_0 \pm j v_x. \end{aligned} \tag{26}$$

The reasoning processes involved in determining beam shapes and ac power flow are identical in this case and yield similar conclusions.

PARAMETRIC AMPLIFICATION

The parametric principle can be applied to obtain a growing fast-cyclotron wave. Since it is necessary to use the fast-cyclotron wave for noise purposes, energy must be transferred to the stream wave for amplification. This is characteristic of a positive ac energy carrier. Energy is delivered to the stream by passing the stream through a cavity, called the pump cavity. The electric

fields in the cavity are principally such as to drive the electrons to larger orbits and thereby increase their energy. This can be done with a suitable rotating electric-field pattern. The rotating electric fields must vary linearly with radius for exponential gain and must rotate in synchronism with the electrons at frequency ω_e. Cavities which are suitable for this purpose are the TE_{11} square guide and the TE_{21} circular guide, each of which generates a rotating quadrupole electric-field pattern. Another possibility is the sinusoidal field pattern present in the TE_{20} rectangular wave-guide mode. The following analysis will assume a quadrupole field pattern for the pump fields.

The force equations in the absence of any pump fields are given by (3) and (4). The electric potential established in a quadrupole pump cavity is given by

$$V=(V_0/a^2)r^2\cos 2\theta\cos\omega_p t. \tag{27}$$

The expressions for electric field can be obtained from (27).

$$\begin{aligned} E_x&=-(V_0/a^2)2x\cos\omega_p t\\ E_y&=(V_0/a^2)2y\cos\omega_p t. \end{aligned} \tag{28}$$

By inserting the resulting values of electric force into the force equations, the basic equations for an analysis of the pump region are obtained.

$$\begin{aligned} &\frac{\partial v_x}{\partial t}+u_0\frac{\partial v_x}{\partial z}+\omega_c v_y=\Omega^2 x(e^{j\omega_p t}+e^{-j\omega_p t})\\ &\frac{\partial v_y}{\partial t}+u_0\frac{\partial v_y}{\partial z}-\omega_c v_x=-\Omega^2 y(e^{j\omega_p t}+e^{-j\omega_p t}) \end{aligned} \tag{29}$$

where Ω^2 is defined as $\eta(V_0/a^2)$.

The solutions to this set of equations are of the form

$$\begin{aligned} v_x&=\sum_{n=-\infty}^{+\infty} v_{x_n}(z)e^{j\omega_n t}\\ v_y&=\sum_{n=-\infty}^{+\infty} v_{y_n}(z)e^{j\omega_n t} \end{aligned} \tag{30}$$

where

$$\omega_n=\omega+n\omega_p. \tag{31}$$

The solutions consist of signal frequency terms and terms resulting from a mixing of the signal and pump frequencies. The displacement quantities x and y are related to v_x and v_y by the familiar definitions

$$\begin{aligned} \left(\frac{\partial}{\partial t}+u_0\frac{\partial}{\partial z}\right)x&=v_x\\ \left(\frac{\partial}{\partial t}+u_0\frac{\partial}{\partial z}\right)y&=v_y. \end{aligned} \tag{32}$$

Combining (29) and (30) and applying the orthogonality relation

$$\int_0^T e^{j\omega_n t}e^{j\omega_m t}dt=\begin{cases}0, & m\neq n\\ T, & m=n\end{cases},$$

one obtains,

$$\begin{aligned} &j\omega_n v_{x_n}+u_0\frac{\partial}{\partial z}v_{x_n}+\omega_c v_{y_n}\\ &\quad-\Omega^2\left[\frac{v_{x_{n-1}}}{j\omega_{n-1}+u_0(\partial/\partial z)}+\frac{v_{x_{n+1}}}{j\omega_{n+1}+u_0(\partial/\partial z)}\right]=0\\ &j\omega_n v_{y_n}+u_0\frac{\partial}{\partial z}v_{y_n}-\omega_c v_{x_n}\\ &\quad+\Omega^2\left[\frac{v_{y_{n-1}}}{j\omega_{n-1}+u_0(\partial/\partial z)}+\frac{v_{y_{n+1}}}{j\omega_{n+1}+u_0(\partial/\partial z)}\right]=0. \end{aligned} \tag{33}$$

These equations must hold for each and every value of n. It is well known that for parametric devices of this sort the two frequencies of interest are the signal and idler frequencies ($n=0, -1$). Taking just the $n=0$ and $n=1$ set of equations from (33) and neglecting terms involving frequencies other than ω and $\omega-\omega_p$, one obtains the following set of four equations. The familiar $e^{-\Gamma z}$ exponential z-dependence is assumed.

$$\begin{aligned} &(j\omega-u_0\Gamma)v_{x0}+\omega_c v_{y0}-\left(\frac{\Omega^2}{j(\omega-\omega_p)-u_0\Gamma}\right)v_{x-1}=0\\ &-\omega_c v_{x0}+(j\omega-u_0\Gamma)v_{y0}+\left(\frac{\Omega^2}{j(\omega-\omega_p)-u_0\Gamma}\right)v_{y-1}=0\\ &\left(\frac{-\Omega^2}{j\omega-u_0\Gamma}\right)v_{x0}+[j(\omega-\omega_p)-u_0\Gamma]v_{x-1}+\omega_c v_{y-1}=0\\ &\left(\frac{\Omega^2}{j\omega-u_0\Gamma}\right)v_{y0}-\omega_c v_{x-1}+[j(\omega-\omega_p)-u_0\Gamma]v_{y-1}=0. \end{aligned} \tag{34}$$

The determinantal equation for Γ is obtained by setting the determinant of the coefficients equal to zero. When this is done, one obtains

$$\frac{1}{2}\left(\frac{u_0}{\Omega}\right)^4=\frac{(j\beta_e-\Gamma)[j(\beta_e-\beta_p)-\Gamma]+\beta_m^2}{(j\beta_e-\Gamma)[j(\beta_e-\beta_p)-\Gamma][(j\beta_e-\Gamma)^2+\beta_m^2][(j(\beta_e-\beta_p)-\Gamma)^2+\beta_m^2]} \tag{35}$$

where

$$\beta_e=\omega/u_0$$
$$\beta_p=\omega_p/u_0$$
$$\beta_m=\omega_c/u_0.$$

The function on the right side of (35) is plotted *versus* Γ in Fig. 5 for $\omega_p\approx 2\omega_c$. The value of the term on the left side decreases as the pump power is increased and is shown as a horizontal dotted line. Intersections of this line and the function of Γ represents solutions to the determinantal equation. There are six imaginary roots shown; two are near $\Gamma=j[\beta_e-(\beta_p/2)]$ and the other four are spaced out in increments of β_m. For no pump power ($\Omega^2=0$), the horizontal line is at plus infinity. As the pump power is turned on and increased, this line drops until the two roots near $\Gamma=j[\beta_e-(\beta_p/2)]$ disappear. This implies that there now exist two complex roots, with the possibility of a growing wave. For a given pump power, the horizontal line will be at a fixed position. Growing waves can also be obtained by varying the pump frequency slightly; this causes the intercept a' to vary. As ω_p approaches $2\omega_c$, the point a' goes to infinity, which allows growing waves to exist for any value of pump fields. The exact relationship between the pump field strength and pump frequency necessary for the establishment of a growing wave is given in the analytical solution which follows.

The next step will be to find an expression for the growing wave predicted by the above graphical reasoning. The interesting waves will occur near $\Gamma=j(\beta_e-\beta_m)$, which is the fast-wave solution for $\Omega^2=0$. Let

$$\Gamma=j(\beta_e-\beta_m)-(\Omega^2/u_0\omega_c)\delta \tag{36}$$

where $\Omega^2\delta/u_0\omega_c$ is a small number. Near $\Gamma=j(\beta_e-\beta_m)$, (35) reduces to

$$[j(\beta_e-\beta_m)-\Gamma][j(\beta_e+\beta_m-\beta_p)-\Gamma]=(\Omega^4/\omega_c^2u_0^2). \tag{37}$$

To allow for deviation from $\omega_p=2\omega_c$, a parameter b is defined by the following equation

$$(\Omega^2/\omega_c)b=2\omega_c-\omega_p. \tag{38}$$

Now (37) is reduced to

$$\delta(\delta+jb)=1. \tag{39}$$

Solving for δ, one obtains,

$$\delta=-j(b/2)\pm[1-(b/2)^2]^{\frac{1}{2}}. \tag{40}$$

It is clear from (40) that maximum gain occurs at $\omega_p=2\omega_c(b=0)$ and that the following inequality must be satisfied in order to set up a growing wave.

$$|2\omega_c-\omega_p|<2(\Omega^2/\omega_c). \tag{41}$$

This corresponds to the point where a' rises above the horizontal line in Fig. 5.

The expression for gain when $b=0$ for both the signal and idler wave is

$$G=-6+8.686(\Omega^2L/\omega_cu_0)db. \tag{42}$$

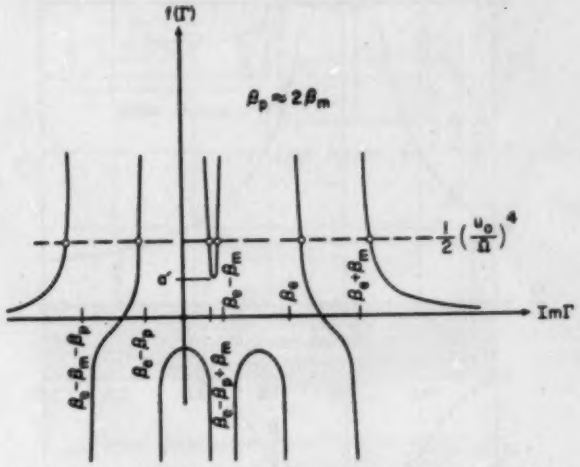

FIG. 5. Plot of determinantal equation for Γ. Intersections on this plot represent solutions to the equation, which occur at intervals of β_m. When all of the mixing terms are taken into account, an infinite series of solutions exists at intervals of β_m. At $\Gamma=j[\beta_e-(\beta_p/2)]$, there are two roots which may become complex, depending on the values of a' and $\frac{1}{2}(u_0/\Omega)^4$.

With no pump ($\Omega^2=0$), there is a fast- and slow-cyclotron wave on the stream. In the presence of quadrupole pump fields, the fast wave splits into one growing and one decaying wave. Amplification of the slow-cyclotron wave is also possible. The presence of the idler wave arises because of mixing of the signal and pump frequencies, and it is important to know whether this new wave is a positive or a negative ac energy carrier (a fast or a slow wave). The signal wave propagates as $\exp j\{\omega t-[(\omega-\omega_c)/u_0]z\}$, from which the signal wave velocity is found to be

$$v_s=\frac{u_0}{1-(\omega_c/\omega)}. \tag{43}$$

The signal wave is obviously akin to the fast-cyclotron wave. The idler wave propagates as $\exp j\{(\omega-\omega_p)t-[(\omega-\omega_c)/u_0]z\}$, from which one can show that

$$v_i=\left[\frac{1-2(\omega_c/\omega)}{1-(\omega_c/\omega)}\right]u_0. \tag{44}$$

These velocities are plotted *versus* ω/ω_c in Fig. 6. The signal wave has the same characteristics as the fast-cyclotron wave. It has the same phase velocity and carries positive ac energy. The idler wave has a radically different phase velocity but still carries positive ac energy in the region $0<(\omega/\omega_c)<2$. However, when $\omega/\omega_c>2$ (i.e., when the signal frequency exceeds the pump frequency) the idler wave becomes a negative ac energy carrier, or a slow wave. This is true because it has a positive phase velocity with $v_p<u_0$ and thereby loses energy as it moves forward. If $v_p>u_0$, it gains energy as it moves forward; if $v_p<0$, it loses energy as it moves backward, Either of these conditions defines a fast wave. The area between 0 and +1 in Fig. 6 is

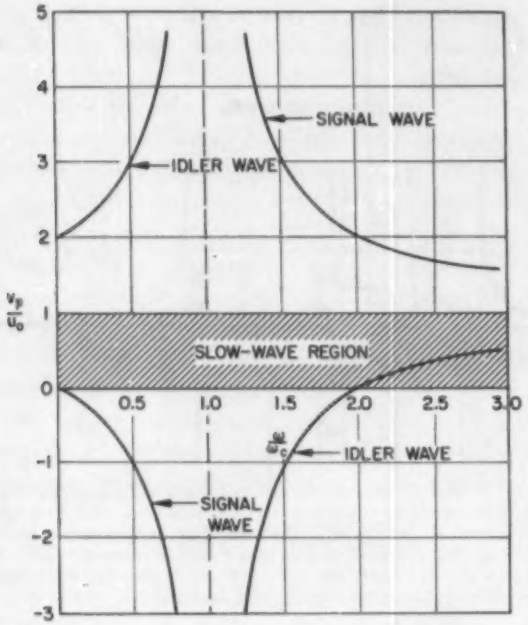

FIG. 6. Idler- and signal-wave velocities in the pump cavity. The idler- and signal-wave velocities are plotted *versus* ω/ω_c.

termed the slow-wave region. (Note that the slow-cyclotron wave in Fig. 2 occupies this region.)

The preceding method of analysis for the quadrupole field pattern can also be used for other types of pump fields. This method was used for the TE_{20} pump cavity, and the results are identical except for a constant multiplier. This constant relates to the strength of the rotating field component generated in each case.

FAST-CYCLOTRON WAVE COUPLERS

The coupling process from a circuit wave to a beam cyclotron wave has been described in a preceding section on a physical basis. Coupling between the wave and beam occurs when the wave velocity approaches the cyclotron-wave velocity. The relative velocity difference between the fast- and slow-cyclotron waves is large over the region of interest (see Fig. 2), in contrast to the separation between the fast and slow space-charge waves. This large difference makes it possible to couple selectively to one of the cyclotron waves with very little coupling to the other wave. It will be assumed in the following analysis that when coupling to the fast-cyclotron wave, the slow-cyclotron wave can be completely neglected.

In coupling to the fast-cyclotron wave for noise-removal purposes, a different type of coupler will be required for different values of ω/ω_c. For $\omega/\omega_c \approx 1$, a coupler with infinite phase velocity is required. For $\omega > \omega_c$, a forward-wave structure is required, and if $\omega < \omega_c$, a backward-wave structure becomes necessary. From the shape of the fast-wave velocity curves it is seen that a device with extended band width is not practical. An additional complication occurs when $\omega \neq \omega_c$, because noise must be removed at two different frequencies, the idler frequency and the signal frequency. This means that two couplers are required, one for the signal frequency and one for the idler frequency.

In this section the coupled-mode analysis of Pierce[8] and Gould[9] will be employed to investigate forward-wave couplers. Backward-wave couplers can be treated in a similar way, but this will not be done here. The electron coupler described by Cuccia[7] will also be considered, and design procedures will be formulated.

If space-charge forces are neglected, the determinantal equation for interaction between an electron stream and a transverse-field circuit is derived by Pierce.[10]

$$(\Gamma^2-\Gamma_1^2)(j\beta_e-\Gamma)^2[(j\beta_e-\Gamma)^2+\beta_m^2] = -j\beta_e\Gamma_1\phi^2\frac{KI_0}{2V_0}[\Gamma^2\{(j\beta_e-\Gamma)^2+\beta_m^2\} - \left(\frac{\phi'}{\phi}\right)^2(j\beta_e-\Gamma)^2]. \quad (45)$$

The following substitutions are made.

$$\begin{aligned} \Gamma &= j\beta \\ \Gamma_1 &= j\beta_1 \\ C^3 &= (\phi^2 KI_0/4V_0) \\ \alpha^2 &= (\phi'/\beta\phi)^2. \end{aligned} \quad (46)$$

Pierce's definition of α^2 involves β_e instead of β. The use of β is necessary here since the beam velocity is not synchronized with the wave velocity. This results in the following expression for α if the usual $e^{j\beta z}$ dependence is assumed.

$$\alpha = j(E_y/E_z). \quad (47)$$

After these substitutions are made, (45) becomes

$$(\beta^2-\beta_1^2)(\beta_e-\beta)^2[(\beta_e-\beta)^2-\beta_m^2] = -2\beta_e\beta_1\beta^2C^3[(\beta_e-\beta)^2(1+\alpha^2)-\beta_m^2]. \quad (48)$$

The region of interest involves only the forward circuit wave and the fast cyclotron wave. The other four waves in (48) can be eliminated by setting $\beta_e-\beta_m \approx \beta \approx \beta_1$. When this is done, (48) reduces to

$$(\beta-\beta_1)(\beta-\beta_e+\beta_m) = \frac{\beta_e\beta^2\alpha^2C^3}{2\beta_m}. \quad (49)$$

In Gould's[9] coupled-mode description of the Kompfner dip condition, he has derived a similar determinantal equation

$$(\beta-\beta_1)(\beta-\beta_e+\beta_m) = \mathfrak{C}^2 \quad (50)$$

where, for complete energy transfer from circuit to

[8] J. R. Pierce, J. Appl. Phys. **25**, 179–183 (1954).
[9] R. W. Gould, IRE Trans. PGED **ED-2**, 37–42 (October, 1955).
[10] J. R. Pierce, *Traveling-Wave Tubes* (D. Van Nostrand Company, Inc., Princeton, New Jersey, 1950).

beam, $\mathfrak{C}L=(\pi/2)$. Therefore, by comparison,

$$\frac{\beta_e\beta^2\alpha^2C^3}{2\beta_m}L^3=\frac{\pi^2}{4}. \tag{51}$$

The parameter C^3 is the coupling parameter based on the longitudinal impedance. The coupling parameter $D^3=\alpha^2C^3$ is the corresponding coupling parameter based on the transverse impedance. When this coupling parameter is used, (51) reduces to

$$(DN)^3=(\beta_mL/16\pi)[1-(\omega_c/\omega)]^{-2}, \tag{52}$$

where $N=\beta_eL/2\pi$. By putting in some practical values for the parameters, it appears that a flattened helix of reasonable length can be used to achieve proper coupling. A helix coupler designed to satisfy (52) would couple the circuit wave onto the fast-cyclotron wave while coupling the stream noise power from the fast wave to the circuit.

A second idler coupler is not required when the idler and signal frequencies are sufficiently close together. In this region the phase velocity of the circuit wave must approach infinity; this involves the use of a cavity-type coupler. The basic interaction is the same, with the cavity fields coupling to the fast-cyclotron wave in such a fashion as to exchange circuit and fast-wave energy.

Smith and Shulman[11] have shown that the electronic conductance presented to a coupling cavity of length L and gap d by the stream is given by

$$G_{el}=\tfrac{1}{8}(L/d)^2(I_0/V_0). \tag{53}$$

In an equivalent circuit representation, as in Fig. 7(a), G_{el} is shunted across the capacitor plates. The cavity is coupled to an external circuit, which presents an admittance across the cavity. At resonance the circuit shown in Fig. 7(b) applies, where G' is the transformed external circuit conductance. In order to match the beam to the cavity properly, one must set

$$G_{el}=G_{sh}+G'. \tag{54}$$

In order to design a cavity to fulfill this requirement, the following equation must be satisfied.

$$(Q_0/Q_L)=(G_{el}/G_{sh}) \quad \text{or} \quad (1/Q_L)=G_{el}(R_{sh}/Q_0). \tag{55}$$

Q_L is the cold-loaded Q, and R_{sh}/Q_0 is the ratio of shunt resistance to unloaded Q. This latter quantity is easily determined by perturbation measurements, and Q_{el} is found from (53). To couple most of the signal power to the beam, G_{sh} must be small compared with G_{el} and G'. This means that in practice the cavity will be overcoupled, with $Q_L \ll Q_0$.

If the cavity is tunable, one may ask what kind of band width can be expected from a cavity-type coupler,

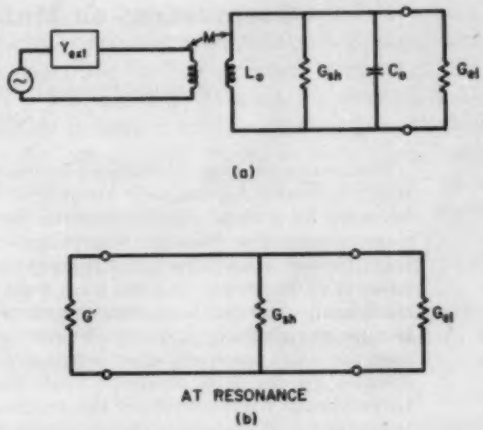

FIG. 7. Equivalent circuit for the cavity-type fast-cyclotron wave coupler.

with good noise characteristics. Smith and Shulman[11] have shown how the electronic admittance varies as the frequency is moved off resonance. The conductance decreases, and a reactance term appears. This electronic reactance will shift the resonant frequency slightly, but more important from a low-noise standpoint, the conductance term cannot decrease much before a mismatch with the circuit becomes damaging. For about a ten-percent reduction in G_{el}, the parameter $\theta=(\omega_c-\omega)L/u_0$ equals one radian. θ is the angle of deviation between the orbiting electron and the rotating cavity field acquired as the electron passes through the cavity. From physical considerations it would seem that only about a one-radian shift could be tolerated. When $\theta=2\pi$, the energy is transferred back to the cavity fields and $G_{el}=0$. Defining band width as

$$BW=\frac{2(\omega-\omega_c)}{\omega_c} \tag{56}$$

and inserting the quantity

$$(\omega_c-\omega)(L/u_0)=1 \text{ radian}, \tag{57}$$

one obtains

$$BW=(2u_0/L\omega_c). \tag{58}$$

Typically, at 3 kMc, BW=one percent. This band width could be utilized only by tuning the cavity or by employing a cavity of sufficiently low loaded Q. Greater band widths can be obtained by matching $G'+G_{sh}$ to G_{el} over the desired frequency range.

ACKNOWLEDGMENTS

The helpful discussions and interest shown by various members of the Electron Dynamics Department of the Hughes Aircraft Company Research Laboratories has been instrumental in the completion of this report. Many suggestions by Roy Gould were particularly enlightening, and part of the analysis in the section on Parametric Amplification was patterned after some of his work.

[11] L. P. Smith and C. I. Shulman, Proc. Inst. Radio Engrs. **35**, 644–657 (1947).

Observations on MnBi Films during Heat Treatment*

LUDWIG MAYER
Mechanical Division of General Mills, Inc., Minneapolis, Minnesota
(Received August 3, 1959)

Observations of magnetic surface phenomena, which were made during the vacuum heat treatment necessary to develop ferromagnetic MnBi films from their nonmagnetic constituents, are described. A vacuum hot stage for a metallurgical microscope was constructed in order to accomplish by means of the Kerr magneto-optic effect this visual observation of incipient ferromagnetism. MnBi films with some areas already magnetic were first observed. The phenomena occurring during evolution of the magnetic state in the areas adjacent to the already magnetic areas could be observed readily and the experiments could be reproduced consistently. Attempts to nucleate this transformation in the vacuum hot stage were only partly successful because reproducibility could not be achieved. Growth of a new magnetic area on MnBi film manifests itself first as an essentially structureless area. This structureless area then becomes an area of antiparallel domains. The size of the domains depends mainly on the duration of the existence of the structureless state. Large domains tend to develop if the structureless state is kept in existence for a short time and vice versa. In addition to the immediate practical goal of improving reproducibility in the preparation of MnBi films such visual observation of the nascent state of ferromagnetism may also be of general interest to the physics of magnetism.

INTRODUCTION AND CONCEPT

THE stoichiometric alloy manganese bismuthide (MnBi) is an interesting material. It has unusual ferromagnetic properties as bulk material as well as in the form of thin films. It is a strongly ferromagnetic intermetallic compound whose constituents are not ferromagnetic. MnBi is magnetically highly anisotropic; the very large magneto-crystalline energy[1,2] in combination with a fine particle size has yielded bulk material with both high coercive force and large energy product.[3] Bulk MnBi would be in many respects an ideal material for permanent magnets. Unfortunately, however, the bulk material corrodes easily when exposed to the atmosphere.[4]

Thin magnetic MnBi films are also of considerable interest. Fortunately and quite surprisingly, MnBi films do not deteriorate when exposed to the atmosphere. MnBi films with a uniaxial direction of easy magnetization normal to the plane of the film can be prepared.[5] Magnetization of the entire film along this easy direction, i.e., normal to the surface, is possible despite the large demagnetization factor involved. Magnetic writing with permanent magnet probes is possible on such MnBi films.[5] The magnetically recorded information can be read optically with high contrast by the Faraday effect and the Kerr magneto-optic effect[5] or electronically with electron mirror microscopical methods.[6] As this magnetically recorded information can also be erased magnetically and storage densities of the order of 10^6 bits/cm^2 appear possible,[5] MnBi films may be basically well suited for magnetic bulk information storage, particularly so because magnetic writing with an electron beam[7] based on Curie-point writing[8] can also be accomplished on MnBi films. This electronic method of magnetic writing and the comparatively high contrast obtainable by optical methods of readout makes MnBi films also inherently well suited for possible applications in display schemes.

There are, however, two major difficulties connected with MnBi films. One difficulty is the problem of erasing, because erasure requires several thousand oersteds. This may not be a severe hindrance, however, because very short magnetic pulses are sufficient to achieve erasure. The other difficulty is connected with the preparation of the right kind of MnBi films. According to experience in this laboratory, reproducibility is very poor and the output of perfect films rather low. The films were prepared after Williams *et al.*[5] by vacuum evaporating onto cover glass disks of 25-mm diam a layer of Bi above a layer of Mn. Usually eight to twelve disks containing this composite Mn-Bi layer were vacuum heat treated in one run. Once in a while a run turned out to be completely successful, all its MnBi films were perfectly uniform across the disks and had the desired magnetic properties, i.e., each film had antiparallel magnetic domains across the entire disc with their direction of magnetization normal to the plane of the film. More often, however, these heat treating runs were either fully or partly unsuccessful. The films turned out to be either nonmagnetic or had, at least in part of the film, the direction of magnetization in the plane of the film rather than normal to it. Even by strict adherence to those procedures which had led to perfect films, reproducibility could not be achieved.

* This research was supported by the U. S. Air Force under Contract No. AF 33(616)-3852 monitored by the Aeronautical Research Laboratory, WCLJL, WADC.
[1] Charles Guillaud, Thesis, University of Strasbourg, 1943, and J. phys. radium **12**, 492 (1951).
[2] Williams, Sherwood and Boothby, Bull. Am. Phys. Soc. Ser. II, **1**, 132 (1956).
[3] Adams, Hubbard, and Syeles, J. Appl. Phys. **23**, 1207 (1952).
[4] Edmund Adams, Proc. Conf. Magnetism and Mag. Materials (AIEE Publication *T*-91, Boston, Massachusetts, 1956), p. 212.
[5] Williams, Sherwood, Foster, and Kelley, J. Appl. Phys. **28**, 1181 (1957).
[6] Ludwig Mayer, J. Appl. Phys. **28**, 975 (1957).
[7] Ludwig Mayer, J. Appl. Phys. **29**, 1454 (1958).
[8] Ludwig Mayer, J. Appl. Phys. **29**, 1003 (1958).

One of the approaches taken to uncover the hidden facts behind this lack of reproducibility is the subject of this paper. The concept of this approach is the following: It would be very desirable to observe visually the Mn-Bi layer when it is in the state of becoming ferromagnetic, i.e., during the vacuum heat treatment. If one were to make accessible to visual observation the magnetic phenomena occurring during the heat treatment, one then should be able to control much more effectively this transformation of a composite nonmagnetic Mn-Bi layer into a film of ferromagnetic MnBi alloy. Whereas in the conventional heat treating procedure the outcome remains in the dark until the heat treatment has been terminated, one could then continuously observe the progress of the transformation through the entire heat treatment schedule and could immediately observe the influence of parameter variations upon the evolution of the magnetic properties and upon the growth of the magnetic areas. If successful, the possibility of observing the nascent state of magnetism might even be of more general significance for the physics of magnetism.

Electron mirror microscopy[9] appeared to be the first choice for such an investigation because it is inherently well suited for the observation of magnetic phenomena[6,10] as well as for the required heat treatment of the specimen. Experiments devised to observe within the electron mirror microscope the formation of magnetic MnBi films during the required heat treatment were unsuccessful however. Growth of Bi whiskers† in combination with the electron mirror microscope's high sensitivity to elevation differences made such observations impossible. It was therefore decided to try the Kerr magneto-optic effect to observe the transformation of the nonmagnetic Mn-Bi layer into the magnetic MnBi alloy film. Such observation with a properly equipped light microscope should be feasible because the Kerr magneto-optic rotation is exceptionally large in MnBi films having an easy direction of magnetization normal to the plane of the film. Whisker growth should not be very disadvantageous for light microscopical observation of the MnBi films during the required heat treatment. The whiskers, being very thin and for the most part very short, appear in the light microscope only according to their actual physical dimensions, whereas the peculiar image formation of the electron mirror microscope depicts these tiny protrusions far out of proportion to their actual size.

What could thus be observed during the vacuum heat treatment in the microscope was very interesting and probably will be of great value in further study. The experiments were not however a complete success. It was possible to observe in a reproducible fashion the phenomena which occurred when an existing area of already magnetic MnBi continued to grow at the expense of a still nonmagnetic area. In some cases it was also possible to initiate this transformation and thereby observe the formation of magnetic MnBi films from the very beginning. It is not yet possible, however, to start this transformation at will in a reproducible manner.

[9] Ludwig Mayer, J. Appl. Phys. **26**, 1228 (1955).
[10] Ludwig Mayer, J. Appl. Phys. **30**, 252S (April suppl., 1959), and J. Appl. Phys. **30**, 1101 (1959).
† Bi whisker growth, interesting in many respects, is under further study; the results of this investigation will be published later.

DESIGN OF VACUUM HOT STAGE

As the heat treatment necessary for the formation of the magnetic MnBi film must be carried out in high vacuum, a complete vacuum hot stage for the light microscope had to be constructed. Figure 1 shows a 1:2.5 cross section of this vacuum hot stage, the heart of which is the furnace *S* made of fused quartz in the shape of an inverted beaker. In the lower half of its cylindrical part a helical groove has been ground into its outer surface. This groove accommodates the windings of a nichrome wire (0.25 mm in diam) which forms the heating coil X.

The flat upper part of the furnace has three holes. A threaded rod P held in the center hole by two nuts Q connects this furnace with the housing cover D. The specimen holder Y consists of two cylinders of fused quartz joined at the bottom. The inner, shorter cylinder supports the specimen V on its upper rim. The outer cylinder is split lengthwise in order to facilitate insertion of the specimen V. The double-walled cylinder assembly with the specimen can be hooked onto three quartz studs U projecting from the cylindrical part of the quartz furnace S, thereby positioning the specimen V close to the center of the furnace's heating coil X.

The specimen is viewed from below through an optically flat Pyrex glass which is sealed to a Pyrex glass cylinder K. An O-ring E around this glass cylinder K permits vacuum sealing of the furnace S with its specimen V by screwing the cover D into the housing H. Vacuum sealing is accomplished by screwing these two brass parts (D and H) together as the O-ring E is thus forced against the glass cylinder H, against the cover

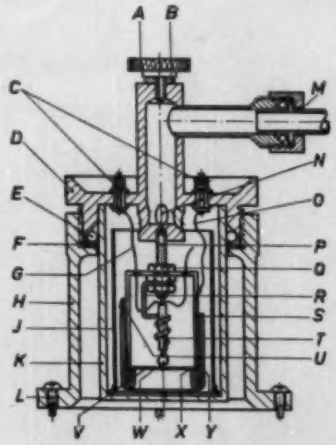

FIG. 1. Vacuum hot stage for metallurgical microscope.

head D and against the brass seat F, which is a brass thrust ring free to turn on a shoulder of the inner wall of the brass housing H. In order to minimize heat radiation losses, a cylindrical mirror-surfaced heat shield J is inserted between the furnace S and the glass cylinder K. This heat shield J rests on three small legs in the corner where the optical flat is sealed to the glass cylinder K. Temperature measurements are accomplished with a thermocouple junction W (Chromel-Alumel) pressing with a slight force against the center of the back side of the specimen V. The thermocouple wires G are fed through a two-hole ceramic tube T, through the two holes in the top of the quartz furnace S and finally through two feed-through terminals, e.g., the left one of the two terminals designated C. Tubular neoprene gaskets hold the terminals C in cover D, serving simultaneously as vacuum seals and insulators. By means of two other feed-through terminals, e.g., the right terminal of two designated C, the electrical connection O is made to the heating coil X of the furnace S. Height adjustment of the furnace S with the specimen V can be accomplished by the nuts Q, one of which also retains wire R holding the thermocouple protection tube T. The brass housing H has in its base four screws L to position it coaxially with the axis of the round table of the metallographic microscope. A vertical tube rising from the center of cover D permits evacuation of glass cylinder K by connecting this tube through the high vacuum coupling M with the high vacuum pump system.

The air leaves the system through four pumping holes N. A knurled screw A seated against a Teflon gasket B serves as an air inlet and the opening may be used for a vacuum gauge if it appears desirable to measure the vacuum directly on the vacuum hot stage. The described vacuum hot stage is set on the table of a metallurgical microscope equipped with Nicol prism polarizer and Nicol prism analyzer (Reichert, type MeF). The connection between the vacuum hot stage proper and the high vacuum system is made with protected flexible bellows, thus permitting the required movement of the microscope table with the vacuum hot stage on it in the three coordinate directions. A vacuum around 2×10^{-5} mm Hg could usually be maintained during the entire heat treatment.

The vacuum hot stage described must be considered as a compromise rather than an ideal solution. For example, the distance from the specimen to the vacuum-enclosing optical flat should, on the one hand, be small in order to allow high magnification which requires small distances between specimen and objective lens. On the other hand, a large distance between specimen and the optical flat through which it is viewed would be desirable in order to immerse the specimen deeply in the vacuum furnace, thus approaching the ideal condition in which the specimen would be completely surrounded by the heated furnace walls. With the present arrangement an objective 8× could be used permitting total magnification up to 100×. As the heater coil of the furnace is rather short compared to the radius of the specimen, an inhomogeneous temperature across the specimen results. This is not too detrimental however because the higher temperatures are at the outer border where one wants to start the transformation reaction. Temperature measurements are rather crude of course because the temperature is not measured at the film which constitutes the specimen proper but at the rear of the glass disks onto which the film has been evaporated. There is however one fact which remedies this situation considerably and makes temperature estimates based on the measured temperatures acceptable although not as accurate as desired. This favorable fact is that tiny melting bismuth whiskers establish a true reference temperature of 271°C within the temperature range of interest. With this one true temperature always observed at the areas viewed at that moment, the other temperatures indicated can be corrected to reasonable accuracy. Another undesirable feature is that the optical glass flat through which the specimen is observed is not at a uniform temperature during the heat treatment of the specimen. The stress caused thereby leads to birefringence in the optical flat which results in general in a decrease in the obtainable contrast.

TYPES OF SPECIMENS

Two types of specimens were observed, by means of the Kerr magneto-optic effect, during their heat treatment in this new vacuum hot stage. The first type of specimens observed were specimens which had been pre-heat-treated so that part of the area of the film had already become magnetic whereas other areas were still nonmagnetic. For the second type of specimen the entire heat treatment required for transformation into magnetic MnBi film was attempted within the vacuum hot stage so that the whole procedure could be observed under the microscope.

The first type of specimen, those already magnetic in parts of the film, were actually specimens taken from normal heat treating runs. As mentioned earlier, some of the heat treating runs were completely successful, whereas others did not yield the right kind of MnBi films. In a few other runs, in which most of the MnBi films were perfect, one or two disks located during the heat treatment at the lower end of the supporting rack, contained good areas exhibiting the desired magnetic properties. These good areas were surrounded however by areas which had apparently not yet become finished, i.e., areas in which the final transformation reaction had not yet taken place. Only within the good areas was magnetic writing with permanent magnet probes possible. Attempts to write magnetically across such a disk resulted therefore in magnetic lines always terminating at the border of the good areas. These borders separating finished and unfinished areas were quite pronounced lines of antiparallel magnetic domains whose average

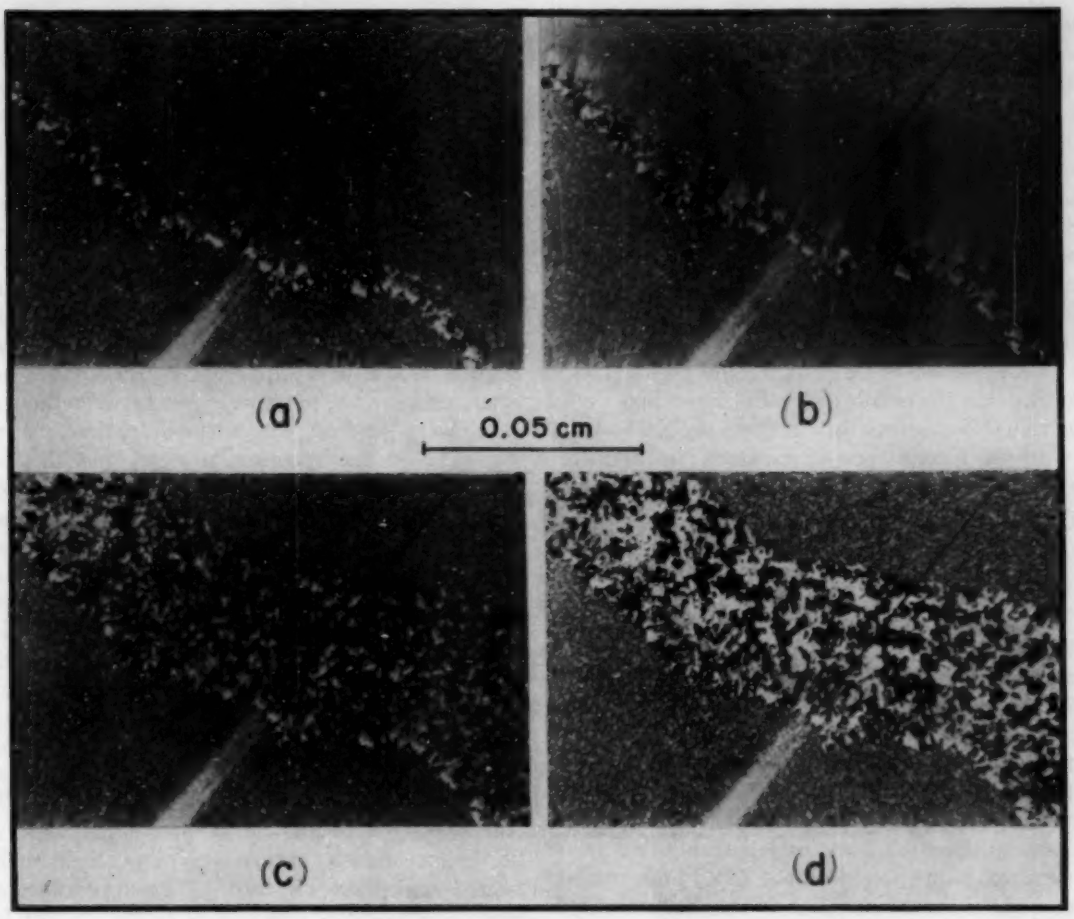

FIG. 2. Growth of an area of large antiparallel magnetic domains on MnBi film.

size was about 10 to 40 times larger than the size of the domains inside the finished areas [see Fig. 2(a)]. Although the borderline was strongly marked, the structures of the areas proper were quite similar and discriminating differences could barely be detected up to magnifications of about 100×. At higher magnifications (350×) one could see, by means of the Kerr magneto-optic effect, that the finished areas consisted of small antiparallel domains, their contrast pattern not being changed by rotation of the film in its plane, whereas the contrast pattern of the unfinished areas changed with rotation around the axis of observation. The white stripe in Fig. 2(a) terminating at the borderline consisting of large antiparallel magnetic domains has been drawn with a Cunife permanent-magnet wire of 0.12-mm diam.‡ The area above the borderline is the unfinished, still nonmagnetic area into which therefore the white stripe of magnetic writing does not continue. The fine dark line in this area, apparently a continuation of the white stripe across the border, is not of magnetic origin; it is actually a scratch which was not apparent immediately after the writing but developed a few days later. It might be mentioned here that when exposed to the atmosphere the stability of the two areas, the magnetic area and the still unfinished nonmagnetic area, is quite different. Immediately after the preparation of such films containing these two types of areas, no difference can be detected between these two areas with the unaided eye. After a few days however the unfinished areas show considerable discoloration, the mirror-like finish becomes somewhat dull and these unfinished areas also become more transparent. The finished magnetic areas however do not show any signs of deterioration, at least not during the period of our observation, i.e., over one year. At the same time as the deterioration in air sets in, marks develop on the unfinished areas which were not visible before, even at high magnification. The scratch mentioned above is an example of such a mark. In the early stages of deterioration the transformation of the nonmagnetic areas into magnetic ones can still be achieved by the appropriate vacuum heat treatment; in advanced stages it is no longer possible however. The fact that the magnetic areas of MnBi films retain their mirror-like appearance without any apparent deterioration, whereas the unfinished areas corrode rapidly, may shed some light on

‡ Kindly supplied by Irvin L. Cooter, Magnetic Measurements Section, National Bureau of Standards.

the surprising fact that magnetic MnBi films are very stable whereas bulk MnBi is known to corrode rapidly when exposed to the atmosphere.

Disks described above with areas already transformed into the desired magnetic MnBi state were used first for further heat treatment in the newly constructed vacuum hot stage. Observation of the continuation of the growth of already existing magnetic areas at the expense of the still nonmagnetic areas was the aim of this first series of experiments. To start the observation with disks already containing areas of the right kind of MnBi film was of course tempting. The probability of success was expected to be considerably higher and it was thought that the results of these observations would provide valuable clues as to what one should look for when, with the second type of specimen, the transformation into the magnetic state is to be observed from the very beginning.

RESULTS AND CONCLUSIONS

The results reported here have been obtained with the first type of specimen described above, i.e., with the preheat-treated, area-wise finished MnBi films. A few micrographs [Figs. 2(a) to 3(d)] will illustrate what has been observed when the heat treatment was continued in the above described vacuum hot stage on the metallurgical microscope.

Figure 2(a) shows the starting condition: a borderline of large antiparallel domains separating two areas which, at a magnification of about 65×, look similar but have quite different properties. The magnetic area contains the white stripe of magnetic writing which terminates as described and explained above at the borderline. When the disk containing these two areas was heated to about 310°C in the vacuum hot stage, an essentially structureless, band-shaped area started to grow from the upper side of the border into the nonmagnetic areas of the film. In about 20 min the essentially structureless band grew about 0.3 mm wide [see Fig. 2(b)]; the heat treatment was then interrupted. During the cooling period antiparallel domains emerged from this structureless area. Figure 2(c) shows the dark areas of one set of domains and the white areas of the other set of domains of opposite magnetization, immersed in the remaining parts of the structureless areas. When the temperature was down to about 250°C, the antiparallel domains had grown together [see Fig. 2(d)] to an average size somewhat larger than the antiparallel domains of the former borderline. Thus, another part of the formerly nonmagnetic area had become magnetic with the same kind of preferred orientation as the previously magnetic areas but with domains corresponding in size to the borderline domains rather than the domains of the interior of the magnetic areas. When the heat treatment was then resumed by heating the disk to a temperature only a few degrees less than before, i.e., to about 305°C, a structureless area started growing anew, this time at about half the former speed [see Fig. 3(a)]. In Fig. 3(b) this structureless area already covers the remaining field of view. This time the vacuum heat treatment was not interrupted for about three hours, during which time the newly transformed band-shaped area grew about 1.5 mm wide. This band did not stay structureless but was transformed into a magnetic structure with the same appearance as those areas which had already been magnetic. This latter transformation started however only after about one hour had elapsed since the particular region had become structureless. There was no pronounced border between regions of this newly developed structure and the still structureless area, the changeover between these regions being very gradual. The antiparallel domains in these newly developed magnetic areas were small, and they had approximately the same size as in the areas which had already been magnetic before the additional heat treatment had been started. After the disk was taken out of the vacuum hot stage, two additional magnetic lines were drawn with the Cunife permanent magnet wire across the MnBi film in a direction parallel to the original line. These newly drawn lines did not terminate at the original borderline [see Fig. 3(c)] but were also apparent across the whole newly developed area, proving that this entire area had become magnetic, consisting of antiparallel domains with their direction of magnetization normal to the plane of the MnBi film. At the border of the newly grown magnetic area a borderline of large antiparallel magnetic domains appeared again [see Fig. 3(d)]. The appearance of this new borderline was very similar to the starting borderline shown in Fig. 2(a), the only difference being that close to this new border a few large antiparallel domains were scattered randomly in the area of principally small domains.

From the experiments described here and from others also made with disks of partly finished MnBi films, one can draw the following conclusions. The phenomena occurring during evolution of the magnetic state in the areas adjacent to already magnetic areas can be readily observed. The new growth starts as an area containing, at the beginning, considerably less structure than either the already magnetic areas or the areas not yet transformed into magnetic areas. Areas which had been for a short time only (less than 30 min) in the structureless state tend to develop into larger antiparallel domains than those areas which are kept for a longer time (more than 60 min) at a temperature at which the structureless area grows. The transition region from large domains into small ones appears to be rather narrow, as no intermediate size domains could be found at the magnetic-area-side of the borderline consisting of the large antiparallel domains.

These experiments observing the continuation in the growth of magnetic areas in MnBi films containing already magnetic areas were rather successful and they could be repeated consistently. The next step, however,

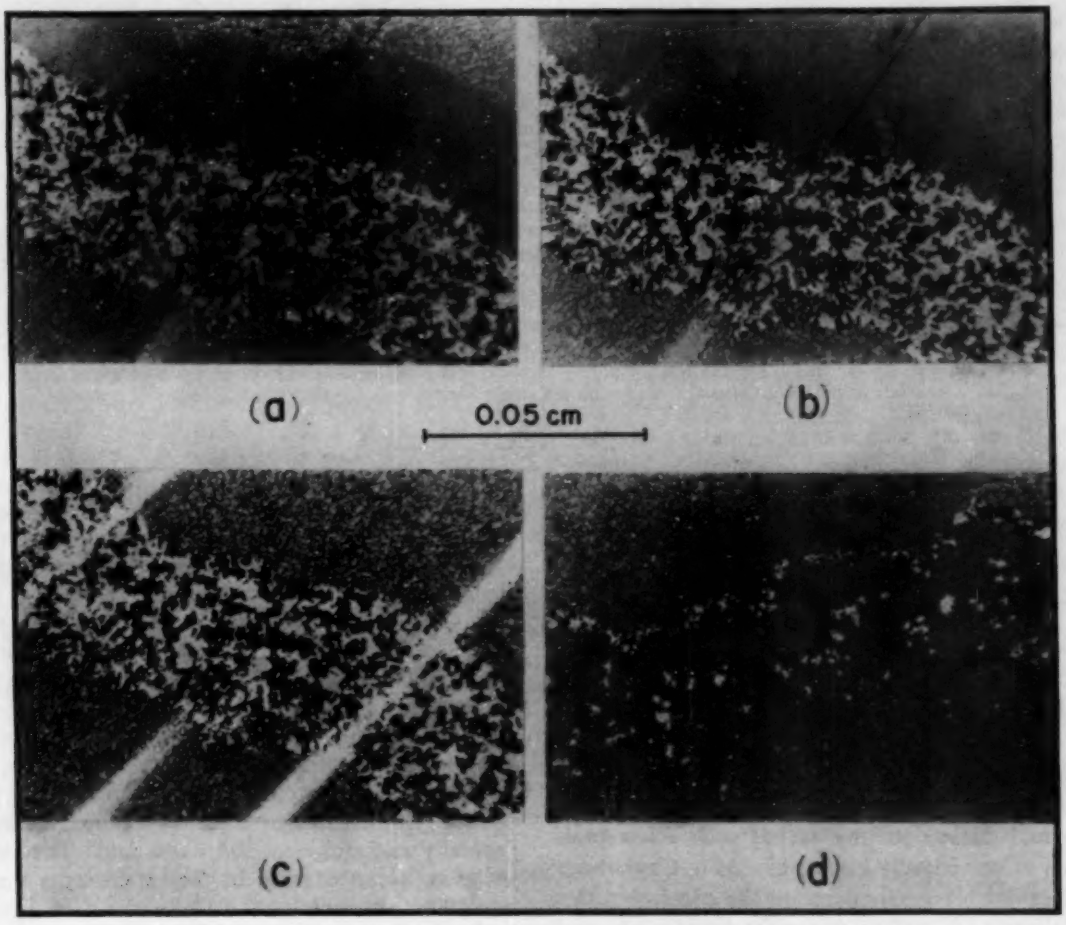

FIG. 3. Growth of an area of small antiparallel magnetic domains on MnBi film.

namely the observation of the very beginning of the nascent state of magnetism in MnBi film has not yet been fully successful because attempts to nucleate the transformation into the magnetic state within the vacuum hot stage have hitherto been only partly successful. In a few cases the goal was achieved. In most cases, however, a surprising, nearly overwhelming variety of phenomena could be observed when heat treatment of a virgin Mn-Bi layer was started in the vacuum hot stage. For a deeper understanding it will become necessary to study these phenomena in detail and to correlate the findings with the results of other methods, particularly with x-ray diffraction analysis.

One now knows definitely what to look for if one wants to let a magnetic MnBi film grow in size at the expense of still nonmagnetic regions. Remaining to be established are the exact conditions necessary for observing the very start of this transformation consistently. If this is done, the visual control then available should permit proper correlation of success or failure with the different parameters involved and should make it possible to uncover the hidden facts which make it so difficult to reproduce good results in the preparation of MnBi films. The possibility of observing the nascent state of magnetism visually might even be of more general interest.

ACKNOWLEDGMENTS

The author wishes to acknowledge gratefully the assistance of Messrs. E. Benz, H. Stenemann, H. Hager, and R. Lund in designing and constructing the vacuum hot stage and in performing the experiments. The editorial assistance provided by Mr. D. Given is also gratefully acknowledged.

Detailed Study of Switching Current in Barium Titanate

M. E. Drougard
IBM Research Laboratory, Poughkeepsie, New York
(Received June 22, 1959)

The polarization reversal process in ferroelectrics has, up to now, been characterized solely by the total switching time and the maximum value of the switching current. The work presented in this paper was aimed at determining how the instantaneous value of the switching current in single crystals of $BaTiO_3$ depends on the applied field, the state of net polarization of the crystal, and possibly other factors. It has been found that the switching current density can be expressed as the product of a function of the polarization, $\phi(p)$, and a function of the electric field, $\exp(-\alpha/E)$. The form of the function $\phi(p)$ indicates a predominance of sideways expansion of 180° domains, with an exponentially increasing domain wall velocity. This last result is shown to be in agreement with a picture of domain wall motion by nucleation of new domain wall layers. This interpretation, together with some details of the switching current pattern, suggests that a crystal, although apparently single-domain, may always retain some small domains of opposite polarization.

I. INTRODUCTION

THE basic studies of the reversal of polarization in barium titanate have been performed by Merz[1] a few years ago. The experiments have yielded a law for the field dependence of the switching time which has not as yet received any satisfactory explanation. Merz[1] has also presented a theory according to which the limiting rate is that of the appearance of nuclei of reverse polarization due to thermal agitation. The only merit of this theory is that it leads to the observed form for the field dependence, but Landauer[2] has shown that this thermal nucleation process has such a low probability as to be virtually impossible. Also, Chynoweth[3] and Miller[4] have recently come to the conclusion that the polarization is reversed mostly by domain wall motion, at least at slow switching speeds (~1 min).

The work presented in the present paper was aimed at gaining some information about the instantaneous dependence of the switching current upon field, polarization and possibly history, which may hopefully shed some light on the switching process.

At any instant of time, we expect the switching current to depend not only on the applied field but also on the state of polarization of the crystal. The history of the sample, that is how the crystal has arrived at its present state of polarization, may also be a relevant factor. Then if i_s is the switching current density, P the net polarization $(-P_s \leqslant P \leqslant +P_s)$ and E the electric field, we can use the symbol h to designate all relevant factors, including the time, having to do with history, and write

$$i_s = dP/dt = F(P,E,h). \quad (1)$$

It is this function F that we propose to analyze experimentally.

[1] W. J. Merz, Phys. Rev. **95**, 690 (1954).
[2] R. W. Landauer, J. Appl. Phys. **28**, 227 (1957).
[3] A. G. Chynoweth, Phys. Rev. **110**, 1316 (1958).
[4] R. C. Miller (to be published).

II. SAMPLES AND TECHNIQUES

The samples used in this investigation were single crystals grown by the standard Remeika method. Their thickness was chosen in the neighborhood of 0.1 to 0.2 mm. Gold strips were evaporated on either side at right angles so that the effective area was about 0.1 mm². The four samples selected have a "good" 60 cps hysteresis loops, that is the loops are square and do not show any opening in the saturated portions. Their switching behavior under constant applied field is characterized by a bell-shape switching current pulse which is very nearly symmetrical, although the current does not generally rise quite as fast as it falls. The range of switching times covered in the experiments was from 2 to 100 microseconds.

The method used in studying the field, polarization and history dependencies of the switching current consists in varying the wave shape of the applied field. The sample is submitted to a pulse train (Fig. 1) which includes four pulses. Two of those pulses (No. 1 and No. 2 in Fig. 1) are of large amplitude (~50 v) and long duration (5 msec), and only serve the purpose of "conditioning" the sample. Crystals of barium titanate are known to become "fatigued" under repetitive pulsing, that is, they seem to lose their ferroelectric response. This may take no more than a few minutes when the amplitude of the pulses is just larger than the 60 cps coercive voltage and their duration just sufficient

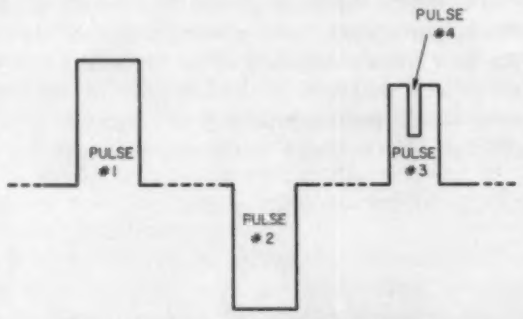

FIG. 1. Basic pulse train used in this study.

to switch the crystal completely. Such a fatigue is avoided by the presence of the large conditioning pulses.

The only pulses actually varied during the experiments are the pulses labeled No. 3 and No. 4 in Fig. 1. Pulse No. 4 is of opposite sign to pulse No. 3 and superposed on it, resulting in a split pulse illustrated in Fig. 2. The No. 3 pulse impresses a field E across the samples for a time t_1. At time t_1, the No. 4 pulse is turned on for a time t', during which the applied field falls to a value E'. Then the No. 4 pulse is turned off, while pulse No. 3 is still on, so that the field goes back to its original value E. Both pulse durations ($t_1+t'+t_2$ and t') can be varied from 1 to 1000 microseconds.

The switching current through the sample is viewed through a series resistor by means of a fast oscilloscope. The polarization may similarly be measured by replacing the viewing resistor with a viewing capacitor. The voltage across the sample is also measured with the help of the oscilloscope by a comparison technique. Even though the output impedance of the generator is low (200Ω) the samples cause a noticeable loading when switched at high speeds, and this loading has to be taken into account for precise measurements. Also, the instantaneous voltage has to be corrected by the corresponding voltage across the viewing resistor.

III. MEASUREMENTS

The possibility of a history dependence of the switching current is eliminated by the following experiment. Keeping the field E (Fig. 2) constant, the times t_1 and t' and the field E' are varied in such a way that the polarization at time t_1+t' is kept constant. As long as E is kept constant, the instantaneous switching current at time t_1+t' remains the same, showing that the switching current is affected only by the instantaneous conditions of polarization and applied field and not by the manner in which those conditions were brought about. The parameter h can then be dropped from equation (1), which can be written

$$i_s=dP/dt=F(P,E). \tag{2}$$

Next, the form of the function $F(P,E)$ is investigated by determining the relationship between i_s and E for different values of P. This is accomplished by turning on pulse No. 4 at a constant time t_1 after the beginning of pulse No. 3 (Fig. 2) and varying its amplitude. The switching current is measured just after the application of pulse No. 4. If $\log i_s$ is plotted against $1/E'$, a straight line results, the slope of which is independent of time t_1, that is, independent of the amount of polarization already reversed. The intercept of the straight line with the $\log i_s$ axis does, of course, depend on the state of polarization of the sample, so that the equation of the straight line is:

$$\log i_s=\log\phi(P)-\alpha/E.$$

This result shows that the switching current depends on the applied voltage only through the multiplying factor $\exp(-\alpha/E)$, where α is a constant (for a given crystal) which is independent of the state of polarization of the sample.

The independence of the coefficient α of P has been demonstrated only, of course, within experimental errors, that is within about 5%. As expected, the value of α is also the same as is found by plotting $\log i_s$ max *versus* $1/E$, as was done by Merz. The value of α on the sample investigated ranges from 5 to 10 kv/cm, which is lower than the value quoted by Merz,[1] but is in good agreement with Landauer's prediction[5] that the low-frequency coercive field should be about 1/10 of α.

For the purpose of the following discussion, it will be convenient to normalize the quantities entering Eq. (2) by introducing the dimensionless parameters:

$$p=\frac{P}{P_s},\ (-1<p<1);\quad j=\frac{i_s}{2P_s}.$$

The direction in which switching is taking place is taken to be the positive direction, so that p varies from -1 at the beginning of the switching to $+1$ at the end of the switching.

Since the function $F(P,E)$ is separable, Eq. (2) now reads

$$j=\frac{dp}{dt}=\phi(p)e^{-\alpha/E}. \tag{3}$$

The function $\phi(p)$ can be obtained simply from any photograph of the switching current *versus* time. The parameter p is easily calculated from the area under the switching current curve. The function $\phi(p)$ is then obtained by plotting the quantity $j\exp(\alpha/E)$ against p, where E is the actual field, taking account of the loading of the pulse generator and of the voltage drop across the viewing resistance.

A typical plot of ϕ *versus* p is shown by a full line in Fig. 3. The dashed lines are the extrapolations to zero current, and the dotted line is the parabola $\phi(p)=1-p^2$. It will be noted that the extrapolations to zero current do not correspond exactly to $p=\pm1$. This feature is common to all such plots, and we will return to this point in the discussion.

The parabola $\phi(p)=1-p^2$ represents a fairly good

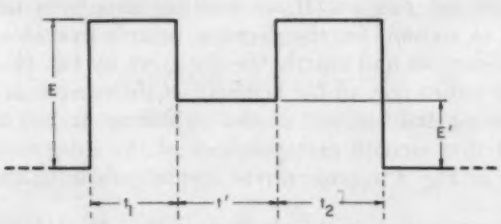

FIG. 2. Detail of split pulse.

[5] Landauer, Young, and Drougard, J. Appl. Phys. 27, 752 (1956).

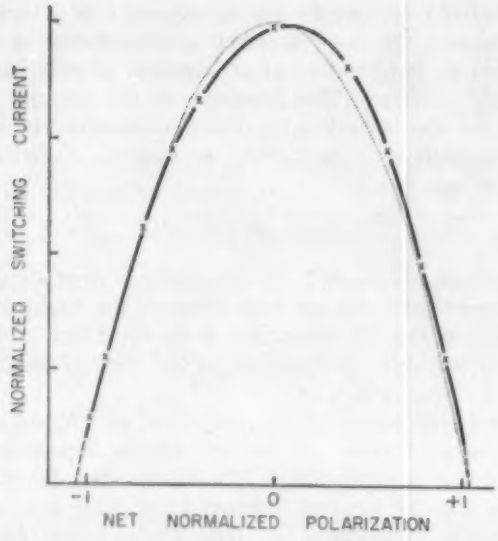

FIG. 3. Actual dependence of j on p (full line) and parabola through the zero current (extrapolated) points in dotted line. Scale factors are such that the areas under the two curves are equal.

fit to the actual curve observed. The actual current actually rises slightly slower than the parabola, but falls down with nearly the same slope. This would seem to indicate that the factor $(1-p)$ is very nearly correct, but that a better fit would probably be obtained if the power of p were taken to be slightly larger than unity (since $0<p<1$).

We can then tentatively write the switching law in the form

$$j=\beta(1-p^2)e^{-\alpha/E} \tag{4}$$

which is equivalent to

$$I_s=Q_s\beta(1-p^2)e^{-\alpha/E}$$

where I_s is the actual switching current at any instant of time, and Q_s the total charge switched during a complete reversal of the polarization. We find that the coefficient β varies from 0.4 to 2.3×10^7 sec^{-1} for the different crystals studied.

IV. DISCUSSION

According to Merz's[1] "nucleation theory" mentioned in the introduction, the switching current should be proportional to $(1-p)$. It seems rather hopeless to try and imagine a mechanism which would also make the nucleation rate proportional to $(1+p)$. On the other hand, Chynoweth[3] has found definite indications that the polarization is reversed mostly by sideways expansion of cylindrical domains. Miller,[4] working on samples with liquid electrodes has unequivocally confirmed this fact in the case of slow switching ($\sim$1 min).

The domain wall velocity at constant field has been found by Miller[4] to be constant. Now, in the early stages of switching, etch patterns show that domains remain nearly circular. This means that the amount of polarization reversed would increase like t^2, that is we would expect j to have the form

$$j=(1-p)(1+p)^1 \tag{5}$$

where the $1-p$ factor accounts for the decrease of the area available to domains to expand. The corresponding curve actually turns out to rise faster than the parabola of Fig. 3, having its maximum at $p=-\frac{1}{3}$, whereas our experimental curve has its maximum for a very small positive value of p.

It should perhaps be mentioned that we are also in disagreement on this point with Pulvari and Kuebler.[6] These authors have found that they could account for the behavior of the switching current with an equation (in the notation of this paper)

$$(dp/dt)=t(1-p)g(E) \quad (A=\text{constant}) \tag{6}$$

which also implies a constant domain wall velocity in the early stages of switching. The corresponding plot is extremely similar to that of Eq. (5), with maximum current at $p=-0.27$, and does not fit our experimental data nearly as well as the parabola.

From our own experiments, we are forced rather to the conclusion that, in the early stages of switching, the current obeys the equation

$$j=(dp/dt)=2\beta(1+p)$$

which implies that $(1+p)$ increases exponentially with time, hence that the domain wall velocity increases exponentially.

This exponential rise of the domain wall velocity appears at first rather surprising. It is, however, in excellent agreement with a suggestion made by Frank[7] that domain wall motion occurs by nucleation of a protuberance or finger on an existing domain wall. (This should be much easier than nucleating a whole domain starting from scratch.) This finger would expand throughout the thickness very rapidly. Then sideways expansion along the domain wall requires much less energy and should occur much faster. The nucleation of the finger would have a probability proportional to the perimeter of the wall, and its expansion would cause a change of polarization also proportional to this perimeter. Hence the time rate of change of the polarization for a single domain would be proportional to the area of the domain. Adding up all contributions from all the domains, we find again that the total rate of change of the polarization would be proportional to the existing polarization. If we multiply this by a factor $1-p$ to account for the decrease in area available for expansion, we find exactly the law given by Eq. (4).

We return now to the behavior of the current at the beginning and the end of the switching. It has been noted that smooth extrapolations of the experimental curve in Fig. 3 to zero current corresponds to values of

[6] C. F. Pulvari and W. Kuebler, J. Appl. Phys. **29**, 1742 (1958).
[7] F. C. Frank (private communication).

p which differ from ± 1. This can be accounted for in a formal way by placing on Eq. (4) the restriction that p may vary not from -1 to ± 1, but only from $(-1+\epsilon_0)$ to $(1-\epsilon_1)$. Physically, if we accept the fact that polarization reversal occurs quite predominantly by domain wall motion, it is tempting to go a step further, and to assume that some regions having the original direction of polarization never disappear. Then, when the field is reversed, these leftover domains start expanding immediately, and the switching current builds up from a small but finite value.

The view that some nuclei never actually disappear from a crystal is supported by a number of facts. Photographs of etch patterns often show what seems to be a very small domain of opposite polarization in the middle of a larger domain (see for instance Fig. 3 of Cameron's article[8]). Cameron has also obtained recently an electron micrograph of a completely switched crystal (shown in Fig. 4) in which small domains of about 1 micron in diameter are clearly visible. Those domains cover about 1% of the area of the whole photograph. Also, the zero current polarization obtained by extrapolating the curve of Fig. 3 to zero current differs from zero or unity by 1 to 3% for all crystal investigated.

The dependence of j upon p illustrated in Fig. 3 throws some doubt on the interpretation given by Chynoweth[3] to Barkhausen pulses. If these pulses did correspond to nucleation of new domains, they should occur at a rate proportional to $1-p$, regardless of how p varies in time. On the other hand, if a Barkhausen pulse resulted from the encounter of two domains expanding sideways, the rate of occurrence of such pulses would be proportional to the area swept by domain walls, hence to the switching current, at least in the case when nuclei are distributed in a perfectly random fashion throughout the area of the crystal. Any deviation from absolute randomness would, of course, result in a deviation from the law of proportionality between rate of occurrence of Barkhausen pulses and switching current. It should be noted that Miller[4] has observed at least *some* Barkhausen pulses which definitely seemed to arise from the merging of two domains.

V. CONCLUSIONS

We have shown that the switching current in barium titanate is determined solely, for relatively fast switching (2–100 μsec), by the conditions of field and polarization in the sample. The switching current is proportional to the product of a function of E, with a function of the net relative polarization, as:

$$j=(dp/dt)=\beta(1-p^2)e^{-\alpha/E}.$$

[8] D. P. Cameron, IBM J. Research and Develop. 1, 2 (1957).

FIG. 4. Electron micrograph of a completely polarized crystal. Magnification is 4000×.

The form of the law just stated is in contradiction with the hypothesis that sideways motion of domain walls plays a negligible part in the switching process. It is in very good agreement with the view that polarization is reversed predominantly if not solely by sideways expansion of domains. If this interpretation is correct, then the wall velocity increases exponentially in the early stages of switching. This would be in excellent agreement with a domain wall motion governed by nucleation. Deviations from this law at the beginning and at the end of the switching suggest that nuclei may never disappear completely. The form of the polarization dependence also favors the interpretation of Barkhausen pulses as arising from the encounter of domain walls.

Further studies of etch patterns together with more detailed studies of the rate of occurrence of Barkhausen pulses may allow to definitely prove or disprove the above conclusions.

ACKNOWLEDGMENTS

The author would like to express his thanks to Dr. R. W. Landauer for suggesting this study, and to Mr. Howard Coons who helped build the the electronic equipment.

JOURNAL OF APPLIED PHYSICS VOLUME 31, NUMBER 2 FEBRUARY, 1960

Decay of Wax Electrets

M. M. PERLMAN*
Whirlpool Corporation, St. Joseph, Michigan
(Received May 28, 1959)

The internal field within an electret can be varied by changing the spacing and arrangement of shielding electrodes ("partial shielding"). The application of this technique to rosin-wax electrets shows that the charge decay observed upon unshielding electrets is caused primarily by volume polarization due to internal field rather than by external ion collection.

INTRODUCTION

WISEMAN and Feaster[1] attributed the decay of an unshielded electret's externally measured charge primarily to volume polarization due to its own internal field, rather than to ion collection. They warmed an initially cool, essentially charge-stable, unshielded Gelva V-7 electret, enabling polarization to occur, resulting in more heterocharge, and thus in decay of the measured charge density. (The electret's homocharge was assumed to remain relatively constant throughout the experiment.) Shielding and cooling tended to preserve static conditions. Warming the shielded electret permitted thermal decay of the heterocharge, resulting in "growth" of measured charge density.

It occurred to the author that a further, more direct test of internal-field self-polarization *vs* ion collection theories would be provided by a study of the effect of the size of this field on the charge decay of electrets. The electret and its shielding electrodes can be regarded as a three-layer capacitor, and equations derived for both the fields in the air gaps, and within the electret.[1,2] As one might expect, these tell us that the internal field should be largest when the electret is completely unshielded, and should decrease as the electrodes are brought closer to the surfaces, having a negligible value on complete shielding. (The field then resides in the small but finite gaps between shields and electret surfaces.) Thus, partial shielding provides a method whereby magnitude of the self-internal field may be varied.

THEORY AND EXPERIMENTAL

Consider the n-electret, $(2n+1)$ layer capacitor with grounded shielding plates of Fig. 1. The internal fields (E) can be shown to be given by

$$E=4\pi\sigma \sum_{j=1}^{n+1} d_{2j-1}/\{K \sum_{j=1}^{n+1} d_{2j-1}+\sum_{j=1}^{n} d_{2j}\},$$

where all d's with odd subscripts are thicknesses of air gaps, all d's with even subscripts are thicknesses of electrets, K is the dielectric constant of the electrets, and σ is the externally measured charge density, assumed equal in magnitude on all electret surfaces.

All 0.25-in.-thick wax electrets were made from the same batch of the "classical" mixture (40% carnauba wax, 40% rosin, 20% beeswax) at 200°F in a field of 6.4 kv/cm. After "growth" to their maximum charges, those electrets with measured charge densities of $\pm 10.2 \pm 0.4$ esu were placed in a desiccator at 5% R.H. and 70°F under storage conditions illustrated in Fig. 2. The storage temperature was not accurately controlled. Fluctuations of a few degrees took place during the course of the experiments.

RESULTS AND DISCUSSION

By using the above equation, one can calculate the percent reduction, R, of the internal field on partial shielding of electrets from its value when they are completely unshielded. In Fig. 3, results are plotted against air-gap spacing for each storage condition of

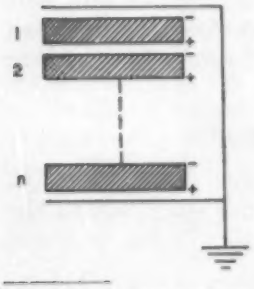

FIG. 1. An n-electret, $(2n+1)$-layer capacitor with grounded shielding plates.

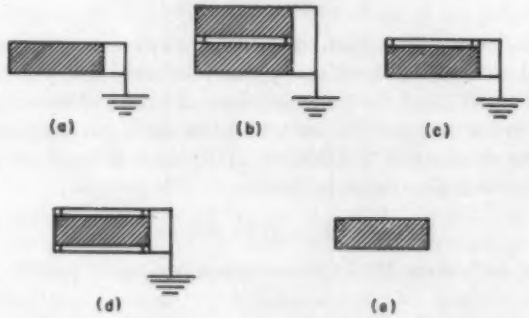

FIG. 2. Diagram showing shielding conditions under which wax electrets were stored in a typical experiment: (a) completely shielded control, (b), (c), (d) partially shielded, (e) unshielded.

* Now at Physics Department, College Militaire Royal, St. Jean, Quebec, Canada.

[1] G. G. Wiseman and G. R. Feaster, J. Chem. Phys. **26**, 521 (1957).

[2] A. N. Gubkin, Soviet Phys.-Tech. Phys. **2**, 1813 (1957).

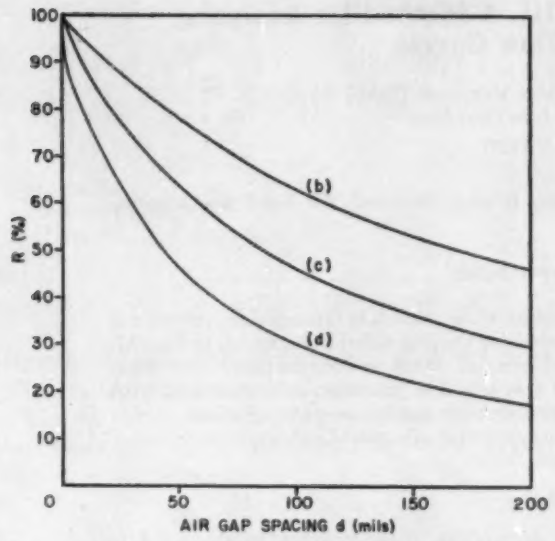

FIG. 3. Percent reduction (R) of internal field (E) from its value when the electret is completely unshielded, as a function of thickness of air gaps. Wax electrets were 0.25-in. thick and of dielectric constant 2.9. (b), (c), (d)—refer to Fig. 2.

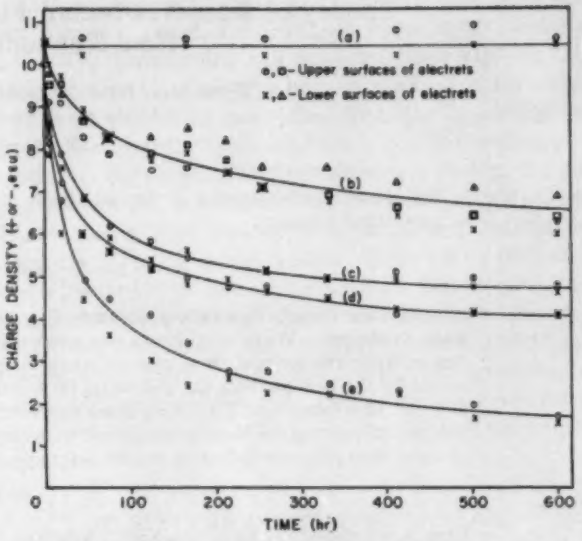

FIG. 4. A typical plot of measured charge density on all surfaces of electrets stored as in Figs. 2 (a)–(e) as a function of time. Air gaps were 0.062 in. This demonstrates that charge decay of electrets is caused primarily by volume polarization due to their own internal fields.

the 0.25-in.-wax electrets of Fig. 2, whose dielectric constant was 2.9.

The internal field of an unshielded electret is simply $E=4\pi\sigma/K$, and in this case is 13.2 kv/cm. That for a completely shielded electret is negligibly small. Spacings of 0.062 in. were used in the typical experiment reported here, yielding R values of 74%, 59%, and 41% for electrets (b), (c), and (d) of Fig. 2, respectively. Typical plots of charge density *vs* time on both upper and lower electret surfaces are shown in Fig. 4 for electrets stored as in Fig. 2. Table I lists initial internal fields and charge densities and their values 260 hr after shielding for cases (a) to (e) of Fig. 2.

One can see that the charge densities on the different wax electrets studied in these experiments are affected by partial shielding in the order to be expected on the basis of strength of internal field, and resulting volume polarization, the larger initial fields yielding larger initial decay rates and lower charge densities. Rapid decay on each of the curves for the first 2 or 3 days is attributed primarily to self internal field, and the following slow decay to a combination of relatively small internal field and perhaps some ion collection.[3]

TABLE I. Internal fields (E) and charge densities (σ) of decaying electrets. (See Fig. 2. Spacing is 0.062-in. Wax electrets are 0.25 in. thick.)

Case	$E(t=0)$ (kv/cm)	$E(t=260$ hr) (kv/cm)	$\sigma(t=0)$ (esu)	$\sigma(t=260$ hr) (esu)
a	0	0	−10.5, +10.2	−10.6, +10.2
b	3.5	2.4	−10.6, +10.6	−7.1, +7.1
			−10.6, +10.6	−7.1, +7.6
c	5.3	2.6	−9.8, +9.8	−5.1, +5.1
d	7.6	3.4	−9.8, +10.2	−4.7, +4.6
e	13.2	3.2	−9.8, +10.6	−2.7, +2.2

The results reported here are qualitatively consistent with the heterocharge-homocharge theory of electrets developed by Gross[4] and Adams. No quantitative agreement was obtained in attempts to establish a proportionality between changes in measured surface charge density, when polarization was nearly complete, and internal field. Further work under more controlled conditions is contemplated.

[3] At 260 hr, Table I shows that the internal fields are roughly the same. The external fields can be calculated from an equation similar to the foregoing and at 260 hr increase in the order (e) to (b) from 0 to 20 kv/cm. Thus, if ion collection were effective, one might expect a progressively increasing slope from (e) to (b). Since Fig. 4 shows that the decay rates after 260 hr are roughly equal, ion collection plays only a minor role.

[4] B. Gross, J. Chem. Phys. 17, 866 (1949).

JOURNAL OF APPLIED PHYSICS VOLUME 31, NUMBER 2 FEBRUARY, 1960

Theory of Non-Newtonian Flow. III. A Method for Analyzing Non-Newtonian Flow Curves

WAN KYUE KIM, NISHIO HIRAI, TAIKYUE REE, AND HENRY EYRING
University of Utah, Salt Lake City, Utah

(Received June 5, 1959)

The historical development of the rate theory of viscosity is briefly reviewed. The Ree-Eyring equation of generalized viscosity,

$$\eta = \sum_{n=1}^{m} (x_n\beta_n/\alpha_n)(\sinh^{-1}\beta_n\dot{s}/\beta_n\dot{s}) \qquad (A)$$

is applied successfully in a variety of cases. (For the definitions of the symbols in this equation, reference is made to the text.) We develop here a new method for determining the parameters x_n/α_n and β_n in Eq. (A). According to the method, these parameters are uniquely determined. When we used the parameters determined by the new method, the viscosities for solutions of poly-γ-benzyl-l-glutamate were calculated from Eq. (A). It is found that Eq. (A) is much superior to other frequently applied viscosity equations.

Upon calculating the Newtonian viscosities η_s for fairly concentrated solutions of polyacrylonitrile and of nitrated pine pulp, the following empirical formula is found:

$$\eta_s \simeq KC^3M\beta_p^3. \qquad (B)$$

Here K is a characteristic constant for a solution; C the concentration; M the molecular weight; and β_p is the "principal" relaxation time. In dilute solutions, Eq. (B) reduces to the form $\eta_s \simeq K'CM$.

INTRODUCTION

BASED on the theory of rate processes, an equation for non-Newtonian viscosity was derived by Eyring.[1] His theory of viscosity was generalized by Powell and Eyring[2] and Ree and Eyring,[3] and was applied to various high polymeric and colloidal systems. The generalized viscosity equation[3] was also applied to synthetic rubber-latex suspensions by Maron and Pierce[4] and Maron and Sisko.[5] Dahlgren[6] applied the generalized equation to a bentonite suspension, and Christiansen, Ryan, and Stevens[7] applied it to the systems: Napalm in kerosens, sodium carboxymethylcellulose in water, and hydrated lime in water. The results were satisfactory in all cases.

In applying the generalized viscosity equation, it is necessary to determine the molecular parameters in the equation. Thus far, the parameters have been determined largely by a method of trial and error.

In this paper, we present (1) a method for the determination of parameters, which gives unique and exact results; (2) the non-Newtonian viscosities of high polymeric systems are calculated from the generalized viscosity equation, using the parameters obtained by the new method; and (3) the results obtained in item (2) are compared with those calculated from other customary viscosity equations.

[1] H. Eyring, J. Chem. Phys. **4**, 283 (1936); Glasstone, Laidler, and Eyring, *The Theory of Rate Processes* (McGraw-Hill Book Company, Inc., New York, 1941), p. 483.
[2] R. E. Powell and H. Eyring, Nature **154**, 427 (1944).
[3] T. Ree and H. Eyring, J. Appl. Phys. **26**, 793 (1955); **26**, 800 (1955).
[4] S. H. Maron and P. E. Pierce, J. Colloid Sci. **11**, 80 (1956).
[5] S. H. Maron and A. W. Sisko, J. Colloid Sci. **12**, 99 (1957).
[6] S. E. Dahlgren, J. Colloid Sci. **13**, 151 (1958).
[7] Christiansen, Ryan, and Stevens, Am. Inst. Chem. Engrs. J. **1**, 544 (1955).

(I) SYSTEMS CONTAINING TWO TYPES OF RELAXING UNITS

We consider a simple system which consists of two kinds of flow units, one is non-Newtonian and the other is Newtonian. This is the case for poly-γ-benzyl-l-glutamate (PBLG) solution which is shown in Fig. 1.

For such systems, the viscosity, η, is represented as a function of shear rate $\dot{s}$ as follows[3]:

$$\eta(\dot{s}) = (x/\alpha)\beta(\sinh^{-1}\beta\dot{s}/\beta\dot{s}) + \eta_N, \qquad (1)$$

where x is the fraction of the area on a shear surface occupied by the non-Newtonian flow units, $\alpha = \lambda\lambda_2\lambda_3/2kT$, $\beta = 1/\{(\lambda/\lambda_1)2k'\}$, k' is the rate constant for the flow process at zero stress, λ_1, λ_2, λ_3, and λ are the molecular distances in the Eyring theory of viscosity,[1] and η_N is the term due to the Newtonian unit.

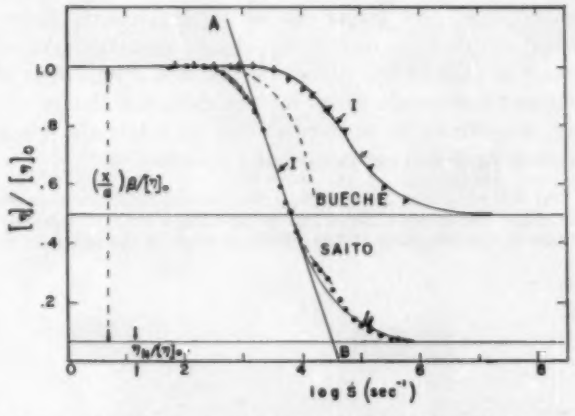

FIG. 1. Non-Newtonian viscosity of poly-γ-benzyl-l-glutamate solution (data from Yang[8]). Open circles represent the observed values in *m*-cresol and circles with dots in dichloroacetic acid. Solid lines are calculated from Eq. (1).

By differentiating Eq. (1) by $\ln \dot{s}$, one obtains

$$\frac{d\eta(\dot{s})}{d\ln\dot{s}}=\frac{x}{\alpha}\beta\left[\frac{1}{\{(\beta\dot{s})^2+1\}^{\frac{1}{2}}}-\frac{\sinh^{-1}(\beta\dot{s})}{\beta\dot{s}}\right] \tag{2}$$

and

$$\frac{d^2\eta(\dot{s})}{d(\ln\dot{s})^2}=\frac{x}{\alpha}\frac{\beta}{\dot{s}^2}\left[\sinh^{-1}(\beta\dot{s})-\frac{\beta\dot{s}}{\{(\beta\dot{s})^2+1\}^{\frac{1}{2}}}-\frac{(\beta\dot{s})^2}{\{(\beta\dot{s})^2+1\}^{\frac{3}{2}}}\right]. \tag{3}$$

Generally the plot of the experimental data of η against $\log \dot{s}$ gives an inflection point, I, where $d^2\eta(\dot{s})/d(\ln\dot{s})^2=0$ (cf. Fig. 1). Hence, from Eq. (3), we obtain the following relation between β and the shear rate at the inflection point, $\dot{s}_i$

$$\beta\dot{s}_i=2.90. \tag{4}$$

If we use this value of $\beta\dot{s}_i$, the slope of the tangent of the curve of η *versus* $\ln\dot{s}$ at I is calculated from Eq. (2), i.e.,

$$\left(-\frac{d\eta(\dot{s})}{d\log\dot{s}}\right)_i=0.290\times2.303\cdot\frac{x}{\alpha}\beta. \tag{5}$$

On combining Eqs. (4) and (5), we get

$$\frac{x}{\alpha}=0.5162\dot{s}_i\left(-\frac{d\eta(\dot{s})}{d\log\dot{s}}\right)_i. \tag{6}$$

Hence, we can determine the parameters, β and x/α, in Eq. (1) from the inflection point of an experimental curve of η *versus* $\log\dot{s}$ and the slope of the tangent at that point.

Yang[8] measured non-Newtonion viscosities of the solutions of PBLG in m-cresol and in dichloroacetate. In the former solvent, the solute molecules exist as rigid, rod-like α helices and as random coils in the latter solvent. Yang tested the merits of the theories of Saito[9] and of Bueche[10] using his results. In his paper, the quantities $[\eta]/[\eta]_0$ were plotted against $\log\dot{s}$. Here $[\eta]$ is the intrinsic viscosity of the solution at the shear rate $\dot{s}$, and $[\eta]_0$ is the value of $[\eta]$ extrapolated to $\dot{s}=0$. In applying our theory to Yang's results, it is thus necessary to replace η by $[\eta]/[\eta]_0$. This replacement brings the parameters, x/α and η_N, in the above equations to $x/\alpha[\eta]_0$ and $\eta_N/[\eta]_0$, respectively, whereas β remains unchanged. From the experimental curve for the solution in *m*-cresol in Fig. 1, we obtain the values: $\log\dot{s}_i=3.575$ and $[d([\eta]/[\eta]_0)/d\log\dot{s}]_i=0.62$. Hence, from Eqs. (4) and (6), the values, $\beta=0.772\times10^{-3}$ sec and $x/\alpha[\eta]_0=1.202\times10^3$, are calculated. The Newtonian term which is equal to $1-x\beta/\alpha[\eta]_0$ is found to be 0.073. The lower solid curve in Fig. 1 is calculated from Eq. (1), using these parameters. The agreement with the experiment is satisfactory over the whole range of shear rates. The broken line is calculated by Yang[8] on the basis of Saito's theory,[9] which is applicable for solid rodlike or ellipsoidal molecules. This theory also gives satisfactory results below $\log\dot{s}=4.5$, but it is not applicable over the range of higher values of $\dot{s}$. In Fig. (1) are also shown the results for the solution of PBLG in dichloroacetic acid. The upper solid curve is calculated from Eq. (1), using the values of $\beta=0.82\times10^{-4}$ sec, $x/\alpha[\eta]_0=0.61\times10^4$ and $\eta_N/[\eta]_0=0.50$. The broken line is calculated by Yang[8] based on Bueche's theory[10] which was developed for randomly coiled molecules. Bueche's theory is not in accord with the experimental values. Thus one sees that the generalized viscosity equation[3] holds regardless of the shape of solute molecules.

(II) SYSTEMS CONTAINING VARIOUS TYPES OF RELAXING UNITS

For the systems containing two or more different types of non-Newtonian relaxing units, the viscosity is given by the following equation[3]:

$$\eta(\dot{s})=\sum_{n=1}^{m}\frac{x_n}{\alpha_n}\beta_n\frac{\sinh^{-1}\beta_n\dot{s}}{\beta_n\dot{s}}, \tag{7}$$

where the subscript n indicates that the quantities belong to a flow unit of the nth mechanism. For a mechanism whose β is so small that $(\sinh^{-1}\beta\dot{s})/\beta\dot{s}\simeq1$), the corresponding viscosity term is reduced to Newtonian viscosity, i.e., $\eta_N=(x\beta/\alpha)_N$.

It is well known that for many high polymeric and colloidal systems,[3-5] the relaxation times of the flow units coexisting in a system are usually separated by two or more decades. In such cases, we can apply the above-mentioned method step by step to the curves of η *versus* $\ln\dot{s}$ of the system. An example is shown below.

In Fig. 2 we plot η against $\log\dot{s}$ for the solution of polyacrylonitrite in diethyl formamide ($M=60\,000$ and $C=8.0\%$). The experimental data were obtained by

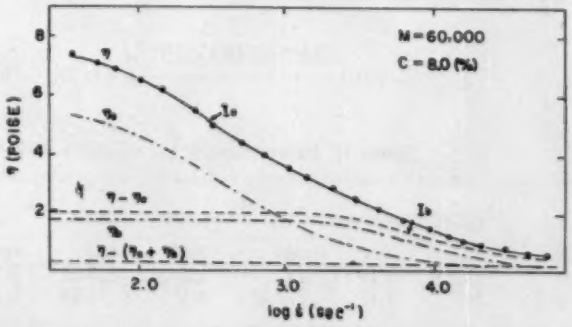

FIG. 2. An analysis of non-Newtonian viscosity of the solution of polyacrylonitrile in diethyl formamide (data from Edelmann[11]). The solid line for η is calculated from Eq. (8).

[8] J. T. Yang, J. Am. Chem. Soc. **80**, 1783 (1958).
[9] N. Saito, J. Phys. Soc. Japan **6**, 297 (1951).
[10] F. Bueche, J. Chem. Phys. **22**, 1570 1954).

TABLE I. Parameters for the solutions of polyacrylonitrile in dimethyl formamide.

C%	$M\times10^{-4}$	I $(x/\alpha)_1\times10^{-3}$	I $\beta_1\times10^{3}$	II $(x/\alpha)_2$	II $\beta_2\times10^{3}$	III $(x/\alpha)_3$	III β_3	Newtonian η_N	Newtonian η_s
8	28	...	...	5310	6.1	415*	0.206*	1.0	118.6
	11	...	...	1645	6.0	408*	0.092*	0.40	47.9
	6	4.010	4.48	538*	9.60*	...	...	0.28	9.24
4	28	1.5	4.50	593.4*	6.05*	25.0	0.029	0.17	5.18
	11	1.1	4.48	227.5*	6.2*	10.22	0.022	0.07	2.17
	6	0.65	4.49*	12.4	6.1	...	...	0.12	0.49

Edelmann.[11] From the original experimental curve of η *versus* $\log\dot{s}$, we can determine an inflection point I_a from which the values $\log\dot{s}_i=2.48$ and $(d\eta/d\log\dot{s})_i=3.478$ are obtained for the first relaxing unit. We call this unit "the principal unit." Equations (4) and (6) are used; we calculate $\beta_a=9.603\times10^{-3}$ sec and $(x/\alpha)_a=5.38\times10^{2}$ dynes/cm^2 for the principal unit. By use of these values, the viscosity resulting from the principal unit $\eta_a=(x\beta/\alpha)_a\sinh^{-1}\beta_a\dot{s}/\beta_a\dot{s}$ is calculated as shown in Fig. 2. We plot the values of $\eta-\eta_a$, which are the viscosity due to the remaining units, against $\log\dot{s}$. One sees that the curve becomes almost flat over the region near I_a. This is the result of the absence of units which satisfy Eq. (4) in this region. On this new curve of $(\eta-\eta_a)$ *versus* $\log\dot{s}$ one finds another inflection point, I_b, which yields $\log\dot{s}_i=3.81$ and $(-d\eta/d\log\dot{s})_i=1.24$. By use of Eqs. (4) and (6), we obtain $\beta_b=4.489\times10^{-4}$ sec and $(x/\alpha)_b=4010$ dynes/cm^2. Hence the viscosity η_b due to the second relaxing unit,

$$\eta_b=(x\beta/\alpha)_b(\sinh^{-1}\beta_b\dot{s}/\beta_b\dot{s}),$$

is calculated as shown in Fig. 2.

When the quantities, $\eta-(\eta_a+\eta_b)$, are plotted against $\log\dot{s}$, we have a horizontal line over the whole range of $\dot{s}$ as shown in Fig. 2. This shows that we have no more relaxing mechanisms over the whole range of $\dot{s}$ in this experiment. The constant value of $\eta-(\eta_a+\eta_b)$ is equal to 0.28 poise and corresponds to the term due to the Newtonian units of the system.

As a result, we have the following viscosity equation for the polyacrylonitrile solution:

$$\eta=537.8\frac{\sinh^{-1}(9.603\times10^{-3}\dot{s})}{\dot{s}}+4010\frac{\sinh^{-1}(4.489\times10^{-4})\dot{s}}{\dot{s}}+0.28. \quad (8)$$

The solid line in Fig. 2 is calculated from Eq. (8). It agrees almost completely with experiment over the whole range of shear rates.

(III) RESULTS OF THE ANALYSIS

Edelmann[11] measured the viscosities of the solutions of polyacrylonitrile in dimethyl formamide and of the solutions of nitrated cellulose in butylacetate. The measurements were made using the polymers with different molecular weights in various concentrations. We now analyze these data according to our method. A part of the results obtained are summarized in Tables I and II. The first column of these tables gives the concentration in percent, and the second column of Table I represents the molecular weight of the polymer. The non-Newtonian units found are classified into the groups I, II, III, etc., according to the values of β. The parameters, x/α and β, belonging to each group are given under the heading of the corresponding group. The last column gives the values of η_N and η_s, the latter being the Newtonian viscosity of the system at $\dot{s}=0$.

In Tables I and II, the parameters for the principal units are indicated by an asterisk. One sees that the principal unit is not necessarily the unit with the highest value of β. As previously mentioned, however, the principal unit is responsible for producing the inflection point of the experimental curve of η *versus* $\log\dot{s}$ for the system, and consequently it is found in the first step of our analysis. It is to be noted that the order of the groups I, II, III, etc., in Tables I and II does not accord with the order in which the units were found, but accords with the increase in the β values.

It also is worthy of note that in Tables I and II the principal unit shifts to the large value of β with increasing concentration and molecular weight. Upon calculating the values of $(x\beta/\alpha)_a$ of a solution, we find

TABLE II. Parameters for the solutions of nitrated pine pulp ($M=294\,000$) in butyl acetate.

C%	I $(x/\alpha)_1$	I $\beta_1\times10^{3}$	II $(x/\alpha)_2$	II $\beta_2\times10^{3}$	III $(x/\alpha)_3$	III β_3	IV $(x/\alpha)_4$	IV β_4	V $(x/\alpha)_5$	V β_5	Newtonian η_N	Newtonian η_s
2	...	...	903	1.45	884	0.0728	318*	1.15*	11.71	7.28	0.14	529.9
1	337.2	1.15	247	1.5	158.2*	0.116*	2.85	1.154	...	...	0.074	25.53
0.5	247	1.45	117.4*	1.4*	1.95	0.115	...		...	...	0.040	2.331

[11] K. Edelmann, *Proceedings of the Second International Congress on Rheology*, edited by V. G. W. Harrison (Academic Press, Inc., New York, 1954), p. 107.

that the corresponding value for the principal unit is the largest of the system. These facts will be discussed in a later publication.

Let the viscosity at $\dot{s}=0$ be η_s, then an equation

$$\eta_s=\sum_n \binom{x}{\alpha}_n \beta_n+\eta_N \tag{9}$$

is derived from Eq. (7). The values of η_s are shown in Table I. The viscosities, η_s, are a function of concentration, molecular weight, and of β_p, the value of β for the principal unit. We obtain the following empirical relation for the concentrated solutions treated here

$$\eta_s=KC^2M\beta_p^{\frac{1}{2}}, \tag{10}$$

where C is the conecntration in percent, M is the molecular weight of the polymer, and K is a constant which is equal to 2.0×10^{-5} for polyacrylonitrile solutions in dimethyl formamide and to 3.2×10^{-4} for nitrated pine pulp ($M=294\,000$) solutions in butyl acetate.

In Fig. 3, we plotted $\log\eta_s$ against $\log C^2M\beta_p^{\frac{1}{2}}$ and obtained straight lines of 45° slope in accord with Eq. (10). In dilute solutions, generally η_s is approximately proportional to C and M, and β_p is approximately independent of concentrations as in the cases of PBLG in *m*-cresol[8] and polystyrene in benzene.[3] DeWitt, Markovitz, Padden, and Zapas[12] pointed out that " the shift factor" for the non-Newtonian viscosity of polyisobutylene solutions in decalin is linear with concentration in the concentrations below 8% and is proportional to the square of concentrations in the range of higher concentrations. The concentration dependence of η_s shown by Eq. (10) seems to be similar to the case of the polyisobutylene solutions in the high concentration range.

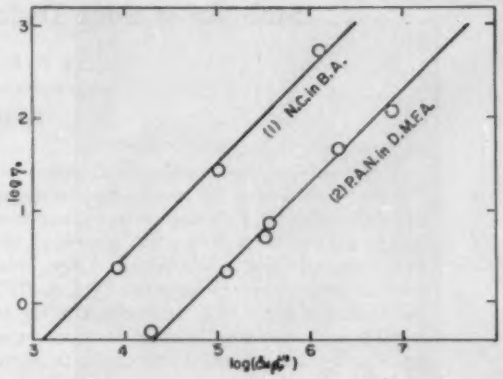

FIG. 3. The dependence of Newtonian viscosity on concentration and molecular weight. (1) Nitrated pine pulp in butyl acetate. (2) Polyacrylonitrile in dimethyl formamide.

ACKNOWLEDGMENTS

The authors wish to express their appreciation to the National Science Foundation for support of this work. This research was also supported in part by a grant from the Petroleum Research Fund administered by the American Chemical Society. Grateful acknowledgement is hereby made to the donors of this fund.

[12] DeWitt, Markovitz, Padden, and Zapas. J. Colloid Sci. **10**, 174 (1955).

Mobility of Edge Dislocations in Silicon-Iron Crystals

DALE F. STEIN AND J. R. LOW, JR.
General Electric Research Laboratory, Schenectady, New York
(Received July 23, 1959)

A method has been developed whereby the velocity of motion of fresh dislocations introduced into a crystal by scratching the surface may be measured as a function of stress. The velocities of unpinned edge dislocations in 3¼% silicon-iron have been measured as a function of stress over a range of five orders of magnitude in velocity from 10^{-7} cm/sec to 10^{-2} cm/sec. The velocity has been found to be very sensitive to the applied stress in this velocity range. Measurements of velocity as a function of stress have been made for four temperatures in the range 78°K to 373°K. It has been found that over this range of temperature the yield stress changes with temperature in the same way as the stress to produce a constant velocity of dislocation motion. From the result it is concluded that the rise in yield stress at low temperatures exhibited by this silicon iron is due primarily to an increase in the lattice resistance to dislocation motion and not to an increase in the Cottrell locking force. Preliminary experiments on pinned dislocations suggest that there may also be an effect of temperature on the strength of pinning by impurities which would be superimposed on the increase in lattice resistance with decreasing temperature.

INTRODUCTION

JOHNSTON and Gilman[1] have recently demonstrated a method for measuring individual dislocation velocities in crystals and have used their method to investigate the effect of stress and temperature on the mobility of dislocations in lithium fluoride. This paper describes the application of the Johnston and Gilman method, modified for our material, to the measurement of dislocation velocities in 3.25% silicon-iron crystals. The principal conclusions of Johnston and Gilman concerning dislocation mobility in lithium fluoride are found to be true also for silicon iron, *viz.*, dislocation velocity is a very sensitive function of the applied stress; the macroscopic yield strength is determined by the dynamic resistance of the lattice to dislocation motion and not by pinning; and glide bands are formed by multiplication, presumably by cross-slip, of the first dislocation to move through a given region of the crystal.

The general method used for the study of silicon iron crystals was to introduce fresh dislocations by scratching the surface of the crystal. A stress pulse was then applied in a three-point bending fixture, the specimen was unloaded, aged to decorate the dislocations, and then etch pitted[2,3] to reveal the position of individual dislocations. Velocity computations were based on the durations of the stress pulses and the distances that the dislocations moved, using the original scratch as a reference mark.

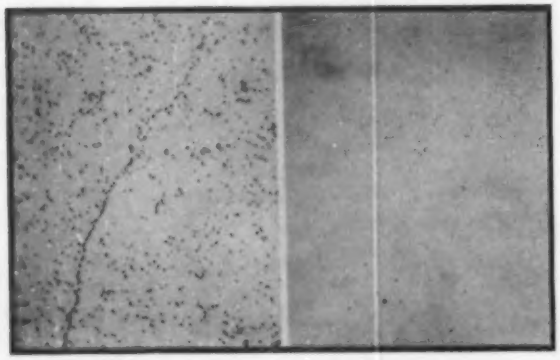

FIG. 1. Dislocation density of undeformed crystals before and after 1300°C anneal. ×250.

[1] W. G. Johnston and J. J. Gilman, J. Appl. Phys. **30**, 129 (1959).

EXPERIMENTAL METHODS

Material

The material that was used was a 3.25% silicon iron single crystal grown by the strain-anneal method of Dunn and Nonken.[4] After it has been grown, about 0.005 weight percent of carbon was added to the crystal by heating it in a sealed quartz capsule containing a measured amount of acetylene. Suits and Low[5] have shown that approximately this amount of carbon must be present in such crystals in order for etch pitting of dislocations to occur.

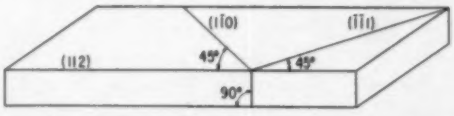

FIG. 2. Orientation of crystals used for study of mobility of edge dislocations. Crystals were scratched on the top, (112), face and bent about an axis normal to the long edge.

The as-grown crystals were found to be imperfect, containing approximately 7×10^6 random dislocations per square centimeter. In this condition the background density of dislocations was too high to permit accurate observation of dislocation motion from a scratch. It was found that annealing the crystals for 16 hours at 1300°C in high-purity argon reduced the dislocation density to

[2] C. G. Dunn and W. R. Hibbard, Acta Met. **3**, 409 (1955).
[3] J. R. Low and R. W. Guard, Acta Met. **7**, 171 (1959).
[4] C. G. Dunn and G. C. Nonken, Metal Progr. **63**, 71 (1953).
[5] J. C. Suits and J. R. Low, Acta Met. **5**, 285 (1957).

approximately 1.4×10^5 per square cm which permitted measurements of dislocation motions. The dislocation densities of the undeformed crystals before and after the 1300°C anneal are shown in Fig. 1.

Specimens were cut from the crystal in such an orientation (Fig. 2) that only single slip occurred when they were bent about an axis normal to the long edge of the specimen, with the slip plane at 45° to the longitudinal axis. Furthermore, this orientation was such that the dislocations normal to the top surface (i.e., those revealed by the etch pitting technique) were *edge* dislocations.

The samples were polished on metallographic polishing papers to remove surface irregularities in the as-grown crystal and were then aged at 150°C for 15 minutes. This allowed local deformation caused by the mechanical polishing to be observed when the crystals were electrolytically etched in the chromic-acetic acid solution. The samples were then electropolished until all traces of surface deformation were removed. This generally required that a layer approximately 20 microns thick be removed.

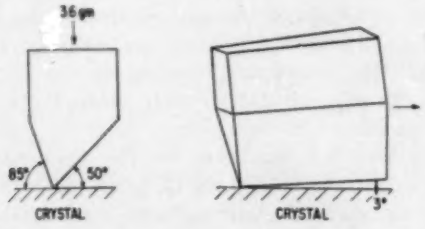

FIG. 3. Shape and orientation of diamond scriber used to introduce dislocations by scratching.

Method of Introducing Fresh Dislocations

The method of rolling a ball over the surface to produce "rosettes" of dislocations which Johnston and Gilman[1] used for lithium fluoride was not found to be satisfactory for silicon iron. This method did introduce dislocations into the proper slip plane but it was very difficult to determine a reference point from which to measure motion. Also, the motion was found to be quite sensitive to the size of the rosette, presumably because of local residual stresses in the vicinity of the rosette.

For the above reasons, other methods of introducing fresh dislocations were explored. The method that was finally adopted was scratching the surface with a special diamond scriber. This method introduced a continuous row of dislocation loops lying in the proper slip plane, i.e., that (110) plane which would have the maximum resolved shear stress in subsequent bending. It was found that a sharp edged scriber such as a razor blade or a diamond polished to a sharp edge was required. Figure 3 illustrates the shape of the scriber that was used and its position relative to the crystal surface. A standard load of 3.6 grams was used to produce the required continuous row of dislocation loops. The scratches, plus the deformed region, were approximately four microns deep and eight microns wide.

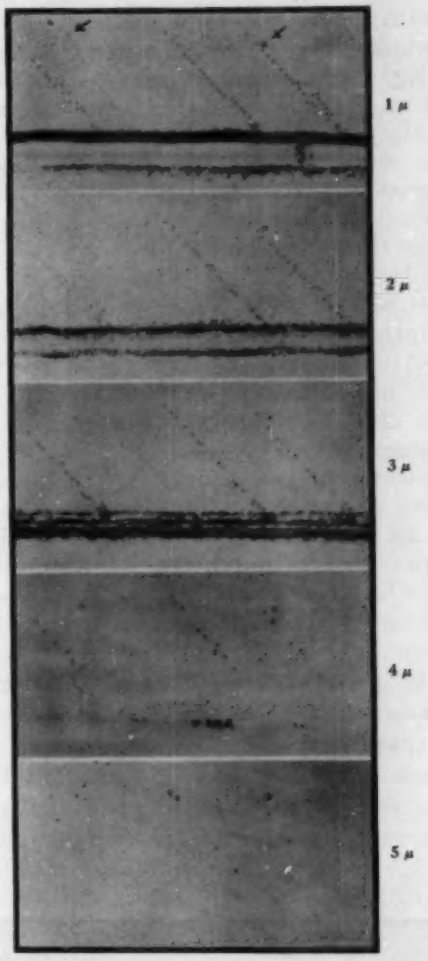

FIG. 4. Dislocation structure of slip bands originating from a scratch at successive levels below the original crystal surface. Distance below surface is shown at the right. The nonmetallic inclusions marked with arrows may be used as reference marks. ×750.

Unless it is otherwise noted, all "fresh" dislocations were introduced by scratching at 78°K and the crystal was then held at this temperature until it was ready for loading. The migration of impurity atoms to the dislocations was thereby prevented and the dislocation velocity measurements can be considered to be for unpinned dislocations. The elapsed time between scratching and loading was never more than five minutes.

Slip Band Structure

The structure of the slip bands was examined by polishing down through a band and etching at successively greater depths below the surface. Figure 4 shows a series of photomicrographs obtained using this procedure for slip bands originating from a scratch. An

important observation to be made in this series of photomicrographs is that, as material is removed by polishing, the outermost dislocations are the last to disappear. We interpret this to mean that the band is formed by a single loop moving out from the scratch and leaving in its wake a series of smaller loops. This conclusion was reached by Gilman and Johnston in their study of slip band formation in lithium fluoride.[6] Just how this multiplication of dislocations occurs is yet to be demonstrated, but the most reasonable model appears to be the double cross-slip mechanism first proposed by Koehler.[7] In any event, since the outermost dislocations appear to have originated at the scratch and to have moved the full length of the slip band, the motion of the outermost dislocations was used in calculating the velocity.

The temperature of deformation was found to have an effect on the character of the slip. This effect is illustrated in Figure 5 which shows the dislocation patterns for temperatures of deformation between 78°K and 373°K. At 78°K there is very little tendency for band formation, but as the temperature is raised, more and more bands appear and fewer and fewer random dislocations. At 373°K most of the dislocations that have moved are in slip bands. This may result because at low temperatures there is less tendency for the screw components of the loops to cross slip and therefore there is less tendency for multiplication. Preliminary experiments on the mobility of screw dislocations (using a differently oriented crystal) indicate that at 78°K, screw dislocation bands are straighter and less dense than at 298°K. This lends some support to the above argument.

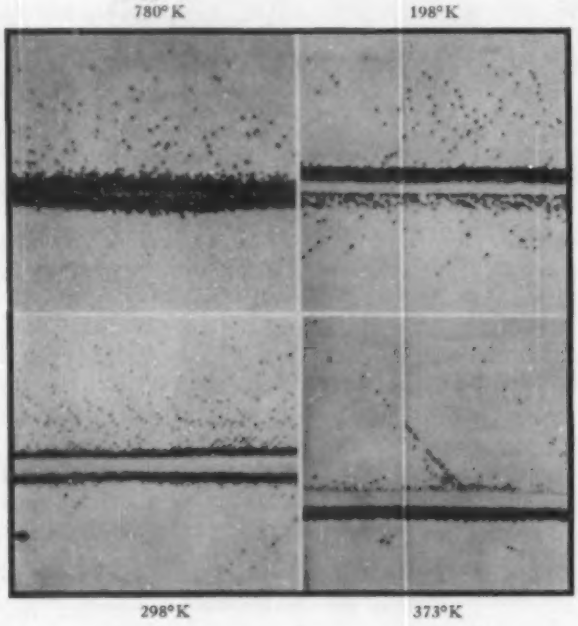

FIG. 5. Character of dislocation motion at various temperatures. ×720.

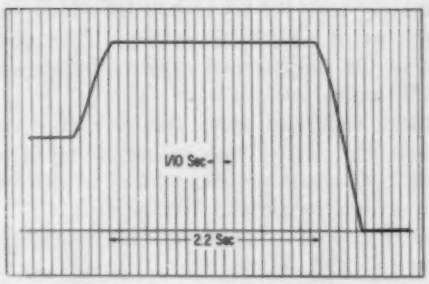

FIG. 6. Oscillograph record of 2.2 second loading pulse applied in tension testing machine.

Method of Loading and Stress Calculation

After the crystals had been scratched at 78°K to introduce dislocations, they were pulse loaded in a three-point bending fixture in a tensile testing machine. The specimens were approximately 30 mm long, 2.5 mm wide, and 0.8 mm thick while the distance between supports of the three-point bending jig was 25 mm. In these experiments all stresses were below the stress for general yielding. Stresses were therefore calculated using the standard equation for the maximum fiber stress in a centrally loaded elastic beam. All stresses are reported as resolved shear stresses, i.e., one-half the maximum tension fiber stress so computed. Since in three-point bending the stress varies continuously from a maximum at the center to zero at the supports, a single bending experiment could be used to measure dislocation movements for a range of stresses. Furthermore, since the stress distribution was symmetrical about the center, a single specimen could be used to check the reproducibility of the measurements. At equivalent positions on the two sides of the center point the movement was found to be the same within about 10%. All measurements were made on the tension surface of the bent specimen.

The time of application of the "pulse" loads varied from two seconds to as long as two hours. For the very short-time loadings an Instron testing machine, modified so as not to overshoot the desired load and equipped with a high-speed recording oscillograph to record the load-time characteristics of the pulse, was used. The record of a typical short-time pulse is shown in Fig. 6. As a check of the validity of the bending method of loading and the method of stress calculation, dislocation velocities were also measured using tension specimens. Spot checks of several stresses at each of three temperatures (198°K, 298°K, and 373°K) indicated that within the accuracy of the method the same velocities were obtained in tension tests as those observed in bending.

[6] J. J. Gilman and W. G. Johnston, *Dislocations and the Mechanical Properties of Crystals* (John Wiley & Sons, Inc., New York, 1957), p. 116.
[7] J. S. Koehler, Phys. Rev. **86**, 52 (1952).

Calculation of Dislocation Velocity

Dislocation velocities were computed by measuring the maximum movement at any given point along the beam, arbitrarily subtracting an eight micron correction factor, and dividing by the time of application of the load. The correction factor was used because it was found that motion within approximately eight microns of the scratch was much more rapid than motion beyond this distance from the scratch. This effect has also been noted by Johnston and Gilman[8] for motion near a rosette and presumably arises from re-enforcement of the applied stress by localized residual stresses in the region immediately adjacent to the scratch.

RESULTS

The Stress Dependence of Dislocation Velocity

The velocity of dislocation motion was found to be a very sensitive function of stress. Figure 7 shows the experimental results for the four different temperatures of testing. These results appear similar to those of Johnston and Gilman[1] for the same velocity range in LiF, in that the logarithm of the velocity varies linearly with the logarithm of the applied stress. The stress to produce dislocation motion is, however, about an order of magnitude higher for silicon-iron than for LiF crystals. Johnston and Gilman also found that at higher stresses and higher velocities ($\bar{V} > \sim 10^2$ cm sec^{-1}) the velocity did not increase as rapidly with increasing stress but tended to approach to an upper limit asymptotically (the velocity of shear wave propagation in their material). This region of higher velocity was not examined for our material.

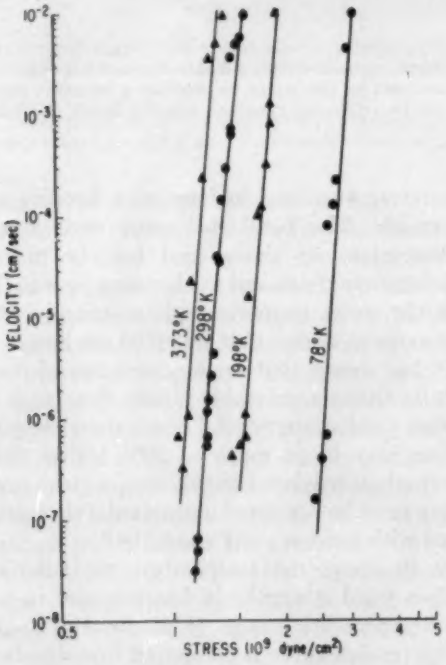

FIG. 7. Stress dependence of edge dislocation velocity at four different temperatures.

[8] W. G. Johnston (private communication).

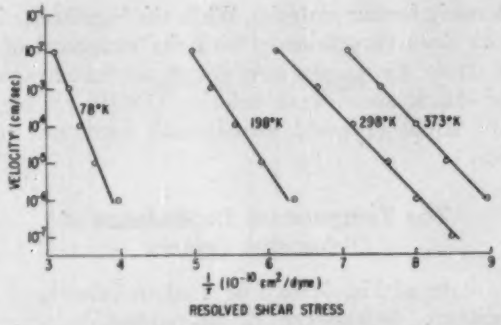

FIG. 8. Variation of dislocation velocity with reciprocal of applied shear stress.

The relationship between velocity and stress shown in Fig. 7 can be written in the form:

$$V = (\tau/\tau_0)^n$$

where V is the velocity, τ is the applied shear stress resolved into the slip plane, and τ_0 is the shear stress for $V = 1$ cm sec^{-1}. The values of the two constants for the four different temperatures are shown in the following:

T(°K)	n	τ_0 (10^9 dynes/cm^2)
78	44	3.8
198	38	2.3
298	35	2.0
373	41	1.5

For the three lowest temperatures n appears to be decreasing systematically as the temperature is increased. It is believed that the high value for 373°K may be incorrect and is connected with the pinning of the dislocations by carbon since this may well have occurred during the testing and would have varied over the range of velocities measured. In general the low velocity points represent times of loading of the order of tens of minutes (i.e., greater pinning), while the high velocity points represent times of loading of the order of seconds. The data for 373°K, therefore, are not thought to be as reliable as those for the lower temperatures since the degree of locking by impurities was not constant. Over this same range of velocities Johnston and Gilman[1] found n to be approximately 25 for LiF.

Gilman[9] in analyzing the dislocation velocity data for LiF found that the velocity obeyed the relationship.

$$V = V_0 e^{-A/\tau}$$

where V_0 is the elastic shear wave velocity for LiF and τ is the applied shear stress. In Fig. 8 the data for silicon iron are plotted in such a way as to test the above

[9] J. J. Gilman, *Conference on Fracture; Swampscott, Massachusetts, April 12–16, 1959* (John Wiley & Sons, Inc., New York, to be published).

relationship for our material. While the logarithm of the velocity does vary linearly with the reciprocal of the shear stress, the curves were found not to extrapolate to the elastic shear wave velocity (5×10^5 cm/sec) at infinite stress ($1/\tau=0$) as Gilman's equation would require.

The Temperature Dependence of Dislocation Velocity

The data of Fig. 7 may be used to investigate the temperature dependence of dislocation velocity at constant stress by cross-plotting the stress for a constant velocity as a function of temperature to obtain a set of constant velocity stress-temperature curves. From such a set of curves one may then plot velocity as a function of $1/T$ for constant stress. Figure 9 shows the result of this method of analyzing the data. At sufficiently low stresses a linear plot is obtained, implying that a single thermally activated process controls the dislocation motion. However, at higher stresses this linear relationship no longer holds. The deviation from linearity increases steadily with increasing stress and suggests that even at the lowest stress levels the linearity may be fortuitous and that one may not be justified in computing a single activation energy for the process controlling the rate of motion of the dislocations.

It may be that the effects shown in Fig. 9 and attributed to a change in stress do not in fact result from the stress change alone. Because of the strong stress dependence of velocity and the large shift on the stress axis with changing temperature (cf. Fig. 7) it was not possible to compare the temperature dependence of velocity over the full range of temperature at a constant stress. For this reason the high stress curves are for the low temperature range only and the low stress curves are for the high-temperature range only. The curvature at high stresses may therefore represent curvature at a low temperature rather than at a high stress. With the present data, it is not possible to choose between these two possibilities. All that can be said is that an Arrhenius type relationship is not obeyed over the full range of the variables investigated.

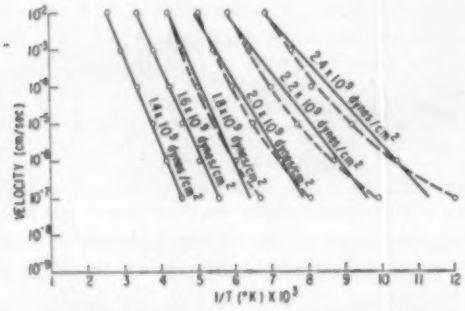

FIG. 9. Log velocity $-1/T$ plot for observed dislocation velocities at various constant applied stresses.

Comparison of Yield Strength and the Stress to Move Unpinned Dislocations

One of the principal objectives of this investigation was to determine whether the rise in yield strength of silicon-iron at low temperatures is due to impurity locking or to a change in the resistance to motion of unpinned dislocations. For this reason, the yield strengths, both in bending and in tension, of the same crystals that were used for the velocity measurements were measured as a function of temperature.

In attempting to measure the yield strengths in tension over the range of temperature 373°K to 78°K, it was found that at the two lowest temperatures tested (78°K, 198°K) twinning preceded slip so that a valid measure of the strength for yielding by slip could not be obtained. In bend tests, however, we were able to obtain yielding by slip at temperatures as low as 125°K without interference due to twinning. Yield strengths

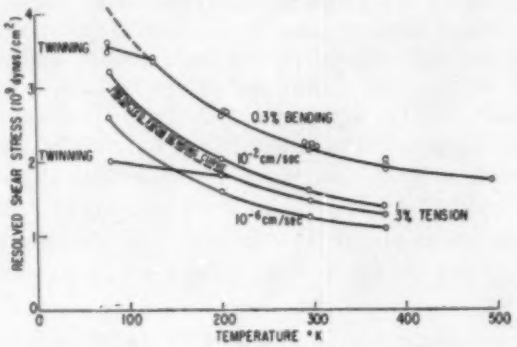

FIG. 10. Comparison of the temperature dependence of the 0.3% offset yield strength in bending and in tension with the temperature dependence of the stress to produce a constant dislocation velocity for two different constant velocity levels (10^{-6} and 10^{-2} cm/sec).

were therefore measured in four-point bending as well as in tension. The bend specimens were about the same dimensions as those used for the dislocation velocity determinations and the bending jig was 1.86 cm between the outer supports with a central constant-bending-moment region that was 0.63 cm long.

Read[10] has shown that for any measure of the yield strength involving appreciable plastic flow (such as the 0.3% offset yield strength used here), the yield strength in bending may be as much as 50% higher than the yield strength in tension. For this reason yield strengths in bending must be corrected downward if they are to be compared with tension yield strengths.*

Figure 10 shows the temperature variation of the 0.3% offset yield strengths in bending and in tension for the temperature range 78°K to 373°K. Below 198°K the tension curve is computed from the bending

[10] W. T. Read, Acta Met. 5, 83 (1957).

* The details of the corrections applied to our results are given in the Appendix.

curve using Read's method. Dislocation velocity-stress curves, for two different velocities, are also plotted in Fig. 10. In comparing these curves it should be kept in mind that the dislocation-velocity-stress curves are for *unpinned* dislocations. It will be noted that these curves closely parallel the yield strength curves over the whole temperature range. *We therefore conclude that most of the rise in yield strength as the temperatures is lowered is due to an increase in the dynamic resistance to dislocation motion and not to impurity locking.*

Effect of Pinning

Some exploratory work has been done on the effect of pinning by deliberately aging a scratch at 150°C for 15 minutes before stressing it to produce dislocation motion. Two observations on the effect of pinning on motion at room temperature can be reported and further experimental work is planned. First, the

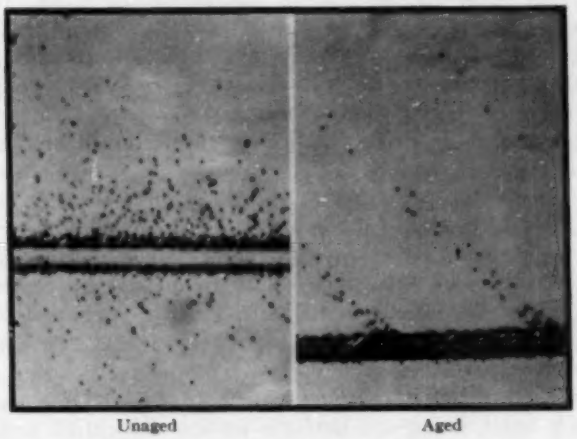

FIG. 11. Difference in motion of dislocations from fresh scratch and scratch aged at 150°C for 15 minutes before loading.

character of the motion of dislocations from the scratch is changed by pinning. This effect is illustrated in Fig. 11. Two scratches on the same specimen were loaded at the same time. One was aged and the other not. The areas shown represent regions subjected to the same applied stress. The dislocations that moved appear to have moved approximately the same distances from both scratches. However, many more dislocations moved from the *unaged* scratch. Also, those that moved from the aged scratch are more sharply confined to slip bands, there being no "random" motion as may be seen in the case of the unaged scratch. The equality of the amounts of motion from the two scratches is better illustrated in Fig. 12. Here the experimental points represent velocity-stress values for an aged scratch and the lines represent the values for motion from an unaged scratch.

It appears that at room temperature pinning prevents the motion of some but not all of the dislocations. Those that do move, move with the same velocity as an

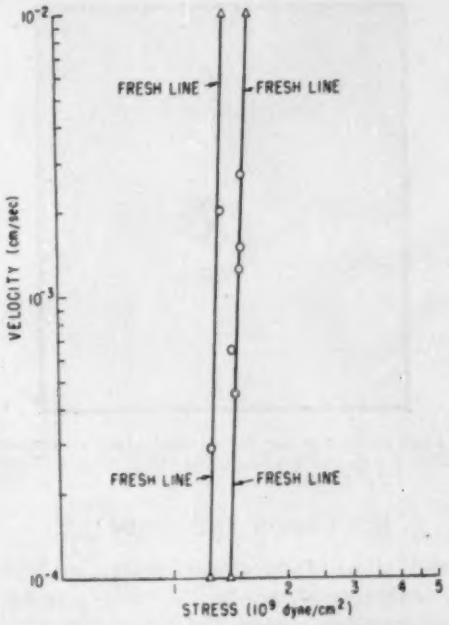

FIG. 12. Comparison of velocities of dislocations from fresh scratch and from scratch aged 15 minutes at 150°C before loading at 298°K and 373°K.

unpinned dislocation. In addition, it was found that at lower temperatures (78°K and 198°K) dislocations could not be moved from a pinned scratch at any stress below that for general yielding of the crystals. Two interpretations of these observations are possible. It may be that in the relatively short time of aging used, not all dislocations in the dense array at the scratch were equally pinned and the weakly pinned dislocations are the ones that moved. Such an explanation does not account for the effect of decreasing the temperature, however, so it would appear that a decrease in temperature has the effect of increasing the strength of pinning. These questions will have to be answered by further experiments using varying aging times and a more detailed study of the effects of temperature.

Before leaving the discussion of general yielding, one other observation is of interest. The crystal used in the present experiments contained nonmetallic inclusions, and it was observed that around each inclusion there was a "cloud" of dislocations. These presumably arose from plastic flow that occurred during cooling from the annealing temperature due to the differential thermal contraction. When the specimens were loaded it was observed that, as the yield stress was approached, slip always began by the motion of dislocations near inclusions. Also, the first slip bands to appear always radiated from inclusions. This effect is illustrated in Fig. 13 where both edge (straight lines) and screw (wavy lines) dislocations can be seen moving away from an inclusion. This result implies that an inclusion-free crystal might be expected to have a somewhat higher yield stress than the present crystals.

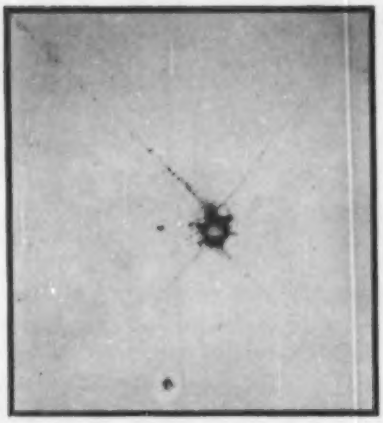

FIG. 13. Edge and screw slip bands originating at nonmetallic inclusion after 2.2 second loading pulse (3.1×10^9 dyne/cm^2). ×250.

DISCUSSION AND SUMMARY

The yield stress of silicon-iron crystals has been found to vary with temperature in the same manner as the stress to move *unpinned* dislocations at a constant velocity. From this we conclude that the principal cause of the increase in yield stress at low temperatures is an increase in the lattice resistance to dislocation motion. The increase in yield stress does not appear to be caused by an increase in the stress needed to overcome the Cottrell locking force. This same conclusion has been reached by Heslop and Petch[11] in their study of the effect of grain size on the yield point of alpha iron over this same range of temperatures. Heslop and Petch found the following relationship to hold:

$$\sigma_{l.y.p.}=\sigma_0+kl^{-\frac{1}{2}},$$

where $\sigma_{l.y.p.}$ is the lower yield point stress and l the grain diameter. σ_0 is interpreted as the resistance to motion of unpinned dislocations, and k as a measure of the locking force due to impurities. These investigators found σ_0 to be strongly temperature dependent, a result which they interpreted to mean that the Peierls-Nabarro force was increasing rapidly as the temperature decreased.

At present there appears to be no theoretical model which will explain these observations. For example, Seeger's[12] model of a moving dislocation cutting a "forest" of grown in dislocations to account for the temperature dependence of the resistance to flow would not be applicable. For the range of motions examined here, the area swept out by a moving dislocation was at the most 10^{-5} cm^2 and in many cases was as little as 5×10^{-7} cm^2. With a measured density of random dislocations of about 1.5×10^{-5} per square centimeter, there would not be enough intersections to account for the temperature effects observed. Recently Schoeck and Seeger[13] have proposed a type of locking by impurity atoms which does not require long-range diffusion and which might conceivably have occurred under our experimental conditions. This model is analogous to the Snoek model for damping due to interstitial impurities. Impurity atoms, by taking up preferred interstitial sites in the region of the stress field of the moving dislocation, can cause a decrease in the energy of the system. Schoeck and Seeger's analysis does not, however, predict a change in the resistance to motion with temperature for a constant velocity which was observed, whereas it does predict a change in stress dependence of velocity at low velocities ($<20\times10^{-8}$ cm/sec) which was not observed in our experiments.

The sources of slip bands at the yield point were nonmetallic inclusions surrounded by arrays of dislocations. Presumably these dislocations are locked by impurities. However, the inclusions act at a stress raisers to unlock the pinned dislocations. Thus, the dislocations can move at low applied stresses, but only in the vicinity of the inclusion where the stresses are high. For general slip-band formation to occur, and macroscopic yielding to be observed, dislocations must move over long distances. This motion is controlled by whatever lattice resistance is characteristic of the temperature of deformation.

It does not appear that the rate controlling step in the motion of dislocations can be characterized by a single activation energy. At low stresses the velocity does obey an Arrhenius equation, but not at higher stresses. Deviations from linearity in the $\log V$ *vs* $1/T$ plots become progressively greater as the stress is increased.

From etch pit patterns at several levels through a slip band, it appears that the leading dislocation loop moving out from a scratch leaves in its wake smaller loops. One possible explanation of this type of slip band structure is that the screw component of the lead dislocations cross slips out of its original slip plane and, by the "double cross slip" mechanism,[3,7] generates new loops on closely adjacent planes. Some further support for this model is provided by the observation that, when the motion of screw dislocations (rather than edges) was observed at several temperatures, it was found that this motion was wavy at 300°K (implying easy cross slip) but quite straight at 78°K. Correspondingly, in the observation of edge dislocation motion, slip bands form readily at 300°K but are not observed at 78°K. At intermediate temperatures, the density of dislocations in the bands which did form increased as the temperature was increased.

When a line of dislocations produced by scratching was pinned by deliberately aging the specimen, it was found that at 298°K and 373°K only a few of the dislocations moved (as compared to an unaged scratch) but that those which did move, moved just as rapidly

[11] J. Heslop and N. J. Petch, Phil. Mag. 1, 866 (1956).
[12] A. Seeger, Phil. Mag. 46, 1194 (1955).
[13] G. Schoeck and A. Seeger, Acta Met. (to be published).

as did the dislocations from an unaged scratch. At 78°K and 198°K no motion was observed up to the stress at which general yielding occurred. This suggests that unpinning may be a thermally activated process which occurs only at the higher temperatures. If so, then by the proper choice of the temperature of loading, such that the time for activation and the time for motion are about the same, a distribution of slip band lengths should be observed for a single applied stress.

ACKNOWLEDGMENTS

We are very grateful to W. G. Johnston, J. J. Gilman, and C. G. Dunn for many helpful discussions during the course of this investigation. We would also like to thank C. G. Dunn for supplying the oriented crystals that were studied.

APPENDIX

Figure 14, taken from Read[10] shows the variation of the bending moment ratio M/M_1, with the ratio K/K_1. M_1 is the bending moment at the proportional limit (yield stress in tension) and M is the bending moment for various small amounts of plastic flow given by the ratio K/K_1 where K is the radius of curvature after some plastic deformation and K_1 is the radius of curvature at the proportional limit. Thus, the apparent yield strength in bending (computed from M) may be as much as 50% greater than the true yield stress as measured in tension. This particular curve is for a tension stress strain curve in which yielding occurs with no further rise in load once the proportional limit is reached (i.e., a "yield point" type of curve). This type of stress strain curve was observed when the silicon iron

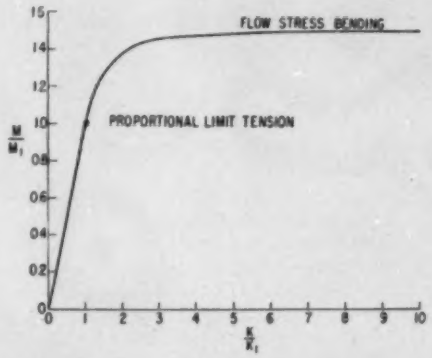

FIG. 14.

crystals used in this investigation were tested in tension.

Since both K_1 and M_1 varied with temperatuer (because of the rise in the yield stress with decreasing temperature) the correction to be applied to the 0.3% offset yield strength in bending was not the same for all temperatures but decreased systematically with decreasing temperature. The correction was obtained from the curve of Fig. 14 using measured curvatures after deformation (K) and computed elastic curvatures (K_1). K_1 was computed from the observed load at the proportional limit in the tension test assuming elastic bending up to the proportional limit. The correction applied to the bending yield stress curve to obtain the tension yield stress curve of Fig. 10 varied from 48% at 373°K to 34% at 78°K. In the range where slip occurred in both tension and bending (298°K–373°K) it was found that the predicted yield strength in tension corresponded quite closely to the observed yield strength.

Single-Velocity Equivalents for Multivelocity Electron Streams*

GLENN A. GRAY
University of California, Berkeley, California
(Received March 27, 1959)

Several electron beam problems which involve a distribution in electron velocities are treated. In each case the actual multivelocity stream is replaced by an equivalent single-velocity stream. Such a procedure provides a common viewpoint for the examples which are considered. For a traveling wave tube, it is found that a distribution of dc electron velocities has the same effect as an increase in the space charge parameter QC, a result which is in agreement with the earlier findings of Watkins and Rynn. Also, agreement with earlier theories is found in the cases of space charge wave propagation on a multivelocity stream, and the double-stream amplifier. In the case of noise fluctuations in high velocity beams, it is found that the time varying part of either the rms or the mean stream velocity may be used to specify the ac velocity modulation on the equivalent single-velocity beam. That is, either value should be equally valid in a first order treatment. Finally, a class of re-entrant beam devices are analyzed, and experimental results are cited as an indication of the validity of the theory.

INTRODUCTION

WHEN dealing with beam-type microwave tubes, it is common practice to treat the electron stream as though all electrons enclosed by any vanishingly small volume have the same velocity. Such a single-velocity theory is indeed often justified, and the majority of beam-type devices have been analyzed on that basis. There are, however, at least three instances in which it is desirable to look more closely into the exact nature of the stream composition. First, one often wishes to estimate the first-order effects of velocity distributions created by space charge potential depression, cathode emission properties (thermal spread), etc. Second, it is desirable to establish a reasonable justification for the use of a single-velocity theory when dealing with such an obviously multivelocity phenomenon as the noise generated by an electron beam interacting with a slow-wave circuit. Third, there exist devices which inherently make use of a distribution of velocities. Examples of these are the double-stream amplifier and re-entrant beam devices.

Frank Gray[1] has set down very clearly the conditions of use of single-velocity equivalents for the first of the above problems—rf behavior of a real beam having normal velocity spread. Hahn in an earlier paper[2] had applied the point of view to obtain useful approximate results for a simple diode. However, in first applications to a traveling-wave tube,[3] results not in agreement with practice were obtained and later work was from the more complete Boltzmann equation. It is consequently important to see that with different assumptions the single-velocity theory can lead to results in first-order agreement with the more complete theory.

The single-velocity theory has so far had its greatest use and most important success in the second of the above listed problems—that of fluctuation noise. It was first introduced by Rack[4] by induction from the asymptotic behavior of an accurate low-frequency statistical analysis and received its clearest verification in the classic Cutler-Quate experiment.[5] Its use has since led to dramatic improvements in the noise figure of traveling-wave tubes. Siegman[6] has given a very clear analysis of the conditions for its validity, so this problem will receive only brief mention here.

It is in the third of the above types of problems—the devices whose operation depends on the use of multivelocity streams—that the use of the single-velocity concept is believed to be new. The double-stream amplifier has of course been analyzed by other methods but is chosen as a first example to develop the physical pictures, especially since it might at first seem to be in direct conflict with such a theory. Finally, the concept is used to develop a very complete small-signal theory of the newer re-entrant beam devices, and experimental verification for this theory is cited.

DYNAMIC EQUATIONS FOR ELECTRON STREAMS

In a one-dimensional analysis of electron beam problems, the single-velocity theory leads to relatively simple equations for the determination of electron motion. The equations of importance can then be written as follows:

$$\begin{aligned} &dv/dt = -\eta E && \text{force equation} \\ &(\partial J/\partial x)+(\partial \rho/\partial t)=0 && \text{equation of continuity} \\ &\partial E/\partial x = \rho/\epsilon && \text{divergence relation} \\ &J=\rho v && \text{definition of space current,} \end{aligned} \tag{1}$$

where E = electric field, ρ = charge density, v = beam velocity, J = beam current, x = coordinate along beam axis, η = charge-to-mass ratio of the electron, and ϵ = dielectric constant. In such a stream, it is assumed

* The research reported herein has been made possible through the support extended by the Electronic Components Laboratory of the Wright Air Development Center under Contract No. AF 33(616)-3278.

[1] Frank Gray, Bell System Tech. J. **30**, 830 (1951).
[2] W. C. Hahn, Proc. Inst. Radio Engrs. **36**, 1115 (1948).
[3] P. Parzen and L. Goldstein, J. Appl. Phys. **22**, 398 (1951).
[4] A. J. Rack, Bell System Tech. J. **17**, 592 (1938).
[5] C. C. Cutler and C. F. Quate, Phys. Rev. **80**, 875 (1950).
[6] A. E. Siegman, J. Appl. Phys. **28**, 1132 (1957).

that motion is confined to the x direction by the application of a large magnetic field.

If the stream is composed of electrons with a distribution of velocities, a set of equations similar to (1) can be derived through the application of the Liouville theorem of statistical mechanics.[7] For the discussion of a stream with a continuous distribution of velocities, the following quantities are defined:

w = velocity coordinate,

$n(x,w,t)dw$ = mass density of particles with velocities lying between w and $w+dw$,

$$N(x,t)=\int_{-\infty}^{\infty} n\,dw = \text{mass density (per unit volume)},$$

$$P(x,t)=\int_{-\infty}^{\infty} nw\,dw = \text{momentum density},$$

and

$$K(x,t)=\int_{-\infty}^{\infty} \tfrac{1}{2}nw^2\,dw = \text{kinetic energy density}.$$

In terms of n, the Liouville theorem in one dimension yields

$$\frac{\partial n}{\partial t}+w\frac{\partial n}{\partial x}+\frac{dw}{dt}\cdot\frac{\partial n}{\partial w}=0. \tag{2}$$

From this relation, Frank Gray[1] has derived the following set of working equations, applicable to any multivelocity stream

$$\begin{aligned}
&\frac{1}{N}\frac{\partial P}{\partial t}+\frac{2}{N}\frac{\partial K}{\partial x}=-\eta E,\\
&\frac{\partial P}{\partial x}+\frac{\partial N}{\partial t}=0,\\
&\frac{\partial E}{\partial x}=-\frac{\eta N}{\epsilon},\\
&J=-\eta P.
\end{aligned} \tag{3}$$

The first equation, which plays the same role as the force equation, is obtained by multiplying Eq. (2) through by w and then integrating over velocity space. The second equation is the equation of continuity, and is obtained by integrating (2) over velocity space directly. It can easily be verified that Eqs. (3) hold also for an electron stream composed of say M discrete velocities U_i. In this case, the distribution function can be written

$$n(x,w,t)=\sum_{i=1}^{M} N_i(x,t)\delta(w-U_i), \tag{4}$$

where $\delta(w)$ is the Dirac delta function, and $N_i(x,t)$ the mass density (per unit volume) of the ith stream. Substituting this definition of n into (2) again leads to the set of Eqs. (3), if we now define

$$\begin{aligned}
N&=\sum_{i=1}^{M} N_i\\
P&=\sum_{i=1}^{M} N_iU_i\\
K&=\sum_{i=1}^{M} \tfrac{1}{2}N_iU_i^2.
\end{aligned} \tag{5}$$

EQUIVALENT SINGLE-VELOCITY STREAMS

Equations (3) are true in general for any multivelocity stream. However, there are a variety of ways one can define an equivalent stream in which, at a given plane x, all electrons travel at the same velocity $U(x,t)$. It turns out that such a stream can then be described by equations similar to (3), but with some additional terms which account for the actual distribution of velocities. Gray[1] has derived the set of relations analogous to (1) appropriate for a single-velocity stream in which it is assumed that the electrons which make up the mass density N all travel at the average, or mean, velocity of the stream. This definition corresponds to the requirement that the momentum density (NU) of the equivalent stream be equal to that of the actual multivelocity stream, i.e., $NU=P$. Inserting this definition of the velocity U into Eqs. (3) yields the following set of working equations:

$$\begin{aligned}
&\frac{dU}{dt}=-\eta\left[E-\frac{2}{\rho}\frac{\partial}{\partial x}(\delta K)\right],\\
&\frac{\partial J}{\partial x}+\frac{\partial \rho}{\partial t}=0,\\
&\frac{\partial E}{\partial x}=\frac{\rho}{\epsilon},\\
&J=\rho u,
\end{aligned} \tag{6}$$

where

$$\rho=-\eta N = \text{charge density}$$

$$\delta K=K-\tfrac{1}{2}NU^2.$$

By comparing (6) with (1), it is seen that the multivelocity stream can be exactly represented by an equivalent single-velocity stream, provided that in addition to the actual electric field E, there is introduced a fictitious electric field

$$E'=-\frac{2}{\rho}\frac{\partial}{\partial x}(\delta K)$$

[7] R. B. Lindsay, *Introduction to Physical Statistics* (John Wiley & Sons, Inc., New York, 1954).

arising as a result of the difference in kinetic energy densities of the single-velocity stream and the actual stream. Spitzer[8] has derived a similar result for a three-dimensional stream, in which he writes the added force term as the gradient of a hydrostatic pressure.[2]

It is clear that similar sets of equations can be derived for other definitions of U. Intuition tells us, however, that if U is defined to be very much different from the mean stream velocity, then large additive terms similar to E' in (6) will be required to compensate for the large differences in kinetic energy and momentum densities between the two streams. We accordingly consider the following definitions of U.

$$U=\left[\frac{\int_{-\infty}^{\infty} nw^m dw}{\int_{-\infty}^{\infty} n dw}\right]^{1/m}. \tag{7}$$

For the case $m=1$, we get the mean velocity, as defined for Eqs. (6) For $m=2$, we obtain the root-mean-square velocity, which can be written

$$U=\left(\frac{2K}{N}\right)^{\frac{1}{2}}. \tag{8}$$

We note that this is also the velocity which gives the equivalent single-velocity stream a kinetic energy density equal to that of the actual stream, making δK in (6) zero. If this rms velocity of Eq. (8) is used, Eqs. (3) lead to another possible set of working equations

$$\begin{aligned}
&\frac{dU}{dt}=-\eta\left[E-\frac{1}{\rho}\left\{\frac{\partial}{\partial t}(\delta P)-U\frac{\partial}{\partial x}(\delta P)\right\}\right]\\
&\frac{\partial J}{\partial x}+\frac{\partial \rho}{\partial t}=0\\
&\frac{\partial E}{\partial x}=\frac{\rho}{\epsilon}\\
&J=\rho u-\eta\delta P,
\end{aligned} \tag{9}$$

where $\delta P=P-NU$ is the difference in momentum densities of the actual and equivalent streams. Thus we note that if we insist that the momentum densities of the actual and equivalent streams be equal, then a term accounting for the differences in kinetic energy densities appears in the equations. Similarly, if the kinetic energy densities are equal, the momentum densities are not. What we have shown so far is that there are several ways in which a multivelocity stream can be described. Thus we could define other velocities by calculating still other moments with respect to w [i.e., other values of m in Eq. (7)]. One may ask which definition of U is the correct one. The answer is that all are exact, and that no one definition is more correct than another as long as the Liouville theorem is properly applied to derive the working equations. The choice of the definitions of U therefore rests either on the simplicity of the resulting equations, or on the ability to calculate δP or δK. If the distribution function n is known, these quantities are calculated from the relations

$$\delta P=\int_{-\infty}^{\infty} n(w-U)dw, \tag{10}$$

$$\delta K=\int_{-\infty}^{\infty} \tfrac{1}{2}n(w-U)^2 dw. \tag{11}$$

If n is not known these quantities must be approximated. In such cases it may even be desirable to formulate the problem in terms of all the moments.

Often the added terms in (6) or (9) can be neglected. This may be a reasonable approximation to make in a beam with only a small spread in velocities. In this case, it makes no difference whether we use the mean or r.m.s. velocity, since the equations for both cases will be the same. However, in those cases mentioned previously it is not possible, *a priori*, to discard these terms. We will therefore devote the remainder of this paper to a detailed consideration of these problems. In the examples to follow, only first-order effects will be considered and time dependence as $e^{j\omega t}$ will be assumed.

TRAVELING WAVE TUBES

The first attempt to determine the effects of a velocity distribution on traveling wave tubes was made by Parzen and Goldstein.[3] Their method consisted of applying Eqs. (6) and retaining the first order terms arising from δK. In their notation, δK was expressed in terms of an equivalent beam temperature T. They considered only the special case $QC=b=d=0$. Although their method was correct, they unfortunately made two unrealistic assumptions. First, in their final calculations they took T to be the cathode temperature T_c, whereas for accelerated beams, such as those used in any practical traveling wave tube, it is really much less than T_c. This assumption led Parzen and Goldstein to predict large reductions in traveling wave tube gain due to velocity distribution. Second, they assumed an isothermal beam within the interaction region, i.e., $\partial T/\partial x=0$. This assumption leads to results which are in error by a factor 3. Watkins and Rynn[9] were the first authors to treat this problem correctly, using a method somewhat different from and apparently more complicated than the one which will be presented here. While these authors have pointed out the errors

[8] Lyman Spitzer, Jr., *Physics of Fully Ionized Gases* (Interscience Publishers, Inc., New York, 1956).

[9] D. A. Watkins and N. Rynn, J. Appl. Phys. **25**, 1375 (1954).

mentioned above, their paper has left the impression in the minds of some workers in the field that the basic method used by Parzen and Goldstein was incorrect. The purpose of the present treatment is to illustrate that correct results are obtained by including the hydrostatic pressure term, the term which we have labeled E', in the usual single-velocity stream analysis.[10]

We now proceed to derive the determinantal equation for the traveling wave tube, without the restriction $QC=b=d=0$. The derivation consists of obtaining a beam equation, which relates the beam current to the circuit field. This equation, plus Pierce's circuit equation[11] [Eq. (2.10)], then yields the determinantal equation. In this section we will use the following notation:

$E_T=E_c+E_{sc}+E'=$ total field,
$E_c=$ circuit field,
$E_{sc}=$ space charge field,
$E'=$ fictitious field, accounting for velocity distribution,
$I_0=$ dc beam current,
$J_1=$ ac beam current,
$K=$ Pierce's impedance parameter,
$n=n_0+n_1e^{j\omega t}$,
$QC=$ Pierce's space charge parameter,
$R=$ space charge reduction factor,
$S=$ velocity distribution parameter,
$u_0=$ dc beam velocity,
$V_0=$ dc beam voltage,
$\Delta=$ half-width for square distribution,
$\beta_e=\omega/u_0$,
$\Gamma=j\beta_e(1+jC\delta)=$ "hot" propagation constant,
$\Gamma_1=j\beta_e(1+Cb-jCd)=$ "cold" propagation constant,
$C=$ Pierce's gain parameter,
$b=$ velocity parameter,
$d=$ loss parameter.

From Pierce's equation (2.22) we can write

$$J_1=\frac{j\beta_eI_0}{2V_0(j\beta_e-\Gamma)^2}E_T. \tag{12}$$

Space charge effects are included in the following way.[12] In a drift tube, all fields are due to space charge and we find that

$$E=jJ_1/\omega\epsilon.$$

We now assume that for the traveling wave tube E_{sc} is related to J_1 in the same way, but reduced by the square of the space charge reduction factor $R=\omega_q/\omega_p$. Then since $\omega_q^2/\omega^2=4QC^3$, we obtain

$$E_{sc}=\frac{2j\beta_eV_0C^2}{I_0}\cdot 4QC\cdot J_1. \tag{13}$$

Next, from Eq. (11), we find that to first order

$$E'=-\frac{\Gamma}{\eta N}\int_{-\infty}^{\infty}n_1(w-u_0)^2dw.$$

This can be written

$$E'=\frac{2j\beta_eV_0C^2}{I_0}\cdot S\cdot J_1, \tag{14}$$

where

$$S=\frac{\int_{-\infty}^{\infty}n_1(w-u_0)^2dw}{u_0^2C^2\int_{-\infty}^{\infty}n_1dw}. \tag{15}$$

Substituting (13) and (14) into (12), the beam equation becomes

$$J_1=\frac{j\beta_eI_0E_c}{2V_0[(j\beta_e-\Gamma)^2+\beta_e^2C^2(4QC+S)]}. \tag{16}$$

Pierce's circuit equation is written

$$J_1=\left(\frac{\Gamma_1^2-\Gamma^2}{\Gamma^2\Gamma_1K}\right)E_c. \tag{17}$$

Combining (16) and (17) then leads to the following determinantal equation (for small C):

$$\delta^2=\frac{1}{-b+jd+j\delta}-(4QC+S). \tag{18}$$

This result is consistent with the findings of Watkins and Rynn,[9] and shows that the parameter S adds directly to $4QC$. For some distributions of course additional roots may appear in the calculation of S. It now remains to be shown that the value of S defined in (15) agrees with Watkins and Rynn's calculations. We shall do this only for the case of a square distribution. First, it is necessary to express n_1 in terms of n_0. This relationship is obtained from Eq. (2)

$$n_1=\eta E\frac{(\partial n_0/\partial w)}{(j\omega+\Gamma w)}.$$

Substituting this expression into (15) then yields for S the value

$$S=(\Delta/u_0C)^2$$

which is the same as the value found by Watkins and Rynn for this distribution.

[10] This fact was also pointed out by Dr. J. Berghammer in a paper presented to the Sixteenth Annual Conference on Electron Tube Research held in Quebec, Canada, in June, 1958.
[11] J. R. Pierce, *Traveling Wave Tubes* (D. Van Nostrand Co., Inc., New York 1950).
[12] This method of taking space charge effects into account was taken from notes of lectures given by Professor J. R. Whinnery at the University of California in 1954.

One final point deserves comment here. It might seem strange at first glance that S depends not only on the relative velocity spread (Δ/u_0), but is also inversely proportional to the coupling parameter C, and hence becomes large for very small C. The physical explanation is believed to be that for very small C, (i.e., small coupling), the gain of the tube becomes very velocity-sensitive. Thus as C is made progressively smaller a point is reached where the range of velocities over which gain is obtainable becomes comparable to or less than the velocity spread of the beam, and interaction then takes place with a progressively smaller number of the velocity classes present.

SPACE CHARGE WAVES

We consider next the case of space charge waves propagating on a stream with a distribution of velocities. This case is treated in a manner similar to the traveling wave tube example given above, but the discussion here starts with an equation which is easily derivable from Maxwell's equation

$$\nabla_T^2 E = -(\Gamma^2+k^2)E + j\omega\mu J_1 - \frac{\Gamma}{\epsilon}\rho_1, \tag{19}$$

where E = electric field (in this case the space charge field E_{sc}), μ = permeability, ϵ = dielectric constant, ρ_1 = ac charge density, ∇_T^2 = transverse Laplacian operator, $k^2=\omega^2\mu\epsilon$, and the subscript 1 refers to ac parts, as before. From Eqs. (6), retaining only first-order terms, we obtain

$$\rho_1 = \frac{\beta}{\omega} J_1 \tag{20}$$

$$J_1 = \rho_1 u_0 + \rho_0 v_1 \tag{21}$$

$$\frac{dU}{dt} = j(\omega-\beta u_0)v_1 = -\eta E_T, \tag{22}$$

where

$$U = u_0 + v_1$$
$$E_T = E + E'$$
$$\Gamma = j\beta.$$

By using Eqs. (20)–(22), and setting $\nabla_T^2 E = 0$ (one-dimensional case), we obtain the following determinantal equation for β:

$$(\beta_e-\beta)^2 = [1+(E'/E)]\beta_p^2.$$

For a finite beam, this becomes

$$(\beta_e-\beta)^2 = [1+(E'/E)]\cdot R^2\cdot\beta_p^2, \tag{23}$$

where

$$R = \omega_q/\omega_p$$
$$\beta_p = \omega_p/u_0$$
$$\omega_p = (\eta I_0/\epsilon u_0)^{\frac{1}{2}}.$$

From Eq. (13), the space charge field E can be written

$$E = \frac{2j\beta_e V_0(\omega_p/\omega)^2}{I_0}\cdot R^2\cdot J_1. \tag{24}$$

Since the gain parameter C has no significance for space charge waves, it is convenient to rewrite Eqs. (14) and (15) as follows:

$$E' = \frac{2j\beta_e V_0(\omega_p/\omega)^2}{I_0}\cdot S'\cdot J_1 \tag{25}$$

$$S' = \frac{\int_{-\infty}^{\infty} n_1(w-u_0)^2 dw}{u_0^2(\omega_p/\omega)^2\int_{-\infty}^{\infty} n_1 dw}. \tag{26}$$

On substituting Eqs. (24) and (25) into (23), we obtain

$$(\beta_e-\beta)^2 = (R^2+S')\beta_p^2.$$

It is now convenient to define a new reduction factor

$$R' = (R^2+S')^{\frac{1}{2}}.$$

In terms of R', the above determinantal equation may be written

$$(\beta_e-\beta)^2 = (R')^2\cdot\beta_p^2. \tag{27}$$

Thus we find that space charge wave propagation on a stream with a distribution of velocities can be described by means of the usual single-velocity theory if we use u_0, the dc part of the average stream velocity, and the reduced plasma frequency $\omega_q' = R'\omega_p$. As an example, consider an electron stream modulated by an rf voltage V_1. From the general theory of space charge waves, and by making use of Eq. (27), we find the resulting ac current to be

$$J_1 = -j\left(\frac{\eta V_1}{u_0}\right)\cdot\frac{I_0}{u_0}\cdot\frac{\omega}{\omega_q'}\cdot\sin\left(\frac{\omega q'}{u_0}x\right)e^{-j(\omega/u_0)x}. \tag{28}$$

Watkins[13] has derived a similar expression, using a series expansion for the ac distribution function. His result to first order,† expressed in terms of u_s, the velocity of the slowest electrons in the stream is

$$J_1 = -j\left(\frac{\eta V_1}{u_s}\right)\cdot\frac{I_0}{u_s}\cdot\left(1-\frac{3}{2}\alpha\right)\cdot\frac{\omega}{\omega_p} \times\sin\left[\left(1-\frac{3}{2}\alpha\right)\frac{\omega_p}{u_s}x\right]e^{-j(1-\alpha)(\omega/u_s)x}, \tag{29}$$

where $\alpha = \frac{1}{2}(kT_c/eV_0)$, k = Boltzmann's constant, and T_c = cathode temperature. We can now compare Eq.

[13] Dean A. Watkins, J. Appl. Phys. **23**, 568 (1952).

† Watkins' analysis (reference 13) was carried out to higher order.

(28) with Eq. (29) by using a square distribution, of velocity width $2\alpha u_0$, in place of the half-Maxwellian distribution. Then we can write

$$u_s = u_0(1-\alpha). \tag{30}$$

For such a square distribution we find that $S' = (\omega/\omega_p\alpha)^2$ and for a narrow distribution S' can be neglected with respect to unity. Then by noting that in Eq. (28) the plasma frequency is defined by $\omega_p = (\eta I_0/\epsilon u_0)^{\frac{1}{2}}$, while in Eq. (29) Watkins has defined this quantity by

$$\omega_p = \left(\frac{\eta I_0}{\epsilon u_s}\right)^{\frac{1}{2}} \simeq (1+\tfrac{1}{2}\alpha)\cdot\left(\frac{\eta I_0}{\epsilon u_0}\right)^{\frac{1}{2}},$$

it is found that Eqs. (28) and (29) are in agreement.

What has been shown in the foregoing example is that the first-order effects of a narrow distribution in electron velocities can be accounted for by means of an equivalent single-velocity stream which travels at the average stream velocity u_0, and which possesses an effective plasma frequency $\omega_p' = R'\omega_p$, where $\omega_p = (\eta I_0/\epsilon u_0)^{\frac{1}{2}}$.

NOISE FLUCTUATIONS IN BEAMS

As noted in the introduction, the single-velocity equivalent for noise has been very successful in the calculation of and improvement in noise figure of traveling-wave tubes. In view of Siegman's very complete treatment of this problem, only a few brief comments will be made here. Let us consider the relative magnitudes of E' and the total electric field. For the traveling wave tube, Eqs. (13), (14), and (16), which are based on the average stream velocity, give

$$\frac{E'}{E_\omega + E_c} = \left(\frac{S}{\delta^2 - S}\right).$$

For a drifting stream, Eqs. (24) and (25) give

$$E'/E = S'/R^2.$$

Typically S and S' are of the order 10^{-2}, while δ^2 and R^2 are of order unity. Thus it seems that for high velocity beams, a first order theory may reasonably use the approximation $S=0$. But $S=0$ also means $\delta K=0$, which is the definition of the rms velocity. Hence it is concluded that for high velocity beams, one may replace noise velocity fluctuations by the time-varying part of either the average or the rms velocity.

DOUBLE-STREAM AMPLIFIER

The theory of operation of the double-stream amplifier, which makes use of an electron stream composed of two distinct velocity classes U_1 and U_2, has long been known.[14,15] Indeed it is possible to arrive at the determinantal equation for the propagation constants of the coupled waves in several different ways. It is interesting, however, to see that the correct result can be obtained also by means of an equivalent single-velocity stream especially since this at first appears to be a contradiction in terms. We shall use the following notation for this derivation:

$$\begin{aligned}
U_1 &= U_{01} + v_1 \\
U_2 &= U_{02} + v_2 \\
\Delta v &= v_1 - v_2 \\
b &= (U_{02} - U_{01})/2U_0 \\
U_0 &= \tfrac{1}{2}(U_{01} + U_{02}) \\
\rho_{01} &= \rho_{02} = \tfrac{1}{2}\rho_0 \\
\omega_p^2 &= -\eta\rho_0/\epsilon \\
\beta &= \beta_0(1+\delta) \\
\beta_0 &= \omega/U_0 \\
x &= (\omega/\omega_p)b \\
n &= N_1\delta(w-U_1) + N_2\delta(w-U_2).
\end{aligned}$$

For the one-dimensional case, the basic form of the determinantal equation [Eq. (23)] becomes

$$\delta^2 = \frac{\omega_p^2}{\omega^2}\left(1+\frac{E'}{E}\right), \tag{31}$$

and the problem consists of determining the quantity E'/E. From Eq. (11) we find

$$2\delta K = \frac{N_1N_2}{N_1+N_2}(U_1-U_2)^2.$$

Retaining only first-order terms, this becomes

$$2\delta K = -\frac{1}{4\eta}[4U_0^2b^2(\rho_1+\rho_2) - 4I_0b\Delta v]. \tag{32}$$

But from Eq. (20),

$$\rho_1+\rho_2 = -\frac{\beta}{\omega}J_1 = -\frac{\beta}{\omega}(-j\omega\epsilon E). \tag{33}$$

Applying the force equation to each stream separately gives

$$\Delta v = j\eta E\left[\frac{1}{\omega-\beta U_{01}} - \frac{1}{\omega-\beta U_{02}}\right]. \tag{34}$$

Then from the definition of E' previously given, Eqs. (32), (33), and (34) lead to

$$\frac{E'}{E} = \frac{\beta^2}{\beta_p^2} - \beta U_0 b\left[\frac{1}{\omega-\beta U_{01}} - \frac{1}{\omega-\beta U_{02}}\right].$$

If this result is substituted into Eq. (31), and use is made

[14] J. R. Pierce, Proc. Inst. Radio Engrs. 37, 980 (1949).
[15] Charles K. Birdsall, Tech. Rept. No. 17, Stanford University, July 30, 1949.

of our previous definitions for β, b, U_0, etc., we obtain

$$\delta^2=\frac{\omega_p^2}{\omega^2}[1+x^2\pm(1+4x^2)^{\frac{1}{2}}] \tag{35}$$

which is identical with the determinantal equation derived by other workers in the past.[14,15]

It is to be noted in the above that the equivalent field E' does bring in the separation in the dc velocities which is fundamental to the gain mechanism; it also is a function of β and so modifies the determinantal equation. This pattern will be seen in the example to follow.

RE-ENTRANT BEAMS

In this section we shall apply some of the preceding concepts to the analysis of microwave devices which use a re-entrant electron beam. One might imagine a general class of such devices in which a part of the output energy, in the form of ac current and velocity modulation in the beam, is returned to the input to be mixed with an injected stream of fresh, or unmodulated, electrons. The magnetron oscillator is perhaps the earliest form of such a device. More recently, the highly efficient Platinotron devices[16] and the Carmatron[17] have aroused considerable interest in re-entrant beams. In order to emphasize beam re-entrancy, we shall consider the model shown in Fig. 1, which contains the essential elements of a class of physically realizable reentrant beam devices utilizing thin ribbon-shaped beams (crossed-field devices) or solid or hollow cylindrical beams (confined-flow devices). One of the principal features of this model is the occurrence (at each point in the beam) of electrons with widely different histories, corresponding to different numbers of transits around the tube. Such a circumstance inevitably leads to a multivelocity stream. Consequently, we shall analyze this model on the basis of an equivalent average-velocity stream. Our problem then is to determine the values of the ac current and the ac part of the average velocity at the input ($Z=0$) in terms of these same quantities at the output ($Z=L$). Let us first consider the nature of the distribution function for such a re-entrant beam. For an ideal beam at the exit from the electron gun (i.e., no velocity spread), one might reasonably suppose the stream to be composed of discrete velocities, a new velocity class being introduced after each complete transit. The distribution function of Eq. (4) would be appropriate, leading to the following

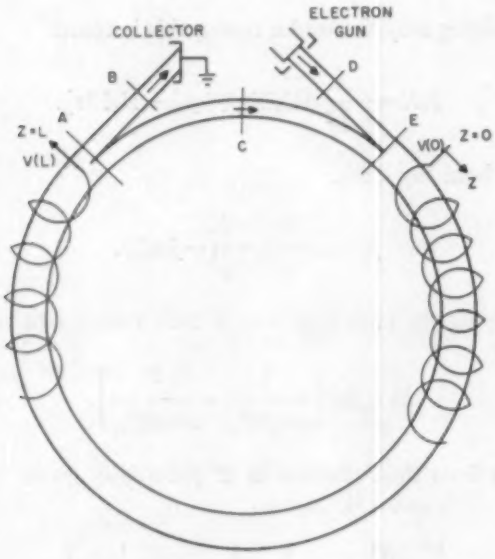

FIG. 1. Model of reentrant beam tube.

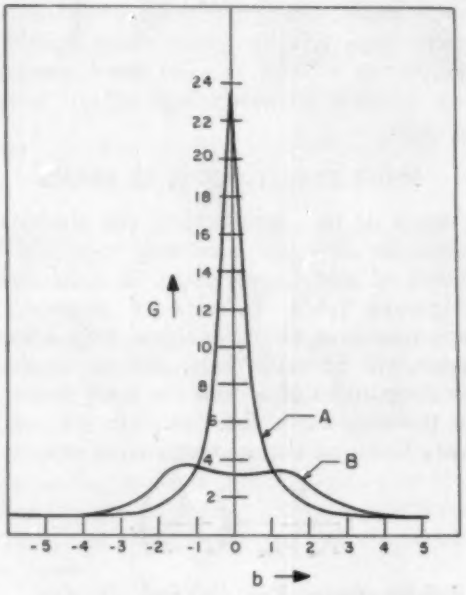

FIG. 2. Gain *versus* beam velocity curves for $\delta\theta=0$ and $\delta\theta=\pi$, with $k'=0.200$.

form for δK:

$$\frac{2\delta K}{N}=\sum_{i=1}^{M}\frac{N_i}{N}[(U_{0i}-U_0)+v_i]^2-v^2,$$

where

$$U_i=U_{0i}+v_i$$

$$U=U_0+v$$

$$U_0=\sum_{i=1}^{M}\frac{N_{0i}}{N_0}U_{0i}.$$

The important point to note here is that for the limiting case of no distribution in dc velocities, only second order terms appear in the above equation, and hence $\delta K=0$, to first order. If the distribution is continuous rather than discrete, we have seen that it is still per-

[16] William C. Brown, Proc. Inst. Radio Engrs. **45**, 1209 (1957).
[17] R. Warnecke *et al.*, Compt. rend. **241**, 695 (1955).

missible to use $\delta K=0$ for a narrow velocity spread ($S\ll 1$). For the analysis, we make use of the following set of assumptions: (1) At the output ($Z=L$) a certain fraction k of the current is split off and returned to the input. This splitting is considered to occur without affecting electron velocities; also, ac currents are assumed to divide proportionally to the dc currents. (2) $\delta P=0$ (definition of average velocity). (3) $\delta K=0$ (small dc velocity spread). (4) Streams C and D mix in such a way that their distribution functions add, i.e., $n_E=n_C+n_D$. (5) All the usual small-signal assumptions appropriate to a linear theory are used. From assumption (2) we can write

$$I_E=I_C+I_D$$

and from assumption (3),

$$I_E U_E=I_C U_C+I_D U_D.$$

Dividing all currents and velocities into dc and ac parts we find the ac modulation conditions at $Z=0$ and $Z=L$

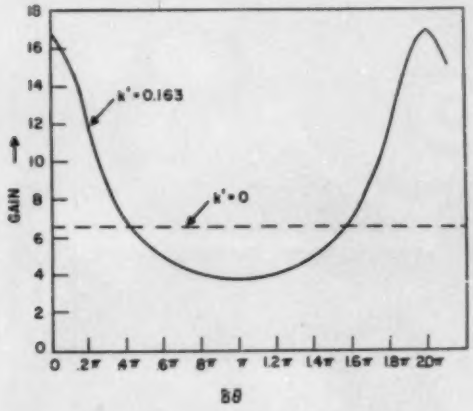

FIG. 3. Theoretical variation of gain with phase.

to be related by

$$\begin{aligned} i(0)&=k\cdot i(L)\\ v(0)&=k\cdot v(L). \end{aligned} \tag{36}$$

These relations may be used as additional equations of constraint in the usual three-wave analysis for a traveling wave amplifier. However, we are particularly interested in backward wave interaction, since such interaction contains an inherent mode separation mechanism. A two-wave coupled-mode theory appropriate for large QC operation, which has been developed by Gould,[18] offers a means of obtaining a simple gain expression for the backward wave case. Using Gould's notation, we let Q and P represent the amplitudes of the two interacting modes; they are defined such that QQ^* and PP^* represent the power carried by the modes. If we let Q represent the backward space harmonic of the circuit field and P the slow space charge wave on the beam, then the boundary conditions [using Eqs. (33)] are given by

$$\begin{aligned} Q&=Q(L) \text{ at } Z=L\\ P&=k\cdot P(L)e^{-j\theta}, \end{aligned}$$

where θ represents the drift angle from output to input. The expression for the complex gain $\bar{A}=Q(0)/Q(L)$ is then found to be

$$\bar{A}=\frac{ky\cos(yL)+jkz\cdot\sin(yL)-ye^{j(zL+\theta)}}{-y\cdot\cos(yL)+jz\cdot\sin(yL)+kye^{-j(zL+\theta)}}, \tag{37}$$

where

$$x=\frac{\beta_q+\beta_p}{2},$$

$$y=\left[\left(\frac{\beta_q-\beta_p}{2}\right)^2+H^2\right]^{\frac{1}{2}},$$

$$z=\frac{\beta_q-\beta_p}{2},$$

and the subscripts q and p refer to the modes Q and P in the absence of coupling. The coupling parameter H is related to the more usual traveling wave tube parameters by

$$HL=\pi CN/(QC)^{\frac{1}{2}}.$$

This same gain expression is also obtained for the crossed-field case, if a neutralized beam model is assumed and if the following correspondences are used:

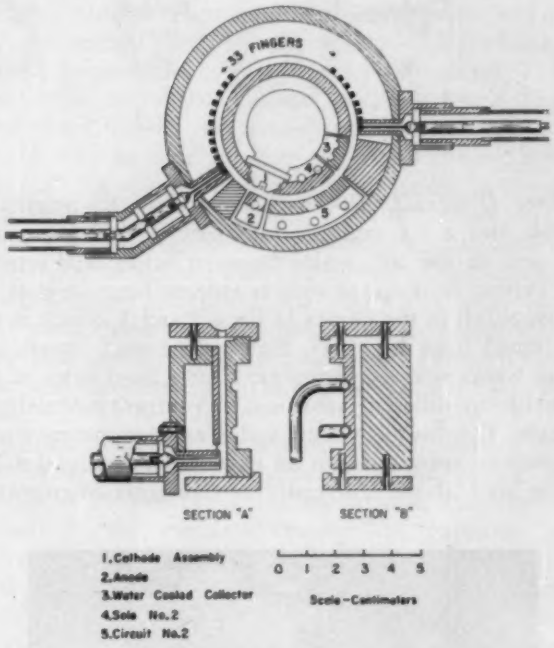

FIG. 4. Re-entrant beam tube.

[18] R. W. Gould, IRE Trans. **PGED-2**(1955).

Confined flow:	Crossed field:
β_q	β_c
β_p	β_e
H	$\beta_e D$
k	k',

where $D^2=(a\rho_0 K/2B)$, a=beam width, B=magnetic field, and $k'=k$ multiplied by any (diocotron) gain present in the drift region between output and input.

Typical behavior of such re-entrant beam devices is exemplified in the curves of Figs. 2 and 3, which were obtained from Eq. (37). Figure 2 presents curves of gain *versus* velocity parameter b for a fixed value of k' and for two different conditions of reentrant modulation phase. The various circuit and beam parameters were chosen to correspond to an experimental crossed-field tube built at the University of California Microwave Tube Laboratory.[19] Curve A represents the case where the re-entrant modulation is in phase with the rf at synchronism ($b=0$). Here the gain drops more rapidly with b than for the nonre-entrant case. This is due to the fact that not only does the beam depart from synchronism as b varies from zero, but also the modulation moves toward an out-of-phase condition. Curve B represents the case where the re-entrant modulation is 180° out of phase at synchronism. The appearance of the double hump is explained physically as follows: As b varies from zero the gain tends to decrease because of the departure of the two waves from synchronism; however, the tendency of the gain to increase because the reentrant modulation approaches more nearly the in-phase condition can, for awhile, more then compen-

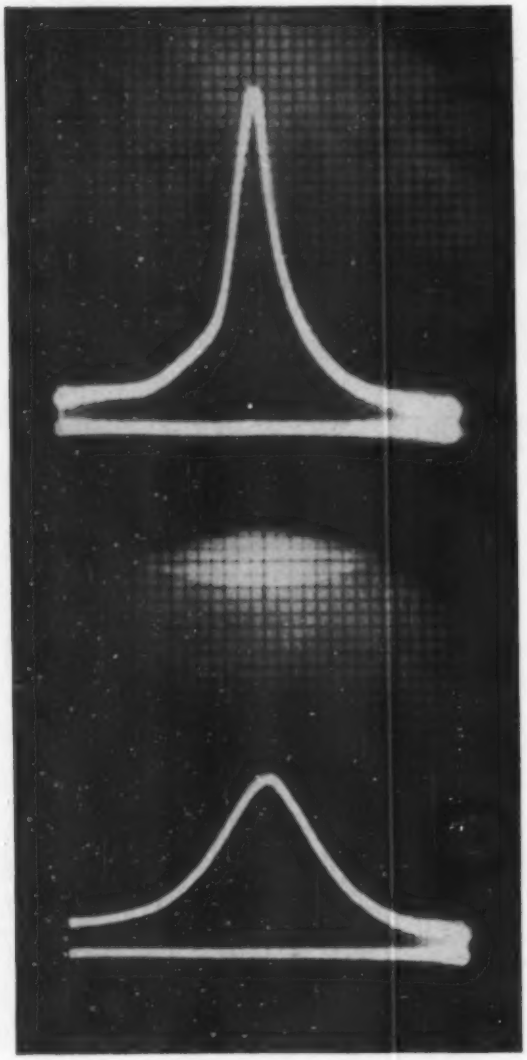

FIG. 5. Gain *versus* beam velocity for $\delta\theta=0$ (upper trace), and for $k'=0$ (lower trace).

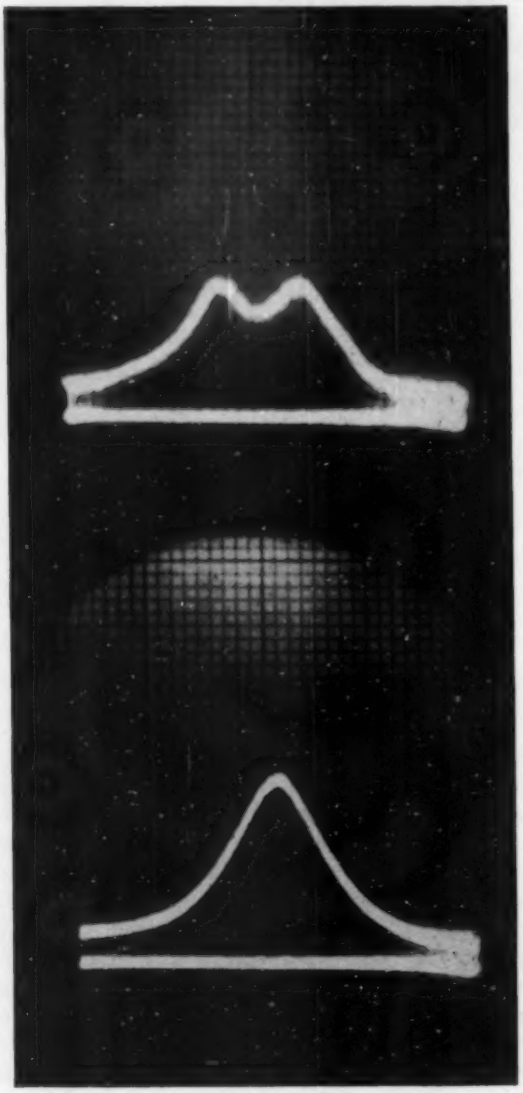

FIG. 6. Gain *versus* beam velocity for $\delta\theta=\pi$ (upper trace).

[19] Glenn A. Gray, Ph.D. dissertation, University of California (1958).

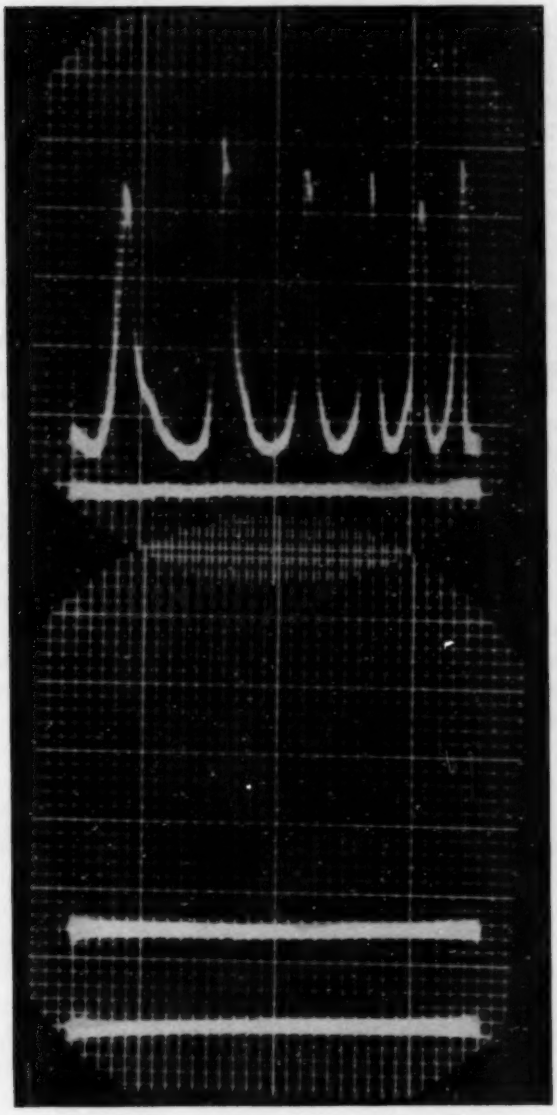

FIG. 7. Gain *versus* re-entrant modulation phase.

sate for this decrease. Hence the appearance of the two humps. Another characteristic of interest is the variation of gain with reentrant modulation phase, beam velocity being maintained at the nonre-entrant synchronous value. This characteristic is given in the curve of Fig. 3, using somewhat different values of the beam and circuit parameters.

In order to obtain a check on the validity of the theory, an experimental crossed-field re-entrant beam tube was constructed. This tube, shown schematically in Fig. 4, utilizes an interdigital slow-wave structure and operates in the frequency range 1100–1700 mc/sec. By varying the collector potential it is possible to control the amount of reentrant current, while the phase of the current can be varied by varying the electric field in the drift space (the space between electrodes 4 and 5 in Fig. 4).

Figure 5 is a photograph of oscilloscope traces which display rf output power *versus* beam velocity, the beam velocity being varied by sweeping the sole voltage. The upper trace is for the in-phase case, i.e., $\delta\theta=0$. The lower trace shows the corresponding nonre-entrant case ($k'=0$). As expected from the simple theory, it is seen that the sensitivity of gain to variations in beam velocity is greater than for the nonre-entrant case. Figure 6 is a photograph which shows a similar oscilloscope traces for the case where the re-entrant modulation is out of phase at synchronism. Again it is seen that the general character of the reentrant case agrees with theoretical predictions, i.e., a decreased sensitivity of gain to beam velocity and the appearance of the double hump.

In order to obtain an experimental verification of the gain *versus* phase relation which is shown in Fig. 3, the phase of the re-entrant modulation was varied through several complete cycles. This variation in phase was brought about by varying the voltage applied to the negative electrode in the drift region, between rf circuit output and input. This electrode will be referred to as sole number 2. The result is shown in the oscilloscope traces of Fig. 7. In the upper trace, the vertical response is proportional to rf output power while the horizontal axis represents the voltage on sole 2. The horizontal axis is also proportional to the average electron velocity through the drift region. Before this experimental curve can be compared directly with theory, it is necessary to express the drift space phase variation of Fig. 3 (i.e., $\delta\theta$) in terms of V_{g-2}, the voltage applied to sole 2. This calculation has been carried out and the result is shown in Fig. 8. It is seen that the experimental curve of Fig. 7 agrees quite well with the theoretical one of Fig. 8. In order to get an idea of the qualitative agreement between these two curves, we can calculate the voltage separations ΔV between gain peaks and compare these with the measured values obtained from Fig. 7. The separation between two successive maxima corresponds to a phase change of 2π, and should therefore be given by

$$(\beta_2-\beta_1)L_d=2\pi.$$

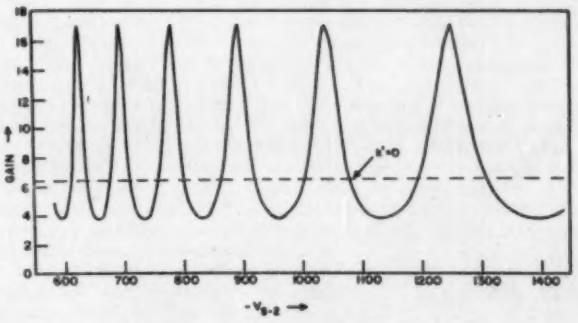

FIG. 8. Theoretical variation of gain with V_{g2}, for the conditions of Fig. 3.

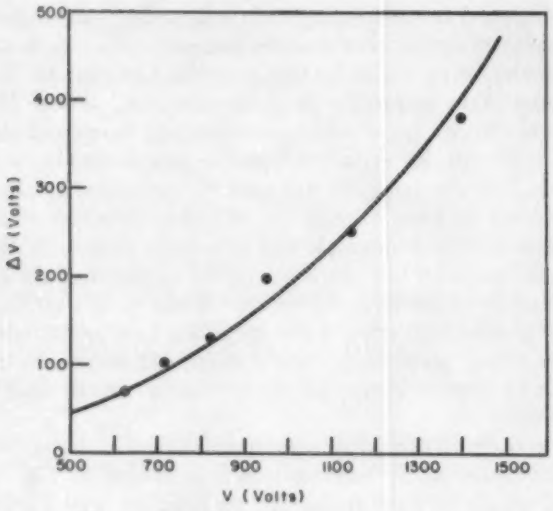

FIG. 9. Voltage separation between gain peaks. Experimental points are taken from Fig. 7.

Since $\beta=\omega/u_0$, the above expression leads to

$$\Delta V = V^2/(FL_dB_d - V),$$

where f=operating frequency, L_d=drift space length, B=magnetic field, and d=circuit-sole spacing. Then if V is the voltage at one peak, ΔV is the voltage separation between it and the next higher peak. In Fig. 9, ΔV is plotted as a function of V for the conditions of Fig. 7. On this same curve are plotted the measured values of ΔV, obtained from Fig. 7. The maximum percentage deviation between the theoretical curve and the measured points is seen to be about 15%, which is about all that can be expected considering the accuracy with which voltages can be determined from the oscilloscope trace.

The above examples are typical of a number of small-signal experiments which have been carried out,[19] and which show generally good qualitative agreement with the simple theory. Thus it is concluded that we are justified in replacing the actual multivelocity stream with its single-velocity equivalent.

ACKNOWLEDGMENTS

The author is greatly indebted to Professor John R. Whinnery for many helpful discussions, and for his constructive criticism of the manuscript. This research was made possible through support extended by the Raytheon Manufacturing Company, and the Wright-Air Development Center.

JOURNAL OF APPLIED PHYSICS VOLUME 31, NUMBER 2 FEBRUARY, 1960

On the Concept of Fictitious Surface Charges of an Electron Beam*

E. L. Chu
Microwave Laboratory, W. W. Hansen Laboratories of Physics, Stanford University, Stanford, California
(Received August 11, 1958)

The electrodynamical phenomena in the boundary strip of a sharply focused electron beam are extremely complicated. This difficulty is usually resolved by postulating a layer of surface current on the boundary of the unperturbed beam while considering the troublesome boundary strip as nonexistent. A critical examination is made of this technique with the result that, if the calculated rf power is to be the same as in the actual beam, a layer of electric dipoles must also be postulated. The discussion begins with the Jacobian and Taylor's expansion, with particular emphasis on the applicability of the latter to the boundary strip, then proceeds to the formulation of a modified problem on an equal-power basis and the specification of the surface conditions which are to be satisfied. Second-order quantities are included in all equations, so that the small-signal beam kinetic quantities can be reliably calculated.

I. INTRODUCTION

IN the small-signal theory of electron-beam devices the time-varying part of any quantity (space-charge density ρ, current density $\mathbf{j}$, electric-field intensity $\mathbf{E}$, etc.) is considered to be small in comparison with the time-independent part of the same quantity. This basic assumption, however, is in most practical cases not satisfied because the electron beam usually has a rather sharply defined boundary surface. With such a beam there exists a region, or strip, partly inside and partly outside the unperturbed beam, in which the space-charge density $\rho(x,t)$ at any fixed point (x,y,z) varies between its maximum value and zero in such an abrupt manner that there are many Fourier harmonic components in the spectrum of $\rho(x,t)$ which have the same order of magnitude as the dc component $\bar{\rho}(x)$. Since the width of the boundary strip varies linearly with the magnitude of the perturbation, the attendant effects of the boundary strip cannot properly be neglected even when the perturbation is vanishingly small.

The well-known technique of treating such problems is to invoke the idea of an equivalent surface current. Imagine that the perturbation is approaching zero; then so is the width of the boundary strip. The current in this strip, whatever it is, would be of the nature of a surface current. As the perturbation increases in magnitude, this surface current is assumed to persist but to increase proportionately in strength. In this way, the problem may be solved strictly as a small-signal problem as if the boundary strip of exceptional nature were not in existence.

This technique was first used by Hahn[1] for an electron beam which was assumed to be completely neutralized by a positive-ion cloud, and then by Feenberg,[2] Buneman,[3] and others[4,5] for pure electron beams. Hahn's original idea[6] was not the same as the concept of an equivalent surface current adopted by later authors. A clear account of the basic assumptions and of the qualitative arguments leading to an equivalent surface current may be found in the work of Warnecke and Guénard.[7] Several different methods of derivation have recently been given by Rigrod,[8] all leading to the same expression for this surface current. Long before this, the concept of an equivalent surface current was considered by most authors as physically obvious and had been used so often and so successfully that this concept may now be invoked without further justification.

Although this technique is indeed very useful in the solution of various specific problems, it is nevertheless true that it is only an artifice and does not fully account for the true state of affairs. This artificial aspect is clearly recognized in Hahn's paper and in Feenberg's report, but has become somewhat obscured in some of the later publications. Lately, this technique has also been used as a rigorous procedure in connection with the proof of small-signal power-conservation theorems.[9,10]

* The research reported in this document was supported jointly by the U. S. Army Signal Corps, the U. S. Air Force, and the U. S. Navy (Office of Naval Research).

[1] W. C. Hahn, G. E. Rev. **42**, 258 (1939).

[2] E. Feenberg, "Notes on velocity modulation" Sperry Gyroscope Company Labs. Rept. No. 5221–1043 (September, 1945).

[3] O. Buneman, J. Electronics and Controls **3**, 1 (1957).

[4] G. G. MacFarlane and H. G. Hay, Proc. Phys. Soc. (London) **B63**, 409 (1950).

[5] W. W. Rigrod and J. A. Lewis, Bell System Tech. J. **33**, 399 (1954).

[6] Hahn postulated the presence of a positive ion cloud, which has the same velocity $\mathbf{v}_0$ and the same magnitude of space charge density ρ_0 as the dc electron stream and which extends far enough beyond the radius b of the latter stream. An unbalanced current ΔI was calculated as the sum of the dc electron current $\pi b^2\rho_0 v_0$ and the total positive-ion current $(-\pi r_b^2\rho_0 v_0)$ contained inside the fluctuating boundary of radius r_b. The unbalanced current $\Delta I \cong -2\pi b\rho_0 v_0(r_b - b)$, being just the negative of the equivalent surface current adopted by Feenberg and later authors. In matching the tangential magnetic fields inside and outside the radius b Hahn introduced another minus sign and thus arrived at the same boundary equation as used subsequently by other authors. If the concept of an equivalent surface current in its present-day version is to be interpreted as a surface effect, Hahn's idea must be explained as a volume effect.

[7] R. Warnecke and P. Guénard, *Les Tubes electroniques à commande par modulation de vitesse* (Gauthier-Villars, Paris, France, 1951), pp. 536–541.

[8] W. W. Rigrod, Proc. Inst. Radio Engrs. **46**, 358 (1958).

[9] H. A. Haus and D. L. Bobroff, J. Appl. Phys. **28**, 694 (1957).

[10] J. W. Klüver, J. Appl. Phys. **29**, 618 (1958).

As it now stands, this concept can only be considered to be an elegant mathematical artifice for modifying the original problem into one which can be solved with ease. The applicability of this procedure to the proof of power theorems would remain doubtful unless it could be proved that the two problems do have the same small-signal beam power.

In a recent letter[11] the author has pointed out that this is not the case, and has briefly indicated how this concept may be revised to lead to the correct expression of beam power. It has later come to our attention that Newton[12] had previously suggested the possibility of a dipole layer in addition to the simple layer of surface charges. Unfortunately, his discussion of the dipole layer was too brief and his expressions of surface charge distribution are not acceptable. According to Newton, the surface charge density should have a negative sign in front of the usual, accepted expression.

Since the beam kinetic quantities and rf power are important characteristics of any electron beam device, we think it is advisable to formulate in detail the method by which these quantities may always be reliably calculated. For this purpose second-order terms will be needed, since without these a unique determination of the kinetic energy-momentum tensor is not possible. Our formulation of the method will be based on the theory of infinitesimal transformations. We shall first discuss the Jacobian, the Taylor expansion, and the applicability of the latter to the boundary strip. Then we shall formulate a modified problem on the basis of equal beam power and, finally, discuss the surface conditions to be satisfied.

II. JACOBIAN AND TAYLOR'S EXPANSION IN PERTURBATION THEORY

Let $\mathbf{r}_0$ and $\mathbf{r}$ be, respectively, the unperturbed and the perturbed position vectors

$$\mathbf{r}_0=\mathbf{i}x_0+\mathbf{j}y_0+\mathbf{k}z_0, \quad \text{and} \quad \mathbf{r}=\mathbf{i}x+\mathbf{j}y+\mathbf{k}z.$$

Likewise, the unperturbed value of any other quantity will also be denoted by the subscript "0," with the exception of time t. In the following it will always be understood that t and t_0 are the same.

An electron at the space-time point (x,t) would be at (x_0,t) were it not for the perturbation. Thus,

$$\mathbf{r}=\mathbf{r}_0+\delta\mathbf{r}=\mathbf{r}_0+\epsilon\mathbf{r}_1+\epsilon^2\mathbf{r}_2+\cdots. \tag{1}$$

where ϵ is a small positive numerical constant[13] ($\epsilon\ll 1$), depending on the magnitude of the perturbation; and $\delta\mathbf{r}$ is a function of (x_0,t).

As in hydrodynamics and the theory of elasticity, the Jacobian and Taylor's series expansion are the principal tools for perturbation calculation. They can be manipulated most concisely by adopting Gibb's vector notations.[14] Thus, the Jacobian $\partial(x,y,z)/\partial(x_0,y_0,z_0)$ may be written as

$$J(x/x_0)=(\mathrm{I}+\nabla_0\delta\mathbf{r})_3 =1+(\nabla_0\delta\mathbf{r})_s+(\nabla_0\delta\mathbf{r})_{2s}+(\nabla_0\delta\mathbf{r})_3. \tag{2}$$

Here I is the idemfactor or the unity dyadic. For any dyadic Φ, there are three fundamental scalar invariants Φ_s, Φ_{2s}, and Φ_3. In particular,

$$(\nabla_0\delta\mathbf{r})_s=\nabla_0\cdot\delta\mathbf{r} \tag{3a}$$

$$(\nabla_0\delta\mathbf{r})_{2s}=(1/2)\,\mathrm{I}:\nabla_0\delta\mathbf{r}\overset{\times}{\times}\nabla_0\delta\mathbf{r} =(1/2)\nabla_0\cdot(\delta\mathbf{r}\nabla_0\cdot\delta\mathbf{r}-\delta\mathbf{r}\cdot\nabla_0\delta\mathbf{r}) \tag{3b}$$

$$(\nabla_0\delta\mathbf{r})_3=\text{determinant of dyadic } \nabla_0\delta\mathbf{r}. \tag{3c}$$

Taylor's expansion is simpler. It may be written in the vector operator form with either a scalar or a vector function as its operand. Let us denote Taylor's operator by Σ; then

$$\Sigma_0=\exp(\delta\mathbf{r}\cdot\nabla_0) =1+\delta\mathbf{r}\cdot\nabla_0+(1/2!)\delta\mathbf{r}\delta\mathbf{r}:\nabla_0\nabla_0+\cdots. \tag{4}$$

From charge conservation, we may at once obtain the perturbed space-charge density $\rho(x,t)$ in terms of the unperturbed space-charge density $\rho_0(x_0)$ and the displacement vector $\delta\mathbf{r}(x_0,t)$, namely,

$$\rho(x,t)=\rho_0(x_0)d\tau_0/d\tau=\rho_0(x_0)/(\mathrm{I}+\nabla_0\delta\mathbf{r})_3, \tag{5}$$

where $d\tau_0$ and $d\tau$ are corresponding infinitesimal volume elements. The velocity $\mathbf{v}(x,t)$ of any electron is simply related to its unperturbed value by

$$\mathbf{v}(x,t)=\mathbf{v}_0(x_0)+d\delta\mathbf{r}/dt, \tag{6a}$$

where

$$d\delta\mathbf{r}/dt=\{\partial/\partial t+\mathbf{v}_0(x_0)\cdot\nabla_0\}\delta\mathbf{r}. \tag{6b}$$

From ρ and $\mathbf{v}$ we immediately obtain the current density

$$\mathbf{j}(x,t)=[\mathbf{j}_0(x_0)+\rho_0(x_0)d\delta\mathbf{r}/dt]/J(x/x_0). \tag{7}$$

Equations (5)–(7) are valid everywhere in the beam regardless of the differentiability of ρ, $\mathbf{v}$, or $\mathbf{j}$. These equations, however, are not quite suitable for calculation, because the two sides of these equations refer to different space points. When (x) is fixed, (x_0) is a function of t, and vice versa. To transform a function of (x,t) to that of (x_0,t) we shall use Taylor's expansion. Thus,

$$\rho(x,t)=\Sigma_0\,\rho(x_0,t) =\Sigma_0\{\rho_0(x_0)+\epsilon\rho_1(x_0,t)+\epsilon^2\rho_2(x_0,t)+\cdots\}. \tag{8}$$

The vector functions $\mathbf{v}(x,t)$ and $\mathbf{j}(x,t)$ can be expanded in a similar manner.

Taylor's expansion is not always valid. The justification of its use will be discussed in the next section.

[11] E. L. Chu, J. Appl. Phys. **30**, 1618 (1959).
[12] R. H. C. Newton, J. Electronics **2**, 441 (1957).
[13] It is very unlikely that the perturbation parameter ϵ may be confused with the dielectric constant ϵ or ϵ_0.
[14] J. W. Gibbs and E. B. Wilson, *Vector Analysis* (Yale University Press, New Haven, 1901).

By combining Eqs. (5) and (8), using Eqs. (1) to (4) inclusive, and collecting terms of the first and second power in ϵ, we obtain

$$\rho_1(x_0,t) = -\nabla_0\cdot(\rho_0\mathbf{r}_1) \tag{9a}$$

$$\rho_2(x_0,t) = -\nabla_0\cdot\{\rho_0\mathbf{r}_2-(1/2)\nabla_0\cdot(\rho_0\mathbf{r}_1\mathbf{r}_1)\}. \tag{9b}$$

Similarly,

$$\mathbf{v}_1(x_0,t) = (d\mathbf{r}_1/dt)-\mathbf{r}_1\cdot\nabla_0\mathbf{v}_0; \tag{10a}$$

$$\mathbf{v}_2(x_0,t) = (d\mathbf{r}_2/dt)-\mathbf{r}_2\cdot\nabla_0\mathbf{v}_0-\mathbf{r}_1\cdot\nabla_0\mathbf{v}_1 - (1/2!)(\mathbf{r}_1\mathbf{r}_1:\nabla_0\nabla_0)\mathbf{v}_0; \tag{10b}$$

$$\mathbf{j}_1(x_0,t) = (\partial/\partial t)(\rho_0\mathbf{r}_1)+\nabla_0\times(\mathbf{r}_1\times\mathbf{j}_0), \tag{11a}$$

$$\mathbf{j}_2(x_0,t) = (\partial/\partial t)\{\rho_0\mathbf{r}_2-(1/2)\nabla_0\cdot(\rho_0\mathbf{r}_1\mathbf{r}_1)\} +\nabla_0\times\{\mathbf{r}_2\times\mathbf{j}_0+(1/2)\mathbf{r}_1\times\mathbf{j}_1 -(1/2)(\mathbf{r}_1\cdot\nabla_0\mathbf{r}_1)\times\mathbf{j}_0\}. \tag{11b}$$

These expressions for ρ and $\mathbf{j}$ satisfy the equations of continuity

$$\nabla_0\cdot\mathbf{j}_n(x_0,t)+\partial\rho_n(x_0,t)/\partial t=0 \quad (n=1, 2, \cdots). \tag{12}$$

This is not surprising because relations (12) are implied in Eq. (5).

All elements of the kinetic energy-momentum tensor of an electron beam can be expressed in terms of $\rho(x_0,t)$ and $\mathbf{v}(x_0,t)$. On the other hand, the perturbed field quantities can be calculated from Maxwell's equations under given boundary conditions (to be discussed in Sec. IV). Thus, every quantity in the perturbed system is expressible (to second order in ϵ) as a function of the unperturbed quantities and the displacement vectors $\mathbf{r}_1$ and $\mathbf{r}_2$. The unperturbed problem is presumed to be soluble rigorously, while the displacement vectors are to be calculated from the Lorentz equation of electron motion in the usual manner. The specific expressions for $\mathbf{r}_1$ and $\mathbf{r}_2$ will depend on the physical nature and geometry of the whole beam system, hence will vary from one problem to another. In the following we shall only be concerned with the general features of the method of solution.

III. TAYLOR'S EXPANSION IN THE BOUNDARY STRIP OF AN ELECTRON BEAM

Equations (9)–(11) are not as general as Eqs. (5)–(7). The former equations are derived from the latter by using Taylor's expansion and would break down in the boundary strip of the beam, where such an expansion as Eq. (8) is not valid.

In the boundary strip, there are regions called "crests" (denoted by C) in which $\rho_0(x)=0$ but $\rho(x,t)\neq 0$. Similarly there are regions called "troughs" (denoted by T) in which $\rho(x_0,t)=0$ but $\rho_0(x_0)\neq 0$. As described in the introductory section, $\rho(x,t)-\bar{\rho}(x)$ in C and $\rho(x_0,t)-\bar{\rho}(x_0)$ in T will be of the same order of magnitude as $\rho_0(x')$ and $\rho_0(x_0')$, respectively, (x') and (x_0') being located in the regular part of the beam (designated as region R), (x') being only a small distance from (x) in C, and similarly (x_0') being very close to (x_0) in T. Since the boundary surface is moving or fluctuating continuously, so are the regions C, T, and R. At a given space point, T and R will change role from time to time. At any given time, $R+T$ make up the whole volume of the unperturbed beam and $R+C$ the whole volume of the perturbed beam. Usually, C and T are small in extent compared with R, a situation apparently implied by calling the exceptional boundary region a strip. The foregoing description, however, can evidently be extended without alteration to other cases, including thin ribbon beams or filament beams for which R is negligibly small in comparison with C or T.

For the sake of clarity, (x_0) will henceforth in this section be restricted to be in the region $R+T$ and (x) in $R+C$. With (x_0) in R, the first few terms of Taylor's expansion as given by Eq. (8), namely,

$$\rho(x,t) = \{1+\epsilon\mathbf{r}_1\cdot\nabla_0+\epsilon^2\mathbf{r}_2\cdot\nabla_0+(\epsilon^2/2!)\mathbf{r}_1\mathbf{r}_1:\nabla_0\nabla_0\}\rho_0(x_0) +(1+\epsilon\mathbf{r}_1\cdot\nabla_0)\epsilon\rho_1(x_0,t)+\epsilon^2\rho_2(x_0,t)+\cdots, \tag{13}$$

may always be assumed to be valid. On the other hand, if (x_0) is in T, Eq. (13) becomes useless because $\rho(x_0,t)$ cannot be considered as a smooth function in passing from region T to region R. Thus Eqs. (9)–(11) are only valid for (x_0) in R, not in T.

By a similar procedure ρ, $\mathbf{v}$, and $\mathbf{j}$ may be expressed in terms of (x,t) instead of (x_0,t); and the resulting equations corresponding to (9)–(11) will, because of similar reasons, be valid only for (x) in R, not in C. The difficulty presented by the boundary surface is of a fundamental nature and appears in both the (x_0,t) and the (x,t) descriptions. These two descriptions are equivalent to each other, and hereafter only the former description given in the last section will be considered.

Formally speaking, the problem should be solved by using Eqs. (5)–(7) directly, which are valid everywhere. This, however, is seldom practicable because of the fact that the solutions inside and outside the beam must be matched on the boundary surface. Indeed, it is this difficulty of matching functions on the fluctuating boundary which dictates the usual method of solution by modifying the original problem so that the boundary surface of the beam may be considered as remaining unperturbed.

We shall now explain how this modification is to be carried out. Perhaps it is simplest to consider the procedure as based on a revision of the definition of the various quantities (ρ, $\mathbf{v}$, and $\mathbf{j}$). After the revision is made, Eq. (8) or (13) and Eqs. (9) to (11) inclusive will all become applicable everywhere in $R+T$. To show that this is really possible, we first change the definition of the space-charge density from the true function $\rho(x_0,t)$ to a different function

$$\rho'(x_0,t)=\rho_0(x_0)+\epsilon\rho_1'(x_0,t)+\epsilon^2\rho_2'(x_0,t)+\cdots$$

such that

$$\rho'(x_0,t)=\rho(x_0,t), \quad (x_0) \text{ in } R \tag{14a}$$

and

$$\Sigma_0\,\rho'(x_0,t)=\rho(x,t)=\rho_0(x_0)/J(x/x_0), \quad (x_0) \text{ in } T. \tag{14b}$$

In other words, $\rho'(x_0,t)$ is so defined that with (x_0) in R it is the same as the true space-charge density $\rho(x_0,t)$; and with (x_0) in T it is derived from $\rho(x,t)$ in the same way as with (x_0) in R by using Eqs. (5) and (8), which represent the law of charge conservation and the Taylor expansion, respectively. Thus, if $\rho_1'(x_0,t)$ and $\rho_2'(x_0,t)$ are substituted for $\rho_1(x_0,t)$ and $\rho_2(x_0,t)$, Eqs. (9a) and (9b) will be applicable everywhere with (x_0) in $R+T$. Without actually making these substitutions we must understand that $\rho_1(x_0,t)$ and $\rho_2(x_0,t)$ do not represent the true space-charge densities except for (x_0) in R. In other words, we are to use Taylor's expansion as if it were generally valid, but we must revise our concept in order to interpret the results correctly.

Similarly, the vector quantities $\mathbf{v}'(x_0,t)$ and $\mathbf{j}'(x_0,t)$ may be defined by the same procedure as the scalar quantity $\rho'(x_0,t)$ is defined. In short, Eqs. (8) to (11) inclusive may be considered as valid everywhere in $R+T$ with the understanding that $\rho_1(x_0,t)$, $\rho_2(x_0,t)$, $\mathbf{j}_1(x_0,t)$, etc. are not the correct functions for (x_0) in T. The same procedure applies also to the field vectors $\mathbf{E}(x_0,t)$ and $\mathbf{H}(x_0,t)$.

IV. MODIFIED PROBLEM ON AN EQUAL-POWER BASIS

Having made the modification, we would naturally hope that the modified problem will be a close approximation (and in a sense, equivalent) to the original problem. To be useful, the modified problem must yield the same small-signal beam power as would be obtained in a solution of the original problem, and we shall require that this be the case. The results obtained in this section are based on this requirement, and lead us to conditions which must be satisfied on the unperturbed beam surface (S_0). These surface conditions are readily interpreted in terms of a surface electric dipole distribution in addition to the usual surface charge and current densities.

Consider a small volume $\delta V=\delta R+\delta C$ of the perturbed beam, which at a given time contains a certain number of electrons. These same electrons would be contained in a corresponding small volume $\delta V_0=\delta R_0+\delta T_0$ in the unperturbed case. Let $d\bar{P}$ denote the difference between the values of electromagnetic power (absorbed if positive) in the perturbed and unperturbed cases for these same electrons

$$d\bar{P}=\int_{\delta V}\mathbf{E}(x,t)\cdot\mathbf{j}(x,t)d\tau-\int_{\delta V_0}\mathbf{E}_0(x_0)\cdot\mathbf{j}_0(x_0)d\tau_0 \tag{15}$$

This expression is the so-called Lagrangian expression of rf beam power. Our objective of formulating the modified problem is to calculate $d\bar{P}$.

As discussed in a previous article[15] there are two alternative definitions of rf beam power. One is the Lagrangian definition given above by Eq. (15). The other definition is called the Eulerian and is given by

$$d\bar{\mathcal{P}}=\int_{\delta V}\{\mathbf{E}(x,t)\cdot\mathbf{j}(x,t)-\mathbf{E}_0(x)\cdot\mathbf{j}_0(x)\}d\tau. \tag{16}$$

For considering scalloped electron beams having sharply defined boundary surfaces it is more desirable to adopt the Lagrangian definition than the Eulerian. In the Lagrangian expression $\mathbf{E}_0(x_0)$ and $\mathbf{j}_0(x_0)$ are smooth functions everywhere in δV_0, while in the Eulerian $\mathbf{E}_0(x)$ and $\mathbf{j}_0(x)$ vary greatly in going from δC to δR. In the forementioned article[15] it has been pointed out that, as far as the usual small-signal rf beam power is concerned, the two definitions are the same. Also discussed therein is the fact that the difference between the two definitions which appears in some cross terms makes no net contribution to the *total* rf power of the whole beam system. The following discussion will be based mainly on the Lagrangian definition.

The first integral on the right of Eq. (15) can be transformed to an integral over δV_0, namely,

$$\int_{\delta V}p(x,t)d\tau=\int_{\delta V_0}J(x/x_0)\{\Sigma_0\,p(x_0,t)\}d\tau_0,$$

where p denotes $\mathbf{E}\cdot\mathbf{j}$. In this equation $p(x_0,t)$ and $\Sigma_0\,p(x_0,t)$ must be understood as *well-behaved* functions in the sense discussed in Sec. III. For the sake of brevity, the functional arguments (x_0,t) and (x_0) will hereafter be omitted.

Let us specifically consider δV_0 as a small section of the dc beam of a certain length (finite or infinitesimal) in the direction of the dc velocity $\mathbf{v}_0$ having a longitudinal boundary surface of area δA_0. The surface enclosing δV_0 will be denoted by $S_0(\delta)$. It consists of δA_0 and two transverse surfaces denoted by $B_0(\delta)$, i.e., $S_0(\delta)=\delta A_0+B_0(\delta)$.

The detailed evaluation of the integrand $J\,\Sigma_0\,p$ is straightforward.[15] This integrand can be expanded into an infinite series in increasing powers (or orders) of ϵ. For calculating the small-signal rf and kinetic power we need only consider the second-order terms. Terms of the first order will vanish on being averaged over time, while those of the third and higher orders are neglected.

Let $d\bar{P}^{(2)}$ denote the second-order part of $d\bar{P}$; we obtain from Eq. (15)

$$d\bar{P}^{(2)}=\int_{\delta V_0}p^{(2)}d\tau_0+\int_{S_0(\delta)}\mathbf{n}_0\cdot[\mathbf{r}_1p^{(1)}+\mathbf{f}_2p^{(0)}]d\sigma_0. \tag{17}$$

[15] E. L. Chu, J. Appl. Phys. **30**, 1617 (1959).

Here $\mathbf{n}_0$ is the unit normal directed outward from the beam surface $S_0(\delta)$;

$$p^{(0)}=\mathbf{E}_0\cdot\mathbf{j}_0\equiv p_{00}, \tag{17a}$$

$$p^{(1)}=\mathbf{E}_0\cdot\mathbf{j}_1+\mathbf{E}_1\cdot\mathbf{j}_0\equiv p_{01}, \tag{17b}$$

$$p^{(2)}=\mathbf{E}_1\cdot\mathbf{j}_1+(\mathbf{E}_0\cdot\mathbf{j}_2+\mathbf{E}_2\cdot\mathbf{j}_0)\equiv p_{11}+p_{02}, \tag{17c}$$

and

$$\mathbf{f}_2=\mathbf{r}_2+(1/2)(\mathbf{r}_1\nabla_0\cdot\mathbf{r}_1-\mathbf{r}_1\cdot\nabla_0\mathbf{r}_1+\mathbf{r}_1\mathbf{r}_1\cdot\nabla_0). \tag{17d}$$

From Eq. (17) it is clear that, in order to obtain the same small-signal power as in the actual (perturbed) beam, an additional amount of power must be added to the volume integral of integrand $p^{(2)}$. This additional power is given by the surface integral in Eq. (17) and is considered as arising from a surface distribution of density $\mathbf{n}_0\cdot(\mathbf{r}_1p_{01}+\mathbf{f}_2p_{00})$. When Eq. (17) is summed over the whole volume V_0 of the unperturbed beam, the domain of integration of the surface integral will become the whole surface S_0 ($S_0=A_0+B_0$) which encloses V_0.

The volume integral in Eq. (17) may further be transformed by using Poynting's theorem. Thus,

$$\int_{\delta V_0}p^{(2)}d\tau_0=-\int_{\delta V_0}[\partial W^{(2)}/\partial t]d\tau_0-\int_{S_0(\delta)}\mathbf{n}_0\cdot\mathbf{S}^{(2)}d\sigma_0. \tag{18}$$

in which $W^{(2)}$ and $\mathbf{S}^{(2)}$ are, respectively, the second-order parts of the electromagnetic energy density and of the Poynting vector. Both $W^{(2)}$ and $\mathbf{S}^{(2)}$ can be written in forms similar to that of $p^{(2)}$ given by Eq. (17c). By substituting Eq. (18) into (17) we obtain

$$d\bar{P}^{(2)}=-\int_{\delta V_0}[\partial W^{(2)}/\partial t]d\tau_0-\int_{S_0(\delta)}\mathbf{n}_0\cdot\mathbf{S}'^{(2)}d\sigma_0 \tag{19}$$

where

$$\mathbf{S}'^{(2)}=\mathbf{S}^{(2)}-(\mathbf{r}_1p_{01}+\mathbf{f}_2p_{00}). \tag{19a}$$

The outward flow of energy density $(\mathbf{n}_0\cdot\mathbf{S}')$ from the longitudinal part (δA_0) of the surface $S_0(\delta)$ must be equal to $[\mathbf{n}_0\cdot\mathbf{S}_{(+)}]$, where $\mathbf{S}_{(+)}=\mathbf{E}_{(+)}\times\mathbf{H}_{(+)}$ is the Poynting vector evaluated at the surface $\delta A_0{}^{(+)}$ just outside δA_0. This is true because the charge densities ρ_0 and ρ vanish outside δA_0. Consequently on an equal-power basis, we arrive at the condition to be satisfied on the longitudinal part of the unperturbed beam surface, namely,

$$\mathbf{n}_0\cdot\mathbf{S}_{(+)}{}^{(2)}=\mathbf{n}_0\cdot\{\mathbf{S}_{(-)}{}^{(2)}-(\mathbf{r}_1p_{01}+\mathbf{f}_2p_{00})\}\ \text{ on }\ A_0. \tag{20}$$

Here $\mathbf{S}_{(-)}{}^{(2)}$ is written in place of $\mathbf{S}^{(2)}$ to indicate that this Poynting vector is to be evaluated at the surface $A_0{}^{(-)}$ just inside A_0.

This condition must then be split into two parts so that the first- and the second-order perturbation calculations can be made in successive steps. For reasons to be explained presently, Eq. (20) is split as follows:

$$\mathbf{n}_0\cdot\{\mathbf{S}_{11}{}^{(+)}-\mathbf{S}_{11}{}^{(-)}\}=-\mathbf{n}_0\cdot\mathbf{r}_1p_{01}\ \text{ on }\ A_0 \tag{21a}$$

$$\mathbf{n}_0\cdot\{\mathbf{S}_{02}{}^{(+)}-\mathbf{S}_{02}{}^{(-)}\}=-\mathbf{n}_0\cdot\mathbf{f}_2p_{00}\ \text{ on }\ A_0. \tag{21b}$$

To obtain the first-order solution, Eq. (21a) is to be used in conjunction with the corresponding relation of the (0,1)th order,[16] i.e.,

$$\mathbf{n}_0\cdot\{\mathbf{S}_{01}{}^{(+)}-\mathbf{S}_{01}{}^{(-)}\}=-\mathbf{n}_0\cdot\mathbf{r}_1p_{00}\ \text{ on }\ A_0. \tag{22}$$

Similarly, to obtain the second-order solution, Eq. (21b) is to be supplemented by the corresponding relation of the next higher order

$$\mathbf{n}_0\cdot\{\mathbf{S}_{12}{}^{(+)}-\mathbf{S}_{12}{}^{(-)}\}=-\mathbf{n}_0\cdot\{\mathbf{r}_1p^{(2)}+\mathbf{f}_2p^{(1)}\}\ \text{ on }\ A_0. \tag{23}$$

Since p_{01} is the first-order power density, it is quite natural that $\mathbf{n}_0\cdot\mathbf{r}_1p_{01}$ should represent the (1,1)th component of surface power density. It is also consistent to consider $\mathbf{n}_0\cdot\mathbf{r}_1p_{00}$ and $\mathbf{n}_0\cdot\mathbf{f}_2p_{00}$ as being, respectively, the (0,1)th and the (0,2)th components. These reasons, however, may seem to be inconclusive, because, for example, $\mathbf{n}_0\cdot\mathbf{r}_1\mathbf{j}_1\cdot\mathbf{E}_0$ can perhaps also be interpreted as belonging to the (0,2)th component. Since the latter interpretation is indeed the same as that used with the usual assumption of a simple surface current, we think it necessary to give here further reasons for taking a variant path.

Consider the Eulerian definition of power given by Eq. (16). Let $\delta\tau$ and the corresponding volume $\delta\tau_0$ be located at all times inside the regular part of the beam. Under this restriction, which implies no difficulty in differentiation, the Eulerian definition of power is as valid as the Lagrangian definition [Eq. (15)]. Omitting the (0,2)th and the higher-order quantities from Eq. (16) and transforming it to the (x_0,t) coordinate system, we obtain

$$d\bar{\mathfrak{P}}=\int_{\delta\tau_0}[\epsilon p_{01}+\epsilon^2\{p_{11}+\nabla_0\cdot(\mathbf{r}_1p_{01})\}]d\tau_0.$$

Thus evidently,

$$(d\bar{\mathfrak{P}})_{11}=\int_{\delta\tau_0}\{p_{11}+\nabla_0\cdot(\mathbf{r}_1p_{01})\}d\tau_0. \tag{24}$$

Equations (17) and (24) tell us that, as long as both definitions are equally valid, $(d\bar{\mathfrak{P}})_{11}$ is the same as $(d\bar{P})_{11}$ provided that $\nabla_0\cdot(\mathbf{r}_1p_{01})$ and $\nabla_0\cdot(\mathbf{f}_2p_{00})$ are considered, respectively, as belonging to the (1,1)th and the (0,2)th components of power density. Near the boundary strip the Eulerian definition becomes dubious for reasons explained in Sec. III. Despite this difficulty, we believe that the scheme of splitting power into different orders should enable the two alternative

[16] See later discussion leading to Eqs. [(30a) and (b)] and [(31a) and (b)].

definitions of rf beam power to agree with each other in the regular region of the beam and should not be altered throughout the remaining regions.

Furthermore, since according to Poynting's theorem

$$\mathbf{n}_0\cdot\mathbf{r}_1\dot{\mathbf{j}}_1\cdot\mathbf{E}_0=-(\mathbf{n}_0\cdot\mathbf{r}_1)\left[\frac{\partial}{\partial t}(\mathbf{E}_0\cdot\mathbf{D}_1)+\nabla_0\cdot(\mathbf{E}_0\times\mathbf{H}_1)\right],$$

the quantity $\mathbf{n}_0\cdot\mathbf{r}_1\dot{\mathbf{j}}_1\cdot\mathbf{E}_0$ accounts for the interaction effect between $(\mathbf{D}_1,\mathbf{H}_1)$ and the dc state as felt by the moving electrons. If this quantity is considered as being of the (0,2)th order, then the first-order calculation will only take account of the interaction effect given by the remaining part of $\mathbf{n}_0\cdot\mathbf{r}_1p_{01}$, namely, $\mathbf{n}_0\cdot\mathbf{r}_1\dot{\mathbf{j}}_0\cdot\mathbf{E}_1$. This effect is felt by the electrons as arising from the interaction between $(\mathbf{E}_1,\mathbf{B}_1)$ and the dc state. Since $(\mathbf{D}_1,\mathbf{H}_1)$ and $(\mathbf{E}_1,\mathbf{B}_1)$ can never appear one without the other, this interpretation is physically untenable.

Equation (21a) differs from the usual surface condition (first postulated by Hahn) in having the additional term $\mathbf{n}_0\cdot\mathbf{r}_1\mathbf{E}_0\cdot\dot{\mathbf{j}}_1$. This term calls for a discontinuity in the tangential electric field across the surface A_0. In order to support this discontinuity the existence of a dipole-moment layer must be postulated.[17] Naturally, the dipole layer will not affect the charge-conservation relations.

To facilitate further discussion of Eqs. [(21a) and (b)] we adopt the following notations for surface charge distributions on A_0:

$$\eta=\mathbf{n}_0\cdot[\mathbf{D}_{(+)}-\mathbf{D}_{(-)}], \tag{25a}$$

$$\chi=\mathbf{n}_0\times[\mathbf{H}_{(+)}-\mathbf{H}_{(-)}], \tag{25b}$$

$$\pi=[\mathbf{E}_{(+)}-\mathbf{E}_{(-)}]\times\mathbf{n}_0=(1/\epsilon_0)\mathbf{n}_0\times\nabla_0\zeta. \tag{25c}$$

Here, η is the surface charge density, χ is the surface current density, ζ is the moment density of a dipole layer, and π measures the discontinuity in the tangential electric field determined by the gradient of ζ. All these quantities are of magnitude $0(\epsilon)$ and can be expanded into different orders.

From Eq. (25c) and the Maxwell equation which relates $\nabla_0\times\mathbf{E}$ to $\partial\mathbf{B}/\partial t$, it follows that

$$\mathbf{n}_0\cdot[\mathbf{B}_{(+)}-\mathbf{B}_{(-)}]=0. \tag{25d}$$

Equations [(25a)–(d)] are the complete set of boundary conditions to be satisfied on A_0. They can be described completely in terms of three surface quantities, η, χ, and $\nabla_0\zeta$ or π. On substituting the expressions of χ and π into the left-hand side of Eqs. [(21a) and (b)] the latter equations become

$$\chi_1\cdot\mathbf{E}_{1(-)}+\pi_1\cdot\mathbf{H}_{1(+)}=\mathbf{n}_0\cdot\mathbf{r}_1p_{01}, \tag{26a}$$

$$\chi_2\cdot\mathbf{E}_0+\pi_2\cdot\mathbf{H}_0=\mathbf{n}_0\cdot(\mathbf{f}_2p_{00}). \tag{26b}$$

[17] J. A. Stratton, *Electromagnetic Theory* (McGraw-Hill Book Company, Inc., New York, 1941), pp. 187–192.

The surface charge density of a given order is determined by the principle of charge conservation. From Eq. (5) it follows that

$$\int_{\delta V_0}\rho_m d\tau_0=-\int_{S_0(\delta)}\eta_m d\sigma_0,\quad (m=1,2,\cdots).$$

Hence,

$$\eta_1=\mathbf{n}_0\cdot\mathbf{r}_1\rho_0 \tag{27a}$$

$$\eta_2=\mathbf{n}_0\cdot\{\mathbf{r}_2\rho_0-(1/2)\nabla_0\cdot(\mathbf{r}_1\mathbf{r}_1\rho_0)\}. \tag{27b}$$

The surface current density χ is related to η through an equation of continuity. The latter equation can easily be derived from Maxwell's equation and is as follows:

$$\partial\eta/\partial t+\mathbf{n}_0\cdot\nabla_0\times(\mathbf{n}_0\times\chi)=\mathbf{n}_0\cdot\mathbf{j}. \tag{28}$$

If both sides of this equation are integrated over a small area and the second term on the left-hand side is transformed into a contour integral, the physical meaning of this equation will become obvious.

Corresponding to η_1 and η_2 we have

$$\chi_1=\eta_1\mathbf{v}_0=\mathbf{n}_0\cdot\mathbf{r}_1\dot{\mathbf{j}}_0 \tag{29a}$$

and

$$\chi_2=\eta_2\mathbf{v}_0+\eta_1\mathbf{v}_{1t}', \tag{29b}$$

where

$$\begin{aligned}\mathbf{v}_{1t}'&=\mathbf{v}_1'\cdot(\mathbf{I}-\mathbf{n}_0\mathbf{n}_0)\\&=(1/2)\{\mathbf{v}_{1t}-(\mathbf{n}_0\cdot\mathbf{v}_1)\mathbf{r}_{1t}/(\mathbf{n}_0\cdot\mathbf{r}_1)\}.\end{aligned}$$

These equations are obtained by using Eq. (28) together with the known expressions of η and $\mathbf{j}$ given by Eqs. [(27a) and (b)] and Eqs. [(11a) and (b)], respectively. Part of the contribution to χ_2 is from η_1 and this part of the surface current flows with a velocity $\mathbf{v}_{1t}'$ which is different from the tangential component of $\mathbf{v}_1$. We may further note that $(\mathbf{n}_0\cdot\mathbf{v}_1)$ does not vanish on A_0, in contrast to the situation at the boundary surface A of the actual beam. The effect of electrons which flow in and out of the surface A_0 is, as far as power is concerned, supposed to be accounted for by the presence of a dipole layer.

Having obtained χ_1 and χ_2 we turn to Eqs. [(26a) and (b)] for determining π_1 and π_2. These equations, however, are not sufficient, because Eq. (26a) only determines one component of π_1 parallel to the tangential component of $\mathbf{H}_{1(+)}$, and Eq. (26b) only determines $\pi_2\cdot\mathbf{H}_0$. In order to determine π_1 and π_2 completely, we must also use Eqs. (22) and (23). Thus, we find

$$\pi_1\cdot\mathbf{H}_0=0, \tag{30a}$$

$$\pi_1\cdot\mathbf{H}_{1(+)}=\mathbf{n}_0\cdot\mathbf{r}_1\mathbf{E}_0\cdot\dot{\mathbf{j}}_1; \tag{30b}$$

$$\pi_2\cdot\mathbf{H}_0=(1/2)\{\mathbf{n}_0\cdot(\dot{\mathbf{j}}_1\mathbf{r}_1-\mathbf{r}_1\dot{\mathbf{j}}_1)\cdot\mathbf{E}_0+(\mathbf{n}_0\cdot\mathbf{r}_1)\nabla_0\cdot(\mathbf{r}_1\dot{\mathbf{j}}_0\cdot\mathbf{E}_0)\}, \tag{31a}$$

$$\pi_2\cdot\mathbf{H}_{1(+)}=\mathbf{n}_0\cdot\{\mathbf{r}_1p^{(2)}+\mathbf{f}_2p^{(1)}\}-\pi_1\cdot\mathbf{H}_{2(+)}-\{\chi_1\cdot\mathbf{E}_{2(-)}+\chi_2\cdot\mathbf{E}_{1(-)}\}. \tag{31b}$$

The dipole layer may be considered as being located just outside the simple layer of surface current, so that the dipole moment ζ does not interact with χ while it creates the required discontinuity in the tangential electric field.[11]

We have thus specified all the boundary conditions on the longitudinal surface of the unperturbed beam, but have not yet completed the formulation of the modified problem. There remains one troublesome aspect which must also be discussed. This is in connection with the boundary conditions on the exit end of the beam. No difficulty is expected from the entrance end, where $\delta\mathbf{r}$ can always reasonably be assumed to vanish.

On the exit end, the electron beam may impinge on a collector plate, may pass through an orifice or a grid plane, or may enter some other device. Generally speaking, the boundary conditions to be satisfied on the exit surface B_0 must depend on the manner in which the beam makes its exit. There are two cases to be considered. In one case, the charge and current densities suffer no discontinuity in going across the exit surface, e.g., in passing through an orifice. In such an instance, the electron beam does not really make its exit in passing across the surface so designated. The situation is simply that the end effect of the beam is to be neglected or, perhaps, it is negligible. Consequently, no restrictive condition is needed on the exit surface.

In the other case as, e.g., with a collector plate, the charge and current densities vary discontinuously in passing across the exit surface. The latter surface B definitely has a fixed position. On the contrary, the position of the corresponding surface B_0 will vary with time. Any position beyond the exit surface B at which $\mathbf{n}\cdot\delta\mathbf{r}<0$ must be conceived as a mathematical fiction. The technical difficulty presented by this fluctuating boundary B_0 is at least as great as that caused by the fluctuating boundary A of V. One solution is to avoid this difficulty by considering the exit surface B_0 as having a fixed position inside of V sufficiently removed from B, so that the short portion of the beam between B_0 and B will be neglected. This, however, may sometimes not be justifiable.

Another solution is to resolve the difficulty by transforming the frame of reference once again, so that in the new coordinate system, say, (x',t), the exit surface B' coincides with the exit surface B and the longitudinal boundary surface A' coincides with A_0. When these requirements are satisfied, it is evident that the boundary conditions on B' will be the same as those on B.

One simple transformation of this kind is as follows:

$$\mathbf{r}_0=\mathbf{r}'-\delta\mathbf{r}\cdot\mathbf{k}_0\mathbf{k}_0 \tag{32}$$

with $\delta\mathbf{r}$ denoting the same displacement vector as defined by Eq. (1), and $\mathbf{k}_0=\mathbf{v}_0(x_0)/|v_0(x_0)|$. Without going into further detail we may mention that the resulting expressions of charge densities, electron velocities, and current densities differ only in second-order terms from the corresponding expressions obtained by simply substituting (x',t) for (x_0,t) in Eqs. [(9a) and (b)], [(10a) and (b)], and [(11a) and (b)]. If the second transformation is not made, so that the complications arising from the exit surface are simply neglected then the error incurred in $(d\bar{P})_{11}$ will be of the third-order of magnitude, while that incurred in $(d\bar{P})_{02}$ will be of the second order. These results serve to justify the usual practice of neglecting the exit boundary conditions for calculating $(d\bar{P})_{11}$.

V. CONCLUDING REMARKS

The concept of a simple layer of surface charges can best be explained as a mathematical artifice by which the troublesome boundary strip of the actual, perturbed beam is resolved in a simple manner. The use of this artifice, however, modifies the problem itself, and is not simply a mathematical approximation. The problem thus modified can only be considered equivalent to the original problem in the following sense: The total charge

$$\int_{\delta V}\rho(x,t)d\tau$$

in the volume δV in the original problem is equal to the sum of the space charges

$$\int_{\delta V_0}\rho'(x_0,t)d\tau_0$$

in the corresponding volume δV_0 and the surface charges $\eta_1=\mathbf{n}_0\cdot\mathbf{r}_1\rho_0$, $\eta_2=\mathbf{n}_0\cdot(\mathbf{r}_1\rho_1'+\mathbf{f}_2\rho_0)$, etc. on the surface $S_0(\delta)$ enclosing δV_0. If (x_0) is in the regular beam region R, then $\rho'(x_0,t)=\rho(x_0,t)$. If (x_0) is in troughs T, then $\rho'(x_0,t)$ must be interpreted as being defined by Eq. (14b). The small-signal power calculated is not the same as that in the actual beam unless $\mathbf{E}_0\cdot\mathbf{j}_1$ vanishes on the surface of the unperturbed dc beam.

By further postulating the presence of a layer of electric dipoles, thus admitting a discontinuity in the tangential electric field in addition to that in the tangential magnetic field, the modified problem can always be required to have the correct beam power. Since a dipole layer does not disturb the relationship between total charges, this revision of the concept would not affect the original sense of equivalence.

Of course, this approximate method of solution, by which the problem itself is modified, leaves something to be desired. The method also has its limitations in practical usefulness, because the conditions to be satisfied on the boundary of the dc beam will become considerably more complicated in successively higher orders of perturbation calculation. When successive calculations are required for solving nonlinear large-signal problems, it may be advisable to abandon the

sharply edged beam model (admitting discontinuous charge- and current-density functions) and to consider, instead, a properly smoothed-out edgeless beam. For a beam of the latter type, Taylor's expansion can easily be justified and the theory of infinitesimal transformations discussed in this paper is particularly useful. All the equations obtained herein remain valid, and become much simplified because all of the fictitious surface charge distributions on the smoothed-out edge of the beam will vanish.

ACKNOWLEDGMENTS

The author is indebted to Dr. G. S. Kino, Dr. O. Buneman, and Dr. W. R. Ayers for helpful discussions during earlier stages of this work, to Dr. K. G. Dedrick and R. Wilson for many recent discussions and helpful criticisms, and to W. Kirk for his valuable assistance in the preparation of the manuscript. The author is also indebted to Dr. T. T. Wu for stimulating discussions concerning several aspects of the perturbation theory.

JOURNAL OF APPLIED PHYSICS VOLUME 31, NUMBER 2 FEBRUARY, 1960

Method for the Detection of Flaws in Yttrium Iron Garnet Crystals

E. Buehler and M. Tanenbaum
Bell Telephone Laboratories, Inc., Murray Hill, New Jersey
(Received June 1, 1959)

Infrared techniques similar to those used in examining silicon crystals have been applied to the examination of yttrium iron garnet crystals. Photographic results for both flux grown and sintered crystals are given.

THE use of infrared radiation to study imperfections in crystals of silicon was introduced by Dash.[1,2] He observed that dislocations would nucleate the precipitation of supersaturated solutions of copper in silicon and that these precipitates were opaque to radiation of approximately 1.1 μ wavelength. Since silicon is transparent at wavelengths greater than 1.1 μ, dislocations could be observed as the locus of strings of opaque precipitates when viewed with an infrared image tube (snooperscope). Recently a similar apparatus has been employed as an aid in the determination of the perfection and purity of yttrium iron garnet crystals.

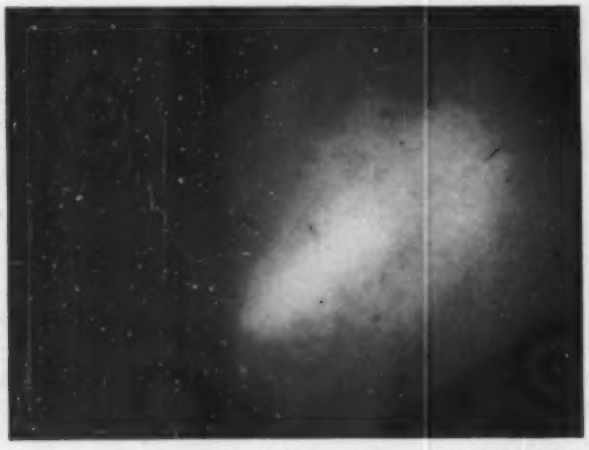

Fig. 1. Single crystal plate (flux grown crystal)—J. W. Nielsen (mag.—11×, thickness—0.049 in., 3 sec exposure in transmitted light from tungsten filament).

[1] W. C. Dash, Phys. Rev. **98**, 1536 (1955).
[2] W. C. Dash, J. Appl. Phys. **27**, 1193 (1956).

The growing of large single crystals of yttrium iron garnet is of conisderable interest.[3] Single crystal specimens are desirable for microwave parametric amplifiers and for other microwave applications. A technique for examining the perfection of crystals was needed to guide the effort to produce large crystals. Yttrium iron garnet crystals are currently grown from solutions of molten salts.[4] The material is also prepared in polycrystalline form as a sintered ceramic[5] and as fused bars. The prior

Fig. 2. Corner of same crystal as in Fig. 1 after 24 hr at 1500°C in air (mag.—11×, thickness—0.028 in., 60 sec exposure in transmitted light from high-intensity arc source).

[3] S. Geller and M. A. Gilleo, Acta Cryst. **10**, 239 (1957); F. Bertant and F. Forrat, Compt. rend. **242**, 382 (1956).
[4] J. P. Remeika, J. Am. Chem. Soc. **78**, 4259 (1956); J. W. Nielsen and E. F. Dearborn, Phys. and Chem. Solids **5**, No. 3, 202–207 (1958).
[5] L. G. Van Uitert and F. W. Swanekamp, J. Appl. Phys. **28**, 1513, 1514 (1957).

techniques used to evaluate these forms have included, (1) ferromagnetic resonance line width measurements on small polished spheres; (2) x-ray diffraction of powder samples; (3) wet chemical analysis; and (4) metallographic studies on polished samples. In addition, magnetic domains[6] can be seen in transmitted polarized light in the visible part of the spectrum by using very thin samples of "good" single crystals.

Single crystal yttrium iron garnet is quite transparent at 1.2 μ,[7] the limit of sensitivity of currently available infrared image tubes. The transparency is dependent upon the stoichiometry of the crystal, the presence of foreign phases and the presence of cracks. Differences in transparency are an indication of the imperfections in the crystal but cannot always be relied upon as a positive means of identification. Fe_3O_4 is completely opaque, while Fe_2O_3 and $YFeO_3$ absorb more strongly in this spectral region than yttrium iron garnet. Cracks are usually opaque and easily identified.

Where corollary information is not available, changes in composition and gross structural defects all appear as opaque regions and cannot be separately identified. However, the presence of any nonuniformity in the transmission indicates that the crystal is not perfect.

The samples were examined in an infrared microscope which consisted of a Leitz (Model PANPHOT) metallograph with carbon arc or tungsten filament illumination. The eyepiece of the metallograph was replaced by an RCA (Model 6032A) infrared sensitive image tube.[5]

FIG. 3. Striations in a r.f.f. sample. Crystal grown by fusion technique (direction of growth ↑, mag.—11×, thickness—0.037 in., 2 min exposure in transmitted light from high-intensity arc source).

[6] J. F. Dillon, Phys. Rev. **105**, 759 (1957).
[7] J. F. Dillon, J. Appl. Phys. **29**, 539–541 (1958); D. L. Wood (to be published).
[8] W. L. Bond (unpublished).

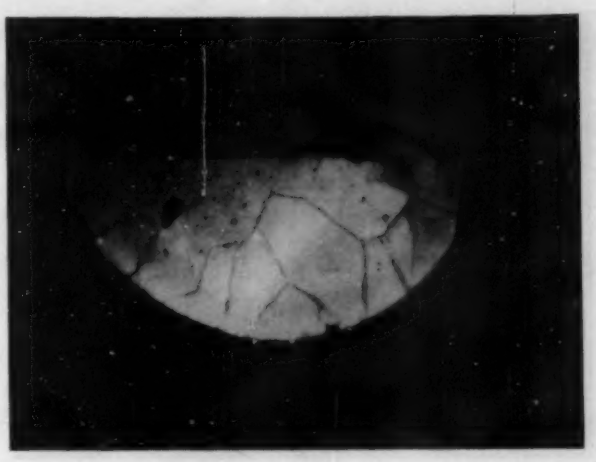

FIG. 4. Grain boundaries. Section from polycrystalline rod 0.030 in. thick (mag.—11×, 10 sec exposure in transmitted light from high-intensity arc source).

Optically polished sample plates $\frac{1}{32}$ in. to $\frac{3}{32}$ in. thick are used for crystals of moderate perfection. Thicker plates can be used from very perfect crystals, i.e., those grown from molten salt solution. The plates are mounted on microscope slides and masked with electrical or optical tape to restrict the field of observation. Light from the source passes through the sample on a microscope stage, is magnified 10–50× and focused on the "snooperscope" screen. The focus can be adjusted to view any desired depth in the sample. By observing the image on the snooperscope screen, the structure of the crystalline garnet can be studied. The image can also be photographed.

A typical photograph of a flux grown crystal is shown in Fig. 1. This sample was 0.049 in. thick. After heating in air for one-half hour at temperatures as high as 1550°C no change in transmission could be detected. However, when heated in air at 1500°C for 24 hr, the same sample became almost completely opaque. It was then thinned to 0.028 in. where it again became transparent enough to permit photographing (see Fig. 2). Numerous rather uniformly distributed dark spots can be seen. These were identified by examination with reflected visible light at 500× as Fe_3O_4 and $YFeO_3$. Although the spots were barely resolved by the metallographic techniques using visible light, they were easily detected with infrared, first as a general loss in overall transmission and secondly as enlarged shadows.

Figure 3 is a photograph taken parallel to the growth direction of a crystal grown by a fusion technique. The striations show that the rate of crystallization was not uniform during the growth of the material.

Grain boundaries in otherwise relatively perfect samples are easily seen. Figure 4 is a photograph of a polycrystalline slab cut perpendicular to the direction of growth. Approximately 12 grains can be discerned.

Photographs of sintered ceramic bar secions are shown

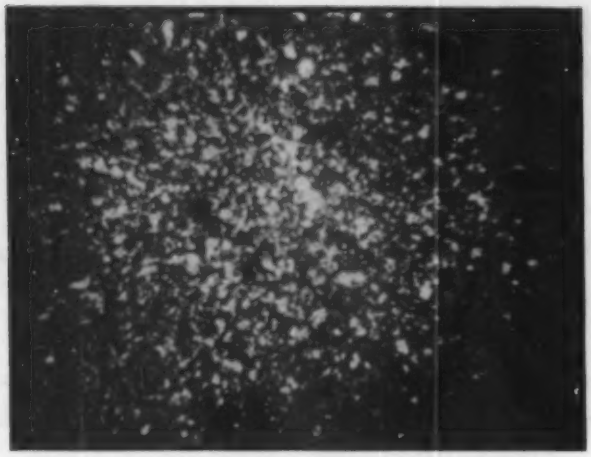

FIG. 5. Section from sintered bar 0.0065 in. thick—M. A. Gilleo (mag.—11×, 7 sec exposure in transmitted light from high-intensity arc source).

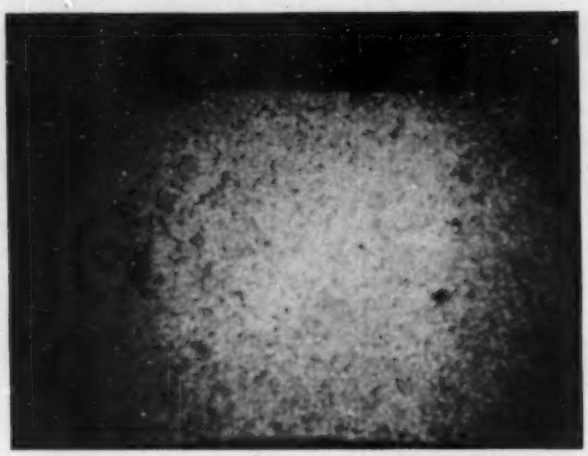

FIG. 6. Section from sintered bar 0.010 in. thick—Van Uitert (mag.—11×, 10 sec exposure in transmitted light from high-intensity arc source).

in Figs. 5 and 6. Samples of this type of material must be made as thin as the largest perfect grains to become transparent. In these samples this thickness usually has to be less than 0.010 in. Again the grain boundaries, the foreign phases, and the cracks can be identified when corollated with the examination in visible reflected light at 500×.

In general the technique provides one additional means of evaluation of the perfection of yttrium iron garnet crystals.

We are indebted to W. L. Bond who made the infrared microscope available to us, to L. G. Van Uitert who provided the sintered ceramic garnet samples and to J. W. Nielsen who provided the single crystal garnets.

Thermal Attenuation of Nonlinear Stress Waves

SVEN TREITEL*
Department of Geology and Geophysics, Massachusetts Institute of Technology, Cambridge, Massachusetts
(Received May 21, 1959)

The work of Knopoff and MacDonald (1958) on the attenuation of nonlinear stress waves in solids has been extended to include thermal losses. The damping of a nonlinear stress wave is completely describable in terms of two attenuation coefficients, a "mechanical" coefficient α_1, and a "thermal" coefficient α_2. The latter is probably small compared to the other, but much high-precision experimental work is required to settle this point definitely.

INTRODUCTION

IN a recent paper the author[1] has shown how stress waves propagating through a real physical solid suffer amplitude decay because a part of the wave energy is conducted away as heat. The resultant attenuation coefficient α was found to be a function of the square of the circular frequency ω. A considerable number of materials, particularly metals, are known to have an attenuation coefficient that behaves in this manner. However, a wealth of experimental evidence suggests that many solids, particularly silicates, do not satisfy such a law. Knopoff and MacDonald[2,†] (1958) have reviewed the laboratory data that has been published, and find that for most silicates α is proportional to the first power of ω. Information for the damping of stress waves in rocks as established from seismograms also appears to confirm the laboratory evidence.[3]

Now K and M have been able to show that any *linear* differential equation with constant coefficients can only lead to an α that is a function of an *even* power of ω. Accordingly these workers were led to investigate the equations of motion and temperature that arise if the linearity restrictions on the stress-strain relation

$$P=f(u,u_p,T) \tag{1}$$

are lifted. Here, P=*total* stress (not necessarily purely elastic), u=elastic displacement, u_p=permanent, or plastic, displacement, and T=absolute temperature. The *total* displacement $\bar{u}$ is given by

$$\bar{u}=u_p+u \tag{2}$$

and the following quantities are easily defined by simple partial differentiation with respect to the space and time variables x and t:

$$\epsilon=\partial u/\partial x=\text{elastic deformation.} \tag{3a}$$

$$\frac{\partial \epsilon}{\partial t}=\partial^2 u/(\partial x\partial t)$$
$$=\text{rate of change of elastic deformation.} \tag{3b}$$

$$c=\partial^2 u_p/(\partial x\partial t)$$
$$=\text{rate of change of permanent deformation.} \tag{3c}$$

$$d=c+\frac{\partial \epsilon}{\partial t}=\frac{\partial^2}{\partial x\partial t}(u_p+u)=\frac{\partial^2 \bar{u}}{\partial x\partial t}$$
$$=\text{rate of change of total deformation.} \tag{3d}$$

For the sake of mathematical simplicity, the present analysis is carried out for plane, one-dimensional stresses only.

K and M have shown that the rate of permanent deformation c can be written

$$c=\frac{\partial^2 u_p}{\partial x\partial t}=\left[\mu_c+\psi_c\left|\frac{\partial^2 u/(\partial x\partial t)}{\partial u/\partial x}\right|\right]M_E\frac{\partial u}{\partial x}, \tag{4}$$

where μ_c and ψ_c are two material constants that have the dimensions of inverse stress and inverse viscosity, respectively. M_E is an elastic modulus given by $M_E=\lambda_E+2\mu_E$. The quantities λ_E and μ_E are the standard Lamé elastic constants.

EQUATIONS OF SMALL AMPLITUDE NONLINEAR STRESS WAVE PROPAGATION IN SOLIDS

The equations of motion and temperature of K and M may be written,

$$\rho_0\frac{\partial^2 u}{\partial t^2}=(\lambda_E+2\mu_E)\frac{\partial^2 u}{\partial x^2}+(\lambda_v+2\mu_v)\frac{\partial^3 u}{\partial x^2\partial t}-\beta k\frac{\partial T}{\partial x}+f_1, \tag{5a}$$

$$\frac{\partial T}{\partial t}=\kappa\frac{\partial^2 T}{\partial x^2}-\frac{k\beta T_0}{\rho_0 c_\epsilon}\frac{\partial^2 u}{\partial x\partial t}+f_2, \tag{5b}$$

where f_1 and f_2 are given by

$$f_1=(\lambda_v+2\mu_v)\frac{\partial^3 u_p}{\partial x^2\partial t}-\rho_0\frac{\partial^2 u_p}{\partial t^2}, \tag{6a}$$

$$f_2=\frac{\lambda_v+2\mu_v}{\rho_0 c_\epsilon}\left(\frac{\partial^2 \bar{u}}{\partial x\partial t}\right)+\frac{\lambda_E+2\mu_E}{\rho_0 c_\epsilon}\frac{\partial^2 u_p}{\partial x\partial t}\frac{\partial u}{\partial x}, \tag{6b}$$

* Present address: Cuba California Oil Company, Apartado 3295, Havana, Cuba.
[1] S. Treitel, J. Geophys. Research **64**, 661–665 (1959).
[2] L. Knopoff and G. J. F. MacDonald, Revs. Modern Phys. **30**, 1178–1192 (1958).
† Hereinafter referred to as K and M.
[3] F. J. McDonal *et al.*, Geophysics **23**, 421–439 (1958).

and where ρ_0 = density of an unstrained solid element, $\lambda_v + 2\mu_v = M_v$ = viscous modulus, β = coefficient of thermal expansion, k = bulk modulus, T_0 = equilibrium temperature, κ = thermal diffusivity, and c_ϵ = specific heat at constant strain. The functionals f_1 and f_2 are seen to incorporate the entire nonlinearities of the equations of motion and of temperature, respectively. The interested reader is referred to the above reference for a detailed derivation of Eqs. (5a), (5b). Solutions to this system of nonlinear partial differential equations can be found by the method of Kryloff and Bogoliuboff[4], provided that the nonlinearities expressed by f_1 and f_2 are small.

We therefore assume that the permanent, plastic strains are small compared to the elastic strains.

K and M have solved Eq. (5a) in the absence of thermal terms and studied the attenuation characteristics of a stress wave described by such a medium. We shall extend their work here, and proceed to investigate thermal attenuation in nonlinear stress wave propagation.

SOLUTION OF NONLINEAR STRESS WAVE EQUATIONS

The approach we shall employ here is a generalization of the theory of first approximation of Kryloff and Bogoliuboff. Essentially the method assumes that wave amplitude and phase are slowly varying functions of the time t, so that they may be approximated by a constant mean value in some interval $(t, t+\tau)$, where τ = period of oscillation. This assumption can be shown to convert the original nonlinear equation into two subsidiary relations, one in amplitude and one in phase. These, although still nonlinear in the general case, are always integrable in terms of elementary functions.

We assume solutions of the system (5a, b) in the form

$$u = A(t)\sin[\sigma x - \omega t + \varphi(t)] = A(t)\sin\theta_1 \qquad (7a)$$

$$T = B(t)\sin[\sigma x - \omega t + \Omega(t)] = B(t)\sin\theta_2 \qquad (7b)$$

where $\sigma = \nu + j\alpha$ is the complex wave number. The amplitudes A, B and the phase angles φ, Ω are functions of time when f_1 and $f_2 \neq 0$, and constants independent of time otherwise. In the latter event, the expressions (7a, b) reduce to the familiar particular solutions for the *linearized* system (5a, b). This case has been treated by the author.[1]

We now substitute the assumed solutions (7a, b) into the system (5a, b) and follow the method of Kryloff and Bogoliuboff. The resulting amplitude equation is,

$$\dot{A} = -\frac{\cos\theta_1}{\rho_0\omega}\Bigg\{(M_v\omega\sigma^2\cos\theta_1)A - (M_E\sigma^2\sin\theta_1)A + (\rho_0\omega^2\sin\theta_1)A - k\beta\sigma\cos\theta_2\left\{\frac{f_2 - [(k\beta T_0/\rho_0 c_\epsilon)\omega\sigma\sin\theta_1]A}{\kappa\sigma^2\sin\theta_2 - \omega\cos\theta_2}\right\} + f_1\Bigg\} \qquad (8)$$

[4] N. Minorsky, *Introduction to Nonlinear Mechanics* (J. W. Edwards Brothers, Ann Arbor, 1947).

or, in more compact form,

$$\dot{A} = -(\cos\theta_1/\rho_0\omega)F(\theta_1,\theta_2) \qquad (9)$$

where the definition of $F(\theta_1,\theta_2)$ is obvious. The dot represents differentiation with respect to time. The derivation of (8) is outlined in the Appendix.

Now the general theory of Kryloff and Bogoliuboff assumes that the right member of (9) may be expanded in a Fourier series of period 2Π. In particular, the theory of first approximation of Kryloff and Bogoliuboff states that, *to first order*, this right member is given by the first term of such an expansion. This is equivalent to averaging the equation over one period, so that higher order terms of the series vanish identically.

If the right member of (9) is expanded in a double Fourier series in the arguments (θ_1, θ_2), *one obtains to first order*,

$$\dot{A} = -\frac{1}{4\pi^2\rho_0\omega}\int_0^{2\pi}\int_0^{2\pi} F(\theta_1,\theta_2)\cos\theta_1 d\theta_1 d\theta_2. \qquad (10)$$

Integrating over all linear terms of (10), one has

$$\dot{A} = -\Bigg[\frac{M_v\sigma^2}{2\rho_0}A - \frac{k\beta\sigma}{4\pi^2\rho_0\omega} \times \int_0^{2\pi}\int_0^{2\pi}\frac{\cos\theta_2[f_2(\theta_1)\cos\theta_1 d\theta_1]}{\kappa\sigma^2\sin\theta_2 - \omega\cos\theta_2}d\theta_2 + \frac{1}{4\pi^2\rho_0\omega}\int_0^{2\pi}\int_0^{2\pi} f_1(\theta_1)\cos\theta_1 d\theta_1 d\theta_2\Bigg]. \qquad (11)$$

The nonlinear functionals f_1 and f_2 are independent of θ_2 since they do not involve the temperature T explicitly.

In order to evaluate the second term of (11), we combine (3d) with (4) and obtain

$$d = \tilde{u}_{xt} = \mu_c M_E u_x + \psi_c M_E\left|\dot{u}_x/u_x\right| u_x + \dot{u}_x, \qquad (12)$$

where the subscript x stands for differentiation with respect to x. If we substitute (12) into (6b), we derive an expression for f_2 in the form

$$f_2 = \frac{M_v}{\rho_0 c_\epsilon}\Bigg[(\mu_c M_E)^2(u_x)^2 + 2(\mu_c\psi_c M_E^2\left|\frac{\dot{u}_x}{u_x}\right|(u_x)^2 + 2\mu_c M_E u_x\dot{u}_x + 2\psi_c M_E\left|\frac{\dot{u}_x}{u_x}\right|u_x\dot{u}_x + \left(\psi_c M_E\left|\frac{\dot{u}_x}{u_x}\right|u_x\right)^2 + (\dot{u}_x)^2\Bigg] + \frac{M_E}{\rho_0 c_\epsilon}\left|\mu_c M_E(u_x)^2 + M_E\psi_\epsilon\left|\frac{\dot{u}_x}{u_x}\right|(u_x)^2\right|. \qquad (13)$$

The quantities u_x and $\dot{u}_x$ are next calculated by the method of Kryloff and Bogoliuboff and the resulting

expressions substituted into (13). One is then able to evaluate the second integral of (11) in closed form, so that this expression may be written

$$\dot{A}=\left[\frac{M_v\omega^2}{2\rho_0 V_p^2}A+\left\{\frac{2M_v M_E^2 k\beta\psi_c}{3\pi\rho_0^2 c_t}\right\}\times\left\{\frac{\psi_c+\dfrac{2(\psi_c+1/M_v)}{\omega}}{1+(\kappa\omega/V_p^2)^2}\right\}\frac{\omega^3}{V_p^3}A^2+\frac{1}{2\pi\rho_0\omega}\int_0^{2\pi} f_1(\theta_1)\cos\theta_1 d\theta_1\right]. \quad (14)$$

The last term has been integrated over θ_2 directly, since f_1 is independent of θ_2. The wave number σ has been replaced by $\sigma=\omega/V_p$ in (14), where V_p = wave velocity $=[(M_E/\rho_0)]^{\frac{1}{2}}$.

K and M have evaluated the last integral of (14) provided that interaction terms between viscosity and permanent deformation can be neglected. They obtained

$$\frac{1}{2\pi\rho_0\omega}\int_0^{2\pi} f_1(\theta_1)\cos\theta_1 d\theta_1=\left\{\tfrac{2}{3}\mu_c\rho_0 V_p^3+\frac{4}{3\pi}\psi_c V_p^2\rho_0\right\}A. \quad (15)$$

If we furthermore assume that

$$1+\left(\frac{\kappa\omega}{V_p^2}\right)^2\approx 1$$

an approximation that is certainly satisfied for all cases of physical interest,[1] Eq. (14) finally becomes

$$\dot{A}=-\left[\frac{M_v\omega^2}{2M_E}A+\left\{\tfrac{2}{3}\mu_c\rho_0 V_p^2+\frac{4}{3\pi}\psi_c\omega V_p^2\rho_0\right\}A+\left\{\frac{2M_v M_E k\beta\psi_c}{3\pi V_p\rho_0 c_t}\right\}\{\psi_c\omega^3+2(\mu_c+1/M_v)\omega^2\}A^2\right]. \quad (16)$$

This equation is nonlinear in the amplitude A, but its solution can be easily found by separation of variables, and is

$$A(x)=\frac{\alpha_1(A_0/A_0\alpha_2+\alpha_1)e^{-\alpha_1 x}}{1-\alpha_2(A_0/A_0\alpha_2+\alpha_1)e^{-\alpha_1 x}} \quad (17)$$

where A_0 is the wave amplitude at $x=0$, and α_1 and α_2 are given by

$$\alpha_1=\tfrac{2}{3}\mu_c\rho_0 V_p+\frac{4}{3\pi}\psi_c V_p\rho_0\omega+\frac{1}{2}\frac{M_v}{M_E}\omega^2 \quad (18a)$$

$$\alpha_2=\frac{2M_v k\beta\psi_c}{3\pi c_t}\{2(\mu_c+1/M_v)\omega^2+\psi_c\omega^3\}. \quad (18b)$$

An involved calculation similar to the one that has been presented shows that, to first order, the amplitude phase angle φ is constant and independent of x and t. Substitution of (17) into (7a) yields the solution for the displacement u in the form,

$$u=\left[\frac{\alpha_1(A_0/A_0\alpha_2+\alpha_1)e^{-\alpha_1 x}}{1-\alpha_2(A_0/A_0\alpha_2+\alpha_1)e^{-\alpha_1 x}}\right]\sin(\sigma x-\omega t+\varphi_0), \quad (19)$$

where φ_0 = constant. The expressions α_1 and α_2 define two separate distance attenuation coefficients. The coefficient α_1 is a function of three terms, proportional respectively to the zeroth, first, and second powers of the circular frequency ω. The zeroth and quadratic factors in ω correspond to the linear terms in the equation of motion (5a) and represent damping in the classical Maxwell and Kelvin-Voigt (viscoelastic) solids, respectively. The factor linear in ω is a direct consequence of the nonlinear stress-strain relationship (4).

The second attenuation coefficient α_2 contains terms proportional to the second and third powers of ω. The first of these is again related to the linear terms of (5a, b) while the second is attributable to the nonlinear portion of the stress-strain equation (5b), expressed by the functional f_2. Again, we find that this nonlinearity introduces terms in the attenuation coefficient that are a function of odd powers of ω. It is evident that the coefficient α_2 introduces additional attenuation arising from the inclusion of thermal damping in our analysis. When $\alpha_2=0$, (19) reduces to

$$u=A_0 e^{-\alpha_1 x}\sin(\sigma x-\omega t+\varphi_0), \quad (20)$$

which is identical to the result of K and M, whose work did not take thermal terms or their interaction effects into account.

It is naturally desirable to gain an idea of the magnitudes of the various parameters that determine the values of α_1 and α_2. Empirical observations are very scarce, particularly for silicates. K and M give the following estimates for rock:

$$\begin{aligned}&\mu_E=3\times10^{11}\text{ dynes/cm}^2,\\&\mu_v=10\text{ dyne sec/cm}^2,\\&\mu_c=10^{-22}\text{ cm}^2/\text{dyne sec},\\&\psi_c=10^{-14}\text{ cm}^2/\text{dyne}.\end{aligned} \quad (21)$$

They calculated that for the frequency range

$$\frac{\pi}{2}\frac{\mu_c}{\psi_c}\ll\omega\ll\frac{8}{3\pi}\psi_c\frac{M_E^2}{M_v} \quad (22)$$

the attenuation coefficient α_1 is essentially a linear function of ω. Assuming that $\lambda_E\approx\mu_E$ and $\lambda_v\approx\mu_v$, substitution of the numerical values for the various parameters into (22) yields

$$10^{-8}\ll\omega\ll10^{9}\text{ rad/sec}.$$

This is the frequency range inside which α_1 varies linearly with ω for rock.

The second attenuation coefficient α_2 is given by (18b). If we take $k=10^{11}$ dynes/cm^2, $c_\epsilon=10^7$ ergs/gram, $\beta=10^{-5}$/°C, and the values (21), one has

$$\alpha_2 \approx 10^{-13}\{\omega^2+10^{-15}\omega^3\}. \tag{23}$$

For these values of the various material constants it is obvious that α_2 will be very small. One may then neglect thermal damping with slight error and use (20) rather than (17) to describe the propagating wave in space and time. However, it must be emphasized that the magnitudes of μ_e and ψ_e are not well known. In particular, the value of μ_e for rock is based on a single calculation of Haskell.[5] If more refined experimental work does show an amplitude decay mechanism faster than is reconcilable with (20) the more exact form (17) should be useful. We notice that if $\psi_e=0$, $\alpha_2=0$. This means that thermal damping is negligible in the Maxwell solid, as has been pointed out by K and M without proof.

CONCLUSIONS

It has been shown that a nonlinear stress wave is subject to mechanical as well as thermal losses as it propagates through any real solid. Preliminary calculations suggest that the latter effect is small, but the question of its importance must remain open until the values of μ_e and ψ_e become better known.

ACKNOWLEDGMENTS

The writer wishes to thank Gordon J. F. MacDonald for continued assistance given in connection with this work, which forms part of the author's doctoral dissertation submitted to the Department of Geology and Geophysics of the Massachusetts Institute of Technology.

APPENDIX

We wish to derive Eq. (8) of the text. Our point of departure is the system (5a, b). In order to forestall a mathematical difficulty which will become evident later, we differentiate both members of (5b) with respect to time. The system to be solved is then

$$\rho_0\frac{\partial^2 u}{\partial t^2}=(\lambda_E+2\mu_E)\frac{\partial^2 u}{\partial x^2}+(\lambda_v+2\mu_v)\frac{\partial^3 u}{\partial x^2\partial t}-\beta k\frac{\partial T}{\partial x}+f_1 \tag{Ia}$$

$$\frac{\partial^2 T}{\partial t^2}=\kappa\frac{\partial^3 T}{\partial x^2\partial t}-\frac{k\beta T_0}{\rho_0 c_\epsilon}\frac{\partial^3 u}{\partial x\partial t^2}+\frac{\partial f_2}{\partial t}. \tag{Ib}$$

[5] N. A. Haskell, Physics **6**, 265–269 (1935).

We assume solutions of this system in the form

$$u=A(t)\sin[\sigma x-\omega t+\varphi(t)]=A(t)\sin\theta_1, \tag{IIa}$$

$$T=B(t)\sin[\sigma x-\omega t+\Omega(t)]=B(t)\sin\theta_1. \tag{IIb}$$

If $f_1=f_2=0$, (Ia, b) would be linear, and solutions (IIa, b) can be found by standard methods. In this case, both the amplitudes A, B and the phase angles φ and Ω are constants independent of time. We now assume that solutions of type (IIa, b) can be found such that (IIa, b) be satisfied when f_1 and $f_2\neq 0$, where the amplitudes A, B and phase angles φ and Ω are explicit functions of time. If expressions for these quantities can be found, their substitution into (IIa, b) yields the desired complete solution. Differentiating (IIa, b) with respect to time, one has

$$\dot{u}=-\omega A\cos\theta_1+\dot{A}\sin\theta_1+A\dot{\varphi}\cos\theta_1 \tag{IIIa}$$

$$\dot{T}=-\omega B\cos\theta_2+\dot{B}\sin\theta_2+B\Omega_t\cos\theta_2 \tag{IIIb}$$

where the dot denotes differentiation with respect to time. In the linear case, where A, B, φ, and Ω are constant, these relations would yield

$$\dot{u}=-\omega A\cos\theta_1, \tag{IVa}$$

$$\dot{T}=-\omega B\cos\theta_2. \tag{IVb}$$

So that (IIa, b) reduce to (IVa, b) in the linear case, we accordingly must require that

$$\dot{A}\sin\theta_1+A\dot{\varphi}\cos\theta_1=0, \tag{Va}$$

$$\dot{B}\sin\theta_2+B\Omega_t\cos\theta_2=0. \tag{Vb}$$

Furthermore, remembering that A, B, φ, and Ω are not explicit functions of x, one calculates from (IIa, b)

$$T_x=B\sigma\cos\theta_2 \tag{VIa}$$

$$T_{xx}=-B\sigma^2\sin\theta_2 \tag{VIb}$$

$$u_x=A\sigma\cos\theta_1 \tag{VIIa}$$

$$u_{xx}=-A\sigma^2\sin\theta_1 \tag{VIIb}$$

and from (IVa, b):

$$\ddot{u}=-\omega^2 A\sin\theta_1-\omega\dot{A}\cos\theta_1+\omega\dot{\varphi}A\sin\theta_1 \tag{VIIIa}$$

$$\ddot{T}=-\omega^2 B\sin\theta_2-\omega\dot{B}\cos\theta_2+\omega\Omega_t B\sin\theta_2 \tag{VIIIb}$$

$$\ddot{u}_x=-\omega^2\sigma A\cos\theta_1+\omega\dot{A}\sigma\sin\theta_1+\omega\dot{\varphi}A\sigma\cos\theta_1. \tag{VIIIc}$$

From (IVb) one has,

$$\dot{T}_x=\omega\sigma B\sin\theta_2 \tag{IXa}$$

$$\dot{T}_{xx}=\omega\sigma^2 B\cos\theta_2 \tag{IXb}$$

and from (IVa),

$$\dot{u}_x=\omega\sigma A\sin\theta_1, \tag{Xa}$$

$$\dot{u}_{xx}=\omega\sigma^2 A\cos\theta_1. \tag{Xb}$$

If relations (IVa, b) and (VI)–(X) be substituted into

the system (Ia, b), one has

$$(\rho_0\omega\cos\theta_1)\dot{A}+(\rho_0\omega A\sin\theta_1)\dot{\varphi}$$
$$=M_E A\sigma^2\sin\theta_1+M_v\omega\sigma^2 A\cos\theta_1$$
$$-\tilde{M}_T B\sigma\cos\theta_2+\rho_0\omega^2 A\sin\theta_1+f_1 \quad \text{(XIa)}$$

$$-(\omega\cos\theta_2)\dot{B}+(\omega\sin\theta_2)\Omega_t+(M_T\omega\sigma\sin\theta_1)\dot{A}$$
$$+(M_T\omega A\sigma\cos\theta_1)\dot{\varphi}=\kappa\omega\sigma^2 B\cos\theta_2+\dot{f}_2 \quad \text{(XIb)}$$

where

$$M_E=\lambda_E+2\mu_E,\quad M_T=\frac{k\beta T_0}{\rho_0 c_\epsilon},$$
$$M_v=\lambda_v+2\mu_v,\quad \tilde{M}_T=k\beta. \quad \text{(XII)}$$

Relations (XIa, b) in conjunction with (Va, b) yield four linear algebraic equations in the unknowns $\dot{A}$, $\dot{B}$, $\dot{\varphi}$, and Ω_t. These may be solved for $\dot{A}$ and $\dot{B}$:

$$\dot{A}=-\frac{\cos\theta_1}{\rho_0\omega}[(M_v\omega\sigma^2\cos\theta_1)A-(M_E\sigma^2\sin\theta_1)A$$
$$+(\rho_0\omega^2\sin\theta_1)A-(\tilde{M}_T\sigma\cos\theta_2)B+f_1], \quad \text{(XIIIa)}$$

$$\dot{B}=-\frac{\cos\theta_2}{\omega}[(\kappa\omega\sigma^2\cos\theta_2)B+\dot{f}_2]. \quad \text{(XIIIb)}$$

Consider now the generalized heat flow equation (5b). Substituting from relations (IV) to (X) into this expression, and solving for $B(t)$, one has

$$B(t)=\frac{f_2-(M_T\omega\sigma\sin\theta_1)A}{\kappa\sigma^2\sin\theta_2-\omega\cos\theta_2}. \quad \text{(XIV)}$$

This formula may be substituted into (XIIIa) to yield

$$\dot{A}=-\frac{\cos\theta_1}{\rho_0\omega}\Bigg[(M_v\omega\sigma^2\cos\theta_1)A-(M_E\sigma^2\sin\theta_1)A$$
$$+(\rho_0\omega^2\sin\theta_1)A$$
$$-\tilde{M}_T\sigma\cos\theta_2\left\{\frac{f_2-(M_T\omega\sigma\sin\theta_1)A}{\kappa\sigma^2\sin\theta_2-\omega\cos\theta_2}\right\}+f_1\Bigg]. \quad \text{(XV)}$$

Expression (XV) is Eq. (8) of the text. We have thus been able to express the rate of change of the wave amplitude, $\dot{A}(t)$, as a function of the circular frequency ω, wave number σ, and the appropriate moduli of the medium. It is now evident why it was necessary to differentiate (5) with respect to time in order to solve the resulting system (Ia, b) for u and T. This step enables us to use (5b) as a separate relation with which to express $\dot{A}$ in (XIIIa) as a function of A and the appropriate constants alone.

Operating Characteristics of a Molecular-Beam Maser*†

H. G. VENKATES‡ AND M. W. P. STRANDBERG
Department of Physics and Research Laboratory of Electronics, Massachusetts Institute of Technology, Cambridge, Massachusetts
(Received April 27, 1959)

General expressions for the emitted power and the frequency pulling in an ammonia maser have been deduced. The operating characteristics of the maser have been deduced by introducing a mean-square time of flight of molecules in the cavity.

I. INTRODUCTION

WE are concerned here with a two-level maser[1,2] in which a molecular beam of ammonia, effusing from narrow channels, passes through an inhomogeneous electric field. We shall assume that the field possesses a cylindrical symmetry about the z axis with its gradient in the radial direction. The two levels in question are those that give rise to the 3-3 inversion line of ammonia. When it emerges from the field (focuser) the beam is state-selected; the molecules transmitted by the focuser are mostly in the inversion state of higher energy. The state-selected beam then enters a tuned microwave cavity in which it emits power by decay into the inversion state of lower energy.

K. Shimoda[3] makes a realistic approach to the theory of the two-level maser by taking into consideration the Maxwell law for the distribution of velocities in the beam. His method consists essentially of treating the focuser as serving a twofold purpose: (a) ideal state selection, and (b) velocity selection of the active molecules by restricting the range of the radial and the axial components of the velocity. This range is determined by the maximum value of the electrostatic field of the focuser, and the dimensions of the focuser and of the cavity. The theory has the merit of simplicity in so far as it avoids the detailed computation of molecular trajectories, and considers only the approximate limiting trajectories of the molecules in the focuser and cavity in order to get reasonably correct relationships among the parameters. In this connection, two classes of molecules are considered—those which pass freely through the cavity, and those which collide with its walls and are reflected away. In order to deal with large power output from the beam, Shimoda has indicated an approximation procedure in which he introduces a certain average velocity of molecules computed from their density in the cavity.

It is shown in the present paper that a closer approximation to the correct theory requires the introduction of a mean-square time of flight in the cavity computed from the flux of molecules in the cavity rather than from the density.

II. GENERAL EXPRESSIONS FOR EMITTED POWER AND FREQUENCY PULLING

An outline of the theory is indicated in Appendix I. We have the following limits for the velocity components for molecules passing freely through the cavity:

$$\begin{aligned} &v_r=0 \text{ to } v_c \\ &v_z=(L/R)v_r \text{ to } (l/2R)v_r; \end{aligned} \tag{1}$$

for molecules colliding with the walls of the cavity

$$\begin{aligned} &v_r=0 \text{ to } v_c \\ &v_z=0 \text{ to } (L/R)v_r. \end{aligned} \tag{2}$$

The approximate limiting trajectories are shown in Figs. 1 and 2.

In expressions (1) and (2) L is the length of the cavity; l, the length of the focuser; R, the cross-section radius of the cavity and the focuser; v_c, the critical velocity in the radial direction determined from the condition $W_c=\frac{1}{2}mv_c^2$, where W_c is the Stark energy corresponding to the maximum value of the field which occurs at the surface of the focuser. With these limits the emitted power is given by

$$P_B=G^2(N\hbar\omega_1)\frac{4\alpha}{\sqrt{\pi}}\frac{AR^2}{L^2}\frac{1}{\Delta^2}\left[\int_{x=0}^{a}\int_{y=y}^{b}\sin^2\left(\frac{\Delta L}{2\alpha}\frac{1}{x}\right)\times\exp(-x^2)xydxdy+\int_{x=0}^{a}\int_{y=0}^{y}\sin^2\left(\frac{\Delta L}{2\alpha}\frac{1}{y}\right)\times\exp(-x^2)xydxdy\right], \tag{3}$$

where N is the density of molecules in the beam in the higher-energy inversion state; α is the most probable velocity in the beam source; $G=(E\bar{\mu}/\hbar)$, with E the rf field amplitude in the cavity, and $\bar{\mu}$ the electric dipole moment of the molecule; A is the cross-section area of the cavity; ω_0 is the resonant frequency of the molecule;

* This work was supported in part by the U. S. Army (Signal Corps), the U. S. Air Force (Office of Scientific Research, Air Research and Development Command), and the U. S. Navy (Office of Naval Research): and in part by the Ministry of Education, Government of India, and the Indian Institute of Technology, Kharagpur, India.

† This paper is based on a thesis submitted to the Department of Physics, Massachusetts Institute of Technology in partial fulfillment of the requirements for the degree of Doctor of Science, August, 1958.

‡ Present address: Department of Physics, Indian Institute of Technology, Kharagpur, India.

[1] Gordon, Zeiger, and Townes, Phys. Rev. **99**, 1264 (1955).
[2] Shimoda, Wang, and Townes, Phys. Rev. **102**, 1308 (1956).
[3] K. Shimoda, J. Phys. Soc. Japan **12**, 1006 (1957).

FIG. 1. Focuser.

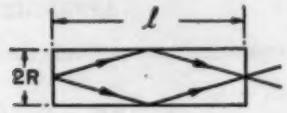

FIG. 2. Cavity.

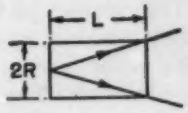

ω_1 is the oscillation frequency; and $\Delta=(\delta^2+G^2)^{\frac{1}{2}}$, with $\delta=\omega_1-\omega_0$.

The variables and limits are defined by

$$x=\frac{v_z}{\alpha};\quad y=\frac{L}{R}\frac{v_r}{\alpha}$$

$$a=\frac{L}{R}\frac{v_c}{\alpha};\quad b=\frac{1}{2}\frac{l}{R}\frac{v_c}{\alpha}$$

and for the frequency pulling we have

$$\frac{\omega_1-\omega_c}{\omega_c}=-8\sqrt{\pi}N\frac{\mu^2\delta}{\hbar\Delta^2}\frac{R^2}{L^2}\times\left\{\int_{y=0}^{a}\int_{x=y}^{b}\left[1-\frac{\sin(\Delta L/\alpha x)}{\Delta L/\alpha x}\right]\times\exp(-x^2)y\,dy\,dx+\int_{y=0}^{a}\int_{x=0}^{y}\left(1-\frac{\sin(\Delta L/\alpha y)}{\Delta L/\alpha y}\right)\times\exp(-x^2)x\,dx\,dy\right\}. \quad (4)$$

III. APPROXIMATION METHODS

The integrals in (3) and (4) are hard to evaluate. Hence it is desirable to consider limiting cases and approximation procedures. If, now, we restrict ourselves to small signals when $\Delta L/\alpha x$ and $\Delta L/\alpha y$ are to be considered small, we obtain for the frequency pulling

$$\frac{\omega_1-\omega_0}{\omega_0}=\frac{\omega_c-\omega_1}{\omega_c}\frac{3}{\langle\tau_0^2\rangle/\langle\tau\rangle}\frac{2Q}{\omega_0}. \quad (5)$$

We also get Shimoda's expression for the emitted power at the resonant frequency:

$$P_B=(G^2/4)(N'\hbar\omega_1)\langle\tau^2\rangle. \quad (6)$$

The quantities $\langle\tau_0\rangle$ and $\langle\tau^2\rangle$ that have the dimension of (time)^2, and $\langle\tau\rangle$ that has the dimension of time, have been defined and evaluated in Appendix II. The flux of molecules and the density of molecules in the cavity are given by

$$N'=\frac{4N\alpha}{\sqrt{\pi}}A\frac{R^2}{L^2}\left[\int_{y=0}^{a}\int_{x=y}^{b}\exp(-x^2)y\,x\,dx\,dy+\int_{y=0}^{a}\int_{x=y}^{b}\exp(-x^2)y\,x\,dx\,dy\right] \quad (7a)$$

and

$$n=\frac{4N}{\sqrt{\pi}}\frac{R^2}{L^2}\left[\int_{y=0}^{a}\int_{x=y}^{b}y\exp(-x^2)dx\,dy+\int_{y=0}^{a}\int_{x=0}^{y}\frac{x^2}{y}\exp(-x^2)dx\,dy\right]. \quad (7b)$$

The evaluation of the integrals involved in the mean times leads to the following expression for P_B in the small-signal case:

$$P_B=\frac{1}{2}G^2\frac{1}{\sqrt{\pi}\alpha^3}(N\hbar\omega_1)AL^2\left(1+\log\frac{l}{2L}\right)v_c^2. \quad (8)$$

In order to put the theory in reasonably explicit form for large signals, we proceed along Shimoda's lines, and consider, first, the case of a beam of uniform velocity v_0 traversing the cavity parallel to its axis. The power emitted is given by

$$P_B=\frac{G^2}{4}(N'\hbar\omega_1)\frac{4}{\Delta^2}\sin^2\left(\frac{\Delta\tau_0}{2}\right), \quad (9)$$

where $\tau_0=(L/v_0)$.

For small signals this formula approximates to

$$P_B=(G^2/4)(N'\hbar\omega_1)\tau_0^2. \quad (10)$$

Upon comparing (10) and (6) we obtain the correspondence

$$\tau_0\rightarrow\langle\tau^2\rangle^{\frac{1}{2}}. \quad (11)$$

In generalizing the theory to large signals in the case involving velocity distribution we can make use of this correspondence. The final result is

$$P_B=\frac{G^2}{4}(N'\hbar\omega_1)\frac{4}{\Delta^2}\sin^2(\tfrac{1}{2}\Delta\langle\tau^2\rangle^{\frac{1}{2}}). \quad (12)$$

This formula replaces, for practical purposes, the complicated general formula (3). Setting $\theta=\frac{1}{2}\Delta\langle\tau^2\rangle^{\frac{1}{2}}$, we obtain

$$\frac{N'}{N_0'}=\frac{\theta^2}{\sin^2\theta} \quad (13)$$

and

$$\frac{v_c}{v_{c0}}=\frac{\theta}{\sin\theta}. \quad (14)$$

In (14) v_{c0} is determined by the potentials on the focuser rods that are required to start the oscillation, and v_c is determined by the higher potentials applied to the rods. The saturation condition, $\theta=\pi$, as given by

(13) and (14) enables plotting of the field amplitude in the cavity agsainst applied potential on which v_e depends. N_0' is the flux corresponding to the minimum oscillation condition. The saturation energy density is given by

$$W_{sat}^{(\theta)}=\frac{\pi^2}{4}\frac{\hbar^2}{\bar{\mu}^2}\frac{l^2}{L}\frac{1}{1+\log(l/2L)}v_e^2. \tag{15}$$

The oscillation condition is given by

$$\frac{1}{Q}\leqslant\frac{4\sqrt{\pi}}{\hbar}\frac{N\langle\mu^2\rangle}{\alpha^3}v_e^3L\left(1+\log\frac{l}{2L}\right)\frac{\sin^2\theta}{\theta^2}. \tag{16}$$

A similar set of formulas has been given by Shimoda[2] with $\beta=\frac{1}{2}\Delta\langle\tau\rangle$ replacing θ in (13) and (14). Thus

$$\frac{N'}{N_0'}=\frac{\beta^2}{\sin^2\beta} \tag{17}$$

and

$$\frac{v_e}{v_{e0}}=\frac{\beta}{\sin\beta}. \tag{18}$$

The saturation energy stored in the cavity is, then,

$$W_{sat}^{(\beta)}=\frac{\pi^2}{32}\frac{\hbar^2}{\bar{\mu}^2}L\left(1+\frac{l}{2L}\right)v_e^2. \tag{19}$$

It may be noted that Shimoda's formulas will follow if we assume the approximate relationship

$$N'=n\Delta L\frac{\langle\tau\rangle}{\langle\tau^2\rangle} \tag{20}$$

between the flux and the density that have been expressed by (7a) and (7b), and then make τ_0 correspond to $\langle\tau\rangle$ by comparing the two formulas for the emitted power, both of which involve the density, one relating to a beam with a velocity distribution, and the other to a beam with uniform velocity.

The two sets of formulas (13), (14), (15) and (17), (18), (19) are different as long as the correspondences $\tau_0\rightarrow\langle\tau\rangle$ and $\tau_0\rightarrow\langle\tau^2\rangle^{\frac{1}{2}}$ are not identical. For a typical case of $l=2L$, $\langle\tau^2\rangle^{\frac{1}{2}}$ is nearly three times as great as $\langle\tau\rangle$. A difference arises, therefore, between the two sets of formulas in regard to the determination of the field amplitude as a function of applied potential, and of the saturation characteristics. In fact, for the typical case we have

$$W_{sat}^{(\theta)}=16W_{sat}^{(\beta)}.$$

Since the density is not so accurately determinable, we may bypass the approximate relationship (20), and hence the density from (7b). We thereby obtain the more accurate relationships (13), (14), and (15) and a closer approximation to the order of magnitude of the output power and saturation characteristics.

APPENDIX I

The emitted power and the frequency pulling are given by

$$P_B=4\pi\omega_1Wx''$$

$$\frac{\omega_1-\omega_c}{\omega_c}=-2\pi x'$$

where ω_c is the resonant frequency of the cavity, W is the energy stored in the cavity, and x' and x'' are the real and imaginary parts of the susceptibility defined by

$$\frac{\int P\dagger\cdot E_a\dagger^*dv}{\int E\dagger\cdot E\dagger^*dv}=x'+jx''.$$

The polarization is given by

$$P=P\dagger e^{j\omega t}+P\dagger^*e^{-j\omega t}=\int p\delta n,$$

where δn is given by Maxwell's law of velocity distribution,

$$\delta n=\frac{AN}{\alpha^3\sqrt{\pi}}\exp(-v^2/\alpha^2)v_r dv_r dv_z,$$

and p is given by

$$p=\int\mu\psi\psi^*dv.$$

The wave functions are those given by Shimoda, Wang, and Townes.[2] The real and imaginary parts of the susceptibility are, then,

$$x'=\frac{4N}{\sqrt{\pi}}\frac{\bar{\mu}^2\delta}{\hbar\Delta^2}\frac{R^2}{L^2}\left\{\int_{y=0}^{a}\int_{x=y}^{b}\left[1-\frac{\sin(\Delta L/\alpha x)}{\Delta L/\alpha x}\right]\times\exp(-x^2)ydydx+\left\{\int_{y=0}^{a}\int_{x=0}^{b}\left[1-\frac{\sin(\Delta L/\alpha y)}{\Delta L/\alpha y}\right]\exp(-x^2)xdxdy\right\}\right.$$

and

$$x''=\frac{2}{L}\frac{4N}{\sqrt{\pi}}\frac{\bar{\mu}^2\alpha}{\hbar\Delta^2}\frac{R^2}{L^2}\left\{\int_{y=0}^{a}\int_{x=y}^{b}\sin^2[(\Delta L/2\alpha)(1/x)]\times\exp(-x^2)xydxdy+\int_{y=0}^{a}\int_{x=0}^{b}\sin^2[(\Delta L/2\alpha)(1/y)]\exp(-x^2)xydxdy\right\}.$$

APPENDIX II

The mean times introduced in the main discussion are defined by

$$\langle\tau^2\rangle=\frac{L^2}{\alpha^2}\frac{\int_{y=0}^{a}\int_{x=y}^{b}\frac{y}{x}\exp(-x^2)dxdy+\int_{=0}^{a}\int_{z=0}^{y}\frac{x}{y}\exp(-x^2)dxdy}{\int_{y=0}^{a}\int_{x=y}^{b}xy\exp(-x^2)dxdy+\int_{y=0}^{a}\int_{x=y}^{y}xy\exp(-x^2)dxdy},$$

$$\langle\tau\rangle=\frac{L}{\alpha}\frac{\int_{y=0}^{a}\int_{x=y}^{b}\frac{y}{x}\exp(-x^2)dxdy+\int_{y=0}^{a}\int_{x=y}^{b}\frac{x}{y}\exp(-x^2)dxdy}{\int_{y=0}^{a}\int_{x=y}^{b}y\exp(-x^2)dxdy+\int_{y=0}^{a}\int_{z=0}^{y}\frac{x^2}{y}\exp(-x^2)dxdy},$$

$$\langle\tau_0\rangle=\frac{4}{\alpha\sqrt{\pi}}\frac{R^2}{L}\left[\int_{y=0}^{a}\int_{x=y}^{b}\frac{y}{x}\exp(-x^2)dxdy+\int_{y=0}^{a}\int_{z=0}^{y}\frac{x}{y}\exp(-x^2)dxdy\right]$$

Explicit expressions for these quantities are

$$\langle\tau^2\rangle=2\left(\frac{L}{l}\right)^2\left(1+\log\frac{l}{2L}\right)\left(\frac{R}{v_c}\right)^2,$$

$$\langle\tau\rangle=4\left(\frac{R}{v_c}\right)\frac{1}{1+(l/2L)},$$

and

$$\langle\tau_0\rangle=\frac{2}{\alpha^3\sqrt{\pi}}Lv_c^2\left(1+\log\frac{l}{2L}\right).$$

In all of this the approximation is made that $a\ll1$ and $b\ll1$.

JOURNAL OF APPLIED PHYSICS VOLUME 31, NUMBER 2 FEBRUARY, 1960

Ion Energies in a Cold Cathode Discharge in a Magnetic Field

JOHN BACKUS AND NORMAN E. HUSTON*
Physics Department, University of Southern California, Los Angeles, California
(Received February 2, 1959)

A cold cathode discharge in a strong magnetic field was studied by means of a pulsing technique. The discharge was run at pressures of a few microns with magnetic fields of 2400 gauss and currents of the order of half an ampere. By means of a multivibrator and amplifier the discharge was pulsed off for 300 μsec at 1000 μsec intervals. During the off period the current flow to the cathodes was observed. Analysis of the current flow shows an approximately Maxwellian distribution of velocities at the cathodes with a temperature of about 0.5 ev. This gives an ion density in the discharge of approximately 20%.

INTRODUCTION

THE investigations to be described below were undertaken to obtain information about the PIG (Philips Ionization Gauge) or Penning type cold cathode discharge in a magnetic field.[1] This type of discharge has frequently been utilized, especially as an ion source, and hence has been studied to quite an extent in its more practical aspects.[2–5] Its instability when subjected to probe measurements and the fact that stable operation requires random fluctuating electric fields in the plasma have made fundamental investigations both difficult and questionable.[6]

DISCHARGE UNIT

The discharge geometry used is shown in Fig. 1, the discharge taking place between the two cathodes K

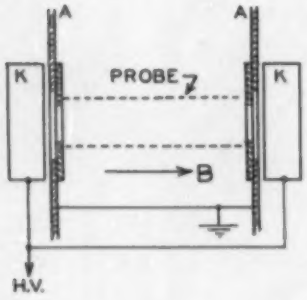

FIG. 1. Discharge geometry.

along the magnetic field B and defined laterally by the holes in the anodes A. The cathodes were ½ in. thick copper blocks provided with an internal network of cooling channels and milled out to take ⅛×1 in. replaceable copper disk inserts which served as the cathode surfaces proper. The anodes were made of 1/16 in. copper sheet bolted to main structure support bars. The discharge defining apertures consisted of ½ in. diam holes drilled in small copper plates which were bolted over 1 in. diam holes in the two anodes. The assembly was mounted on a one-inch Bakelite plate which was bolted to one side of a vacuum chamber mounted between the poles of a magnet so that the discharge could be run in magnetic fields up to strengths of 3500 gauss.

PULSER

The discharge was operated with the anodes grounded and the cathodes at high negative voltage. A positive voltage pulse of the proper magnitude applied to the cathodes served to shut off the discharge. The discharge

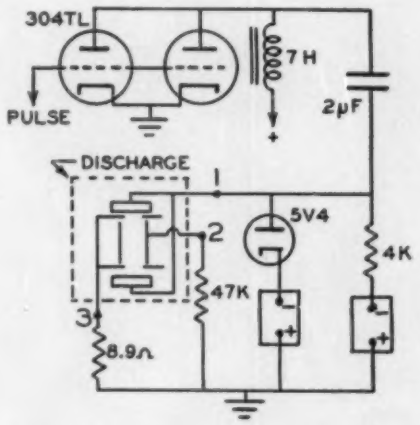

FIG. 2. Power amplifier and discharge circuit.

was operated with a 4000 ohm bank of resistors in series with the cathode as a ballast. This served as a load across which to apply the positive pulse. The pulser consisted of a multivibrator followed by a stage of voltage amplification and an output stage of power amplification. Figure 2 shows the power amplifier stage and the schematic of the discharge circuit. The output pulse of the voltage amplifier drove the grids of the power amplifier stage below cutoff for 300 μsec once every 1000 μsec. The power amplifier consisted of two 304TL triodes connected in parallel, with a 7 henry choke as the plate load.

The output of the power amplifier was capacitively

* Now at Atomics International, Canoga Park, California.
[1] F. M. Penning, Physica **4**, 71 (1937).
[2] F. M. Penning and J. H. A. Moubis, Physica **4**, 1190 (1937).
[3] P. Lorrain, Can. J. Research A. **25**, 338 (1947).
[4] R. Keller, Helv. Phys. Acta **21**, 170 (1948).
[5] R. Keller, Helv. Phys. Acta **22**, 78 (1949).
[6] J. Backus, in *Gaseous Electrical Discharges in Magnetic Fields*, edited by A. Guthrie and R. K. Wakerling (McGraw-Hill Book Company, Inc., New York, 1949), Chap. II, p. 347.

coupled to the discharge cathodes. By varying the amount of current through the plate inductance, the voltage pulse at the cathodes of the discharge could be controlled. The plate line of the power amplifier was essentially a constant current source, this current flow ing to ground through the 304TL tubes when they were conducting. When these were shut off by the 300 μsec negative pulse on their grids, the current was then shunted through the ballast resistors in the cathode line of the discharge and thus supplied a voltage pulse to the cathodes to shut off the discharge.

As will be discussed below, the mode of plasma decay was quite sensitive to the potential assumed by the cathode during the pulse (cathode pulse voltage). The voltage across the discharge in operation has random fluctuations of the order of a few percent.[6] Since the voltage pulse from the power amplifier is constant, the variation in discharge voltage results in a variation of the cathode pulse voltage from pulse to pulse. To remove this variation a clamper diode was connected as shown in Fig. 2, with the diode plate connected to the

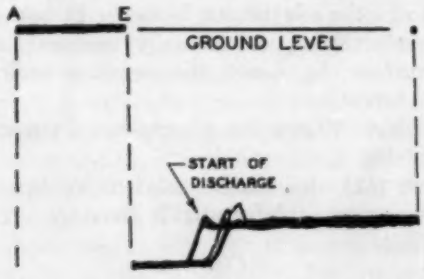

FIG. 3. Oscillogram of cathode voltage pulse. *A* denotes start of pulse, *E* end of pulse 300 μsec later. Vertical scale arbitrary.

discharge cathode and the clamper cathode biased to an adjustable negative potential. The discharge cathode could thus be driven to a predetermined value near ground regardless of the fluctuation in operating value. Because of the current decay in the inductance-ballast resistor circuit, the cathode pulse voltage is not constant but becomes more negative by a few volts during the pulse.

OPERATION OF DISCHARGE AND PULSER

The discharge studied consists of a plasma extending between the cathodes and defined by the apertures in the anodes because of the magnetic field. Electrons are liberated at the cathodes by various emission mechanisms; the current to the anodes is predominantly electronic, while that to the cathodes is predominantly ionic.[6]

A cylindrical probe was positioned coaxially around the discharge to monitor the voltage pulse of the plasma when the discharge was cut off. The probe was grounded through a 47 000 ohm resistor so that it was essentially floating at the plasma potential. The radius of the probe was $\frac{1}{8}$ in. larger than the radius of the

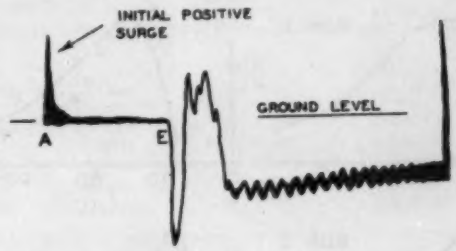

FIG. 4. Oscillogram of probe voltage pulse. *A* denotes start of pulse, *E* end of pulse 300 μsec later. Vertical scale arbitrary.

discharge plasma cross section, and resulted in no difference in the characteristic of the discharge current-voltage curve.

With the discharge on and the pulser operating, the wave forms of the cathode voltage, probe voltage, and anode current were observed on a Dumont 248A oscilloscope. Typical traces are shown in Figs. 3, 4, and 5; they were taken using a driven sweep triggered by a synchronizing pulse obtained from a pickup "antenna" placed near the cathode line of the discharge.

Figure 3 shows the voltage pulse on the discharge cathodes as taken from a voltage divider connected to point 1 of Fig. 2. The trace length is 1000 μsec and includes several pulses. The "discharge on" part of the trace is distinguished as the fluctuating portion near the end. It is of interest to notice the variation in the delay from the instant that full voltage was reapplied until the discharge reached steady operating conditions. This delay frequently extended into the next pulse period.

The plasma voltage pulse on a 1000 μsec trace taken at the cylindrical probe (point 2 of Fig. 2) is shown in Fig. 4. An initial positive surge of the plasma is quite evident. The discharge voltage was pulsed off at point *A*, and pulsed on again at *E*.

The plasma current decay pulse was taken from a small resistance (8.9 ohms) between the anodes and ground (at point 3 of Fig. 2). A typical trace covering a number of pulses is shown in Fig. 5. The pulse has been extended by the dashed line to show the behavior

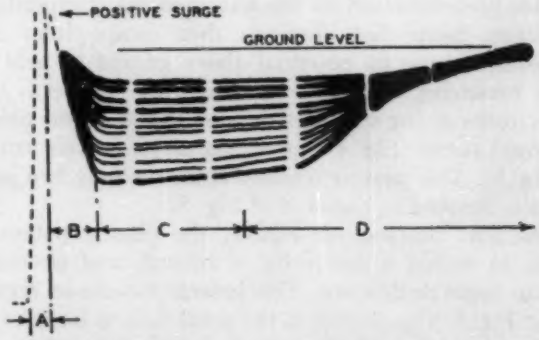

FIG. 5. Oscillogram of anode current decay pulses. Markers are at 10 μsec intervals. Vertical scale proportional to current through anode resistance to ground.

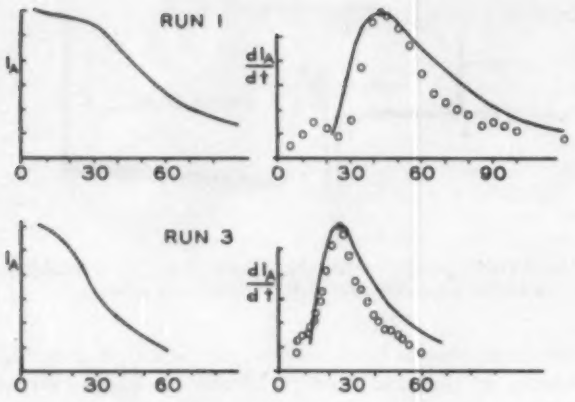

FIG. 6. Decay curves and slopes of ion current to cathodes during pulse. Curves on the left are anode current decay curves taken from oscillograms of Fig. 5. Circles on the right are measured slopes of these decay curves; curves on the right are calculated from an assumed Maxwellian distribution. Vertical scales are arbitrary; horizontal scale are in μsec.

at the start of the pulse. This portion is clearly shown on sweeps covering a number of pulses, but an expanded trace is used here to show the details of the plasma decay. The marker interval is 10 μsec.

The above wave forms were photographed with the discharge running in argon at a pressure of 3×10^{-3} mm Hg in a magnetic field of 2400 gauss; the discharge current was 495 ma and the discharge voltage 1080 v.

PLASMA DECAY DURING THE PULSE

Just before the pulse is applied, the discharge is in its steady state condition, the plasma being at ground potential and the cathodes at a high negative potential, the precise value fluctuating somewhat. The electrons in the plasma are a mixture of fast electrons produced at the cathode surfaces and falling through the discharge voltage, and slow electrons produced by ionization of the neutral gas atoms; the electrons move freely along the magnetic field but are held in the plasma by the ion sheaths at the ends.

The application of the pulse raises the potential of the cathodes in less than one μsec to a low negative value predetermined by the setting of the clamper bias voltage. Some fast electrons then escape from the plasma, raising its potential above ground to hold in the remaining electrons. Ions can then escape to the electrodes giving the positive pulse shown on the probe current curve (Fig. 4) and on the anode current curve (Fig. 5). This process requires approximately two μsec and is denoted as region A of Fig. 5.

As ions continue to escape, the plasma potential falls to within a few volts of ground, and electrons again begin to flow out. This process appears as region B of Fig. 5. The current to the probe falls to zero at the time when ions and electrons flow to it at equal rates; the clamper is adjusted so that the total current to the probe remains zero during the pulse after the initial positive surge, as shown in Fig. 4. (The ground level on all traces was determined by using an electronic switch and applying ground to one input terminal and the desired signal to the other with the switch output displayed on the oscilloscope.)

At the end of region B of Fig. 5 the plasma has reached a quasi-equilibrium condition during which it disappears as ions and electrons flow out at equal rates, its potential remaining substantially constant. The flow to the somewhat negative cathode will be a mixture of ions and those electrons of sufficient energy to reach it; the relative proportion of each will depend on the conditions in the discharge at the start of the pulse. Fluctuations of these initial conditions result in the spread of decay curves shown in Fig. 5.

Meanwhile, the cathode is becoming more negative, as pointed out above, and eventually the electron current to the cathodes disappears, leaving only an ion current. The lowermost curve of Fig. 5 is then presumed to be that having initially the smallest accompanying electron flow, and the region D of this curve (of admittedly imprecise beginning) is then assumed to be the ion current I_C to the cathodes during this period. (What was actually measured was the anode current I_A, hence the negative ordinate for positive current.)

After about 80 μsec the plasma has disappeared, as shown by Fig. 5.

Assume that the number of ions contained in a velocity component differential is given by

$$NF(v_x)dv_x, \tag{1}$$

where N is the total number of ions, dv_x is the differential element, and F is some function of v_x, the velocity component toward the cathode. If the plasma is now pictured as composed of superimposed uniform assemblies of ions in distinct velocity component groups, the current collected at the cathode at a time t, where $t=0$ at the time the discharge is pulsed off, will be given by

$$I_c(t)=e\int_0^{L/t} Nv_xF(v_x)dv_x, \tag{2}$$

where L is the length of the plasma column, and e is the electronic charge. We differentiate Eq. (2),

$$\begin{aligned}(d/dt)[I_C(t)]&=-Ne(L^2/t^3)F(L/t)\\&=-(B/t^3)G(t)=-(d/dt)[I_A(t)].\end{aligned} \tag{3}$$

For comparison, a Maxwellian distribution of velocity components toward the cathode may be assumed and transformed to the form of Eq. (3). This leads to

$$(d/dt)[I_A(t)]=(C/t^3)\exp(-T_m^2/t^2), \tag{4}$$

where $T_m=L/v_m$ with v_m the most probable speed of a Maxwellian distribution, and C is a constant. The maximum value of the right side of Eq. (4) occurs at

TABLE I. Compilation of results.

Run number	I (amp)	t_{max} (μsec)	T_m (μsec)	Temperature V_e (ev)	B (gauss)	P (μ-Hg)	Gas	Gas density (n/cm³)	Ion density (n/cm³)
1	0.43	43	52	0.41	2400	3	Argon	1.1×10^{14}	2.0×10^{12}
2	0.50	36	45	0.55	2400	3	Argon	1.1×10^{14}	2.0×10^{12}
3	0.75	26	38	0.77	2400	3	Argon	1.1×10^{14}	2.2×10^{12}
4	0.47	35	43	0.59	3400	3	Argon	1.1×10^{14}	2.0×10^{12}
5	0.62	21	26	0.16	2400	24	Helium	8×10^{14}	1.4×10^{12}

time t_{max} given by

$$t_{max}=0.816T_m. \tag{5}$$

The temperature V_e (electron volts) of a Maxwellian distribution is related to the most probable speed by:

$$Mv_m^2/2e=V_e, \tag{6}$$

where M is the particle mass.

RESULTS OF PLASMA DECAY STUDIES

At each current level studied, a series of photographs was taken of the plasma current decay curves. A trace was made of the largest decay pulses in each case. These traces were normalized, averaged, and a resultant curve plotted for each current level. The resultant curves were then graphically differentiated. The current decay curves and their time derivatives for runs 1 and 3 are typical of the results obtained and are shown in Fig. 6. The observed decay curves for the anode current I_A are shown on the left. The measured slopes dI_A/dt are shown by circles on the right. For comparison the curve of Eq. (4) is shown, fitted to the experimental values at the point of maximum slope. The pertinent data and results of all runs are presented in Table I.

The experimental curves obtained indicate that the ions arriving at the cathodes after the discharge is shut off have an approximately Maxwellian distribution of energy of about 0.5 ev (for argon). The ion energy distribution in the normally operating discharge will presumably be somewhat different from this. Loss of ions to the other electrodes has not been taken into account; however, other work at this laboratory shows that the ion current in the discharge is predominantly along the magnetic field[7] so this should not be an important factor. Loss of ion energy by collisions after the discharge is shut off and before the ion is collected has also not been taken into account; the effect of this would presumably be to degrade the energy of the distribution as the ions are being collected so that the actual ion distribution in the normally operating discharge should have a higher energy than given in Table I.

The determination of the average ion velocity enables a calculation of the ion density. The ratio of positive ion current to the cathodes to the total measured discharge current is about 0.75.[7] By using this, the values of ion density required for the measured discharge currents and ion velocity components were calculated. These are tabulated in Table I along with the gas particle density as calculated from the ion gauge readings for the vacuum chamber. The calculated ion densities indicate that the ionization in the plasma region is approximately 20%.

It was hoped that a discharge could be run at the same pressure in helium as that used in the argon runs, and that equivalent currents could be obtained. However, as can be seen in Table I, the pressure necessary to obtain a steady plasma condition for the helium discharge was from 6 to 10 times as large as that used for the discharge in argon. This prevented operation under equivalent conditions so that no comparison or conclusions could be made.

ACKNOWLEDGMENTS

This work was jointly supported by Research Corporation and by the Office of Naval Research, and their assistance is gratefully acknowledged.

[7] John Backus (to be published).

JOURNAL OF APPLIED PHYSICS VOLUME 31, NUMBER 2 FEBRUARY, 1960

Structure in Vitreous Silicate Fibers as Shown by Small-Angle Scattering of X-Rays

W. O. Statton and L. C. Hoffman
Pioneering Research Laboratory, Textile Fibers Department, E. I. du Pont de Nemours and Company, Inc., Experimental Station, Wilmington, Delaware

(Received April 11, 1958)

The relation of the x-ray diagram at small angles to the preparation conditions of glass fibers from molten silicates is studied. The composition $Na_2O \cdot MgO \cdot 3SiO_2$ is studied extensively, and fibers are also studied in which K_2O replaces Na_2O, and CuO and PbO replace MgO.

Most of the diagrams are characterized by very intense, shaped, diffuse scattering. Also, fibers which had certain thermal histories show intense, unshaped diffraction maxima.

The diffuse scattering is interpreted as due to voids which are elongated by the spinning process. The discrete diffraction corresponds to a Bragg spacing of about 30 A but is not associated with short-range order. It is concentrated on the surface or accessible to liquid penetration from the surface. It is either frozen in by quenching, produced by quenching, or produced by a combination of quenching and reaction with the atmosphere. No interpretation of the structure responsible for it is given.

INTRODUCTION

In a previous paper,[1] it was shown that the small angle x-ray technique can elucidate structure in powdered massive glass samples. Diffuse scattering, varying with composition and thermal history, was interpreted as arising from voids or pores. Discrete diffraction (30-A Bragg spacing) was also observed in some of these samples but no unambiguous interpretation could be made. It was also shown that commercial, Owens-Corning "E" "Fiberglas" showed diffuse scattering resulting from inhomogeneities elongated in the direction of the fiber axis. It was suggested that this was confirmation of the existence of elongated "cracks" or "flaws" as postulated by Griffith[2] to explain the unexpectedly high strength of glass fibers.

We now wish to present the results of a study of small angle patterns obtained for a variety of "homemade" silicate fibers which extend the previous findings for powders and demonstrate that a similar structural situation exists generally for silicate fibers.

EXPERIMENTAL METHODS

Preparation of Glass Compositions and Spinning of Fibers

The glasses were prepared by melting together C. P. Na_2CO_3, K_2CO_3, $MgCO_3$, $PbCO_3$, CuO, and "potters-flint." Flint was used as a source of pure SiO_2. Melting was done in 50-ml platinum crucibles except for the CuO- and PbO-bearing glasses. These latter glasses, known to attack platinum, were melted in kyanite crucibles. Melting was accomplished in a box-type "globar" furnace at 1200–1300°C. Melting and stirring was continued until threads of uniform diameter, free from unmelted batch, could be drawn from the melt. The melt was then poured into a graphite crucible and allowed to cool and solidify.

The spinning apparatus was of simple design based on pulling a monofilament from an elongated spinneret tube. Figure 1 is a schematic sketch. The silicates were remelted in a platinum crucible which had a platinum "blowpipe" tip with a 0.050-in. hole pressed through the crucible bottom. The crucible was supported on an alumina tube which was supported by the bottom of the furnace. A water cooled, hollow copper cylinder surrounded the "spinneret" tip to prevent passage of furnace heat to the spinning threadline. Heating was accomplished by globars. A thermocouple was placed in close proximity to the crucible but all spinning temperatures referred to in this paper were determined by an optical pyrometer reading of the glass temperature at the tip of the orifice.

In practice, the remelted glass was allowed to flow down through the spinneret by gravity until a drop formed on the end. This drop was seized with a pair of tweezers and a thick thread was pulled quickly down through the copper coil and led to a rapidly rotating windup "bobbin" some seven feet below the spinneret. If the temperature of the glass melt was in the spinnable range, the sudden jerk as the fiber wrapped around the bobbin merely attenuated the rod to a fine fiber. If the temperature was too low the fiber broke, and if the temperature was too high the fiber diameter was reduced

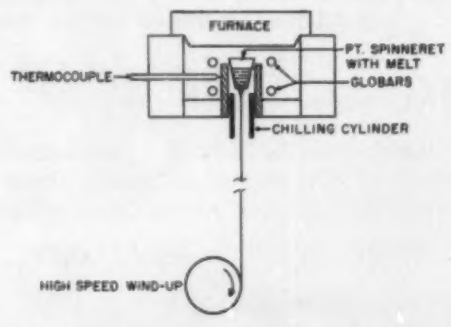

FIG. 1. Diagram of spinning apparatus for silicate fibers.

[1] L. C. Hoffman and W. O. Statton, Nature **176**, 561 (1955).
[2] A. A. Griffith, Phil. Trans. Roy. Soc. (London) **A221**, 163 (1920).

to zero. Fiber spins were accomplished in this way for up to two-hour periods without threadline breakdown. Fibers had diameters in the range of 0.008 to 0.013 mm.

Many fibers were prepared in this way for the composition $Na_2O \cdot MgO \cdot 3SiO_2$. Spinning was possible from 950° to 1260°C at windup speeds of up to 1000 yards per min. 1060°C was found experimentally to be a convenient temperature for long spins. Many of the fibers studied were produced from melts at this temperature after the effect of varying temperature was investigated.

Some fibers were also spun from melts in which K_2O replaced Na_2O and in which CuO and PbO were substituted for MgO. These melts were spun from a temperature in the middle of the spinnable range for the composition being studied.

X-Ray Scattering at Small Angles

The techniques for obtaining x-ray patterns at small angles from inorganic glass fibers were very similar to those used for organic polymer fibers.[3] Since the mass absorption coefficient is relatively high for inorganic fibers, a small sample size and long exposure times were necessary. The following conditions were used for most of the samples reported here: sample-to-film distance = 17.0 cm in vacuum; exposure time (Kodak No-Screen film) = 64 hr; sample thickness = 0.010 in.; collimating pinholes = 0.025 in. diameter, 6 in. apart; Cu$K\alpha$ radiation, Ni filtered, at 40-kv peak and 20 ma.

Intense diffuse scattering was found around the undiffracted beam at very small angles. The intensity was greatest at the smallest angles which were obscured by the trap for the unscattered x-ray beam; therefore, no accurate integrated intensity measurements can be given for all of the scattering. The amount of the scattering registered on the film is a measure of the amount of electron density inhomogeneity[4] in the scattering medium. A plot of scattered intensity *vs* scattering angle can be used with certain important assumptions to measure the sizes of the inhomogeneities causing the scattering.[3-5] Such size measurements are not related in any way to Bragg diffraction spacings.

The diffuse scattering diagram is rarely completely circular in shape for fibrous materials. A shaping or elongation of this scattering is observed when drawing occurs; even spinning tension alone is usually sufficient to elongate a portion of this scattering. Thus, the inhomogeneities giving rise to this scattering are shaped or elongated, with their long dimension in the direction of the fiber axis.[3] This streak on the equator is not due to specular reflection from the smooth surface of the glass fibers since all such totally reflected intensity would occur at less than 20 minutes of arc (the critical angle for glass).[6] This scattering angle is not recorded on our diagrams since the beam trap extends to 32 minutes; the streaks we observe extend, on the average, to at least 1° and may extend to 2°. The patterns may be described as "diamond" if the majority of the inhomogeneities are equally shaped, or "ball and streak" if the shaping is mixed so that some of the inhomogeneities are highly elongated and others spherically uniform.

[3] W. O. Statton, J. Polymer Sci. **22**, 385 (1956).

[4] A. Guinier and G. Fournet, *Small Angle Scattering of X-Rays* (John Wiley & Sons Inc., New York, 1955).

[5] For example: Kratky, Porod, Sikora, and Paletta, J. Polymer Sci. **16**, 163 (1955); A. N. J. Heyn, J. Appl. Phys. **26**, 519 (1955); Heikens, Hermans, van Velden, and Weidinger, J. Polymer Sci. **11**, 433 (1953).

RESULTS

In general, both diffuse scattering and discrete diffraction were found in these silicate fibers. For clarity the two types are separated in discussion.

$Na_2O \cdot MgO \cdot 3SiO_2$ Fibers

Typical small angle patterns for glass fibers of $Na_2O \cdot MgO \cdot 3SiO_2$ are shown in Fig. 2. Extremes of windup speed produced different patterns. The data for these and other fibers of $Na_2O \cdot MgO \cdot 3SiO_2$ are summarized in Table I.

Diffuse Scattering

All the fibers produced an intense scattering diagram, higher than that found for melt spun organic fibers such as 66 nylon. It was found that annealing reduced the amount of this central scattering.

The effect of high windup speed usually was to produce a fiber showing ball and streak diffuse scattering as in Fig. 2(a). Filaments spun at lower windup speed usually gave diamond shaped diffuse scattering, as in Fig. 2(b). Following the interpretation used for organic fibers, this indicates that the spinning process elongated the inhomogeneities but not all the inhomogeneities were equally affected if the windup speed was high.

Discrete Diffraction

Effect of Spinning Conditions

The effect of high windup speed was to produce a fiber showing a discrete diffraction maximum corresponding to a Bragg spacing of about 30 A. This ring never showed orientation under any spinning or other processing variations. Slowly woundup fibers did not show the ring. Figures 2(a) and 2(b) show these differences.

Effect of Aftertreatments

Quenching and Annealing.—All attempts to introduce the diffraction maximum into fibers which did not show it originally were unsuccessful. Slowly drawn $Na_2O \cdot MgO \cdot 3SiO_2$ fibers (without the ring) were heated to a temperature just below their softening range (about

[6] A. H. Compton, Phil. Mag. **45**, 1121 (1923).

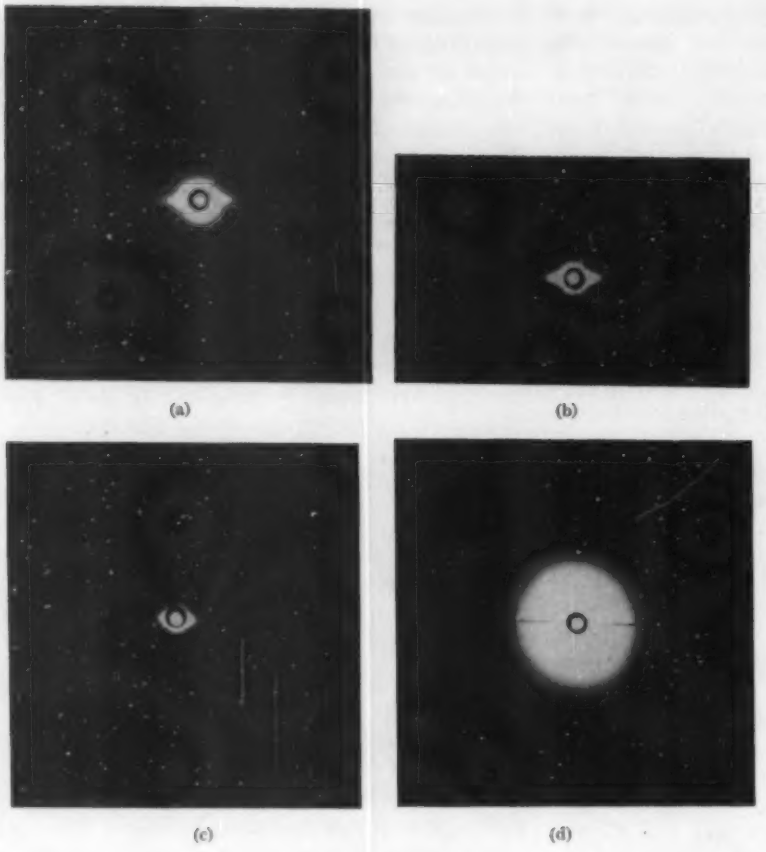

FIG. 2. Small angle x-ray diagrams of $Na_2O \cdot MgO \cdot 3\,SiO_2$ fibers (fiber axis vertical) (a) 1000 ypm windup speed; (b) 153 ypm windup speed; (c) 1000 ypm windup speed—after attack by 10% HF for 30 sec; (d) 1000 ypm windup speed—after attack by 0.02*N* NaOH for 30 seconds.

500°C below the spinning temperature) and quenched by dropping into mercury. No discrete maximum resulted, showing that sudden quenching alone from this temperature is not sufficient to produce the unusual structure. Conversely, however, heating high-speed spun fibers (which showed the maximum) to 525°C was sufficient to remove it.

Water Vapor.—Fibers which showed a diffraction maximum were stored for 30 days over desiccators of H_2SO_4-water solutions of known vapor pressures, as listed in Table I. It was found that a relative humidity of 3% was sufficient to cause a disappearance of the maximum.

Immersion in Liquid of High Density.—Fibers which showed the maximum were sealed into glass capillaries (0.012-in. diameter) filled with bromoform to obtain their small-angle diagram during immersion. Since bromoform has about the same x-ray density as glass, it would suppress total reflections from the surface of the individual fibers and/or fill or surround the inhomogeneities.

Both the diffuse scattering and the discrete scattering were changed upon immersion. The equatorial diffuse streak and the discrete ring were both eliminated; the remainder (the ball) of the diffuse scattering was unchanged. No permanent structural changes were caused by this immersion as the diffuse streak and discrete ring returned to the diagram after the bromoform was evaporated. This leads to the conclusion that the factors responsible for both types of scattering are either concentrated in the surface of the glass fibers or are interior inhomogeneities which are capable of being filled or surrounded with a liquid.

Etching with HF.—The surface of these glass fibers showing the diffraction ring was removed by a reaction with 10% aqueous HF for 30 sec. The discrete diffraction was eliminated, as shown in Fig. 2(c). It was a permanent removal, as it did not return upon aging the fiber. This again indicates that the only way to introduce the ordering is by quenching from the melt. Since the diffuse scattering also showed a decrease (indicating a net increase in the average size of the voids) it is possible that interior etching of inhomogeneities also occurred; therefore, it cannot be concluded definitely that the ordered structure is concentrated in the surface of the fibers.

Attack by NaOH and HCl Solutions.—The attack by NaOH solutions on glass is particularly severe because the alkali-silicate products are soluble in water and are carried away from the glass surface. Fibers showing the diffraction maximum were boiled for 30 min in 0.02*N* NaOH solution. This attack was sufficient to produce an 11.8% weight loss. The resulting small-angle diffraction pattern is shown in Fig. 2(d). The 30-A ring was

TABLE I. Small angle x-ray patterns of $Na_2O \cdot MgO \cdot 3\ SiO_2$ fibers.

Preparation (from melt at 1060°C unless noted)	Diffuse scattering: Integrated intensity[a]	Diffuse scattering: Void elongation parameter[b]	Diffuse scattering: Type of diagram	Discrete scattering: Relative intensity	Discrete scattering: Spacing, A[c]
153 ypm windup speed	high	1.5	ball and streak	weak	32
166 ypm windup speed	medium	1.9	diamond	weak	32
166 ypm windup speed (heated to 525°, quenched in Hg)	low	1.9	diamond	none	...
475 ypm (melt at 1175°)	high	1.6	ball and streak	weak	29
				strong	44 oriented[d]
657 ypm (melt at 1120°)	very high	1.5	ball and streak	very strong	29
785 ypm (melt at 1258°)	high	1.2	ball and streak	medium	28
813 ypm (melt at 1140°)	high	1.3	ball and streak	weak	32
1000 ypm	high	2.8	ball and streak	strong	27
1000 ypm after standing 6 weeks	medium	2.6	ball and streak	weak	30 oriented[d]
1000 ypm	high	1.7	diamond	weak	29
1000 ypm in 3% RH for 30 days	medium	2.5	diamond	none	...
1000 ypm in 37% RH for 30 days	medium	2.1	diamond	none	...
1000 ypm in 100% RH for 30 days	very high	1.0	ball	none	...
1000 ypm boiled in NaOH	extremely high	1.0	ball	very strong	12.1±0.05
1000 ypm boiled in HCl	high	1.2	ball and streak	none	...
1000 ypm in 10% HF, 30 sec	low	1.7	diamond	none	...
1000 ypm immersed in $CHBr_3$	high	1.0	ball	none	...
1000 ypm immersed in $CHBr_3$ dried	high	1.5	diamond	very strong	30

[a] Estimated visually. The higher the integrated intensity, the greater the void content.
[b] Measured visually as the ratio of length of streak along the equator to the length of blackening along the meridian. The higher the value of the parameter, the greater the void elongation for diagrams of the same type.
[c] Measured visually from the peak intensity of the rings and calculated by the Bragg equation ($\lambda = 2d \sin\theta$). The accuracy is ±0.5 A.
[d] This orientation is shown by an arc across the equator. It could be caused by elementary fibrils which are regularly spaced or sized. Oriented overgrowths of decomposition products could also be the cause of this unusual diffraction. These samples had been in laboratory air for six weeks before obtaining the x-ray diagram.

eliminated, but a new diffraction maximum was found; it was very sharp and intense and corresponded to a Bragg spacing of 12.1 A. Thus, attack had occurred which resulted in a major change in structure. No wide-angle diffraction was observed for the product; it was still vitreous, even though it exhibited this unusual "intermediate period ordering" the nature of which is unexplained.

The attack by HCl solution eliminated the maximum at 30 A, similar to the above attack with HF.

Both NaOH and HCl attacks produced a great increase in diffuse scattering, indicating a large increase in porosity which is the known result of such treatments.[7,8]

Fibers of Other Compositions

Table II lists the results obtained from the small-angle patterns for fibers whose compositions were changed by substituting K_2O (partially or wholly) for Na_2O, or CuO and PbO for MgO. These patterns showed, in general, less elongation of inhomogeneities and less intense discrete scattering than corresponding $Na_2O \cdot MgO \cdot 3SiO_2$ fibers.

The substitution of CuO for MgO reversed the shape-windup speed relation in the diffuse scattering pattern; the slow windup now produced the mixed "ball and streak" pattern which was found for the fast windup fibers of $Na_2O \cdot MgO \cdot 3SiO_2$. Also, the relation of windup speed and existence of the discrete scattering was reversed in a similar way.

The greatest effect was observed when PbO was substituted for MgO. In this case, there was no discrete scattering and only a very small amount of diffuse scattering in contrast to all other fibers studied here. This decrease in diffuse scattering was not due to increased mass absorption, as might be suspected, since the many exposures were adjusted to equal the previous intensities at wide angles in the diagram.

DISCUSSION

Diffuse Scattering

The inhomogeneities in electron density are not distinguished by scattering theory as either (1) particles, clumps (regions of greater density within the solid) or (2) holes, voids, pores (less dense regions). The electron micrographs of Prebus and Michener[9] show dense clumps which are of the size that would scatter x-rays. Evidence by Porai-Koshits and Filipovich,[7] by Ritland and Beeman,[8] by Porai-Koshits and Andreyev,[10] and by Brumberger and Debye[11] favors voids as a source of diffuse scattering. Brumberger and Debye also observe similar results in Corning Glass No. 7740, a borosilicate,

[7] E. A. Porai-Koshits and V. N. Filipovich, Bull. Acad. Sci. U.S.S.R. Div. Chem. Sci. S.S.R. **1955**, 19, No. 1.
[8] W. N. Ritland and W. W. Beeman, "Small angle scattering of x-rays by several glasses," paper presented at Pittsburgh Diffraction Conference, November 4, 1954.
[9] A. F. Prebus and J. W. Michener, Ind. Eng. Chem. **46**, 147 (1954).
[10] E. A. Porai-Koshits and N. S. Andreyev, Nature **182**, 335 (1958).
[11] H. Brumberger and P. Debye, J. Phys. Chem. **61**, 1623 (1957).

TABLE II. Small angle x-ray patterns of fibers.

Composition	Melt temp. °C	Spinning speed, ypm	Diffuse scattering			Discrete scattering	
			Integrated intensity[a]	Void elongation parameter[b]	Type of diagram	Relative intensity	Spacing, A[c]
$1/2Na_2O \cdot 1/2K_2O \cdot MgO \cdot 3SiO_2$	1080	500	low	2.6	ball and streak	none	···
$1/2Na_2O \cdot 1/2K_2O \cdot MgO \cdot 3SiO_2$	1080	1000	medium	2.1	ball and streak	very weak	···
$K_2O \cdot MgO \cdot 3SiO_2$	1155	500	medium	1.4	diamond	weak	30
$K_2O \cdot MgO \cdot 3SiO_2$	1155	1000	medium	1.4	ball and streak	medium	29
$Na_2O \cdot CuO \cdot 3SiO_2$	1010	500	medium	1.4	ball and streak	very weak	···
$Na_2O \cdot CuO \cdot 3SiO_2$	1010	1000	medium	1.4	diamond	none	···
$Na_2O \cdot PbO \cdot 3SiO_2$	897	500	extremely low	···	streak	none	···
$Na_2O \cdot PbO \cdot 3SiO_2$	897	1000	extremely low	···	streak	none	···
Owens *E* fiber	?	?	low	1.9	diamond	none	
Owens *E* fiber respun	1226	500	low	2.0	diamond	none	···
Owens *E* fiber respun	1226	1000	low	2.5	diamond	none	···

[a] See footnote a, Table I.
[b] See footnote b, Table I.
[c] See footnote c, Table I.

and ascribe them to strains present in the glass. Pores were shown to exist by Leont'ev and Luk'yanovich.[12]

An interpretation of the inhomogeneities as regions of low electron density agrees best with our experimental data and our experience with other fibers of viscous melts.[13] The Si-O-Si network does not fill all space; there are regions which contain fewer (or no) atoms. The inhomogeneities are shaped by spinning in such a fashion that their long axes are aligned parallel with the fiber axis. Thus, spherical pores are pulled out into ellipsoids by spinning. The void elongation parameter in Tables I and II is a measure of the relative lengths of the major and minor axes of these ellipsoids.

Those treatments which are known to cause compaction of glass reduced the size of the inhomogeneities.[1,11] Slow cooling of $Na_2O \cdot MgO \cdot 3SiO_2$ powder yielded diffuse scattering which was characterized[1] as 77% due to 24-A diameter pores. Fast cooling gave scattering characterized as 55% due to 68-A pores. It seems reasonable to assume that high windup speed in spinning fibers is analogous to fast cooling of powders. Variation in the windup speed was found to have a greater affect on the amount of elongation of the voids than on their size. For $Na_2O \cdot MgO \cdot 3SiO_2$ high windup speed produced a mixed elongation of the voids. Many voids remained essentially spherical, which could indicate a nonuniform response to the sudden pull on the melt, either in the nature of "dilatancy" or because of higher stress in the surface of the forming fiber. In addition, a higher melt temperature had the same effect of producing mixed elongations. Slow windup speed produced a more uniform void elongation.

When the fiber samples were attacked by NaOH, HCl, HF or H_2O, the elongation apparent in the scattering diagram was reduced. When the fibers were simply immersed in bromoform, there was a loss of the equatorial streak without the loss of the spherical scattering. These facts strongly suggest that elongated voids are at the surface of the fiber and sealed spherical holes are in the interior.

Variation in chemical composition of the glass changed its response to given spinning conditions. In $Na_2O \cdot MgO \cdot 3SiO_2$, the higher speed spinning showed greatest void elongation. When one-half the sodium ions were replaced by postassium ions, the lower speed spinning showed greatest elongation. In $K_2O \cdot MgO \cdot 3SiO_2$ the spinning speed showed no effect; the void elongation is slight for either low or high speeds. Mixed alkali glasses show other abnormal or extreme properties as a function of composition; minima are obtained for the plots of composition *vs* electrical conductivity,[14] solubility,[15] and the temperature necessary to attain a given viscosity.[16]

When MgO was replaced by CuO in $Na_2O \cdot MgO \cdot 3SiO_2$ glass, the effect of spinning speed was reversed. That is, high-speed spinning produced moderate elongation of all voids; at low speeds some voids were greatly elongated and others were unaffected. This reversal is not due to viscosity or difference in activation energies, since the glasses were spun at about equal viscosities and their activation energy (viscous flow) is about equal.[16]

Discrete Diffraction

The existence of a discrete ring in many of the small angle diagrams for both powders and fibers requires an ordered position of some structural feature to produce a Bragg diffraction. This large lattice could follow the Bragg law without local ordering within the structural feature at the lattice site. The nature of this structural feature in terms of a model cannot be given at this time, since none of the experiments designed to detect it were unambiguous. The disappearance of the ring by bromoform immersion may indicate a surface structure, although filling of voids or surrounding of surface clusters have equal validity as explanations. The

[12] E. A. Leont'ev and V. M. Luk'yanovich, Doklady Acad. Nauk S.S.S.R. **103**, 1039 (1955).
[13] W. O. Statton, J. Polymer Sci. (to be published).
[14] G. Gehloff and M. Thomas, Z. tech. Physik **6**, 544 (1925).
[15] C. J. Peddle, J. Soc. Glass Technol. **4**, 120 (1920).
[16] Hoffman, Kupinski, Thakur, and Weyl, J. Soc. Glass Technol. **36**, 196 (1952).

permanent disappearance resulting from NaOH or HF attack requires an assumption as to what is being attacked.

The mechanism of formation of this ordering also leads to ambiguity in interpretation. For $Na_2O \cdot MgO \cdot 3SiO_2$ powders and fibers the more drastic the quench, the more intense the ring, provided the sample was exposed to the atmosphere. This poses the following basic questions which are not answered at present: Does the long-period order exist at the elevated temperatures, being merely frozen in by the quenching? Or, is the ordered structure produced by the sudden cooling? Or, is it produced by a combination of sudden cooling and reaction with the atmosphere? None of the fibers used for the diffraction study was protected from the atmosphere in any special way, allowing opportunity for reaction with moisture, for example.

It can be conjectured that the ordered structural feature is related to some of the various proposals in the literature for "cluster melts,"[17] "vitrons,"[18] "structons,"[19] discrete ions,[20] or others.[21]

SUMMARY

The variations of diffuse and discrete small angle scattering showed that two new structural features must be considered in a description of these vitreous materials:

1. A relatively high inhomogeneity in electron density existed in practically all the samples studied. These inhomogeneities are interpreted as voids of submicroscopic size (20 to 500 A). The porosity resulting from these voids is greater in bulk or fibrous silicates than in products of other viscous melts (such as nylon or polyethylene terephthalate polymers or fibers). The size distribution of these voids shifted toward smaller dimensions when the samples were annealed, showing a compaction of the matter. These voids were elongated into ellipsoids or cracks by the spinning operation; the greater the windup speed, the greater this elongation in the direction of the fiber axis. These elongated voids are probably concentrated in the surface. When these fibers were chemically attacked, these ellipsoids were etched into a more spherical shape. Changes in chemical compositions of the melts produced varying amounts and varying elongation of these voids.

2. A long-period order of about 30 A existed in many amorphous silicates. This ordered structure is interpreted as a regularity of placement of inhomogeneities in electron density. It is perhaps concentrated in the surface. No crystalline, local order (1 to 10 A) was found in any of the products which showed this long-period ordering. It cannot be stated at this time whether this order is a regularity of voids or of dense clumps; evidence was found for either interpretation. It was conclusively shown that for $Na_2O \cdot MgO \cdot 3SiO_2$ powders or fibers the long-period order was the most pronounced when the most drastic quenching technique was used. This raises these basic questions: Does the long-period order exist at the elevated temperature, and is it merely frozen in by quenching? Or, is the ordered structure produced by the sudden cooling?

ACKNOWLEDGMENTS

The authors would like to thank Professor W. A. Weyl and Professor M. J. Buerger for helpful discussions.

[17] J. S. Lukesh, Proc. Natl. Acad. Sci. U. S. **28**, 277 (1942).
[18] L. W. Tilton, J. Research Natl. Bur. Standards **59**, 139 (1957).
[19] M. L. Huggins, J. Phys. Chem. **58**, 1141 (1954).
[20] Bockris, Mackenzie, and Kitchener, Trans. Faraday Soc. **51**, 1734 (1955).
[21] "Structure of Glass" Papers presented at a conference convened by the Institute of Silicate Chemistry, Academy of Sciences, U.S.S.R. Trans. from the Russian, Glass Division of the Am. Ceramic Soc., New York, 1958.

JOURNAL OF APPLIED PHYSICS VOLUME 31, NUMBER 2 FEBRUARY, 1960

Precision Lattice Parameter Measurements of Cold-Worked Metals

ROBERT ASIMOW
Division of Engineering, California Institute of Technology, Pasadena, California
(Received February 12, 1959)

A technique is developed for precise measurement of interplanar spacings under conditions such that both crystal imperfections and the finite x-ray spectrum contribute significantly to the broadening of the diffraction peaks. This is accomplished by considering the variation of the interference function in the neighborhood of a reciprocal lattice point. A weighted average value of $\sin\theta$, which corresponds to the interference function centroid, is calculated from the usual intensity *versus* angle data for a diffraction peak. Comparison of this measurement, with that obtained by using the position of maximum intensity, indicates that errors greater than 0.1% may be expected with the latter technique depending on the shape of the diffraction peak.

INTRODUCTION

SEVERAL fields of research require the precise determination of interplanar spacings in materials with a sufficiently imperfect crystal structure to cause broad diffraction peaks. Under these conditions, there is no simple relationship between interplanar spacings and the angular location of the corresponding diffraction peaks. Experimentally this difficulty is manifested by the computation of slightly different interplanar spacings depending on the particular procedure used. At the present time, a large number of techniques are in use (graphical peak separation, position of intensity maxima, centroid position, etc.) none of which have a sound theoretical foundation.

Some aspects of this problem have been investigated by Lang[1] and by Pike[2]; however, both these analyses contain limitations which make their application difficult under many experimental conditions. Both papers consider the imperfect crystal to be composed of large crystallites of slightly differing lattice parameters. The applicability of such a model to cold worked metals is uncertain. Further, the precedures developed by Lang and Pike cannot be applied when the broadening caused by the finite distribution of x-ray wavelengths and that caused by the lattice imperfections are both appreciable. In the present paper, we assume only that the lattice imperfections are of a type which may be characterized by a distribution of small lattice strains. It then becomes possible to calculate the mean interplanar spacing $\bar{d}_{hkl}$ from scattered intensity *versus* angle data for the (hkl) diffraction peak.

To determine $\bar{d}_{hkl}$, it is convenient to consider the variation of intensity of the interference function surrounding the (hkl) reciprocal lattice point. For a large perfect crystal, the interference function is symmetric about the (hkl) point; therefore, the centroid of the interference function coincides with the reciprocal lattice point. For the imperfect crystal, we define the position of the (hkl) reciprocal lattice point by the mean reciprocal (hkl) interplanar spacing $\bar{\rho}$. Then, we see by superposition of intensities that for crystals containing only the Lang type of imperfection, the interference function broadens out; however, its centroid position remains at the reciprocal lattice point. Thus, for this case, any change in the average unit cell dimensions is reflected by a corresponding change in the interference function centroid position.*

For the lattice where the strains cannot be considered constant over large numbers of unit cells, the relationship between the centroid position and the reciprocal lattice point is by no means obvious. However, Asimow[3] has shown that in fact the centroid of the interference function does coincide very nearly with the reciprocal lattice point.† Therefore, if it is possible to determine the position of the centroid from diffraction data; the mean interplanar spacing can be calculated.

APPLICATION TO A POWDER SPECIMEN

The centroid position can be most readily determined using a powder specimen in conjunction with an x-ray diffractometer. Warren and Averbach[4] have derived a relationship between the scattered intensity P, at the Bragg angle θ, and the corresponding value of the interference function I_0, for this case:

$$P(2\theta)=(MjR\lambda^2F_{hkl}^2/16\pi c^*v\sin^2\theta)I_0(\zeta), \qquad (1)$$

where ζ is a distance along the reciprocal lattice coordinate c^*, λ is the wavelength of the incident radiation, M is the number of crystals scattering radiation, F_{hkl}^2 is the structure factor in electron units for the (hkl) planes, and v is the volume of the unit cell. As Warren[5] has shown, if the coordinate directions in reciprocal lattice space are properly chosen, we are concerned only with values of the interference function very near the c^* axis; therefore,

$$c^*\zeta\lambda=2\sin\theta, \qquad (2)$$

[1] A. R. Lang, J. Appl. Phys. **27**, 485 (1956).
[2] E. R. Pike, Acta Cryst. **12**, 87 (1959).

* Lang has shown that for small lattice strains $\bar{d}=1/\bar{\rho}$.
[3] R. M. Asimow, Ph.D. dissertation, University of California at Los Angeles (1958).
† The percentage deviation has been shown to be of the same magnitude as the mean cubed strain between neighboring atoms in the crystal.
[4] B. E. Warren and B. L. Averbach, J. Appl. Phys. **21**, 595 (1950).
[5] B. E. Warren, Acta Cryst. **8**, 483 (1955).

since $c^*=\bar{\rho}$ by choice. On differentiating Eq. (2) and substituting in Eq. (1), we find

$$P(2\theta)d2\theta=(K\lambda^3/\sin2\theta\sin\theta)I_0(\zeta)d\zeta, \quad (3)$$

where $K=MjRF_{hkl}^2/16\pi v$.

Equation (3) applies only when the incident radiation is monochromatic, a situation never realized in practice. Even if characteristic K_{α_1} radiation is used, the range of λ present is comparable to the broadening of the reciprocal lattice spot due to lattice distortions. In the past, the Stokes method has often been used to correct for the line broadening introduced by this factor.[6] For the present problem, a new method turns out to be experimentally easier to apply and capable of greater accuracy. Let $G(\lambda)$ be the intensity distribution of the incident radiation as a function of λ, then

$$P_t(2\theta)d2\theta=(K/\sin2\theta\sin\theta)\times\int_{\lambda_1}^{\lambda_2}G(\lambda)\lambda^3I_0(2\sin\theta/\lambda c^*)d\lambda d\zeta, \quad (4)$$

where P_t is the total intensity at the angle 2θ and λ_1 and λ_2 are the limits of the incident wavelength spectrum. Integration of Eq. (4) leads to the result

$$\int_{\theta_1}^{\theta_2}P_t(2\theta)\sin2\theta\sin\theta d2\theta=K\int_{\lambda_1}^{\lambda_2}\int_{2\sin\theta_1/\lambda c^*}^{2\sin\theta_2/\lambda c^*}G(\lambda)\lambda^3I_0(\zeta)d\lambda d\zeta. \quad (5)$$

In performing the integration, it has been assumed that F_{hkl}^2 varies sufficiently slowly with ζ so that it can be treated as a constant. No essential difficulty would be encountered in including both F_{hkl}^2 and the polarization factor in the integration.

The limits of integration in Eq. (5) are determined by the conditions that the diffraction peak is contained within the angular range θ_1 to θ_2. For all values of λ present in the spectrum, it follows therefore, that the interference function must be zero for $\zeta\geqslant\sin\theta_2/c^*\lambda_2$ and $\zeta\leqslant\sin\theta_1/c^*\lambda_1$. Thus the variable limits of integration can be replaced by the fixed limits ζ_1 and ζ_2, where $\zeta_1=\sin\theta_1/\lambda_1c^*$ and $\lambda_2=\sin\theta_2/\lambda_2c^*$, so that

$$\int_{\theta_1}^{\theta_2}P_t(2\theta)\sin2\theta\sin\theta d2\theta=K\int_{\lambda_1}^{\lambda_2}\int_{\zeta_1}^{\zeta_2}G(\lambda)\lambda^3I_0(\zeta)d\zeta d\lambda,$$

$$=KNH\langle\lambda^3\rangle, \quad (6)$$

where N is the number of unit cells contributing to the diffraction peak, H is the area under the $G(\lambda)$ curve, and $\langle\lambda^3\rangle$ is the third moment of the wavelength distribution.

[6] A. R. Stokes, Proc. Phys. Soc. (London) **61**, 382 (1948).

From Eqs. (2) and (3), it can be shown that

$$P(2\theta)\sin2\theta\sin^2\theta=(K\lambda^4c^*/2)I_0(\zeta)d\zeta. \quad (7)$$

Then on using the same reasoning that lead to Eq. (6) from Eq. (3)

$$2\int_{\theta_1}^{\theta_2}P_t(2\theta)\sin2\theta\sin^2\theta d2\theta=(Kc^*NH\langle\lambda^4\rangle\bar{\zeta}/2). \quad (8)$$

The ratio of Eq. (8) to Eq. (6) yields an expression for $\bar{\zeta}c^*$ in terms of quantities measurable with high precision. Since $\bar{\zeta}c^*$ corresponds to the centroid of the interference function; it follows from previous discussion that $\bar{\zeta}c^*=\bar{\rho}=1/d$ so that this ratio can be expressed as

$$d=(\langle\lambda^4\rangle/2\langle\lambda^3\rangle)\left\{\int_{\theta_1}^{\theta_2}P_t(2\theta)\sin2\theta\sin\theta d2\theta\right\}\Big/\left\{\int_{\theta_1}^{\theta_2}P_t(2\theta)\sin2\theta\sin^2\theta d2\theta\right\}. \quad (9)$$

Equation (9) provides a means for computing the mean interplanar spacing from experimentally obtained data on broad diffraction peaks. For absolute parameter measurements, the value of $\langle\lambda^4\rangle/\langle\lambda^3\rangle$ corresponding to any given tube voltage and target material can be determined by the use of a well-annealed crystalline powder of known lattice parameter.

MEASUREMENT ERRORS FOR THE PEAK POSITION METHOD

Equation (9) is dimensionally similar to the Bragg equation, however, it differs in the values of λ and $\sin\theta$

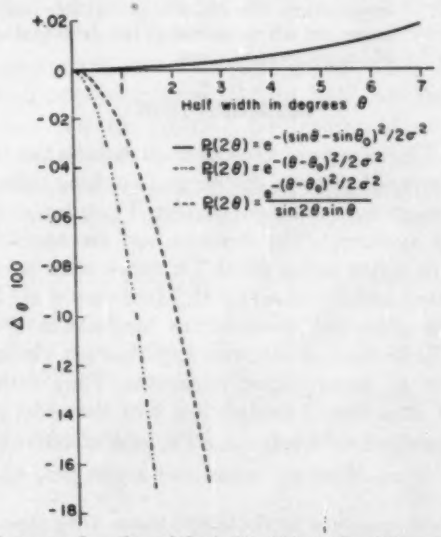

FIG. 1. Δ_θ as a function of the half-width of the diffraction curve. The percentage errors made in the determination of interplanar spacings as a function of the half-width of the diffraction peak (width at half-maximum intensity) for three different peak shapes are shown. In all cases the observed intensity maximum occurs at $2\theta=150°$; however, for 2θ greater than 90°, Δ_θ does not vary greatly with peak position.

used. In the limiting case, when monochromatic radiation is diffracted from a perfect crystal, the two equations are identical. For all other conditions, the error resulting from the peak position method is

$$E=[(\lambda_p/2\sin\theta_p)-(\langle\lambda^4\rangle/2\langle\lambda^3\rangle\bar{\theta})]/(\langle\lambda^4\rangle/2\langle\lambda^3\rangle\bar{\theta}), \quad (10)$$

where θ_p is the value of θ corresponding to maximum intensity, λ_p is the value of λ which maximizes $G(\lambda)$, and $\bar{\theta}$ is the ratio of the two integrals in Eq. (9). Expressing $\lambda_p\langle\lambda^3\rangle/\langle\lambda^4\rangle$ as $1+\Delta_\lambda$ and $\bar{\theta}/\sin\theta_p$ as $1+\Delta_\theta$ where Δ_θ and Δ_λ are small compared to one, Eq. (10) becomes

$$E=\Delta_\lambda+\Delta_\theta. \quad (11)$$

Approximating $G(\lambda)$ by a Gaussian curve, $\Delta_\lambda\sim\sigma^2/\lambda_p^2$ where σ is the standard deviation. For the usual K_{α_1} radiations, this quantity is negligibly small ($\sim5\times10^{-5}$). However, Δ_θ is a sensitive function of the diffraction peak shape, and may be of significant size. Values of Δ_θ, for three different peak shapes, are shown in Fig. 1. If both K_{α_1} and K_{α_2} wavelengths are present, further errors are encountered with the peak position method because of the decreased resolution between the broadened peaks. There is no similar problem with the interference function centroid method as long as the angular range of integration is made sufficiently large to include the same wavelength spectrum irrespective of the broadening.

ACKNOWLEDGMENTS

The writer wishes to express his sincere appreciation to Professor Daniel Rosenthal for his pertinent comments and frequent help in carrying out this work. Financial support for the project was obtained through an Air Force contract.

JOURNAL OF APPLIED PHYSICS VOLUME 31, NUMBER 2 FEBRUARY, 1960

Microwave Study of Afterglow Discharge in Water Vapor*

SUSUMU TAKEDA† AND ARWIN A. DOUGAL
Department of Electrical Engineering, University of Illinois, Urbana, Illinois
(Received January 27, 1959)

Results of a microwave investigation of decaying plasmas produced in water vapor H_2O are reported. Electron loss processes prevailing in these decaying water vapor plasmas were interpreted. In the electron density range from 10^{10} to 10^{8} per cm³, electron-ion recombination prevails as the dominant electron loss process with a coefficient of 10^{-6} to 10^{-5} cm³/sec. For vapor pressures up to 7.0 mm Hg, electron attachment to water vapor molecules or their derivatives was too small to be detectable, i.e., an attachment probability less than 10^{-7}. The electron collision probability for momentum transfer collisions with water vapor molecules was measured to be 2300 ± 500 cm^{-1} mm Hg^{-1} for electrons near thermal energies at room temperature. The collision probability steeply decreases with increasing electron energy in the low energy range. An interpretation of the de-ionization processes in TR tubes filled with admixtures of water vapor and noble gases is given.

INTRODUCTION

WATER vapor is used as a quenching gas in commercial gaseous discharge switching tubes, such as the microwave transmit-receive TR tubes employed in radar systems.[1] The deionization mechanisms prevailing in water vapor filled TR tubes were previously interpreted and discussed by H. Margenau *et al.*[2] In that work the principal deionization mechanism was concluded to be that of electron loss through electron attachment to water vapor molecules. They deduced a value of attachment probability h of the order of 10^{-4} from experimental results in a TR tube which contained an admixture of water vapor and argon gas, where an electron-ion recombination coefficient of 10^{-14} cm³/sec was assumed.

The electron attachment probability h in the relatively higher electron energy range is known through measurements by Townsend's method. However, h in the lower electron energy range for mean electron energies near thermal is not otherwise known. This has handicapped the understanding of the TR tube, as well as the possible influence of water vapor impurities in gaseous discharges. Water vapor is considered to be one of the most probable impurities which may be present in gaseous discharge tubes.[3]

We report here an experimental investigation of deionization mechanisms in the afterglow period of electrical discharge through water vapor. Guided microwave transmission measurements were performed directly in a distintegrating water vapor plasma. The prevailing electron loss processes are identified, and the results tend to clarify the deionization mechanisms in

* Research sponsored by the United States Army Signal Corps Engineering Laboratories.
† Visiting from Yokohama National University, Yokohama, Japan.
[1] L. D. Smullin and C. G. Montgomery, *Radiation Laboratory Series* (McGraw-Hill Book Company, Inc., New York, 1948), Vol. 14.
[2] H. Margenau *et al.*, Phys. Rev. **70**, 349 (1946).
[3] K. B. Perrson and S. C. Brown, Phys. Rev. **100**, 729 (1955).

water vapor plasma. In addition, the momentum transfer collision probability of slow electrons with H_2O molecules was determined by microwave interaction techniques.

EXPERIMENTAL RESULTS OF ELECTRON LOSS RATES

The experimental instrumentation is similar to that used and reported by Anderson and Goldstein.[4,5] The method provides the means to determine the electron density and electron collision frequency by the phase shift and the attenuation measurements of low level microwave signal through the plasma of interest. The electron density is proportional to the phase shift and the effective collision frequency is proportional to the ratio of the attenuation and the phase shift. An improved and refined method of measuring small microwave phase shifts and attenuation of the probing signal through the plasma was developed. This may be reported elsewhere. Photographic recording of an oscilloscope display of the time-dependent standing wave pattern and the transmitted wave amplitude resulting from the probing signal which passes through the plasma, provided the basic phase shift and attenuation data. From this, the electron density n and the effective electron-molecule collision frequency ν_e were determined. Electron densities in the range from 10^{10} to 10^8 per cm^3 were measured by the use of x-band microwaves (8200 to 12 400 Mc).

Electron loss during the afterglow of a pulsed discharge in water vapor was measured in the first step of this work with an adequately low level microwave probing signal which did not disturb the prevailing thermal electron energies. Typical results for the shift of the detector and the attenuation of the probing microwave *versus* time in the water vapor afterglow are given in Fig. 1.

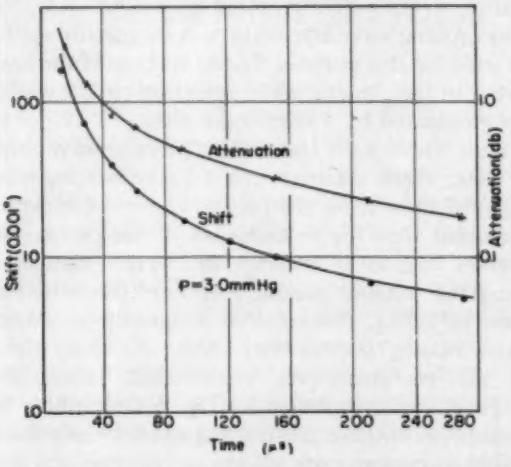

FIG. 1. Shift of detector and attenuation *versus* time.

[4] J. M. Anderson and L. Goldstein, Phys. Rev. **100**, 1037 (1955).
[5] J. M. Anderson and L. Goldstein, Phys. Rev. **102**, 532 (1956).

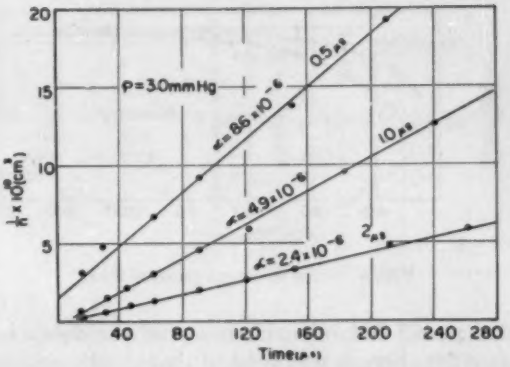

FIG. 2. Inverse value of electron density plotted with time for different pulse widths of discharges.

Examination of the time dependence of the observed phase shift as the plasma disintegrates, and the associated electron density $n(t)$, shows that the reciprocal $1/n(t)$ is completely linear with time t. Figures 2 and 3 give $1/n(t)$ *versus* t for different pulse widths, and peak currents, of the discharge, respectively. The time t is measured from the termination of the pulsed discharge current, and ranges from 15 μsec to approximately 250 μsec. The electron loss mechanism identified with a linear time dependence of $1/n(t)$ is electron-ion recombination. The slope $(1/n(t))/dt$ yields the electron-ion recombination coefficient. The recombination coefficient α appears to be dependent upon the active discharge conditions during the pulsed discharge. It increases with decreasing discharge pulse widths, and decreasing peak discharge currents.

Data was collected for water vapor pressures ranging from 0.5 to 7.0 mm Hg. The recombination coefficients are summarized in Table I, with the applicable peak discharge current and discharge pulse width. The α's vary from approximately 10^{-8} to 10^{-5} cm^3/sec. Such high values for the electron-ion recombination coefficient in water vapor at room temperature are not unreasonable since, as is well known, values of the same order have already been reported in other ionized mo-

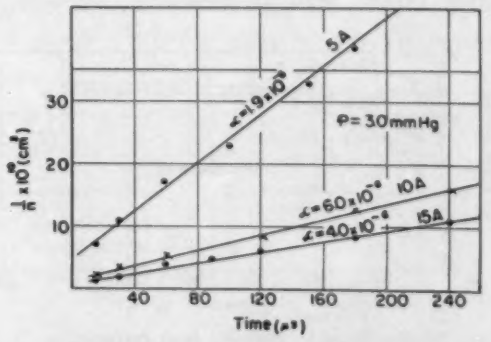

FIG. 3. Inverse value of electron density plotted with time for different peak current of discharges.

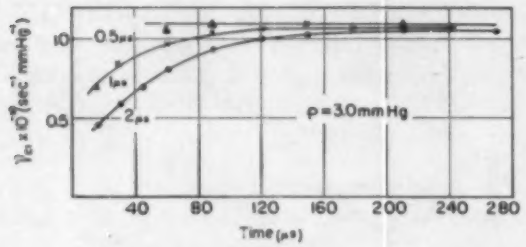

FIG. 4. ν_{e1} for different pulse widths.

lecular gases.[6] Before concluding that the decay is due to recombination, it was verified that this decay cannot be due principally to higher order diffusion modes. The effect of diffusion in the dominant diffusion mode was taken into account, in calculating the electron density at the lower water vapor pressures.

Regarding electron attachment in these water vapor discharges, *contribution of attachment to the electron loss rate was too small to be detectable compared with that of recombination even at the highest pressure of 7 mm Hg.* Here the mean electron energies are near thermal equilibrium with the neutral water vapor at about 300°K. The estimated value of h from the log plot of the electron density decay in the later period should be less than 1×10^{-7}. Therefore, we conclude from these results that h for electrons having mean energies near 0.04 ev is less than 10^{-7}.

EXPERIMENTAL RESULTS OF ELECTRON COLLISION FREQUENCY

Microwave attenuation of the probing wave was measured as a function of time in the decaying water vapor plasma. From this data the electron-molecule momentum transfer collision frequency per unit pressure ν_{e1} was calculated, and appears in Figs. 4 and 5, respectively, for a water vapor pressure of 3.0 mm Hg. In water vapor, the electron temperature should rapidly become equal to the gas temperature after the pulsed discharge because of the relatively large value of $\nu_e G$, where G is the energy loss factor in collisions of electrons with water vapor molecules. In Figs. 4 and 5, it is noted that ν_{e1} changes slowly with time in the earlier afterglow period. Also, the asymptotic value of ν_{e1} as

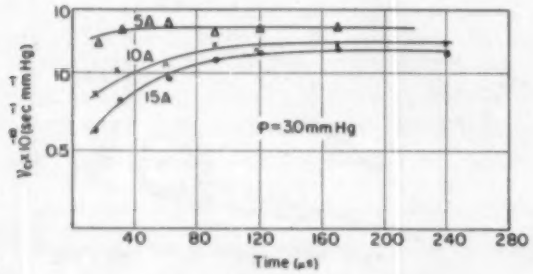

FIG. 5. ν_{e1} for different peak currents.

[6] L. B. Loeb, *Basic Processes of Gaseous Electronics* (University of California Press, Berkeley, California, 1955), p. 562, Table 6.4.

time elapses decreases slightly for higher peak currents or wider pulse widths of the discharge current as is shown in Table I. This is explained upon recognizing that the neutral water vapor temperature itself is slightly higher than the room temperature, and the temperature deviation will increase with increasing peak current or pulse width. In the following section it will be shown that ν_{e1} steeply decreases with increasing electron temperature, which here thermalizes with the neutral gas. The maximum value of ν_{e1} shown in Table I was $(1.5\pm0.3)\times10^{10}$ sec^{-1} mm Hg^{-1} which corresponds to an electron temperature near 300°K.

EXPERIMENTAL DETERMINATION OF THE ENERGY DEPENDENCE OF THE ELECTRON COLLISION PROBABILITY

The variation of the microwave attenuation of the probing wave was measured when a second heating wave at a different frequency was simultaneously propagated

TABLE I. The determined values of effective collision frequency per unit pressure ν_{e1} and the recombination coefficient α for different discharge conditions.

Pressure (mm Hg)	Peak current (A)	Pulse width (μsec)	ν_{e1}(sec^{-1}mm Hg^{-1})	α(cm^3 sec^{-1})
7.0	15	2	0.9×10^{10}	3.4×10^{-6}
5.0	13	2	1.0×10^{10}	4.0×10^{-6}
3.0	20	0.5	1.1×10^{10}	8.6×10^{-6}
3.0	20	1.0	1.05×10^{10}	4.8×10^{-6}
3.0	20	2.0	1.05×10^{10}	2.4×10^{-6}
3.0	5	2	1.3×10^{10}	1.9×10^{-5}
3.0	10	2	1.2×10^{10}	6.0×10^{-6}
3.0	15	2	1.15×10^{10}	4.0×10^{-6}
1.2	15	2	1.5×10^{10}	5.5×10^{-6}
1.2	7.5	2	1.5×10^{10}	1.2×10^{-5}
0.5	15	2	...	1.7×10^{-6}

through the plasma. A comparatively strong heating wave power was required to perturb the electron temperature to the extent required for a detectable change in the probing wave attenuation. A magnetron oscillator was used for this purpose. Direct leakage of the heating wave into the probing wave detection circuit was carefully eliminated by a microwave filter.

Figure 6 shows the transmitted probing wave through the water vapor plasma when a 2 μsec heating wave is employed to increase the plasma electron temperature. It is noted that the transmission of the probing wave increases due to an increase in electron temperature during the heating period, therefore, the attenuation decreases. Thus, the collision frequency ν_e *decreased with increasing electron temperature.* At these electron and ion concentrations, electron-ion collisions are negligible. For comparison, in Fig. 6 the probing wave transmission without plasma and the reference for zero probing wave power are shown.

The energy loss factor G for electrons colliding with water vapor molecules is required for calculating the electron temperature rise[3] due to the heating wave

power. No attempt was made to measure G independently in this experiment due to the very short time constants ($\tau = 1/\nu_e G$) prevailing, and it is otherwise not yet reported. Here, we extrapolated to lower electron energies the previous values of G measured by Bailey[7] at somewhat higher electron energies. G for electrons in water vapor is relatively large and of the order of magnitude of 10^{-2}; that is, 10^3 times larger than $2m/M$ for elastic collisions. This is clearly the reason why a relatively high heating wave power was required to heat the electrons. The large value of G is to be attributed to the numerous inelastic collisions of these slow electrons with water vapor molecules. There are indeed many rotational energy transitions in the infrared[8] and microwave region[9] of water vapor.

The calculated electron temperature rise in water vapor plasma using these G's is shown in Fig. 7 as a

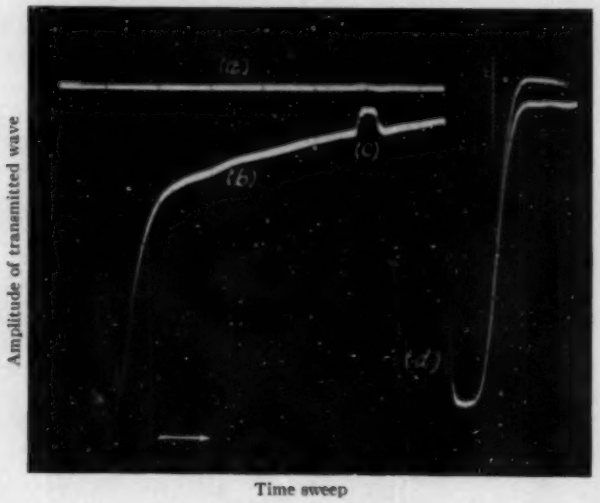

FIG. 6. Transmitted wave through the decaying plasma when a heating pulse is added. (a) Base line without plasma. (b) Transmitted wave with plasma. (c) The decrease of attenuation when the heating wave is added. (d) Cutoff pulse as a reference.

function of the heating wave power. In this calculation ν_e is assumed to be small compared to the angular frequency ω of the heating wave. This holds only for the lower pressures reported here. At the higher pressures the calculation of electron temperature becomes more complicated because ν_e itself is an implicit function of the temperature. For our interpretation here, the water vapor pressure of 1 mm Hg was chosen, where ν_e is small compared to ω. However, at the pressure of 1 mm Hg, the attenuation measurements were obtainable only during the earlier periods of the decaying plasma where the electron-molecule collision frequency ν_e was varying with time. The measured values of the attenuation, which are proportional to ν_e, were corrected here for

[7] V. A. Bailey and W. E. Duncanson, Phil. Mag. **10**, 145 (1930).
[8] H. M. Randall, Phys. Rev. **52**, 160 (1937).
[9] J. H. Van Vleck, Phys. Rev. **71**, 425 (1947).

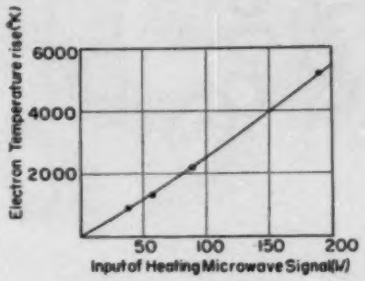

FIG. 7. Electron temperature rise with input power of microwave.

the higher temperature by knowledge of the ν_e variation with time. Figure 8 shows the measured and corrected probing wave attenuation *versus* the electron temperature calculated from the pulsed heating wave power. Two examples for different times of the heating wave power, 15 and 25 μsec after the discharge pulse are shown. The corrections of the temperature were 300°K and 180°K at 15 and 25 μsec, respectively. The corrected probing wave attenuation from Fig. 8 yields the electron temperature dependence of the collision frequency as

$$\nu_{e1} = (1.5 \pm 0.3) \times 10^{10} (Te/300)^{-1} \text{ sec}^{-1}\text{mm Hg}^{-1}.$$

Therefore, ν_{e1} is approximately inversely proportional to the electron temperature from 300 to 3500°K.

The electron-molecule collision probability for momentum transfer per unit pressure, P_m will be expressed by the previously reported method[3] as

$$P_m = (2300 \pm 500)(V/0.04)^{-1}\text{cm}^{-1}\text{mm Hg}^{-1},$$

where V is the mean electron energy in electron volts. P_m is plotted in Fig. 9. It decreases steeply with increasing electron energy in the lower electron energy range starting from 0.04 ev and intersects the earlier result obtained by Bailey[7] at the higher electron energies.

DISCUSSION OF EXPERIMENTAL RESULTS

The measured electron-ion recombination coefficient α was found to be dependent upon the active discharge conditions, including the pulse width and peak current, during the pulsed discharge. If a single species of ion were produced and prevailed throughout the post discharge period, α would be expected to be independent of the active discharge conditions in the absence of

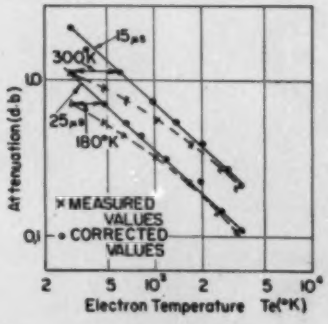

FIG. 8. Attenuation *versus* electron temperature.

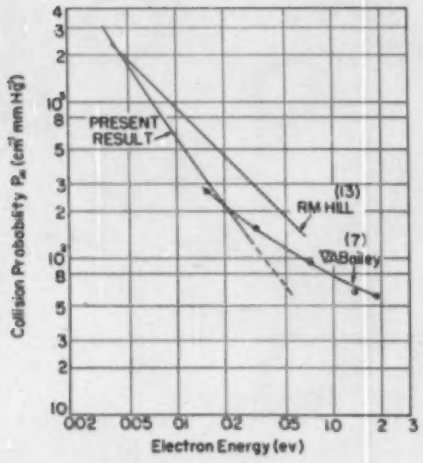

FIG. 9. Collision probability per unit pressure *versus* electron energy.

other secondary processes. Therefore, it appears to be reasonable to assume that varying amounts of positive ions of different species are produced by the discharge. Then the measured electron loss rate is the sum effect of electron-ion recombination with the respective ion species. The following positive ions which are derivatives of the water vapor molecules H_2O have been identified,[10] and their appearance potentials in volts are H_2O^+ (13.0), OH^+ (18.7), O^+ (18.6), H_3O^+ (13.8), H^+ (15.5), and H_2^+ (23.0). Unfortunately, the detection and identification of respective ions, and their concentrations, have not yet been achieved for the transient, time-dependent, type of experiment reported here.

It may not be unreasonable to assume that H_2O^+ or OH^+ ions will dissociate to O^+ or H^+ in stronger discharges. Then the resultant electron-ion recombination rate will be decreased because of the smaller electron-atomic ion recombination coefficient known to apply. This explains in part the observed decrease in α in Figs. 2 and 3 for increasing discharge pulse width or peak discharge current. This interpretation may be not different from that of Schulz-Du Bois[11] who showed that the ambipolar diffusion and electron-attachment coefficients in molecular oxygen O_2 plasmas were dependent upon the active discharge types.

[10] Mann, Hustrulid, and Tate, Phys. Rev. **58**, 340 (1940).
[11] E. Schulz-Du Bois, Z. Physik. **145**, 69 (1958).

It is appropriate to make a few comments regarding the interpretation of deionization in the TR tubes in view of the experimental results reported here. We restrict our attention to those TR tubes using an admixture of water vapor and a noble gas such as argon. It is not self-evident that there exists an electron-attachment mechanism in a water vapor-noble gas mixture which would be greatly different from that occurring in a pure water vapor plasma. In view of the very small electron-attachment probability implied here, where $h<10^{-7}$, in the pure water vapor plasma, *the role of electron-attachment in the over-all deionization process may be insignificant compared with recombination.* We found that addition of small amounts of water vapor to noble gases in our experiments greatly increased the electron loss rates in agreement with other experimental results. However, this is consistent with the large electron-ion recombination rather than with electron-attachment in water vapor. Due to complex molecular ion formation[12] from the noble gas constituents, the full interpretation of deionization in water vapor-noble gas admixtures may be more complicated.

In determination of the electron-molecule collision probability P_m *versus* electron energy, we used an extrapolated value of the energy loss factor G from Bailey's data in the calculation of the electron temperature rise in the microwave heating field. This extrapolation was made into the lower electron temperature range prevailing in these experiments. The collision probability P_m determined by this approximation is compared in Fig. 9 with that reported recently by Hill,[13] and it appears to be in better agreement with the low energy results of Bailey. Altshuler[14] gave a theory for this probability in water vapor and compared the theoretical values to the existing experimental values in the electron energy range from 0.36 to 1.0 ev. He showed that $P_m v^2 =$ constant where v is the electron velocity. This however is in a somewhat higher energy range than that reported here.

ACKNOWLEDGMENT

The authors are deeply appreciative of the encouragement and suggestions by Professor L. Goldstein.

[12] U. Weimer, Doctoral dissertation, Eberhart Kurts University (1957).
[13] R. M. Hill, abstracts of the 11th Annual Gaseous Electronics Conference. C-8 (October, 1958), New York.
[14] S. Altshuler, Phys. Rev. **107**, 114 (1957).

Absorption and Reflection Spectrum of a Plasma*

W. D. HERSHBERGER
University of California, Los Angeles, California
(Received May 4, 1959)

A series of absorption and reflection peaks for plasmas, cylindrical in form, and occurring at electron densities lower than that required for the conventional plasma frequency, has been reported by various workers such as Tonks, Rommel, and Dattner. This paper describes experiments at a wavelength of 10 cm in which the multiple resonances are observed both within a wave guide and in free space. The electric field of the incident microwave is perpendicular to the axis of the plasma column. The positions of the absorption peaks are given by the interference-dispersion relationship,

$$2n/(2n+1)=[1-(f_0/f)^2]^{\frac{1}{2}}.$$

The mode spectrum is found by assigning integral values, including zero, to n. When $n=0$, we obtain the conventional plasma frequency f_0, but for $n>0$, the frequencies, and electron densities for higher order modes are obtained. The relationship identifies a distinctive set of ratios between the phase velocity of a plasma wave and the rms velocity of the electrons such that simultaneously the conditions are met for the existence of a standing plasma wave and a stationary pattern of electron motion. Application of the relationship to radar echoes from meteor trails is indicated.

I. OBSERVATIONS ON ABSORPTION SPECTRA OF PLASMAS

PLASMA oscillations were described by Tonks[1,2] in 1931, and he reported multiple resonance peaks at that time instead of a single resonance peak. Tonks distinguished between "plasma-electron resonance" which depends solely on electron density and "plasma resonance" which depends both on electron density and the geometrical configuration of the plasma.

Rommel[3] in 1951 made a detailed study of the multiple peak resonance phenomenon working with reflections in free space at 1000 Mc from a cylindrical discharge tube. The tube was 3.2 cm in diam and 80 cm long and when the discharge current was 0.93 amp, the main reflection peak was elicited at approximately the calculated current density for this type of resonator. However, for lower electron densities, for which the operating frequency was higher than the calculated plasma frequency, Rommel found a set of additional resonance peaks. From the reflection curves given in his paper, it is noted that for the first two of these subsidiary resonances, the currents drawn by the discharge tube were just slightly less than 60% and 40%, respectively, of that required for the principal resonance.

Dattner[4] reported on experiments, both absorption and reflection, in which an extended series of peaks was obtained from a plasma in a wave-guide system operating at 6 cm. One of his discharge tubes, on which many experiments were performed, was cylindrical in cross section and had an inside diam of 5 mm and an outside diam of 6.5 mm. In addition, he investigated extensively the effect on the absorption spectrum of a variety of geometrical cross sections for his resonators, as well as the effect of an externally applied magnetic field. He commented on the absence of a theoretical explanation for the multiple absorption and reflection peaks that he observed. It is to be noted that the diameter of the discharge tube used is smaller by a factor of 10 than the wavelength.

In Dattner's experiments a cylindrical gas discharge tube containing mercury vapor was placed across a wave guide, as shown schematically in Fig. 1, so the applied microwave electric field was perpendicular to the axis of the discharge tube. As the current through the tube was varied, standing wave measurements were made. These formed the basis for calculations on the impedance of the plasma in the wave-guide system as a function of the ratio I/I_0, where I_0 is the current associated with the electron density for the main resonance peak.

At the same time, the power transmitted to the receiver was measured as a function of I/I_0. Figure 2 shows the received power as a function of the normalized current and is Fig. 5 from Dattner's paper. The impedance of the plasma may be represented by a smooth many-turn spiral on a graph in which the normalized reactance of the tube is plotted against its normalized resistance. When I/I_0 is unity, the main resonance peak is found, the plasma is purely resistive, and it constitutes almost a short circuit across the wave guide, since the VSWR—the voltage standing wave ratio—is approximately 20. As I/I_0 is reduced from unity to zero,

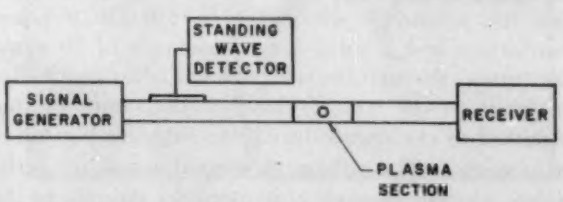

FIG. 1. Microwave system used in studying plasma resonance.

* Work supported in part by a grant from the National Science Foundation.

[1] L. Tonks, Phys. Rev. **37**, 1458 (1931).
[2] L. Tonks, Phys. Rev. **38**, 1219 (1931).
[3] D. Rommel, Nature **167**, 243 (1951).
[4] A. Dattner, Ericsson Technics No. 2, Stockholm, 310 (1957).

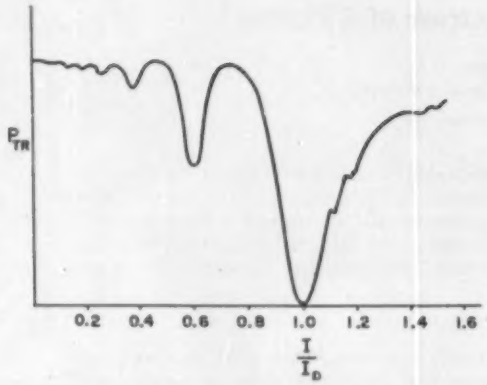

FIG. 2. Relative power at the receiver as a function of normalized plasma current.

a situation in which the conventional plasma resonance frequency is always lower than the fixed operating frequency, the impedance of the plasma changes from a low resistive value, through a range of inductive-resistive values, crosses the resistance axis near (R/Z_0) equal to unity, then through a range of capacitive-resistive values to a low resistive value for the second resonance peak, and so on for succeeding turns on the spiral and their associated resonance peaks.

The purpose of the present experimental study was to make an independent check on the experimental results of Rommel and Dattner and also to develop a theory for the additional resonance peaks. The experiments here reported were carried out at frequencies in the range from 2750 to 2950 Mc, but the results did not depend in any critical fashion on the actual frequency used other than to shift the position of the resonances, as predicted, to an appropriate value of electric charge density. A plasma tube modeled closely after that used by Dattner was constructed using approximately the dimensions he employed. The wave guide used was a standard S-band guide with nominal outside dimensions of 3.0 by 1.5 in. and an 0.080-in. wall. An unmodulated klystron with output of the order of 50 mw was used. In preliminary work in which the plasma tube was disposed across the wave guide with the electric field perpendicular to the tube axis, the multiple peaks could be elicited by manually varying current through the discharge tube, while meter readings on output power were noted. The preferred method permitted the resonance spectrum to be viewed on a cathode-ray oscilloscope. In this arrangement, a steady dc source through the discharge tube was connected in series with the secondary winding of a 110–220 v power transformer and a small series resistance of 10 ohms. The current through the tube was varied by controlling the input to the transformer, but the lamp was not permitted to extinguish during the negative portion of the ac period. The voltage developed across the series resistor was fed through a dc amplifier directly to the deflection plates of the oscilloscope, so current through the discharge tube was indicated directly by the horizontal deflection of the electron beam. The S-band klystron was unmodulated so the only modulation impressed on the microwaves arose as a result of varying the current through the plasma tube to elicit its absorption and reflection spectrum. Audio frequency amplification of the 60 cycle fundamental and the first 30 harmonics was adequate for obtaining a signal for vertical deflection of the beam. The signals were large so no problems were presented in signal amplification. Large values of attenuation were used between klystron and plasma tube and between plasma tube and the crystal detector to avoid standing waves and an interaction between a varying load and the microwave generator.

The three photographs shown were taken by this method and display the selective characteristics for microwaves of the plasma tube as a function of current drawn. Since very nearly the same trace was obtained on proceeding from low current density through the resonances to high current density as by proceeding in the reverse direction, the reverse trace was blanked off during the observations. The experiments were carried

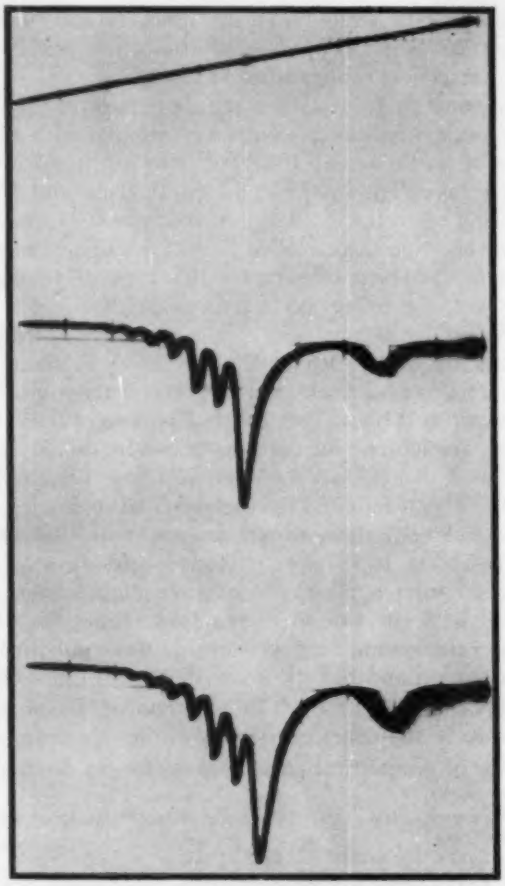

FIG. 3. Resonant response of cylindrical plasma placed in a wave guide midway between top and bottom.

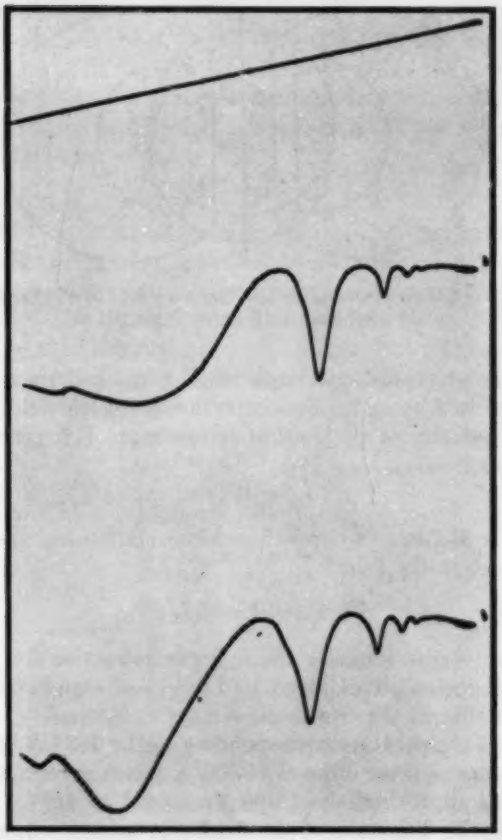

FIG. 4. Resonant response of cylindrical plasma placed in a constricted wave guide so tube fills $\frac{3}{4}$ of space between top and bottom of guide.

on in a number of fashions of which three variants are considered particularly significant.

Figure 3 shows the resonant response when the plasma tube was placed across the guide, midway between top and bottom of the guide. The peaks reported by Dattner appear on the low-current side of the main resonance peak and these peaks appeared in all the experiments. However, a fine structure, sinusoidal in appearance is found on the high-current side of the main resonance peak. This structure changed in a marked fashion as several wave-guide configurations were used. Figure 4 was obtained when a taper section was employed such that the plasma tube filled approximately $\frac{3}{4}$ of the space between top and bottom of the guide. The effect here is to enhance the peaks reported by Dattner on the low-current side of the main resonance peak and to widen the main resonance peak so it was 100 ma wide. The main resonance occurred when the current was approximately 500 ma. Also with the tapered wave-guide section, the subsidiary structure on the high-current side of the main peak disappeared to form one large peak. Inasmuch as the reflection cross section of the plasma column at resonance is large, the constricted wave guide merely served to accentuate the subsidiary resonant peaks and to distort and widen the main peak.

Accordingly, the experiment was varied to resemble more nearly the free-space work of Rommel. The plasma tube was placed in the open, and it was irradiated by the klystron using the open end of the guide as a horn. As before, large values of attenuation were used in both the transmitting and receiving guides. The receiving guide was also open ended so as to serve as a horn, and both horns were pointed in approximately the same direction towards the plasma tube so it served to reflect energy from the transmitter to the receiver. The spectrum on reflection is shown in Fig. 5. The peaks reported both by Dattner and Rommel are present, but the fine structure on the high-current side of the main resonance shown in Fig. 3 is largely absent. This curve resembles closely the spectrum reported by Dattner including very small subsidiary resonances on the high-current side of the main peak. The pattern is affected by moving material about in the proximity of the plasma tube or in the direct radiation path. Stray, but unmodulated, radiation feeds directly from the transmitting horn to the receiving horn to furnish a

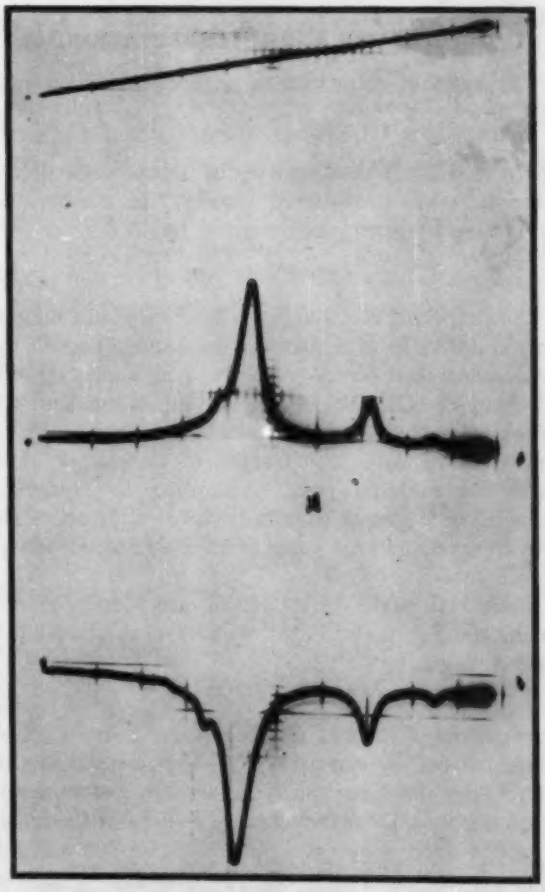

FIG. 5. Reflection from cylindrical plasma placed in open and irradiated by 10-cm waves.

reference microwave phase; as a result, the pattern on the oscilloscope goes through cylic changes as distance from plasma tube to the microwave equipment is varied. These changes are repetitive at half wavelength intervals and are consistent with the vectorial addition of a direct wave and a reflected wave. The pattern inverts at the quarter-wave positions, and Fig. 5 shows two patterns obtained at positions differing by a quarter wave measured from the horns.

The results in Fig. 5 are considered more significant than those depicted in Fig. 3 and 4, since the latter are somewhat vitiated by the proximity of the resonating dipole to large masses of metal. A resonant dipole enclosed within a cavity may be expected to display quite different characteristics from one in free space. A pattern almost identical to the one shown in Fig. 5 was obtained on placing the plasma tube across the wave guide but adjacent to the top, and then using a tuner to adjust the main peak for minimum width and for symmetry.

The multiple reflection and absorption peaks are not predicted by the usual theory of plasma resonance, but their existence and locations are firmly established by the experiments of Rommel and Dattner and are confirmed in the present work.

II. THEORY AND INTERPRETATION

The index of refraction of an unbounded plasma is

$$\eta = c/v_t = [1-(f_0/f)^2]^{\frac{1}{2}}, \tag{1}$$

where v_t is the phase velocity of a transverse electromagnetic wave propagated through the plasma. f_0 is the plasma frequency and is given by

$$f_0^2 = e^2N/4\pi^2\epsilon_0 m. \tag{2}$$

The proper or characteristic frequency of a bounded plasma differs from that of the unbounded plasma by a factor dependent on its geometry, which for a cylindrical plasma is $\sqrt{2}$. Also, its reaction on an incident wave differs from that of the unbounded plasma in that it may resonate after the fashion of an electric dipole displaying external poles. According to Herlofson,[5] diameter of a plasma column becomes large at its resonant frequency with a value of $8\lambda/\pi$ and is independent of column diameter.

Additional modes of oscillation are found by introducing the Bohm and Gross[6] dispersion relationship for plasma waves

$$\omega^2 = w_0^2 + (3kt/m)K^2, \tag{3}$$

where $K=\omega/V_L$ and V_L is the phase velocity. These plasma waves are essentially one-dimensional in character,[7] they are longitudinal resembling compressional sound waves, they travel in the direction of the motion

[5] N. Herlofson, Arkiv Fysik 3 (15), 247 (1951).
[6] D. Bohm and E. P. Gross, Phys. Rev. 75, 1851 (1949).
[7] Lyman Spitzer, *Physics of Highly Ionized Gases* (Interscience Publishers, Inc. New York, 1956), Chap. 4.

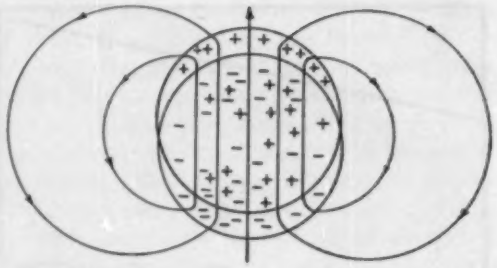

FIG. 6. Charge distribution and restoring field in a cylindrical plasma subject to a transverse electric field.

of the electrons associated with them, and they may be excited by an incident alternating electric field. The rms velocity of electrons at temperature T is given by the expression

$$\bar{V}_e^2 = 3kT/m. \tag{4}$$

The Bohm and Gross dispersion relationship may be written in the form

$$\bar{V}_e/V_L = [1-(f_0/f)^2]^{\frac{1}{2}}, \tag{5}$$

which is also formally the index of refraction for electromagnetic waves given in Eq. (1) although the f's are unlike in the two cases.

The temperature corresponding to the 2537 A line of mercury is of the order of 11 000°K which gives a value of $\bar{V}_e$ approximately 1/400 the speed of light. Thus while the diameters of the discharge tubes used in the experimental work are approximately 1/10 the wavelength of the incident electromagnetic waves, the diameter may be as much as 40 times greater than the wavelength of the plasma waves within the column depending on the operating frequency. The particular mode of plasma oscillation which is excited by an incident electromagnetic wave, for the geometry used, has as its direction of propagation that diameter of the column which is parallel to the electric vector of the applied field. This is also the direction of motion of that class of electrons coupled most closely both to the incident field and the plasma oscillations.

A plasma cylinder, subject to a uniform polarizing field along a diameter, displays an external dipolar field as depicted in Fig. 6 taken from Herlofson's paper. Higher order modes, involving both the setting up of a stationary pattern for the motion of the electrons and the setting up of standing plasma waves within the column, are believed to constitute a mechansim adequate to account for the selective transmission and reflection phenomena observed experimentally. The additional resonances are noted at fixed operating frequency at charge densities lower than that appropriate for the main plasma resonance.

Consider the class of electrons moving with mean speed $\bar{V}_x$ in the direction of propagation of a longitudinal plasma wave taken to be the x direction,

$$E_x = E_0 \cos(\omega t - Kx). \tag{6}$$

Let the electrons with mean speed $\bar{V}_x$, as a result of successive reflections at the plasma sheath taken to be a velocity node,[8] make $2n$ round trips across the plasma in time t_0 so they travel a distance $4nD$ where D is a characteristic length and is approximately the column diameter. Then

$$t_0 = 4nD/\bar{V}_x.$$

In short, we have a stationary pattern which describes the electron motion. Electron temperature of course is related to rms electron speed which is a constant under a set of specified experimental conditions, so t_0 is a definite time interval.

Consider a plasma wave which is the time interval t_0 makes $(2n+1)$ round trips across the plasma column. That is, let

$$t_0 = [2(2n+1)D/V_L].$$

This condition is satisfied only if

$$(\bar{V}_x/V_L) = (2n/2n+1), \tag{7}$$

or if

$$2n/2n+1 = [1-(f_0/f)^2]^{\frac{1}{2}}. \tag{8}$$

If n is integral, in time t_0, the electrons have lagged behind the plasma wave the distance $2D$, and then the cycle is repeated. This happens when the interference-dispersion relationship of Eq. (8) is satisfied, and this relationship identifies a set of characteristic velocity ratios, independent of the distance D, for the simultaneous existence of a stationary pattern of electronic motion and a standing plasma wave associated with the electronic motion.

The interaction between plasma wave and the electrons arises because during the time interval the plasma wave travels $(2n+1)$ wave lengths, the electrons of interest have traveled only $2n$ plasma wavelengths and thus are subjected to an alternating electric field for one complete period. During this time interval, neglecting collisions, the electrons neither gain nor lose momentum on the average but merely exchange energy with the wave. For an extended or unbounded plasma, there are no distinctive velocity ratios for which this exchange takes on a maximum value, but rather the momentum exchange is a monotonically varying function of index of refraction.

In the experimental work, f for the most part is higher than f_0, although the experiments are conducted at fixed frequency, while electron density is varied by controlling the current through the discharge tube. If we assume that electron density is proportional to the current drawn by the tube, the dispersion function given in Eq. (5) in terms of measured quantities becomes

$$m = [1-I/I_0]^{\frac{1}{2}}, \tag{9}$$

where I/I_0 is the normalized current.

Table I shows the observed values of I/I_0 for the various absorption peaks and the predicted values of I/I_0 based on Eq. (8) and (9). The experimental values are read in part from Dattner's Fig. 5, and in part from the impedance spiral in his paper and agree well with the predicted values.

TABLE I. Theoretical and observed values of normalized current through the plasma for resonance peaks of various order.

n	I/I_0 (observed)	I/I_0 (calculated)
0	1.00	1.00
1	0.56	0.56
2	0.36	0.36
3	0.27	0.27
4	0.21	0.20

If we consider the electrons which have made only two instead of $2n$ round trips—a condition adequate to insure a stationary pattern of electron motion—the velocity differential between wave and electron becomes large. In one mode of operation the class of electrons making $2n$ round trips have been subjected to one acceleration-deceleration cycle, while in another mode the electron making only two trips are subjected to $(2n+1)$ such cycles. With the fixed mass of the electron, the response would thus fall off as $1/(2n+1)$ while these responses would also lie quite close to the main peak where $f=f_0$. The weak interactions with these electrons thus would not be distinguishable experimentally from the principal resonance. If the difference between electron velocity and the plasma-wave velocity is low we have the condition for maximum energy interchange between electrons and wave,[9] and at frequencies well removed from f_0. By specifying the set of velocity ratios given in Eq. (8), when n is integral (including zero) we satisfy the condition for cyclic excitation of the plasma and with response and excitation in phase: the condition which characterizes resonance in general. If n is nonintegral, the in-phase character of the interaction between electrons and wave is not satisfied.

When n is zero, phase velocity and plasma wave length become infinite, so irrespective of the value of $\bar{V}_x$, all of the electrons take part in the interaction so the momentum exchange between waves and electrons attains its absolute maximum value. This is the conventional plasma frequency, the resonator displays the properties of a resonating dipole and acts as a low resistance placed across the wave guide.

Whether D represents the diameter of the plasma column is not known from the experiments since it cancels out and thus serves only as a characteristic length common to the path of the electrons and the propagation of the attending plasma wave.

In the wave-guide system in which the reaction of the plasma resonator on an incident field takes place, a resonance is observed for each value of n. Retardation

[8] D. Bohm and E. P. Gross, Phys. Rev. **75**, 992 (1950).

[9] D. Bohm and E. P. Gross, Phys. Rev. **75**, 1864 (1949).

of the microwaves in the plasma does not arise as a result of the travel of a wave through an actual physical path length, but equivalent retardations are realized by successive resonances within the plasma itself. The retardation measured in periods becomes evident if we examine the magnitude and the phase of the reflections from the plasma as revealed by the standing wave measurements.

When n is integral, the electric field vector for the reflected microwave, and arising from plasma resonance, is 180° out of time phase with the electric field of the incident wave, while for nonintegral values of n, the phase angle of the reflection coefficient has values other than 180° and may be read from Dattner's impedance spiral.

Thus a mode spectrum is displayed by a cylindrical plasma and in terms of the ratio of f_n to f_0 we have as an expression for this spectrum

$$f_n/f_0=(2n+1)/(4n+1)^{\frac{1}{2}}. \tag{10}$$

For the lower order members of the spectrum, we have

$$f_n/f_0=1.0,1.34,\ 1.67,\ \text{etc.}$$

These results should be applicable to the reflections from a cylindrical meteor trail with a specified electron density whose diameter is small compared to wavelength, and whose axis is perpendicular to the axis of the beam of a search radar used for meteor detection as well as perpendicular to the electric vector of the incident wave. That is, a series of resonant responses are predicted for the meteor trail.

It is of some interest to calculate the focal length of a large cylindrical plasma when considered as a lens for which the dispersion function or index of refraction, is restricted to integral values of n in Eq. (8). This situation may arise when microwaves are used to study large plasma columns. The focal length F of a cylindrical lens of radius r is given by the relationship,

$$F/r=\eta/2(\eta-1).$$

Under these circumstances

$$F/r=-n. \tag{11}$$

The multiple focal lengths, all negative since the index of refraction is less than unity, are reminiscent of the multiple focal lengths found in optical zone plates.

ACKNOWLEDGMENTS

Acknowledgments particularly are due Irene Petroff and Charles Stelzried for their contributions to the experimental part of the investigation and for helpful discussions.

JOURNAL OF APPLIED PHYSICS VOLUME 31, NUMBER 2 FEBRUARY, 1960

Monoenergetic Neutron Irradiation of Germanium

O. L. Curtis, Jr., and J. W. Cleland
Solid State Division, Oak Ridge National Laboratory, Oak Ridge, Tennessee*
(Received March 2, 1959)

A study has been made on 14-Mev neutron-irradiated germanium, using lifetime, Hall, and resistivity measurements to determine the nature of the radiation-induced defects and to compare the damage with that produced by neutrons from a fission spectrum. The electron removal rate in high-resistivity, n-type material is $\sim 8/\text{cm}^{-3}$ per incident neutron/cm^2, measured at 77°K. Lifetime measurements have been made on n- and p-type material. On the basis of simple recombination theory, assuming no variation of capture probabilities with temperature, the results for n-type material indicate that a recombination level is located 0.32 ev above the valence band near the center of the energy gap. Assuming an introduction rate of recombination centers equal to one-half the electron removal rate in n-type material, the following values of recombination capture cross sections are obtained: $\sigma_n = 2.2\times10^{-17}$ cm^2; $\sigma_p = 6\times10^{-15}$ cm^2, the latter value being correct only within about a factor of two. The ratio of the cross sections, σ_p/σ_n, which is independent of the method of determining the number of recombination centers, is ~ 300, indicating that the recombination centers are negatively charged. The lifetime measurements for p-type germanium are not so readily analyzed. Possible explanations for observed behavior are discussed.

I. INTRODUCTION

PREVIOUS investigations[1,2] have shown that minority carrier lifetime is a useful tool in investigating the nature of energy levels introduced into the forbidden gap of germanium by radiation-produced defects. Lifetime measurements are one of the most sensitive detectors of those levels. Due to this high sensitivity, it has been felt that studies of the recombination centers induced by monoenergetic neutrons would be feasible. In addition to the simplification due to the presence of only one neutron energy, monoenergetic neutron doses can be determined more accurately than doses in a reactor. Results from monoenergetic neutrons should aid in the analysis of reactor irradiation. The most attractive source of monoenergetic neutrons in terms of available dose is the $D(t,n)He^4$ reaction, which produces 14-Mev neutrons.

The flux which can be obtained with available equipment is sufficient to produce changes in the carrier concentration as well as the lifetime. Measurements of the carrier removal rate and effects on lifetime have been made.[3] Hall effect, restivity, and lifetime have been measured as a function of temperature for n- and p-type specimens. By using the results obtained, an attempt has been made to determine the characteristics of the recombination center, i.e., the position of the recombination level in the forbidden gap, and the capture cross sections for electrons and holes.

II. EXPERIMENTAL PROCEDURE

The Biology Division of this laboratory maintains a Cockroft-Walton accelerator for use as a neutron source. At a distance of 7.5 cm from the target an irradiation time of from one to two hr is required to produce 10^{11} neutrons/cm^2 at the sample, with an accuracy in the flux determination of 5–10%. Greater fluxes can be obtained closer to the tube with resultant decrease in the accuracy of flux determinations. The neutron flux is determined independently by two methods: the neutrons are counted directly by a long counter located some distance from the target, and the alpha particles produced simultaneously with the neutrons are detected by a second counter.

The optical shutter used for previous measurements[2] of carrier lifetime transmitted a constant background of light and thus provided a low, steady state excess carrier density. For accurate analysis of the data this is undesirable. This problem has been eliminated by using a xenon discharge tube. An infrared filter was necessary to eliminate an afterglow. The decay time resulting was less than a μsec. The light intensity being very high, it was possible to insert a germanium filter ($\sim$1 mm) to produce a more uniform distribution of excess carriers throughout the sample. These lifetime measurements were made in a dry helium atmosphere. Other experimental details of the lifetime measurements are reported in previous papers.[1,2]

III. RESULTS

A. Carrier Concentration Measurements

Figure 1 shows the conductivities of two n-type samples and one p-type sample of germanium at 77°K as a function of the integrated incident flux of 14 Mev neutrons. The slopes are essentially linear. The incident flux actually decreased somewhat during irradiation as the target was exhausted, and the incident flux also varied slightly as a result of the beam shifting to different portions of the rotating target.

The samples of Fig. 1 were slowly warmed to room temperature after irradiation and were then recooled

* Oak Ridge National Laboratory is operated by Union Carbide Corporation for the U. S. Atomic Energy Commission.

[1] Curtis, Cleland, Crawford, and Pigg, J. Appl. Phys. **28**, 1161 (1957).

[2] Curtis, Cleland, and Crawford, J. Appl. Phys. **29**, 1722 (1958).

[3] O. L. Curtis, Jr., and J. W. Cleland, Bull. Am. Phys. Soc. Ser. II, **4**, 47 (1959).

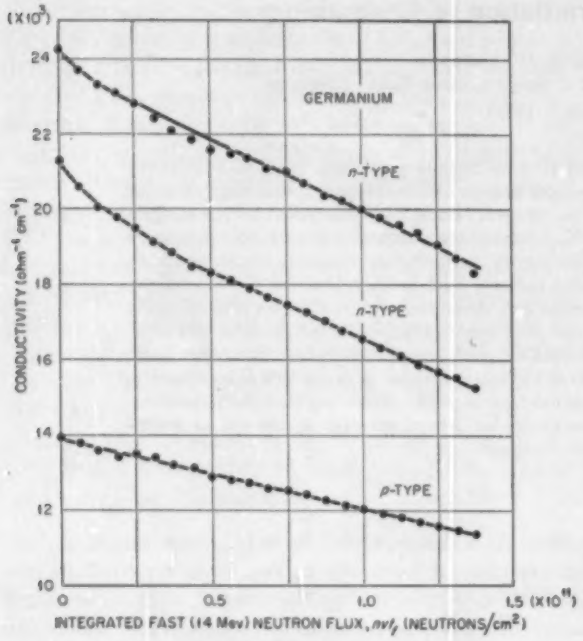

FIG. 1. Conductivity of n- and p-type germanium at -196°C *vs* flux of 14 Mev neutrons.

to 77°K. No evidence of thermal instability of defects or annealing was observed. No dark-conductivity effects due to trapping were observed, which is to be contrasted with low-temperature reactor irradiation results, where extensive minority-carrier trapping effects have been observed.[4] This is presumably due to a lack of ionizing radiation, which is always present in a reactor, and indicates an added advantage in using this type of neutron source. The conductivity of the two n-type specimens returned to the post-irradiation value at 77°K following thermal cycling to room temperature. The p-type sample could not be measured, apparently because of a loose resistivity probe. The two n-type samples were not appreciably photosensitive at 77°K prior to exposure; however they became extremely photosensitive at 77°K as a result of the irradiation, indicating that minority-carrier traps were introduced.

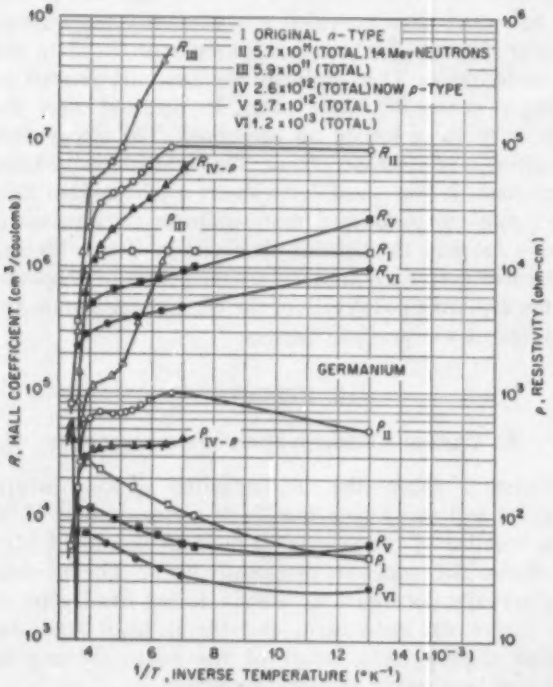

FIG. 2. Hall coefficient and resistivity *vs* reciprocal temperature of initially n-type germanium after successive irradiations of 14 Mev neutrons.

Figure 2 shows the Hall coefficient and resistivity of a typical n-type sample of germanium as a function of the inverse temperature for a series of irradiations. The electron removal rate as determined at 77°K following irradiation at room temperature for this and other samples averages about 8 per incident 14-Mev neutron. This value has only been determined for high-purity material with an initial extrinsic carrier concentration of 2.6×10^{14} electrons cm^{-3} or less, because of the low total flux available. The removal rate may be a function of the initial carrier concentration; however, the small total available flux limits one to high-purity specimens; so the dependence on carrier concentration cannot be determined.

Conversion from n-type to p-type is also indicated in Fig. 2. Continued irradiation increased the hole concentration and decreased the low-temperature slope of the Hall coefficient and resistivity curves. The addition rate of holes as determined at 77°K following irradiation at room temperature for several initially high-resistivity, p-type samples was about 1.5 per incident 14-Mev neutron. In this case the value was only determined for material with an initial extrinsic carrier concentration of $\sim2\times10^{13}$ holes cm^{-3}.

B. Lifetime Measurements

Figure 3 illustrates the dependence of lifetime upon temperature for n-type germanium irradiated with 14 Mev neutrons. Here lifetime is plotted logarithmically *vs* reciprocal temperature. Results are shown for three specimens having room-temperature resistivities of 35, 7, and 2 ohm-cm. These specimens had initial room temperature lifetimes of 1070 μsec, 410 μsec, and 170 μsec, respectively. The slopes of the linear portions of the curves are 0.35 ev, the value being essentially the same for the range of resistivities measured.

Similar data are shown in Fig. 4 for a 14 ohm-cm sample for a series of irradiations. The initial room-temperature lifetime for the specimen was 960 μsec. The irradiations given were 1.05, 2.2, and 4.5×10^{11} total neutrons/cm^2. The observed slopes for the linear

[4] Cleland, Crawford, and Pigg, Phys. Rev. **98**, 1742 (1955).

portions of the curves were essentially the same as for Fig. 3, in this case being listed as 0.36 ev.

Figure 5 is a similar plot for three p-type specimens having room-temperature resistivities of 40, 6.5, and 2 ohm-cm. Here the room-temperature lifetimes before irradiation were 760 μsec, 460 μsec, and 220 μsec, respectively. Slopes of nearly linear portions of the curves are given for comparison.

IV. DISCUSSION

As obtained from Fig. 2 and other data, the removal rate for electrons from high-resistivity, n-type germanium is ~8 per incident neutron.[5] In comparison,

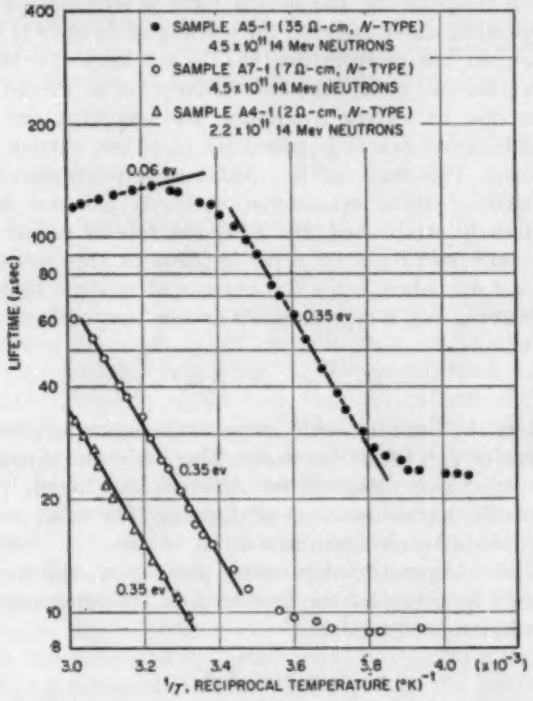

FIG. 3. Minority carrier lifetime τ vs reciprocal temperature $1/T$ for three n-type, 14 Mev neutron-irradiated specimens of germanium.

the removal rate of conduction electrons in n-type germanium has been listed as ~3.2 per incident fast neutron as obtained in a cylindrical uranium doughnut or fission chamber located in Hole 51N of the Oak Ridge National Laboratory Graphite Reactor.[4] Monoenergetic neutrons of 1.7-, 3.2-, and 4.8-Mev energy have been reported[6] to remove 21, 12, and 12 conduction electrons, respectively, at 77°K following irradiation at 77°K. These data, compared with the value of

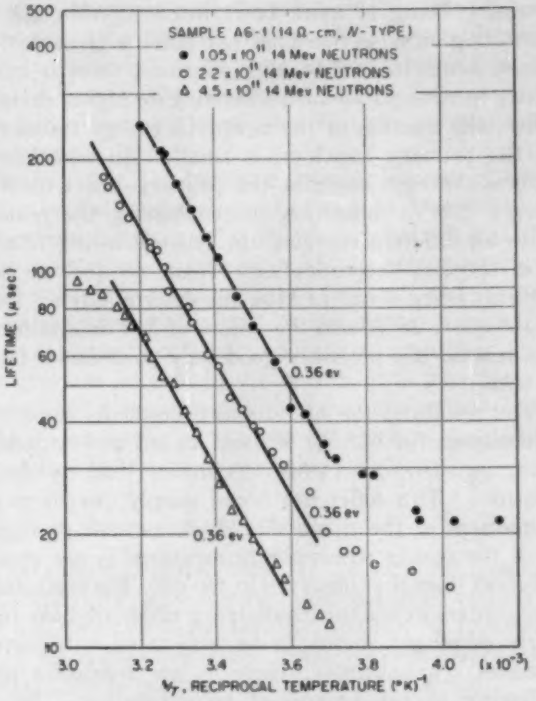

FIG. 4. Minority carrier lifetime τ vs reciprocal temperature $1/T$ for an n-type, 14 Mev neutron-irradiated specimen of germanium.

8 per incident 14 Mev neutrons, would seem to indicate that the removal rate of conduction electrons in n-type germanium is not a sensitive function of the incident neutron energy. However, it is difficult to draw quantitative conclusions regarding the relative effectiveness of primary knock-ons having different energies, this

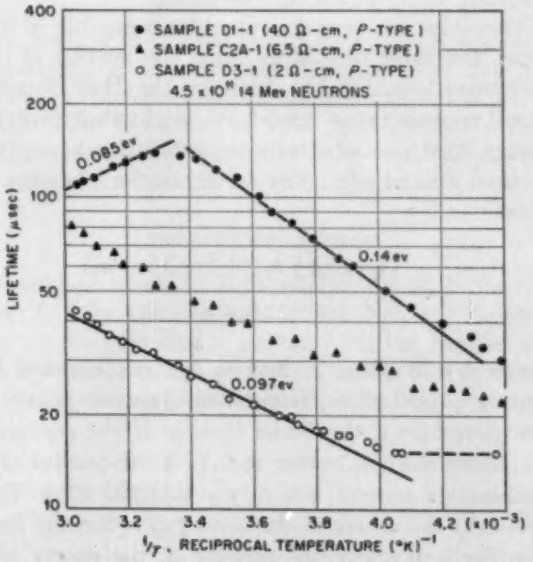

FIG. 5. Minority carrier lifetime τ vs reciprocal temperature $1/T$ for three p-type, 14-Mev neutron-irradiated specimens of germanium.

[5] A. V. Spitsyn and V. S. Vavilov [Zhur. Eksptl. i. Teoret. Fiz. 34, 530 (1958)] have made room-temperature resistivity and lifetime measurements on 14 Mev neutron-irradiated germanium. While their changes in room-temperature lifetime agree well with those we observe, their data indicate an electron removal rate several times that which is reported here.

[6] Ruby, Schupp, and Wolley, Phys. Rev. 111, 1493 (1958).

quantity being of more basic interest. Although the scattering cross section does not differ a great deal for fission neutrons and 14-Mev neutrons, there is a tendency to stronger forward scattering for higher energies. Thus, the fraction of the neutron's energy transferred to the primary knock-on is smaller. In addition, at sufficiently high energies the primary knock-on loses energy due to ionization. In comparing the removal rates for different energies, the greatest source of error is in the flux determinations. While we feel we have 10% accuracy in our 14 Mev flux determinations, Ruby *et al.*[6] quote 25%, and the values of flux determined in the reactor are probably good only to about a factor of two.

The results of the lifetime measurements show that minority-carrier lifetime is about an order of magnitude more sensitive to 14-Mev neutrons than to fission neutrons.[5] This difference is not simply due to an enhancement of the number of displacements produced, since the carrier removal rate measured is not greatly different from that observed in the pile. The recombination centers in reactor-irradiated germanium have been fairly definitely shown to be associated with carrier removal; consequently, there is an indication of a difference in the process of recombination. The dependence of lifetime upon carrier concentration is observed to be different from that for reactor neutron-induced centers. The most striking difference in the two cases is illustrated by Figs. 3 and 4, in which $\ln \tau$ is plotted as a function of $1/T$. The temperature dependence is much stronger than for the case of reactor irradiation, showing an activation energy of about 0.32 ev (correcting for a $T^{\frac{1}{2}}$ term in the density of states function), compared to 0.20 ev previously obtained.[2] It is clear, then, that the nature of the recombination centers is different for the two cases.

This slope has been measured for a number of specimens, the value of 0.32 ev being the average of these determinations. On the basis of the Hall[7]-Shockley-Read[8] recombination model, we might then expect an energy level associated with recombination located 0.32 ev from a band edge. The recombination equation can be written

$$\tau=\frac{(1/c_n)(p+p_1)(+1/c_p)(n+n_1)}{N_t(n+p)}, \tag{1}$$

where τ is lifetime, c_n and c_p are electron and hole capture probabilities, respectively, n_1 and p_1 are the concentrations if the Fermi level is at the position of the recombination center and N_t is the number of recombination centers. For n-type material $n \gg p$. For a level near the center of the band gap, when the Fermi level lies well above the position of the energy level, $p_1 \gg p$, $n \gg n_1$. The recombination equation reduces to

$$\tau=\frac{p_1}{c_n N_t n}+\frac{1}{c_p N_t}. \tag{2}$$

From the first term we see that the temperature dependence measures the position of the recombination center from the valence band; therefore, on the basis of the observed data, the recombination center has an energy level lying 0.32 ev above the valence band. Thus, the position is uniquely determined, in contrast with the usual case,[2] where it is not possible to determine from which band edge the energy level is measured. Aside from the possibility of a variation of c_p with temperature, the second term is temperature independent and represents the leveling off of the τ *vs* $1/T$ curve at low temperature. We do not know N_t. However, we can make the same assumption as we did for the case of reactor irradiation and say that one recombination center is added for each two carriers removed. This may not be a valid assumption since the nature of these recombination levels has not been definitely established. By using the rate of carrier removal herein reported, 8 per incident 14 Mev neutron, $N_t=4\ nvt$, where nvt is the number of incident 14-Mev neutrons. For n-type samples at low temperatures we have

$$\tau=(1/c_p N_t), \quad \text{or} \quad c_p=(1/\tau N_t), \tag{3}$$

where the limiting value for several specimens gives a value of $c_p \sim 1\times10^{-7}$ cm³/sec. There is some variation in the value obtained for different specimens, presumably due to the onset of trapping. The value given is probably correct within a factor of two.

The temperature-dependent portion of the curve should be given by the first term in the foregoing recombination equation,

$$\tau=p_1/c_n N_t n. \tag{4}$$

By knowing n and using the same assumption as in the foregoing to determine N_t, we need only to calculate p_1 to determine c_n. We have

$$p_1=N_v \exp(E_v-E_t/kt). \tag{5}$$

Inserting values for different specimens, we obtain $c_n=2.4\times10^{-9}$ cm³/sec. The error here is estimated to be less than 10%, assuming proper counting of N_t. From the relationship $c=\sigma\langle v\rangle$, where $\langle v\rangle$ is the mean carrier velocity (1.8×10^7 cm/sec for holes and 1.1×10^8 cm/sec for electrons) and σ is the capture cross section, we obtain $\sigma_n=2.2\times10^{-17}$ cm² and $\sigma_p=6\times10^{-15}$ cm². Although these values for cross sections may be in error due to improper counting of the recombination centers, the ratio σ_p/σ_n is independent of the manner in which N_t is determined. The value of this ratio is found to be $\sim$300, indicating that the recombination center is negatively charged.

[7] R. N. Hall, Phys. Rev. **87**, 387 (1952).
[8] W. Shockley and W. T. Read, Phys. Rev. **87**, 835 (1952).

Although the results for n-type germanium are quite readily explained on the basis of a simple, one-level recombination model, the results are more complicated for p-type germanium. This was true before in the case of fission neutron and gamma-irradiated material.[2] Figure 5 shows the variation of lifetime with temperature for three p-type specimens. The results are similar to those observed before and can be explained on the same basis, i.e., a two-level recombination center. There remain two other possibilities that must be considered: a possible variation in capture probability with temperature and the existence of an ~0.1 ev level which acts as a recombination center for sufficiently high hole concentrations.

Suppose that the same recombination center observed in n-type germanium is effective in p-type material; then Eq. (1) gives for p-type germanium, in which the Fermi level lies well below the recombination level,

$$\tau=\frac{1}{c_n N_t}+\frac{n_1}{c_p N_t p}, \tag{6}$$

but $c_p \gg c_n$ and $p \gg n_1$. Therefore,

$$\tau=1/c_n N_t, \tag{7}$$

which should be temperature independent. The dependence observed might be due to a variation in electron capture probability, c_n. We do not think this is likely. However, if it is true, then the analysis of the results for n-type germanium is invalid and the results cannot be analyzed on the basis used. The p-type specimens do not exhibit the temperature behavior expected if the center were located lower in the energy gap, and if the level is higher in the gap (e.g., $E_v-E_t\sim 0.2$ ev) then hole capture must almost certainly be the limiting process. σ_p would, in general, not exhibit the same temperature dependence as σ_n. Therefore, if it were true that the temperature behavior in p-type material is due to a variation of σ_n with temperature, the position of the energy level and σ_p could not be determined from present data. In this case it would be necessary, however, that σ_p vary in the same sense as σ_n.

The alternate possibility is that an energy level located ~0.1 ev above the valence band becomes the recombination center as the sample becomes increasingly more p-type. Through the high-resistivity range the 0.32 ev level could share in the recombination process. The data of Fig. 5 could be explained in this manner, as could the dependence of lifetime on carrier concentration. Furthermore, Hall measurements (Fig. 2) indicate the existence of such a shallow level. Using 0.1 ev as the energy level responsible for recombination predicts, however, an electron capture cross section of $\sim 3\times 10^{-13}$ cm^2. This extremely large value in itself casts some doubt as to whether this process might be occurring.

Finally, since the behavior in p-type material is so similar for the case of fission neutron, 14-Mev neutron, and gamma irradiation,[2] it might be expected that the same recombination process might be occurring in all three cases. The data for fission neutron and gamma irradiation, however, indicated that neither a variation in cross section nor recombination at a shallow level was sufficient to explain the results. It is felt then, as before, that a more complicated recombination center probably consisting of two coupled levels is most likely responsible for the observed behavior.

V. SUMMARY

The carrier removal rate for 14-Mev neutrons in high-resistivity, n-type germanium has been measured and found to be ~8 per incident neutron (as measured at 77°K), indicating that about four vacancy-interstitial pairs are produced per incident neutron.

On the basis of the Hall[7] Shockley-Read[8] recombination theory and neglecting any variation of capture probabilities with temperature, the recombination process in n-type germanium may be explained on the basis of a recombination level located 0.32 ev from the valence band. Assuming the number of recombination centers to be given by one-half the number of carriers removed (this assumption may not be valid), we obtain $\sigma_n=2.2\times 10^{-17}$ cm^2, $\sigma_p=6\times 10^{-15}$ cm^2. The ratio σ_p/σ_n, which is independent of the manner in which N_t is determined, is ~300, indicating the center to be negatively charged.

It is possible to analyze results for p-type germanium by including either a strong dependence of capture probability on temperature or recombination at a shallow level. However, it seems more probable that the behavior is due to a recombination center having two coupled levels.[2]

ACKNOWLEDGMENTS

We wish to thank M. L. Randolph and D. L. Parrish of the Biology Division, Oak Ridge National Laboratory, for their generosity in supplying the irradiations used in this work. We especially thank J. H. Crawford, Jr., for his encouragement and interest.

Microwave Determination of Plasma Density Profiles*

CHARLES B. WHARTON AND DONALD M. SLAGER†
Lawrence Radiation Laboratory, University of California, Livermore, California
(Received April 30, 1959)

A method for the rapid determination of the average electron density and of the spatial electron density distribution in plasmas is presented. The technique employed permits time-resolved measurements over a wide range of electron densities, introducing little or no perturbation into the gaseous discharge. The quantities measured by the described techniques have been correlated previously with other plasma measurements and show reasonably good agreement.

INTRODUCTION

THE propagation of an electromagnetic wave in a plasma is characterized by a complex propagation "constant," $\gamma=\alpha+j\beta$, which is determined by the electron density, temperature, average collision frequency and the external magnetic field.[1-3] In many plasma experiments[4] the collision frequency is negligibly small. If, in addition, the wave propagation can be either transformed to or approximated by a plane wave, with its electric field parallel to the external magnetic field, the low-temperature propagation coefficient can be expressed simply as

$$\beta=\frac{\omega}{c}\left(1-\frac{\omega_p^2}{\omega^2}\right)^{\frac{1}{2}}, \tag{1}$$

where ω=microwave radian frequency, ω_p=plasma radian frequency$=(\rho e^2/m_e\epsilon_0)^{\frac{1}{2}}$, ρ=electron density, electrons per meter[3] m_e=electron mass, 9.11×10^{-31} kg, e=electron charge, 1.6×10^{-19} coulombs or

$$f_p=(\omega_p/2\pi)=8.97\times10^3 n^{\frac{1}{2}}, \tag{2}$$

where n=electrons per cm^3.

The wave propagates with a phase velocity greater than c when $\omega_p/\omega<1$ and is cut off when $\omega_p/\omega>1$.

UNIFORM DENSITY CASE

Figure 1 sketches the plane wave geometry in a plasma slab. The d dimension is assumed large compared to a wavelength. Any external magnetic field lies in the y direction.

To determine the electron density in such an idealized uniform plasma, the sample is placed in one arm of a microwave interferometer[1,5] (Fig. 2) and the phase change due to insertion is recorded.

For example, many laboratory plasma experiments deal with transient plasmas, whose density rises rapidly from zero to a fairly high value and then decays slowly away, as sketched in Fig. 3. If the microwave frequency is such that $\omega_p/\omega>1$ at peak density, the interferometer response will resemble that at the bottom of Fig. 3.

The successive maxima and minima are caused by the interferences of the waves from the two paths combining at the comparison point, much as in an optical interferometer. By analogy these periodic variations are called "fringes."

Since the plasma density is uniform over the test path, the calculation of the electron density is straightforward; one simply counts fringes and works backwards. The phase change due to introducing plasma into the path is

$$\begin{aligned}\Delta\Phi&=\Phi_0-\Phi\\&=\beta_0 d-\beta d\\&=\frac{\omega}{c}d\left[1-\left(1-\frac{\omega_p^2}{\omega^2}\right)^{\frac{1}{2}}\right]\\&=\frac{\omega}{c}d\left[1-\left(1-\frac{n}{n_c}\right)^{\frac{1}{2}}\right],\end{aligned} \tag{3}$$

where n_c is the density necessary to reach cutoff. The electron density is then

$$n=n_c\left[\frac{2Nc}{fd}-\frac{N^2c^2}{f^2d^2}\right]=n_c\left[2\frac{N}{N_{c0}}-\left(\frac{N}{N_{c0}}\right)^2\right], \tag{4}$$

where N is the number (whole or fractional) of fringes

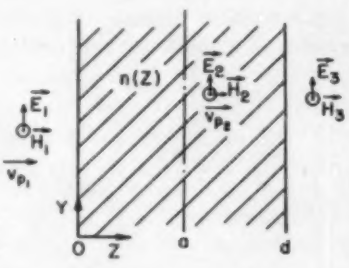

FIG. 1. Plane wave incident on a plasma slab of thickness d.

* Work done under the auspices of the U. S. Atomic Energy Commission.
† Los Alamos Scientific Laboratory, Los Alamos, New Mexico.
[1] C. B. Wharton, University of California Radiation Laboratory Rept. UCRL-4836 Rev. (September, 1957).
[2] L. Spitzer, *Physics of Fully Ionized Gases* (Interscience Publishers, Inc., New York, 1956).
[3] J. Drummond, Stanford Research Institute Report LTR 014-57 (1957).
[4] R. F. Post, Proc. Inst. Radio Engrs. **45**, 134-160 (1957); Revs. Modern Phys. **29**, 338 (1956).
[5] R. F. Whitmer, Phys. Rev. **104**, 572-575 (1956).

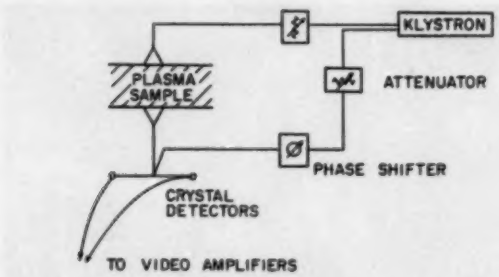

FIG. 2. Microwave interferometer circuit, with plasma in one leg.

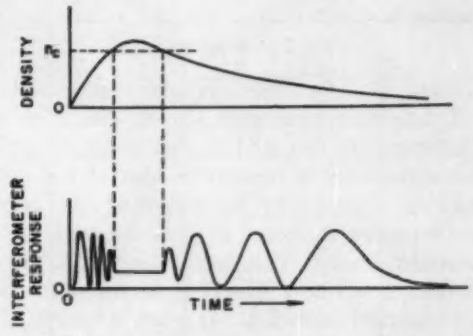

FIG. 3. Interferometer response to a transient plasma.

counted. Table I indicates the range of measurable densities as a function of frequency and path length d.

NONUNIFORM DENSITY CASE

In general, however, the electron density will not be uniform throughout the discharge. Each discharge configuration will have its own particular spatial distribution, in both density and temperature. It is the density distribution function and the maximum density n_0 which we shall attempt to determine by our methods.

The phase change when plasma (which has any arbitrary density distribution that is slowly varying compared to wavelength) is introduced into the test path will be (see Figs. 1 and 2)

$$\Delta\Phi=\Phi_0-\Phi$$
$$=\frac{\omega}{c}\left[d-\int_0^d\left(1-\frac{n(Z)}{n_c}\right)^{\frac{1}{2}}dZ\right], \tag{5}$$

where $n(Z)$ is the density distribution function.

The integration of Eq. (5) is, in general, difficult. For example,

$$\text{Cosine:}\quad \Phi'=\Phi\frac{c}{\omega}=\frac{1}{d}\int_0^d\left[1-\frac{n_0}{n_c}\cos\left(\frac{\pi}{2}\frac{Z-a}{a}\right)\right]^{\frac{1}{2}}dZ. \tag{6a}$$

$$\text{Cosine squared:}\quad =\frac{1}{d}\int_0^d\left[1-\frac{n_0}{n_c}\cos^2\left(\frac{\pi}{2}\frac{Z-a}{a}\right)\right]^{\frac{1}{2}}dZ. \tag{6b}$$

$$\text{Bessel:}\quad =\frac{1}{d}\int_0^d\left[1-\frac{n_0}{n_c}J_0\left(K\frac{Z-a}{a}\right)\right]^{\frac{1}{2}}dZ. \tag{6c}$$

$$\text{Parabolic:}\quad =\frac{1}{d}\int_0^d\left[1-\frac{n_0}{n_c}\frac{d^2-4(Z-a)^2}{d^2}\right]^{\frac{1}{2}}dZ. \tag{6d}$$

$$\text{Gaussian:}\quad =\frac{1}{d}\int_0^d\left[1-\frac{n_0}{n_c}\exp\{-[(Z-a)/a]^2\}\right]^{\frac{1}{2}}dZ. \tag{6e}$$

$$\text{Triangular:}\quad =\frac{1}{d}\int_0^d\left[1-\frac{n_0}{n_c}\left(1-\frac{|Z-a|}{a}\right)\right]^{\frac{1}{2}}dZ. \tag{6f}$$

We have carried through some of these integrations and have plotted the results in Fig. 4.

From experimental observations of various plasma configurations it has been found that a combination of triangular and uniform distributions, making up a trapezoidal distribution, fits a surprisingly large number of cases. Figure 5 sketches the trapezoidal configuration.

The phase term for this distribution is simply the sum of the proportionate contributions from the triangular and rectangular distributions.

$$\Phi=2\frac{\omega}{c}\int_0^b\left[1-\frac{n_0}{n_c}\left(\frac{Z}{b}\right)^{\frac{1}{2}}\right]dZ+\frac{\omega}{c}\int_b^c\left(1-\frac{n_0}{n_c}\right)^{\frac{1}{2}}dZ$$
$$=\frac{\omega}{c}\frac{4b}{3}\frac{n_c}{n_0}\left[1-\left(1-\frac{n_0}{n_c}\right)^{\frac{3}{2}}\right]+\frac{\omega}{c}(c-b)\left(1-\frac{n_0}{n_c}\right)^{\frac{1}{2}}. \tag{7}$$

The phase shift due to inserting a plasma with this

distribution is

$$\Delta\Phi=\Phi_0-\Phi \text{ as in (5).}$$

Equation (7) for the "regular trapezoid" case ($b=d/3$) has been plotted in Fig. 4. The close coincidence between this case and the cosine case is apparent.

In an experiment a reasonable idea of the distribution may be deduced by the following data analysis: 1. The frequency is chosen so that the path is cut off at maximum density. This establishes n_0. 2. The number of fringes actually observed is compared to the number expected from Eq. (4) when $n=n_c$. 3. Choose from Fig. 5 the distribution curve that most closely matches the total phase shift for $n_0=n_c$. 4. The maximum density at any other phase shift then follows the distribution curve chosen, unless the experimental distribution changes during decay. 5. Additional checks on the distribution should be obtained by using several frequencies simultaneously, so that cutoff is reached at different times.

Figure 6 shows the response of a 25-kMc interferometer to a transient plasma. Twelve fringes are present. The dimension d was 12 in. or 25λ, giving a Φ' of 0.53 in Fig. 4. An additional measurement, taken at 35 kmc, fits the cosine distribution curve fairly well. The amplitude decrease in the vicinity of cutoff is due to a combination of scattering and absorption. The vertical assymetry is due to the square-law response of the crystal detector.

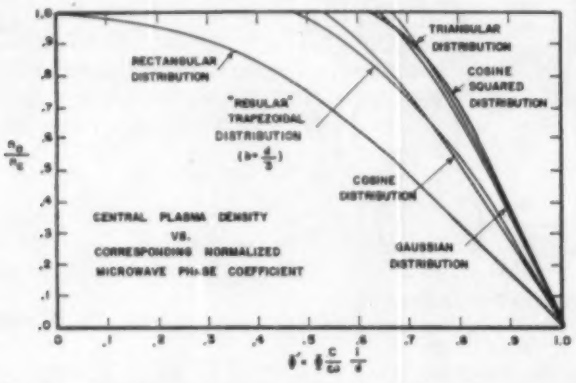

Fig. 4. Central plasma density as a function of the observed microwave normalized phase shift, for several spatial distributions.

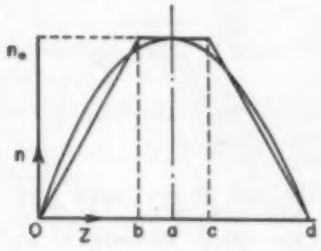

Fig. 5. General symmetrical trapezoidal distribution with cosine superimposed.

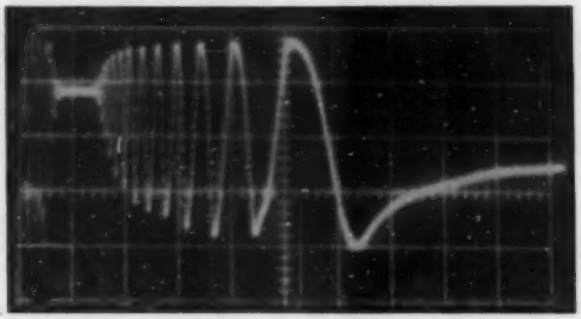

Fig. 6. Oscilloscope record of a microwave interferometer response to a transient plasma.

Table I. Measurable densities as a function of frequency and path length.

Frequency in kmc	Maximum density of electrons/cc (cutoff)	Minimum detectable density ($\pi/10$ phase shift) electrons/cc 1 in. path	3 in. path	6 in. path	9 in. path
2.5	7.7×10^{10}	3.7×10^{10}	1.2×10^{10}	6.2×10^{9}	4.1×10^{9}
10	1.2×10^{12}	1.5×10^{11}	5×10^{10}	2.5×10^{10}	1.6×10^{10}
25	7.7×10^{12}	3.7×10^{11}	1.2×10^{11}	6.2×10^{10}	4.1×10^{10}
35	1.5×10^{13}	5.2×10^{11}	1.7×10^{11}	8.7×10^{10}	5.8×10^{10}
50	3.1×10^{13}	7.4×10^{11}	2.5×10^{11}	1.2×10^{11}	8.2×10^{10}
70	6.1×10^{13}	10^{12}	3.5×10^{11}	1.7×10^{11}	1.2×10^{11}
100	1.2×10^{14}	1.5×10^{12}	5×10^{11}	2.5×10^{11}	1.6×10^{11}
150	2.8×10^{14}	2.2×10^{12}	7.4×10^{11}	3.7×10^{11}	2.5×10^{11}
250	7.7×10^{14}	3.7×10^{12}	1.2×10^{12}	6.2×10^{11}	4.1×10^{11}

Φ' is obtained from the relation

$$\Phi'=1-\frac{Nc}{fd}$$

where units are as defined in the foregoing.

CONCLUSIONS

This data analysis is at best semiquantitative. The technique is based upon an approximation to a slab geometry. The finite dimensions of an experimental plasma may permit scattering around it, which limits the interpretability of results. Also, there is an ambiguity in that if the discharge were hollow this data analysis would be badly in error, since all of the region inside the shell which is at cutoff would be inaccessible.

In spite of the shortcomings, however, the method permits nonperturbing, rapid diagnostics on a wide variety of discharge configurations, and in many cases affords by far the most meaningful measurement technique.

Letters to the Editor

Improvement of Semiconductor Surfaces by Low Melting Glasses, Possibly Functioning as Ion Getters

S. S. Flaschen, A. David Pearson, and I. L. Kalnins
Bell Telephone Laboratories, Inc., Murray Hill, New Jersey
(Received August 17, 1959)

It has been suggested by Bardeen[1] and subsequently demonstrated by a number of workers that the presence of adsorbed ionic contaminants at semiconductor surfaces can strongly affect surface state energy levels and properties of semiconductor devices dependent thereon. In the commonly employed etching and water-washing techniques of cleaning semiconductor surfaces, concentrations of residual contaminants of the order of 10^{14}/cm^2 have been indicated.[2] The drift of these contaminants under the influence of high fringing electrostatic fields is suspected to be a major cause of instability of semiconductor properties, and the catastrophic deterioration observed in the presence of a dissociating solvent such as water. This letter is a preliminary report of the effects observed in the treatment of semiconductor surfaces with chemical systems designed to decrease the activity and/or the concentrations of these residual surface contaminants. In this work, we have been concerned with a study of the effectiveness of recently developed low-melting sulfide and iodide inorganic glasses.[3]

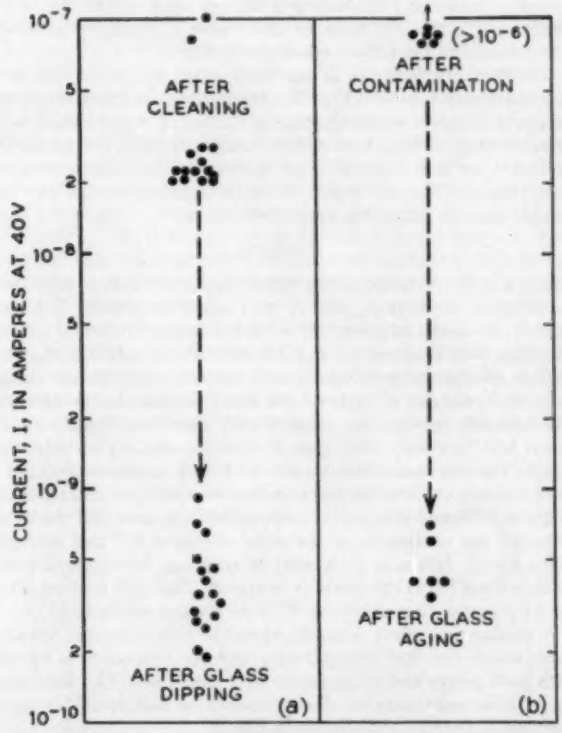

FIG. 1. (a) Low melting glass processing of 56 v $n+p$ 0.035 in. diam Si diodes. "After cleaning" refers to processing by a modified CP-4 etch followed by deionized water rinse cleaning, drying, and measurement of reverse current at 40 v under dark vacuum. "After glass dipping" refers to reverse currents obtained following a 90 sec, 320°C, dip coating of the cleaned diodes in a 24% As, 67% S, 9% I glass melt. (b) Study of glass treatment effects on surface contaminated diodes. Following exposure of cleaned diodes to organic & inorganic vapor contaminants, reverse currents obtained are in excess of 1 μamp at 40 v. "After glass aging" refers to currents following dip coating of the contaminated diodes and aging at 275°C for 64 hr.

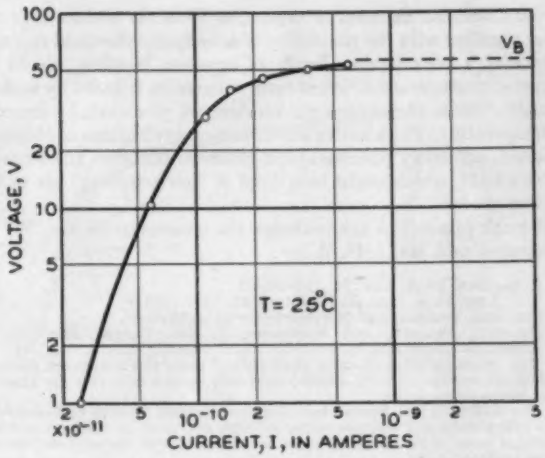

FIG. 2. Reverse V-I characteristic of a low melting glass processed $n+p$ 0.035 in. diam diffused junction Si diode. Measurement temperature 25°C.

The semiconductor test units of this report were 56 v breakdown $n+p$ diffused junction silicon diodes, consisting of silicon disks 0.035 in. diam with gold thermal-compression bonded leads. The diodes were treated with a modified CP-4 etch followed by deionized water cleaning. After etching and washing, the reverse currents were measured with the units in a dark evacuated chamber. They were then immersed into high purity glass melts prepared from the end members in the ternary systems AS-S-I[3] or As-S-T[4] contained in clean fused silica crucibles. Processing temperatures ranged from 250°C to 350°C for periods of time of from 30 to 90 sec. The units were next withdrawn from the melts in the form of glass coated test vehicles[5] or allowed to cool directly within the crucibles for subsequent high temperature studies. Precautions were taken both in synthesis and subsequent high temperature exposure, or use of the glass to avoid alkali, silver, or copper contamination. Free circulation of air over the molten glasses was minimized. In these studies, the concentration of the cationic contaminants was maintained below 5 ppm, as determined spectroscopically.

The reverse currents of a group of etched and washed units, measured at approximately 80% of the breakdown voltage in a dark vacuum chamber are indicated at the top of Fig. 1(a). Coating the units with glass† resulted in a reduction in these currents of about two orders of magnitude to the extremely low values shown at the bottom of Fig. 1(a). To date, some 200 test units have been studied which exhibited reductions in reverse currents of this general magnitude after coating with a variety of low-melting glass compositions. Figure 2 shows the reverse current-voltage characteristic of a representative unit from the group depicted in Fig. 1(a).

In Fig. 1(b), a group of six units following etching and aqueous cleaning were exposed to a mixture of deleterious vapors. The reverse currents following exposure to contamination and measured under dry conditions were in excess of 10^{-6} amp with breakdown voltages erratic over the range 40–50 v. Reverse currents were reduced to the level of 10^{-8} to 10^{-7} amp and breakdown voltages were improved by immersion in a glass melt for 90 sec. Aging of the diodes in the glass melts at 275°C resulted in a further reduction of currents to levels [Fig. 1(b)] comparable with those of the noncontaminated diodes and attainment of full 56 v breakdowns. In screening studies of other silicon and germanium structures including $n+p$ and $p+n$ diodes of both types, no evidence has been found for reactions with the "fast" surface states.

The authors believe that the low levels of reverse currents observed for glass treated units can be explained by the removal of contaminants from the semiconductor surface and/or the deactivation of ionic and other contaminants by the glass environ-

ment. Chemical diffusion of impurities from the surface into the glass together with the possibility of subsequent chemical reaction involving a considerable degree of covalent bonding, would be expected to cause reduction of reverse currents induced by surface charges. These phenomena are accelerated, of course, by increase in temperature. The kinetics and relative contributions of chemical reaction, solubility processes, and chemical diffusion gradients to these effects, which might be a form of "ion gettering" are under further study.

We are pleased to acknowledge the assistance of Mr. W. R. Northover and Mr. J. H. Wiley.

[1] J. Bardeen, Phys. Rev. 71, 717 (1947).
[2] J. T. Law, Proc. Inst. Radio Engrs. 42, 1367 (1954).
[3] Flaschen, Pearson, and Northover (to be published).
[4] Flaschen, Pearson, and Northover, J. Am. Ceram. Soc. (to be published).

* The characteristics of such glass coated units remain stable through 8000 hours storage at 98% relative humidity, which indicates the absence of moisture permeation.

† The sulfide-iodide glasses, including the visually opaque compositions, show substantial transmission in the infrared and must be further coated or protected from light during measurements, because of the photosensitivity of the enclosed units.

High-Power Effects in Ferrimagnetic Resonance*

P. E. Seiden, *Lockheed Missiles and Space Division, Palo Alto, California, and Microwave Laboratory, W. W. Hansen Laboratories of Physics, Stanford University, Stanford, California*

AND

H. J. Shaw, *Microwave Laboratory, W. W. Hansen Laboratories of Physics, Stanford University, Stanford, California*

(Received May 1, 1959)

THE premature saturation of a ferrimagnetic sample under resonance conditions was observed by Damon,[1] and by Bloembergen and Wang,[2] and was interpreted by Suhl[3] as a result arising from the growth of specific spin waves from their thermal level. In performing further experiments at high powers in yttrium iron garnet[4] (YIG), we have observed small, sharp declines in susceptibility superposed upon the continuous decline observed by Damon, and by Bloembergen and Wang.

The experimental measurements yield the reflection coefficient by a comparison of the incident power and the power reflected from a cavity containing the sample, as devised by Artman and Tannenwald[5] (with certain modifications made necessary by use of a pulsed source). Figure 1 shows a moving film record taken on a polycrystalline sphere of a YIG sample. Point 1 is the onset of the Suhl instability, which is usually determined by direct oscilloscope measurement, since the decline in the susceptibility is very gradual. Point 2 shows a sharp change in reflected power, demonstrating a change in the susceptibility of the sample. Point 3 shows a much smaller discontinuity in reflected power occurring at a higher power level. A number of these discontinuities have been found, as many as nine occurring for one sample. The size of the discontinuity and the number observable are roughly inversely proportional to the line width of the sample.

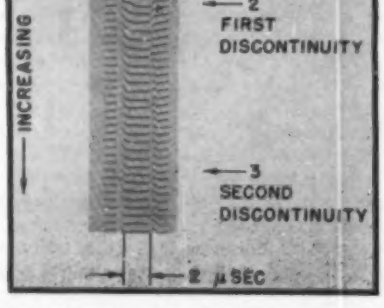

FIG. 1. Pulses of reflected power minus incident power, at ferrimagnetic resonance, recorded by a moving film oscilloscope camera. Power increases by 0.1 db between pulses as one goes down the film. Measurements are made in the central flat portion of the pulse. Frequency modulation on the rise and fall of the pulse causes the irregular regions seen on each edge of the pulse.

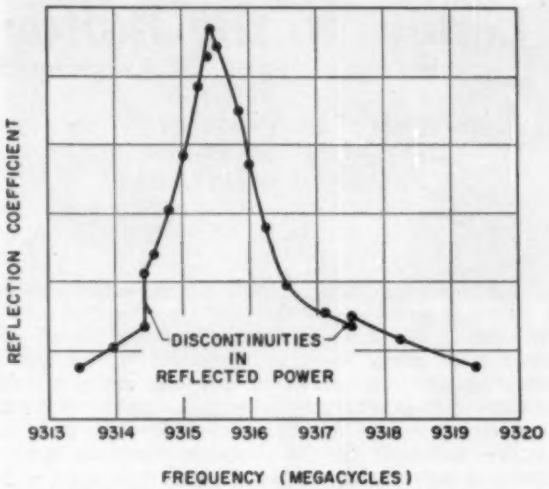

FIG. 2. Reflection coefficient of the cavity as a function of frequency, above the first discontinuity, at constant power level and dc magnetic field.

The first discontinuity is observed where the susceptibility is approximately 0.6 to 0.7 of the small-signal susceptibility, and occurs in a region where the rate of change of susceptibility with power is large. The square of the rf magnetic field (h^2) across the sample is between 5 and 20 times that required for the onset of the Suhl decline. The occurrence of the discontinuities for any one sample seem to follow the empirical relation

$$h^2 = Ke^{n/c},$$

where n is the number of the discontinuity when it is numbered in order of occurrence, and K and c are constants. The constant c, for most samples which have a large number of discontinuities, falls between 1.2 and 3.2. Green[6] has recently reported similar effects in gadolinium and yttrium iron garnet single crystals. A number of higher order discontinuities show the opposite behavior in that the susceptibility increases slightly as the power level is raised. This type of discontinuity is generally very small. The discontinuities shown in Fig. 1 were observed in a cavity with a Q_0 of 8000. The experiment was repeated in cavities of Q's of 3000 and 900, and the discontinuities were still observed, although not necessarily at the same values of h_{rf}^2 and susceptibility for all values of Q. A shift of resonant field toward lower fields is observed as the power is increased. This shift is about 80 oe for a polycrystalline sphere of YIG with a line width of 43 oe.

A similar new effect is noted when the power level is set at a point above the first discontinuity and the frequency is varied, with both power and dc magnetic field kept fixed. The resonance curve observed contains discontinuities in susceptibility as a function of frequency as shown in Fig. 2.

A final effect observed is the occurance of a region of instability in reflected power just after the first discontinuity. If the power level is set in this region, the level of reflected power varies from pulse to pulse. This effect appears to be due to the coupling between the ferroresonant sample and the cavity, in the region of large change in susceptibility with respect to power level. For example, a slight disturbance of the direction of the magnetization which, say, increases the precession angle, will result in a decreased

susceptibility and an increased Q for the cavity (the cavity is always operated undercoupled), accompanied by an increase in the magnetic field in the cavity. This greater field will in turn augment the initial disturbance of the precession angle, and if this effect is greater than the initial disturbance the magnetization will be unstable. The situation is similar, of course, for an initial decrease in precession angle. This effect is not the same as that reported by Weiss[7] for disks, since the experiments are done on spheres and the resonance curve does not fold over in this case. Weiss actually gets an oscillation while in this case the system is trying to achieve a stable state. At lower Q's the transient state dies out rapidly, and instead of a region of instability from pulse to pulse, we see just two states corresponding to the boundaries of the unstable region.

* This research was supported in part by the U. S. Air Force under Contract AF49(638)-415 and in part by Lockheed Missiles and Space Division, monitored by the Air Force Office of Scientific Research of the Air Research and Development Command.

[1] R. W. Damon, Revs. Modern Phys. 25, 239 (1953).
[2] N. Bloembergen and S. Wang, Phys. Rev. 93, 72 (1954).
[3] H. Suhl, J. Phys. Chem. Solids 1, 209 (1957).
[4] The YIG samples were supplied by the Solid State Physics and Technical Ceramics Sections of Lockheed Missiles and Space Division.
[5] J. O. Artman and P. E. Tannenwald, J. Appl. Phys. 26, 1124 (1955).
[6] J. J. Green, Bull. Am. Phys. Soc. Ser. II, 4, 177 (1959).
[7] M. T. Weiss, Phys. Rev. Letters 1, 239 (1958).

Flow of Magnesium Oxide Single Crystals

D. S. Thompson and J. P. Roberts
Ceramics Division, Houldsworth School of Applied Science, University of Leeds, England
(Received August 28, 1959)

A NUMBER of investigations of the room-temperature flow properties of magnesium oxide single crystals have been reported.[1-5] We shall describe a study of the effect of temperature on the plasticity of these crystals, and in particular the effect on the yield stress.

Bars (~2.5×0.25×0.025 cm) were cleaved {100} by hand from crystals (~99.8% MgO) grown from the melt in the industrial process for making fused magnesia. They were stressed in bend under four-point loading (stressing rate in the outer fibers 2–8×10^5 dyne cm^{-2} sec^{-1}), deflection being measured by microscope. The apparatus was constructed in sintered alumina and included a small platinum furnace. Low temperatures were obtained by cooling with liquid nitrogen.

The effect of temperature on the stress-strain relation is shown typically in Fig. 1. Figure 2 shows that bars cleaved from different crystals and tested at the same temperature gave markedly different stress-strain curves. However, the curves for bars from the same parent crystal were reproducible, as is shown for six bars from crystal No. 2.

Typical variation of yield stress (σ) with temperature (T) is shown in Fig. 3. The results were compared with relations predicted by theories of yielding, but no single such relation satisfactorily described the results for every crystal studied. Each of the relations

$$\sigma=\sigma_0 e^{-aT} \tag{1}$$

$$\sigma=\sigma'/T+c \tag{2}$$

$$\sigma=\sigma'' e^{Q/kT}, \tag{3}$$

where σ, a_0, σ', c, σ'', Q, and k are constants, fitted some of the data.

Equation (1) was derived by Petch,[6] who considered the variation of the Peierls-Nabarro stress over a limited temperature range, assuming dislocation width to vary linearly with temperature. This relation is fitted to a set of results in Fig. 3 (continuous line).

Seeger's consideration of the resistance to motion of a dislocation cutting through a forest of dislocations[7] led to a linear relation between yield stress and temperature but none of the present results fitted this. However, Friedel[8] has modified Seeger's theory by taking into account the variation of "tree" spacing with the applied stress. He arrived at a hyperbolic dependence of yield stress on temperature [cf. Eq. (2) and the broken line in Fig. 3].

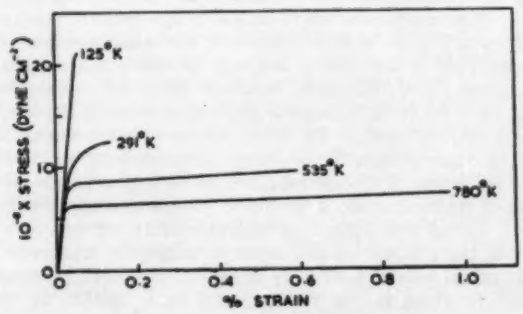

FIG. 1. The effect of temperature on the stress-strain behavior of a magnesia crystal.

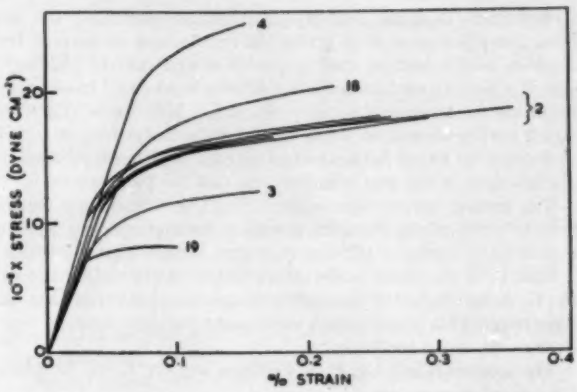

FIG. 2. The room-temperature behavior of specimens cleaved from five different parent crystals. The reproducibility of the stress-strain curve for crystal No. 2 is also shown.

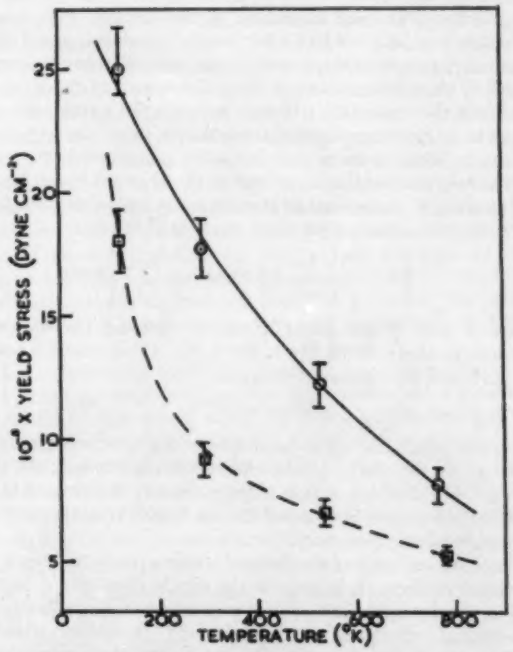

FIG. 3. The effect of temperature on the yield stress of specimens from two crystals.

Equation (2), again, and Eq. (3) (these are essentially the same from the point of view of fitting the results) can be derived from theories which assume that impurity atoms control yielding[8,10]. But it is hard to see how impurity atmospheres could have a major influence in determining the yield stress here, since the stress-strain curves showed no sharp yield point and, further, no correlation could be found between the contents of either iron or silicon (believed to be the major impurities) and the yield stress.

The present results thus suggest that the temperature-dependence of yield stress (and its variation among crystals) is better explained in terms of substructure than simple impurity locking.

Change of the room-temperature plastic strain at fracture with the time elapsing after cleavage of magnesium oxide bars has been reported.[1,2] This phenomenon was sought but not observed over a time range of 0.5 to 500 hr.

The authors thank Dr. P. A. Feltham and Dr. R. W. Armstrong for helpful discussions.

[1] Gorum, Parker, and Pask, J. Am. Ceram. Soc. **41**, 161 (1958).
[2] Lad, Stearns, and Del Duca, Acta Met. **6**, 610 (1958).
[3] P. J. Anderson and F. P. Clarke (private communication, 1958).
[4] E. Sommerfeldt, Zentr. Mineral. Geol. u. Paläontol. **7**, 212 (1907).
[5] O. Müggе, Neues Jahrb. Mineral. Geol. u. Paläontol. 24 (1920).
[6] N. J. Petch, Phil. Mag. **3**, 1089 (1958).
[7] A. Seeger, "Dislocations and mechanical properties of crystals," in *Lake Placid Conference, September 6–8, 1956*, edited by Fisher, Johnston, Thomson, and Vreeland (John Wiley & Sons, Inc., New York, 1958).
[8] J. Friedel, see reference 7.
[9] A. H. Cottrell and B. A. Bilby, Proc. Phys. Soc. (London) **A62**, 49 (1949).
[10] J. C. Fisher, Trans. Am. Soc. Metals **47**, 451 (1955).

Thermal Stress Analysis and Grueneisen's Relation

A. M. FREUDENTHAL
Columbia University, New York, New York
(Received September 10, 1959)

THERMAL stress analysis in the elastic or the inelastic continuum is usually performed under the assumption of elastic compressibility of the medium expressed by the equation,

$$e-3\alpha T=p/K=3p(1-2\nu)/E, \tag{1}$$

or its time derivative, where $e=\epsilon_{kk}$, $p=\frac{1}{3}\sigma_{kk}$, α denotes the coefficient of linear thermal expansion, K the (elastic) bulk modulus, ν Poisson's ratio, $E=3K(1-2\nu)$ Hooke's modulus, and $T(x_i)$ the local temperature with respect to a uniform reference temperature at which the medium is stress-free. The combination of this relation with the respective relations between the stress- and strain-deviations, the compatibility conditions, and the equilibrium equations, using a stress-function ϕ for plane problems, leads to well-known differential equations of the thermal stress problem; for elastically compressible homogeneous viscoelastic media, for instance, this equation for plane stress is of the form[1]

$$\left[\mathcal{P}+\frac{(1-2\nu)}{2(1+\nu)}\mathcal{Q}\right]\nabla^4\phi=-\frac{3\alpha E}{2(1+\nu)}\mathcal{Q}\nabla^2T \tag{2}$$

where $\mathcal{P}$ and $\mathcal{Q}$ are linear operators defining the viscoelastic response in shear. With $\mathcal{P}=1$, $\mathcal{Q}=1$, Eq. (2) is transformed into the standard thermoelastic equation:

$$\nabla^4\phi=-\alpha E\nabla^2T. \tag{3}$$

For plane strain the right-hand side of Eq. (3) is multiplied by $1/(1-\nu)$. In the elastic-plastic thermal stress problem, the stress-intensity in the plastic region is also primarily determined by that in the elastic region because of the conditions of continuity along the elastic-plastic boundary.

Thus, the intensity of the thermal stresses (as distinct from their distribution) depends largely on the elastic constants E and ν as well as on the coefficient α, in combinations such as (αE), (one-dimensional restraint) or $[\alpha E/(1-\nu)]$ (two-dimensional restraint), the tacit assumption being that the three constants are independent. On the basis of this assumption, meaningful solutions of the thermal stress equations can usually be obtained even for an assumedly incompressible medium. Equation (1) with $\nu\to\frac{1}{2}$ while $K\to\infty$, such that $E=3K(1-2\nu)$ remains finite and becomes $e=3\alpha T$, while the right-hand sides of Eqs. (2) and (3) remain different from zero.

This physical inconsistency can be removed by considering that the three constants E, ν, and α are not independent, but are related through the Grueneisen equation,[2]

$$3\alpha KV/C_v=3\alpha K/\rho c_v=\gamma \tag{4}$$

where (C_v/V) denotes the specific heat at constant volume per unit volume and is equal to ρc_v (c_v being the heat capacity per unit mass), and γ the dimensionless, Grueneisen constant, which is of the order of $1.2<\gamma<3$ depending on the valence forces, and largely independent of temperature. By introducing $\beta=\rho c_v\gamma$ as a new constant,

$$3\alpha K=\beta=\text{const.} \tag{5}$$

Equation (1) can be written in the form,

$$e-\beta T/K=p/K, \quad \text{or} \quad e=1/K(p+\beta T). \tag{6}$$

For $K\to\infty$, this relation becomes $e=0$ rather than $e=\alpha T$. Similarly, the factors $\alpha E=\beta(1-2\nu)$, $\alpha E/(1-\nu)=\beta(1-2\nu)/(1-\nu)$ vanish for $\nu=\frac{1}{2}$, while the factor associated with three-dimensional restraint $\alpha E/(1-2\nu)=\beta$ remains finite instead of becoming infinite. The order of magnitude of this factor is obtained by considering that, for instance, for iron $\rho c_v=3.3$ joule per cm^3 and $\gamma=1.6$. Hence, $\beta=5.3$ joule per cm^3 $=54$ kg per cm^2, which represents the hydrostatic stress associated with a temperature-change of 1°C under conditions of three-dimensional restraint.

Written in the proposed form, with β as an independent constant rather than α, the inconsistencies inherent in the conventional formulation of the thermal stress problem with respect to incompressibility are removed, and the fact is clearly established that the assumption of incompressibility is associated with vanishing thermal stresses, except in the limiting case of complete three-dimensional restraint. This conclusion may be of importance in connection with the admissibility, in thermal stress-analysis, of inelastic stress-strain relations implying elastic incompressibility such as the approximation of the Prandtl-Reuss relations by the Mises-Levy relations.

This research was supported by a U. S. Air Force Contract, monitored by the Materials Laboratory WADC, Wright Patterson Air Force Base, Ohio.

[1] A. M. Freudenthal and H. Geiringer, *Handbuch der Physik* (Springer-Verlag, Berlin, Germany, 1958), Vol. 6, p. 298.
[2] E. Grueneisen, Ann. Physik **26**, 393 (1908).

Elastic Moduli of Face-Centered Cubic Cobalt

R. DEAN DRAGSDORF
Department of Physics, Kansas State University, Manhattan, Kansas
(Received July 16, 1959)

THE transformation of cobalt from the stable hexagonal phase at room temperature to the stable face-centered cubic phase above 420°C must be accomplished by the cobalt atoms on every second close-packed plane slipping by one atom site in the hexagonal [21·0] direction. Similarly then, the transformation from the cubic to the hexagonal phase upon lowering the temperature would result when the cobalt atoms on every second close-packed plane slipped by one-sixth the periodicity in the cubic $[\bar{2}11]$ direction. A speculation could be made about these relative rates of transformation if the wave velocities or specifically the elastic moduli were known for both crystalline systems.

It is the purpose of this letter to relate the transverse and longitudinal velocities of nearly equivalent directions in hexagonal cobalt to those in the face-centered cubic system to obtain the cubic elastic moduli. Using an ultrasonic pulse technique, McSkimin[1] determined the transverse and longitudinal velocities

TABLE I. The square of the velocities of elastic waves in hexagonal and cubic crystals.

Phase	Vibrational mode	Direction of wave propagation	Direction of particle displacement	Square of the wave velocity
Hexagonal	Transverse	[00·1]	[10·0]	C_{44}^H/ρ^H
Hexagonal	Longitudinal	[10·0]	[10·0]	C_{11}^H/ρ^H
Hexagonal	Longitudinal	[21·0]	[21·0]	C_{11}^H/ρ^H
Cubic	Transverse	[110]	[1$\bar{1}$0]	$(C_{11}^c-C_{12}^c)/2\rho^c$
Cubic	Transverse	[100]	...	C_{44}^c/ρ^c
Cubic	Longitudinal	[110]	[110]	$(C_{11}^c+C_{12}^c+2C_{44}^c)/2\rho^c$
Cubic	Longitudinal	[$\bar{2}$11]	[$\bar{2}$11]	$\frac{5}{4}C_{11}^c+\frac{1}{4}C_{12}^c+2C_{44}^c+\frac{\sqrt{3}}{4}[3(C_{11}^c)^2+11(C_{12}^c)^2+16(C_{44}^c)^2-2C_{11}^cC_{12}^c-8C_{11}^cC_{44}^c+24C_{12}^cC_{44}^c]^{\frac{1}{2}}/3\rho^c$

for sound waves propagated in different directions in three single cobalt crystals. From these velocities the elastic moduli of hexagonal cobalt were derived. Engler,[2] Street,[3] and more recently Fine and Greener[4] have determined Young's modulus of polycrystalline cobalt.

Relations.—Table I gives various relations for the propagation of elastic waves in cubic and hexagonal crystals which have been known for some time. The superscripts H and c refer to the hexagonal and cubic crystal systems, respectively, and the ρ's are the mass densities. If then the transverse velocity of a wave in the [110] direction in the cubic system for a particle displacement in the [1$\bar{1}$0] direction is equated to the transverse velocity of a wave in the [00·1] direction in the hexagonal system for a particle displacement in the [10·0] direction, the following equation is obtained

$$\frac{C_{11}^c-C_{12}^c}{2\rho^c}=\frac{C_{44}^H}{\rho^H}.$$

If the longitudinal velocity of a wave in the [110] direction in the cubic system is equated to the longitudinal velocity in the [10·0] direction in the hexagonal system, another equality occurs as

$$\frac{C_{11}^c+C_{12}^c+2C_{44}^c}{2\rho^c}=\frac{C_{11}^H}{\rho^H}.$$

The reason the foregoing particle displacements were chosen is that they are the nearest neighbor directions in both close-packed systems. If the transverse velocity of a wave in the [100] direction in the cubic system for a particle displacement anywhere in the (100) plane is equated to the transverse velocity of a wave in the [00·1] direction in the hexagonal system for a particle displacement anywhere in the (00·1) plane, the third equation for the three unknowns becomes

$$C_{44}^c/\rho^c=C_{44}^H/\rho^H.$$

The choice to equate these latter transverse waves was made to relate particle motion in planes of two layered stacking.

TABLE II. Elastic moduli of hexagonal cobalt at 25°C in dynes/cm².

$C_{11}=3.071\pm0.015\times10^{12}$
$C_{12}=1.650\pm0.008\times10^{12}$
$C_{13}=1.027\pm0.015\times10^{12}$
$C_{33}=3.581\pm0.018\times10^{12}$
$C_{44}=0.755\pm0.004\times10^{12}$

Results.—The elastic moduli for hexagonal cobalt at 25°C with $\rho^H=8.836$ g/cc found by McSkimin[1] are listed in Table II. If these values are substituted into the above three equations, the three cubic elastic moduli can be determined. A density of 8.739 g/cc was used for cubic cobalt. The resulting values are listed in Table III. Substituting these new cubic along with the hexagonal elastic moduli into the equality between the longitudinal wave velocities in the [$\bar{2}$11] cubic and the [21·0] hexagonal directions as given by

$$\frac{C_{11}^H}{\rho^H}=\frac{5}{4}C_{11}^c+\frac{1}{4}C_{12}^c+2C_{44}^c+\frac{\sqrt{3}}{4}[3(C_{11}^c)^2+11(C_{12}^c)^2+16(C_{44}^c)^2-2C_{11}^cC_{12}^c-8C_{11}^cC_{44}^c+24C_{12}^cC_{44}^c]^{\frac{1}{2}}/3\rho^c$$

gives $(0.348\pm0.002)\times10^{12}=(0.353\pm0.016)\times10^{12}$, an apparently excellent check.

Engler,[2] Street,[3] and Fine and Greener[4] have all determined a value of 2.1×10^{12} dynes/cm² for polycrystalline hexagonal cobalt at room temperature. This value is significantly lower than either of the two elastic moduli, C_{11} or C_{33}, reported by McSkimin. Fine and Greener also have determined Young's modulus for polycrystalline cubic cobalt above 400°C. Extrapolating their determinations on the cubic phase back to room temperature, a value of 2.2×10^{12} dynes/cm² is obtained for Young's modulus. This is lower than the value reported here for the cubic elastic modulus C_{11}. It is most likely that the small shear modulus, elastic modulus C_{44} for both the hexagonal and cubic phase, would cause the apparently small Young's modulus observed in polycrystalline cobalt.

Discussion.—Because of the difference in relative positions of the six second nearest neighbors all at $\sqrt{2}$ "a" from each other in the cubic and hexagonal close-packed structures, the accuracy of the determined elastic moduli might be questioned. Also there is a difference in the number and position of the third nearest neighbors, twenty four with a $\sqrt{3}$ "a" separation, in the face-centered cubic structure as compared to the third and fourth nearest neighbors, two with a $(2\sqrt{2})/\sqrt{3}$ "a" and eighteen with a $\sqrt{3}$ "a" separation, respectively, in the hexagonal close-packed structure. Here "a" designates the nearest neighbor distance or the atomic diameter. The force constants for the six second nearest neighbors in both structures would not be too different. On the other hand, the force constants associated with the third and fourth nearest neighbors in the two phases would be quite different but quite small compared to the force constants for the first and second neighbors. This would indicate that the difference in lattice energy in the two crystal phases is small. In substantiation of this Edwards and Lipson[5] have indicated that the Helmholtz free energy for hexagonal and cubic cobalt phases must be nearly the same below 400°C. Their conclusion was made after many samples of cobalt were observed to have up to 20% of the face-centered cubic phase remaining at room temperature. The amount of the residual cubic phase depended mainly on the lattice strain present in their various sized samples. Some fifty cobalt whiskers have been examined at room temperature by this laboratory. In every case a small residual cubic phase was similarly apparent. The velocities related herein, therefore, have a good foundation, at least for cobalt.

The symmetry of the first and second nearest neighbors and the small force constants associated with the more distant atoms might imply that cubic cobalt would be isotropic. The isotropy of the cubic elastic moduli is inherent in the related velocities.

Finally, mention should be made of the fact that the cubic elastic moduli were calculated from the hexagonal elastic moduli determined at 25°C. A question might arise as to the feasibility of relating the lattice wave velocities in the hexagonal to those in the cubic system at this temperature since the transition temperature in pure cobalt occurs at approximately 400°C. As is well

TABLE III. Elastic moduli of cubic cobalt in dynes/cm².

$$C_{11} = 3.037 \pm 0.023 \times 10^{12}$$
$$C_{12} = 1.543 \pm 0.023 \times 10^{12}$$
$$C_{44} = 0.747 \pm 0.004 \times 10^{12}$$

known, the cubic phase can be obtained at room temperature by either cold working the lattice or introducing a small quantity of impurity atoms into the cobalt within the limits of solid solubility of the alloy. Both methods give rise to cubic cobalt at room temperature due to the local lattice strain that is present. The cubic elastic moduli found would therefore be most appropriate for such induced cobalt lattices. The moduli, too, could be modified for use at higher temperatures.

[1] H. J. McSkimin, J. Appl. Phys. 26, 406 (1955).
[2] O. Engler, Ann. Physik 31, 145 (1938).
[3] R. Street, Proc. Phys. Soc. (London) 60, 236 (1948).
[4] M. E. Fine and E. H. Greener, Trans Am. Inst. Mining Met. Engrs. 212, 476 (1958).
[5] O. S. Edwards and H. Lipson, J. Inst. Metal 69, 177 (1943).

Effect of Gas Pressure and Cone Angle on the Velocities of Electrically Excited Shock Waves

PHILIP J. HART
Lockheed Missiles and Space Division, Palo Alto, California
(Received June 24, 1959)

SHOCK waves in a gas have been produced by a variety of electromagnetic methods. The systematic investigation reported in this letter is restricted to certain experimental configurations having plasma-accelerating electrodes of axial symmetry.[1-4]

The experimental arrangement is shown schematically in Fig. 1. The variables consist of the pressure of the gas (air) in the shock tube, and of the cone angle and material of the replaceable conical insulators. The capacitor is charged to 30 kv prior to each discharge, and the ringing frequency of the circuit is 220 kc.

Shock velocities were determined from streak photographs produced with an image converter camera at initial gas pressures of 0.03, 0.1, 0.3, 1.0, and 3.0 mm Hg. Average velocities obtained with insulating cones of Teflon plastic are presented in Fig. 2. The data scatter lies within about ±10% of the given curves for cones of small angle, but is somewhat greater for larger angles.

A qualitative explanation of the dependence of shock velocity on cone angle follows. For large angle cones (half-angles near 90°) one may expect the magnetic force acting in the axial direction on the nearly radial current to be dominant over forces due to Joule heating, the latter being minimized because the current is less confined. Since the magnetic force is essentially independent of gas pressure (the ringing frequency being nearly constant), a volume of plasma of less density will have higher acceleration because of its lower inertia. Thus, large angle cones should be more effective at lower gas pressures. Conversely, for small angle cones one may expect the Joule heating, which is favored by a longer and more constricted discharge channel, to be dominant over the magnetic force which now acts largely in the radial direction. Thus,

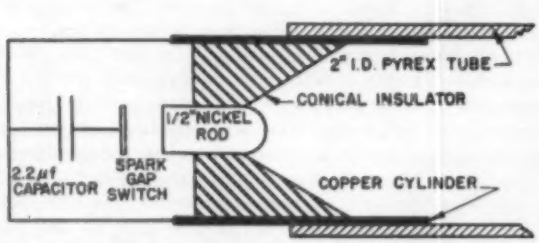

FIG. 1. Schematic arrangement of circuit and electrode system.

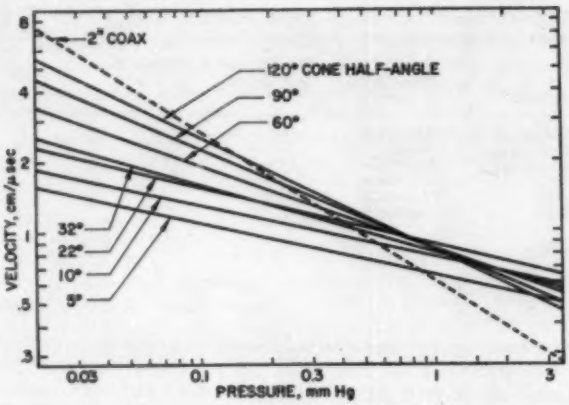

FIG. 2. Shock velocities in air obtained with Teflon cones. The curves represent average velocities of the first shock pulse for the arbitrary interval between markers placed 10 and 20 cm distant from the electrodes.

since Joule heating increases with pressure, small angle cones should be relatively more effective at higher pressures. These predictions are substantiated in general by Fig. 2 in which the curves cross at about 1 mm Hg pressure, except that the entire curves for the smallest angles are displaced downward. At higher pressures, the 22° curve rises above the other curves, probably because for this case the shock velocity coincides with the rate of travel of the pinch, an effect observed in a more pronounced form by Josephson[1] for deuterium at a cone half-angle of about 10°.

The material of the insulating cone has a marked effect on shock velocities. A uniform electrical breakdown at the surface of the insulator leads to symmetric and reproduceable shocks, while a concentrated discharge along one side of, say, a large angle cone ejects less plasma but at a higher velocity and in such a direction that it may strike a tube wall and be deflected at reduced speed, thus giving a wide variation in measured speeds. Transverse streaking pictures and other evidence show that shock waves from Teflon cones at pressures below 1 mm Hg are symmetric and uniform, but that glass cones produce highly erratic results and alumina ceramic cones somewhat less so.

Figure 3 shows average shock velocities obtained with the alumina cones. The dotted lines (shown only in part) for 10° and 20° half-angles, represent velocities first found for these angles with clean alumina. However, when graphite lines were drawn on the alumina cones in order to investigate the effect of increased surface conductivity, the results for larger angles were duplicated but the curves for 10° and 20° then fell into their "normal" sequence as shown by the solid lines. Presumably, the discharge

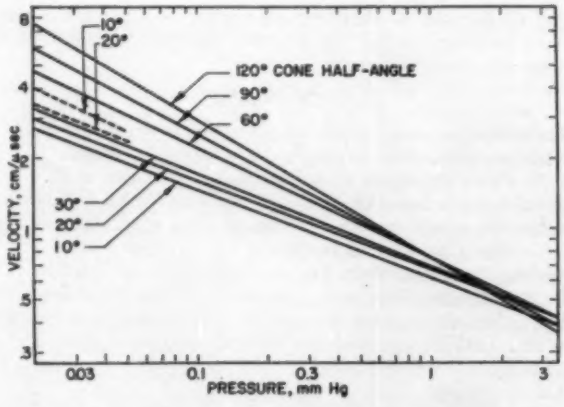

FIG. 3. Shock velocities in air obtained with alumina cones for the 10 to 20 cm interval down the shock tube.

path over the surface of the clean alumina can become so long that electrical breakdown occurs preferentially through the body of the gas, the current then spreading out near the outer end of the cone to simulate a cone of larger angle.

The dotted curve of Fig. 2 is for a coaxial electrode system formed by extending the center electrode about 5 cm through a plane insulator. The rather involved sequence of phenomena relating to shock formation, which occur as the pressure is reduced, will be reported subsequently.

Further modifications of the electrode systems, not reported here, indicate that shock formation is determined largely by the region of the discharge adjacent to the center electrode and that the outer region of the insulating cone has little effect.

Further details of this study may be found in the Lockheed research report, LMSD 288000.

[1] V. Josephson, J. Appl. Phys. 29, 30 (1958).
[2] Scott, Basman, Little, and Thomson, in *The Plasma in a Magnetic Field*, edited by R. K. M. Landshoff (Stanford University Press, Stanford, California, 1958), p. 110; see also Kash, Gauger, Starr, and Vali., *ibid.*, p. 99.
[3] G. S. Janes and R. M. Patrick, *The Production of High Temperature Gas by Magnetic Acceleration* (AVCO Research Laboratory, Everett, Massachusetts, 1958), Research Report 27.

Observation of Néel Walls in Thin Films*

HARVEY RUBINSTEIN, HARRISON W. FULLER, AND MURRAY E. HALE
Computer Products Division, Laboratory for Electronics, Incorporated, Boston, Massachusetts
(Received September 24, 1959)

A PRINCIPLE of ferromagnetic domain theory that is frequently applied is the condition that through the wall the variation of magnetization proceeds in such a manner that the component of magnetization normal to the wall does not change.[1,2] The existence of this principle is due to Néel,[3] who has shown by calculation that for a bulk material the energy of a wall which meets this condition is less, by an order of magnitude, than one which violates it. If the condition is met the wall energy is due to anisotropy and exchange. If this condition is violated, a large number of magnetic poles will exist in the wall and these volume poles will give rise to a magnetic field. The energy of the wall then arises from a magnetostatic contribution in addition to anisotropy and exchange contribution.

Further, in discussing the wall of a bulk material, the forces arising when a wall intersects the surface of the material are assumed to be negligible. These forces are due to fields produced by poles on the crystal surface, and are small because these surface poles are far removed from the majority of spins in the material. They are, of course, important for operation of the Bitter powder technique.

When the problem of domain walls in thin films was studied,[4] the above principle and assumption were found to be inapplicable, since the effect of surface poles is much greater compared with that of volume poles because of the far greater ratio of surface to volume of a thin film. Moreover, it was found that the contribution

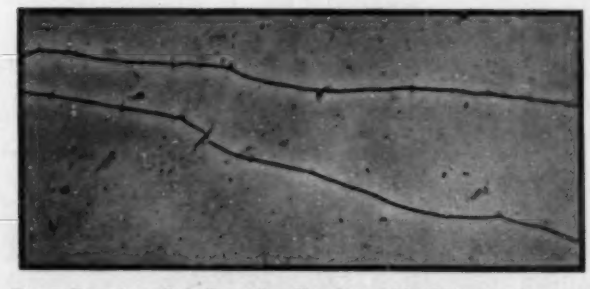

FIG. 1. Domain walls in Permalloy film observed by Bitter powder pattern with no external field applied.

FIG. 2. Néel-wall segments of walls of Fig. 1 shown by application of an external field in the plane of the film and perpendicular to the walls.

of the magnetostatic energy of the surface poles could overshadow the contribution from the anisotropy energy for a wall formed according to the principle mentioned above. Calculations showed that a sufficiently thin film should have walls which do indeed have volume poles, and that minimize or eliminate surface poles.

From the above considerations there resulted two possible pictures of a wall in a thin film. The first, which is expected to occur in thicker films, is the same as the picture of a wall in bulk material, and is denoted as a Bloch wall. Here the spins in the wall rotate about an axis that is in the plane of the film. The second, which is expected to occur in thinner films, has spins rotating in the plane of the film and is called a Néel wall.

Before proceeding with the discussion of Néel wall observations, mention should be made that the direction of rotation of the

FIG. 3. Néel-wall segments as in Fig. 2 showing reversal of segment intensification as a result of reverasing the direction of the applied field.

magnetization within a wall can be clockwise or counterclockwise. It would be expected that if one proceeded along a wall, the sense of rotation would be constant unless the wall runs through a film imperfection. Hence when a wall is observed, it is possible to observe segments of opposite rotation. Such an observation for Bloch walls has been reported.[5] The present observations indicate such occurrences for Néel walls.

The Néel walls were observed[6] in a 450 A film from a 4–79 Permalloy melt deposited on glass substrate heated to a temperature of 150°C. The coercive force of this film was about 2.9 oersteds and the anisotropy field was 4.3 oersteds. The observations of the wall were made by using the standard Bitter powder

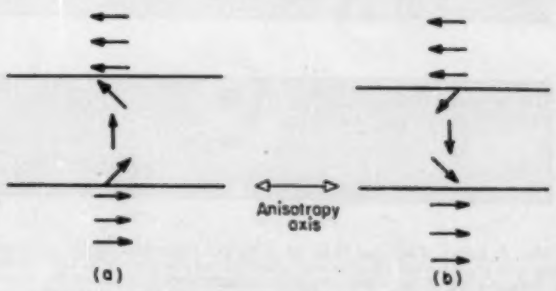

FIG. 4. 180° Néel walls of opposite directions of rotation.

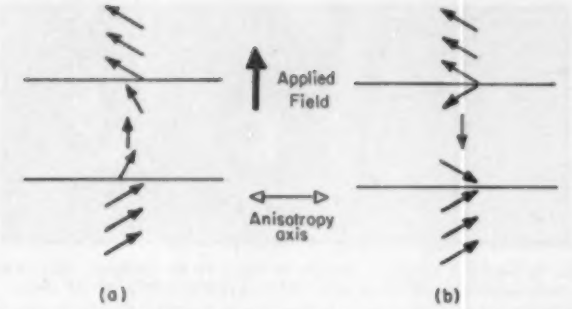

FIG. 5. Effect of external applied field on Néel walls of opposite directions of rotation. In (a) the magnetization rotates less than 180° while in (b) the magnetization rotates more than 180°.

technique in conjunction with an applied field in the plane of the film and normal to the plane of the wall. Figures 1 to 3 show the appearance, respectively, of the wall in zero field, in a field applied normal to the wall and in a field applied in the opposite direction normal to the wall. Note the reversal of the dark and light segments with the reversal of the field.

These reversals in light and dark segments indicate the existence of the Néel wall in the following way. Consider the two possible 180° Néel walls depicted in Figs. 4(a) and 4(b). These figures show the magnetization surrounding the wall and in the wall in the absence of applied field. If a field is applied in the plane of the film and normal to the wall, the magnetization distribution shown in Fig. 4 would change to that shown in Fig. 5. Figure 5(a) shows the case in which the applied field is directed parallel to the magnetization in the wall, while in Fig. 5(b) the field is antiparallel to the magnetization in the wall, while in Fig. 5(b) the field is antiparallel to the magnetization in the wall. We note that in Fig. 5(a) the magnetization must rotate through an angle less than 180°, while in Fig. 5(b) the magnetization now rotates through an angle larger than 180°. The case of Fig. 5(a) then contains a smaller number of magnetic poles than the case shown in Fig. 5(b). Hence, the external field in Fig. 5(b) would be larger than the external field in Fig. 5(a) and this in turn indicates that the case of Fig. 5(b) would collect more magnetite than the case shown in Fig. 5(a). A second mechanism for a change in particle concentration with an applied field is operative if the size of the particle is such that portions of the particles are sufficiently distant from the film, for then the field at the particle may have a component parallel to the film. The applied field will then serve to reduce the local external field of Fig. 5(a) and increase the field of Fig. 5(b).

As a check on Néel's theory, the data for the above described film were used and, following Néel, the thickness was calculated at which the transition from the Bloch to the Néel wall should occur.

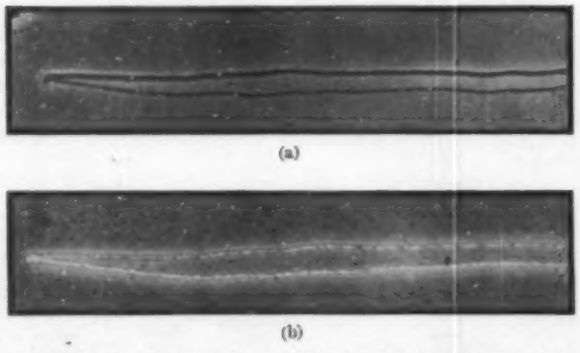

FIG. 6. Effect of applied fields on Néel-wall segments. In (a) the applied field is in the plane of the film and perpendicular to the walls, and the effect is different on Néel segments with magnetization rotating in opposite directions. In (b) the applied field is normal to the film and the effect is the same on both segments.

The computed value was 200 A, below which one could expect to find Néel walls. For a thickness larger than this, one would expect to find Bloch walls. The discrepancy of theory and experiment is probably not serious, for the Néel theory is quite approximate and pertains to cubic anisotropy.

It was also observed in films having a higher coercive force than the film described above that the direction of the magnetization in the middle of the wall can reversibly be changed with an applied field in the plane of the film and perpendicular to the wall.

Application of a field normal to the plane of the film causes only an increase in the number of particles along a Néel segment regardless of the direction in which the magnetization rotates through the wall, as seen in Fig. 6. Bloch wall segments would be intensified or diminished with such a normal field in accordance with the direction of magnetization in the center of the segments.[5]

* This work was supported in part by the Office of Naval Research under Contract Nonr-2676(00), and Bell Helicopter Corporation under Contract Nonr-1670(00).

[1] Williams, Bozorth, and Shockley, Phys. Rev. **75**, 174 (1949).
[2] L. Néel, Cahiers phys. **25**, 14 (1944).
[3] See reference 1, p. 12.
[4] L. Néel, Compt. rend. **241**, 533 (1955).
[5] H. W. Williams and M. J. Goertz, J. Appl. Phys. **23**, 316 (1952).
[6] H. Fuller and H. Rubinstein, J. Appl. Phys. **30**, 84S (1959).

Three-Dimensional Wedge Impact on a Compressible Fluid

S. F. BORG
Civil Engineering Department, Stevens Institute of Technology, Hoboken, New Jersey

(Received August 28, 1959)

IN a recent paper,[1] a new solution is given for the initial impact of a two-dimensional wedge on a compressible fluid. The solution utilized a similarity transformation, and represented essentially a superposition of compressible, viscous-elastic effects.

The present note extends the method to the three-dimensional case.

In terms of the parameter $\xi=r/t$, the continuity and momentum equations for spherical compressible flow become

$$-\xi(d\rho/d\xi)+d(\rho u)/d\xi+2\rho u/\xi=0 \tag{1}$$

and

$$-\xi(du/d\xi)+u(du/d\xi)=-(1/\rho)(dp/d\xi). \tag{2}$$

In addition, the velocity of small disturbances is given by

$$C=(dp/d\rho)^{\frac{1}{2}}. \tag{3}$$

The solution to (1), (2), and (3) is (see Fig. 1)

$$u=2(\xi_0-\xi) \tag{4}$$

$$\rho=\rho_0\frac{\xi_0^2}{\xi^2} \tag{5}$$

$$p=2\rho_0\xi_0^2\left[3\ln\frac{\xi_0}{\xi}-2\left(\frac{\xi_0}{\xi}-1\right)\right]. \tag{6}$$

The above satisfy, in addition to Eqs. (1), (2), and (3), the following boundary and physical requirements:

(a) The velocity of the outer wave is ξ_0, the velocity of sound in the fluid.
(b) The particle velocity at the outer wave is zero.
(c) The pressure along the outer boundary is zero.
(d) The density along the outer boundary is ρ_0, the undisturbed free-stream density.
(e) The velocity of the inner boundary, the wedge, is $\xi_i=\frac{2}{3}\xi_0$, i.e., two-thirds the velocity of sound.

Thus, all physical and boundary requirements for a solution are satisfied, except along the free surface where we have a pressure distribution given by (6) instead of zero pressure as required. It

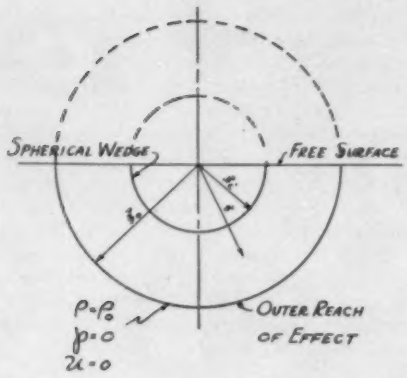

FIG. 1. The impacting spherical similar wedge in the ξ plane.

is, therefore, necessary to add to the solution thus far obtained, another one which will cancel the free-surface pressure (6) without introducing a violation of any of the other conditions. This is done by superposing on the above solution an approximate elastic-hollow-sphere solution, as follows.

A hollow sphere subjected to a pair of equal opposite diametral concentrated pressure forces on the inside surface will give pressures approximately equal and opposite to (6). If these concentrated forces are then "smoothed out" to vary linearly from the free surface to the stagnation point, with the free surface value taken equal and opposite to the free surface value given by (6) in order that the pressure on the wedge be zero at this point as required, we find that at the stagnation point,

$$p_{\text{elastic}} = (13/8)p_l \tag{7}$$

so that the total pressure at the wedge stagnation point, the sum of (6) and (7), is given by

$$\frac{p_s}{\frac{1}{2}\rho_0 \xi_3^2} = 5.2 \tag{8}$$

and the pressure varies linearly with angle to zero at the free surface.

The solution given holds best for sharp pointed wedges entering the fluid at a velocity equal to two-thirds the velocity of sound in the undisturbed fluid. For blunt wedges entering at different velocities, a combination of the Prandtl-Glauert pressure coefficient correction and a suitable superposition of the given solutions may be utilized. See reference 1 for a more complete discussion of this. See also reference 1 for a discussion of the period-of-importance of compressibility effects as compared to incompressible effects.

The work reported upon herein was supported by a National Science Foundation Research Grant.

[1] S. F. Borg, J. Appl. Phys. **30**, 1432 (1959).

On the Reflection of Electromagnetic Waves from a Medium Excited by Acoustic Waves

HANS J. SCHMITT AND DIPAK L. SENGUPTA
Gordon McKay Laboratory of Applied Science, Harvard University, Cambridge, Massachusetts

(Received September 25, 1959)

THE reflection of electromagnetic waves incident normally on the wave fronts of a semi-infinite acoustic wave is observed experimentally and an approximate theory is developed in order to ascertain the nature of such a reflection. In the following communication this phenomenon is at first discussed from physical considerations. Whenever necessary relevant theoretical formulas are quoted without giving their derivations. Secondly, the experimental arrangement is discussed. The details of both the theory and the experiment will be published in the form of a report by one of the authors.[1]

In a right-handed rectangular coordinate system, let the $y=0$ plane be the interface between medium 1 ($z>0$) and medium 2 ($z<0$) having dielectric constants ϵ_1 and ϵ_2, respectively. In the present case medium 1 is air and medium 2 is assumed to be a liquid (water) having negligible acoustic absorption. A plane acoustic wave (angular frequency ω_A) propagating along the positive z direction in medium 2 is reflected back into the medium due to the discontinuity in acoustic impedance at the interface. This produces in the liquid a standing wave along the z direction. The local variation of density and temperature in the liquid caused by the acoustic wave produces regions of maximum and minimum dielectric constant. These regions are parallel to the interface and are separated by a distance $\lambda_A/2$, λ_A being the acoustic wavelength in the liquid. The relative variation of dielectric constant in the liquid caused by the acoustic wave may be calculated from the Lorenz-Lorentz relation; the final result is obtained in the following form:

$$\left|\frac{\Delta\epsilon_2}{\epsilon_2}\right| = \frac{\Delta p}{\rho C_A^2}\left|\frac{(\epsilon_2-1)(\epsilon_2+1)}{3\epsilon_2}\right|$$

where ρ is the density of medium 2, Δp is the amplitude of the acoustic pressure, and C_A is the sound velocity in medium 2. $|\Delta\epsilon_2/\epsilon_2|$ is of the order of magnitude of 10^{-3} for even the highest sound intensities (for water $\Delta\epsilon_2/\epsilon_2 \approx 31.2\times10^{-4}$ with $\Delta p = \frac{1}{3}$ atmosphere).

The electromagnetic waves propagating in the negative z direction in medium 1 are reflected partly from the interface and partly from the regions of extreme values of ϵ_2 in medium 2. Provided the ratio of the electromagnetic to the acoustic wavelength is chosen properly, the waves reflected from the subsequent regions reinforce one another and thereby produce a substantial over-all reflection. This may be looked upon as a sort of Bragg reflection in optics. Owing to the periodic disappearance of these regions this part of the reflection appears as a modulation of the total reflected signal. It can be shown that the reflected signal consists of a component at the electromagnetic frequency ω and two side bands at frequencies $(\omega+\omega_A)$ and $(\omega-\omega_A)$. The first component is due to the usual reflection at the interface, the two side bands are produced

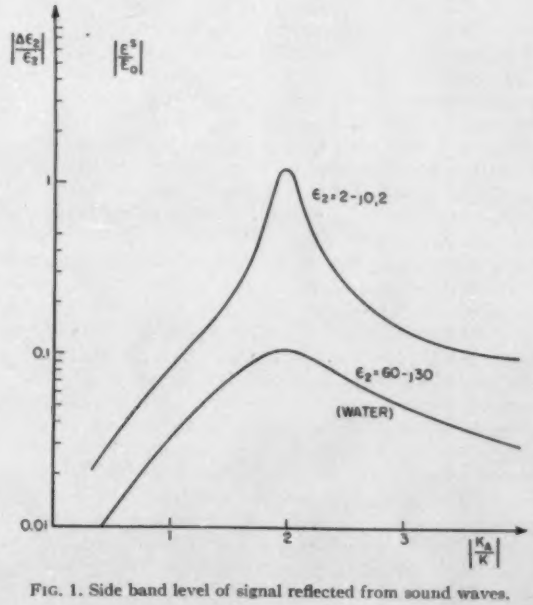

FIG. 1. Side band level of signal reflected from sound waves.

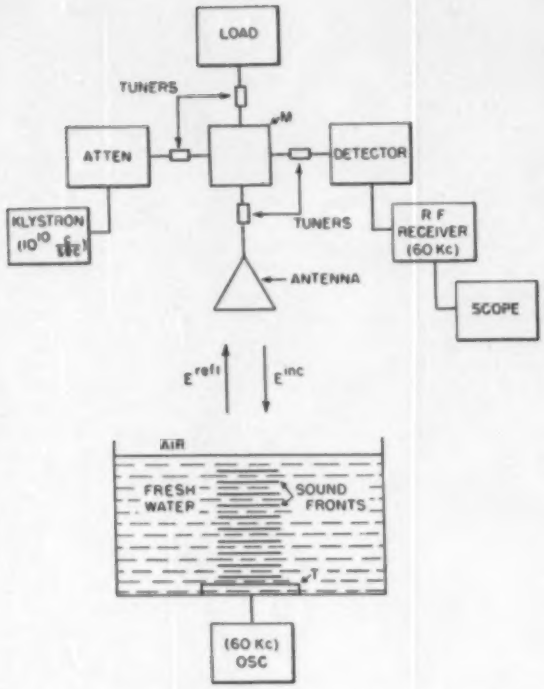

FIG. 2. Block diagram of the experimental arrangement.

by the internal Bragg reflections. The normalized field-strength in the side band is given by the following expression:

$$\left|\frac{E^s}{E_0}\right| = \frac{(Z_2/Z_1)(k_A/k)\,|\Delta\epsilon_2/\epsilon_2|}{[(Z_2/Z_1)+1]^2[4-(k_A/k)^2]}$$

where Z_1 and Z_2 are the electromagnetic wave impedances of media 1 and 2, respectively; $k_A(=2\pi/\lambda_A)$ and $k(=2\pi/\lambda)$ are the propagation constants of the acoustic and electric waves in medium 2.

$|E^s/E_0|$ has been computed for different media as a function of $|k_A/k|$ and is plotted (see Fig. 1) in terms of the ratio $\Delta\epsilon_2/\epsilon_2$. It is found that the maximum of the modulated part of the reflected signal lies, for small loss tangents, at $\lambda/\lambda_A=2$; i.e., the electric wavelength in the sound perturbed medium is exactly twice the acoustic wavelength, as required by the Bragg condition in optics.

The modulated component of the reflected signal has been observed clearly. The schematic diagram of the experimental arrangement used is as shown in Fig. 2. A steel tank ($1.54\times2.13\times0.26$ meter^3) filled with fresh water contains a magnetostrictive underwater sound transducer with a circular aperture of radius 8.3 cm. The transducer has a resonant frequency of 60 kc/sec ($\lambda_A=2.56$ cm in water). It is fed by a 200 watt rf oscillator which can be operated in a pulsed or a cw condition. In order to set up standing sound waves the transducer is placed at the bottom of the tank and is directed against the water surface.

The electromagnetic system consists of a two-resonator klystron (Varian X21b, $\lambda=3.2$ cm) with a power output of about 2 watts. The microwave energy is fed through a variable attenuator into the series arm of a magic T where it is separated into two parts in the equal branches of the T. The signal from one branch is radiated by a rectangular horn (9.5×15 cm^2) directed toward the air-water interface. The horn is rigidly mounted at a height of 1 m above the interface and in line with the standing acoustic wave. It also serves to receive the reflected signals. In the second branch of the T a fixed wave-guide load in conjunction with a sliding screw tuner provides for the introduction of any desired amplitude and phase of reflection to the signal traveling into this branch. The output branch of the T leads directly through a crystal demodulator into a tunable rf receiver which has a sensitivity of 10^{-8} volts at 60 kc/sec for the minimum detectable signal. The response after demodulation is maximized by adjusting the canceling signal from the auxiliary arm of the magic T in such a way that the total carrier signal at the crystal detector has the proper phase relation. The output from the receiver is connected to an oscilloscope for visual observation.

After proper adjustment of the entire system, the modulation of the reflected electromagnetic wave by the 60 kc sound wave was clearly observed on the oscilloscope. The response on the scope was about 20 db above the noise level produced mainly by the klystron and partly by the receiver. The response was found to be of the same amplitude for pulsed as for steady sound waves. It would disappear if the sound transducer was tilted or moved away from the correct position directly underneath the electromagnetic antenna.

It may be concluded that an electromagnetic wave incident normally on the wave fronts of an acoustic wave suffers a modulation both in amplitude and phase. The amount of modulation, although very small, may be observed experimentally. A more sensitive experimental set up is necessary in order to obtain quantitative conclusions.

The authors wish to thank Professor R. W. P. King and Professor F. V. Hunt for support of this work and numerous stimulating discussions.

[1] Hans J. Schmitt, "Reflection of electromagnetic waves from sound waves," Technical Report No. 310, Gordon McKay Laboratory, Harvard University, Cambridge, Massachusetts (to be published).

Bulk Densities of Separated Copper Isotopes

D. D. SNYDER*
Physics Department, Research Laboratories, General Motors Corporation, Warren, Michigan
(Received September 25, 1959)

IN connection with contemplated studies on the effects of isotopic composition on the electrical and magnetic properties of copper it was desired to know the bulk densities of the two stable isotopes of copper. This note is written to report these results and to point out that the drawing of copper into a fine wire may give rise to trapped gases which can produce some anomalous effects. The samples were purchased from Oak Ridge National Laboratory which also provided the isotopic and chemical analyses. For the copper-63 sample, the percent isotopic composition was Cu^{63}, 99.69 ± 0.05; Cu^{65}, 0.31 ± 0.05; and the main chemical impurity was, in weight percent, Ca, 0.1. For the copper-65 enriched sample, the percent isotopic composition was Cu^{63}, 6.9 ± 0.5; Cu^{65}, 93.1 ± 0.5; and the chemical impurities were all less than 0.07 weight percent. Natural copper has an isotopic composition of Cu^{63}, 69.1%; Cu^{65}, 30.9%.

The samples were prepared by ORNL in the form of metallic wires approximately 0.018 in. in diameter which were drawn from vacuum cast nuggets. They were subsequently drawn until the diameter was 0.008 in. The diameter was checked for uniformity and found to vary not more than $\pm2\%$.

The first density measurements were made on the wire by simply weighing and measuring it as received after the final drawing. These data gave values of 7.95 and $7.17\pm3\%$ g/cm^3 for isotopes 63 and 65, respectively. These results are to be compared with the accepted value[1] of 8.93 g/cm^3 for natural copper. The wires were then vacuum annealed at 500°C for four hours and showed no change in density. The discrepancy between the isotopically enriched samples and the cited value for natural copper was thought to be due to trapped gases. Consequently, some of each sample was vacuum melted in an effort to reduce this trapping. The samples were then cleaned in nitric acid, weighed in air, in distilled water and in acetone, the two liquids serving as a cross check on the measurements. Considerable care was needed to prevent the sample from trapping air around its support. Care

TABLE I. Density of copper (g/cm³, at 20°C).

Material	Bulk density	Crystal density
Copper-63	8.83 ±0.05	8.846
Copper-65	9.12 ±0.05	9.127
Copper-nat	(8.933[a])	8.933

[a] See reference 1.

was also taken to minimize surface tension and buoyancy effects on the support wire. Correction for the calcium impurity in the Cu^{63} sample was made on the assumption that it was of normal density (1.55 g/cm³). The correction for the Cu^{63} in the copper-65 enriched sample was also made. The corrections for the isotopic impurity in the copper-63 sample and the chemical impurities in the copper-65 sample were both much less than the accuracy of the other data. The resulting values are given in Table I. The crystal densities given in Table I are calculated using the crystallographic and isotopic data given in the *American Institute of Physics Handbook*.[2]

Calculation of the density of natural copper from the densities of the separated isotopes gives a value of 8.92 g/cm³. This computed density and the measured densities of the separated isotopes are slightly smaller than the respective crystal densities. This relationship has been observed before in lithium[3] and is, in general, to be expected.

* Present address: Physics Department, Emmanuel Missionary College, Berrien Springs, Michigan.

[1] Kahlbaum, Roth, and Sidler, Z. anorg. u. allgem. Chem. **29**, 177 (1902).
[2] *American Institute of Physics Handbook*, edited by D. E. Gray *et al.* (McGraw-Hill Book Company, Inc., New York, 1957), Sec. 2, p. 48 and Sec. 8, p. 8.
[3] D. D. Snyder and D. J. Montgomery, J. Chem. Phys. **27**, 1033 (1957).

Reciprocity Law Failure in ZnO and Se

JOZE KOSTELEC*
Physics Research Laboratories, Ansco Division of General Aniline & Film Corporation, Binghamton, New York
(Received December 12, 1958)

EXTENSIVE use for ZnO and Se has been found in electrophotographic systems such as "xerography"[1] and "Electrofax."[2] Validity of the Bunsen-Roscoe reciprocity law in such systems is of importance and has been investigated as far as known by two groups. Gerritsen *et al.*,[3] report that for changes of exposure times from 100 to 10^{-2} sec, no change of quantum yield was observed in ZnO dispersed in a dielectric resin. The accuracy of their instrument was such that a change of a factor of two would have been detected. However, V. M. Fridkin and co-workers[4] reported results where the Bunsen-Roscoe law was not obeyed. Fridkin[4] also used ZnO finely dispersed in a resin as well as dye-sensitized ZnO. Both high and low intensity reciprocity law failures were observed by this group.

In view of this apparent disagreement, a series of experiments was conducted in order to see whether long and low intensity exposures caused a voltage drop of charged ZnO and Se layers, which would be different from that caused by short, high intensity exposures. Exposure is defined as the product of intensity and time. The total number of incident photons was kept constant in all cases. The results were plotted in the familiar manner. The logarithm of the exposure required for equal drop in surface potential is plotted against the logarithm of the applied intensity. If the reciprocity law holds, then this exposure is independent of the applied intensity and the reciprocity curve is a straight line, parallel to the logarithm of intensity axis.

The surface charge was obtained by means of a corona discharge, positive for Se and negative for ZnO samples. This was done in the dark. When exposed to light, the surface charge was dissipated. The change of the surface potential due to illumination was measured by means of a dynamic electrometer, with stationary electrode and moving charged surface. A 300 w tungsten projection lamp was used as the light source. The amount of light reaching

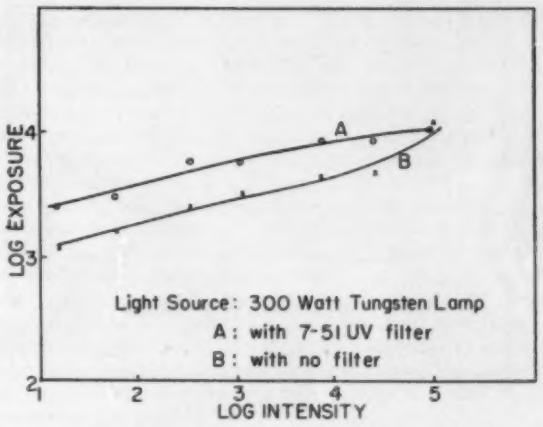

FIG. 2. Reciprocity law curves for "Green Seal" ZnO imbedded in dielectric resin and deposited on paper support. A: Illumination applied through a uv transmitting 7-51 Corning Glass filter. B: The total tungsten spectrum applied to the sample.

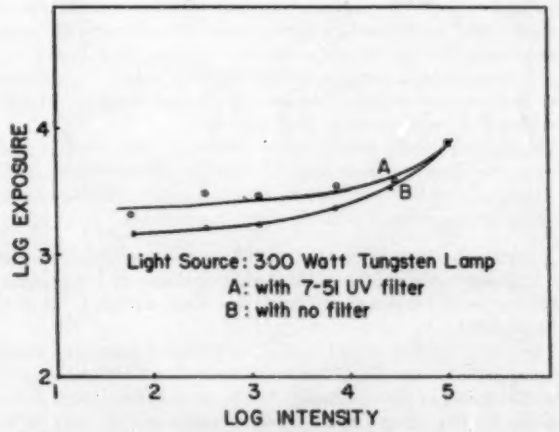

FIG. 1. Reciprocity law curves for "Green Seal" ZnO imbedded in dielectric resin and deposited on aluminum support. A: Illumination applied through a uv transmitting 7-51 Corning Glass filter. B: The total tungsten spectrum applied to the sample.

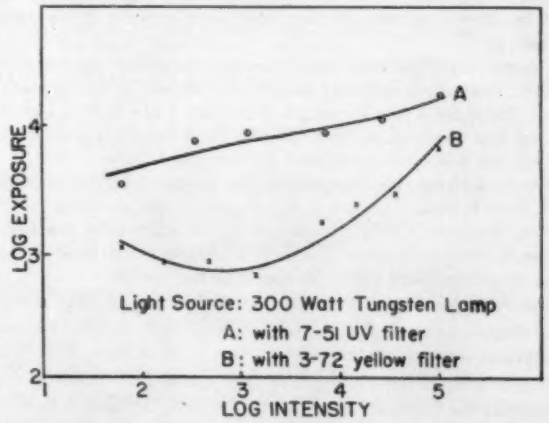

FIG. 3. Reciprocity law curves for Rose Bengal sensitized "Green Seal" ZnO, imbedded in dielectric resin and deposited on paper support. A: Illumination applied through a uv transmitting 7-51 Corning Glass filter. B: Illumination applied through a uv absorbing 3-72 Corning Glass filter.

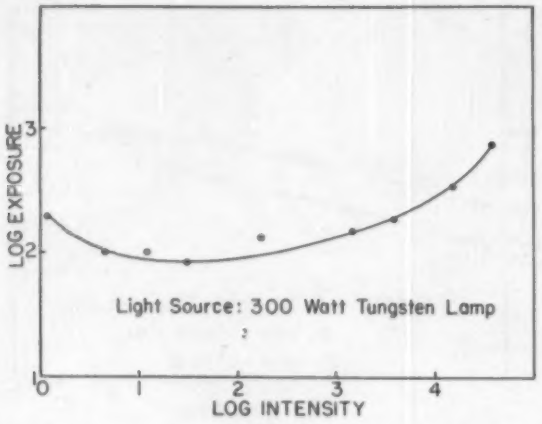

FIG. 4. Reciprocity law curve for Se coated metal plate (manufactured by Haloid Corporation). The total tungsten spectrum applied to the sample.

the sample was controlled by neutral density Wratten filters. For exposure in the absorption band of ZnO, a 7–51 Corning Glass filter was used transmitting from 310 to 420 mμ. For exposing dye-sensitized ZnO samples, a 3–72 Corning Glass filter was used which transmits from 440 mμ up.

Illumination was applied to the sample in pulses of 7 msec duration and at 50 msec intervals. After each light pulse the sample passed the electrode and the surface potential was recorded. Thus, the number of light pulses required to reduce the initial surface charge to one half of the original value was measured for different applied intensities.

In the case of Se, a commercially available xerographic Se plate manufactured by the Haloid Corporation was used. The applied surface charge was positive.

In case of ZnO, "Green Seal" ZnO, manufactured by New Jersey Zinc Company, was used. The ZnO powder was dispersed in SR82 Silicone Resin (General Electric Company). In some cases, the ZnO powder was sensitized with Rose Bengal and then dispersed in the resin. About 15 μ thick layers were deposited both on the paper and on aluminum. Negative surface charges were used for ZnO layers.

Figure 1 represents results obtained with ZnO dispersion deposited on aluminum and Fig. 2 contains data of the dispersion posited on paper. In both instances, curves *A* were obtained by inserting the 7–51 uv filter in the path of the light beam. Curves *B* were obtained without the filter; i.e., the total tungsten spectrum reached the charged surface. It can be seen that the presence of the visible portion of the spectrum affects the shape of the reciprocity curves by initially changing their slope with decreasing intensity.

Curves *A* in Figs. 1, 2, and 3 show high intensity reciprocity law failure. For certain intensity ranges, the reciprocity law appears to hold. The same is true for curves *B* in Figs. 1 and 2. It can be concluded that the backing material and the presence of a sensitizing dye do not affect the intrinsic ZnO absorption band.

Figure 3 shows the reciprocity law curves for ZnO sensitized with Rose Bengal. Curve *A* in Fig. 3 is quite similar to the other *A* curves. However, curve *B* is different. The reciprocity law failure is much more prominent for ZnO sensitized with Rose Bengal. Also, a low intensity failure is observed in this case.

Figure 4 shows the reciprocity law failure for Se. The curve is very similar to curve *B* of Fig. 3, i.e., both high and low intensity reciprocity law failure occur.

It is evident from curves *B* in Fig. 3 and Fig. 4 that at high intensities the exposure must be increased by at least a factor of 10 to obtain the same drop of the surface potential.

It should be mentioned that the relative displacement of the curves in relation to others cannot be taken as evidence of differences in quantum efficiency. The tungsten light source provides a smaller number of short wavelength photons than longer wavelength photons.

The high intensity reciprocity law failure can at least partially be attributed to the fact that the lifetime of an electron before direct recombination with the hole is decreasing with increasing intensity of applied illumination.[5] The results, as presented here, are not corrected for dark decay. If such a correction is made, it would not explain the low intensity reciprocity law failure, which remains a rather peculiar phenomenon and merits further investigation.

The author wishes to express his appreciation to Dr. H. F. Nitka for many informative conversations throughout the course of this investigation. He also wishes to thank Mr. D. A. Nepela for helpful suggestions and Mr. M. Reynolds for helping with the experiments.

* Now at Machlett Laboratories Inc., Springdale, Connecticut.

[1] Dessauer, Mott, and Bogdenoff, Phot. Eng. **6**, 250-269 (1955).
[2] C. J. Young and H. G. Greig, RCA Rev. **15**, 469–484 (1954).
[3] Gerritsen, Ruppel, and Rose, Helv. Phys. Acta **30**, 504–512 (1957).
[4] Fridkin, Delova, Gerasimova, and Bilyaletdinov, Zhur. Nauch. i Priklad Fot. i Kinematografii **2**, 286–292 (1957); Chem. Abstr. **57**, 6991 (1958).
[5] Charles Kittel, *Introduction to Solid State Physics* (John Wiley & Sons, Inc., New York, 1956), second edition, pp. 514, 515.

"Spontaneous Magnetic Anisotropy" in Polycrystalline Thin Films

W. ANDRÄ, Z. MÁLEK, W. SCHÜPPEL, AND O. STEMME
Institute of Magnetic Materials, German Academy of Sciences, Jena, Germany, and Institute of Physics, Czechoslovak Academy of Sciences, Prague, Czechoslovakia

(Received May 19, 1959)

THIN ferromagnetic films produced in a magnetic field parallel to their surface show a uniaxial magnetic anisotropy as found in the case of evaporated[1] and electrolytically deposited[2] films.

The following experimental results show that this anisotropy is not caused or influenced immediately by the external magnetic field, but by the spontaneous magnetization in the film.

(1) Nickel films (thickness $d \approx 1000$ A) produced electrolytically at the same conditions, but in external magnetic fields H_e of different strengths ($0.1 > H_e^{\min} \leq H_e \leq 3500$ oe) possessed nearly the same values of the constant K^* of uniaxial anisotropy $K^* = (2.8 \pm 0.4) \times 10^3$ erg cm^{-3}.

(2) Evaporated Permalloy and electrolytically deposited nickel films ($d = 400$ to 10 000 A) shielded magnetically while being produced ($H_e < 0.10\,e$) or shielded and rotating around an axis perpendicular to the surface during production showed K^* values that are smaller, but not an order smaller than those in (1).

(3) Rotating in a strong external magnetic field during production films showed values of anisotropy constants the mean value of which is an order smaller than that in (1).

(4) Electrolytically produced Ni films that were kept at room temperature in an external field ($H_e = 600$ to 800 oe) either parallel or pendicular to the original axis (parallel to the film plane) show an increase or decrease of K^* in time, respectively.[3]

A similar increase or decrease of K^* in time was observed when the films were saturated parallel or perpendicular to their original anisotropy axis, respectively, and then held shielded (at room temperature).

This observed anisotropy cannot be a kind of geometric anisotropy as reported by Knorr and Hoffman[4] and Smith,[5] because it was also found at films rotating during production (point 2) and because of the aging (point 4). The results (1—4) may be explained by the formation of an easy axis parallel to the direction of spontaneous magnetization in each domain during and after film production. We suppose as a preliminary that this spon-

taneous anisotropy is caused by a kind of substructure of orientation[6] influenced by the spontaneous magnetization.

The authors are indebted to Miss C. Hermann for assistance in measurements.

[1] H. J. Williams and R. C. Sherwood, J. Appl. Phys. **29**, 296 (1958); D. O. Smith, J. Appl. Phys. **29**, 264 (1958); Andrä, Málek, Schüppel, and Stemme, Naturwissenschaften **46**, 257 (1959); W. Schüppel and Z. Málek, Naturwissenschaften **46**, 423 (1959).
[2] N. V. Kotel'nikov, Doklady Akad. Nauk S.S.S.R. **113**, 97 (1957); O. Stemme and W. Andrä, Naturwissenschaften **46**, 352 (1959).
[3] Málek, Schüppel, Stemme, and Andrä, Ann. Phys. (N.Y.) **4** (1959) (to be published).
[4] T. G. Knorr and R. W. Hoffman, Phys. Rev. **113**, 1039 (1959).
[5] D. O. Smith, J. Appl. Phys. **30**, 2645 (1959).
[6] L. Néel, J. phys. radium **15**, 225 (1954).

Pulsed Field Millimeter Wave Maser*

L. R. Momo, R. A. Myers,† and S. Foner
Lincoln Laboratory, Massachusetts Institute of Technology, Lexington, Massachusetts
(Received September 10, 1959)

THE frequency range of the previously reported[1] pulsed field ruby maser has been extended to the 70 kMcps range, and the peak output power has been increased, by a factor of about ten, to several milliwatts. These results demonstrate the feasibility of generating pulses of coherent millimeter wavelength radiation with an inverted spin population which extracts energy from a pulsed magnetic field. Operation at 4.2°K extends over a broad band of discrete frequencies with pulsed fields as high as 30 koe. From these observations upper limits of the magnetic field dependence of the spin-lattice relaxation time have been estimated.

In normal operation, the dc biasing field is set at H_0 (see Fig. 1) and levels 1 and 3 are saturated at $\nu_1 = 12.7$ kMcps which corresponds to the TE_{101} mode of the solid ruby cavity. A pulsed magnetic field is then applied to the paramagnetic system, increasing the energy difference between the inverted levels 1 and 2; the pump source is gated off within 10 μsec of the start of the field pulse. Maser oscillations are observed whenever the energy difference ν_{12} corresponds to the frequency of a favorable cavity mode, e.g., ν_2 (TE_{102}) and ν_3 (TE_{103}) in Fig. 1.

Extension of maser operation to the millimeter wave region was attained by systematically increasing the peak pulsed field. Oscillations at the two lowest TE_{10n} modes, 12.7 kMcps and 19.2 kMcps, have been identified; above these frequencies, identification of cavity modes was not feasible. Lower frequency limits were ascertained by means of microwave cutoff filters introduced into the detection system, and the emission frequencies were calculated by comparing the magnitude of the applied field at emission with the energy difference ν_{12}. The highest frequency attained thus far is 75±5 kMcps; operation at higher frequencies has been limited by the available peak magnitude of the pulsed field. As many as 14 different emission frequencies have been observed in the 12 to 70 kMcps range, with up to six distinguishable emission frequencies during a given field traversal.

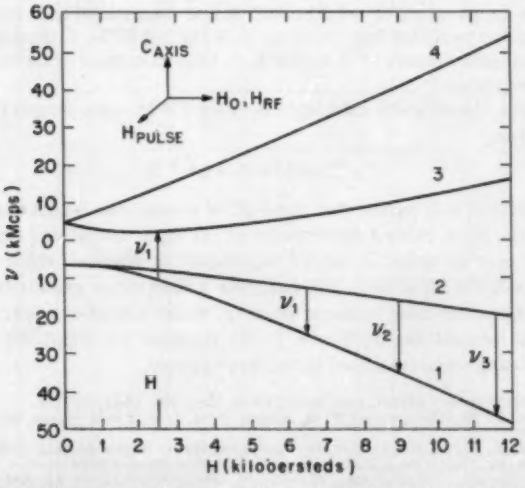

FIG. 1. Energy level diagram for Cr^{3+} in Al_2O_3 for applied field perpendicular to the c axis. Orientation of the magnetic fields with respect to the crystal is indicated in the insert.

The size of the single coupling iris has proven a critical variable for the operation of this maser, determining both which modes are observed and the power output. Increased cavity coupling and somewhat greater pump power have increased the earlier reported power[1] by 10 db; peak output power of more than 2.5 mw has been obtained at 12.7 and 19.2 kMcps; and more than 0.025 mw has been detected at about 40 kMcps. The results in the millimeter wave range are underestimated by a large factor because a non-optimum hybrid microwave system of both K_u- and K_a-band components was employed.

During preliminary attempts to obtain inversions of successive levels by adiabatic rapid passage, the biasing dc magnetic field was reduced from H_0 (see Fig. 1) before the pulsed magnetic field was applied. To permit such operation it was, of course, necessary to delay gating off the klystron until the pump transition was traversed. Under these conditions saturation (or, perhaps, partial inversion) of the normal pump transition at H_0 was obtained on a transient basis, and the millimeter wavelength output remained substantially unaffected. In this experiment, millimeter wave maser operation was observed when the biasing dc field was reduced by as much as 700 oe.

Maser oscillations were detected at the peak of pulsed fields as high as 29.2 koe, for which the field rise-time was 600 μsec. This observation requires that any field dependence of the spin-lattice relaxation time in ruby be small, if not entirely negligible, for pulsed fields up to 29.2 koe. Such field dependence has not been extensively studied, either experimentally or theoretically, but it has been suggested[2] that it is of the form

$$1/T_1 = (1+bH^n)/T_0.$$

If this is true, either $bH^n \ll 1$, or n is small. In the latter case, it is possible to show that $n \lesssim 1.1$ for $bH^n \gg 1$ by using our result in conjunction with a value of $T_1 = 25$ msec at 4.2°K and 4 koe obtained by Kikuchi *et al.*[3] In order to investigate the field dependence, more detailed measurements of $T_1(H)$ are being made at high dc magnetic fields.

We are indebted to B. Feldman and J. J. Kelley for valuable assistance, and to Dr. S. Shapiro of the Arthur D. Little Company, Cambridge, Massachusetts, for informative discussions.

* The work reported in this paper was performed at Lincoln Laboratory, a center for research operated by Massachusetts Institute of Technology with the joint support of the U. S. Army, Navy, and Air Force.
† Permanent address: Harvard University, Cambridge, Massachusetts.
[1] Foner, Momo, and Mayer, Phys. Rev. Letters **3**, 36 (1959).
[2] J. H. Van Vleck, Phys. Rev. **57**, 426 (1940).
[3] Kikuchi, Lambe, Makhov, and Terhune, Project Michigan Report No. 2144-377-T, March, 1959 (unpublished).

Noise Temperature Measurement on a Traveling-Wave Maser Preamplifier

R. W. DeGrasse and H. E. D. Scovil
Bell Telephone Laboratories, Incorporated, Murray Hill, New Jersey
(Received February 12, 1959)

NOISE temperature measurements have been performed by McWhorter *et al.*[1,2] on cavity-type solid-state masers in which a circulator is required[3] to obtain low system noise temperatures.

A system-noise measurement on a traveling-wave solid-state maser is herein reported. The traveling-wave maser (TWM)[4] employs a comb-type slow-wave structure and uses ruby as the

active maser material. The TWM has both nonreciprocal gain and reverse attenuation; thus, it is essentially a unilateral two-port amplifier. Consequently, input and output mismatches do not produce gain instability or oscillation, and no room temperature isolation is required when the amplifier is employed in a receiving system.

The experimental arrangement is shown in Fig. 1. The measurement was performed with the maser tuned to a signal frequency of 5815 mc and the maser gain was 20.6 db with a band width of 25 mc.

Two noise sources which are matched loads maintained at different temperatures are alternatively connected to the TWM input with an electrically operated wave-guide switch. Isolators were included at the input and output of the TWM. Although the TWM is short circuit stable, small gain fluctuations can be produced by changes in the input VSWR. Since gain fluctuations on the order of 0.02 db are significant in this measurement, an input isolator was included to eliminate gain changes when the wave-guide switch is operated. An isolator was included on the

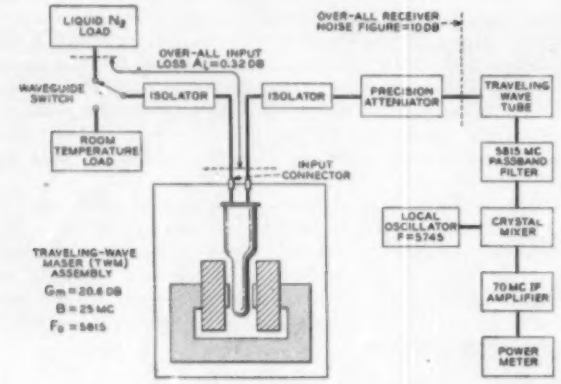

FIG. 1. The experimental arrangement.

output of the TWM to insure that no excess noise from the traveling-wave tube (TWT) would be fed back into the TWM and to prevent maser gain changes due to the precision attenuator setting.

The microwave detecting system consisting of the TWT, filter, crystal mixer, etc., had an over-all noise figure of 10 db. As in previous noise temperature measurements, gain variations were a substantial source of error. However, in this experiment the gain variations in the receiving system only, i.e., TWT, mixer, etc., were a limiting factor. There was no detectable difference between the gain variations of the receiving system with and without the TWM.

Referring to the experimental system of Fig. 1, the noise temperature input to the TWT, T_{TWT}, is

$$T_{TWT}=(T_L+T_M)G_MA+T_R(1-A) \quad (1)$$

where T_L is the effective temperature of the maser input load. T_M is the effective temperature of the maser referred to the input, G_M is the maser gain, A is the loss in the precision attenuator, and T_R is room temperature.

Since there is loss A_i between the cold input load which is maintained at liquid nitrogen temperature, and the maser the effective temperature of the cold maser input load is

$$T_L=T_R(1-A_i)+A_i\,77.3^\circ \quad (2)$$

where A_i is incurred at room temperature. The effective temperature of the room temperature load is, of course, not changed by the input loss A_i.

The noise temperature measurement procedure is to first set the power meter output to some reference value with the cold load switched to the maser input and the precision attenuator set to some initial loss A_C, typically 5 db. The wave-guide switch is then operated to connect the room temperature load to the maser input and the precision attenuator is reset to bring the power meter back to the reference value. The resulting setting of the precision attenuator, A_H, is recorded. With this procedure the noise of the detecting system, i.e., the traveling wave tube, mixer, etc., does not enter into the measurement. The noise temperature input to the TWT, T_{TWT}, is constant and using (1) the maser effective temperature is

$$T_M=\frac{A_HT_R-A_CT_L+(A_C-A_H)T_R/G_M}{A_C-A_H}. \quad (3)$$

The numerical values for our experiment were $T_R=297.1^\circ$K, $A_i=0.32\pm0.02$ db, $T_L=92.9\pm0.4^\circ$K, $G_M=114.8\pm8.2$, $A_C=0.309$, $A_H=0.1023\pm0.0116$.

The greatest error in the above measured values occurs in A_H. It is estimated that approximately half of the rms deviation is due to fluctuations in the gain of the detecting system and half due to manual setting error. The above value of A_H was obtained from 37 measurements taken over a period of about 30 min. Thus we find from (3)

$$\begin{aligned} T_M &= 10.7\pm\underset{A_H}{1.6}\pm\underset{T_L}{0.6}\pm\underset{G_M}{0.08} \\ &= 10.7\pm2.28. \end{aligned}$$

Since this is the noise temperature referred to the input at room temperature, the useful TWM noise figure is

$$F=1.037\pm0.008\,(0.16\pm0.03\text{ db}).$$

The TWM employs ½-in. diam 50Ω coaxial input and output leads of low heat conductivity Monel to reduce heat loss from the liquid He bath which was maintained at a temperature of 1.6°K. The coaxial cables were silver plated and polished to reduce microwave losses. The input cable, 30 in. long, had a room temperature loss of 0.28 ±0.02 db. The actual input cable temperature gradient was monitored with 12 thermometers throughout its length. A calculation using these data and taking into account the known variation of the resistivity of silver with temperature, shows that a noise temperature of 9±1°K is produced by the input cable losses.

Another possible source of noise is that fed back into the TWM output from the isolator at room temperature. In the TWM this produces a negligible contribution at the input because of the reverse isolation.

The noise contributed by the maser proper depends upon the spin temperature of $-1.70\pm0.05^\circ$K and the ratio of spin system gain to the circuit loss occurring at $+1.60\pm0.02^\circ$K. A theoretical noise temperature of $2.4\pm0.2^\circ$K is thus calculated from maser noise theory.[5-7]

The theoretically calculated over-all TWM noise temperature is then

$$T_M(\text{theory})=11.4\pm1.2^\circ\text{K}.$$

Since it is apparent that most of the above noise is contributed by the input cable a modification of the input circuit will reduce the over-all noise. A second experiment is planned which will exclude the input cable loss and allow a more direct measurement of the actual noise temperature of the maser amplifier proper.

We should like to thank J. M. Hammer for supplying the traveling wave tube used in the measurement.

[1] McWhorter, Meyer, and Strud, Phys. Rev. **108**, 1642 (1957).
[2] A. L. McWhorter and F. R. Arams, Proc. Inst. Radio Engrs. **46**, 913 (1958).
[3] F. R. Arams and G. Krayer, Proc. Inst. Radio Engrs. **46**, 912 (1958).
[4] R. W. DeGrasse, I.R.E. Wescon Convention Record 1958.
[5] Shimoda, Takahasi, and Townes, J. Phys. Soc., Japan **12**, 686–700 (1957).
[6] R. V. Pound, Ann. Phys. (N.Y.) **1**, 24–32 (1957).
[7] M. W. P. Strandberg, Phys. Rev. **106**, 617–620 (1957).

Penetration Depth Investigation of Gas Cleanup with Radioactive Tracers

C. V. BARTHOLOMEW, *Bell Telephone Laboratories, Allentown, Pennsylvania,*
AND
A. R. LAPADULA, *Western Electric Company, Allentown, Pennsylvania*
(Received August 28, 1959)

GAS cleanup in glow discharge has been under investigation for some time.[1] It is allied to the phenomenon of ion pumping, in which ions also penetrate into the tube electrodes.[2,3] Cleanup rates have been investigated using a radioactive tracer gas, krypton-85.[4]

During investigation of some special problems connected with gas discharge tubes, data on depth of penetration of cleaned-up gases were obtained using krypton-85 as a tracer. The experimental tube had a plane nickel cathode which was operated for 24 hr in a discharge of 30 mamp at 150 v in neon-argon gas mixture containing about 0.0001% by volume of krypton-85. It is believed that some of the krypton-85 is positively ionized and penetrates the cathode surface; the anode does not show measurable radioactivity. Radioactivity of the cathode was then checked as the surface was removed in a series of steps using fine abrasives. Figure 1 is a semilog plot of density of krypton-85 in arbitrary units as a function of depth of penetration from the surface.

It is seen from Fig. 1 that the density is down to 10% of its surface value at a penetration distance of 0.03 mil. In addition, the density distribution as a function of penetration distance appears to be exponential within the experimental accuracy. The data for deep penetrations are not as reliable as that for shallow penetrations because of background effects.

This observed penetration represents several thousand atomic layers and seems surprisingly large. A rough calculation indicates that diffusion is not a likely explanation for this deep penetration. Auto radiographs taken before and after the grinding process indicate that the radioactivity was uniform over the cathode surface, and that grain boundary diffusion did not play an important role.

Work is continuing in applying the krypton-85 tracer technique to the study of gas discharges.

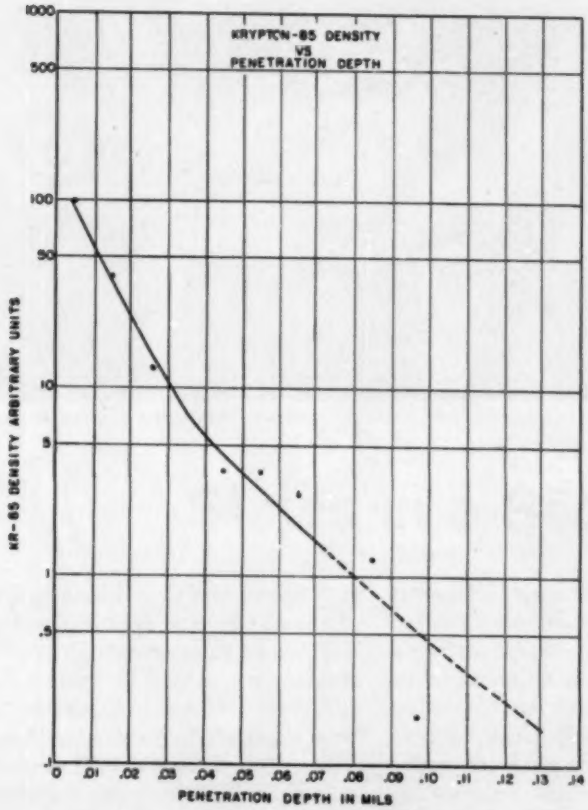

FIG. 1. Krypton-85 density vs penetration depth.

[1] D. Alpert, *Handbuch der Physik* (Springer-Verlag, Berlin, Germany, 1958), Vol. 12.
[2] S. Dushman, *Scientific Foundations of Vacuum Technique* (John Wiley & Sons, Inc., New York, 1949).
[3] J. H. Carmichael and E. A. Trendelenburg, J. Appl. Phys. **29**, 1570 (1958).
[4] D. J. Harris and P. O. Hawkins, Nature **177**, 285 (1956).

Erratum: Diffraction by a Slit

ROBERT PLONSEY AND HWEI-PIAO HSU
Case Institute of Technology, Cleveland, Ohio
[J. Appl. Phys. **30**, 1468 (1959)]

THE caption of Fig. 1 should read as follows: Relative intensity at the center of a slit as a function of slit width.

———— Exact solution.
- - - - - - - - - Geometric optics approximation.
— — — — Calculation by Karp and Russek method.
— — — — — Hadlock's result.

Books Reviewed

Prompt, noncritical reviews appear in this column. Critical reviews of many of the books described here will appear in Physics Today, The Review of Scientific Instruments, *or* American Journal of Physics.

Astronomy. THEODORE G. MEHLIN. Pp. 368+xxiv. John Wiley & Sons Inc; New York, 1959. Price $9.95.

Designed as a text for undergraduate survey courses, this volume covers the field of astronomy extensively and almost entirely nonmathematically. Among the topics discussed are the sun and the solar system, galaxies (including our own), stellar distances and motions, binary star systems, the characteristics of the planets, and comets and meteors. The book ends with a chapter delineating the different theories current today of the origin of the solar system. This text is full of fine illustrations and also includes two appendices which give the reader important background information in capsule form.

Nucleonics Fundamentals. DAVID B. HOISINGTON. Pp. 348 +lxii. McGraw-Hill Book Company, Inc; New York, 1959. Price $9.50.

This text is designed for use in undergraduate and survey courses. Among the topics developed are basic atomic and nuclear physics, radioactivity, particle accelerators, radiation protection, instrumentation, fission, reactor principles, research and power reactors, thermonuclear power, nuclear explosives and isotope separation. The treatment of the subject matter is not highly mathematical, although the derivation of many expressions is indicated for those with a knowledge of calculus.

Advances in Electronics and Electron Physics. Vol. XI. L. MARTON, EDITOR. Pp. 523. Academic Press, Inc., New York, 1959. Price $15.

This excellent series continues to provide concise and authoritative reviews of current problems in electron physics.

That the editors are interpreting their field liberally is indicated by the article on parity nonconservation in weak interactions. Other articles cover photoemission, quantum efficiency of radiation detectors, automatic data processing, operational amplifiers, radio telemetry, electron diffraction as a tool for structure analysis, and secondary electron emission. The extensive lists of references continue to be a valuable feature of these volumes.

The Magnetodynamics of Conducting Fluids. DANIEL BERSHADER, EDITOR. Pp. 145. Stanford University Press, Stanford, California, 1959. Price $4.50.

This is the third volume of a series stemming from the Lockheed Symposia on Magnetohydrodynamics. The seven papers included here were presented at the Symposium in November, 1958. The volume, therefore, represents a concise summary of the state of this branch of fluid mechanics at that time. The papers are mostly theoretical, the single exception being the contribution of Fishman, Lothrop, Patrick, and Petschek, which presents the results of shock-tube experiments. The theoretical studies are concerned with existence and stability, wave propagation, and steady and unsteady flows of both perfect and imperfect conductors in various idealized geometries.

Books Received

The Structure and Evolution of the Universe: An Introduction to Cosmology. G. J. WHETROW. Pp. 197+xxv. Harper and Brothers (Torchbooks) New York, 1959. Price $1.45.

Relativity for the Layman. JAMES A. COLEMAN. Pp. 127. The Macmillan Company, New York, 1959. Price $3.50.

Science & Human Values. J. BRONOWSKI. Pp. 94. Harper and Brothers (Torchbooks), New York, 1959. Price $.95.

Ancient Science and Modern Civilization. GEORGE SARTON. Pp. 111. Harper and Brothers (Torchbooks), New York, 1959. Price $.95.

Science Since 1500. H. T. PLEDGE. Pp. 325+xxxi. Harper and Brothers (Torchbooks), New York, 1959. Price $1.85.

Soap Bubbles and the Forces Which Mold Them. C. V. BOYS. Pp. 156. Doubleday Anchor Books (Science Study Series), Garden City, New York, 1959. Price $.95.

Magnets: The Education of a Physicist. FRANCIS BITTER. Pp. 155. Doubleday Anchor Books (Science Study Series), Garden City, New York, 1959. Price $.95.

The Neutron Story. DONALD J. HUGHES. Pp. 158. Doubleday Anchor Books (Science Study Series), Garden City, New York, 1959. Price $.95.

How Old is the Earth? PATRICK M. HURLEY. Pp. 160. Doubleday Anchor Books (Science Study Series), Garden City, New York, 1959. Price $.95.

This common game is a sequential machine. Its inputs are the possible moves at a given state. Its state is the arrangement of numbers at a given time.

States in a Sequential Machine

A "sequential machine" is any device producing prescribed sequences of outputs in response to given sequences of inputs. The theoretical problem of designing a machine, satisfying certain specifications with the fewest possible number of states, is now under study by IBM scientists.

The operation of a sequential machine is not necessarily completely specified. Some states may have no specified transitions for certain inputs, and some states may have no assigned outputs. For this general case, a technique has been developed for reducing a given machine to an equivalent machine with a minimum number of states. The procedure is to construct a state diagram of the machine which describes input and output sequences. Then through the use of a transition-matrix representation, a minimum-state diagram is obtained, which is equivalent to the original machine in the sense that it will produce the same sequences of outputs for the given sequence of inputs.

Earlier reduction procedures have been applicable only to state diagrams having known transitions for each input at each state. The extension of the procedure is important since many practical sequential machines (such as computers) require a specified operation for only a certain set of sequences of inputs.

IBM. RESEARCH

Investigate the many career opportunities available in exciting new fields at IBM.
International Business Machines Corporation, Dept. 579N, 590 Madison Avenue, New York 22, New York

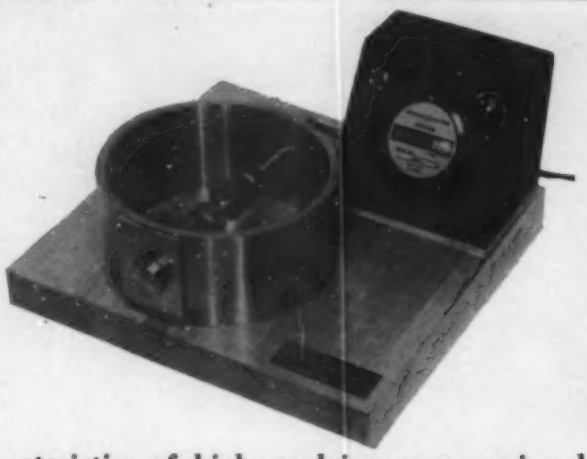

STATIC FATIGUE TESTS WITH GREGG TENSION RING

The Gregg Tension Ring is a small and simple device for applying and maintaining a load on a notch stress rupture specimen. The load is applied to the test specimen through the elastic ring and is measured by the change in diameter. The ring and time control base is shown on the left and the ring and loading fixture is below. Tests can be conducted to evaluate the effects embrittlement or delayed failure characteristics of high applying compression loads on the loading assembly by machine and measuring the corresponding inside diameter.

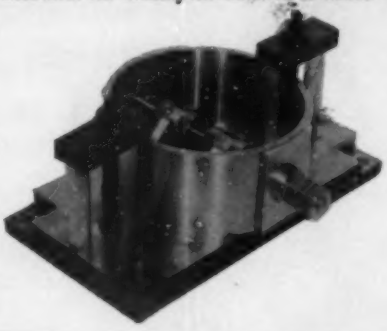

Model No.	Wall Thickness	Outside Diameter	Max. Load
CS-106 A	0.250 in.	7.125 in.	3,000 lbs.
CS-106 B	0.375 in.	7.125 in.	10,000 lbs.

Write for Brochure and Price.

CUSTOM SCIENTIFIC INSTRUMENTS, INC.
541 Devon Street **Kearny, N. J.**

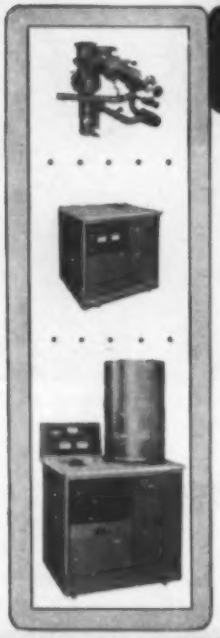

You're guaranteed 10^{-6} mm Hg *fast* with . . .

THE MODULAR "400" SERIES 4" VACUUM SYSTEMS & EVAPORATORS

GUARANTEED PERFORMANCE:
5×10^{-6} in 45 sec. Less than 5×10^{-7} ultimate (blanked port)
5×10^{-6} in 4 min. Less than 10^{-6} ultimate (18" x 30" Bell Jar)

MODULAR CONSTRUCTION:
Buy exactly what you need, from basic plumbing to complete Evaporators and Bakeout Systems. Incorporate additional equipment as your requirements grow.

TROUBLE-FREE PERFORMANCE:
Each VE-400 System undergoes a full week (168 hrs.) of test run and inspection before shipment.

FREE "400" SERIES BROCHURE contains complete performance data and design specifications on the 4" building block components and modular systems. Write Department A-1436.

Veeco VACUUM CORP.
86-J Denton Avenue, New Hyde Park
Long Island, New York
HIGH VACUUM & LEAK DETECTION EQUIPMENT

Visit our Booths #3001-#3002 **I.R.E. Show, N.Y.C.**

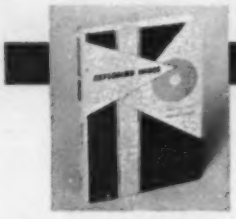

The FIRST Book on . . .

EXPLODING WIRES

Edited by William G. Chace and Howard K. Moore

The increasing contemporary importance of this scientific phenomenon was dramatically indicated by the unexpectedly large attendance at the Conference on Exploding Wires. This volume, a complete record of the conference, includes reports of theoretical research in the field as well as new developments and applications.

In this book—the first ever published on the subject *in any language*—scientists, students, and technologists will find a wealth of incisive material dealing with high-speed photographic techniques, shock waves, and the physics of fluids.

cloth **374 pp.** **profusely illus.** **$9.50**

PLENUM PRESS
227 W. 17TH ST. • NEW YORK 11, N.Y.

Electronic Engineers / Physicists

Senior level positions available with the Scientific Research Staff and the Applied Research and Development Division of REPUBLIC AVIATION

The Scientific Research Staff

Here, theoretical and experimental studies are performed in the various disciplines of the physical sciences. Research scientists and engineers with masters' or doctors' degrees are invited to participate in current programs or to initiate new studies. Our interests include research in such areas as electromagnetic radiation, information theory, data transmission, quantum mechanical electronic devices, solid state physics, and infrared which will lead to a product technology applicable to space exploration and weapons utilization components and systems.

Applied Research & Development Division

Here, conceptual thinking is translated into practical methods which will eventually result in prototypes of advanced ballistic missile systems, strategic orbital systems, space vehicle programming and tracking systems, and lunar observatory reconnaissance stations.

Openings at all levels (including top level supervisory) in nearly every area of Electronics related to Advanced Flight & Weapons Technology:

Navigation & Guidance Systems	**Countermeasures**
Radar Systems	**Digital Computer Development**
Information Theory	**Telemetry-SSB Technique**
Radio Astronomy	**Radome & Antenna Design**
Solid State & Thermionic Devices	**Microwave Circuitry & Components**
Radiation & Propagation (RF, IR, UV)	**Receiver & Transmitter Design**
	Miniaturization-Transistorization

Address your resume in confidence to:
Mr. George R. Hickman
Engineering Employment Manager, Dept. 17-B

REPUBLIC AVIATION

Farmingdale, Long Island, New York

Available now

TORONTO Symposium *Proceedings*

■ The proceedings of the International Electromagnetic Theory Symposium, which was sponsored by U.R.S.I. (Union Radio Scientifique Internationale), The University of Toronto, and the Institute of Radio Engineers' Professional Group on Antennas and Propagation, held at the University of Toronto, Canada, June 15–20, 1959, may be ordered now.

■ It will comprise 400 pages and contain over 60 papers. Topics covered include: Diffraction and Scattering Theory, Radio Telescopes, Surface Waves, Boundary Value Problems, The Propagation of Waves Through Various Media, and Antennas. As an example, it may be noted that the portion of the volume devoted to Surface Waves contains contributions by the following authorities:

Carlos M. Angulo
H. Bremmer
J. Brown
A. L. Cullen
L. B. Felsen
Bernard Friedman
K. Furutsu
George Goubau
A. Hessel
A. E. Karbowiak
H. M. Marlow
A. A. Oliner
Gerhard Piefke
S. A. Schelkunoff
James R. Wait
F. J. Zucker

Send for your copy today.
The rates are:
Libraries $12.00;
Individuals $16.00.

Mr. Delmer C. Ports
Jansky and Bailey, Inc.
1339 Wisconsin Ave., N. W.
Washington 7, D. C.

Enclosed is a check in the amount of $ ..... Please send me ..... copy(ies) of the Proceedings of the 1959 Toronto Symposium.

NAME .....

ADDRESS .....

.....

.....

.....

MICRO MANIPULATORS

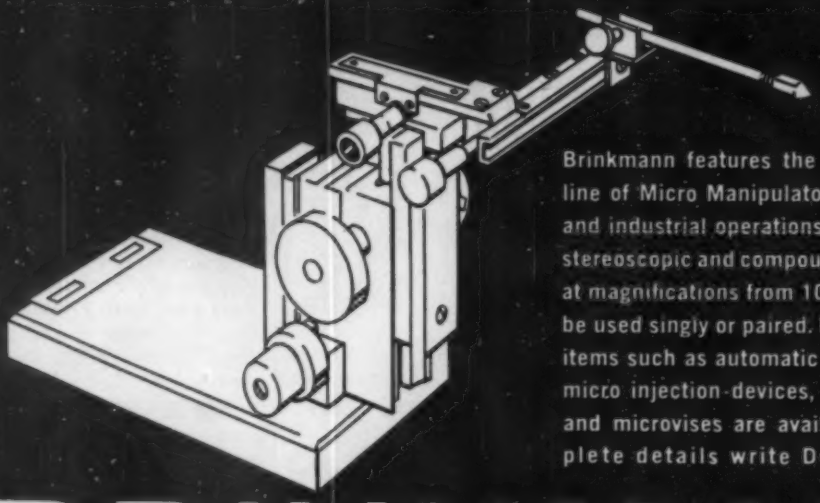

Brinkmann features the most complete line of Micro Manipulators for scientific and industrial operations. Available with stereoscopic and compound microscopes at magnifications from 10 to 1000 x. Can be used singly or paired. Many accessory items such as automatic pipette pullers, micro injection-devices, pipette holders and microvises are available. For complete details write Department M.

BRINKMANN

INSTRUMENTS INC., 115 CUTTER MILL ROAD, GREAT NECK, NEW YORK

High Performance ELECTROMAGNETS and Power Supplies

RUGGEDNESS

4" Electromagnet Type A
(4" pole diameter)
Fields up to 25,000 gauss.
Homogeneity of at least 1 part in 10^6 in ½ cc.

ROTATION

Rotating Base Type AE
360° scale.
Positive friction lock.

STABILITY

Current-Stabilized Power Supply Unit Type B.
Two models:
B.4—Stability 1 part in 10^4.
B.5—Stability 1 part in 10^5.

Also available:—
1½" Electromagnet Type C—for Teaching purposes.
7" Electromagnet Type E—for Electron Resonance Work.
8" Electromagnet Type D—for Electron Resonance and Nuclear Magnetic Resonance work.
Direct Reading Magnetometer Type G.
Proton Resonance Magnetometer Type P.

NEWPORT INSTRUMENTS
(Scientific & Mobile) Ltd.
NEWPORT PAGNELL, BUCKS, ENGLAND
Telephone: NEWPORT PAGNELL 401/2

NEW VACUUM METALLIZER

- For research or small scale deposition of metals and salts on metals, glass, plastics, ceramics, etc.
- Permits multiple source evaporations and close control of filament voltage from 0 – 40 V.
- Power, high voltage, thermocouple, work positioning, etc. feed-throughs are easily relocated at any of 17 points.

Packaged 35" x 48" x 112" unit is easy to install, operate, and maintain. Geared hoist takes work out of raising 18" shielded Pyrex or 24" O.D. mild or stainless 30" high bell jar. Vibration-isolated, 6" pumping system with optical baffle cold trap gives fast, "clean" pump-down to 10^{-6} mm. Hg. Write today for details on NRC Model 3144.

NRC
NRC EQUIPMENT CORPORATION

A subsidiary of National Research Corporation
Dept. 20-N, 160 Charlemont St., Newton 61, Massachusetts • DEcatur 2-5800

JARRELL-ASH
MICROFOCUS
X-RAY UNIT

Features

BETTER FOR . . .

- High Resolution
- Low Angle Studies
- High Speed
- Microradiography
- Lattice Defect Studies
- Microsamples

The Jarrell-Ash Microfocus X-Ray unit is the best instrument for all photographic defraction work. It is manufactured in the U.S.A. exclusively by Jarrel-Ash Co.*

* licensed by Hilger & Watts, Ltd.

WRITE FOR CATALOGUE MF12-59

SALES OFFICES IN:

Costa Mesa, Cal. — Dearborn, Mich.
San Mateo, Cal. — New Brunswick, N. J.
Atlanta, Ga. — Pittsburgh, Pa.
Glen Ellyn, Ill. — Dallas, Tex.
Toronto, Canada

JARRELL-ASH CO.

26 FARWELL STREET, NEWTONVILLE 60, MASS.

ENGINEERS and SCIENTISTS

Dynamic new division of **Ford Motor Company** is now in initial stages of expanding military and commercial programs. Positions are at Aeronutronic's new $22 million Research Center, at Newport Beach in Southern California. Work in an intellectual environment as stimulating as the location is ideal—close to most of Southern California's cultural, educational, and recreational centers. Outstanding growth opportunities for qualified engineers and scientists are open in the following fields:

RESEARCH OPERATIONS

Research is being conducted in hydrodynamic and radiation processes in tenuous gases at very high temperatures, ionization produced by soft X-radiation, hydrodynamics of solids at high pressures including studies of equations of state, infrared properties of the atmosphere and of hot gases, conversion of chemical energy into sound and the condensation rate of supersaturated vapors. Theoretical physicists are needed to work in these fields. Specific experience is not necessary, however a general background in theoretical and mathematical physics is required.

You are invited to address inquiries to Dr. Lloyd P. Smith, General Operations Manager, Research Operations Staff, Aeronutronic Bldg. 15, Ford Road, Newport Beach, California.

Other unusual opportunities are open for qualified engineers and scientists in the following areas:

SPACE TECHNOLOGY OPERATIONS

Astrodynamics · Space Environment · Theoretical Physics · Electronics · Radar · Information Links · Automatic Controls · Mathematics · Propulsion Research · Combustion · Materials · Aeromechanics

COMPUTER OPERATIONS

Input-Output Equipment · Storage Units · Display Devices

TACTICAL WEAPON SYSTEMS OPERATIONS

Infrared Systems and Components · Optical Systems · Transistor Circuitry Development · Aerodynamics · Thermodynamics

Qualified applicants for the above three operations are invited to send resumes and inquiries to Mr. Jim Harris, Aeronutronic Bldg. 15, Ford Road, Newport Beach, California. Telephone ORiole 3-2520.

AERONUTRONIC

a Division of FORD MOTOR COMPANY
NEWPORT BEACH,
SANTA ANA, AND MAYWOOD, CALIFORNIA
NATICK, MASSACHUSETTS

Since final quality of your production of ferrites, electronic cores, and magnetic recording media depends on proper use of 3 specialized groups of magnetic materials . . . you'll find it mighty helpful to have all the latest, authoritative technical data describing the physical and chemical characteristics of each. This information is available to you just for the asking. Meanwhile, here are highlights of each product group.

PURE FERRIC OXIDES—For the production of ferrite bodies, we manufacture a complete range of high purity ferric oxide powders. These are available in both the spheroidal and acicular shapes, with average particle diameters from 0.2 to 0.8 microns. Impurities such as soluble salts, silica, alumina and calcium are at a minimum.

MAGNETIC IRON OXIDES—For magnetic recording—audio, video, instrumentation etc.—we produce a group of special magnetic oxides with a range of controlled magnetic properties. Both the black ferroso-ferric and brown gamma ferric oxides are available.

MAGNETIC IRON POWDERS—For the fabrication of magnetic cores in high-frequency, tele-communication, and other magnetic applications, we make a series of high purity iron powders.

If you have problems involving any of these materials, please let us go to work for you. We maintain fully equipped laboratories for the development of new and better inorganic materials. Write . . . stating your problem . . . to C. K. Williams & Co., Dept. 38, 640 N. 13th St., Easton, Penna.

WILLIAMS
COLORS & PIGMENTS
C. K. WILLIAMS & CO.
E. ST. LOUIS, ILL. • EASTON, PA. • EMERYVILLE, CAL.

NEW LOW COST
GETTERING VACUUM PUMP

Cartridge only $135

Complete assembly including metal gaskets $215

- For use in ultra-high vacuum or continuously pumped closed systems.
- Pumps through chemical action — no fluids to contaminate system.
- Operating range 10^{-1} -10^{-9}mm. Hg. Speed approx. 5 l/s.
- No backing pump or expensive power supply needed.

Gases are removed by chemical reaction with titanium film which is intermittently deposited by low voltage filament.

Available either as a cartridge for mounting directly in vacuum chamber, or with stainless steel housing where deposits of titanium are objectionable or for external mounting. Write today for technical details on NRC Model 2202-02 Titanium Adsorber Pump.

NRC
EQUIPMENT CORPORATION
A subsidiary of National Research Corporation
Dept. 20-N, 160 Charlemont St., Newton 61, Massachusetts • DEcatur 2-5800

FOR EXPLORING MICROWAVE OPTICS . . .
CENCO®
MICRO-WAVE APPARATUS

A valuable new teaching aid for school and laboratory that demonstrates principles of physical optics at a meter stick rather than microscope level. Also illustrates basic radar. Special manual outlines 17 experiments. Write for details.

No. 80422 Micro-Wave Apparatus, with transmitter tube.....each **$293.00**

cenco®
CENTRAL SCIENTIFIC CO.
1718-A Irving Park Road • Chicago 13, Illinois
Branches and Warehouses — Mountainside, N. J. Boston • Birmingham • Santa Clara • Los Angeles • Tulsa Houston • Toronto • Montreal • Vancouver • Ottawa

Engineers and Scientists
STRETCH YOUR IMAGINATION

...at Beckman Instruments, last refuge of the Non-Organization Man. Here's a company that is concerned with the man, his mind and his original contributions.

Commercial, industrial and military projects tickle the fancy of unconstrained intellects at these Beckman Divisions:

Beckman / *Scientific and Process Systems Division*
Helipot Division

Don't get crushed in the Organization Mill ...look into these imagination stretching positions...

ENGINEERS/SCIENTISTS...

at all levels in the fields of precision electronic components and analytical instrumentation for engineers and scientists with degrees in engineering or physical science. Some of our specific needs include project engineers and senior electronic engineers. We also have openings for exceptional recent graduates.

And you can stretch your legs in Orange County, too, where you and your family will enjoy Southern California living at its barbecuing best.

Overcome your own organizational inertia... phone, wire or write Mr. T. P. Williams for all the parameters.

Beckman Instruments, Inc. Fullerton, Calif. Telephone TRojan 1-4848; from Los Angeles OWen 7-1771 ©B.I.I. 1960.

NEW *micro* SIZE!

CENCO®

LAB-JACK

Excellent for micro techniques. Supports up to 5 lbs. with precision control of vertical adjustments thru an elevation of more than 3". 3x3" stainless top and bottom auxiliary plates for quick attachment. Model 19086 each $18.75.

CENCO the most complete line of scientific instruments and laboratory supplies in the world.

cenco®

CENTRAL SCIENTIFIC CO.
1718-A Irving Park Road • Chicago 13, Illinois
Branches and Warehouses — Mountainside, N. J. Boston • Birmingham • Santa Clara • Los Angeles • Tulsa Houston • Toronto • Montreal • Vancouver • Ottawa

HIGH IN RESOLVING POWER, EASIER TO MAINTAIN THAN ANY OTHER ELECTRON MICROSCOPE

BENDIX TRONSCOPE TRS-50 E1

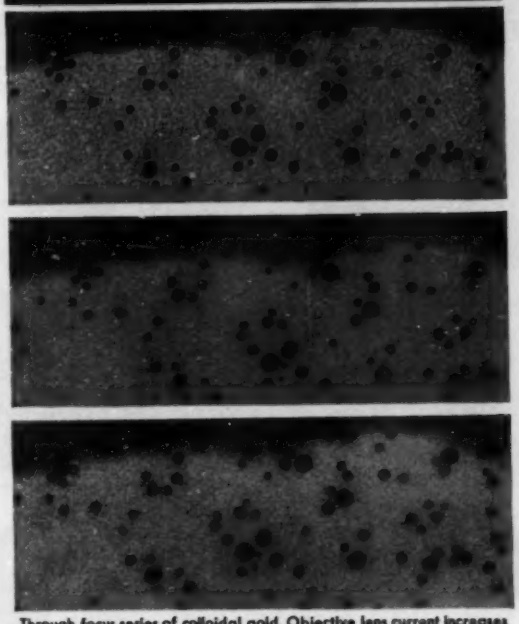

Through focus series of colloidal gold. Objective lens current increases from top to bottom.

BENDIX TRONSCOPE demonstrates 20Å resolving power with no adjustments.

BENDIX TRONSCOPE is first electron microscope with absolutely no decrease in resolving power from adjustments.

BENDIX TRONSCOPE is the most trouble-free electron microscope in the world.

BENDIX TRONSCOPE, including electron tubes, is *warranted unconditionally* for one year against defects in materials and workmanship. Service is available after warranty period on either a contract or a transportation, per diem, parts basis.

FULL DETAILS can be obtained by writing Dept. EMS11.

Cincinnati Division
3310 Wasson Road • Cincinnati, Ohio

Bendix

Export Sales & Service:
Bendix International, 205 E. 42nd St., New York 17, N. Y.
Canada:
Computing Devices of Canada, Ltd., Box 508, Ottawa 4, Ont.

EPLAB

Thermopiles

For many years the thermopile has been the accepted instrument for measuring Radiant Heat from Radiant Heaters at the American Gas Association Testing Laboratory in Cleveland, Ohio. Since 1930, when Vandaveer first described his work in this field,* an Eppley thermopile has been used for this purpose in hundreds of tests and the results have been consistent and accurate to within 1 per cent.

This is but one of the many applications in the field of radiant energy measurements for which Eppley Thermopiles are ideally suited. They may be obtained with windows of different materials, and various types of black are available for receiver coatings.

All Eppley Thermopiles are supplied with a certificate of calibration, this calibration being made against a Standard Lamp from the National Bureau of Standards.

If you have a problem involving the measurement of radiant energy we invite you to write us, describing your problem in as much detail as possible. We will be glad to make recommendations and there will be no obligation.

*Vandaveer, *Industrial & Engineering Chemistry*, Vol. 22, page 596, June 1930.

BULLETIN NO. 3 ON REQUEST
ADDRESS: 6 SHEFFIELD AVE., NEWPORT, R. I.

THE EPPLEY LABORATORY, INC.
SCIENTIFIC INSTRUMENTS
NEWPORT, RHODE ISLAND, U. S. A.

NOW!
Easy Demonstration of basic Gas Laws
CENCO Kinetic Theory Apparatus

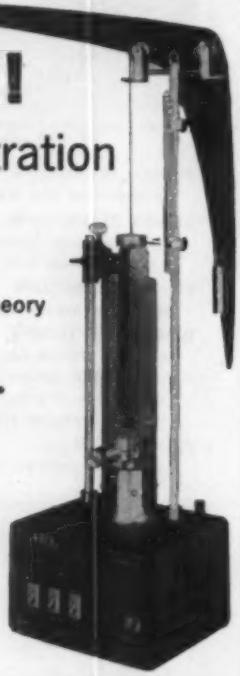

Permits quantitative determination of the most fundamental principles of gas mechanics. Adapted from a design by H.F Meiners of Rensselaer Polytechnic Institute. Plot p-V and p-T curves, measure molecular diameters, verify the fundamental gas laws and Van der Waals Corrections.

No. 77722 without stroboscope, $295.00

cenco®
CENTRAL SCIENTIFIC CO.
A Subsidiary of Cenco Instruments Corporation
1718-A Irving Park Road • Chicago 13, Illinois
Branches and Warehouses—Mountainside, N. J
Boston • Birmingham • Santa Clara • Los Angeles • Tulsa
Houston • Toronto • Montreal • Vancouver • Ottawa

Outstanding opportunity for men with development experience in

SOLID STATE DEVICES

If you are a Physicist, Chemist, Metallurgist or Electrical Engineer, and have experience in solid state development, or in related fields, you are invited to investigate one of the several very interesting positions now open at IBM.

We are greatly expanding our development work in the theory, design and technology of solid state devices for use in new advanced computer systems.

This is an outstanding opportunity for experienced scientists and engineers who wish to undertake new and interesting work in this field. Recent graduates, who have done work in this field, are also invited to apply.

Please write, outlining briefly your qualifications and experience, to:

Mr. B. N. Slade, Dept. 579N1
Product Development Laboratory
IBM Corporation, Box 390
Poughkeepsie, N. Y.

IBM®
INTERNATIONAL BUSINESS MACHINES CORPORATION

Now!

a new concept in

Compound High Vacuum Pumps

- PRECISION
- RUGGEDNESS
- QUIET OPERATION
- VIBRATION-FREE
- SMOKELESS EXHAUST

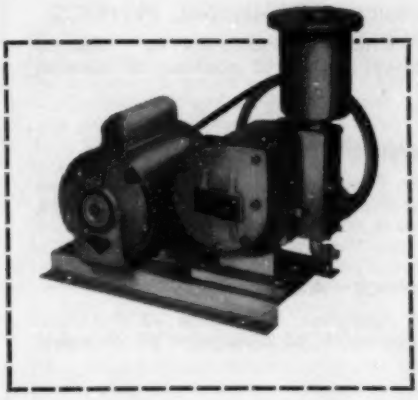

New Stokes Compound High Vacuum Pumps combine the sturdy, reliable construction demanded in an industrial pump with the precision performance of a laboratory unit. Lightweight, compact design. Fast pumping. Exceptionally low vacuums. Vapor-free discharge. Quiet, smooth operation. No vibration! Displacement: 2.3 and 3.7 cfm. Prices: $230 and $245.

Write for full information

High Vacuum Division
F. J. STOKES CORP.
5565 Tabor Road
Phila. 20, Pa.

STOKES

NOW— 15,000°F. PLASMA FLAME SPRAY IN YOUR OWN PLANT

Apply coatings of high melting point materials such as tungsten, tungsten carbide, molybdenum, chromium carbide, titanium oxides, calcium zirconate, rare earth oxides. Operates at 10,000°-15,000°F.

Plasma flame spraying hi-temperature crucible

Now any material that can be melted without decomposing can be sprayed. Despite high melting temperature, object sprayed stays cool.

High fluidity of particles and high velocity of impingement bond the particles together to produce high density coatings semi-fused to work. Absence of air eliminates oxidation.

The METCO Plasma Flame Spray Gun is a valuable new tool for the metalworking research department or production line. Operates on inexpensive inert gases with high electrical power conversion efficiency, long component life. Continuous gas streams, as high as 30,000°F., with accurate control of temperature, generated at costs of ⅛ to ½ those of oxygen-fuel gas equipment for equivalent heat output. No combustion—uses inert gases. No flashback or explosion hazards—push-button operation.

Write today for free bulletin describing the METCO Plasma Flame Gun.

METCO

Metallizing Engineering Co., Inc.
Flame Spray Equipment and Supplies
1143 Prospect Avenue, Westbury, Long Island, N. Y.
In Great Britain METALLIZING EQUIPMENT CO., Ltd.
Chobham-near-Woking, England

Please send me free bulletin on the Metco Plasma Flame Spray Gun.

Name _____ Title _____

Company _____

Address _____

City _____ Zone _____ State _____

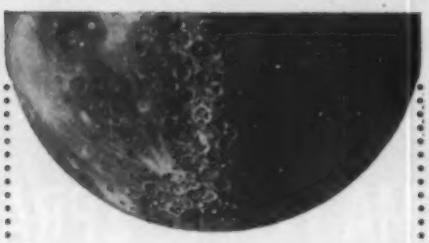

THEORETICAL AND EXPERIMENTAL PHYSICISTS

Rocketdyne is expanding its electrical propulsion activities, openings exist for:

ION ROCKET ENGINE

Project Leader for Ion Thrust Device—Challenging position to direct the experimental research of a long-term development program on: Ion sources; Ion Species; Electrical discharge phenomena; Field phenomena; Ion acceleration and collimation; Sputtering; and Ion-electron recombination.

Senior Research Specialist—To conduct experimental research on: Auxiliary space powerplants; and Electrostatic generators.

Senior Research Specialist—To conduct analytical studies on: Ion beam dynamics; Direct Power conversion; and Electrical propulsion systems.

MAGNETOGASDYNAMICS

Senior Research Specialist—To conduct experimental and theoretical research directed toward development of a thermo-dynamic plasma jet for satellite and space propulsion.

Desired qualifications: MS or PhD degree and from one to five years of related experience.

Address inquiries to:
Mr. J. C. Peck
Dept. SE 596
6633 Canoga Avenue
Canoga Park, California

ROCKETDYNE
A DIVISION OF NORTH AMERICAN AVIATION, INC.
First with Power for Outer Space

TRANSLATIONS OF . . . .

SOVIET JOURNALS

Published by the American Institute of Physics with the cooperation and support of the National Science Foundation.

SOVIET PHYSICS—JETP
Monthly. Complete translation of "Zhurnal Eksperimental'noi I Teoreticheskoi Fiziki" of Academy of Sciences, U.S.S.R.

SOVIET PHYSICS—SOLID STATE
Monthly. Complete translation of "Fizika Tverdogo Tela" of Academy of Sciences, U.S.S.R.

SOVIET PHYSICS—TECHNICAL PHYSICS
Monthly. Complete translation of "Zhurnal Tekhnicheskoi Fiziki" of Academy of Sciences, U.S.S.R.

SOVIET PHYSICS—DOKLADY
Bimonthly. Complete translation of the Physics Section of Proceedings of Academy of Sciences, U.S.S.R.

SOVIET PHYSICS—ACOUSTICS
Quarterly. Complete translation of "Akusticheskii Zhurnal" of Academy of Sciences, U.S.S.R.

SOVIET PHYSICS—CRYSTALLOGRAPHY
Bimonthly. Complete translation of "Kristallografiya" of Academy of Sciences, U.S.S.R.

SOVIET PHYSICS—USPEKHI
Bimonthly. Complete translation of "Uspekhi Fizicheskikh Nauk" of Academy of Sciences, U.S.S.R.

SOVIET ASTRONOMY—AJ
Bimonthly. Complete translation of "Astronomicheskii Zhurnal" of Academy of Sciences, U.S.S.R.

For subscription prices and other information, address

American Institute of Physics
335 East 45 Street, New York 17, N. Y.

Industrial Research PHYSICISTS and Electronic Engineers

Electronics . Optics
Sonics . Instrumentation
Automation . Measurements

—If you are a physicist or electronic engineer and have broad technical interest in any of the above fields, then the Physics Department of Continental Can Company offers you a unique opportunity for interesting non-defense work and professional growth.

THE POSITIONS

We have openings for both recent graduates and more experienced individuals and one, with the title of General Physics Laboratory Director, for an outstanding man who has demonstrated considerable creative ability.

THE WORK

We are pioneering long-range and radically new processes and products arising out of the company's major position in high-speed fabrication of metal, glass, paper, fiber, cork and plastic containers, and other products. In addition, we render consulting services to other divisions.

THE BENEFITS

Salary structure is excellent, and there are numerous benefits including company-paid hospitalization and life insurance, relocation assistance. Staff members are *encouraged* to keep ahead in their profession.

THE LOCATION

The division's new laboratories are located within easy reach of the University of Chicago, The John Crerar Library, Argonne National Laboratory and of the finest southern and western residential suburbs.

You are invited to investigate these opportunities at Continental Can Company, in complete confidence. A few minutes now can mean a jump of years in your professional progress.

Please write or call collect to Dr. Harold K. Hughes, Director of Physics Research

CONTINENTAL CAN COMPANY, INC.

Central Research & Engineering Division
7622 S. Racine Avenue
Chicago 20, Illinois
Vlcennes 6-3800, Ext. 305

of major interest to all researchers in low temperature physics . . .

A Supplement to "HELIUM"

by E. M. Lifshits and E. L. Andronikashvili.

TRANSLATED FROM RUSSIAN

This notable volume consists of two supplementary chapters, by these outstanding Soviet physicists, which were added to the Russian translation of *W. H. Keesom's* classic book *"Helium."*

The first chapter, by *Lifshits,* presents a concise resume of the Landau theory of superfluidity. The second chapter reports in detail the experimental work conducted by *Peter Kapitza and E. L. Andronikashvili.*

cloth **175 pp.** **$7.50**

now available . . .

A New Method in the Theory of SUPERCONDUCTIVITY

by N. N. Bogoliubov, V. V. Tolmachev, D. V. Shirkov.

TRANSLATED FROM RUSSIAN

The Soviet authors put forth a systematic presentation of a new method in the theory of superconductivity, developed as a result of the research of *N. N. Bogoliubov and V. V. Tolmachev*—based on a physical and mathematical analogy with superfluidity. This new method is a generalization of the method developed by *Bogoliubov* in formulating a microscopic theory of superfluidity.

The authors give calculations for the energy of the superconducting ground state using *Frohlich's Hamiltonian,* as well as of the one-fermion and collective elementary excited states. A detailed analysis of the role of the *Coulomb* interaction between the electrons in the theory of superconductivity is included. The authors also demonstrate how a system of fermions is treated with a fourth-order interaction *Hamiltonian* and establish the criterion for its superconductivity.

cloth **130 pp.** **$5.75**

CONSULTANTS BUREAU, INC.
227 W 17th ST. NEW YORK 11 N. Y.

INDEX TO ADVERTISERS

Name	*Page*
AERONUTRONIC, DIV. OF FORD MOTOR CO.	xxxi
APPLIED PHYSICS CORP.	xx
BECKMAN INSTRUMENTS, INC.	xxxiii
BECKMAN & WHITLEY, INC.	Cover 2
BELL TELEPHONE LABS.	v
BENDIX AVIATION CORP. CINCINNATI DIV.	xxxiii
BRINKMAN INSTRUMENTS INC.	xxx
CENTRAL SCIENTIFIC CO.	xxxii, xxxiii, xxxiv
CONSULTANTS BUREAU	xxxvii
CONTINENTAL CAN CO.	xxxvii
CORNELL-DUBILIER ELECTRIC CO.	xxii
CUSTOM SCIENTIFIC INSTRUMENTS, INC.	xxviii
DELCO RADIO DIV., GENERAL MOTORS CORP.	vi
DEWEY CORP., G. C.	vii
ELECTRO-OPTICAL SYSTEMS, INC.	xxv
EPPLEY LAB., INC.	xxxiv
GENERAL ELECTRIC CO., KAPL	x
GENERAL RADIO CO.	Cover 3
HUGHES AIRCRAFT CO.	iv, xvii
I.B.M. CORP.	xxvii, xxxiv
JANSKY & BAILEY, INC.	xxix
JARRELL-ASH CO.	xxxi
KEITHLEY INSTRUMENTS, INC.	ix
LOCKHEED MISSILES AND SPACE DIV.	xii
LOS ALAMOS SCIENTIFIC LAB.	xix
McGRAW-HILL BOOK CO., INC.	xvi
METALLIZING ENGINEERING CO., INC.	xxxv
MITRE CORP.	viii
NRC EQUIPMENT CORP.	xxx, xxxii
NATIONAL COMPANY, INC.	iii
NEWPORT INSTRUMENTS LTD.	xxx
OLDSMOBILE, DIVISION OF GENERAL MOTORS	xviii
PLENUM PRESS	xxviii
RAMO-WOOLDRIDGE	Cover 4
REPUBLIC AVIATION	xxix
ROCKETDYNE, DIV. OF NORTH AMERICAN AVIATION	xxxvi
STOKES CORP., F. J.	xxxv
TIFFEN OPTICAL CO.	xiii
UNITED AIRCRAFT CORP.	xxiii
VARIAN ASSOCIATES	xi, xiv, xv
VEECO VACUUM CORP.	xxviii
WELCH SCIENTIFIC CO., W. M.	xxvi
WESTINGHOUSE BETTIS ATOMIC POWER LAB.	xxi
WILLIAMS & CO., C. K.	xxxii

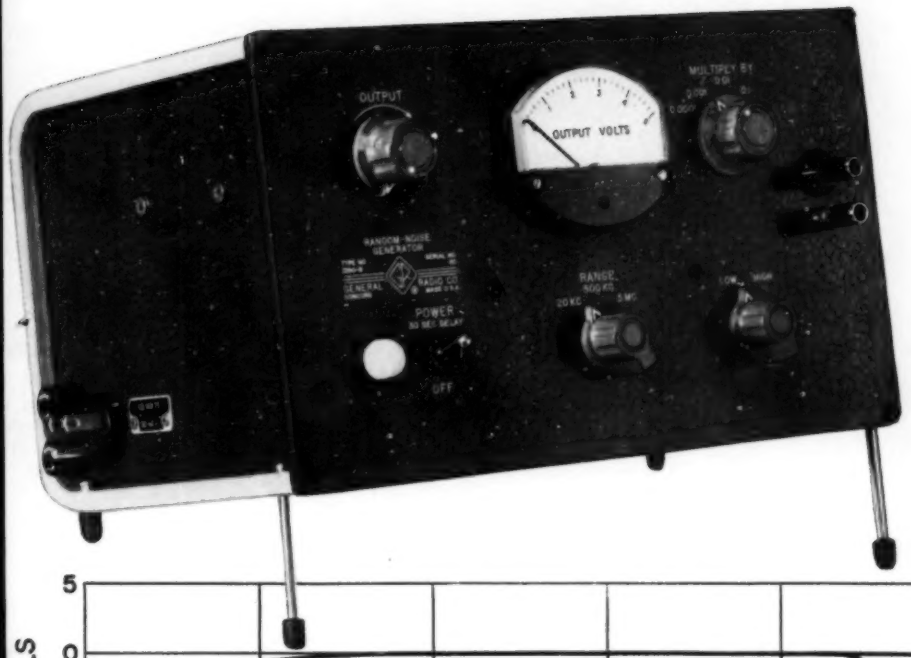

NEW Random-Noise Generator

Type 1390-B . . . $295

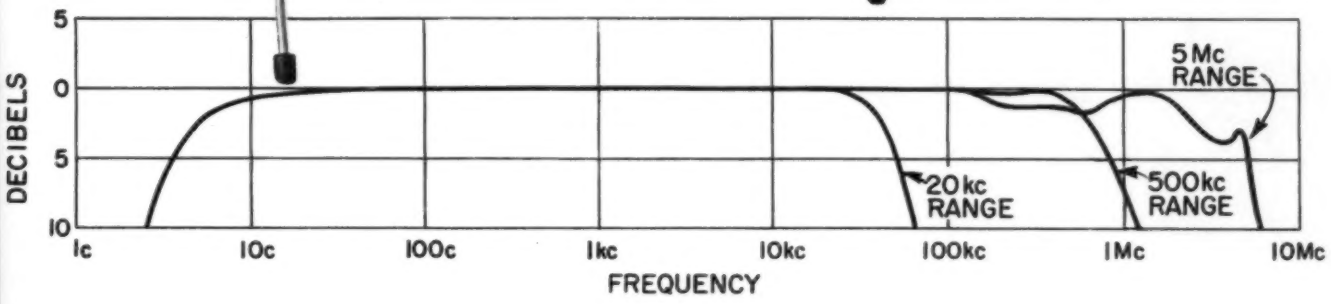

Incorporates these wanted features:

- ★ Wide-Band Noise of Uniform Spectrum Level
- ★ Three Frequency Bands — 20c to 20 kc; 20c to 500 kc; 20c to 5 Mc
- ★ High Output Level — at least 3v for 20-kc range, 2v for 500-kc range, and 1v for 5-Mc range
- ★ Extended low-frequency range down to 5 cps.
- ★ Built-in 80-db attenuator—supplements output meter to provide metered output levels from over 3 volts to below 30 μv.
- ★ Automatic time-delay relay in on-off switch circuit insures long life for noise-producing gas tube.
- ★ Built-in extendible legs tilt panel for easy viewing.
- ★ Panel extensions supplied for relay-rack mounting.

The Random-Noise Generator's amplitude distribution closely approximates the statistical amplitude distribution of speech, music, and many other sounds and electrical disturbances which occur naturally. Consequently, this instrument is extremely useful in obtaining realistic measurements of the performance of audio-frequency equipment of all types. Moreover, since noise is a common form of interference limiting the threshold of electrical operation, a controlled noise generator can be extremely useful for measurements of communications systems and detection apparatus.

The Random-Noise Generator is also widely used to drive shake tables for mechanical testing; to test microphones and speakers in the acoustics laboratory; for study of filter characteristics; and in transmission-engineering work involving crosstalk measurements.

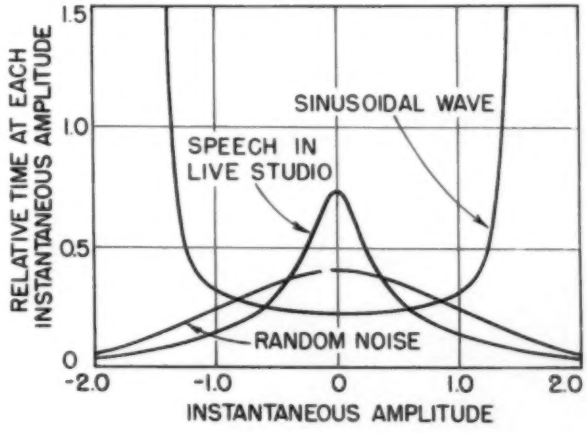

Write for Complete Information

GENERAL RADIO COMPANY

Since 1915 — Manufacturers of Electronic Apparatus for Science and Industry

WEST CONCORD, MASSACHUSETTS

NEW YORK AREA: Tel. N. Y. WOrth 4-2722, N. J. WHitney 3-3140 **CHICAGO:** Tel. VIllage 8-9400
PHILADELPHIA: Tel. HAncock 4-7419 **WASHINGTON, D. C.:** Tel. JUniper 5-1088
SAN FRANCISCO: Tel. WHitecliff 8-8233 **LOS ANGELES 38:** Tel. HOllywood 9-6201
In CANADA, TORONTO: Tel. CHerry 6-2171

We started selling binding posts and "banana" Type 274 Plugs in 1923, and they are still compatible with the tens of thousands of their modern counterparts sold by us this year. Incidentally, the ¾" binding post spacing first introduced by GR is an industry standard today.

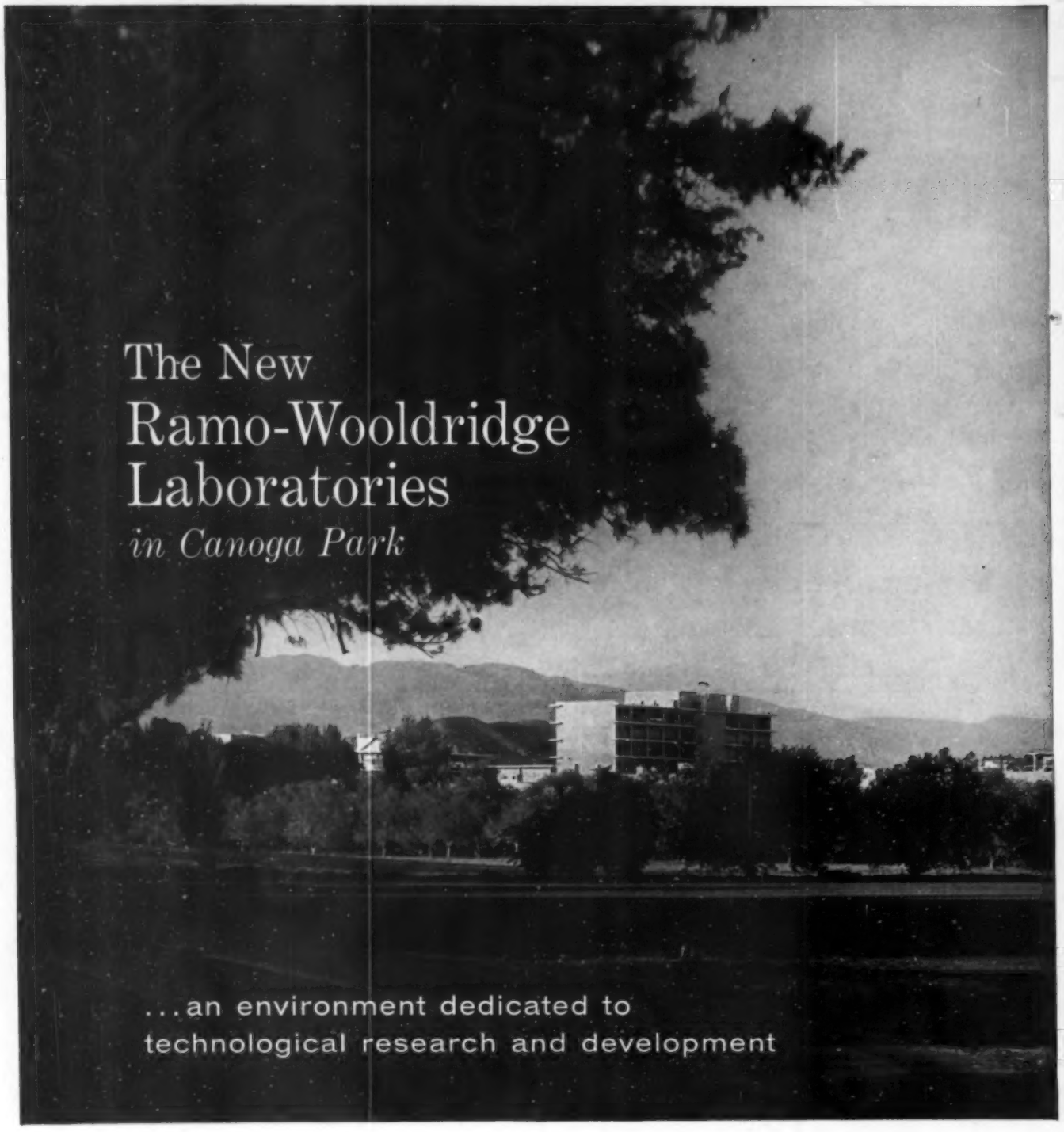

The new Ramo-Wooldridge Laboratories in Canoga Park, California, will provide an excellent environment for scientists and engineers engaged in technological research and development. Because of the high degree of scientific and engineering effort involved in Ramo-Wooldridge programs, technically trained people are assigned a more dominant role in the management of the organization than is customary.

The ninety-acre landscaped site, with modern buildings grouped around a central mall, contributes to the academic environment necessary for creative work. The new Laboratories will be the West Coast headquarters of Thompson Ramo Wooldridge Inc. as well as house the Ramo-Wooldridge division of TRW.

The Ramo-Wooldridge Laboratories are engaged in the broad fields of electronic systems technology, computers, and data processing. Outstanding opportunities exist for scientists and engineers.

For specific information on current openings write to Mr. D. L. Pyke.

THE RAMO-WOOLDRIDGE LABORATORIES

8433 FALLBROOK AVENUE, CANOGA PARK, CALIFORNIA